



PST 2025

CONFERENCE PROCEEDINGS

The 8th International Conference and
Exhibition on Pharmaceutical Sciences
and Technology 2025
at Ambassador Hotel Bangkok, Thailand

"Advancing Pharmaceutical Frontiers: Collaboration,
Innovation, and Patient-Centric Solutions"

June 12 - 13, 2025



คณะเภสัชศาสตร์ มหาวิทยาลัยศิลปากร
FACULTY OF PHARMACY • SILPAKORN UNIVERSITY
LEARN TOGETHER, GROW TOGETHER

Table of Contents

Innovations in Drug Development and Delivery	5
Formulation and Characterization of Taste-Masked Cannabis Extract Thin Film for Active Coating Application.....	6
Effect of Solvent Composition on the Formation and Drug Association Efficiency of Silymarin-Loaded Niosomes..	11
Study of Self-Assembled Hyaluronic Acid Based Nanogel as Controlled Drug Delivery and Stabilization System	16
Investigation of the Effect of Binding Liquid Composition on the Formation of Montmorillonite-Based Pellets	21
Process Optimization of Butyric Acid-Conjugated Hyaluronic Acid Nanoparticles Loading Curcumin for Colorectal Cancer Therapy.....	26
Formulation and Evaluation of a Diclofenac Sodium Pain Relief Stick Using a Eutectic Mixture System.....	31
Thermal Treated Mung Bean Starch Used as Binder and Disintegrant in Wet Granulation Tablet.....	36
Preformulation Study of Montelukast Sodium for the Development of Chewable Tablets.....	41
Development and Evaluation of a Povidone-iodine Throat Spray: Physicochemical Properties and Stability.....	46
Development and Characterization of Tablets Prepared from Directly Compressible Piroxicam-Impregnated Neusilin® US2 Fabricated Using Fluidized Bed Impregnation.....	51
Efficacy of Calcium Hydroxylapatite in Hand Rejuvenation, a Prospective 3-month Study.....	56
The Efficacy of Hyperdiluted Calcium Hydroxylapatite for the Treatment of Horizontal Neck Wrinkle.....	60
Development of PEG-modified Phytosome of Naringin for Improving Physical Properties, Stability and Cytotoxicity in Caco-2 Cells.....	65
Influence of Polymer Molecular Weight on Physical Properties and Cytotoxicity of Folic Acid Conjugated Hyaluronic Acid Nanoparticles Loading Curcumin.....	70
Advances in Pharmaceutical Sciences, Analysis, and Medicinal Chemistry	74
Green and Rapid Stability-Indicating HPLC Method for Determination of Rosmarinic Acid in <i>Thunbergia laurifolia</i> Leaf Extract.....	75
Determination of Anti-Aging Amino Acids via High-Performance Liquid Chromatography Using 2-Hydroxynaphthaldehyde as a Derivatizing Agent.....	80
Anti-Inflammatory and Antioxidant Activities of Commercial Saffron Tea products.....	85
Development of a Microcontroller-Driven Automated Titration System for the Quantitative Assay of Sodium Bicarbonate Tablets.....	90
Screening of Colorimetric Reagents for Rapid Detection of Bisacodyl on Paper-Based Device.....	95
Study on Biological Activities of Medium-Ripe and Ripe <i>Pouteria campechiana</i> Fruit Extracts for Use as Cosmetic Raw Materials.....	100

Patient-Centric Approaches in Biopharmaceutics, Pharmacology, and Toxicology.....105

The Functional Analysis of *UGT1A1**80 and *93 Polymorphisms on Deferasirox Metabolism and Transcriptional Regulation.....106

Analysis of the Effects of Transforming Growth Factor- β , a Main Component of Platelet-Rich Plasma, on Pain-Related Diseases Using Network Pharmacology.....111

Cutting-Edge Technologies in Drug discovery, Natural Products, Cosmetics, and Nutraceuticals.....116

Isolation and Characterization of Chemical Constituents from *Pinalia densa* and Evaluation of Their Cytotoxic Activity Against Human Prostate Cancer Cell Lines.....117

Green Extraction of Bioactives from Thai Traditional Plant *Clinacanthus nutans* (Burm.f.) Lindau.....121

The Role of Topical Nicotinamide Adenine Dinucleotide (NAD⁺) in Alleviating Short-Term Skin Damage Following Uvb Exposure in Mice.....126

The Role of Topical Nicotinamide Adenine Dinucleotide (NAD⁺) in Alleviation of UVB-induced Acute Sun damage in Mice.....131

The Efficacy of Nicotinamide Adenine Dinucleotide (NAD⁺) in Mitigating Long-term Skin Side Effects from UVB Radiation in Mice.....136

Investigation of Trikatu Remedy: Potential Anti-Amyloid Beta and Antioxidant Effects in a *Caenorhabditis elegans* Alzheimer's Model.....141

A Comparative Study of Total Flavonoid Content, Total Phenolic Content, and Antioxidant Potentials of *Aegle marmelos* (L.) Corrêa Extracts from Thailand's Floristic Regions Using Optimized Ultrasonic-Assisted and Heat Reflux Extraction Methods.....146

Isolation and Identification of Phenolic Compounds from *Cylindrolobus mucronatus* and their Cytotoxic Activity Against Glioblastoma Cells.....151

Development of Pyrrolidinyl Diaminopyrimidine Oxide Microemulsion System for Enhancing Solubility in Hair Care Applications.....155

Enhancing α -Gel Stability: The Role of Surfactant Ratios, Heating, and Stirring Conditions.....160

Nanofibril Cellulose from Pineapple Core: A Sustainable Solution For Antimicrobial Air Filtration.....165

Exploring the Combined Pharmacological Potential of *Mimosa pudica* L. and *Centella asiatica* in Hyperglycemic Wound Healing: A Hyperglycemic Planarian Regeneration Model Approach.....170

Innovative Extraction of Phenolic Compounds from Longan Seeds Using Ultrasonic-Assisted Extraction and Response Surface Methodology.....175

Development of Film-Forming Spray Containing Herbal Mixture for Hair Coloring.....180

Antioxidant and Anti-tyrosinase Activities of *Morus nigra* L. Fruit Extract and Mixed Extract for Use as Cosmetic Raw Materials.....185

Potential of *Peristrophe bivalvis* (L.) Leaf Extracts for Cosmeceutical Applications: Biological Activity and Safety Profile.....190

Antioxidant and Anti-inflammatory Effects of <i>Ipomoea pes-caprae</i> (L.) R.Br. Extracts from Eco-Friendly Extraction	195
Characterization of Cannabis Flower Wax for Cosmetic Production	200
Cosmetic Applications of Silk Cocoon Extracts: Enzyme-Assisted Extraction and Development of Nanostructured Lipid Carriers	205
Emerging Trends in Biotechnology and AI	210
Evaluation of Picosecond Nd:YAG Laser Parameters on Laser-Induced Optical Breakdown (LIOB) Formation and Tissue Response	211

Innovations in Drug Development and Delivery

Formulation and Characterization of Taste-Masked Cannabis Extract Thin Film for Active Coating Application

Samuel Wirajaya Prawinata¹, Sornkanok Vimolmangkang^{2,3,4}, Varin Titapiwatanakun^{5,6,}*

¹Graduate Program of Pharmaceutical Sciences and Technology, Faculty of Pharmaceutical Sciences, Chulalongkorn University, Bangkok 10330, Thailand

²Department of Pharmacognosy and Pharmaceutical Botany, Faculty of Pharmaceutical Sciences, Chulalongkorn University, Bangkok, 10330, Thailand

³Center of Excellence in Plant-Produced Pharmaceuticals, Chulalongkorn University, Bangkok, 10330, Thailand

⁴Research Cluster for Cannabis and Its Natural Substances, Chulalongkorn University, Bangkok, 10330, Thailand

⁵Department of Pharmaceutics and Industrial Pharmacy, Faculty of Pharmaceutical Sciences, Chulalongkorn University, Bangkok, 10330, Thailand

⁶Cyclodextrin Application and Nanotechnology-based Delivery Systems Research Unit, Chulalongkorn University, Bangkok, 10330, Thailand

Author Email: samuelwepe@gmail.com

*Corresponding author Email: varin.t@pharm.chula.ac.th

Abstract. Cannabis extract, one of the herbal medicine products on the national list of essential medicines, offers various therapeutic benefits such as analgesic, antiemetic, neuroprotective, anti-inflammatory and psychiatric treatment; however, it has unpleasant taste, and the products are available as liquid preparation which can significantly reduce patient compliance and drug effectiveness. This research aims to develop taste-masked films as oral solid dosage form, incorporating the extract using Eudragit E100 (E100) and Kollidon VA64 (KVA64) as taste-masking polymers. Plasticizers with different chemical structures, including polyethylene glycol (PEG-400), triacetin, and diethyl phthalate, were used to modify various film characters. The films were formed via the solvent casting method. 20% of cannabis extract (5% THC) was added into the formulation. Physical, mechanical, chemical, and thermal properties were characterized. E100:triacetin and KVA64:PEG400 combinations were identified as the most promising due to their favorable mechanical properties and film-forming characteristics. Fourier Transform Infra-Red (FTIR) analysis demonstrated the presence of THC within the film, no interactions between each compound inside the film, and no peaks of THC degradant. KVA64:PEG-400 formulation showed the highest flexibility, four times more flexibility than other plasticizers. Notably, a significant glass transition temperature decrease was found in the film formulations; thus, this may cause stickiness while coating at high temperatures. This study highlights the importance of plasticizer selection on film characteristics, which can be applied for active cannabis extract coating on granules or tablets, to ensure an effective and easier way of processing.

Keywords: Cannabis Extract, Active Coating, Taste-masked polymer, Oral Film Characterization

INTRODUCTION

Cannabis, a plant with a long history of medicinal, recreational, and industrial use, has gained increasing attention in recent years due to its therapeutic potential. The plant contains a wide array of bioactive compounds, including cannabinoids such as Delta-9-tetrahydrocannabinol (THC) and cannabidiol (CBD), as well as various terpenes. THC, as the main component, is a potent active ingredient with various therapeutic benefits, but it presents formulation challenges due to poor solubility and a resinous consistency. These characteristics can significantly affect the drug formulation process, such as making the drug hard to formulate and possibly causing drug interactions in medical cannabis therapies. The resin state of THC can make oral products like edibles, capsules, and oils less palatable.

Taste masking is an interesting alternative in the development of cannabis-based therapies. Taste masking polymers work by creating a physical barrier around bitter drug particles, preventing them from dissolving in saliva and interacting with taste buds. This reduces the perception of bitterness, enhancing the drug's palatability and improving patient compliance with medication regimens. By improving the palatability of these formulations, taste masking can significantly enhance patient adherence, acceptance, and overall therapeutic outcomes.

As the field of medical cannabis continues to evolve, the development of cannabis-based formulations with taste-masking polymer strategies will be essential in ensuring that patients can benefit from the therapeutic potential of cannabinoids without the barrier of unpleasant taste. This, in turn, will contribute to the broader acceptance and integration of cannabis-based therapies in the pharmaceutical area.

This study aims to analyze the casted film from cannabis extract by utilizing either Eudragit E100 (water insoluble polymer) and Kollidon VA64 (water soluble polymer) as the taste-masking polymers and incorporating PEG-400, triacetin, and diethyl phthalate as plasticizers. The study aims to develop optimal film characteristics. By varying the type of taste-masking polymers and plasticizers, this study will help identify the optimal formulation of cannabis extract. The film characteristics, such as the chemical interaction, will be critical in determining how the main component, THC, interacts with other excipients, providing compatibility between each compound. Other characteristics tests such as thermal characterization, can provide information on the application of this film into another form of drug delivery, such as active coating. Overall, the integration of chemical analysis, thermal analysis, moisture evaluation, and characterization provides a comprehensive foundation for the rational design of THC-loaded films intended for further processing via fluid bed as an active coating technology.

MATERIALS AND METHODS

Materials

Cannabis extract (51%THC) was provided from the Center of Excellence in Plant-Produced Pharmaceuticals, Chulalongkorn University (Bangkok, Thailand). Analytical-grade acetone and isopropanol were sourced from Sigma-Aldrich (St. Louis, USA). HPLC-grade ethanol was obtained from Burdick & Jackson (Ulsan, South Korea). Eudragit®E100 (E) was obtained from Evonik GmbH & Co. KG (Darmstadt, Germany). Kollidon®VA64 (vinylpyrrolidone-vinyl acetate copolymers; K) was received from BASF (New Jersey, USA).

Methods

Raw material preparation

Cannabis extract (51% THC) with a resin-like state will be kept in a sealed vial in a dark room at room temperature. Due to formulation constraints, the extract was diluted with acetone: isopropanol (4:6) until it reached the concentration of 5% THC for easier handling and formulation accuracy.

Formulation screening by solvent casting

Solvent casting were done according to Lin 1991^[1] with a slight modification. Two polymers were used for this casting, which is a hydrophobic polymer, (Eudragit E100 (E) and a hydrophilic polymer, Kollidon VA64 (K). Taste masking polymer was dissolved in the mixture of acetone and isopropanol (2:3) for 30 minutes. The other excipient(s) were added and were mixed in constant stirring at 250 rpm, room temperature, for 2 hours, sealed with parafilm, according to Table 1 below. To evaluate the influence of different classes of plasticizers on film properties, four distinct plasticizers were individually incorporated: PEG-400 (poly-ol polymer-based plasticizer), triacetin (glycerides-based plasticizer), rice bran oil (natural vegetable oil-based plasticizer), and diethyl phthalate (organic ester plasticizer). Each plasticizer was selected to represent a specific chemical class with differing mechanisms of plasticization. 10 grams of film liquid preparation were poured into a Teflon cast and left at room temperature for 24 hours. Dried film was peeled and kept in a dark and sealed plastic container until further characterization as described in Table 2^[2]

Table 1 Film Formulation

Code	E100 (gr)	Kollidon (gr)	THC 5% (gr)	Rb oil (gr)	PEG-400 (gr)	Triacetin (gr)	Diethyl Phtalate (gr)	Ace+Iso (4:6) (gr)	Total weight (gr)
E1 (C)	1.00	-	0.2	-	-	-	-	8.8	10.00
E2	1.00	-	0.2	0.15	-	-	-	8.65	10.00
E3	1.00	-	0.2	-	0.15	-	-	8.65	10.00
E4	1.00	-	0.2	-	-	0.15	-	8.65	10.00
E5	1.00	-	0.2	-	-	-	0.15	8.65	10.00
K1 (C)	-	1.00	0.2	-	-	-	-	8.8	10.00
K2	-	1.00	0.2	0.15	-	-	-	8.65	10.00
K3	-	1.00	0.2	-	0.15	-	-	8.65	10.00
K4	-	1.00	0.2	-	-	0.15	-	8.65	10.00
K5	-	1.00	0.2	-	-	-	0.15	8.65	10.00

(c): Control

Characterization of taste-masked films

1. Physical Appearance

The dried films were visually examined for attributes such as transparency, smoothness, fragility, and peelability using the subjective visual analysis described in Table 2 below.

Table 2 Subjective Film Characterization Parameter

Parameter	Characterization
Transparency	Subjective visual transparency (transparent/opaque) Subjective visual colour (white/yellow/brown)
Smoothness	(-) surface not uniform (+) surface uniform but found bubbles (++) surface uniform and no bubbles
Fragility	(--) Break when peel (-) Break in the middle

Parameter	Characterization
	(+) Didn't break but deformity happened (++) Peeled successfully
Peelability	(-) can't be peeled (+) can be peeled but crack into pieces (++) can be peeled, still one piece but crack in the middle (+++) successfully peeled and have no crack at all

Dry Weight Analysis

The dried weight of each film was measured and compared to the theoretical dry weight to help identify any residual organic solvent in the film.^[3]

Thickness

Five random spots were selected from the film for thickness measurement. Thickness was measured at five different locations for each spot: four at the corners and one at the centre of the film sheet. A manual micrometer (TEclock SM-112, Japan) was used to measure film thickness to the nearest 0.01 mm.^[4]

2. Moisture Content

0.5 mg of the film was put on the moisture analyzer (Mettler Toledo HR83, America). The moisture content of the film was measured to make sure the organic solvent residue will be lower than 2%.^[3]

3. Folding Endurance

A 3x1 cm section of the selected film was manually folded repetitively 100 times at the same location. The number of folds the film could endure before breaking was recorded as the folding endurance value. The test was performed in triplicate.^[6]

4. Fourier Transform Infrared (FTIR)

FTIR spectroscopy was utilized to investigate the interactions between the materials used in the film. The analysis was performed using a Nicolet iS20 instrument (Nicolet Instruments, Madison, USA) in attenuated total reflectance/ATR mode, 64 scans in the range 400–4,000 cm⁻¹ at a resolution of 4 cm⁻¹. The spectra were analyzed using the instrument's provided software.^[6]

5. Differential Scanning Calorimetry (DSC)

DSC was used to assess the interaction of each compound of each film under several steps of temperature using a PerkinElmer Diamond DSC instrument (Shelton, CT, USA). Samples of each preferred film were prepared by weighing 5 mg of each using a Mettler ToledoTM Excellence Plus analytical balance (model no. XP 204). These samples were then sealed in aluminium crimped pans (Kit 0219–0062, PerkinElmer Instruments, Shelton, CT, USA) and heated in the range from 25–150°C at a rate of 5°C/min under a nitrogen gas with a flow rate of 30 mL/min.^[7]

RESULTS AND DISCUSSION

Table 3 Film Characterization

Parameter	E1	E2	E3	E4	E5	K1	K2	K3	K4	K5
Transparency	Opaque, Yellowish	Opaque, Yellowish	Clear, Yellowish	Opaque, Brownish	Opaque, Brownish	Opaque, Yellowish	Clear	Clear	Clear	Clear
Smoothness	++	++	++	++	+	++	++	++	++	++
Fragility	--	--	+	++	++	--	--	++	-	-
Peelability	+	+	+++	+++	+++	-	+	+++	++	++
Thickness (mm)	N/A	0.41±0.04	0.23±0.01	0.27±0.04	0.25±0.03	N/A	N/A	0.34±0.033	0.38±0.06	0.36±0.053
Weight (gr)	1.34	1.06	1.1	1.02	1.06	1.24	1.06	1.02	1.1	1.06
Moisture Content (%)	0.32	0.43	0.23	0.22	0.23	0.42	0.88	0.85	0.95	0.92
Folding Endurance	-	-	✓	✓	✓	-	-	✓	-	-

* N/A = no thickness measurement due to film cracking

The characteristics of polymer films formulated with various plasticizers are summarized in Table 3. All samples displayed similar smoothness, thickness, and color consistency within each polymer group. E appeared as yellowish granules, while K was a colorless fine powder, consistent with prior reports.^[9,10] Eudragit-based formulations showed compatibility with PEG-400, triacetin, and diethyl phthalate (DEP), with E3 and E5 passing the folding endurance test, although peeling resulted in film deformities, indicating mechanical limitations. In contrast, K demonstrated compatibility only with PEG-400, likely due to both substances' hydrophilic nature, which enhances miscibility. K films exhibited higher moisture content compared to their Eudragit counterparts. This behavior is attributed to the presence of vinylpyrrolidone units in K, which form hydrogen bonds with water molecules and increase moisture uptake^[11]. On the other hand, E, composed mainly of hydrophobic methacrylate derivatives, showed lower affinity for moisture absorption. Although higher moisture content can improve flexibility and plasticization, it may compromise product stability, especially for moisture-sensitive compounds such as THC, where humidity exposure may lead to degradation, loss of potency, and reduced shelf-life. Based on mechanical performance, peelability, and fragility, two formulations—E4 (Eudragit with triacetin) and K3 (Kollidon with PEG-400)—were selected for further study involving THC incorporation.

Following film casting, Fourier-transform infrared (FTIR) spectroscopy was employed to evaluate the incorporation of

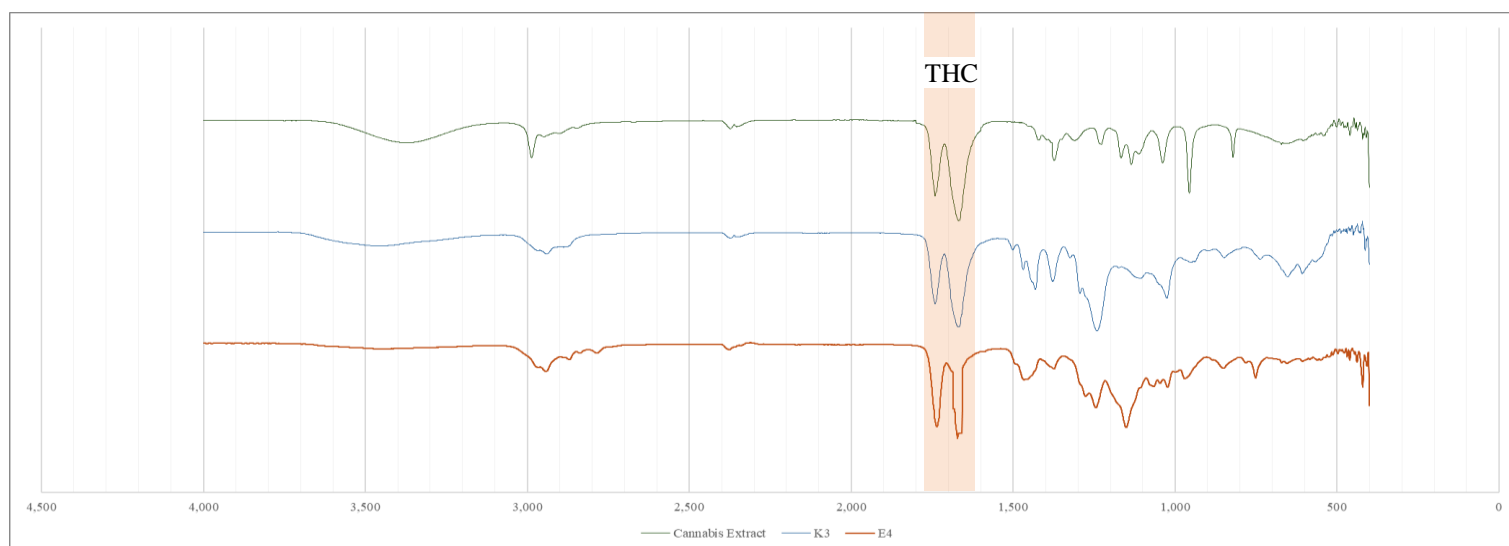


Figure 1 FTIR result of cannabis extract, E4 and K3

THC within the polymeric matrix, by confirming the presence of THC-specific absorption bands. K3 and E4 samples exhibit distinct spectral characteristics indicative of THC. Two significant peaks were expected to be observed at specific wavenumbers: notably around 1740 cm^{-1} and 1660 cm^{-1} ^[13], which are associated with the carbonyl and aromatic functional groups in THC, respectively. This finding shows that THC is incorporated during the solvent casting process. Considering the API was a plant extract, FTIR can provide valuable information for detecting THC in cannabis extracts, but the complexity and variability of the extract's composition may necessitate careful analysis and consideration of potential interferences from other compounds.

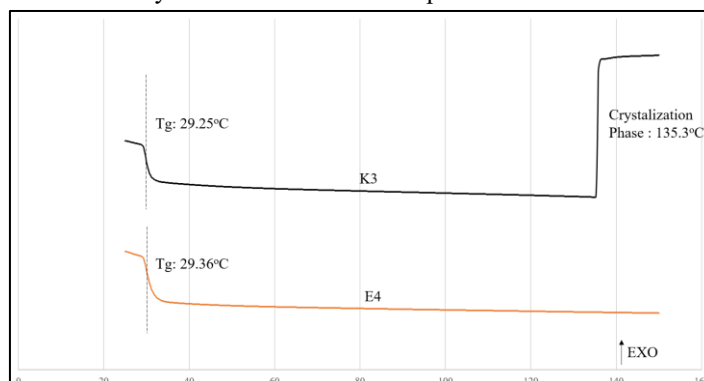


Figure 2 DSC of E4 and K3

As part of the film characterization, Differential Scanning Calorimetry (DSC) was conducted to determine the glass transition temperature (T_g) of the formulations. Understanding T_g is essential to optimize processing conditions and to ensure film stability

during subsequent fluid bed as an active coating application. The DSC data revealed that K3 exhibited Tg of 29.25 °C, while E4 demonstrated a comparable Tg of 29.36 °C. Notably, both compounds did not show any significant thermal events up to 135.3 °C where crystallization was observed for K3, indicating a distinct thermal behavior. Markedly lower than the Tg of the unmodified polymers (48 °C for Eudragit E-100 and 115 °C for Kollidon VA64)^[11], indicating successful plasticization. The findings also suggest that E4 and K3 may tend to face a challenge with their operating conditions in pharmaceutical applications such as active coating, which typically involve elevated temperatures. This thermal characteristic necessitates stringent control of the coating process, as product temperatures exceeding the Tg could induce polymer chain mobility, leading to tackiness, particle agglomeration, and compromised film quality. It is therefore imperative that process temperatures are suggested to be maintained below the measured Tg to ensure discrete particle coating, consistent film formation, avoidance of operational issues, and protect heat- or moisture-sensitive actives such as THC.^[14] Additionally, crosslinking agents or other stabilizing additives could be explored to increase the Tg and enhance the overall thermal stability of the films.

CONCLUSION

This study successfully developed taste-masked films incorporating cannabis extract, demonstrating favorable properties for an active coating. The findings underscore the importance of plasticizer selection in optimizing film characteristics, paving the way for more effective and palatable cannabis-based medicinal products. Although subjective analysis provided an initial evaluation of the thin film formulations, it is acknowledged that objective, instrument-based characterization is required to validate these findings. Future work should include more comprehensive physical, mechanical, and chemical analyses to establish reproducible and scientifically robust results. However, future challenges also include ensuring the long-term stability of these films and optimizing formulations for various pharmaceutical applications.

ACKNOWLEDGMENTS

The author acknowledges support from the Pharmaceutical Sciences Faculty, Chulalongkorn University, Thailand, and the scholarship funding from the Chulalongkorn University's Graduate Scholarship Programme for ASEAN or Non-ASEAN Countries

REFERENCES

1. Lin SY, Lee CJ, Lin YY. The effect of antibiotics on gut microbia. *Phar Res.* 1991;8(9):1137-43
2. Coban O, Ozcan K, Tatar B, Soylu M. Formulation and evaluation of triamcinolone acetonide loaded oral disintegrated film with different polymers via solvent casting methods. *Turk J Pharm Sci.* 2024;21(5):440-8.
3. Krisai K, Kitisak. Increasing levodopa and carbidopa loading quantity in oral pullulan thin film. Chulalongkorn Univ Theses Dissertations. 2019:8673.
4. Pak ES, Ghaghelestani SN, Najafi MA. Preparation and characterization of a new edible film based on Persian gum with glycerol plasticizer. *J Food Sci Technol.* 2020;57(9):3284-94.
5. Karki S, Kim H, Na SJ, et al. Thin films as an emerging platform for drug delivery. *Asian J Pharm Sci.* 2016;11(1):559-74.
6. Cui SJ, Zhang Z, Rodrigue D. Release of delta-9-tetrahydrocannabinol from polyvinylalcohol hydrogels and its safe interaction with human skin fibroblasts. *Front Drug Deliv.* 2024;4(1):1-12.
7. Zhu YC, Mehta KA, McGinity JW. Influence of plasticizer level on the drug release from sustained release film coated and hot melt extruded dosage forms. *Phar Dev Tech.* 2006;11(9-20):285-94.
8. Citti C, Braghiroli D, Vandelli MA, Cannazza G. Pharmaceutical and biomedical analysis of cannabinoids: A critical review. *J Pharm Biomed Anal.* 2018;1(1):565-79.
9. Pharma Excipients. Eudragit E-100. Available from: <https://www.pharmaexcipients.com/news/eudragit-e-100/>
10. BASF Pharma Solutions. Kollidon VA 64. Available from: <https://pharma.basf.com/products/kollidon-va-64>
11. Gupta SS, Meena A, Parikh T, Serajuddin ATM. Investigation of thermal and viscoelastic properties of polymers relevant to hot melt extrusion-I: Polyvinylpyrrolidone and related polymers. *J Excip Food Chem.* 2016;5(1):1001.
12. Liu G, McEnnis K. Glass transition temperature of PLGA particles and the influence on drug delivery applications. *Polymers.* 2022;14(5):993.
13. Geskovski N, Stefkov G, Gigopulu O, Stefov S, Huck CW, Makreski P. Mid-infrared spectroscopy as process analytical technology tool for estimation of THC and CBD content in Cannabis flowers and extracts. *Spectrochim Acta A Mol Biomol Spectrosc.* 2021;251:119422.
14. Feldstein MM, Shandryuk GA, Platé NA. Relation of glass transition temperature to the hydrogen-bonding degree and energy in poly(N-vinyl pyrrolidone) blends with hydroxyl-containing plasticizers. Part 1. Effects of hydroxyl group number in plasticizer molecule. *Polymer.* 2001;42(3):971-9.

Effect of Solvent Composition on the Formation and Drug Association Efficiency of Silymarin-Loaded Niosomes

Pantakarn Jarunyakorn¹, Vipaporn Panapisal^{1,}*

¹Department of Pharmaceutics and Industrial Pharmacy, Faculty of Pharmaceutical Sciences, Chulalongkorn University, Bangkok, Thailand

*Corresponding author Email: vipaporn.p@chula.ac.th

Abstract. Silymarin, a flavonolignan with antioxidant and anti-inflammatory properties, has limited water solubility and permeability, posing formulation challenges for dermal delivery. This study examines the influence of ethanol:chloroform solvent mixtures on the physicochemical characteristics of Span 60-based niosomes (cholesterol-to-surfactant ratio 7:3) prepared by thin-film hydration. A solubility study identified ethanol:chloroform as a suitable solvent system, and ratios of 1:1, 2:1, and 3:1 were selected based on their polarity and volatility profiles. The resulting niosomes were characterized for particle size, polydispersity index (PDI), zeta potential, and percentage of supernatant-associated drug (%SA). Higher ethanol content led to reduced particle size and improved size uniformity, while zeta potential remained consistent across formulations. The 2:1 ethanol:chloroform ratio demonstrated the highest %SA, suggesting enhanced drug association under these conditions. These findings emphasize the role of solvent composition in tailoring niosomal formulations and may guide further development of silymarin-based dermal delivery systems.

Keyword: Niosomes; Silymarin; Thin-Film Hydration; Solvent Ratio; Drug Delivery

INTRODUCTION

Niosomes are non-ionic surfactant-based vesicular systems that have gained significant attention in drug delivery due to their ability to enhance the solubility and stability of poorly water-soluble compounds[1]. These vesicles are composed of surfactants and cholesterol, which contribute to their structural integrity and controlled drug release properties[2]. Among various bioactive compounds, silymarin, a standardized flavonolignan extract from *Silybum marianum*, exhibits skin protective[3], antioxidant[4], and anti-inflammatory properties[5]. However, its poor water solubility and low permeability limit its therapeutic potential[6]. Encapsulation within niosomes offers a promising strategy to improve silymarin's stability and enhance its delivery for dermal applications.

Thin-film hydration is a widely used technique for preparing niosomes, allowing for efficient drug entrapment and controlled vesicle size[7]. The selection of solvents and their ratios plays a crucial role in film formation, vesicle characteristics, and drug association efficiency. Ethanol and Transcutol® have demonstrated high silymarin solubility, but only ethanol was suitable for thin-film formation. The ethanol:chloroform ratios (1:1, 2:1, and 3:1) were selected based on their complementary physicochemical properties and established use in niosome formulation. Ethanol dissolves hydrophilic compounds, while chloroform efficiently solubilizes lipophilic components like cholesterol and surfactants. Their combination ensures a homogeneous mixture for uniform thin-film formation. Chloroform's high volatility supports rapid solvent removal, while ethanol's polarity and water miscibility aid in film hydration. A study by Cakir et al., 2024[8] also demonstrated the effectiveness of ethanol:chloroform mixtures in producing stable niosomes with desirable characteristics. The impact of ethanol:chloroform ratios on niosomal properties, such as particle size, polydispersity index (PDI), zeta potential, and supernatant-associated drug (%SA), remains an area of interest for optimizing formulation parameters.

This study aims to investigate the effect of varying ethanol:chloroform ratios (1:1, 2:1, and 3:1) on the physicochemical properties of silymarin-loaded niosomes. The findings are expected to provide insights into the influence of solvent composition on niosomal characteristics, contributing to the development of more effective dermal drug delivery systems for poorly water-soluble compounds.

MATERIALS AND METHODS

Materials

Silymarin was received from Berlin Pharmaceutical Industry Co., Ltd. Sorbitan Stearate (Span 60) was purchased from Chanjao Longevity Co., Ltd. Thailand. Cholesterol was purchased from Sigma-Aldrich (St. Louis, USA). Methanol (HPLC grade), ethanol (AR grade), and chloroform (AR grade) were purchased from RCI Labscan (Thailand). Orthophosphoric acid 85% (AR grade, KEMAUS, Australia) and glass beads (3 mm, Germany) were purchased from CT Laboratory Co., Ltd. (Thailand).

Methods

1. Saturated solubility of silymarin by shake flask method[9]

An excess amount of silymarin will be added to each solvent, including ethanol, methanol, Transcutol®, and chloroform. The mixtures will then be placed in a rotary shaker for 24 hours at 25°C. After this period, the solutions will be centrifuged at 3000 rpm and 25°C for 15 minutes. The supernatants will be analyzed for silybin A and B using the validated HPLC method. The solvent

with the highest solubility will be selected for preparing solvent mixtures that maximize silymarin solubilization and loading in the niosomes.

2. Preparation of niosomes

2.1 Thin film formation method modified from Thabet et al., 2022[7]

Silymarin, surfactants, and cholesterol will be dissolved in a mixture of the selected solvent and chloroform in a round-bottom flask. The organic solvents will be evaporated under reduced pressure using a rotary evaporator with a water bath at 60°C and 70 rpm for 2 hours, forming a thin film on the inner surface of the flask. The formation of the film will be documented with photographs to assess its appearance and completeness. Afterward, the flask will be sealed with parafilm and foil, then placed in a desiccator overnight. The dryness of the film will be documented with photographs before proceeding to the rehydration steps.

2.2 Film hydration and Size reduction

The thin film will be hydrated with PBS (pH 7.4), using a rotary evaporator in a water bath at 60°C for 1 hour. The rehydration solution will be documented with photographs and then subjected to microfluidization for size reduction of the niosomes, with 5 cycles at 2000 bar. Photographs will be taken before and after overnight equilibration of the solution, followed by further characterization.

3. Physical Characterization

3.1 Appearance

The thin film formation, niosome dispersion after rehydration, and microfluidization will be visually observed and photographed after preparation.

3.2 Particle size and size distribution[10]

Particle size and size distribution will be determined using dynamic light scattering (DLS) with a Malvern Zetasizer Nano ZS (Malvern Instruments, UK) to measure the average size (Z-Ave) and polydispersity index (PDI). Samples will be diluted with ultrapure water at a 1:100 v/v ratio, and all experiments will be conducted in triplicate at 25°C.

3.3 Zeta potential[10]

Zeta potential measurements will be conducted using a Malvern Zetasizer Nano ZS (Malvern Instruments, UK). Samples will be diluted with ultrapure water at a 1:100 v/v ratio, and all experiments will be performed in triplicate at 25°C.

4. Chemical Characterization

4.1 Silymarin content (mg/g) as Silybin A and B[11]

After preparing the niosomal dispersion, the formulation was allowed to equilibrate at room temperature for 24 hours. A slight precipitation of silymarin was observed at the bottom of the container. To ensure accuracy and consistency, only the homogeneous upper phase of the dispersion was carefully collected and analyzed to determine the total silymarin content prior to centrifugation. The niosome dispersion will be quantified using a verified HPLC method at 288 nm after appropriate dilution with methanol. The silymarin content in the niosomal formulation was calculated to express the amount of silymarin (in milligrams) present in 1 gram of the niosome sample. The following equation was used:

$$\text{Silymarin content (mg/g)} = \left(\frac{\text{Amount of silymarin loaded (mg)}}{\text{Total weight of niosome sample (g)}} \right) \times 100$$

Where:

- Amount of silymarin loaded (mg) refers to the actual amount of silymarin encapsulated or associated with the niosomes.
- Total weight of niosome sample (g) refers to the overall weight of the formulation sample, including both the encapsulated silymarin and the other formulation components.

4.2 Supernatant-Associated Drug (%) modified from Pandey et al., 2021[12]

The niosomal dispersion was subjected to ultracentrifugation at 40,000 rpm for 30 minutes at 4 °C using a Hitachi CP100NX ultracentrifuge. Following centrifugation, the supernatant was carefully collected, diluted with methanol, and analyzed for silymarin content using a validated HPLC method at 288 nm. The total silymarin content was determined from the initial homogeneous dispersion prior to centrifugation. To evaluate the extent of drug association with vesicles in the supernatant, dynamic light scattering (DLS) was performed on the supernatant sample. A monomodal size distribution with a relatively broad polydispersity index (PDI) was observed. Based on these findings, the supernatant-associated drug (%) was calculated using the following formula:

$$\text{Supernatant-associated drug (\%)} = \left(\frac{\text{Silymarin in supernatant}}{\text{Total silymarin content}} \right) \times 100$$

Where:

- Silymarin in supernatant refers to the drug content measured in the supernatant after centrifugation, believed to be primarily niosome-associated.
- Total silymarin content refers to the initial drug content in the full dispersion prior to centrifugation.

To further assess separation efficiency, centrifugation was repeated at 60,000 rpm for 3 hours under the same temperature conditions (4 °C). However, HPLC analysis indicated that silymarin was still present in the supernatant.

Statistical analyses

All experiments will be conducted in triplicate (n=3) and presented as the mean \pm standard deviation. Mean values will be compared using one-way analysis of variance (ANOVA), followed by post-hoc Tukey's test for multiple comparisons. Statistical significance will be considered at $p < 0.05$, using SPSS software.

RESULTS AND DISCUSSION

Results and discussions

Saturated Solubility of Silymarin in Various Solvents

The saturated solubility of silymarin was determined in different solvents using the shake flask method. The solubility values at 25 °C were as follows: ethanol, 193.65 ± 5.16 mg/mL; Transcutol®, 193.46 ± 6.16 mg/mL; methanol, 107.60 ± 6.78 mg/mL; and chloroform, 2.37 ± 0.20 mg/mL. Silymarin exhibited the highest solubility in ethanol and Transcutol®, indicating their strong solubilizing effects. In contrast, silymarin showed very low solubility in chloroform, suggesting its limited affinity for nonpolar solvents. The high solubility of silymarin in ethanol and Transcutol® suggests their potential as co-solvents for thin-film formation in niosome preparation. The moderate solubility in methanol and low solubility in chloroform indicate silymarin's partial lipophilic nature, with a preference for polar organic solvents over nonpolar ones. These findings provide valuable insights for selecting optimal solvents to enhance silymarin solubilization during thin-film hydration, thereby improving niosomal encapsulation efficiency.

Preparation of silymarin loaded niosomes by thin film hydration method

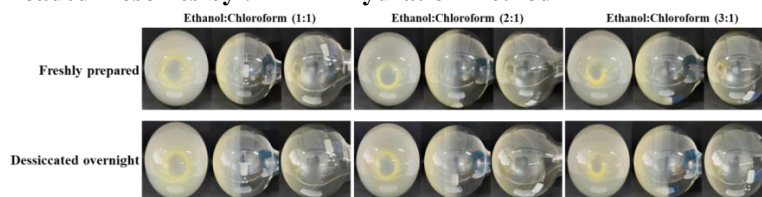


Figure 1. Visual comparison of niosome films at varying ethanol:chloroform ratios (1:1, 2:1, 3:1) before and after desiccation.

The formation of the thin film at different ethanol:chloroform ratios was visually assessed and is shown in **Figure 1**. The 1:1 ethanol:chloroform ratio yielded the most complete and quickly dried film, likely due to balanced solvent volatility. Higher ethanol ratios (2:1 and 3:1) slowed evaporation, requiring additional drying, supporting previous findings on solvent effects in film formation[13]. All formulations showed yellow silymarin residue, likely due to limited solubility or crystallization, but this did not impede film formation. Similar observations have been reported in phytochemical-loaded vesicles[14]. These results highlight the need to optimize solvent ratios for effective film quality and drug loading.

Rehydration steps



Figure 2. Niosome dispersions after microfluidization and overnight equilibration.

All niosome formulations (1:1, 2:1, and 3:1 ethanol:chloroform ratios) exhibited no precipitation of silymarin immediately after microfluidization. However, following overnight equilibration, silymarin began to precipitate in all formulations, as shown in **Figure 2**. This precipitation is likely attributed to the portion of silymarin that could not be encapsulated within the hydrophobic region of the niosomes.

Upon exposure to PBS buffer (pH 7.4), the non-encapsulated silymarin, which is insoluble in the aqueous solution, precipitated out. To enhance the encapsulation efficiency and minimize drug precipitation, optimization of the niosome formulation is essential. This includes adjusting the surfactant-to-cholesterol ratio, employing appropriate hydration techniques, and incorporating stabilizers to prevent drug leakage. Addressing formulation variables and employing advanced preparation techniques may enhance drug encapsulation and stability in niosomal systems.

Physicochemical Characterization of Silymarin-Loaded Niosomes

The particle size, polydispersity index (PDI), zeta potential, silymarin content, and supernatant-associated drug (%) of silymarin-loaded niosomes were evaluated. The results are summarized in **Table 1**.

Table 1. Physicochemical Properties of Silymarin-Loaded Niosomes

Solvent ratios (Ethanol:Chloroform)	Particle Size (nm)	PDI	Zeta Potential (mV)	Silymarin Content (mg/g dispersion)	Supernatant- Associated Drug (%)
1:1	208.50 ± 10.26 ^{*,a}	0.35 ± 0.02 ^{*,a}	-51.88 ± 3.77	0.37 ± 0.02 ^{*,a}	83.40 ± 3.30 ^a
2:1	191.54 ± 7.11 ^b	0.31 ± 0.04 ^b	-53.02 ± 1.48	0.38 ± 0.01 ^{ab}	87.70 ± 2.75 ^{**,b}
3:1	190.52 ± 5.96 ^b	0.29 ± 0.05 ^b	-53.60 ± 3.62	0.39 ± 0.01 ^b	85.85 ± 0.85 ^{ab}

* $p < 0.05$, with the 1:1 group differing significantly from both the 2:1 and 3:1 groups.

** $p < 0.05$, with the 2:1 group differing significantly from the 1:1 group but no significant difference between the 3:1 groups.

Superscript letters (a, b) indicate statistically significant differences between groups in the same column ($p < 0.05$, one-way ANOVA with Tukey's post hoc test). Values sharing at least one letter are not significantly different.

Particle Size, PDI, and Zeta Potential

The ethanol:chloroform ratio significantly influenced the particle size and polydispersity index (PDI) of the silymarin-loaded niosomes (**Table 1**). One-way ANOVA confirmed that the solvent ratio had a significant effect on particle size ($p < 0.05$). Tukey's HSD post hoc analysis further revealed that the 1:1 group was significantly different from both the 2:1 and 3:1 groups ($p < 0.001$), while no significant difference was observed between the 2:1 and 3:1 groups. This suggests that increasing the ethanol content beyond a 2:1 ratio does not further reduce particle size significantly. Similarly, the PDI decreased with higher ethanol content, indicating improved size uniformity. The differences were statistically significant ($p < 0.05$), with the 1:1 group differing significantly from both the 2:1 and 3:1 groups ($p < 0.001$), while 2:1 and 3:1 were not significantly different. These findings align with previous studies reporting that ethanol improves solubilization of lipids and surfactants, enhancing molecular dispersion and leading to smaller, more homogenous vesicles[14]. All formulations exhibited high negative zeta potential values, ranging from -51.88 ± 3.77 mV to -53.60 ± 3.62 mV, indicating good electrostatic stability of the niosomes. Although there was a slight increase in the magnitude of zeta potential with higher ethanol content, the differences were not statistically significant ($p > 0.05$), suggesting that the solvent ratio did not substantially impact the surface charge of the vesicles. This is consistent with previous reports indicating that surfactant and cholesterol composition primarily dictate zeta potential rather than solvent system[15].

Silymarin Content

The amount of silymarin in the homogeneous upper phase of the dispersion showed slight variation across formulations, with the highest content observed in the 3:1 ethanol:chloroform ratio (0.39 ± 0.01 mg/g); however, this was not significantly greater than that observed with the 2:1 ratio, but it was significantly higher compared to the 1:1 ratio. These results suggest that increasing the proportion of ethanol enhances silymarin incorporation, although the effect plateaus beyond a 2:1 ratio. The observed silymarin content was lower than the theoretical amount based on the initial 0.05 g of silymarin used during formulation, indicating some loss of active compound throughout the preparation process. Analysis of silymarin content at different stages of production revealed that, after the rehydration step, the content ranged from 0.39 to 0.46 mg/g of dispersion. Following microfluidization, the content further decreased to approximately 0.38 mg/g. These findings suggest that silymarin loss occurred during both the rehydration and microfluidization steps, likely due to degradation, retention on equipment surfaces, or precipitation. Visual evidence of precipitation can also be seen in **Figure 2**, supporting the notion of drug loss during processing.

Supernatant-Associated Drug

The percentage of supernatant-associated drug was significantly influenced by the solvent ratio. The 2:1 ethanol:chloroform formulation exhibited the highest value (87.70 ± 2.75%). One-way ANOVA confirmed a significant effect of solvent ratio on the percentage of supernatant-associated drug ($p < 0.05$). Post hoc Tukey's test revealed a significant difference between the 1:1 and 2:1 formulations ($p = 0.004$), whereas no significant difference was observed between the 2:1 and 3:1 groups. These results suggest that ethanol-rich solvent systems enhance drug encapsulation, with the 2:1 ethanol:chloroform ratio emerging as the most favorable.

Despite the application of high-speed ultracentrifugation, complete separation of untrapped silymarin from vesicle-associated drug was not achieved. Even after extended centrifugation at 60,000 rpm for 3 hours, measurable amounts of silymarin remained in the supernatant. This suggests that the drug in the supernatant was likely retained within vesicles that were not sedimented. Several observations support this conclusion. Firstly, silymarin exhibits low aqueous solubility in the phosphate buffer used for rehydration, making it unlikely that substantial amounts of free drug remained in solution post-centrifugation. Secondly, the formulation contained minimal surfactant, reducing the likelihood of micelle formation. Lastly, dynamic light scattering (DLS) analysis of the supernatant revealed a monomodal particle distribution with a relatively broad polydispersity index (PDI), indicative of vesicular particles. By contrast, the supernatant from a control formulation containing silymarin with Span 60 alone (without cholesterol) showed a distinct peak at ~8 nm, suggesting micelle formation rather than niosomes (data not shown).

Therefore, the drug quantified in the supernatant is presumed to be primarily encapsulated within niosomes that remained suspended due to incomplete sedimentation—a known limitation when separating small vesicles using standard ultracentrifugation

protocols. Accordingly, the percentage of supernatant-associated drug was used as a practical surrogate for encapsulated drug content, offering a more reliable and representative measure under these experimental conditions than traditional entrapment efficiency calculations.

CONCLUSIONS

The solvent composition significantly influences the formation and performance of silymarin-loaded niosomes. An increase in the ethanol proportion from a 1:1 to a 2:1 ethanol:chloroform ratio resulted in notable improvements in particle size, polydispersity index (PDI), silymarin content, and supernatant-associated drug percentage. However, further increasing the ethanol content to a 3:1 ratio did not yield additional significant benefits. These findings suggest that a 2:1 ethanol:chloroform ratio is the optimal solvent composition for producing stable and efficient niosomal formulations.

ACKNOWLEDGMENTS

The authors gratefully acknowledge Berlin Pharmaceutical Industry Co. Ltd. for generously supplying silymarin used in this study. We also thank the Chulalongkorn University Drug and Health Products Innovation & Promotion Center (CUDHIP) for providing access to the instrumentation and facilities essential for the completion of this work.

REFERENCES

1. Ge X, Wei M, He S, Yuan W-E. Advances of Non-Ionic Surfactant Vesicles (Niosomes) and Their Application in Drug Delivery. *Pharmaceutics*. 2019;11(2):55.
2. Nowroozi F, Almasi A, Javidi J, Haeri A, Dadashzadeh S. Effect of Surfactant Type, Cholesterol Content and Various Downsizing Methods on the Particle Size of Niosomes. *Iran J Pharm Res*. 2018;17(Suppl2):1-11.
3. Vostálová J, Tinková E, Biedermann D, Kosina P, Ulrichová J, Rajnochová Svobodová A. Skin Protective Activity of Silymarin and its Flavonolignans. *Molecules*. 2019;24(6):1022.
4. Kim J, Lee YN, Lee J, Lee SG, Kim H, Choi YS, et al. Efficacy and safety of silymarin containing antioxidant serum as an adjuvant treatment of mild-to-moderate acne vulgaris: A prospective, open-label pilot study. *J Cosmet Dermatol*. 2023;22(2):561-8.
5. Boira C, Chapuis E, Scandolera A, Reynaud R. Silymarin Alleviates Oxidative Stress and Inflammation Induced by UV and Air Pollution in Human Epidermis and Activates β -Endorphin Release through Cannabinoid Receptor Type 2. *Cosmetics*. 2024;11(1):30.
6. Hung CF, Lin YK, Zhang LW, Chang CH, Fang JY. Topical delivery of silymarin constituents via the skin route. *Acta Pharmacol Sin*. 2010;31(1):118-26.
7. Thabet Y, Elsabahy M, Eissa N. Methods for Preparation of Niosomes: A Focus on Thin-Film Hydration Method. *Methods*. 2021;199.
8. Cakir N, Ozturk N, Kara A, Zarrabi A, Mustafaoglu N. Optimizing Niosomal Formulations for Enhanced Cellular Applications. *Advances in Pharmacological and Pharmaceutical Sciences*. 2024;2024.
9. Kumari P, Rachna, Kumar U, Ravikant, Gupta A, Sagheer R. Development, Characterization and Validation of Silymarin Loaded Solid Lipid Nanoparticles for the Treatment of Liver Cirrhosis. 2023.
10. Sağiroğlu AA. Preparation and characterization of topical niosomal formulation containing retinyl palmitate and squalane for enhanced skin delivery. *Journal of Research in Pharmacy*. 2023;27(5):1821–30.
11. United States Pharmacopeia. Powdered Milk Thistle Extract. In: USP-NF 2023. Rockville, MD: United States Pharmacopeia; 2024. Available from: https://doi.org/10.31003/USPNF_M54066_05_01.
12. Pandey SS, Shah KM, Maulvi FA, Desai DT, Gupta AR, Joshi SV, et al. Topical delivery of cyclosporine loaded tailored niosomal nanocarriers for improved skin penetration and deposition in psoriasis: Optimization, ex vivo and animal studies. *Journal of Drug Delivery Science and Technology*. 2021;63:102441.
13. Uchegbu IF, Vyas SP. Non-ionic surfactant based vesicles (niosomes) in drug delivery. *Int J Pharm*. 1998;172(1-2):33–70. doi:10.1016/S0378-5173(98)00169-0.
14. Moghassemi S, Hadjizadeh A. Nano-niosomes as nanoscale drug delivery systems: an illustrated review. *J Control Release*. 2014;185:22–36. doi:10.1016/j.jconrel.2014.04.015.
15. Raeiszadeh M, Pardakhty A, Sharififar F, Farsinejad A, Mehrabani M, Hosseini-Nave H, et al. Development, physicochemical characterization, and antimicrobial evaluation of niosomal myrtle essential oil. *Res Pharm Sci*. 2018;13(3):250-61.

Study of Self-Assembled Hyaluronic Acid Based Nanogel as Controlled Drug Delivery and Stabilization System

May Thu Thu Kyaw^{1,4}, Kittipong Sanookpan², Kittipong Tonghatta^{1,4}, Sirikool Thamniem¹, Tisana Kaewruethai⁴, Chavee Laomeephol⁴, Jittima Luckanagul^{1,5,6,*}

¹Department of Pharmaceutics and Industrial Pharmacy, Faculty of Pharmaceutical sciences, Chulalongkorn University, Bangkok 10330, Thailand

²Department of Pharmacology and Physiology, Faculty of pharmaceutical sciences, Chulalongkorn University, 10330, Thailand

³Department of Biochemistry and Microbiology, Faculty of Pharmaceutical sciences, Chulalongkorn University, Bangkok 10300, Thailand

⁴Pharmaceutical Sciences and Technology Program, Faculty of Pharmaceutical sciences, Chulalongkorn University, Bangkok 10330, Thailand.

⁵Center of Excellence in Biomaterial Engineering in Medical and Health, Chulalongkorn University, Bangkok 10330, Thailand

⁶Center of Excellence in Plant-Produced Pharmaceuticals, Chulalongkorn University, Bangkok 10330, Thailand

*Corresponding author: Jittima.L@pharm.chula.ac.th

Abstract. Cannabidiol (CBD), a major phytocannabinoid present in *Cannabis sativa*, possesses multiple effective pharmacological activities, such as neuroprotective, cardioprotective and anti-inflammatory properties. However, its hydrophobic nature and rapid degradation mechanisms limit its clinical usefulness. Encapsulation of lipophilic compounds inside modified polymers with hydrophilic properties can improve the aqueous solubility and stability of drugs in specific environments. Therefore, this study focused on self-assembled poly N-isopropyl acrylamide (pNIPAM) grafted hyaluronic acid (HA) nanogels for encapsulating CBD. At the highest concentration 0.25 % w/w of HA-g-pNIPAM, encapsulation efficiency (% EE) of CBD 87.57 % was achieved compared to other two formulations 0.15 % w/w with 59.01 % EE and 0.1 % w/w with 44.4 % EE. Nanoparticle characterizations (morphology studies by a transmission electron microscopy, size measurement by a nanoparticle tracking analysis and dynamic light scattering, in vitro release study and stability) were analyzed. Nanogel formulation increased the aqueous solubility and significantly raised the release rate at 37°C over 25°C due to thermos responsive activity. It was also more stable over formulation without polymer for 5 days. The profitable development of this nanogel will lead to modernized formulations that can be functionalized and adjusted for target drug therapy and controlled drug delivery of biomolecules and small molecules.

Keywords: HA-g-pNIPAM; thermoresponsive; nanogel; controlled-delivery; CBD.

INTRODUCTION

Hyaluronic acid (HA) is an abundant, ubiquitous biopolymer found in mammals that functions as an extracellular matrix to support cell viability, motility, metabolism and differentiation. HA also serves as a lubricant in synovial fluid of the joint and controls the homeostasis of the cartilage tissue. Due to its biocompatibility and biodegradability, HA is utilized as a drug carrier system for targeted controlled drug delivery system or tissue engineering. [1, 2]

Cannabidiol (CBD) is the phyto cannabinoid isolated from *Cannabis sativa* and the recent studies has been confirmed their psychotic safety profile in comparison with other cannabinoids. CBD is consumed as promising therapeutic compound for analgesic, anti-convulsant, anti-inflammatory, neuroprotective, anti-oxidant, anxiolytics and anti-cancer activities. Even though CBD has high therapeutic potency, its efficacy has been limited due to its poor chemical stability such as photo and thermal sensitivity, low water solubility, deriving to reduce and poor bioavailability. Therefore, synthetic delivery routes are needed to provide effective CBD loaded delivery system and overcome its limitations.[3, 4]

Several nanotechnology-based drug delivery systems such as liposomes, polymeric nanoparticles, micelles, solid lipid nanoparticles, macromolecular conjugates, liposomes and self-emulsifying drug delivery systems have been emerged for targeted and controlled drug delivery. These systems can promote pharmacokinetics, physical and chemical stability and therapeutic targeting of the active ingredient. Nanogels are nano size physically and chemically cross-linked networks with high surface area and water volume which are biocompatible and harmonizable. Drugs are loaded into the particles via hydrogen bonding, van der waals and hydrophobic chemical bonding. Hydrophilic polymers are intended to carry hydrophobic drugs in the form of amphiphilic polymer and increase aqueous solubility and drug loading amount by preventing them from metabolic effects. Poly N-isopropyl acrylamide (pNIPAM) is a thermos responsive polymer with both hydrophilic (-CONH) and hydrophobic functional groups (-CH(CH₃)₂) and possesses lower critical solution temperature (LCST) at 32°C. Below LCST, amide group incorporates water molecules and polymer becomes hydrophilic. Above the LCST temperature, hydrogen bond becomes weakened and the reaction mechanism of (-CH(CH₃)₂) getting stronger.

Natural polysaccharides such as chitosan and hyaluronic acid (HA) are commonly used in nanoparticles due to their hydrophilicity, biocompatibility and biodegradability and can be conjugated with stimuli responsive polymers to create bipolar nanogels. Hyaluronic acid grafted poly N-isopropyl acrylamide (HA-g-pNIPAM) is a hydrophilic polymer which can provide not only hydrophilic but also hydrophobic drug loading and support biocompatibility and drug release under physiological environment as LCST is similar to body temperature 37°C. LCST behavior HA-g-pNIPAM was successfully proved by Win et.al and Charoenkanburkang et.al in their study and also provided sharp size transitions directly related to concentration of polymer. They also indicated about stability of drug encapsulated inside polymer is more than that of free drug existence. Curcumin release increment along with temperature was also tested by Kaewruethai et.al and sustained release of drug at physiological condition had been confirmed. [1, 2, 5, 6]. In the present study, we discussed about thermos responsive HA-g-pNIPAM nanogel for CBD delivery with 0.25% w/w of polymer concentration. The characterization, efficacy and stability of polymer were provided.

MATERIALS AND METHODS

Materials

The 3.36 % w/v CBD containing *Cannabis sativa* ethanolic extract (CBD3E) (Genuine full spectrum flower extract) and lyophilized HA-g-pNIPAM were supported from Nabsolute Co.,ltd, Bangkok, Thailand. Acetonitrile HPLC grade was purchased from Lichrosolv, Merck co.,ltd, Germany and concentrated sulphuric acid (analytical grade) was from J.T.baker Co.ltd, USA and methanol (HPLC grade) were from Honeywell, Bangkok, Thailand.

Method

Preparation of CBD-loaded HA-g-pNIPAM nanogel

Nanogel was prepared at three polymer concentrations of (0.1 % w/w, 0.15 % w/w and 0.25 % w/w) using a simple sonication method and kept at 4°C overnight. 3 % w/w of polysorbate 20, 0.15% w/w of phenoxy ethanol and 0.01 % w/w of hemp extract were added to the polymer solution and stirred at 300 rpm till a clear nanogel was obtained. The final product, nanogel, was then stored at 4°C and named as CBD HA-g-pNIPAM 0.1, CBD HA-g-pNIPAM 0.15 and CBD HA-g-pNIPAM 0.25. A control group without HA-g-pNIPAM was also prepared.

Entrapment efficiency (% EE) and loading capacity (% LC) determination by HPLC

CBD content was analyzed using Agilent 1260 infinity II HPLC with a Cancep C C18 column at UV detection wavelength 210 nm with reverse phase chromatography. The mobile phase was ACN and 0.1% sulfuric acid in water (68:32, v/v), with a flow rate of 1 ml/min at 25°C. Absolute methanol was used as a solvent to dilute both standard and sample solutions. % EE was determined by centrifugal ultrafiltration using a 30 kDa membrane. CBD-loaded nanogels were centrifuged at 14000 x g, then extracted with methanol for 1h and analyzed by HPLC.

Thermal analysis and Morphology

Polymer which gave highest encapsulation efficiency was used for below characterizations comparison with control group. The particle size distribution of control and CBD HA-g-pNIPAM 0.25 were measured by dynamic light scattering (DLS) and nanoparticle tracking analysis (NTA) at 25°C. Blank nanogels were diluted 2.3 times with ultrapure water (UPW), while CBD HA-g-pNIPAM 0.25 was diluted 200 times for DLS and 100 times for NTA. The morphology was examined by using transmission electron microscopy (TEM) with 0.5% (w/v) uranyl acetate.

Stability study of drug loaded nanogels

Drugg stability analysis was performed at 4°C as long term and 25°C as accelerated study for one month according to ICH Q1A R2 guideline.

In vitro drug release study

Sink condition was firstly determined by detection of solubility of CBD in sink media that contains phosphate buffer saline (PBS) pH (7.4) with 5% polysorbate 20. Drug release profile was analyzed by dialysis diffusion method by using 14kDa cellulose acetate membrane at 200 rpm inside incubator at 25°C and 37°C in sink condition. 10 ml of sample inside dialysis bag was put in 120 ml of sink condition. 1 ml of sample was collected at selected time intervals and analyzed by HPLC.

Statistical analysis

All experiments were performed in three replicates and statistically analyzed by one way anova using SPSS software.

RESULTS AND DISCUSSIONS

Entrapment efficiency and loading capacity determination by HPLC

CBD-HA-g-pNIPAM 0.15 and 0.25 showed significantly higher %EE than CBD-HA-g-pNIPAM 0.1 nanogel. It can be discussed that %EE was higher in nanoparticles prepared from higher polymer concentration. Nevertheless, %LC was significantly larger in nanogel formulation with lower polymer concentration 0.1% w/w as

CBD may not be completely soluble in 0.1% of nanogel and filaments are dispersed and stabilized by small nanogel concentration. %LC measurement was calculation based on mole of CBD that can be held by one mole of polymer, therefore mole division calculation can create higher number over 100 %. [1]

Thermal analysis and Morphology

LCST of HA-g-pNIPAM alone solution occurred sharp transition around 30°C with around 1200 nm from 600nm at 29 °C. Meanwhile CBD-loaded formulation showed a gradual size increment instead of distinct changes. This may be due to its high loading of additives and hydrophobic constituent in the formulation which can interfere with transforming behaviour of polymers. Win.et.al. study described comparably LCST disruption due to high asiatic acid content and Coughlan.et.al and Gandhi.et.al. also discussed salting out effect of hydrophobic ingredients which disrupted the swelling behaviour of the particles. The particle sizes from DLS aligned with measurement from NTA and TEM assays. For the TEM analysis, CBD-loaded nanogel particles showed well-defined spherical shape particles with around 200-500 nm in size, however, without CBD, particle size was only around 200 nm. From NTA analysis, CBD-loaded nanogel showed around 300 nm and drug free particles for 200 nm. By concluding all three analyses, loading of CBD into HA-g-pNIPAM can increase the particle size over polymer only nanoparticles due to incorporating of drug into hollow particles.

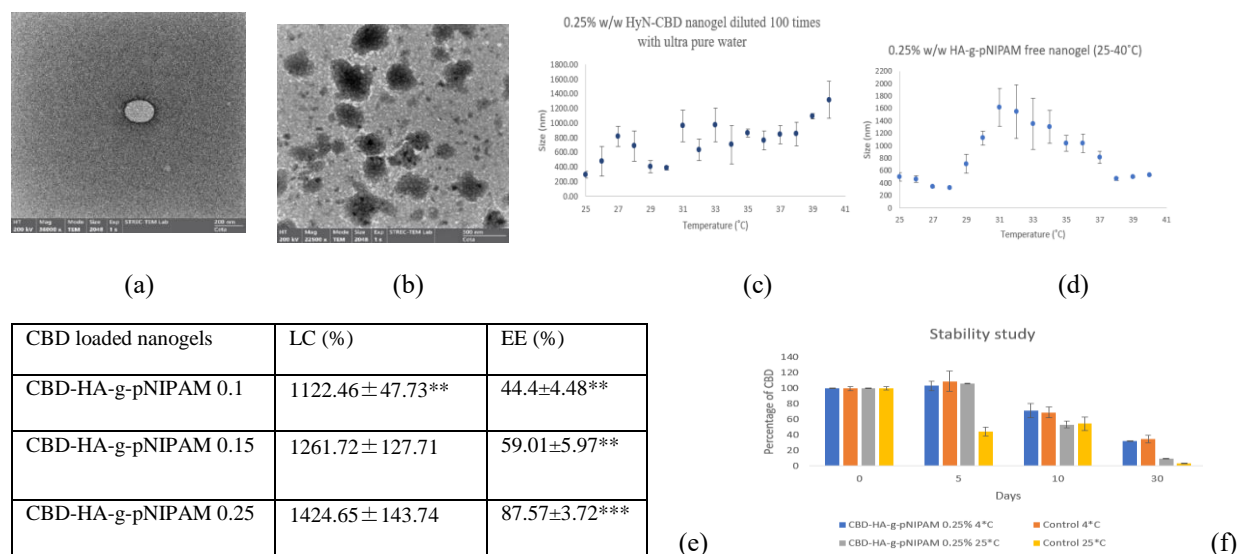


Figure 1. TEM images of self-assembled nanogel (a) 0.25% w/w HA-g-pNIPAM (b) CBD-HA pNIPAM 0.25% w/w and thermoresponsive action measurement by DLS (c) 0.25% w/w HA-g-pNIPAM (d) CBD-HA-g-pNIPAM 0.25% w/w (e) %EE and %LC determination (f) stability study at 4° C and 25° C.

Stability study of drug inside nanogels

The CBD-HA-g-pNIPAM 0.25 maintained significantly higher percentage compared to the polymer-free formulation at day 5 and day 30 at 25°C significantly p value < 0.05 . The encapsulation HA-g-pNIPAM can protect the loaded CBD from environmental degradations. Both formulations showed degradation starting from day 10 and CBD levels dropped under detectable limits after day 30. At 4°C, the degradation mechanism of both formulations are not significantly different as CBD was more stable at refrigerated condition over room temperature.

In vitro release study

Drug release was observed at sink condition for 24 h. The result revealed that CBD could not release rapidly into media according to its preferences to inside formulation containing both HA-g-pNIPAM and 3% w/w Tween 20. Taboon et.al., discussed in their study that entrapment of CBD inside highly viscous oleoyl macroglycerides retard the drug release according to pore clogging and aggregation of surfactant molecules can also slow down abrupt release profile. However, drug release by diffusion was facilitated by thermoresponsive action of the nanogel. High error bar indicated about higher standard deviation between replicates due to dynamic behaviour of nanogel which indicates

different release rate, however all replicates got larger mass release over 25°C where as 25°C showed only around 10 to 20 ug and 37 °C showed nearly 30 to 130 ug. Only release profile from nanogel due to responsive factor was analyzed in this study instead of kinetic model calculations. [6] [7]

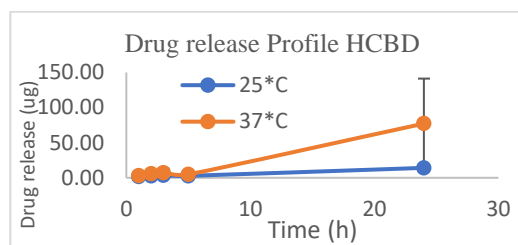


Figure 2. In vitro release study of CBD loaded 0.25% w/w HA-g-pNIPAM at 25° C and 37°C for 24 h

CONCLUSION

Consumption of high polymer concentration 0.25 % w/w of HA-g-pNIPAM in formulation can promote drug loading and solubility of CBD in water compared to lower polymer concentrations and can provide thermoresponsive drug release at specific physiological condition. Therefore, it can be considered for future hydrophobic drugs formulations.

ACKNOWLEDGEMENT

Author would like to show deepest thanks to Nabsolute Co., Ltd and TSRI Fund (CU_FRB640001_01_32_1 for supporting funding for this research. The author would like to give gratitude to the Research instrument center of the Faculty of Pharmaceutical sciences, Chulalongkorn University and department of pharmaceutics and industrial pharmacy for providing research facilities, presentation funding and Asean and non-Asean scholarship from Pharmaceutical science and Technology Program, Chulalongkorn University, Bangkok, 10330, Thailand. Funding support for this research has received from the NSRF via the Program Management Unit for Human Resources & Institutional Development, Research and Innovation (PMU-B) [grant number B13F660137].

REFERENCES

1. Win YY, Charoenkanburkang P, Limprasutr V, Rodsiri R, Pan Y, Buranasudja V, et al. In Vivo Biocompatible Self-Assembled Nanogel Based on Hyaluronic Acid for Aqueous Solubility and Stability Enhancement of Asiatic Acid. *Polymers (Basel)*. 2021;13(23).
2. Luckanagul JA, Ratnatilaka Na Bhuket P, Muangnoi C, Rojsitthisak P, Wang Q, Rojsitthisak P. Self-Assembled Thermoresponsive Nanogel from Grafted Hyaluronic Acid as a Biocompatible Delivery Platform for Curcumin with Enhanced Drug Loading and Biological Activities. *Polymers (Basel)*. 2021;13(2).
3. Moqejwa T, Marimuthu T, Kondiah PPD, Choonara YE. Development of Stable Nano-Sized Transfersomes as a Rectal Colloid for Enhanced Delivery of Cannabidiol. *Pharmaceutics*. 2022;14(4).
4. Demisli S, Galani E, Goulielmaki M, Kyrilis FL, Ilic T, Hamdi F, et al. Encapsulation of cannabidiol in oil-in-water nanoemulsions and nanoemulsion-filled hydrogels: A structure and biological assessment study. *J Colloid Interface Sci*. 2023;634:300-13.
5. Charoenkanburkang P, Kaewruethai T, Rojsitthisak P, Luckanagul JA. The study of physical properties and formulation of self-assembling nanogel from grafted hydrophilic polymer backbone as stabilization system for curcumin. *The Thai Journal of Pharmaceutical Sciences*. 2021;45(1):50-3.
6. Kaewruethai T, Lin Y, Wang Q, Luckanagul JA. The Dual Modification of PNIPAM and beta-Cyclodextrin Grafted on Hyaluronic Acid as Self-Assembled Nanogel for Curcumin Delivery. *Polymers (Basel)*. 2022;15(1).
7. Tabboon P, Pongjanyakul T, Limpongsa E, Jaipakdee N. In Vitro Release, Mucosal Permeation and Deposition of Cannabidiol from Liquisolid Systems: The Influence of Liquid Vehicles. *Pharmaceutics*. 2022;14(9).

Investigation of the Effect of Binding Liquid Composition on the Formation of Montmorillonite-Based Pellets

Sonha Seam¹, Jittima Chatchawalsaisin^{1,}*

¹ Department of Pharmaceutics and Industrial Pharmacy, Faculty of Pharmaceutical Sciences, Chulalongkorn University, Bangkok, THAILAND

*Corresponding author Email: Jittima.C@chula.ac.th

Abstract. Montmorillonite (MMT) is a type of smectite clay with a layered structure and interlayer spaces that can accommodate water, ions and organic molecules. When hydrated, MMT adsorbs water molecules, providing lubricity and plasticity, which could make it a suitable aid for pellet formation in the extrusion-spheronization process. In this study, MMT was used to prepare pellets, and the effects of binding liquids on the properties of MMT-based pellets were investigated. Pellets were formulated with metformin hydrochloride (MF), MMT, and Eudragit® L100 using two solvent systems: 1:2 ethanol-to-water and 1:2 ethanol-to-10⁻⁶ M NaOH solution. The resultant pellets were characterized for surface morphology, particle size distribution, in vitro drug release in water, and molecular interaction using FTIR spectroscopy. Results demonstrated that both binding liquids successfully formed pellets, but the alkaline system produced a narrower size distribution and a smoother surface. Drug release exhibited a similar pattern, reaching a plateau after 30 min. After 3 h, cumulative drug release was approximately 36% for pellets prepared with the ethanol-water mixture, and 31% for those prepared with the ethanol-NaOH solution. Although the decrease in drug release was not statistically significant, the observed difference may be attributed to the deprotonation of Eudragit® L100's carboxyl groups, facilitating interactions with MF. FTIR analysis supported this, showing the disappearance of the C=O stretching band in the alkaline-treated pellets, indicating carboxyl group dissociation under basic conditions. These findings highlight the feasibility of using MMT for pellet formation and the influence of binding liquid composition on pellet characteristics and drug release.

Keywords: Extrusion; Montmorillonite; Pellets; Solvent; Spheronization

INTRODUCTION

Montmorillonite (MMT) is a clay mineral belonging to the smectite group. It consists of two-dimensional layered sheets stacked on top of one another, with interlayer gaps of approximately 1 nm (Figure 1 (a)). Each MMT layer carries a strong negative charge, which is balanced by exchangeable counterions, such as Na⁺, Ca²⁺, Mg²⁺, and K⁺. Recently, MMT has gained significant interest in drug delivery [1], particularly due to the potential formation of electrostatic interactions between the negative charges on the planar surface and cationic molecules, which may affect the overall performance, including drug release, of the drug delivery system. MMT, when wet, also has excellent swellability, lubricity, and plasticity [2], making it a potentially ideal aid in pellet formulation via the extrusion-spheronization process. As a major component in bentonite, MMT has been reported as an excipient in pellet formulation [3]. However, pelletization of MMT using water as a binding liquid resulted in stickiness due to excessive swelling of this material; subsequently, upon drying, the resultant pellets shrank [4]. These drawbacks may be overcome by modifying the polarity of the binding liquid properties through mixing water with a water-miscible organic solvent, such as ethanol, and the addition of a polymer to strengthen the pellet structure [5]. Eudragit® L100 is an anionic copolymer of methacrylic acid and methyl methacrylate (1:1) (Figure 1 (b)) that is soluble in ethanol and aqueous solutions with a pH greater than 6.5. In basic environment, the carboxyl groups can dissociate, forming an anionic moiety that interacts with cationic molecules. To our knowledge, no studies have investigated the effect of binding liquids containing an anionic polymer on the ability of MMT to form pellets and their impact on drug release. In this study, MMT was used to form pellets of metformin hydrochloride (MF) (Figure 1 (c)), which was employed as a model cationic drug with high solubility (approximately 300 mg/mL) across a broad pH range of 1.2 to 6.8. The drug was dissolved in either water or 10⁻⁶ M NaOH solution and added to pellet formulations resulting a difference in the alkalinity of the overall binding liquid in the wet mass.

MATERIALS AND METHODS

Materials

The materials used in this study included a pharmaceutical-grade montmorillonite (MMT), Veegum® HS, purchased from Vanderbilt Minerals; metformin hydrochloride (MF) obtained from Harman Finocem Limited, India; Eudragit® L-100 supplied as a gift from Evonik (Thailand) Ltd.; sodium hydroxide and absolute ethanol (99.9%, EMSURE®) obtained from Sigma-Aldrich, UK. Ultrapure water was produced by Pacific TII 12 UV system (Thermo Scientific, Germany).

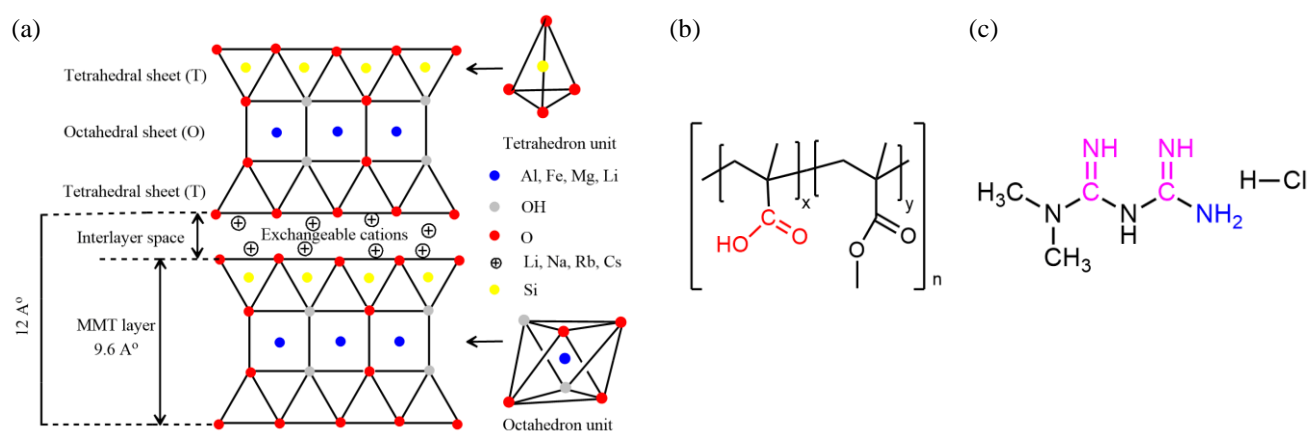


Figure 1. The structure of (a) montmorillonite modified from [6]; (b) Eudragit® L100; (c) metformin hydrochloride

Methods

Pellet preparation

Pellets containing 10% MF, 90% MMT, and 5% Eudragit® L100 solutions were prepared with two solvent systems: 1:2 ethanol-to-water (EtOH/H₂O) and 1:2 ethanol-to-10⁻⁶ M NaOH solution (EtOH/NaOH). Briefly, pellet formulations, as shown in Table 1, were processed through four main steps: wet mass preparation, extrusion, spheronization, and drying. Prior to preparing the wet mass, 20 g of MF was dissolved in either 75 g of water or 75 g of 10⁻⁶ M NaOH solution, and 10 g of Eudragit® L100 was dissolved in 38 g of absolute ethanol. The wet mass was prepared in a planetary mixer (Model 5K5SS, KitchenAid, USA) by mixing MMT with MF solutions for 10 min. Then, the polymer solution was added, and mixing continued for a further 10 min. Finally, a 1:2 ethanol-to-water or a 1:2 ethanol-to-10⁻⁶ M NaOH solution, corresponding to the ethanol-to-water (or 10⁻⁶ M NaOH solution) used in the polymer and MF solution, was added to adjust the consistency of the wet mass, and mixing continued for a further 2 min. The wet mass was then extruded using a screw extruder (Model EXKS-1, Fuji Paudal, Japan) equipped with 1 mm x 1 mm (diameter x length) dies. Extrudates were rounded on a 25 cm cross-hatched plate of a spheronizer (Aeromatic-Fielder, Type S320, England) at a speed of 170 rpm for 15 min. Resultant pellets were then dried in a hot air oven at 50 °C for 20 h.

Table 1. Pellet formulation

Composition	Amount/per batch	Solvent systems	
		EtOH/H ₂ O	EtOH/NaOH
MMT	180 g	-	-
MF	20 g	water (75 g)	10 ⁻⁶ M NaOH solution (75 g)
Eudragit® L100	10 g	absolute ethanol (38 g)	absolute ethanol (38 g)
Final binding liquid	-	1:2 ethanol-to-water (40 g)	1:2 ethanol-to-NaOH (40 g)

Pellet characterization

Appearance and surface morphology of the dried pellets was examined using an optical microscope (Nikon Eclipse E200, Japan) at 4x magnification. A scale bar was added to the image using ImageJ software (National Institutes of Health, USA).

Size distribution of pellets was determined using sieve analysis. A sieve shaker (Model FT-200M, Spain) equipped with sieves of varying aperture sizes (0.50, 0.71, 1.00, 1.18, 1.40, and 1.70 mm) was used. Eighty grams of pellets were mechanically vibrated for 10 min. The weight of pellets retained on each sieve was measured and expressed as a percentage of the total weight. Pellets between 0.71 and 1.00 mm were chosen for further characterization and dissolution testing.

Fourier transform infrared (FTIR) spectra were acquired using a Nicolet iS20 spectrometer (Thermo Scientific, USA) in ATR mode. Each sample was scanned over the range of 400–4000 cm⁻¹ with 64 scans.

In-vitro drug release from pellets was determined using a USP Apparatus II with a rotating paddle speed of 50 rpm in 900 mL of ultrapure water, maintained at 37 ± 1 °C. For each vessel, 1 g of pellets, equivalent to 100 mg of MF, was tested. Aliquots of 10 mL were withdrawn at 5, 15, 30, 60, 120, and 180 minutes, and the drug concentration was determined using a UV–Vis

spectrophotometer (UV-1800, Shimadzu, Japan) at 233 nm. Dissolution was performed in triplicate, reported as mean \pm SD. An independent two-tailed t-test ($\alpha = 0.05$) was applied at 180 min using Microsoft Excel 2019.

RESULTS AND DISCUSSION

Pellet appearance and size distribution

Pellets were successfully formed using both solvent systems, with generally round shapes. However, pellets formed with EtOH/NaOH had a smoother surface and better size uniformity, with approximately 75% in the 0.71–1.4 mm range, compared to about 55% for EtOH/H₂O (Figure 2 (a) and (b)). The superior appearance and uniformity may result from the better solubility of Eudragit® L100 in the mildly alkaline binding liquid (pH 6.6), compared to the more acidic EtOH/H₂O binding liquid (pH 5.3). The improved solubility of Eudragit® L100 likely facilitated the distribution of materials and contributed to better binding properties during pellet formation.

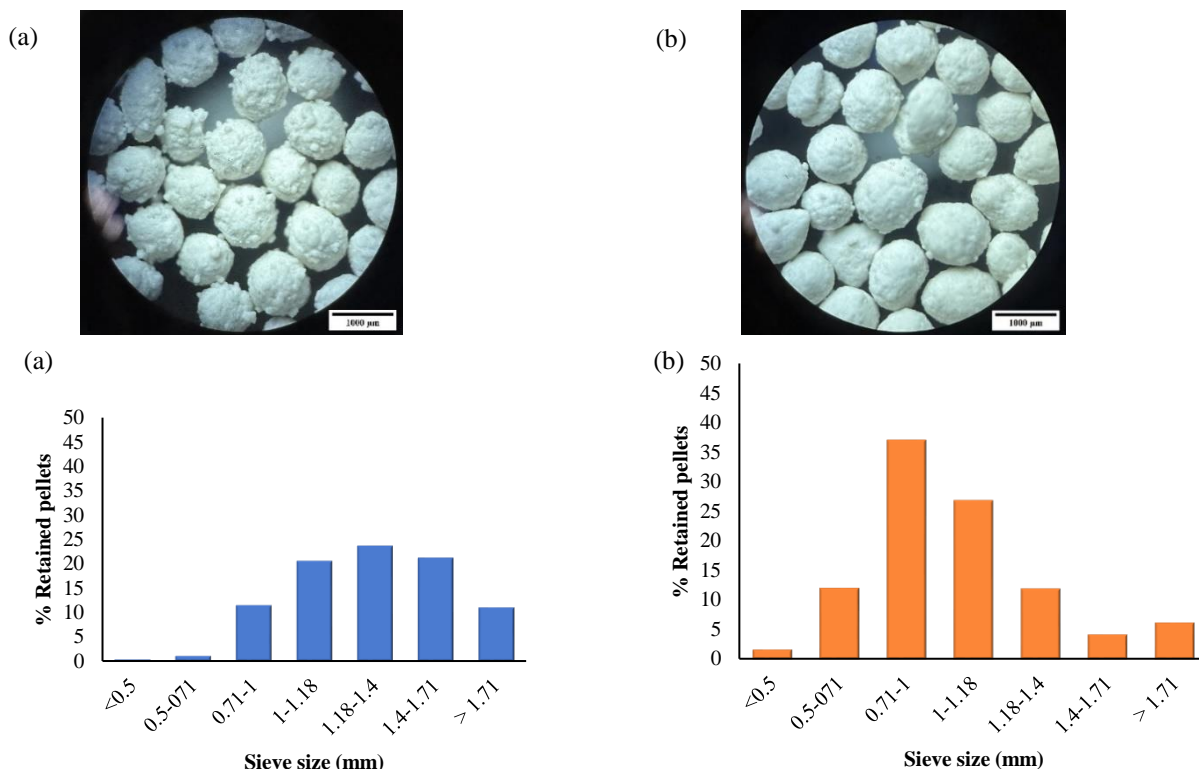


Figure 2. Microscopic photographs (4x magnification) and size distribution of pellets formulated with (a) EtOH/H₂O and (b) EtOH/NaOH

Drug release

The drug release profiles of both pellet types were similar, with a gradual initial release reaching a plateau after 30 min. After 3 h, the cumulative release was approximately 31% for pellets formed with EtOH/NaOH and 36% for those produced with EtOH/H₂O, with a p-value of 0.06, indicating no statistically significant difference between the two formulations. Incomplete drug release was observed in both cases, likely due to the high proportion of MMT in the formulation, which behaved as a matrix, hindering drug diffusion. Additionally, the cationic MF may adsorb with the negatively charged surface of MMT's layered structure, forming a composite structure that further limited drug release [7]. The cumulative drug release from pellets from the more alkaline system was slightly lower. This may be explained by greater ionization of Eudragit® L100 in EtOH/NaOH, leading to stronger interactions with MF or MMT, forming a denser matrix that lowered the drug release. As reported by Rebitski et al. MF release from the MF-MMT composite varies with pH, typically showing higher release under acidic conditions [8]. In this study, dissolution testing was performed only in deionized water, which may not fully represent the gastrointestinal environment. Therefore, further studies using simulated gastric and intestinal media with varying pH and ionic strength are recommended.

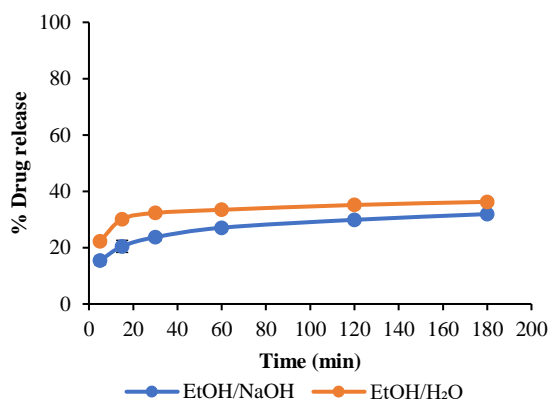


Figure 3. Drug release profiles of pellets formulated with EtOH/H₂O and EtOH/NaOH (mean \pm SD, n =3)

FTIR Spectra

The FTIR spectrum of MF exhibited characteristic N–H stretching peaks at 3385.79 cm^{-1} and 3309.42 cm^{-1} , as well as C=N stretching bands from the imine groups at 1631.18 cm^{-1} and 1554.07 cm^{-1} [9] (Figure 4 (a)). For MMT, a small peak at 3644.95 cm^{-1} corresponded to the O–H stretching of silanol groups [10], while a weak band at 1645.29 cm^{-1} indicated O–H stretching of adsorbed water [11], and the peak at 1005.38 cm^{-1} was attributed to a strong Si–O–Si stretching [12]. A distinct peak corresponding to the carbonyl (C=O) stretching of Eudragit® L100 was observed at 1721.86 cm^{-1} . In pellets prepared using EtOH/NaOH as the binding liquid, this peak disappeared, whereas in those treated with EtOH/H₂O, it remained visible but showed a slight upward shift to 1726.69 cm^{-1} . The disappearance of the C=O peak could be attributed to the deprotonation of the carboxyl group in Eudragit® L100, forming carboxylate anions (COO⁻), which may subsequently form ionic interactions with the protonated amine groups of MF (Figure 4 (b)). This interaction can disrupt the resonance of the C=O bond, effectively diminishing its double bond character in the FTIR spectra. A similar disappearance of polymeric C=O stretching due to ionic interactions with basic drug amine groups such as MF has been reported in previous studies [13]. In pellets of the EtOH/H₂O system, the observed shift of the C=O band to a higher wavenumber may result from weaker hydrogen bonding interactions [14]. Unlike the more alkaline EtOH/NaOH solution, the EtOH/H₂O binding liquid is likely insufficient to deprotonate the carboxyl groups of Eudragit® L100, thereby minimizing ionic interactions and preserving the C=O bond character.

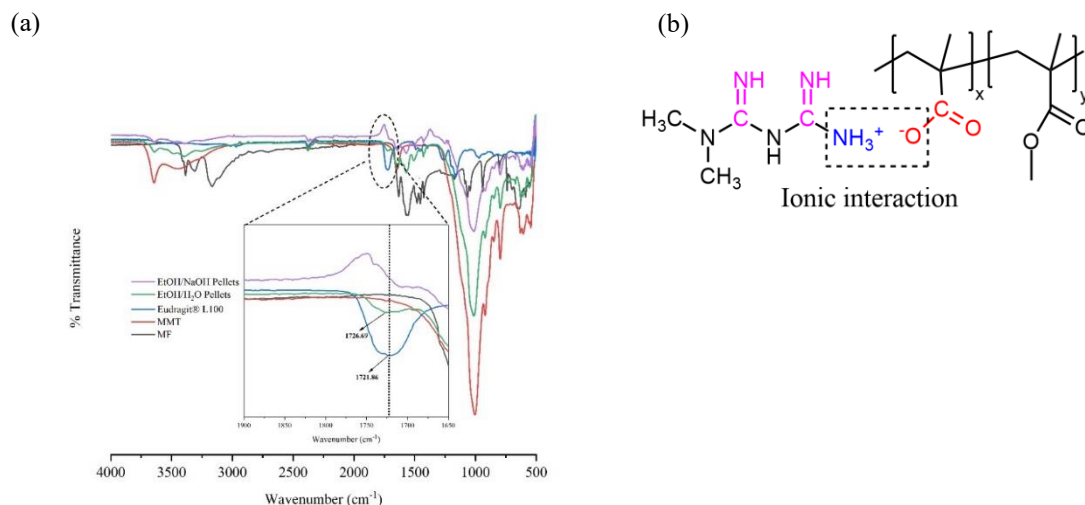


Figure 4. (a) Overlay FTIR spectra of pellets; (b) Proposed ionic interaction between metformin HCl (MF) and Eudragit® L100

CONCLUSIONS

This study investigated the effects of binding liquid composition on the formation of montmorillonite-based pellets containing metformin hydrochloride and Eudragit® L100. Both ethanol-to-water and ethanol-to-NaOH solutions successfully formed pellets, with the alkaline system yielding a narrower size distribution and smoother surface. The performance of pellets, in terms of drug release from both formulations can be attributed to the deprotonation of the carboxyl groups in Eudragit® L100 under basic conditions, which facilitates ionic interactions with metformin and alters the polymer's characteristics. Overall, MMT proves to be a promising excipient for pellet formation. The findings underscore the importance of binding liquid composition in modifying the properties of montmorillonite-based pellets and the release behavior of the cationic drug in water. Further studies may explore the influence of the formulation variables on the long-term stability and manufacturing scalability of these pellets. In addition, due to MMT's high adsorption capacity and its potential for ionic interactions with various compounds, the practical application of MMT-based pellets requires that the effects on drug release and bioavailability under environmental challenges in the gastrointestinal tract, such as variations in pH, ionic strength, food components, and co-administered drugs, should be carefully considered and systematically evaluated.

ACKNOWLEDGMENTS

This research is funded by Thailand Science Research and Innovation Fund Chulalongkorn University.

REFERENCES

1. Park, J.H., et al., *Application of montmorillonite in bentonite as a pharmaceutical excipient in drug delivery systems*. Journal of Pharmaceutical Investigation, 2016. **46**(4): p. 363-375.
2. Al-Ani, T. and O. Sarapää, *Clay and clay mineralogy*, in *Physical-chemical Properties and Industrial Uses*. 2008. p. 11-65.
3. Fielden, K.E. and J.M. Newton, *Extrusion and extruders*, in *Encyclopedia of Pharmaceutical Technology*, J. Swarbrick and J.C. Boylan, Editors. 1992, Marcel Dekker, Inc.: New York.
4. Weerakul, P., *Formation of pellets by extrusion/spheronization process using smectite as pelletization aid*, in *Department of Pharmaceutics and Industrial Pharmacy*. 2020, Chulalongkorn University.
5. Panda, G.P., et al., *Response of high swelling montmorillonite clays with aqueous polymer*. Minerals, 2023. **13**(7): p. 933.
6. Tagiev, D.B., et al., *Comparative study of the physical and chemical properties of natural bentonite clay of the dash-salakhli deposit and synthetic montmorillonite*. Glass Physics and Chemistry, 2022. **48**(2): p. 140-150.
7. Ainurofiq, A. and S. Choiri, *Application of montmorillonite, zeolite, and hydrotalcite nanocomposite clay-drug as drug carrier of sustained release tablet dosage form*. Indonesian Journal of Pharmacy 2014; 25 (3): 125, 2014. **131**.
8. Rebitski, E.P., et al., *Theoretical and experimental investigation on the intercalation of metformin into layered clay minerals*. Applied Clay Science, 2020. **186**: p. 105418.
9. Sabbagh, B.A., et al., *Determination of metformin in fixed-dose combination tablets by ATR-FTIR spectroscopy*. Chemical Data Collections, 2022. **39**: p. 100868.
10. Chen, G., et al., *FTIR spectra, thermal properties, and dispersibility of a polystyrene/montmorillonite nanocomposite*. Macromolecular Chemistry and Physics, 2001. **202**(7): p. 1189-1193.
11. Rebitski, E.P., et al., *Intercalation of metformin into montmorillonite*. Dalton Transactions, 2018. **47**(9): p. 3185-3192.
12. Acemana, S., N. Lahav, and S. Yariv, *A thermo-FTIR-spectroscopy analysis of Al-pillared smectites differing in source of charge, in KBr disks*. Thermochimica Acta, 1999. **340-341**: p. 349-366.
13. Abd-El Hafeez, S.I., et al., *Design and optimization of metformin hydrophobic ion pairs for efficient encapsulation in polymeric drug carriers*. Scientific Reports, 2022. **12**(1): p. 5737.
14. Kaushal, A.M., A.K. Chakraborti, and A.K. Bansal, *FTIR studies on differential intermolecular association in crystalline and amorphous states of structurally related non-steroidal anti-inflammatory drugs*. Molecular Pharmaceutics, 2008. **5**(6): p. 937-945.

Process Optimization of Butyric Acid-Conjugated Hyaluronic Acid Nanoparticles Loading Curcumin for Colorectal Cancer Therapy

Chatchapong Tangjidapichai¹, Patravadee Buranatrakul¹, and Duangratana Shuwisitkul^{1,}*

¹Faculty of Pharmacy, Srinakharinwirot University, THAILAND

*Corresponding author Email: duangrats@g.swu.ac.th

Abstract. Butyric acid, a fatty acid, played a role in colorectal cancer and was selected to target the free fatty acid receptor (FFAR) which was often overexpressed on colorectal cancer cells. This study aimed to optimize the preparation process of butyric acid (BA)-conjugated hyaluronic acid (HA)-based nanoparticles (NPs) for targeted curcumin (CUR) delivery. The process optimization involved the sequence of conjugation of BA to HA under varying conjugation times. The effect of HA:BA ratios was also investigated. Chemical conjugation was used as a method for attaching BA and CUR to HA. The physical properties including size, size distribution, zeta potential and conjugation efficiency, were evaluated. HPLC-DAD was utilized to analyze the conjugation efficiency of both BA and CUR. All developed NPs had sizes ranging from 20-200 nm with polydispersity index (PDI) less than 0.5 and zeta potential between -25 to -60 mV. The conjugation efficiencies were found to be approximately 40-70% across all formulation for CUR and 20-30% for BA. Interestingly, larger particle size, less negative surface charge and higher CUR conjugation efficiency were found when CUR was first attached, while different conjugation times did not influence characteristics of NP. In conclusion, the study exhibited the impact of conjugation times, conjugation sequence and HA:BA ratios on the properties of NPs. These findings provided insights for optimizing HA-based nano-formulations for targeted colorectal cancer therapy. Further study on drug release, cytotoxicity and cellular uptake are necessary.

Keywords: Butyric Acid, Hyaluronic Acid, Curcumin, Nanoparticles, Conjugation

INTRODUCTION

Colorectal cancer (CRC), a life-threatening disease, was the 3rd most diagnosed and 2nd fatal disease among all cancers. Interestingly, lipid reprogramming in CRC cells was beneficial in facilitating the developing systems to deliver anti-cancer agents targeted to the uncontrollably overgrowing cells [1]. Fatty acid, including butyric acid (BA), normally served as an energy source for colon cells, played an important role as fuel in driving cancerous cell progression through the butyrate paradox effect [2,3]. Taking advantage of the CRC's dependency on fatty acids for growth and survival, BA could be used as a specific ligand in drug delivery system via the interaction to its free fatty acid receptor (FFAR) 1 and 2 [2].

Hyaluronic acid (HA)-based nanoparticles (NPs) were widely used in various pharmaceutical formulations especially for targeted drug delivery in cancer therapy [4]. HA is well-known for its biocompatibility, biodegradation and non-immunogenicity [4]. Moreover, the specific interaction between HA and CD44, which was commonly overexpressed on the surface of many cancer cells [5], supported both passive and active targeting strategies of HA-NPs [6]. HA was also an optimal polymer for conjugation with cytotoxic agents and targeting ligands. From the high lipid energy demand in CRC and the advantages of HA including improved physiological stability and enhanced solubility of curcumin (CUR) [1,7], BA-conjugated HA-based NPs were considered a good candidate for increasing specificity of CUR delivery in CRC therapy. However, there is no scientific research using both HA and BA as dual ligands in the literature. Therefore, this study aimed to optimize the preparation process of BA-conjugated HA-based NPs for targeting CUR delivery under varying BA concentration, reaction times and conjugation sequence. The previously reported simple conjugation method for HA-CUR was adapted and modified for application in the more complex HA-BA-CUR systems [7].

MATERIALS AND METHODS

Materials

Hyaluronic acid (Mw 1,000 kDa) was purchased from Shanghai Huiwen Biotech Corp., Ltd., China. Butyric acid ($\geq 99.9\%$), 1,3-dicyclohexylcarbodiimide (DCC) and curcumin were obtained from Sigma Aldrich, China. 4-dimethylaminopyridine (DMAP) was sourced from Sigma Aldrich, USA. Methanol (HPLC grade) from LiChrosolv®, Germany, was used as a diluent for sample preparation for HPLC analysis. Acetonitrile (HPLC grade) from LiChrosolv®, Germany, and potassium dihydrogen phosphate (KH_2PO_4) from Loba Chemie Pvt. Ltd., India were used as mobile phase components.

Methods

Preparation of nano-formulation from HA BA and CUR conjugates

In the first sequence BA was conjugated prior to CUR. HA (40 mg) was dissolved in a 1:1 (v/v) mixture of H₂O: DMSO to reach the concentration of 0.2 % w/v. BA was activated by DCC and DMAP at a molar ratio of 1:0.1:0.01, respectively, and mixed at 50 °C for 24 h. The activated BA was then added to HA solution to achieve a molar ratio of HA:BA in 1:10,000. The mixture was constantly shaken at 60 °C. Varying reaction times (2, 4 and 6 h) were determined. In the next step, HA was also activated by adding DCC (25 mg) and DMAP (10 mg). The solution was stirred for 1 h and 12.5 ml of 6 mM curcumin in DMSO was slowly added. The reaction was carried out at 60 °C for an additional 6 h to obtain HA-BA-CUR solution. A reverse conjugation sequence, HA-CUR-BA, was also prepared using the previously mentioned method, but CUR was conjugated before BA. All formulations were incubated and shaken under a nitrogen atmosphere using an incubator shaker (IKA® Works (Thailand) Co. Ltd., Thailand). Additionally, HA:BA molar ratios of 1:5,000 and 1:7,500 were also formulated. The resulting conjugated solutions were dispersed in aqueous medium using sterile water for injection (SWI) to form micellar NPs. Final solutions were purified from unreacted materials by centrifugation using an Amicon® stirred cell (Merck KGaA, Germany) (MWCO = 100,000 Da).

Characterization of prepared NPs

Particle size, polydispersity index (PDI) and zeta potential were characterized by dynamic light-scattering technique (Zetasizer, Malvern US). Formation of particles was confirmed by photographing with nano-tracking analyzer (NanosightPro, Malvern US). The conjugation efficiency of both BA and CUR onto HA was evaluated by HPLC-DAD (Nexera LC-40 series, Shimadzu Japan) using a gradient elution system. The chromatographic conditions for the measurement of free BA and CUR are detailed in table 1. Drug conjugation efficiency (DCE) was calculated according to the following equation.

$$\text{DCE (\%)} = (\text{Ct} - \text{Cs}) / \text{Ct} \times 100$$

where Ct represented the total drug concentration in formulation, and Cs referred to the concentration of the unconjugated (free) drug.

Table 1. Chromatographic conditions and gradient elution system.

HPLC parameters	Detailed conditions		
Column	ACE 5 C18-AR (250 x 4.6 mm id)		
Flow rate	1.0 ml./min		
DAD detection	210 nm for BA and 423 nm for CUR determination		
Injection volume	20 µl		
Run time	60 min		
Mobile phase	A = Acetonitrile and B = KH ₂ PO ₄ 10 mM pH 2.4		
	Time (min)	Mobile phase A (%)	Mobile phase B (%)
	0	5	95
	15	5	95
	20	50	50
	40	50	50
	45	5	95
	60	5	95

RESULTS AND DISCUSSION

Results

HA-based formulations were successfully synthesized using the conjugation method. The unconjugated materials, free BA and CUR, were collected and diluted 10-fold with methanol. The unconjugated BA and CUR were determined quantitatively using HPLC-DAD. Different BA amounts yielded comparable conjugation efficiencies (Table 2). The HA:BA molar ratio of 1:10,000 was selected for further study due to its highest efficiency. The percentage of conjugation of BA remained consistent across all formulations, regardless of reaction time and conjugation sequences for HA-BA conjugates (Table 3). However, CUR showed interesting results. The conjugation efficiency of CUR was similar among different reaction times but differed between HA-CUR-BA and HA-BA-CUR sequences. The strategy of conjugation CUR prior to BA resulted in higher efficiency compared to the beginning with the conjugation of HA-BA. There was approximately 70.96-73.07 % conjugation for HA-CUR-BA, while 46.40-51.62 % was observed for HA-BA-CUR.

The size of NPs, PDI and zeta potential were summarized in Table 3. The conjugated solutions were dispersed in SWI to form NPs. Various dilution factors (25-, 50- and 100-fold) were performed. The particle size tended to decrease with increasing dilution, while the PDI also showed a declining trend. The particle size and PDI seemed constant at the above 100-fold of the dilution factor. A lower PDI indicated a narrower size distribution meaning that the particles were closer to being monodispersed [8]. This result reflected a more representative estimation of the actual particle size across the population. The 1:100 dilution was then selected, as it provided the lowest PDI values for both HA-BA-CUR and HA-CUR-BA ranging from 0.19 to 0.39. The result showed that the size and zeta potential of developed NPs were not different between each reaction times of HA-BA conjugates (Table 3). HA-CUR-BA exhibited a larger size compared to HA-BA-CUR, while the zeta potential of HA-CUR-BA was less negative than that of HA-BA-CUR.

Table 2. Conjugation efficiency of BA onto HA

Formulations	Conjugation times (Hour)	BA conjugation efficiency (%)
HA-BA (1:5000)	2	18.33
HA-BA (1:7500)	2	15.48
HA-BA (1:10000)	2	24.71

Table 3. Particle size, PDI, zeta potential and conjugation efficiency of developed NPs

Formulations	Conjugation times (Hour)	Size* (nm)	PDI*	Zeta potential* (mV)	BA conjugation efficiency (%)	CUR conjugation efficiency (%)
HA-CUR-BA	2	160.56 \pm 9.22	0.30 \pm 0.06	-29.24 \pm 4.58	26.44 \pm 1.54	72.94 \pm 0.10
HA-CUR-BA	4	163.00 \pm 2.29	0.37 \pm 0.05	-31.54 \pm 0.75	25.34 \pm 0.95	70.96 \pm 0.10
HA-CUR-BA	6	159.00 \pm 2.77	0.39 \pm 0.04	-31.72 \pm 2.13	25.04 \pm 0.05	73.07 \pm 0.07
HA-BA-CUR	2	104.10 \pm 1.36	0.19 \pm 0.01	-50.22 \pm 1.50	26.22 \pm 1.28	46.40 \pm 0.17
HA-BA-CUR	4	99.79 \pm 3.02	0.20 \pm 0.01	-49.14 \pm 1.10	27.29 \pm 2.51	51.62 \pm 0.12
HA-BA-CUR	6	99.20 \pm 1.98	0.20 \pm 0.01	-45.97 \pm 1.08	26.32 \pm 1.35	51.23 \pm 0.26

*NPs were carried out at a 100-fold dilution.

Confirmation of HA-based nanoparticles forming as prepared in this study was conducted utilizing capturing images by nano-tracking analyzer as illustrated in Figure 1. The size of NPs used in targeted drug delivery was a vital factor to be considered. NPs could extravasate through the fenestrated vasculature surrounding tumor, where endothelial gaps typically ranged from 200-800 nm and they could be unable to permeate through normal vessels (2-4 nm) for serving passive targeting strategy [9]. Moreover, the excessively small NPs would be excreted via renal clearance (threshold 6-8 nm), while too large NPs would be eliminated by reticuloendothelial systems (RES) (threshold >500 nm) [9]. The formulated NPs had sizes ranging from 99.2-210.2 nm across all dilution folds, which aligned within the optimal size range of approximately 20-200 nm, indicating that they would not be destroyed through renal clearance or RES and ensuring the optimal circulation time [10].

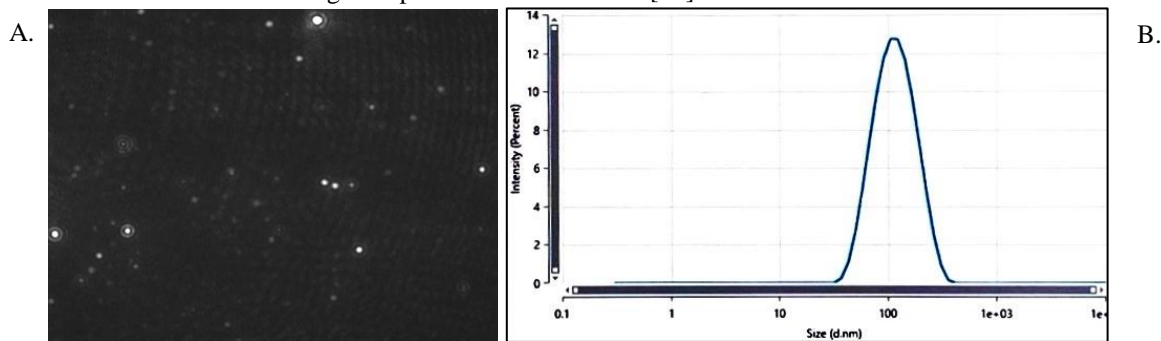


Figure 1. A: Captured image of HA-BA-CUR NPs (with HA-BA conjugation time of 2 h) at a 1000-fold dilution, obtained using a nano-tracking analyzer, B: Size distribution peak of HA-BA-CUR NPs (with HA-BA conjugation time of 2 h) at a 100-fold dilution analyzed using a zetasizer.

Discussions

The size of HA-CUR-BA was larger than that of HA-BA-CUR, which corresponded to the higher CUR conjugation efficiency in the HA-CUR-BA sequence (Table 3). Zeta potential, which represents the surface charge of NPs, was found to be less negative in the HA-CUR-BA formulations. The results were also consistent with their higher percentage of conjugation (Table 3). The conjugation of BA and CUR on the HA backbone was based on the esterification reaction. The carboxylic acid of BA interacted with the hydroxyl of HA, while the hydroxyl of CUR reacted with the carboxylic acid of HA [7,11]. The negative charge on NPs surface originated from the activated carboxylic acid on the HA polymer [12]. The zeta potential shifted to a less negative value as the percentage of CUR conjugation increased. This finding was due to a greater number of carboxyl groups on HA being utilized to form ester bonds with the hydroxyl groups of CUR, thereby reducing the amount of HA's free carboxyl groups available. Thus, it led to a reduction in the negative surface charge. However, all formulations exhibited highly negative zeta potentials (< -30 mV) indicating sustained stability [13].

Conjugation efficiency of CUR in HA-CUR-BA was higher in comparison to HA-BA-CUR. Due to the structure of CUR, it likely caused stronger steric repulsion to BA-preconjugated HA than BA, which was smaller, and thus induced less steric force to CUR-preconjugated HA [14]. It resulted in a lower percentage of CUR conjugation when it was attached onto HA after BA. In contrast, a consistent BA conjugation efficiency was observed in both sequences, likely due to the smaller size of BA, which may have been less affected by steric forces and more capable of interacting with HA.

The predicted 3D structures of HA-BA and HA-CUR conjugates (Figure 2) suggested that prior conjugation with BA created a narrower space between the BA molecule and HA's carboxyl group compared to the larger distance between the CUR molecule and HA's hydroxyl group when CUR was first conjugated. These findings supported the idea that when BA was conjugated first, it became more difficult for CUR to access its interaction site. Conversely, BA more easily accessed its binding site when HA-CUR had been previously formed.

Furthermore, the previously attached ligands on HA could have caused stronger steric hindrance, making it more difficult for subsequent ligands or reagents to access the HA's functional groups [15]. In the conjugation of HA-CUR, DCC, which was used as a coupling reagent, interacted with the carboxyl group of HA to form an *O*-acylisourea intermediate, which was highly reactive toward CUR's hydroxyl group [16]. The previously attached BA could have also sterically hindered HA's carboxyl group from interacting with DCC. Even if DCC was able to access the HA site, the presence of BA could still have interfered sterically with the reactive intermediate, thereby reducing the amount of CUR that reacted. In contrast, during the conjugation of HA-BA, DCC interacted with the carboxyl group of BA. The highly reactive intermediate could form via the freely available BA molecule without interference from other ligands, thereby allowing easier interaction with HA.

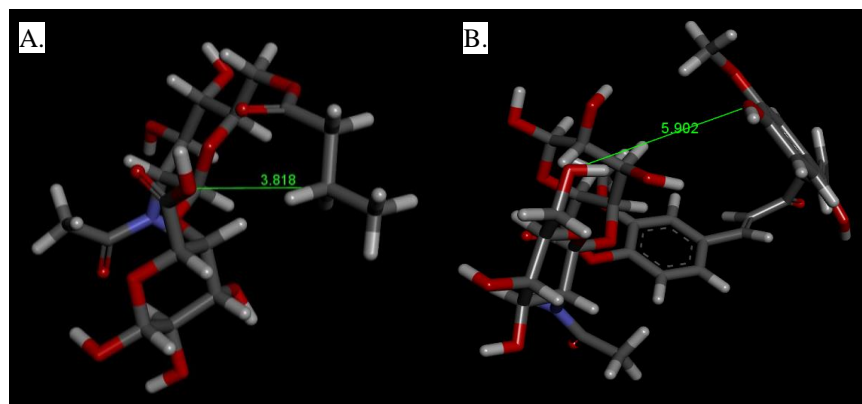


Figure 2. A: The predicted 3D structure of HA-BA conjugates and B: The predicted 3D structure of HA-CUR conjugates (2D structures were initially drawn by SwissDrugDesign and subsequently converted to 3D using NovoPro. The conjugated structures of BA or CUR onto HA monomer were then analyzed using BIOVIA Discovery Studio Visualizer 2024)

CONCLUSIONS

The sequence of conjugation played a vital role in the formulation of butyric acid (BA)-conjugated hyaluronic acid (HA)-based nanoparticles (NPs) for targeted curcumin (CUR) delivery. The impact of the parameter affected physicochemical properties of prepared NPs including particle size, zeta potential and conjugation efficiency. The addition of CUR prior to BA resulted in larger particle size, a less negative surface charge and higher percentage of CUR conjugation. Conversely, varying reaction times

did not affect any of the measured NPs' properties. The FT-IR and/or NMR spectrum should be performed for the confirmation of ester bonds between HA, BA and CUR. These findings provided insights for optimizing HA-based nano-formulations for targeted colorectal cancer therapy. Further studies on drug release, cytotoxicity in CRC cell line and cellular uptake are necessary.

ACKNOWLEDGMENTS

We would like to thank the graduate school and Faculty of Pharmacy, Srinakharinwirot university, for funding this research project.

REFERENCES

1. Salita T, Rustam YH, Mouradov D, et al. Reprogrammed Lipid Metabolism and the Lipid-Associated Hallmarks of Colorectal Cancer. *Cancers* [Internet]. 2022 [cited 2025 Apr 11];14(15). Available from: <https://doi.org/10.3390/cancers14153714>
2. Li Y, Huang Y, Liang H, et al. The roles and applications of short-chain fatty acids derived from microbial fermentation of dietary fibers in human cancer. *Frontiers in Nutrition* [Internet]. 2023 [cited 2025 Apr 11];10. Available from: <https://doi.org/10.3389/fnut.2023.1243390>
3. Belcheva A, Irrazabal T, Robertson SJ, et al. Gut microbial metabolism drives transformation of MSH2-deficient colon epithelial cells. *Cell* [Internet]. 2014 [cited 2025 Apr 11];158(2):288–299. Available from: <https://doi.org/10.1016/j.cell.2014.04.051>
4. Matalqah S, Lafi Z, Asha SY. Hyaluronic Acid in Nanopharmaceuticals: An Overview. *Current Issues in Molecular Biology* [Internet]. 2024 [cited 2025 Apr 11];46(9):10444–10461. Available from: <https://doi.org/10.3390/cimb46090621>
5. Misra S, Hascall VC, Markwald RR, et al. Interactions between Hyaluronan and Its Receptors (CD44, RHAMM) Regulate the Activities of Inflammation and Cancer. *Frontiers in Immunology* [Internet]. 2015 [cited 2025 Apr 11];6:201. Available from: <https://doi.org/10.3389/fimmu.2015.00201>
6. Gavas S, Quazi S, Karpiński TM. Nanoparticles for Cancer Therapy: Current Progress and Challenges. *Nanoscale Research Letters* [Internet]. 2021 [cited 2025 Apr 11];16(1). Available from: <https://doi.org/10.1186/s11671-021-03628-6>
7. Manju S, Sreenivasan K. Conjugation of curcumin onto hyaluronic acid enhances its aqueous solubility and stability. *Journal of Colloid and Interface Science* [Internet]. 2011 [cited 2025 Apr 11];359(1):318–325. Available from: <https://doi.org/10.1016/j.jcis.2011.03.071>
8. Mudalige T, Qu H, Van Haute D, Ansar SM, Paredes A, Ingle T. Chapter 11 – Characterization of nanomaterials: tools and challenges. In: López Rubio A, Fabra Rovira MJ, Martínez Sanz M, Gómez Gómez-Mascaraque L, editors. *Nanomaterials for food applications*. Amsterdam: Elsevier; 2019. p. 313–353. Available from: <https://doi.org/10.1016/B978-0-12-814130-4.00011-7>
9. Bazak R, Houry M, Achy SE, et al. Passive targeting of nanoparticles to cancer: A comprehensive review of the literature. *Molecular and Clinical Oncology* [Internet]. 2014 [cited 2025 Apr 11];2(6):904–908. Available from: <https://doi.org/10.3892/mco.2014.356>
10. Attia MF, Anton N, Wallyn J, et al. An overview of active and passive targeting strategies to improve the nanocarriers efficiency to tumour sites. *The Journal of Pharmacy and Pharmacology* [Internet]. 2019 [cited 2025 Apr 11];71(8):1185–1198. Available from: <https://doi.org/10.1111/jphp.13098>
11. Coradini D, Pellizzaro C, Miglierini G, et al. Hyaluronic acid as drug delivery for sodium butyrate: improvement of the anti-proliferative activity on a breast-cancer cell line. *International Journal of Cancer* [Internet]. 1999 [cited 2025 Apr 11];81(3):411–416. Available from: [https://doi.org/10.1002/\(sici\)1097-0215\(19990505\)81:3<411::aid-ijc15>3.0.co;2-f](https://doi.org/10.1002/(sici)1097-0215(19990505)81:3<411::aid-ijc15>3.0.co;2-f)
12. Kumar R, Singh M, Meena J, et al. Hyaluronic acid - dihydroartemisinin conjugate: Synthesis, characterization and in vitro evaluation in lung cancer cells. *International Journal of Biological Macromolecules* [Internet]. 2019 [cited 2025 Apr 11];133:495–502. Available from: <https://doi.org/10.1016/j.ijbiomac.2019.04.124>
13. Shnoudeh AJ, Hamad I, Abdo RW, et al. Chapter 15 - Synthesis, Characterization, and Applications of Metal Nanoparticles. In: *Biomaterials and Bionanotechnology*. 2019 [cited 2025 Apr 11];527–612. Available from: <https://doi.org/10.1016/B978-0-12-814427-5.00015-9>
14. Exner O, Böhm S, Decouzon M, et al. Small steric effects in isolated molecules: alkyl-substituted benzonitriles. *J Chem Soc Perkin Trans 2* [Internet]. 2002 [cited 2025 May 15];(1):168–172. Available from: <http://dx.doi.org/10.1039/B104856M>
15. Ossipov DA, Gustafsson O, Lüchow M, et al. Combination of coordination and releasable covalent binding for the delivery of antisense therapeutics by bisphosphonate-hyaluronan-oligonucleotide conjugates. *ACS Appl Polym Mater* [Internet]. 2021 [cited 2025 May 15];3(4):2197–2210. Available from: <https://pubs.acs.org/doi/10.1021/acsapm.1c00243>
16. Verdoliva V, Muzio G, Autelli R, et al. Microwave-assisted, solid-state procedure to covalently conjugate hyaluronic acid to curcumin: validation of a green synthetic protocol. *ACS Polymers Au* [Internet]. 2024 [cited 2025 May 15];4(3):214–221. Available from: <https://doi.org/10.1021/acspolymersau.3c00047>

Formulation and Evaluation of a Diclofenac Sodium Pain Relief Stick Using a Eutectic Mixture System

Juthamas Thungchan¹, Nichapa Watthanachanobon¹, Sathit Niratisai¹, Kanawan Pochanakom¹, Vipaluk Patomchaivivat¹, Jankana Burana-osot¹, Panadda Phattanawasin¹, Somlak Kongmuang^{1,*}

¹Department of Industrial Pharmacy, Faculty of Pharmacy, Silpakorn University, Nakhon Pathom, THAILAND 73000

*Corresponding author Email: somlak.kongmuang@gmail.com

Abstract. This study aimed to develop a convenient pain relief stick utilizing diclofenac sodium (DS) as the active ingredient. To enhance absorption and provide a cooling effect, a eutectic mixture system was incorporated, consisting of menthol (M) and camphor (C) in a 1:1 ratio. A 1% DS formulation was prepared using an oleaginous base composed of cetyl alcohol (CA), stearic acid (SA), soft paraffin (SP), beeswax (B), and propylene glycol (PG) in varying concentrations. The formulation process involved heating and solidification before molding into six different variations. Physical evaluations, including hardness, weight variation, and stickiness tests, identified the optimal formulation containing 1.00% DS, 24.55% CA, 24.55% SA, 24.95% SP, 11.98% PG, 9.98% B, 1.50% M, and 1.50% C. This formulation exhibited superior physical properties, with a hardness of 0.70 ± 0.14 N, a weight of 3.31 ± 0.06 g, and minimal stickiness. Content uniformity analysis via HPLC confirmed a label claim percentage of $99.36 \pm 5.29\%$ per stick. IR spectroscopy revealed no interactions between the active drug and the base components. Additionally, X-ray powder diffraction may not have detected crystalline structures, possibly due to the low drug concentration or instrument limitations. Drug release studies, conducted using USP Apparatus V with a phosphate buffer medium at pH 5.5, showed a release of $5.73 \pm 0.48\%$ within 60 minutes. Further refinement of the eutectic system may be necessary to improve drug release efficiency.

Keywords: Pain relief stick; Diclofenac sodium; Eutectic mixture; Formulation; Drug release

INTRODUCTION

Diclofenac is one of the widely used non-steroidal anti-inflammatory drugs (NSAIDs) for treating pain and inflammation. It is commonly used in the form of its sodium salt due to its better solubility. Although diclofenac sodium (DS) is well absorbed in the stomach, it may cause irritation to the gastrointestinal tract [1]. This side effect can be avoided by administering the drug through the skin. Currently, topical 1% DS products are available in the form of creams or gels packaged in tubes [2]. The development of drugs with new drug delivery systems (NDDS) could enhance drug safety and effectiveness, allowing for rapid action, ease of use, and affordability [3]. One approach to this development is formulating drugs in stick form, which offers practical benefits, including convenience for daily use and portability [3]. Additionally, stick formulations can be carried on airplanes, as air travel regulations restrict the amount of liquid products allowed and impose weight limitations on luggage. The stick formulation in this study were based on a preliminary study using standard lipstick formulations with an oleaginous base to provide structural solidity. Moreover, a previous report has found that eutectic substances can enhance transdermal absorption [4]. Therefore, eutectic-forming substances are incorporated into the formulation in this study. Various substances can be used to create eutectic mixtures; however, it has been found that a 1:1 ratio of menthol and camphor forms a complete eutectic mixture while also providing a cooling effect on the applied area [5]. Thus, the objective of this study is to develop a 1% DS stick formulation with desirable properties as an alternative to existing dosage forms.

MATERIALS AND METHODS

Materials

DS standard and raw material were kindly supported by Medicine Supply Company, Thailand. CA, SA, SP, PG, B, M, C, Ethyl alcohol, Phosphoric acid, Monobasic sodium phosphate, Potassium dihydrogen phosphate AR grade, Disodium hydrogen phosphate, Methanol AR grade were purchased from SIGMA by PC Drug Center company as a distributor. The HPLC-grade methanol and acetonitrile were purchased from Merck (Darmstadt, Germany). All other chemicals and solvent used were of analytical grade. High purity water was prepared by using a Milli-Q RO system (Millipore, Bedford, MA, USA).

Methods

Formulation Preparation Procedure

To develop the formula, preliminary experiments were conducted based on the principles of lipstick formulation and

prior literature, as cited in references [3-5]. It was observed that increasing the amount of eutectic substance in the initial stage led to reduced solidification of the stick. Consequently, the amount of eutectic substance was limited to 3%. The DS stick was prepared using a preliminary formula containing 1.00% DS, along with CA, SA, SP, PG, B, M, and C. In the preparation process, M and C were mixed together in a beaker until they became a liquid. DS was then added to this mixture to form a liquid. This liquid was subsequently combined with the liquid part that is the base at a temperature of 60°C. The resulting liquid mass was poured into a lipstick mold and allowed to solidify. The stick was obtained by removing the solid mass from the mold. The formulation details are shown in Table 1.

Table 1. The formula of DS sticks (% by weight)

Ingredients	F1	F2	F3	F4	F5	F6
DS	1.00	1.00	1.00	1.00	1.00	1.00
CA	26.95	21.96	31.93	26.95	29.54	24.55
SA	26.95	21.96	31.93	26.95	29.54	24.55
SP	29.94	29.94	19.96	19.96	24.95	24.95
PG	11.98	11.98	11.98	11.98	11.98	11.98
M	1.50	1.50	1.50	1.50	1.50	1.50
C	1.50	1.50	1.50	1.50	1.50	1.50
B	0.00	9.98	0.00	9.98	0.00	9.98

Physical Appearance Evaluation

The formulation's color and external physical characteristics, such as greasiness, smoothness, stickiness, and adhesion to the skin, were assessed through sensory perception and visual inspection.

Weight Variation

The study involved randomly selecting three sticks per formulation. Each stick was weighed, and the measurements were recorded. The recorded weights were then compared with the average weight to assess weight variation with standard deviation.

Hardness

The hardness of the samples was measured in Newtons (N) using a Texture Analyzer. A higher force reading indicated greater hardness. Three samples from each formulation were tested. The procedure was as follows: The "T.A. Exponent 32" program was opened, and the force was calibrated using a 2 kg weight until the display showed a current weight of 0 kg. A needle-type probe was selected and connected to the adaptor, which was then attached to the Texture Analyzer. The height was calibrated to define the distance between the probe and the sample base. Hardness measurements were performed by pressing the probe onto the surface of each sample at three distinct and evenly spaced positions. The resulting force was recorded in Newtons (N).

Uniformity of Drug Content

This test determined the content of DS in a single stick formulation. Ten sticks were randomly selected and extracted for drug content measurement using High-Performance Liquid Chromatography (HPLC) under specified analytical conditions.

In Vitro Dissolution Test

The Paddle over-disc model (USP apparatus V) was applied for determination of a release of DS stick. The medium of this study was 500 mL of phosphate buffer pH 5.5 at temperature of 32 °C. The sample was analyzed by HPLC to determine the percentage drug release of DS using the standard curve method. The average amount of DS released was calculated from triplicate measurements.

Chemical Analysis

Instrumentation and chromatographic conditions

The HPLC-DAD system consisted of an Agilent 1100 series pump, an on-line solvent degasser (Model G1311A), an autosampler (Model G1313A), a photodiode-array detector (DAD) (Model G13158) and a Chemstation software Version A.08.01 (Agilent Technologies, USA). A reversed-phase column, 250 mm×4.6 mm packed with 5 µm, Phenomenex C18 modified silica (Phenomenex, USA) and a guard column, 20 mm x 3.9 mm packed with 5 µm, C18 were used. The separation was carried out under isocratic elution with acetonitrile: 40 mM phosphate buffer pH 4 (30:70, v/v) at a flow rate of 1.0 ml min⁻¹. The column was operated at room temperature, the wavelength was monitored at 215 nm, and the injection volume was 20 µl.

XRD study

XRPD was performed with an X-ray diffractometer (Miniflex, Japan). The diffraction pattern was recorded in the interval $3^\circ < 2\theta < 40^\circ$ in a step scan mode of 0.02° per step every second. The samples were side loaded in the sample holder. The XRD patterns of DS powder, base, DS with physical mixture with base and DS stick were obtained.

Differential scanning calorimetry (DSC)

Differential scanning calorimetry (DSC) studies were performed on the base, the drug, a physical mixture of the drug with the base, and F6 using a DSC-60 calorimeter (Shimadzu Corporation, Japan). The instrument was calibrated with indium and zinc standards. Samples were initially heated from 10°C to 300°C at a rate of $25^\circ\text{C}/\text{min}$ to eliminate thermal history. They were then rapidly cooled to 10°C and reheated from 10°C to 300°C under a nitrogen flow at a heating rate of $10^\circ\text{C}/\text{min}$.

Fourier-transform infrared spectroscopy (FT-IR) study

The FT-IR spectra (range $650\text{--}4000\text{ cm}^{-1}$) of DS powder, base, DS with base by a physical mixture and DS stick, were recorded using an FT-IR spectrophotometer (Thermo Electron Corporation, model Nicolet 4700). The sample was mounted on the sample stage, and pressure was applied by turning the top of the arm of the sample stage to create a flat surface, ensuring intimate contact between the sample and the stage. The spectra obtained were averaged over four scans at a resolution of 1 cm^{-1} .






Statistical evaluation

The Excel program was used for statistical analyses. The ANOVA was chosen for comparing data with the 95 % confidential interval.

RESULTS AND DISCUSSION

The experiment revealed that all six prepared formulas had a white cloudy appearance in stick form and a pleasant camphor scent as shown in Table 2. However, there were differences in hardness and stickiness. The weight of each stick did not differ significantly across the six formulas when tested with ANOVA ($p < 0.05$), likely due to the uniform mold size and precisely defined substance quantities. Significant differences in hardness ($p < 0.05$) were observed, possibly due to the varying amounts of hardening agents, with beeswax providing the most suitable hardness. Formula 6 exhibited the least stickiness, making it suitable for further study.

Table 2. The physical appearance of DS stick

Formulation	Physical Appearance	Picture	Weight Variation (g)	Hardness (N)	Stickiness
F1	White, glossy, and slippery surface with slight flaking.		3.3874 ± 0.0885	1.27 ± 0.02	+++
F2	Opaque white with a highly glossy, slippery surface (more slippery than F1); sticky to the touch and non-flaking.		3.3851 ± 0.0658	0.66 ± 0.03	+++
F3	White, glossy, and slippery surface with a smooth touch; harder than other formulations and non-flaking.		3.3574 ± 0.0683	1.76 ± 0.25	++
F4	Opaque white with a less glossy surface than F3, dry, non-slippery and non-flaking.		3.3219 ± 0.0308	0.87 ± 0.06	++
F5	White with a slippery, glossy surface; brittle and easily breakable.		3.4052 ± 0.0355	1.32 ± 0.06	++

F6 Opaque white with non-slippery surface not brittle, and non-flaking.



3.3071 0.70±0.14 +
±0.0608

The experimental results suggest that Formulation 6 is the most suitable for practical application. The investigation into the changes in the drug's crystalline structure using IR, DSC (unpublished data), and X-ray diffraction revealed the following findings:

From the IR spectrogram, the IR spectrogram pattern of DS was conformed the previous study [6] as shown in the Figure 1. It was found that there was no change in the drug's peak when it was prepared in both physical mixture and stick form.

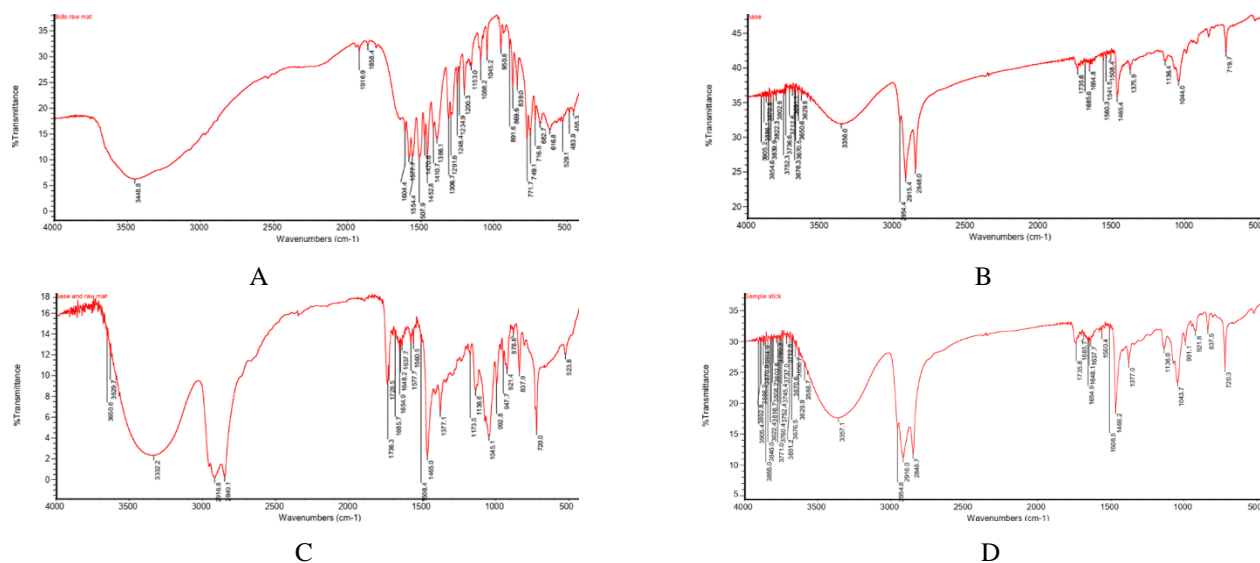


Figure 1. FT IR spectrum of A: DS, B: base, C: DS with base by physical mixture, and D: DS stick

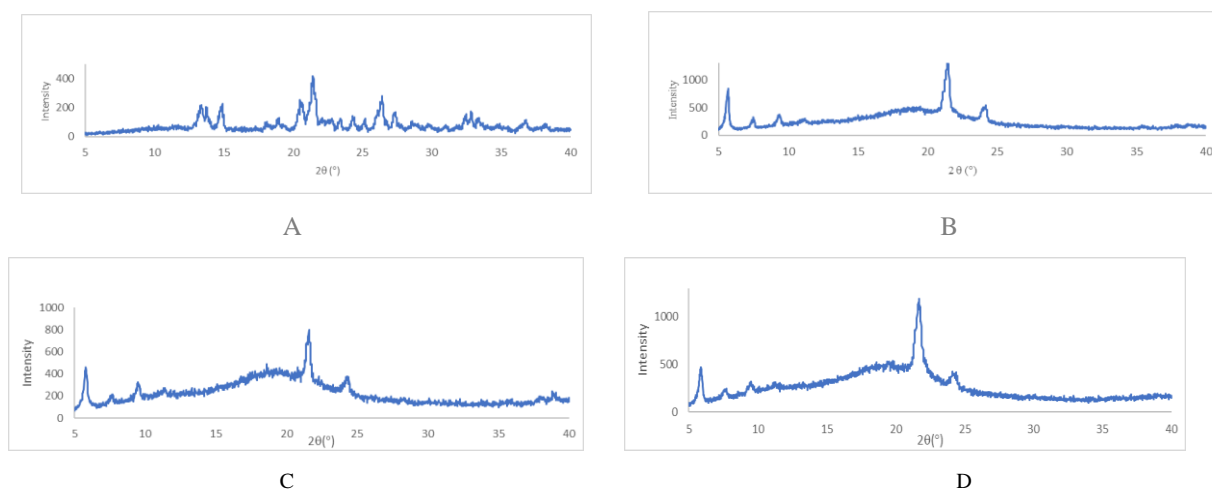


FIGURE 2. XRD diffractogram of A: DS, B: base, C: DS with base by physical mixture and D: DS stick

Regarding the XRD results shown in Figure 2, the diffractogram of DS was consistent with previous studies [6], confirming its crystalline nature. However, no crystalline structures were detected when DS was incorporated into the base, either in the stick formulation or the physical mixture. This absence could be due to the low drug concentration (1%), making it undetectable or limitations of the instrument's analytical sensitivity. This is particularly relevant to polycrystalline samples, where each crystallite can contribute to multiple diffraction peaks simultaneously, resulting in the whole diffraction profile building

from a limited number of crystallites [7]. However, the DSC results (unpublished data) shown in Figure 3 revealed that the base began to burn as the temperature increased to 200°C. Since the melting point of DS is reported range of 283—285°C [6] which is higher than the burning temperature of the base, the sample's melting point could not be analyzed using this DSC method.

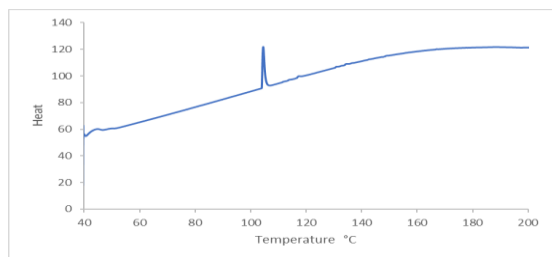


Figure 3. DSC thermogram of base

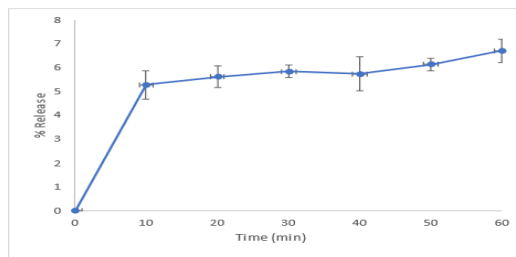


Figure 4. The dissolution profile of DS sticks with USP Apparatus V, pH 5.5 at 32 °C

Ten stick samples were randomly selected and analyzed for the active ingredient (API) content in each stick using HPLC. The average API content was $99.36 \pm 5.29\%$, with a %R.S.D. of 5.36 ($n=10$). The results were satisfactory, showing that the drug percentage in the sticks matched the label's claim. This indicates that the DS was homogeneously mixed within the sticks.

Using USP Apparatus V, $5.73 \pm 0.48\%$ of the drug was released within 60 minutes. The eutectic mixture did not enhance drug release as expected, possibly due to the amount or type of eutectic substance used. Increasing the amount of eutectic substance might affect the hardness of the stick hardness. Additionally, the low drug release might be due to its low solubility in acidic medium. It was found that the pH of the dissolution medium might affect drug solubility, with alkaline pH increasing solubility. Therefore, this could be another factor contributing to the low drug release observed [8]. Alternatively, the drug might dissolve better in a stick base, leading to reduced release [9].

CONCLUSION

The study shows that DS can be prepared in stick form, but the drug release remains low. Future studies may find that using a eutectic mixture to enhance solubility and absorption is still insufficient. Increasing the quantity or using other substances might be necessary to improve drug release.

ACKNOWLEDGMENT

We would like to thank Professor Dr. Praneet Opanasopit for her providing the cell member for the dissolution study.

REFERENCES

- Robert A. and Donald D., Diclofenac. [Internet]. 2014 [Cited 11 Oct 2023]. Available form: [https://www.ncbi.nlm.nih.gov/books/NBK557879/ournal Article](https://www.ncbi.nlm.nih.gov/books/NBK557879/ournal%20Article)
- Jean-Luc K., Systemic bioavailability of topical diclofenac sodium gel 1% versus oral diclofenac sodium in healthy volunteers. [Internet]. 2009 [Cited 11 Oct 2023]. Available form: Systemic bioavailability of topical diclofenac sodium gel 1% versus oral diclofenac sodium in healthy volunteers - PubMed (nih.gov)
- Nagalakshmi R., Formulation and Evaluation of Medicated Analgesic Sticks. [Internet]. 2017 [Cited 11 Oct 2023]. Available form: <https://zenodo.org/records/1036422>
- GOHEL M. C. and NAGORI S. A., Resolving Issues of Content Uniformity and Low Permeability Using Eutectic Blend of Camphor and Menthol, Indian Journal of Pharmaceutical Sciences, November - December 2009: 622- 629
- Phaechamud T., Tuntarawongsa S., and Caressas P., Evaporation Behavior and Characterization of Eutectic Solvent and Ibuprofen Eutectic Solution., AAPS Pharm Sci Tech, Vol. 17, No. 5, October 2016 (# 2015), 1213-1220
- Christianah M.A. and Pui-Kai Li, Diclofenac Sodium, Analytical Profile of Drug Substances, Academic Press., Inc, The Squibb Institute for Medical Research New Brunswick, New Jersey, vol 19,1990, p 123-144
- Paul F. F.,The Limits of X-ray Diffraction Theory, Crystals 2023, 13(3), 521; <https://doi.org/10.3390/cryst13030521>
- Maja K., Marija M., Marjan V. and et al., Study of Physicochemical parameters affecting the releases of diclofenac sodium from lipophilic matrixtablets, Acta Chim. Slov. 2004, 51, 409–425
- Anita K., Fanni F., and Attila G. et al, Formulation and investigation of hydrogels containing an increased level of diclofenac sodium using risk assessment tools, European Journal of Pharmaceutical Sciences 193 (2024) 106666

Thermal Treated Mung Bean Starch Used as Binder and Disintegrant in Wet Granulation Tablet

Thaksaphon Renu¹, Thanaporn Promma¹, Papichaya Kulwichien¹, Chanunchida Sangchart¹, Padungkwan Chitropas², and Wanassnant Kajthunyakarn^{3,*}

¹Pharmacy student, Faculty of Pharmaceutical Sciences, Khon Kaen University, THAILAND

²Division of Pharmaceutical Technology, Faculty of Pharmaceutical Sciences, Khon Kaen University, THAILAND

³Department of Pharmaceutical Technology, Faculty of Pharmacy, Srinakharinwirot University, THAILAND

*Corresponding author Email: wanassnant@gmail.com

Abstract. Starch is widely used as an excipient in tablets produced by wet granulation. The objective of this study was to evaluate the properties of thermally treated mung bean starch (MMBS) as a binder and a disintegrant in tablet formulations, comparing its effectiveness with commercial products. The results indicated that MMBS exhibited higher swelling capacity and viscosity compared with unmodified mung bean starch. For the binder evaluation, lactose monohydrate was used as a filler. Increasing the MMBS concentration (1-5%) led to enhanced tablet hardness and prolonged disintegration, while reducing friability. Remarkably, tablets containing 3% MMBS showed a higher hardness/friability disintegration time ratio (HFR/DT index). Therefore, 3% MMBS was selected as the optimal binder concentration for comparison with other binders. The hardness and disintegration time of tablets containing MMBS were lower than those of tablets containing polyvinylpyrrolidone K30 (PVP-K30) and starch 1500[®]. Drug release of MMBS tablets was superior to those containing PVP-K30 and Starch 1500[®] as binders. In the disintegrant evaluation, dibasic calcium phosphate was used as a filler. Tablets formulated without a disintegrant did not disintegrate. Disintegration times for tablets containing 1%, 3%, and 5% MMBS were less than 8, 3, and 1 minute, respectively. Therefore, 3% MMBS was selected for comparison with other disintegrant. Disintegration time of tablets containing MMBS was longer than that of those containing EXPLOTAB[®]. Drug (hydrochlorothiazide) release of tablets containing MMBS was comparable to those containing EXPLOTAB[®] as a disintegrant. In conclusion, MMBS is a promising binder and disintegrant for tablets produced by wet granulation.

Keywords: Thermal modification; Mung bean starch; Binder; Disintegrant; Tablet

INTRODUCTION

Mung bean starch (MBS) is obtained from *Vigna radiata*, which is grown in Thailand. Native starch exhibits a high swelling factor and high viscosity in hot water [1-3]. These properties limit its use in wet granulation tablets. Therefore, modification of starch is essential to enhance its properties. Thermally treated mung bean starch (MMBS), a physically modified starch derived from MBS, is particularly interesting for use as an excipient in tablet formulations, especially as a binder and disintegrant. The objective of this study was to evaluate the properties of MMBS as a binder and disintegrant in tablet formulations, comparing its effectiveness with commercial products.

MATERIALS AND METHODS

Materials

Hydrochlorothiazide was purchased from Suzhou ausun chemical Co., Ltd. (China). Native MBS was purchased from Sitthinan Co., Ltd. (Thailand). Lactose monohydrate was purchased from VWR BDH chemical Co., Ltd. (Belgium). Dibasic calcium phosphate was purchased from Maxway Co., Ltd. (Thailand). Pregelatinized starch (Starch 1500[®]) and sodium starch glycolated (EXPLOTAB[®]) were purchased from Rama Production Co., Ltd. (Thailand). Magnesium stearate was purchased from Fluka Chemika Co., Ltd. (Switzerland). Polyvinylpyrrolidone K30 (PVP-K30), hydrochloric acid (RCI Labscan), sodium hydroxide (RCI Labscan), potassium dihydrogen orthophosphate (Kemaus) were purchased from RPC Intertrade Co., Ltd. (Thailand).

Methods

Preparation of MMBS

Native MBS was dispersed in deionized water (DI water) to achieve a concentration of 5 % w/w. After that, it was heated at 80 °C for 5 minutes. The dispersion was cast onto a tray and dried in a hot air oven until it was completely dry. Then the dried starch was milled and passed through a sieve with a mesh size no.100, resulting in what was called MMBS. The MMBS was kept in a desiccator at room temperature.

Characterization of MMBS

Swelling property

MMBS was studied for its swelling properties in three media: DI water, 0.1 N hydrochloric acid (0.1 N HCl), and phosphate buffer pH 6.8 (PPB pH 6.8). One gram of MMBS was weighed, placed in a cylinder and the initial volume was recorded, followed by the addition of the medium until the total volume reached 10 mL. The swelling of MMBS was measured at 1, 5, 15, 30, 45, and 60 minutes. The swelling capacity of MMBS was compared with that of Starch 1500[®], PVP-K30 and EXPLOTAB[®]. Swelling capacity was calculated using the following equation (n=3):

$$\text{swelling capacity} = \frac{\text{swelling volume} - \text{initial volume}}{\text{initial volume}} \times 100 \quad (1)$$

Viscosity property

The viscosity of MMBS was investigated in three media: DI water, 0.1 N HCl, and PPB pH 6.8. The MMBS was weighed, prepared at a concentration of 5 %w/w in each medium, then continuously stirred for 30 minutes until completely swollen. The MMBS dispersions were measured using a Brookfield viscometer compared with those of Starch 1500[®], PVP-K30 and EXPLOTAB[®] (n=3).

Effect of MMBS concentrations used as a binder

Tablet preparation

The tablets were prepared using a wet granulation technique, utilizing a hydraulic press machine set to 160 kgf/cm². Lactose monohydrate served as a diluent, while magnesium stearate was used as a lubricant at a concentration of 1%. MMBS, dispersed in DI water to a concentration of 15 %w/w was used as binder solution. The binder solution was added to the diluent to achieve 0, 1, 3, and 5 %w/w of MMBS in the tablet formulation. Each tablet weighed a total of 400 mg.

Following preparation, the tablets were evaluated for uniformity of weight, thickness, hardness, friability, disintegration time, and the hardness/friability disintegration time ratio (HFR/DT index). Additionally, PVP-K30 and Starch 1500[®], both commercial products, were prepared at a concentration of 3% to compare their binding properties with MMBS. The tablets used for comparison with commercial products contained 25 mg of hydrochlorothiazide (HCTZ) as the active pharmaceutical ingredient.

Drug release

Tablets containing 0% and 3% binder were selected for drug release studies. *In vitro* drug release from the tablets was assessed using the USP dissolution apparatus I (basket method) with 900 mL of dissolution medium. The dissolution medium consisted of 0.1 N HCl and phosphate buffer pH 6.8 (PPB pH 6.8). The temperature of the system was maintained at 37.0 ± 0.5 °C, and the baskets were rotated at 100 rpm. The dissolution test was conducted until complete drug release was achieved. The HCTZ concentration was analyzed by UV-Visible spectrophotometer at a wavelength of 272 nm.

Effect of MMBS concentrations used as a disintegrant

Tablet preparation

The tablets were prepared using a wet granulation method with a hydraulic press machine set to 80 kgf/cm². The total weight of the tablets was 400 mg per tablet. The tablets consisted of dibasic calcium phosphate as a filler, and magnesium stearate (1%) as a lubricant. MMBS in varying concentrations of 0%, 1%, 3%, and 5% were chosen as extra-granular disintegrants in the tablets. After preparation, the tablets were evaluated for uniformity of weight (n = 20), thickness (n = 10), hardness (n = 10), friability (not less than 6.5 g), and disintegration time (n = 3). Commercial disintegrants at 3% concentration, Starch 1500[®] and EXPLOTAB[®], were evaluated for comparison with MMBS. HCTZ (25 mg) was also added to the tablets used for comparison with commercial disintegrants.

Drug release

To study the effect of disintegrant on drug release, tablets containing 0% and 3% disintegrants (MMBS, Starch 1500[®] and EXPLOTAB[®]) were evaluated using the USP dissolution apparatus I (basket method) with 900 mL of dissolution medium (n = 3). The dissolution medium and *in vitro* study conditions were based on the evaluation of MMBS as a binder during drug release.

Statistical analysis

All data are represented as mean ± standard deviation (SD). The statistical analysis was performed using one-way ANOVA with the least significant difference (LSD) for multiple comparisons. The significance of the difference was determined by 95% confidence interval ($p < 0.05$).

RESULTS AND DISCUSSION

Characterization of MMBS

MMBS was prepared by heating the mung bean starch suspension. The viscosity and swelling properties of MMBS are greater compared to unmodified mung bean starch. The viscosity of 5 % w/w MMBS in DI water, 0.1 N HCl, PPB pH 6.8 ranged from 10 to 14 cps. The swelling of MMBS in DI, 0.1 N HCl, PPB pH 6.8 were approximately 6.8, 3.5, and 11.8 times, respectively. In hot water, hydrogen bonds between starch molecules were disrupted, resulting in swelling and the formation of a sticky starch gel. Thus, MMBS was suitable for use as a binder and disintegrant in wet granulation tablets.

Effect of MMBS concentration used as a binder

For the binder evaluation, the results are shown in Table 1 and 2 and Figure 1. MMBS (1-5 % w/w in the tablets) was used as a binder in lactose monohydrate tablets. With increasing concentrations of MMBS, tablet hardness increased while friability decreased. The disintegration time of tablet containing 1-3 % MMBS was shorter ($p < 0.05$) than that of tablets without MMBS due to the swelling property of MMBS [4]. At 5 % MMBS, the disintegration time was the longest ($p < 0.05$), attributed to its viscosity. In general, the binder enhanced binding properties and reduced disintegration time. Therefore, the hardness /friability disintegration time ratio (HFR/DT index) should be considered. Based on this, 3% MMBS, which had the highest HFR/DT index, was selected as the optimal binder concentration for comparison with commercial binders. The hardness of tablets containing MMBS was lower than those tablets containing PVP-K30 and Starch 1500®. Moreover, the MMBS-containing tablet provided the shortest disintegration time. This result was due to the swelling properties of MMBS being higher than that of Starch 1500® [5]. However, PVP-K30 might have dissolved in water. Dissolution testing was performed using 0.1 N HCl and PPB pH 6.8 as medium. The drug release from HCTZ tablets containing MMBS was significantly superior to that from tablets using PVP-K30 and Starch 1500® as binders, especially in acidic condition. These results suggested that MMBS has potential for use as a binder in wet granulation tablet formulations.

Table 1. Effect of MMBS concentration used as a binder on the physical properties of lactose monohydrate tablets

Properties of tablets	Concentration of MMBS			
	0%	1%	3%	5%
Uniformity of weight (mg \pm SD)	398.3 \pm 0.5	397.4 \pm 1.7	398.2 \pm 0.9	398.9 \pm 0.6
Thickness (mm \pm SD)	3.56 \pm 0.02	3.56 \pm 0.01	3.58 \pm 0.02	3.57 \pm 0.02
Hardness (kP \pm SD)	11.2 \pm 0.6	12.8 \pm 0.9	19.0 \pm 1.2	21.0 \pm 1.6
Friability (%)	0.68	0.70	0.34	0.37
Disintegration time (min \pm SD)	8.87 \pm 3.06	3.63 \pm 0.68	2.23 \pm 0.11	16.74 \pm 1.23
HFR/DT index	1.85	5.04	25.01	3.38

Table 2. Effect of different binder types on physical properties of HCTZ tablets using lactose monohydrate as a diluent

Properties of tablets	Types of binders (3% in tablet)			
	No binder	MMBS	PVP-K30	Starch 1500®
Uniformity of weight (mg \pm SD)	399.2 \pm 0.4	399.0 \pm 0.5	399.8 \pm 0.6	399.5 \pm 0.6
Thickness (mm \pm SD)	3.55 \pm 0.01	3.54 \pm 0.01	3.52 \pm 0.02	3.54 \pm 0.02
Hardness (kP \pm SD)	8.8 \pm 0.9	15.8 \pm 1.4	21.0 \pm 1.2	17.7 \pm 1.9
Friability (%)	0.84	0.34	0.35	0.35
Disintegration time (min \pm SD)	21.06 \pm 0.79	7.31 \pm 1.08	22.24 \pm 0.98	> 30
HFR/DT index	0.5	6.36	2.70	NA

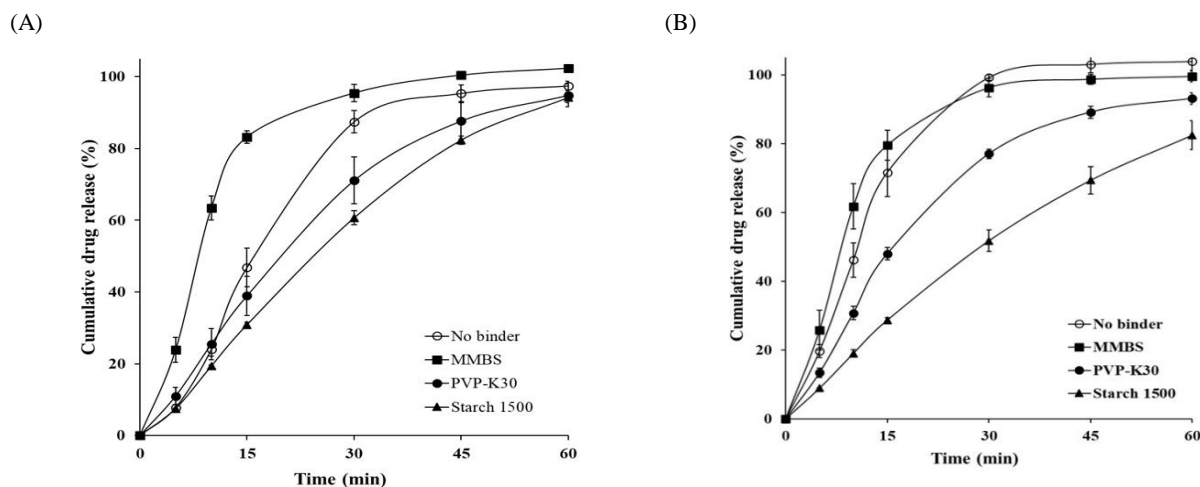


Figure 1. Dissolution profiles of HCTZ tablets containing various types of binders (3 %w/w in tablet): (A) in 0.1 N HCl and (B) in PPB pH 6.8

Effect of MMBS concentration used as a disintegrant

For the disintegrant evaluation, the results are presented in Table 3 and 4 and Figure 2. MMBS (1-5 % w/w in the tablets) was incorporated as an extragranular disintegrant in dibasic calcium phosphate tablets. Typically, tablets formulated with dibasic calcium phosphate exhibit low hardness, high friability, and fail to disintegrate in deionized water. MMBS, due to its swelling properties, was investigated as a potential disintegrant. As the concentration of MMBS increased, tablet hardness slightly decreased ($p > 0.05$), while disintegration time significantly decreased ($p < 0.05$). The disintegration times for tablets containing 1%, 3%, and 5% MMBS were 7.75 ± 0.91 , 2.87 ± 0.75 , and 0.90 ± 0.42 minutes, respectively. Based on these results, 3% MMBS was selected for comparison with commercial disintegrants. The disintegration times for tablets containing 3% MMBS, EXPLOTAB[®], and Starch[®] 1500 were 1.37 ± 0.35 , 0.63 ± 0.22 , and 1.73 ± 0.58 minutes, respectively. Drug release from tablet using dibasic calcium phosphate as a filler depended on both the solubility of the filler in the dissolution medium and the swelling ability of the disintegrant^[6,7]. Drug release from HCTZ tablets containing disintegrants was significantly higher than those without disintegrant. Additionally, the drug release of tablets containing MMBS was comparable to that of tablets containing EXPLOTAB[®]. These results suggest that MMBS shows potential as an effective extra-granular disintegrant in wet granulation tablet formulations.

Table 3. Effect of MMBS concentration as a disintegrant on the physical properties of dibasic calcium phosphate tablets

Properties of tablets	Concentration of MMBS			
	0%	1%	3%	5%
Uniformity of weight (mg \pm SD)	398.3 \pm 0.6	398.1 \pm 0.7	397.7 \pm 2.7	398.8 \pm 0.6
Thickness (mm \pm SD)	2.66 \pm 0.04	2.67 \pm 0.01	2.70 \pm 0.02	2.73 \pm 0.04
Hardness (kP \pm SD)	3.3 \pm 0.3	3.2 \pm 0.2	2.8 \pm 0.2	2.6 \pm 0.4
Friability (%)	2.92	2.17	2.17	2.62
Disintegration time (min \pm SD)	> 30	7.75 \pm .091	2.87 \pm 0.75	0.90 \pm 0.42

Table 4. Effect of types of disintegrants on the physical properties of HCTZ tablets using dibasic calcium phosphate as a diluent

Properties of tablets	Types of disintegrants (3% in tablet)			
	No disintegrant	MMBS	EXPLOTAB [®]	Starch 1500 [®]
Uniformity of weight (mg \pm SD)	398.3 \pm 0.6	398.8 \pm 0.9	398.7 \pm 0.5	398.8 \pm 0.5
Thickness (mm \pm SD)	2.69 \pm 0.01	2.73 \pm 0.01	2.71 \pm 0.03	2.72 \pm 0.02
Hardness (kP \pm SD)	3.5 \pm 0.2	3.0 \pm 0.3	3.4 \pm 0.2	3.0 \pm 0.3
Friability (%)	2.29	2.46	1.96	2.05
Disintegration time (min \pm SD)	> 30	1.37 \pm 0.35	0.63 \pm 0.22	1.73 \pm 0.58

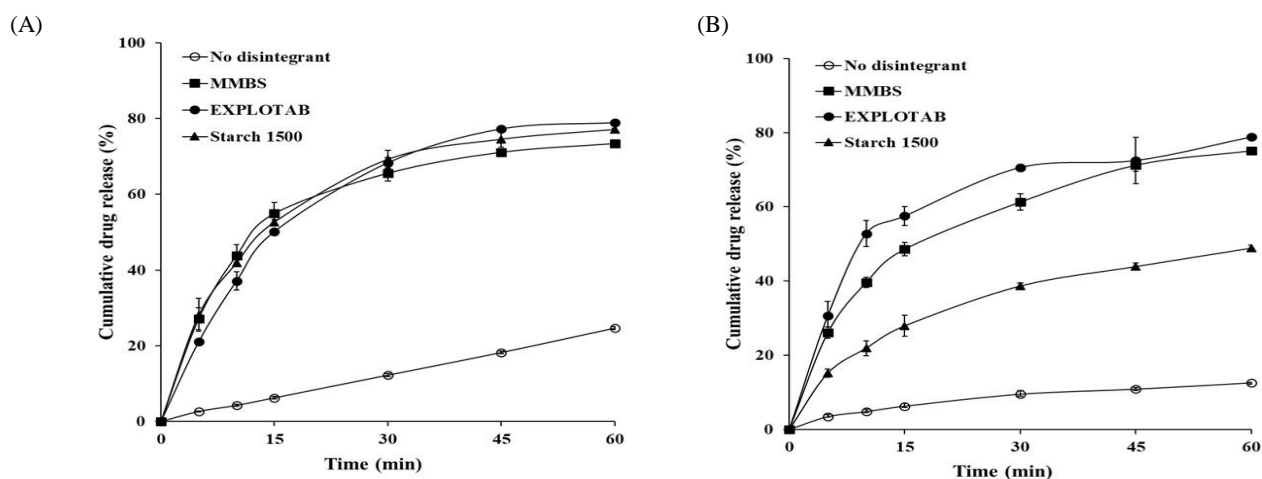


Figure 2. Dissolution profiles of HCTZ tablets containing various types of disintegrants (3 % w/w in tablet): (A) in 0.1 N HCl and (B) in PPB pH 6.8

CONCLUSIONS

MMBS was prepared by thermal modification of mung bean starch. It exhibited high swelling and viscosity properties, making it suitable for use in wet granulation tablets, particularly as a binder and disintegrant. A concentration of 3% MMBS was found to be optimal for comparison with commercial binders. The HCTZ tablets containing 3% MMBS exhibited the shortest disintegration time compared to those with commercial products. Furthermore, the drug release from the MMBS tablets was faster than that of tablets formulated with other binders in both 0.1 N HCl and PPB pH 6.8. In the disintegrant study, MMBS was used as an extra-granular disintegrant and compared with commercial disintegrants. The disintegrant properties of MMBS were comparable to those of the commercial products, which may be attributed to the solubility of the filler and the swelling properties of disintegrant in the dissolution medium. In conclusion, MMBS exhibits potential as an excipient for use in wet granulation tablets intended for immediate-release formulations.

ACKNOWLEDGMENTS

This research would not have been possible without the help and support of Assist.Prof. Padungkwan Chitropas, whose extensive scientific knowledge guided me throughout the project. I would also like to thank Mr. Chiravut Pathumthanasup and Mr. Att Meephairin, officers at Faculty of Pharmaceutical Sciences, for their valuable technical assistance. Special thanks are extended to Dr. Sansanee Pongwai for her diligent assistance in language refinement and proofreading of this manuscript.

REFERENCES

1. Hoover R, Li Y, Hynes G, Senanayake N. Physicochemical characterization of mung bean starch. *Food Hydrocoll.* 1997; 11(4): 401-408.
2. Halim A, Torley PJ, Farahnaky A, Majzoobi M. Investigating the effects of acid hydrolysis on Physicochemical properties of Quinoa and Faba Bean starches as compared to Cassava starch. *Foods.* 2024; 13 (23): 3885.
3. Hoover R, Vasanthan T. Effect of heat-moisture treatment on the structure and physicochemical properties of cereal, legume, and tuber starches. *Carbohydr Res.* 1994; 252: 33-53.
4. Thanaketsapaisarn O, Sethabouppha B, Phadungpattanakoon N, Jantakat A. Comparative study on binding capacity of some natural binders using paracetamol tablet produced by wet granulation method as a model. *Int J Pharm Sci.* 2017; 13.
5. Mimura K, Kanada K, Uchida S, Yamada M, Namiki N. Formulation study for orally disintegrating tablet using partly pregelatinized starch binder. *Chem Pharm bull.* 2011; 59 (8): 959-964.
6. Boonwatcharapan Y, Srisuk P, Palladino P, Sutthiparinyanont S, Chitropas P. Preparation and evaluation of alcohol-alkaline-treated Rice starch as a tablet disintegrant. *Trop J Pharm Res.* 2016; 15 (2): 221-229.
7. Pathumthanasup C, Srisuk P, Chitropas P. Microwave-treated glutinous rice starch as a tablet binder. *Thai Pharm Health Sci J.* 2020; 15(2): 75-80.

Preformulation Study of Montelukast Sodium for the Development of Chewable Tablets

Sinatinee Dulalumpa¹, Wanchai Chongcharoen¹, Narueporn Sutanthavibul^{1,}*

¹Faculty of Pharmaceutical Sciences, Chulalongkorn University, Bangkok, Thailand

*Corresponding author Email: dmee9559@gmail.com

This research aims to obtain preformulation data of montelukast sodium (MTKs) for the development of MTKs chewable tablets. The study is important to assess stability, excipients compatibility, and optimize heat and moisture conditions during tablet manufacturing. Powder X-ray diffraction (PXRD) analysis demonstrates an amorphous structure of MTKs raw material. Stability under high temperature and humidity was tested. The MTKs samples were exposed to heat (70°C for 12 hours), moisture (dispersed in water and dried), and both (80°C over a water bath for 4 hours). The USP 2023 HPLC method was subsequently applied to evaluate impurities in MTKs and perform a PXRD analysis. PXRD results demonstrated that the solid-state morphology of MTKs remained unchanged, whereas HPLC results indicated increased levels of impurities. Specifically, samples exposed to both conditions showed 0.08% sulfoxide and 0.07% montelukast ketone impurities. Compatibility, MTKs were mixed with various excipients in specified ratios and conditions. Mixtures included 1:1 at 70°C for 24 hours with mannitol, microcrystalline cellulose, hydroxypropyl cellulose, croscarmellose sodium, sodium starch glycolate, acesulfame potassium (ACE-K); 1:100 at 70°C for 24 hours with erythrosine, sunset yellow; 1:100 at 30°C for 24 hours with magnesium stearate, orange and strawberry flavor. Analyses were performed using FT-IR and HPLC. All samples exhibited identical FT-IR spectral as the initial. However, HPLC results indicated potential increases in impurities with ACE-K. In conclusion MTKs can be formulated into a chewable tablet with careful consideration of using ACE-K sweetener and exposure to heat, moisture during processing, as it affects the stability and overall quality of the final product.

Keywords: Montelukast sodium; Chewable tablet; Powder X-ray diffraction; Amorphous

INTRODUCTION

Montelukast sodium, first approved by the US FDA in 1998 under the brand name Singulair, remains widely used globally, including in Thailand. It is a leukotriene receptor antagonist used for prophylaxis and chronic treatment of asthma ⁽¹⁾, prevention of exercise-induced bronchoconstriction ⁽²⁾, relief of symptoms of allergic rhinitis both seasonal and perennial ⁽³⁾ in adults and pediatric patients. The recommended dose for patients aged 6 to 14 years is 5 mg, available as chewable tablets. Caution is advised for patients with phenylketonuria, as these tablets contain phenylalanine (Aspartame) ⁽⁴⁾. The chemical structure of MTKs is 2[1-[(R)-[3-[2(E)-(7-chloroquinolin-2-yl) vinyl] phenyl]-3-[2-(1-hydroxy-1-methylethyl) phenyl]propyl-sulfanylmethyl] cyclopropyl] acetic acid sodium salt (Fig. 1), the molecular formula C₃₅H₃₆ClNO₃Na. It is white to off-white hygroscopic powder, freely soluble in ethanol, methanol and water.

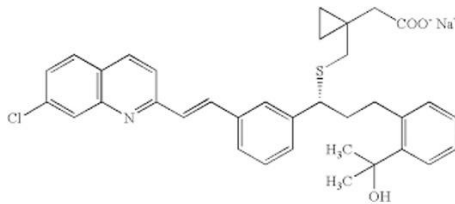


Figure 1. Chemical structure of MTKs

The previous study examined the effects of light and heat on the stability of montelukast in solution and solid forms. It found that montelukast is unstable in solution, with the best stability in 70% methanol. Light exposure leads to the formation of montelukast *cis*-isomer in both solution and solid forms, with UV light having the most significant effect, while neon light has no effect. In solid form was found to be stable at 65°C for 70 days, with more than 99% of the montelukast remaining. Only sulfoxide impurity was detected, at a level of 0.2%. Additionally, the presence of hydrogen peroxide clearly results in sulfoxide impurity ⁽⁵⁾. The United States Pharmacopeia (USP) official monograph for montelukast sodium chewable tablet describe the HPLC method for the test of impurities where seven impurities were reported. Among them the sulfoxide, montelukast ketone and *cis*-isomer were calculated the percentage ⁽⁶⁾. This research aims to gather preformulation data for developing montelukast sodium chewable tablets, focusing on various excipients as an option for the formulators, especially the sweetener Ace-K which could be a choice

for phenylketonuria patients. The study is crucial to assessing drug-exipient compatibility, stability, effect of heat and moisture conditions to select the suitable manufacturing process.

MATERIALS AND METHODS

Materials

Pharmaceutical grade Montelukast sodium (Zhejiang Tianyu Pharmaceutical, China), manitol (SPI Pharma, U.S.A.), hydroxypropyl cellulose (Ashland, U.S.A.), microcrystalline cellulose 101 (Accent, India), croscarmellose sodium (Mingtai Chemical, Taiwan), sodium starch glycolate (DFE Pharma, Germany), magnesium stearate (FACI Asia Pacific, Singapore), strawberry and orange powder (T.Hasegawa, Japan), erythrosine CI45430 (Adinop, Thailand), sunset yellow (Sensient Colors S.A., Mexico), acesulfame potassium (Anhui Jinhe Industrial, China), acetonitrile and methanol HPLC grade (Duksan, Republic of Korea), trifluoroacetic acid AR grade (Thermo Fisher Scientific, U.K.)

Methods

Sample preparation

Stability testing of MTKs under high temperature and humidity. It is widely recognized that thermal and humidity conditions play an important role in the tablet manufacturing process. Therefore, this study investigates the stability of MTKs by subjecting them to a temperature of 70 °C and moisture level of 25% for 12 hours, following the most rigorous granule drying standards employed in the industry. Initially, the study examines each factor independently, followed by an investigation of the combined effects of both factors. However, due to the limitations of the equipment and the time constraints in studying both factors simultaneously, stress conditions were chosen instead. Specifically, the experiment was conducted by subjecting the sample to a temperature of 80 °C and a moisture level of 25% in a water bath for 4 hours. The samples were prepared as follows:

For heat condition, the MTKs samples were wrapped with aluminum foil and heat in hot air oven at 70°C for 12 hours. For moisture condition, MTKs powder 10 g were mixed with water 2.5 ml, protected from light and dried at control room temperature (25°C) for 12 hours. For a combination of both heat and moisture condition, MTKs powder 10 g were mixed with water 2.5 ml in the crucible then placed in a water bath at 80°C for 4 hours.

Compatibility study, MTKs were physically mixed with various excipients in specified ratios and conditions. The selection of the proportion and the conditions tested are based on the use of substances in chewable tablet formulations, using quantities exceeding the maximum amount to clearly observe compatibility and the related manufacturing processes.

Mixtures included MTKs physical mixed in ratio 1:1 at 70°C for 24 hours with mannitol, microcrystalline cellulose, hydroxypropyl cellulose, croscarmellose sodium, sodium starch glycolate, acesulfame potassium (ACE-K); 1:100 at 70°C for 24 hours with erythrosine, sunset yellow; 1:100 at 30°C for 24 hours with magnesium stearate, orange and strawberry flavor.

Powder X-ray diffraction (PXRD) analysis

The Rigaku MiniFlex II powder diffractometer and Rigaku's D/teX Ultra 1D silicon strip detector with condition scan angle (2 θ) 1° to 50° continuous. The sample of MTKs powder and all three samples from the stability testing of MTKs under high temperature and humidity were prepared into powder by carefully grinding in the ceramic mortar then spread and pressed on the glass slide. The PXRD patterns were recorded and analyzed.

HPLC analysis

HPLC method and calculation for the test of impurities was proceeded as directed in the USP 2023 official monograph for montelukast sodium chewable tablet. Preparing the sample solution (for 5-mg chewable tablets) nominally 0.25 mg/ml of montelukast. A high-performance liquid chromatograph system 1290 Infinity II (Agilent, USA.) with photodiode array detector with Agilent OpenLab CDS ChemStation software, column C18 XBridge BEH Phenyl 100 x 4.6 mm, 3.5 μ m, (Waters, USA.) were used.

Fourier Transform Infrared Spectroscopy (FT-IR)

Using the FT/IR-4100 (Jusco, UK) to analyze compatibility study on sample of MTKs and all excipients. The sample was mixed with KBr and pressed to obtain disc then scan under wavenumber [cm^{-1}] Start 650 to 3800 cm^{-1} with resolution of 4 cm^{-1} . The FT-IR spectra were recorded.

RESULTS AND DISCUSSION

Results

Powder X-ray diffraction (PXRD) analysis demonstrates an amorphous structure of MTKs raw material (Fig.2). The obtained PXRD pattern exhibits broad, diffused peaks or "halos" instead of sharp, distinct peaks typically observed in crystalline substances⁽⁷⁾. The MTKs samples exposed to heat, moisture and the combination of both conditions, PXRD results of all samples showed unchanged in MTKs solid state morphology (Fig.3) the PXRD patterns were comparable to the MTKs raw material. While HPLC tested impurities results indicated increased impurities (0.08% sulfoxide, 0.07% montelukast ketone) in samples exposed to both conditions (Table 1).

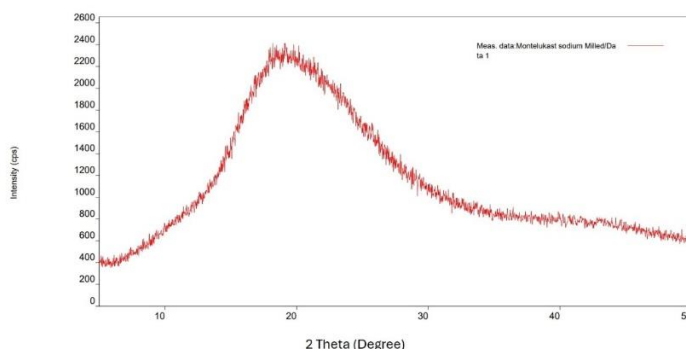


Figure 2. Powder X-ray diffraction (PXRD) pattern of MTKs raw material.

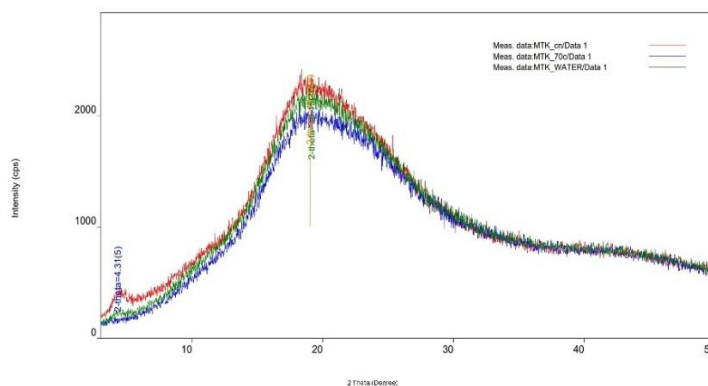


Figure 3. Powder X-ray diffraction (PXRD) pattern of; blue graph obtained from the MTKs sample treated by heat condition (70°C for 12 hours), green graph obtained from the MTKs treated by moisture condition (mixed with water and dried), red graph, the MTKs treated by both heat and moisture conditions (80°C in water bath for 4 hours).

Table 1. HPLC analysis results of MTKs samples testing the effect of heat and moisture conditions

Condition / MTKs Treated by	% Assay	% of impurities observed
Control sample	100.27	Not detected
Heat / 70°C for 12 h	99.47	Not detected
Moisture / mixed with water and dried for 12 h	99.27	MTK ketone (0.03%)
Both heat and moisture / 80°C in a water bath for 4 h	99.55	Sulfoxide (0.08%), MTK ketone (0.07%)

Compatibility study, the analysis results were obtained using FT-IR and HPLC. All samples exhibited identical FT-IR spectral as the initial. However, HPLC results indicated potential increases in impurities with ACE-K (Fig.4). The obtained chromatograms were summarized as the identified peak and its retention time (Table 2).

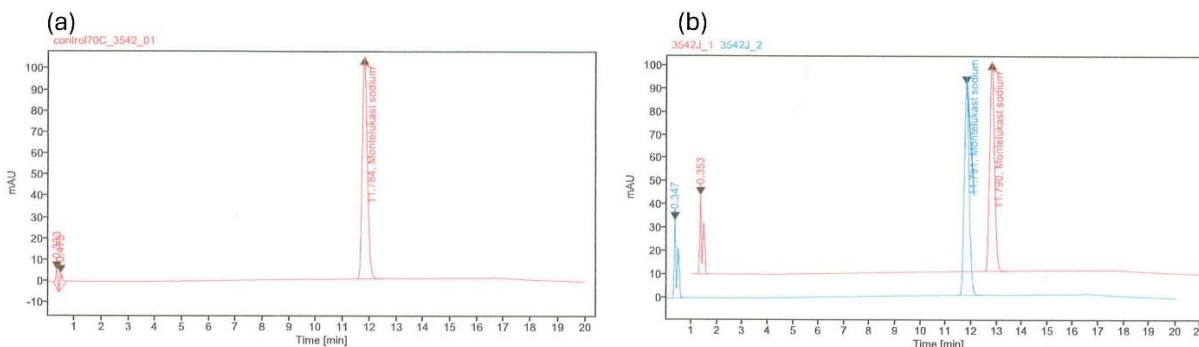


Figure 4. (a) HPLC chromatogram of MTKs at 70°C for 24 h. (b) HPLC chromatograms of mixture MTKs with ACE-K at 70°C for 24 h obtained from 2 replicated sample injections.

Table 2. Peaks obtained from HPLC chromatograms of compatibility samples testing

Substances	MTKs physical mixed ratio	Storage condition	Peak identified / Retention time (min)
MTKs control_01	-	70°C for 24 h	MTKs / 11.784
MTKs control_02	-	30°C for 24 h	MTKs / 11.385
Mannitol	1:1	70°C for 24 h	MTKs / 11.810
MCC 101			MTKs / 11.818
Hydroxypropyl cellulose			MTKs / 11.817
Croscarmellose sodium			MTKs / 11.810
Sodium starch glycolate			MTKs / 11.803
ACE-K			MTKs/11.790, unknown impurity/0.35
Erythrosine	1:100	70°C for 24 h	MTKs / 11.790
Sunset yellow			MTKs / 11.789
Magnesium stearate	1:100	30°C for 24 h	MTKs / 11.383
Orange flavor			MTKs / 11.390
Strawberry flavor			MTKs / 11.390

Discussions

The previous study found that the impurities sulfoxide and montelukast ketone were formed through oxidation and hydrolysis mechanisms ⁽⁸⁾. Increased levels of both impurities under heat and moisture exposure indicate that heat contributes to the rise of these impurities. This information is useful for understanding the conditions leading to higher impurity levels and can assist in optimizing process parameters during tablet manufacturing to reduce these effects. Furthermore, the use of antioxidants might benefit reducing sulfoxide impurity in formulation. In compatibility study, the mixture containing ACE-K showed increased impurity, which may be caused by excessive usage. Typically, the sweetener is used in chewable tablets at a lower amount than what was tested. Therefore, further experiments should be conducted.

CONCLUSIONS

In conclusion, MTKs can be formulated into a chewable tablet with careful consideration of using Acesulfame Potassium (ACE-K) as a sweetener and controlling exposure to heat and moisture during processing when the wet granulation is selected. The study confirmed that both thermal and humidity conditions significantly impact the stability of MTKs during the tablet manufacturing process. However, further research is required for formulation, including determining the suitable amount of ACE-K, selecting appropriate antioxidants, optimizing and monitoring critical process parameters, choosing suitable packaging and product stability evaluating to ensure consistent stability of the chewable tablets.

ACKNOWLEDGMENTS

This research was funded by Vesco Pharmaceutical Co., Ltd. and the Higher Education for Industry Consortium (Hi-FI) project collaboration with the Industrial Pharmacy Program, Chulalongkorn University.

REFERENCES

1. Sánchez G, Buitrago D. Effect of Montelukast 10 mg in Elderly Patients with Mild and Moderate Asthma Compared with Young Adults. Results of a Cohort Study. *Open Respir Med J.* 2018; 12:67-74.
2. de Benedictis FM, Vaccher S, de Benedictis D. Montelukast sodium for exercise-induced asthma. *Drugs Today (Barc).* 2008 Nov;44(11):845-55.
3. Krishnamoorthy M, Mohd Noor N, Mat Lazim N, Abdullah B. Efficacy of Montelukast in Allergic Rhinitis Treatment: A Systematic Review and Meta-Analysis. *Drugs.* 2020 Nov;80(17):1831-1851.
4. <https://www.ncbi.nlm.nih.gov/books/NBK459301/>
5. Mahmoud M. Al Omari, et al. Effect of light and heat on the stability of montelukast in solution and in its solid state. *Journal of Pharmaceutical and Biomedical Analysis.* 2007;45: 465 - 471.
6. Montelukast sodium chewable tablet monograph. In: United States Pharmacopeia [Internet]. 43rd ed. Rockville, MD: USP Convention; 2023 [cited 2023 Aug 1]. Available from: <https://www.uspnf.com>
7. Bates S, Zografi G, Engers D, Morris K, Crowley K, Newman A. Analysis of amorphous and nanocrystalline solids from their X-ray diffraction patterns. *Pharm Res.* 2006 Oct;23(10):2333-49
8. Mohan P, Sharath Babu H, et al. Stability-indicating liquid chromatography method development and validation for impurity profiling of montelukast sodium in bulk drug and tablet dosage form. *Biomedical Chromatography.* 2022;36: e5330.

Development and Evaluation of a Povidone-iodine Throat Spray: Physicochemical Properties and Stability

Suwannee Panomsuk^{1,2}, Phuvamin Suriyaamporn^{1,2}, Korakod Budnampet², Jinnipa Sirinukulpipat², Chayanit Pattanapong², and Malai Satiraphan^{2,3,*}

¹PDGIG Research Group, Faculty of Pharmacy, Silpakorn University, Nakhon Pathom 73000, THAILAND

² Department of Industrial Pharmacy, Faculty of Pharmacy, Silpakorn University, Nakhon Pathom 73000, THAILAND

³ AiM Research Group, Faculty of Pharmacy, Silpakorn University, Nakhon Pathom 73000, THAILAND

*Corresponding author Email: satiraphan_m@su.ac.th

Abstract. Throat spray formulations were specifically used as topical treatments for alleviating sore throat symptoms or disinfecting the oral cavity. These sprays, formulated with diverse active ingredients ranging from chemical drugs to herbal extracts, were widely available. Formulations incorporating povidone-iodine as a key ingredient typically exhibited a relatively high acidity, with a pH of approximately 2. The slightly acidic to neutral pH of the oral cavity makes it prone to irritation from these sprays. This study aimed to develop and optimize a povidone-iodine throat spray formulation, focusing on its physicochemical properties (appearance, spray characteristics, pH, and iodine content) and stability. The effects of formulation components and storage conditions (room temperature and 2-8 °C) on these properties were also evaluated. The study revealed that all tested formulations were effectively delivered as a fine mist via spraying, exhibiting pH values between 3 and 5. Formulation stability was significantly influenced by both processing steps and formulation components. Several factors contributing to higher residual iodine levels included separation of the buffer system, the addition of potassium iodide, the use of a citrate buffer, and low buffer concentration. An 8-week stability study demonstrated that formulations stored at refrigerated temperatures (2-8 °C) exhibited greater stability than those stored at room temperature. In conclusion, this study successfully formulated a povidone-iodine throat spray with desirable physicochemical properties and good stability, achieving a pH range of 3-5, which closely approximates the environment of the oral cavity.

Keywords: Throat spray; Povidone-iodine; Oral cavity; Stability

INTRODUCTION

Pharyngitis, or sore throat, is a common ailment, characterized by symptoms such as pain, irritation, and itchiness of the throat [1] and caused by viral (like rhinovirus, influenza) or bacterial pathogens (particularly *Staphylococcus aureus*, *Streptococcus pyogenes*, and *Pseudomonas aeruginosa*) [2,3]. Povidone-iodine (PVP-I) throat sprays are effective due to their extensive antimicrobial properties, providing rapid relief by targeting the throat's mucosal lining [4]. PVP-I, a biocidal agent, disrupts pathogen replication by binding to cell walls and inhibiting protein synthesis. It's used in various applications, including wound treatment and surgical preparation, and is effective against bacteria, fungi, viruses, and protozoa [5]. With over 30 years of use, PVP-I has shown no toxic report, with free iodine content below 3 ppm.

Current PVP-I formulations include 0.5% mouthwash, 0.5% nasal spray, and 0.45% throat spray [3,4]. Existing throat sprays like Kamillosan® (a blend of herbs), Propoliz® (propolis extract), and Betadine (4.5 mg PVP-I/mL) are available. PVP-I solution in oral medication forms has been listed in current hospital pharmacopeia [6]. The pH of Betadine is around 2.0, aligning with USP standards (pH1.5-6.5) [7]. The pH-stability profile indicated stability within a pH range of 2-4. However, the solution with too acidic might irritate the oral cavity. In a previous study, Lugol's solution formulation for treating patients with Graves' disease was developed and contained 5% PVP-I and 10% potassium iodide (KI), which were mixed and dissolved in distilled water with appropriate pH range [8, 9].

This research aims to develop a PVP-I throat spray with a higher pH, better suited for the oral cavity, and to examine its physicochemical properties (appearance, spray characteristics, pH, and iodine content). The effects of formulation components and stability under different storage conditions (room temperature and 2-8 °C) were also explored.

MATERIALS AND METHODS

Materials

Povidone-iodine (PVP-I), citric acid, glycerine, sodium saccharin (SS), and eucalyptus oil were purchased from P.C.Drug Center Co., Ltd. (Bangkok, Thailand). Sodium phosphate dibasic anhydrous (Na₂HPO₄), potassium iodide (KI), and sodium thiosulphate were purchased from KemAus™ (New South Wales, Australia). Other chemicals and reagents were analytical grade.

Methods

Preparation of PVP-I throat spray

The ingredients listed in Table 1 were used to prepare the PVP-I throat spray. Two preparation methods were employed to observe and compare their effects on physicochemical properties. In the first method (method 1 - direct mixing), only formulations Rx1 and Rx2, all ingredients were dissolved sequentially in water. First, PVP-I and KI were dissolved, followed by the addition of the citrate buffer (citric acid/ Na_2HPO_4), sweetening agents (SS), glycerin, and eucalyptus oil, with continuous stirring until a homogeneous solution was achieved. In the second method (method 2 - separation mixing), for Rx1-Rx4, the process involved three separate beakers. Beaker one contained PVP-I and KI dissolved in water. Beaker two contained the citrate buffer (citric acid/ Na_2HPO_4) dissolved in water. Beaker three contained the remaining ingredients dissolved in water. The contents of beakers two and three were then gently added to beaker one, with continuous stirring. The resulting PVP-I throat sprays, prepared by both methods, were then evaluated for physicochemical properties, including pH, spray ability, and iodine content.

Table 1: The ingredients of PVP-I throat spray formulations.

Formulations	Ingredients (%w/v)							
	PVP-I	Citric acid	Na_2HPO_4	KI	SS	Glycerine	Eucalyptus oil	Water q.s. to
Rx0	0.45	-	-	-	-	-	-	100
Rx1*	0.45	0.50	-	0.23	0.50	5	0.1	100
Rx2	0.45	0.92	1.32	-	0.50	5	0.1	100
Rx3	0.45	0.92	1.32	0.23	0.50	5	0.1	100
Rx4	0.45	0.50	0.72	0.23	0.50	5	0.1	100

* The formulation Rx1 was adjusted to pH 3.5 with a 4% sodium hydroxide solution, while the other formulations were not subjected to this pH adjustment.

Physical appearance and pH measurement of PVP-I throat spray

The physical appearance of each PVP-I throat spray formulation was visually inspected. Formulations exhibiting any signs of incompatibility or precipitation were excluded from further analysis. The pH of each remaining formulation was then measured using a pH meter (Horiba LAQUAtwin, Kyoto, Japan). Finally, each formulation was compared to a control (Rx0). Any formulations demonstrating unstable physical appearance or pH (<2.8) were also excluded.

Spray ability of PVP-I throat spray

The spraying ability of the PVP-I throat spray was evaluated by spraying the formulation onto moistened Kimwipes paper (Kimtech® Science™, Texas, USA), using a modified technique based on the study of Sugibayashi K. et al. Briefly, a single 6 μL spray was dispensed from a distance of 3 cm onto the moistened paper. The diameter of the resulting brown stain, caused by the PVP-I, was then measured to assess the spray's dispersion [10].

Iodine content determination.

Iodine content was quantified using redox titration with an automatic titrator (Metrohm 848 Titrino Plus). A 0.02N sodium thiosulfate solution served as the titrant, and the endpoint was determined potentiometrically using a platinum-calomel electrode system. The sodium thiosulfate titrant was standardized against potassium iodate, a primary standard. A blank titration was also performed. This method leverages the redox reaction between iodine and thiosulfate under controlled conditions to ensure precise iodine quantification [7].

Stability of PVP-I throat spray.

Stability testing of the PVP-I throat spray was performed in amber glass bottles stored at $5 \pm 3^\circ\text{C}$ and $25 \pm 2^\circ\text{C}/60 \pm 5\%$ RH for eight weeks. Following the stability period, the physicochemical properties of each formulation, including physical appearance, spray characteristics, pH, and iodine content, were evaluated [11].

Statistical analyses.

All experimental trials were tested in triplicate. The results are presented as the mean \pm SD. Statistical analysis was conducted using one-way ANOVA, followed by Tukey's HSD post-hoc test for multiple group comparisons. Independent *t*-tests were used for binary comparisons. A *p*-value of less than 0.05 was considered statistically significant. All statistical analyses were performed using Microsoft Excel 2021.

RESULTS AND DISCUSSION

Results

Characteristics of PVP-I throat spray.

Initially, all PVP-I throat spray formulations (Rx1-Rx4) were clear, dark brown solutions, regardless of the preparation method (Figure 1). The control formulation (Rx0) had a pH of 2.80 ± 0.00 . Formulation Rx1, buffered solely with citric acid, was adjusted to a pH of 3.50. In contrast, formulations Rx2-Rx4, buffered with a citrate/phosphate mixture, maintained a pH of approximately 4.00 without any adjustment (Table 2).

Table 2: The characteristics of PVP-I throat spray with different preparation methods. (Day 0)

Formulations	Characteristics of PVP-I throat spray				
	Physical appearance	Incompatibility	pH	Spray diameter (cm)	% initial I ₂ (%w/v)
Rx0	Clear dark brown	No	2.80 ± 0.00	4.90 ± 0.18	0.0482 ± 0.0007
Method 1: Without separation mixing technique					
Rx1	Clear dark brown	No	3.50 ± 0.00	5.30 ± 0.05	0.0463 ± 0.0004
Rx2	Clear dark brown	No	4.00 ± 0.00	4.55 ± 0.31	0.0416 ± 0.0004
Method 2: With separation mixing technique					
Rx1	Clear dark brown	No	3.50 ± 0.00	4.27 ± 0.10	0.0463 ± 0.0000
Rx2	Clear dark brown	No	3.97 ± 0.06	4.48 ± 0.28	0.0420 ± 0.0001
Rx3	Clear dark brown	No	3.97 ± 0.06	5.00 ± 0.18	0.0463 ± 0.0004
Rx4	Clear dark brown	No	3.97 ± 0.06	4.97 ± 0.18	0.0461 ± 0.0002

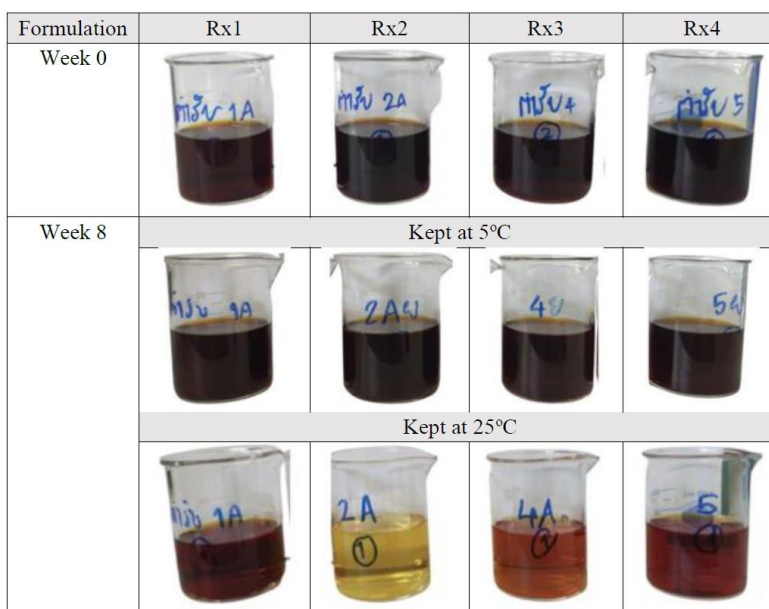


Figure 1. The physical appearance of the PVP-I throat spray prepared by method 2 after 8 weeks of stability testing.

Spray ability of PVP-I throat spray.

The spray ability of the PVP-I throat spray, regardless of the preparation method, exhibited no significant differences across all formulations. This indicates that the sprays were easily dispensed from the nozzle and effectively spread across moistened Kimwipes paper. The spray diameter for each formulation ranged from 4.27 ± 0.10 cm to 5.30 ± 0.05 cm. Detailed spray diameter measurements are presented in Table 2.

Iodine content determination.

The initial iodine percentage of each formulation (at Day 0, Table 2) was determined and defined as 100% iodine remaining to establish a baseline for the stability study.

Stability of PVP-I throat spray.

After eight weeks of stability testing, formulations prepared using method 1 showed unstable physical appearances across both storage conditions, with a color change from clear dark brown to faded brown. In contrast, method 2 formulations remained stable in appearance at 5°C but exhibited a color change to clear light brown or yellow at 25°C (Figure 1). While the pattern of iodine loss was consistent across all formulations, the extent of loss varied. At 5°C, method 2 formulations retained significantly higher percentages of iodine compared to method 1 formulations (Figure 2). Temperature assessment revealed that method 2 formulations stored at 5°C demonstrated superior stability, with iodine retention ranging from $78.19 \pm 0.02\%$ to $85.17 \pm 0.30\%$, compared to those at 25°C (Figure 3). Throughout the stability study, pH and spray ability remained unchanged for all formulations from week zero.

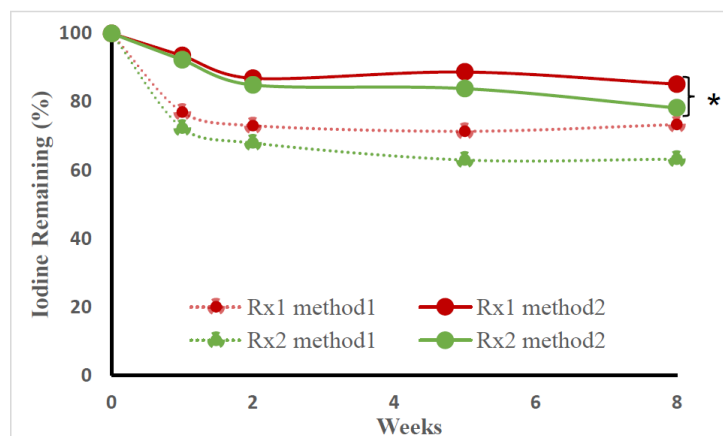


Figure 2. The iodine remaining percentage in the PVP-I throat spray after 8 weeks when prepared by different methods. *indicates a significantly higher percentage of remaining iodine when compared across each formulation ($p < 0.05$).

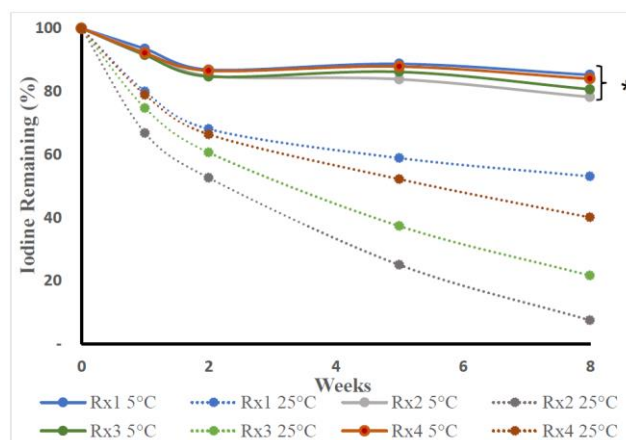


Figure 3. The percentage of iodine remaining in the PVP-I throat spray prepared by method 2 after 8 weeks of stability testing. *indicates significantly higher stability when stored at 5°C compared to being kept at 25°C for each formulation ($p < 0.05$).

Discussions

The developed PVP-I throat spray formulations exhibited suitable physical stability, showing no phase separation (Figure 1). All formulations maintained a mildly acidic pH (3.5 to 4.0) (Table 2), which aligns with USP standards (1.5 to 6.5) for PVP-I solutions, ensuring safety and comfort for the oral and throat cavities [7]. Notably, the pH of these formulations was higher than commercially available PVP-I throat sprays. The formulations demonstrated good spray ability, easily discharging and providing wide coverage within the oral cavity. An optimal spray diameter of 2-8 cm is considered suitable for oral cavity application. Diameters below this range may not reach all areas, while diameters exceeding it may fail to reach deeper sites [10]. Furthermore, iodine content analysis confirmed that the formulation procedures effectively preserved the integrity and therapeutic potency of iodine in the throat sprays [3].

The eight-week stability testing of the PVP-I throat spray revealed significant differences in physicochemical stability based on preparation method (Figure 2) and storage conditions (Figure 3). Formulations prepared using method 1 (direct mixing) showed decreased stability, characterized by a color change from clear dark brown to faded brown and a reduction in iodine content. This suggests potential degradation or reactivity among formulation components during prolonged storage, potentially compromising therapeutic efficacy [12]. The direct mixing of citric acid (acidic) and Na_2HPO_4 (basic) may have led to localized, drastic pH fluctuations, potentially accelerating PVP-I structure hydrolysis and thus reducing iodine content [13]. Method 2, employing a separation mixing technique, addressed this issue by pre-mixing the buffer components to the desired pH before adding them to the PVP-I solution, thus minimizing extreme pH shifts during formulation. Moreover, potassium iodide inclusion is known to enhance PVP-I solution stability (Rx3 VS Rx2), improve iodine solubility and efficacy, and minimize irritation, making it a valuable component in antiseptic formulations [14].

As seen in Figure 3, temperature significantly impacted PVP-I throat spray stability. Formulations stored at 5°C maintained greater stability than those at 25°C. This observation aligns with the understanding that elevated temperatures can accelerate PVP-I degradation, potentially through hydrolysis, leading to reduced iodine content [15]. Notably, the control formulation (Rx0) without any buffer (pH 2.80) exhibited higher initial iodine compared to those with a buffer. This suggests that buffer systems, particularly those with higher pH, might contribute to PVP-I degradation [13]. However, all method 2 formulations maintained a pH within the reported stability range of 3.50-4.00, as indicated by the pH values of Rx1-Rx4. Furthermore, buffer systems are

essential for controlling pH to ensure oral cavity compatibility. Increasing buffer concentration has a slight positive effect on the initial iodine content but negatively impacts long-term stability (Rx3 VS Rx4). It is important to consider the type and the optimal buffer volume that maximizes both initial iodine content and stability. Rx4, compared to Rx3, consisted of an effective buffer component at an appropriate concentration and demonstrated superior long-term performance.

This emphasizes the critical role of temperature control in pharmaceutical spray storage, consistent with the observed physical stability profiles. While temperature influenced iodine content and appearance, pH levels, and spray capabilities remained stable, demonstrating the robustness of the formulations' functional properties under the testing parameters. Consequently, optimizing preparation and storage conditions is crucial for enhancing throat spray stability and efficacy. This optimization is vital for achieving positive clinical outcomes in the treatment of pharyngitis and related conditions.

CONCLUSIONS

This study demonstrated the significant influence of formulation and storage conditions on PVP-I throat spray stability and efficacy. Formulations prepared using the separation mixing technique and stored at controlled temperatures exhibited enhanced physicochemical stability and higher iodine retention, crucial for therapeutic effectiveness. Notably, Rx4, formulated with the separation mixing technique and stored at 5°C, emerged as the most stable. These findings validated the importance of controlled pH and buffer capacity in preventing active ingredient degradation and highlighted the necessity of precise temperature control during storage. This research advances the development of stable and effective throat sprays, offering significant potential for improved treatment outcomes in pharyngitis and related conditions. Future studies should explore alternative buffer systems to further enhance iodine retention. Comprehensive evaluations, including drug permeation, antimicrobial testing, cytotoxicity, and clinical trials, are also warranted.

ACKNOWLEDGMENTS

This research was supported by the Faculty of Pharmacy, Silpakorn University for facilities and financial support.

REFERENCES

1. Sykes EA, Wu V, Beyea MM, et al. Pharyngitis. Approach to diagnosis and treatment. *Can Fam Physician*. 2020;66(4):251-7.
2. Luo R, Sickler J, Vahidnia F, Lee Y-C, Frogner B, Thompson M. Diagnosis and Management of Group A Streptococcal Pharyngitis in the United States, 2011–2015. *BMC Infectious Diseases*. 2019;19(1):193.
3. Kanagalingam J, Feliciano R, Hah JH, et al. Practical use of povidone-iodine antiseptic in the maintenance of oral health and in the prevention and treatment of common oropharyngeal infections. *Int J Clin Pract*. 2015;69(11):1247-56.
4. Lepelletier D, Maillard JY, Pozzetto B, et al. Povidone Iodine. Properties, Mechanisms of Action, and Role in Infection Control and *Staphylococcus aureus* Decolonization. *Antimicrob Agents Chemother*. 2020;64(9):e00682-20.
5. Eggers M. Infectious Disease Management and Control with Povidone Iodine. *Infect Dis Ther*. 2019;8(4):581-93.
6. Amtha R, Kanagalingam J. Povidone-Iodine in Dental and Oral Health: A Narrative Review. *J Int Oral Health*. 2020;12(5):407-12.
7. Pharmacopeia US. USP Monographs, Povidone–Iodine Topical Aerosol. USP-NF. Rockville, MD: United States Pharmacopeia; 2024.
8. Lotfipour F, Valizadeh H, Shademan S, et al. Efficacy and Physicochemical Evaluation of an Optimized Semisolid Formulation of Povidone Iodine Proposed by Extreme Vertices Statistical Design; a Practical Approach. *Iran J Pharm Res*. 2015;14(4):1015-29.
9. Calissendorff J, Falhammar H. Lugol's solution and other iodide preparations: perspectives and research directions in Graves' disease. *Endocrine*. 2017;58(3):467-73.
10. Sugibayashi K, Yamamoto N, Itakura S, et al. Development of Spray Formulations Applied to the Oral Mucosa Using Non-lamellar Liquid Crystal-Forming Lipids. *Chem Pharm Bull (Tokyo)*. 2020;68(11):1025-33.
11. Group IEW. Stability testing of new drug substances and products Q1A(R2). ICH Harmonised tripartite guideline. USA2023.
12. Moniruzzaman M, Razu MH, Rahman SAR, et al. Stability, homogeneity and measurement uncertainty estimation of PVP-I solutions for the application on oro and nasopharynx against SARS-CoV-2. *Sci Rep* 2024;14(1):7268.
13. Thakur SS, Bai A, Chan D, Lu J, et al. Ex vivo evaluation of the influence of pH on the ophthalmic safety, antibacterial efficacy and storage stability of povidone-iodine. *Clin Exp Optom*. 2021;104(2):162-6.
14. Makhayeva DN, Irmukhametova GS, Khutoryanskiy VV. Polymeric Iodophors: Preparation, Properties, and Biomedical Applications. *Rev J Chem*. 2020;10(1):40-57.
15. Dattilo S, Spitaleri F, Aleo D, Saita MG, Patti A. Solid-State Preparation and Characterization of 2-Hydroxypropylcyclodextrins-Iodine Complexes as Stable Iodophors. *Biomol*. 2023;13(3).

Development and Characterization of Tablets Prepared from Directly Compressible Piroxicam-Impregnated Neusilin® US2 Fabricated Using Fluidized Bed Impregnation

Malina Thepphaya¹ and Veerakiet Boonkanokwong^{2,}*

¹Graduate Program of Industrial Pharmacy, Faculty of Pharmaceutical Sciences, Chulalongkorn University, Bangkok 10330, THAILAND

²Department of Pharmaceutics and Industrial Pharmacy, Faculty of Pharmaceutical Sciences, Chulalongkorn University, Bangkok 10330, THAILAND

*Corresponding author Email: veerakiet.b@pharm.chula.ac.th

Abstract. This research aimed to develop piroxicam (PRX) tablets manufactured from particles containing PRX impregnated onto Neusilin® US2 as a highly porous carrier by using fluidized bed (FB) impregnation and direct compression. FB impregnation was employed to prepare PRX-impregnated Neusilin® US2 composites owing to the capability to produce an amorphous solid dispersion (ASD) of PRX within the carrier and the convenient single operation that had advantages over conventional granulation and drying processes. FB impregnation process parameters were studied, and results suggested that pump speed, nozzle air pressure, inlet temperature, and weight of the porous carrier influenced the actual PRX loading capacity. PRX was successfully impregnated into Neusilin® US2 pores and formed ASD with the greatest loading capacity of $16.91 \pm 0.22\%$ w/w. Physicochemical properties of PRX-impregnated Neusilin® US2 particles were investigated showing that particle size (d_{90}) was $9.46 \mu\text{m}$ with span of 2.48, specific surface area was $250.27 \text{ m}^2/\text{g}$, and total pore volume was 1.27 mL/g . Subsequently, PRX-impregnated Neusilin® US2 composites were directly compressed to produce PRX tablets which had weight of $170.10 \pm 1.22 \text{ mg}$, thickness of $2.72 \pm 0.02 \text{ mm}$, hardness of $6.37 \pm 0.08 \text{ kp}$, and friability of 0.47% . The examined tablets disintegrated within $13.31 \pm 0.12 \text{ min}$. Compared to PRX raw material, PRX-Neusilin® US2 tablets could improve the dissolution rate of PRX and had $79.67 \pm 7.14\%$ drug dissolved within 45 min.

Keywords: Fluidized bed impregnation; Piroxicam; Neusilin® US2; Amorphous solid dispersion; Direct compression

INTRODUCTION

Amorphous solid dispersion (ASD) is a valuable pharmaceutical formulation technique that can be employed to improve dissolution and thus oral bioavailability of poorly water-soluble drugs. Piroxicam (PRX), a white or slightly yellow crystalline powder, belongs to the Biopharmaceutics Classification System (BCS) Class II drug, possessing low solubility despite having high permeability¹. To address the challenge of its solubility limitation, impregnation was chosen as an effective and safe method to develop ASD of PRX. Incipient wetness impregnation is a process of filling the internal voids of porous carriers with active pharmaceutical ingredients (APIs) by capillary forces, resulting in stabilization of amorphous drugs within solid particles^{2,3}. In recent years, Neusilin®, a synthetic amorphous form of magnesium alumino-metasilicate with high surface area and excellent flowability, has been explored as a less expensive excipient to improve drug dissolution via impregnation⁴. This study aimed to produce ASD of PRX particles using Neusilin® US2, a white, neutral granule form of Neusilin®⁵ as a porous carrier, and ethanol as a solvent for dissolving PRX (solubility of PRX in ethanol is $3.4 \pm 0.3 \text{ mg/mL}$ at room temperature)⁶ due to its safety when being used for fluidized bed (FB) impregnation. FB impregnation is a one-step process that can be accomplished by spraying API solution droplets onto a dry porous carrier followed by a drying process to remove the excessive solvent^{3,4} for several cycles. To achieve an appropriate impregnated product, FB impregnation process parameters, such as pump speed, nozzle air pressure, and inlet temperature were studied. Physicochemical properties including solid-state characterization of PRX-impregnated particles were investigated. Subsequently, a suitable impregnated formulation was directly compressed to produce PRX tablets. Tablet properties, *in vitro* drug dissolution profile, and short-term stability were then evaluated to examine for their quality over time.

MATERIALS AND METHODS

Materials

PRX raw material (manufactured by Apex Healthcare Limited, India) was a grateful gift from Putchubun Dispensary Co., Ltd. (Putchubun Osoth pharmaceutical factory), Thailand. Magnesium alumino-metasilicate (Neusilin® US2, granule form) was kindly given as a sample from Fuji Chemical Industries Co., Ltd., Japan. Acetonitrile (HPLC grade) (Honeywell - Burdick & Jackson®, South Korea), ethanol (AR grade) (QReC®, New Zealand), acetone (AR grade) and methanol (HPLC grade) (MACRON, Norway) were purchased for experiments.

Methods

Preparation of PRX-impregnated composites via fluidized bed impregnation

Forty milligrams of PRX raw material were first dissolved in 50 mL of ethanol. The amount of drug was determined based on the desired amount of Neusilin[®], which in this case was 200 mg, to achieve 20% target drug loading (defined as % weight of API per % weight of porous carrier). The impregnation process was carried out in a VFC-LAB Micro FLO-COATER[®] (Freund-Vector Corporation, USA), a FB dryer equipped with a top spray nozzle. The procedure consisted of these following steps: (1) Load the FB dryer with the preferred amount of Neusilin[®] US2. (2) Start FB and set pump speed, nozzle air pressure, and inlet temperature to desired values which would be varied to investigate the effects of FB impregnation process parameters and conditions. Meanwhile, air flow and air pressure were fixed process parameters throughout the study. (3) Begin spraying pure solvent to reach a constant product temperature. (4) Switch to spray PRX solution onto Neusilin[®] US2. (5) After finishing impregnation and obtaining the desired drug loading, switch back to spraying pure solvent. (6) Dry the impregnated product for a specific time, cool down, and unload it.

Morphology examination

The scanning electron microscope and energy dispersive X-ray spectrometer (SEM-EDS) Model JEOL JSM-IT300 (JEOL Ltd., Japan) with an acceleration voltage at 10.0 kV was used to assess the surface morphology and obtain the images of samples based upon the previous work's protocol⁷. SEM images of the samples were captured at the 500× magnification.

Particle size measurement

Particle size and particle size distribution of samples were determined using Morphologi 4-ID[™] (Malvern Panalytical Ltd., UK). Each sample was dispersed on a glass plate by the instrument using a pressure of 4 bar. The individual particles were counted within a 20 mm × 20 mm area and measured the circular-equivalent (CE) diameters of each particle.

Specific surface area, total pore volume, and pore size measurement

The measurement was conducted by a surface area analyzer, Model Quantachrome, Autosorb-IQ-MP (Anton Paar QuantaTec Inc., USA). The Brunauer-Emmett-Teller (BET) standard method under N₂ adsorption was applied to determine the specific surface area in m²/g and total pore volume in mL/g of the samples, and the Barrett-Joyner-Halenda (BJH) model was employed to evaluate an average pore diameter (nm) of the samples⁸. The samples were degassed for approximately 30 h at 180°C before measurement.

Chromatographic conditions

Shimadzu SIL-20AHT high-performance liquid chromatography (HPLC) system (Shimadzu Corporation, Japan) was used with the following conditions: LC column, 150 × 4.6 mm; mobile phase of 1 mL of phosphoric acid in water and acetonitrile; flow rate of 0.5 mL/min; UV determination at $\lambda = 340$ nm. A five-point calibration curve was generated ($R^2 = 0.9999$).

Drug loading determination

To extract PRX, 200 mg of the fabricated impregnated sample was transferred into a 100-mL volumetric flask using 70 mL of methanol as a diluent. The flask was sonicated in an ultrasonic sonicator for 1 h. The mixture was diluted with methanol to 100 mL, mixed again, and then left for 24 h at room temperature to equilibrate. Subsequently, the mixture was centrifuged to obtain a clear supernatant before being placed in a vial. The actual drug loading was analyzed using the HPLC system as described above.

Solid-state characterization by FT-IR, XRPD, and DSC

To evaluate chemical interactions between PRX and Neusilin[®], Fourier transform infrared spectra of the samples were recorded in a Nicolet iS20 FT-IR spectrometer (ThermoFisher Scientific, USA) using the diamond Attenuated Total Reflectance (ATR) within the range of 500–4000 cm⁻¹ with 4 cm⁻¹ resolution under 64 scans/measurement⁷. X-ray powder diffraction patterns of the samples were collected, using Rigaku Miniflex II[™] (Rigaku[™], Japan) with monochromatic Cu-K α -radiation at 15 mA and 30 kV, following conditions: a scan range (2 θ) of 5°–40° with a scan speed of 2°/min. Thermal analysis of samples was conducted by a DSC Model DSC822e (Mettler-Toledo[™], Switzerland). A sample (approximate weight of 2–5 mg) was enclosed in a pin-hole aluminum pan under a dry N₂ atmosphere and heated in the range of 50°C–220°C at a heating rate of 10°C/min^{8,9}.

Preparation of PRX-impregnated tablet

PRX-impregnated Neusilin[®] US2 composite was mixed with 2% crospovidone (as a disintegrant) and then compressed by direct compression with a single punch tablet machine. Physical properties of tablets were subsequently studied.

In vitro dissolution study

PRX-impregnated tablets were immersed in 900 mL of simulated gastric fluid without pepsin. USP Apparatus I (Basket) was chosen for PRX raw material which was manually weighed and filled into hard gelatin capsules (size 0), and USP Apparatus II (Paddle) was used for impregnated tablets at 37±0.5°C, stirring under constant rotation speed of 50 rpm. Five milliliters of the sample were then withdrawn from each vessel at given time point intervals (3, 5, 15, 30, 45, 60, 90, 120, 180, and 240 min) with a syringe and replaced with the 5.0 mL of the fresh medium. The sample concentrations were subsequently analyzed by HPLC, the same protocol as the drug loading determination. The drug dissolution profiles were plotted, presenting the average percentage of drug dissolved and the standard deviation (SD) at each time point.

Short-term stability study

PRX-impregnated tablets were kept in a stability chamber (BINDER Inc., USA) at an accelerated storage condition ($40^{\circ}\text{C} \pm 2^{\circ}\text{C}$ / $75\% \text{ RH} \pm 5\% \text{ RH}$) ¹⁰ for a period of 1 month. *In vitro* drug release was then evaluated for dissolution deceleration of the sample.

Statistical analysis

The independent samples *t*-test via IBM® SPSS® statistics software at the 95% confidence interval ($p < 0.05$) was used to assess the statistical significance of surface area, total pore volume, and average pore diameter.

RESULTS AND DISCUSSION

Preparation of PRX-impregnated composites via fluidized bed impregnation

The experiment of 5.00 g Neusilin® US2 loaded, 50 RPM pump speed, 2.0 PSI nozzle air, and 65°C inlet temperature (with constant 37 LPM air flow and 4 bar air pressure) could produce $16.91 \pm 0.22\%$ drug loading PRX-impregnated particles, which were closest to the target drug loading of 20%. Inlet temperature and pump speed were also increased to 75°C and 100 RPM, respectively to study for more different conditions. However, the results showed their lesser actual drug loading, which might be due to the drug solution being dried in the air or the drug stuck to the chamber before reaching the porous carrier particles.

Morphology and particle size measurement

SEM images revealed differences in morphology of samples (see Figure 1). While PRX powder (Figure 1(a)) appeared to have an irregular shape and a rough surface, the pure Neusilin® US2 (Figure 1(b)) showed a perfectly spherical shape with a smooth porous surface. Although the SEM image of PRX-impregnated particles (Figure 1(c)) revealed a spherical shape similar to the pure Neusilin® US2 (Figure 1(b)), PRX-impregnated sample appeared slightly larger in size with differences in porous surface appearance, which might be due to some drug coating or deposition on surface occurring during the process. Furthermore, the particle size and size distribution, as shown in Table 1, suggested that the particle size slightly changed during the impregnation.

Table 1. Particle size, BET surface area, total pore volume, and average pore diameter of as-received pure Neusilin® US2 and PRX-impregnated composites via FB.

Sample No.	Sample	Particle Size (μm)			Span	Surface Area (m^2/g sample)	Total Pore Volume (mL/g sample)	Pore Diameter (nm)
		d_{10}	d_{50}	d_{90}				
1	Pure Neusilin® US2	1.50	3.95	7.60	1.54	323.31	1.64	20.24
2	PRX-impregnated Neusilin® US2 via FB	1.51	3.21	9.46	2.48	250.27	1.27	21.05

Specific surface area, total pore volume, and pore size measurement

Pure Neusilin® US2 possesses the largest surface area (see Table 1). After the impregnation process, PRX-impregnated Neusilin® US2 product had significantly lower surface area ($p < 0.05$) compared to the pure Neusilin® US2. This was due to the drug filled into the Neusilin® US2 pores. The total pore volume of the impregnated particles also decreased in agreement with the decrease in the specific surface area. The average pore diameter of the impregnated composites showed no statistically significant difference ($p > 0.05$) compared to pure Neusilin® US2, which could imply that the drug stayed in the pores of the solid matrix and obstruction from the impregnation process did not occur.

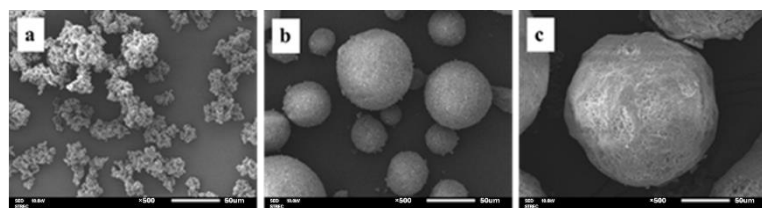


Figure 1. SEM images of (a) PRX raw material powder, (b) pure Neusilin® US2, and (c) PRX-impregnated Neusilin® US2 particles fabricated from FB impregnation (with $500\times$ magnification and scale bars of $50 \mu\text{m}$).

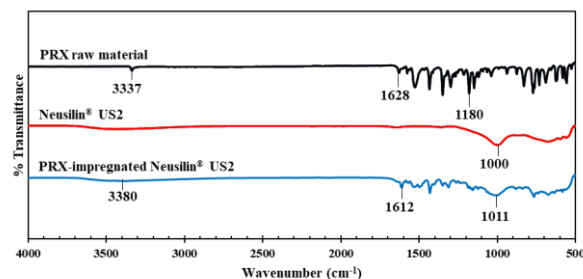


Figure 2. FT-IR spectra within the range of $500\text{--}4000 \text{ cm}^{-1}$.

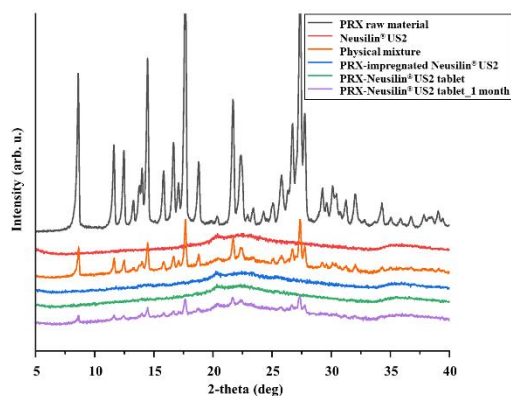


Figure 3. XRPD patterns of PRX raw material, pure Neusilin® US2, physical mixture, PRX-impregnated particles, PRX-Neusilin® US2 tablet, and PRX-Neusilin® US2 tablet after 1-month storage.

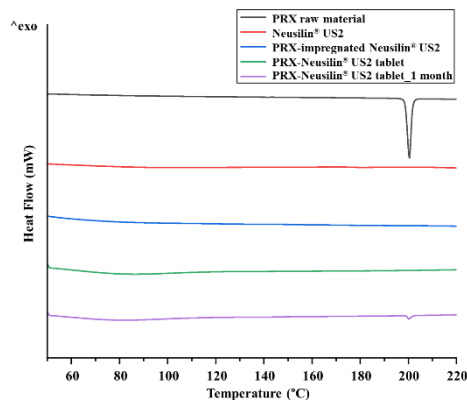


Figure 4. DSC thermograms of PRX raw material, pure Neusilin® US2, PRX-impregnated particles, PRX-Neusilin® US2 tablet, and PRX-Neusilin® US2 tablet after 1-month storage.

Solid-state characterization by FT-IR, XRPD, and DSC

FT-IR was conducted to study chemical interactions between the drug substance and Neusilin® US2 (see Figure 2). For PRX-impregnated Neusilin® US2 particles, there were Si-O-Si linkages of Neusilin® US2 presented at around 1000 cm^{-1} . The absorption bands at 1628 cm^{-1} corresponding to the stretching of amide carbonyl groups (C=O) and 1180 cm^{-1} corresponding to the sulfonyl groups (S=O) asymmetric stretching of benzothiazine ring of PRX were shifted and broadened in the sample. Furthermore, the FT-IR spectra of PRX-impregnated particles indicated that the characteristic peak of PRX at 3337 cm^{-1} , associated with the bands of N-H of amide group and enolic O-H¹¹, was reduced in intensity due to probable H-bonding between PRX and Neusilin® US2.

XRPD patterns (see Figure 3) of PRX-impregnated particles displayed the disappearance of all sharp peaks, which proved that impregnation could transform PRX from a crystalline to an amorphous nature. DSC thermograms (Figure 4) of PRX-impregnated particles showed no endothermic melting peak. Therefore, both results suggested that impregnation could produce ASD of PRX.

Tablet properties study

The PRX-impregnated tablets were successfully compressed, which had weight of $170.10 \pm 1.22\text{ mg}$, thickness of $2.72 \pm 0.02\text{ mm}$, hardness of $6.37 \pm 0.08\text{ kp}$, and friability of 0.47% . Six examined tablets disintegrated within $13.31 \pm 0.12\text{ min}$.

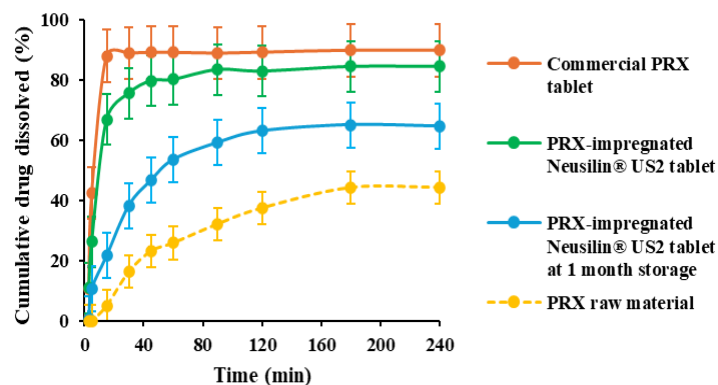


Figure 5. *In vitro* dissolution profiles of PRX raw material, PRX-impregnated tablets (freshly prepared, and at 1-month storage), and commercial PRX tablet (mean \pm SD, $n = 3$).

In vitro dissolution study

The dissolution results showed that PRX-impregnated Neusilin® US2 tablet could improve the dissolution rate of PRX (see Figure 5). In this study, PRX-impregnated tablets had $79.67 \pm 7.14\%$ drug dissolved within 45 min, while PRX raw material had only $23.12 \pm 10.25\%$ dissolved drug at 45 min. Commercial PRX tablets were also tested, showing $88.95 \pm 0.65\%$ drug dissolution at 45 min, which may depend on the unknown excipients in its formulation.

Short-term stability study

The accelerated stability study of PRX-impregnated tablet was conducted afterwards. The results (see Figure 5) displayed that PRX dissolution from the impregnated tablets after 1-month storage decreased to $46.63 \pm 6.37\%$ drug dissolved at 45 min, which could be attributed to drug recrystallization, as confirmed by the XRPD and DSC results (see Figures 3 and 4).

CONCLUSIONS

FB was employed to successfully manufacture amorphous PRX-impregnated Neusilin® US2 composites within a fast, single unit operation. The FB impregnation process parameters including pump speed, nozzle air pressure, and inlet temperature as well as the material attribute (i.e., the weight of the porous carrier) had an impact on the actual PRX loading capacity. PRX could be successfully filled into the pores of Neusilin® US2 with the actual drug loading capacity closed to the expected value, and solid-state characterizations showed an amorphous form of PRX impregnated inside the porous solid carrier indicating complete transformation of crystalline PRX to ASD formulations with acceptable physicochemical properties. The ASD of PRX-impregnated Neusilin® US2 particles was subsequently compacted by direct compression method producing PRX tablets with good physical properties. Dissolution profiles revealed that PRX-impregnated Neusilin® US2 tablets had a comparable dissolution rate to that of the commercial product and an enhanced dissolution rate compared to PRX starting material. However, solely including the drug into a porous carrier might lead to a lack of satisfaction in preventing the recrystallization of the drug. Further studies on combining other excipients such as amorphous stabilizers in the impregnated ASD formulation may be necessary to improve stability of the drug and ensure the desired dissolution profiles. Impregnation time and drying time in FB impregnation process also needed to be investigated further to diminish the possibility of coating, spray drying, or granulation that might happen instead of impregnation and achieve better impregnated product with higher actual drug loading.

ACKNOWLEDGMENTS

This work (Grant No. RGNS 64 – 018) was supported by Office of the Permanent Secretary, Ministry of Higher Education, Science, Research and Innovation (OPS MHESI), Thailand Science Research and Innovation (TSRI) and Chulalongkorn University. The authors thanked the Pharmaceutical Research Instrument Center and the Drug and Health Products Innovation Promotion Center (CUDHIP), Faculty of Pharmaceutical Sciences, Chulalongkorn University. We gratefully thanked Putchubun Dispensary Co., Ltd. (Putchubun Osoth pharmaceutical manufacturing company) for supporting piroxicam raw material.

REFERENCES

1. USFDA. M9 biopharmaceutics classification system-based biowaivers guidance for industry [Internet]. CDER, CBER: USFDA; 2021 [updated 2021 May; cited 2024 May 29]. Available from: <https://www.fda.gov/media/148472/download>.
2. Omar TA, Oka S, Muzzio FJ, Glasser BJ. Manufacturing of pharmaceuticals by impregnation of an active pharmaceutical ingredient onto a mesoporous carrier: impact of solvent and loading. *J Pharm Innov*. 2018;14:194-205.
3. Grigorov P, Glasser B, Muzzio F. Formulation and manufacture of pharmaceuticals by fluidized-bed impregnation of active pharmaceutical ingredients onto porous carriers. *AIChE*. 2013;59(12):4538-52.
4. Grigorov P, Glasser B, Muzzio F. Improving dissolution kinetics of pharmaceuticals by fluidized bed impregnation of active pharmaceutical ingredients. *AIChE*. 2016;62(12):4201-14.
5. Fuji Chemical Industries. The specialty excipient Neusilin® [Internet]. 2015 [updated 2015 Sep; cited 2024 May 29]. Available from: https://www.fujichemical.co.jp/english/medical/medicine/neusilin/neusilin_brochure.pdf.
6. De Zordi N, Kikic I, Moneghini M, Solinas D. Piroxicam solid state studies after processing with SAS technique. *J Supercrit Fluids*. 2010;55(1):340-7.
7. Aung WT, Kopongpanich P, Boonkanokwong V. Supersaturable solid self-microemulsifying delivery systems of astaxanthin via spray drying: effects of polymers and solid carriers. *AAPS PharmSciTech*. 2023;24(8):218.
8. Javadzadeh Y, Bairami Atashgah R, Barzegar-Jalali M, Soleimani F, Mohammadi G, Sabzevari A, et al. Inclusion of piroxicam in mesoporous phosphate glass-ceramic and evaluation of the physiochemical characteristics. *Colloids Surf B Biointerfaces*. 2014;116:751-6.
9. Mostafa GAE, Al-Dosseri AS, Al-Badr AA. Chapter seven-piroxicam. In: Brittain HG, editor. *Profiles of drug substances, excipients and related methodology*. 45: Academic Press; 2020. p. 199-474.
10. ASEAN. ASEAN guideline on stability study of drug product (R1) [Internet]. ASEAN; 2010 [cited 2024 May 9]. Available from: <https://asean.org/wp-content/uploads/2018/01/25PPWG-ANNEX-7-iv-Final-ASEAN-Guideline-on-Stability-Study-Drug-Product-R2.pdf>.
11. Stulzer HK, Tagliari MP, Cruz AP, Silva MAS, Laranjeira MCM. Compatibility studies between piroxicam and pharmaceutical excipients used in solid dosage forms. *Pharm Chem J*. 2008;42(4):215-9.

Efficacy of Calcium Hydroxylapatite in Hand Rejuvenation, a Prospective 3-month Study

Punyaphat Sirithanabadeekul^{1,*}, Napasorn Weerayuttwilai¹

¹Chulabhorn International College of Medicine, Thammasat University (Rangsit Center)
99 Moo 18, Paholyothin Road, Klongnong, Klongluang, Pathumthani 12120 Thailand

*Corresponding author Email: penyaphats.cicm@gmail.com

Abstract. This study aimed to evaluate the efficacy of calcium hydroxylapatite (CaHA) biostimulator for hand rejuvenation in a prospective 3-month study. Ten participants received CaHA treatment on the dorsum of the hand, and outcomes were evaluated using the Merz Hand Grading Scale (MHGS), skin moisture levels, wrinkle severity, skin texture analysis, skin depression volume, and melanin levels at baseline, at 4 weeks, and 12 weeks post-treatment. The results demonstrated significant improvements in all objective parameters across the study period, indicating the potential of CaHA as an effective treatment for hand rejuvenation.

Keywords: Calcium hydroxylapatite; Hand rejuvenation; Aging hand; Biostimulator

INTRODUCTION

Aging hands are another aspect that people are paying more attention to nowadays, as they are a part of the body that is frequently used and easily noticeable. The aging process is most prominent in the dorsum of the hand. Characteristics of an aging hand consist of loss of subcutaneous fat, prominence of superficial veins and extensor tendons, prominence of bony contours of the metacarpal and proximal phalangeal bones, thinning of the dermis, irregular surface pigmentation, and age spots appearance.¹ There is disorganization of collagen and elastin fibers in hand aging as in facial skin aging.²

Currently, there are various therapeutic options available for dorsal hand rejuvenation, including topical acids (tretinoin and vitamin C, among others), laser therapy, vein sclerotherapy, chemical peeling, autologous fat grafting, and filler injections.^{3,4} Injecting fillers for dorsal hand rejuvenation is a popular procedure and has high patient satisfaction. They provided an approach for restoring volume loss and improving the appearance of prominent veins and tendons. The relatively common minor early-onset complications of soft tissue fillers include swelling, bruising, and paresthesia^{5,6,7}, while more serious and long-term complications include surface irregularities, granuloma formation, and skin necrosis. Among the various types of injectable fillers, calcium hydroxylapatite (CaHA) has gained considerable attention due to its unique biostimulatory properties.⁸

Calcium hydroxylapatite fillers (Radiesse®, Merz Aesthetics), currently the only one approved by the FDA for hand augmentation, are composed of 30% CaHA microparticles in 70% aqueous carboxymethylcellulose (CMC) gel carrier. The particles are relatively large, ranging from 25-45 µm in size, which limits macrophage phagocytosis and provides durability. The carrier gel disperses within 2-3 months after injection, whereas the CaHA remains, stimulates fibroblast growth and collagen formation around the microspheres.⁹

The high viscosity and high elastic (G') of CaHA filler leads to immediate volume correction and its unique radiopaque properties and white color allow it to blend well with the skin and result in more optical masking of veins and tendons as compared with other fillers.⁸ When injecting CaHA, most practitioners will dilute the product 1:1 with 0.9% NaCl and lidocaine mixture. One longevity study showed evidence of CaHA microspheres surrounded by neocollagenesis for 72 weeks.¹⁰ Associated adverse events typically include swelling, pain, redness, and bruising, with nearly all events resolving without intervention within the first 2 weeks of treatment.^{11,12}

This prospective study investigates the efficacy of CaHA for hand rejuvenation over a 3-month period, focusing on objective measures of skin quality and aesthetic improvement.

MATERIALS AND METHODS

Materials

The primary material used in this study was calcium hydroxylapatite (CaHA) biostimulator (Radiesse®, Merz Aesthetics). The assessment tools included the Merz Hand Grading Scale (MHGS)¹³, MoistureMeterD® (Delphin Technologies Ltd., Kuopio, Finland) for measuring skin moisture levels and Antera 3D® (Miravex Ltd., Dublin, Ireland) for assessing wrinkle severity, skin texture analysis, skin depression and melanin levels.

Methods

Experiment

Ten participants with aging hands, defined as a Merz Hand Grading Scale (MHGS) score of 2 or higher, were enrolled in this single-arm, prospective study. Exclusion criteria included a history of allergic reaction to CaHA, previous hand rejuvenation treatments within the past 6 months, the presence of active skin infections or inflammatory conditions in the treatment area, pregnancy, and breastfeeding. Prior to treatment, informed consent was obtained from all participants, and standardized photographs of the dorsal hands were taken for objective assessment. The treatment area was cleansed with chlorhexidine solution, and topical anesthesia was applied for 30 minutes to minimize discomfort. The 0.75ml of CaHA (Radiesse®, Merz Aesthetics) mixing with 0.75ml of 2% Lidocaine CaHA (Radiesse®, Merz Aesthetics) was injected into the dorsal hands using a 25-gauge needle and a retrograde-fanning technique¹⁴, primarily in the dorsal superficial lamina (DSL) plane¹⁵, targeting areas of volume loss and prominent veins. The total injected volume was 1.5ml. Following the injection, the treatment area was gently massaged to ensure even distribution of the product. The Merz Hand Grading Scale (MHGS), skin moisture levels (MoistureMeterD®), wrinkle severity (Antera 3D®), skin texture analysis (Antera 3D®), skin depression volume (Antera 3D®), and melanin levels (Antera 3D®) were assessed at baseline, 4 weeks, and 12 weeks post-treatment.

Statistical analyses

Data were analyzed using STATA/SE 14 (Stata Corp LP). Statistical analysis was performed using paired t-tests to compare baseline, 4-week, and 12-week values. A p-value of less than 0.05 was considered statistically significant. Sample size

RESULTS AND DISCUSSION

Results

The demographic data of 10 participants with Merz Hand Grading Scale (MHGS) score of 2 or higher, primarily female (80%), were enrolled. The mean age of participants was 48 ± 11.6 years.

Table 1. Demographic characteristics of participants

Characteristics	n = 10
Sex	
Female	8 (80%)
Male	2 (20%)
Age	48 ± 11.6

The treatment resulted in notable and statistically significant improvements across several key metrics related to hand appearance and skin health. Specifically, the Merz Hand Grading Scale (MHGS) scores, which assess the overall appearance of the hands, demonstrated a significant decrease at both 4 and 12 weeks compared to baseline, indicating a visible improvement in hand appearance. Skin moisture levels also exhibited a substantial increase, suggesting enhanced hydration of the treated skin. Furthermore, the severity of wrinkles was significantly reduced, and the overall skin texture was visibly improved. There was also a reduction in skin depression volume, suggesting that the treatment effectively restored volume to areas where it had been lost. Finally, melanin levels decreased significantly, indicating a reduction in pigmentation and a more even skin tone. These positive changes, observed at both the 4-week and 12-week marks post-treatment, provide strong evidence of CaHA's effectiveness in rejuvenating the hands.

Table 2. Comparison of outcomes

Outcome Measure	Baseline (Mean \pm SD)	4 Weeks (Mean \pm SD)	12 Weeks (Mean \pm SD)	p-value (4 Weeks vs Baseline)	p-value (12 Weeks vs Baseline)
MHSG	2.70 \pm 0.82	1.20 \pm 1.23	1.44 \pm 0.88	< 0.001	< 0.001
Skin Moisture	45.17 \pm 2.77	48.53 \pm 3.46	47.67 \pm 3.62	< 0.001	< 0.001
Wrinkle	53.85 \pm 22.33	42.94 \pm 21.03	45.64 \pm 16.56	< 0.001	< 0.001
Skin Texture	59.65 \pm 25.74	47.07 \pm 23.52	50.13 \pm 18.24	< 0.001	< 0.001
Depression	41.71 \pm 20.89	31.18 \pm 20.24	34.14 \pm 15.71	< 0.001	< 0.001
Melanin level	0.433 \pm 0.074	0.417 \pm 0.066	0.406 \pm 0.056	< 0.05	< 0.05

Table 3. Percentage mean change of each parameter from baseline

Outcome Measure	%change from baseline	
	4 Weeks	12 Weeks
MHSG	-55.56%	-46.30%
Skin Moisture	7.44%	6.11%
Wrinkle	-20.26%	-16.97%
Skin Texture	-21.10%	-17.80%
Depression	-25.24%	-20.16%
Melanin level	-3.69%	-7.39%

The percentage change is calculated at 4 weeks and 12 weeks after the initiation of the treatment. A negative percentage indicates a reduction in the measured value, which generally signifies an improved outcome (e.g., a decrease in wrinkle score, a decrease in depression). A positive percentage indicates an increase in skin moisture.

No serious side effects were observed, such as nodules or skin infection, with only one patient experiencing a bruise that resolved within 2 weeks without any treatment.

Discussions

The results of this prospective 3-month study provide evidence supporting the efficacy of CaHA for hand rejuvenation. The significant improvements observed in MHGS scores, a validated scale for assessing hand aging, indicate a noticeable reduction in volume loss and improved overall aesthetic appearance. The increase in skin moisture levels suggests that CaHA may also contribute to enhanced skin hydration, which is crucial for maintaining skin health and elasticity. The reduction in wrinkle severity and improvement in skin texture further support the rejuvenating effects of CaHA on the hands. The decrease in skin depression volume indicates that CaHA effectively restores volume loss in the hands, leading to a more youthful contour. The reduction in melanin levels suggests that CaHA may also have a beneficial effect on skin pigmentation, contributing to a more even skin tone.

These findings are consistent with previous studies that have demonstrated the efficacy of CaHA for hand rejuvenation. The biostimulatory properties of CaHA, which promote collagen synthesis, likely contribute to the improvements in skin quality and volume observed in this study. While the 3-month study period allowed for observing initial effects, it's important to acknowledge this is a relatively short follow-up period. Longer-term collagen stimulation following CaHA injection is a key area for further investigation. It is possible that continuous collagenesis beyond 3 months could lead to even greater improvements in skin quality and volume. Conversely, it's also conceivable that over time, the initial improvements could plateau or even decline due to natural aging processes or the gradual degradation of CaHA. Therefore, studies with extended follow-up periods are crucial to fully understand the longevity of CaHA's effects and to identify any potential need for maintenance treatments.

CONCLUSIONS

This prospective 3-month study demonstrates that CaHA is an effective treatment for hand rejuvenation, leading to significant improvements in various objective parameters, including MHGS scores, skin moisture levels, wrinkle severity, skin texture, skin depression volume, and melanin levels. These findings suggest that CaHA can effectively address multiple signs of aging in the hands, resulting in a more youthful and rejuvenated appearance. While valuable, future research should compare CaHA with other biostimulators and explore combination therapies. Crucially, longer-term studies (6-12+ months) are needed to assess the durability of CaHA's effects and the potential need for maintenance. Further research should investigate optimal injection techniques and volumes for best outcomes. Furthermore, increasing the sample size and employing standardized protocols would enhance the reliability and generalizability of these findings, ultimately improving patient outcomes in hand rejuvenation.

ACKNOWLEDGMENTS

The author would like to express sincere gratitude to Merz Aesthetics Thailand company for providing product support for this research study.

REFERENCES

1. Jakubietz RG, Kloss DF, Gruenert JG, Jakubietz MG. The ageing hand. A study to evaluate the chronological ageing process of the hand. *J Plast Reconstr Aesthet Surg*. 2018;61(6):681-6.
2. Fisher GJ. The pathophysiology of photoaging of the skin. *Cutis*. 2005;75 Suppl 2:5-9.
3. Shamban AT. Combination hand rejuvenation procedures. *Aesthet Surg J*. 2009;29(5):409-13.
4. Butterwick K, Sadick N. Hand rejuvenation using a combination approach. *Dermatol Surg*. 2016;42 Suppl 2:S108-18.
5. Park TH, Yeo KK, Seo SW, Kim JK, et al. Clinical experience with complications of hand rejuvenation. *J Plast Reconstr Aesthet Surg*. 2012;65(12):1627-31.
6. Fantozzi F. Hand rejuvenation with fat grafting: a 12-year single-surgeon experience. *Eur J Plast Surg*. 2017;40(5):457-64.
7. Frank K, Koban K, Targosinski S, Erlbacher K, et al. The anatomy behind adverse events in hand volumizing procedures: retrospective evaluations of 11 years of experience. *Plast Reconstr Surg*. 2018;141(6):650e-62e.
8. Kühne U, Imhof M. Treatment of the ageing hand with dermal fillers. *J Cutan Aesthet Surg*. 2012;5(3):163-9.
9. Rivkin AZ. Volume correction in the aging hand: role of dermal fillers. *Clin Cosmet Investig Dermatol*. 2016;9:225-32.
10. Marmur ES, Phelps R, Goldberg DJ. Clinical, histologic and electron microscopic findings after injection of a calcium hydroxylapatite filler. *J Cosmet Laser Ther*. 2004;6(4):223-6.
11. Goldman MP, Moradi A, Gold MH, Friedmann DP, et al. Calcium hydroxylapatite dermal filler for treatment of dorsal hand volume loss: results from a 12-month, multicenter, randomized, blinded trial. *Dermatol Surg*. 2018;44(1):75-83.
12. Busso M, Moers-Carpi M, Storck R, Ogilvie P, et al. Multicenter, randomized trial assessing the effectiveness and safety of calcium hydroxylapatite for hand rejuvenation. *Dermatol Surg*. 2010;36(6):790-7.
13. Carruthers A, Carruthers J, Hardas B, et al. A validated hand grading scale. *Dermatol Surg*. 2008;34 Suppl 2:S179-S183.
14. Pavicic T, Cotofana S. Hands. In: Logham JV, editor. *Calcium Hydroxylapatite Soft Tissue Fillers: Expert Treatment Techniques*. CRC Press; 2020. p. 139-143.
15. Bidic SM, Hatf DA, Rohrich RJ. Dorsal hand anatomy relevant to volumetric rejuvenation. *Plast Reconstr Surg* 2010;126:163-8.

The Efficacy of Hyperdiluted Calcium Hydroxylapatite for the Treatment of Horizontal Neck Wrinkle

Punyaphat Sirithanabadeekul^{1,}, Kanokphan Kulprueksri¹*

¹Chulabhorn International College of Medicine, Thammasat University (Rangsit Center)
99 Moo 18, Paholyothin Road, Klongnong, Klongluang, Pathumthani 12120 Thailand

*Corresponding author Email: punyaphats.cicm@gmail.com

Abstract. There has been rising in popularity of non-invasive treatments horizontal neck lines. Injection procedures such as botulinum toxin, Hyaluronic acid, and biostimulators. These are proving effective and safe, reduced risk of side effects compared to invasive procedures. Calcium hydroxylapatite (CaHA) is a one of choice. It is a biocompatible, biodegradable, and resorbable. Recommendations the use of diluted is 1:2. However, there is little research on CaHA in hyperdiluted treating in neck area. From the above reasons, The author therefore studied about the effectiveness and safety of 1:4 hyperdiluted CaHA for the treatment of horizontal neck wrinkle in 8 patients. By enrolling 8 patients with none or mild neck sagging on Merz Neck Volume Scale and mild to moderate on neck Horizontal neck wrinkle (HnWs) scale. Then injected CaHA 1:4 (CaHA 0.75 ml + diluent 3 ml; to NSS 2.5 ml and 0.5 mL of 2% lidocaine total 3.75 ml) to subdermal using blunt cannula. Photographic was done at baseline, after injection at 1, 3, 6 months. Antera 3D was measures at follow up visits. The main outcomes were graded by blinded dermatologist assessment Global aesthetic improvement scale (GAIS) and Antera 3D wrinkle. After injection, The results showed significant improvement of GAIS and decrease of wrinkle size by Antera3D at 1, 3 months post treatment, with sustained at 6 months after the procedure. No one developed severe adverse effects such as granuloma nodule. It can be concluded that CaHA is effective treatment for improved horizontal necklines, with sustained until 6 months. No serious side effects.

Keywords: Neck rejuvenation, Calcium hydroxyapatite, Horizontal neck wrinkle

INTRODUCTION

Nowadays, when talking about the increasing importance of beauty standards. People not only value an appearance on face. But it also gives importance to other areas of the body. The neck is the area closest to the face [1,2,3] and can be easily noticed of aging. People are beginning to pay more attention to the quality of the skin around their necks.

Wrinkles on the neck It is like other wrinkles. You might see them around your mouth, eyes, hands, or forehead. Although wrinkles are a natural part of aging, but it is not the only factor. Neck wrinkles can be found in teenagers. or more children from frequently bending your neck to look at your cell phone, tablet, or book. This can cause wrinkles caused by repeated folding of the skin.[4]

Biostimulators represent a recent trend in dermatology innovation. Dermatologists are interested in their dual functionality, as they not only offer immediate skin filling similar to Hyaluronic acid fillers [5,6] but also have ability to sustainably stimulate the ongoing production of natural collagen within the skin layers. This dual action is seen as a promising approach to promoting long-term youthfulness and overall skin health. [7,8]

In recently, There are more research studies about Calcium hydroxylapatite from its ability to stimulate the endogenous collagen production, generating long-term tissue remodeling by the CaHA microspheres and volumization[7,8]. Although CaHA use for neck treatment is off-label, its ability to induce extracellular matrix remodeling after subdermal injection may have a significant impact on reducing fine wrinkling, improving skin quality, and promoting local skin tightening with evidence from one study, researchers described a method for treating horizontal neck lines using Calcium Hydroxylapatite (CaHA) injections. Changes in skin mechanical properties were assessed using ultrasound scanning and cutometry. Immunohistochemical analysis showed increased collagen and elastin production, which correlated with improved skin elasticity and pliability as assessed by cutometry, while ultrasound scans revealed increased dermal thickness. [7]

Consensus recommendations regarding the use of diluted and hyperdiluted CaHA have been developed by panels of global expert aesthetic physicians. For the treatment of the neck, the panel recommend a dilution of 1:2 is

indicated, and a short linear threading technique using a needle is an alternative option for product application, following a gentle massage. [7,8]

However, there is little research on Calcium hydroxylapatite in hyperdiluted treating in neck area. The purpose of this study was to assess the effectiveness and safety of 1:4 hyperdiluted calcium hydroxylapatite for the treatment of horizontal neck wrinkle.

MATERIALS AND METHODS

Methods

Prospective Randomized double-blinded study performed at Benchakitti Park Hospital, Bangkok, Thailand from July 2024 to December 2024. The 8 participants were recruited with none or mild neck sagging on Merz Neck Volume Scale and mild to moderate on neck Horizontal neck wrinkle (HnWs) scale. Use Cohen formula to calculated sample size (at least 7 persons). All patients provided informed consent prior to enrollment. The study participants comprised of only female with ages ranging 35.50 ± 10.62 (Table1). Participants were injected with diluted 1:4 CaHA (CaHA 0.75 ml plus diluent 3 ml divided to NSS 2.5 ml and 0.5 mL of 2% lidocaine solution total 3.75 ml. Using a 22 Gauge cannula with a length of 70 mm in the subdermal plane with fanning technique.

Photography, Antera 3D, Moisturemeter, Corneometer, Tewameter will be taken before the treatments at baseline and follow up at 1 month, 3 months and 6 months for analysis by blinded dermatologists. In all follow-up visits, the patients were asked to report any side effects.

Data were analyzed using STATA/SE version 14. Quantitative results were presented as mean \pm standard deviation (SD) and mean difference (95% confidence interval). Qualitative data were expressed in percentages. Statistical significance was set at a p-value of < 0.05 . The independent t-test was used to compare differences between groups.

RESULTS AND DISCUSSION

Results

Patient Demographic Data 8 participants with none or mild neck sagging on Merz Neck Volume Scale and mild to moderate on neck Horizontal neck wrinkle (HnWs) scale, comprising females 100%, were enrolled. The mean age of participants was 35.50 ± 10.62 years. And it was an experiment on the right side 5 persons (62.5%) and on the left side 3 persons (37.5%) showed in table 1

Table 1. Baseline characteristics of participants

Characteristics	Dilute1:4 (n = 8)
Gender	
Female	8 (100)
male	0 (0.0)
Age (years)	35.50 ± 10.62
Side	
Right side	5 (62.5)
Left side	3 (37.5)

Clinical assessments were done by blinded dermatologists through comparative photographs using a Global Aesthetic Improvement Scale: GAIS (1 = very much improved, 2 = much improved, 3 = improved, 4 = no change, 5 = worse) and Antera 3D to measure wrinkle size and texture, Moisturemeter, Cutometer to measure these parameters; Corneometer, Tewameter.

The mean scores of the Global Aesthetic Improvement Scale based on dermatologist assessments showed a peak much improvement at 1 month and still improved until 6 months after treatment compared with baseline before the procedure (Table 2).

Table 2. Efficacy on Global Aesthetic Improvement

GAIS	Dilute1:4 (n = 8)
1 month	
Grade 1 (very much improved)	0 (0.0)
Grade 2 (much improved)	4 (50.0)
Grade 3 (improved)	2 (25.0)
Grade 4 (no change)	2 (25.0)
3 months	
Grade 1 (very much improved)	1 (14.3)
Grade 2 (much improved)	1 (14.3)
Grade 3 (improved)	4 (57.1)
Grade 4 (no change)	1 (14.3)
6 months	
Grade 1 (very much improved)	1 (12.5)
Grade 2 (much improved)	1 (12.5)
Grade 3 (improved)	5 (62.5)
Grade 4 (no change)	1 (12.5)

The result of cutometer showed a significant improvement of Tewameter parameter at 1, 3 months after procedure (p-value <0.05) as seen in the table 3. At the 1 month follow- up, Tewameter increased by an average of 2.83 (95%CI: 1.06, 4.59) with statistical significance (p-value = 0.002), whereas at 3 months Tewameter increased by an average of 2.24 (95%CI: 0.40, 4.09) with statistical significance (p-value = 0.017). Then, decline in improvement was seen at the 6- month follow- up, compared with before the experiment (Table 3). However, they were showed no differences in Moisturemeter, Corneometer, Wrinkle size, and Texture before and after 1, 3, and 6 months (Table 3). On the contrary, the patient's assessment scores as satisfied score showed very satisfied at 1,3 months after treatment. Similarly, a decline in satisfied was seen at the 6 months follow- up (Figure 1).

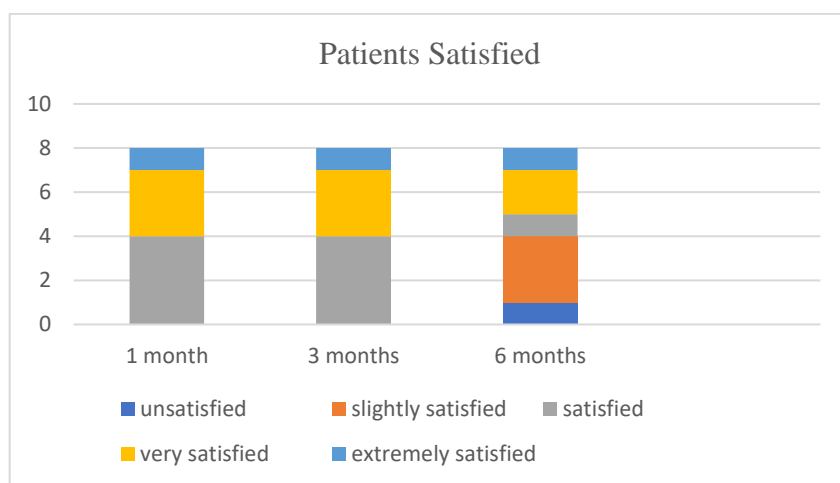


Figure 1. Patients' satisfaction

Table 3. Comparison of Moisturemeter, Cutometer, Tewameter, Wrinkle size and Texture before and after

Outcomes	Dilute1:4 (n = 8)		
	Mean \pm SD	Change from baseline (95% CI)	p-value
Moisturemeter			
Baseline	39.13 \pm 4.14	Reference	
1 month	39.56 \pm 4.50	0.44 (-2.22, 3.09)	0.747
3 months	41.47 \pm 2.41	1.35 (-1.61, 4.30)	0.371
6 months	39.30 \pm 6.47	0.18 (-3.22, 3.57)	0.920
Cutometer			
Baseline	75.66 \pm 13.04	Reference	
1 month	73.57 \pm 10.77	-2.09 (-11.64, 7.47)	0.669
3 months	67.18 \pm 10.38	-7.96 (-17.97, 2.05)	0.119
6 months	70.19 \pm 12.91	-5.47 (-15.39, 4.45)	0.280
Tewameter			
Baseline	3.30 \pm 2.13	Reference	
1 month	6.13 \pm 2.14	2.83 (1.06, 4.59)	0.002
3 months	5.73 \pm 3.53	2.24 (0.40, 4.09)	0.017
6 months	3.36 \pm 1.87	0.06 (-1.71, 1.83)	0.945
Wrinkle size			
Baseline	41.45 \pm 14.65	Reference	
1 month	35.94 \pm 12.59	-5.51 (-18.04, 7.02)	0.389
3 months	39.91 \pm 14.83	-2.39 (-16.81, 12.03)	0.745
6 months	39.70 \pm 16.33	-1.75 (-19.67, 16.17)	0.848
Texture			
Baseline	26.12 \pm 3.53	Reference	
1 month	22.20 \pm 5.28	-3.93 (-8.32, 0.47)	0.080
3 months	24.03 \pm 4.61	-2.13 (-6.72, 2.47)	0.365
6 months	25.12 \pm 4.80	-1.01 (-5.44, 3.43)	0.657

Adverse Effects

There was 1 patient who experienced minor side effects such as bruising immediately after the injection, but this resolved without any treatment within 1 week. No serious adverse effects, such as granuloma, infection or scarring, were observed throughout the study.

Discussion

Neck aging, much like facial aging, is a complex condition influenced by various factors such as sun exposure, gravity, hormonal shifts, genetic predisposition, and postural habits. These elements collectively contribute to the decline in dermal collagen and elastin. Clinically, cervical aging presents as thinning skin, loss of firmness, discoloration, and the formation of wrinkles, commonly cited as concerns in medical consultations for aesthetic purposes. Now, there is a lacking of systematic studies on the assessment of rejuvenation procedures for the neck.

Recently, biostimulator has become an important role in rejuvenation this neck. Calcium hydroxylapatite is a one of choice. that's biocompatible, biodegradable, and resorbable substance. In Undiluted or slightly diluted it provides immediate correction by volume augmentation and stimulate the endogenous collagen production through neocollagenesis, elastin production, angiogenesis, and dermal cell proliferation. But in Hyperdiluted form (1.5mL of product plus ≥ 1.5 mL of diluent) has a minimal or absent immediate volumizing effect, generating only long-term tissue remodeling by the CaHA microspheres.

In this study's proposal is an expansion of a prior pilot study on the use of hyperdiluted Calcium hydroxylapatite(1:4) for treating horizontal neck wrinkles, and it includes a well-designed examination with the

expectation of more precise results that will be beneficial for alternatively treating patients with Calcium hydroxylapatite in the future.

It's demonstrated a reduction in neck wrinkle size measured by Antera 3D starting at 1 month after injection to 3 months and remaining stable at 6 months.

In addition, it was further discovered that the effect of hyperdiluted Calcium hydroxylapatite not only helps in generating long-term tissue remodeling or stimulating collagen but also significantly effective in retaining moisture in the skin layer from the experimental results measured by Tewameter at 1 month sustained until 3 months after injection with no any side effects such as granuloma, hematoma, infection or scarring.

Furthermore, the majority of patients noted clinical improvement of neck as assessed by a dermatologist on the GAIS scale, reporting that the neck continued to improve from 1 month to 6 months after injection

CONCLUSIONS

In conclusion, this prospective study confirms that a single treatment with hyperdiluted CaHA injections leads to a noticeable improvement in the appearance of horizontal neck lines. The most prominent results are typically seen between 1 and 3 months after the procedure, though the rejuvenating effects can persist until 6 months with no serious side effects.

ACKNOWLEDGMENTS

The author would like to thank Merz Aesthetics Thailand for supporting the research product.

REFERENCES

1. Ferneini, Elie. Applied Head and Neck Anatomy for the Facial Cosmetic Surgeon. 2021.
2. Kohan, E. J. Wirth, G. A. "Anatomy of the neck." Clin Plast Surg 41.1 (n.d.): 1-6.
3. Narayan, Deepak. Surgical and Perioperative Management of Patients with Anatomic Anomalies. 2021.
4. Patel, Bhupendra C. K. "Aesthetic Surgery of the Aging Neck: Options and Techniques." Orbit 25.4 (2006): 327-356.
5. Lee, S. K. "Correction of horizontal neck lines: Our preliminary experience with hyaluronic acid fillers." J Cosmet Dermatol 17.4 (2018): 590-595.
6. Rongthong, A., et al. "Efficacy and safety of hyaluronic acid filler on the treatment of horizontal neck lines." J Cosmet Dermatol 22.2 (2023): 433-438.
7. de Almeida, A. T. "Consensus Recommendations for the Use of Hyperdiluted Calcium Hydroxyapatite (Radiesse) as a Face and Body Biostimulatory Agent." Plast Reconstr Surg Glob Open 7.3 (2019): e2160.
8. Trindade de Almeida, A. R. "Efficacy and Tolerability of Hyperdiluted Calcium Hydroxylapatite (Radiesse) for Neck Rejuvenation: Clinical and Ultrasonographic Assessment." Clin Cosmet Investig Dermatol 16 (2023): 1341-1349.

Development of PEG-modified phytosome of naringin for improving physical properties, stability and cytotoxicity in Caco-2 cells

Somboon Tiranupan², Thitianan Kulsirirat¹, Thanu Thongnopkoon^{2,}*

¹Department of Biopharmacy, Faculty of Pharmacy, Srinakharinwirot University, Nakhon Nayok, Thailand

*Corresponding author Email: thanu@g.swu.ac.th

²Department of Pharmaceutical Technology, Faculty of Pharmacy, Srinakharinwirot University, Nakhon Nayok, Thailand

Abstract. This study aimed to develop phytosome of naringin (NG) by adding polyethylene glycol (PEG) derivatives to improve physical properties, stability and cytotoxicity in Caco-2 cells. The molar ratios of naringin to phosphatidylcholine (PTC) were varied at 1:1, 1:2, 1:3, and 1:4 with a constant concentration of cholesterol. Phytosomes were prepared using thin-film hydration method. The optimal formulation was selected and subsequently modified by incorporating PEG 400, PEG 1500, PEG 4000, and lauroyl PEG-32 glycerides. The modified formulations were examined for stability studies and the most stable formulation was evaluated for cytotoxicity in Caco-2 cells. The results indicated that the formulation containing NG:PTC at 1:4 was the suitable formulation, exhibiting a particle size of 170.93 ± 1.87 nm with PDI of 0.28 ± 0.01 , zeta potential of -34.57 ± 0.57 mV, and entrapment efficiency of $86.12 \pm 0.22\%$. Among the PEG-modified formulations, PEG 400 demonstrated the most favorable properties, i.e. a particle size of 136.00 ± 1.54 nm, PDI of 0.28 ± 0.01 , zeta potential of -52.95 ± 0.27 mV, and entrapment efficiency of $96.74 \pm 0.01\%$. Stability studies at 4°C revealed that the entrapment efficiency of the PEG 400-modified formulation significantly decreased to $68.55 \pm 0.07\%$, whereas the particle size and PDI were relatively unchanged for 2 months. Regarding the cytotoxicity study in Caco-2 cells, the PEG 400-modified phytosome of naringin showed the significantly increased cytotoxicity when compared with the unprocessed naringin. The cytotoxicity was evidently increased with increasing phytosome concentration.

Keyword: Naringin, Phytosome, Polyethylene glycol, Caco-2 cells

Introduction

Naringin (NG), a naturally occurring flavonoid found in citrus fruits, exhibits a broad spectrum of pharmacological activities, including antioxidant, anti-inflammatory, anticancer, and hepatoprotective effects (1). However, its clinical utilization is hampered by poor aqueous solubility, low oral bioavailability, and susceptibility to degradation under physiological conditions (2). To overcome these drawbacks, phospholipid-based nanocarriers have been developed to enhance the solubility and membrane permeability of hydrophobic compounds (3). Phytosome, a complex of bioactive molecules with phosphatidylcholine (PTC), facilitates better interaction with biological membranes, thereby promoting absorption and bioavailability (4). Further improvement can be achieved through PEGylation conjugating polyethylene glycol (PEG) to the formulation to enhance colloidal stability, prolong circulation time, and reduce immune clearance (5). The physicochemical properties and performance of PEGylated phytosomes depend on the choice of PEG derivatives, making rational selection critical. Therefore, this study aimed to develop naringin-loaded phytosome by adding PEG derivatives to improve physical properties, stability and cytotoxicity in Caco-2 cells.

Material and methods

Materials

Naringin (NG), hydrogenated phosphatidylcholine (PTC), and cholesterol (CHO) were purchased from Myskinrecipes, Bangkok, Thailand. Polyethylene glycol 400 (PEG 400), polyethylene glycol 1500 (PEG 1500), and polyethylene glycol 4000 (PEG 4000) were bought from PC drug center, Bangkok, Thailand. Lauroyl PEG-32 glycerides (Gelucire® 44/14) was purchased from Gattefossé, Neuilly-Sur-Seine, France. Absolute ethanol and sodium hydroxide were from RCI Labscan, Bangkok, Thailand. Dulbecco's modified eagle medium (DMEM) high glucose, penicillin, streptomycin and phosphate-buffered solution (PBS) tablets were purchased from Gibco® by Life Technologies™, NY, USA. Fetal bovine serum (FBS) was bought from Gibco®, EU Approved Origin South America. MTT(3-(4,5-dimethylthiazol-2-yl)-2,5-diphenyltetrazolium bromide) was purchased from AppliChem GmbH, Darmstadt, Germany. Dimethyl sulfoxide (DMSO) was bought from Wako Pure Chemical Industries, Ltd., Osaka, Japan

Methods

Preparation of phytosomes containing naringin

In order to study the optimal ratio of naringin (NG) to phosphatidylcholine (PTC), phytosomes of naringin were prepared by thin-film hydration method using the ratios of NG:PTC of 1:1, 1:2, 1:3 and 1:4 by mole. Table 1 shows the components used to prepare phytosomes of naringin. PTC and cholesterol (CHO) were dissolved in 25 mL of absolute ethanol in beaker 1, whereas NG

was dissolved in 10 mL of absolute ethanol in beaker 2. The two solutions were mixed together and sonicated for 10 min. Then, the mixture was stirred using a magnetic stirrer for 2 h until a clear solution was obtained. The solution was subsequently evaporated by placing it in a water bath at 70°C for 5 h to form a thin film at the bottom of the beaker. Then, 80 mL of purified water was added to hydrate the sample and sonicated for 30 min to create phytosome particles.

Preparation of naringin-loaded phytosomes with the addition of polyethylene glycol (PEG) derivatives

In this study, PEG 400, PEG 1500, PEG 4000, and Gelucire® 44/14 (lauroyl PEG-32 glycerides) were selected as PEG derivatives for modification of phytosomes. PEG 400 represents a low-molecular-weight PEG with high aqueous solubility, which may enhance nanoparticle stability and bioavailability (6). PEG 1500 and PEG 4000 were included to investigate the impact of increasing chain length on the physicochemical behavior of the phytosomes. Gelucire® 44/14 was chosen for its amphiphilic nature and self-emulsifying properties, which may enhance dissolution of poorly water-soluble compounds (7). The phytosome formulation with the most suitable ratio of NG:PTC was selected to study the effect of PEG derivatives on phytosome properties. The preparation of naringin phytosomes with PEG derivatives was carried out in the same way as the preparation of naringin phytosome. The weights of PEG derivatives used in each formulation were fixed to a ratio of 1:1 to CHO (Table 1).

Table 1. Components of naringin phytosomes and naringin phytosomes containing PEG derivatives.

Ingredient (mg)	Blank (PB)	Molar ratio of NG:PTC				Phytosomes containing PEG derivatives			
		1:1 (P1)	1:2 (P2)	1:3 (P3)	1:4 (P4)	P400	P1500	P4000	G4414
PTC	500.00	133.68	267.36	401.03	534.71	534.71	534.71	534.71	534.71
CHO	150.00	40.10	80.21	120.31	160.41	160.41	160.41	160.41	160.41
NG	-	100.00	100.00	100.00	100.00	100.00	100.00	100.00	100.00
PEG 400	-	-	-	-	-	163.11	-	-	-
PEG 1500	-	-	-	-	-	-	163.11	-	-
PEG 4000	-	-	-	-	-	-	-	163.11	-
Gelucire® 44/14	-	-	-	-	-	-	-	-	163.11

Remark: The molar ratio of PTC:CHO is fixed.

Physicochemical studies of naringin-loaded phytosomes

Particle size and zeta potential of phytosomes. The particle size distribution and zeta potential of phytosomes were studied using photon correlation spectroscopy (Zetasizer Pro, Malvern Instruments, Worcestershire, UK). The sample volume of 1 mL was pipetted and distributed in 10 mL of deionized water. All data were expressed as the mean and standard deviation from triplication.

Molecular interaction in phytosomes. The molecular interaction especially between NG and PTC was studied using Fourier Transform Infrared Spectroscopy (FT-IR) (Perkin-Elmer, Waltham, MA, USA). The phytosome samples were dried using vacuum dryer (Mettler, Germany) for 24 h and collected for analysis against the unprocessed ingredients and the co-evaporated sample of PTC and NG. FT-IR spectra were obtained from 256 scans over the range of 4000-600 cm⁻¹.

Encapsulation efficiency (%EE) of naringin in phytosomes. The encapsulation efficiency of NG in phytosomes was studied by the indirect method adapted from Xiao-Lei Yu et al. (2023) (8). The phytosomes were first centrifuged at 15,000 rpm for 60 min at 4°C to separate the unencapsulated NG in the supernatant. The supernatant (500 µL) was pipetted into a 10-mL test tube, then 5 mL of absolute ethanol and 100 µL of 4 M NaOH were added and mixed with a vortex mixer. The volume was adjusted to 10 mL with deionized water, and the sample was heated with a water bath at 40°C for 10 min. The sample turned yellow. The sample was then allowed to cool to room temperature and analyzed with a UV-visible spectrophotometer (Shimadzu UV-2700i, Kyoto, Japan) at 242 nm. The percentage of encapsulation efficiency (%EE) was calculated using the equation 1.

$$\%EE = [(Total\ added\ NG - Unencapsulated\ NG) / Total\ added\ NG] \times 100 \quad \text{Equation 1}$$

Stability study of naringin phytosomes. The phytosome formulations were stored at 30°C to follow the long-term storage condition according to ICH guideline, and at 4°C (2-8°C) which is the refrigerated conditions of the long-term storage of active ingredients according to ICH guideline. The stability study was conducted for 2 months and the formulations were characterized for particle size, zeta potential, and encapsulation efficiency.

Cytotoxicity study on Caco-2 cell line

The cell culture used Caco2 cell line (human Caucasian colon adenocarcinoma ATCC Cat. No. HTB-37). Cells were maintained in Dulbecco's Modified Eagle Medium (DMEM) containing 10% fetal bovine serum, 2 mM L-glutamine, 0.1 mM non-essential amino acid, 1% penicillin/streptomycin. Cells were incubated at 37°C and 5% CO₂. The toxicity of naringin phytosomes was evaluated by MTT (3-(4,5-Dimethylthiazol-2-yl)-2,5-Diphenyltetrazolium Bromide) cell viability assay. Caco-2 cells were plated 24 h before the treatment in 96-well plates at a concentration of 2 x 10⁴ cells per well. Then, different concentrations of phytosome samples (125–1,125 µg/mL of NG) were added into each well and cultured for 24 h. DMEM without the sample were

used as a negative control. At the end of the incubation period, the treatments were removed. The MTT solution (PanReac AppliChem ITW Reagents, Spain) at the concentration of 0.5 mg/mL was then added to each well for 3 h at 37°C and 5% CO₂. After 3 h of the incubation period, the media were removed, and 50 µL of DMSO was added to dissolve the formazan crystals. The absorbance was determined at 570 nm using a microplate reader (ClarioStar Multimode Microplate Reader, BMG Labtech, Germany). The percentage of cell viability was calculated using the equation 2.

$$\% \text{ Cell viability} = \frac{(\text{Absorbance of treated cells})}{(\text{absorbance of negative control cells})} \times 100 \quad \text{Equation 2}$$

Results and discussion

Regarding the optimization of the NG:PTC ratio to generate the appropriate phytosome (Table 2), it was found that all formulations (P1-P4) showed the particle size which was smaller than that of the blank formulation (PB). The particle size reduction in drug-loaded formulations might be due to molecular interactions between drug and lipid components (9). All formulations exhibited low polydispersity index (PDI) values, indicating monodisperse systems with narrow size distributions. The low PDI values are crucial for pharmaceutical applications as they ensure reproducible drug delivery and predictable in vivo behavior (9). The zeta potentials beyond ± 30 mV generally provide sufficient electrostatic repulsion to prevent particle aggregation, suggesting the superior stability (11). All formulations showed the zeta potential values near and lower than -30 mV, which might be attributable to phosphate of PTC. This suggested the stability of the prepared phytosomes. It can be seen that the use of higher ratio of PTC resulted in better encapsulation efficiency. The higher ratio of PTC might provide a higher number of the moieties to interact molecularly with NG. A suitable concentration of PTC may optimize the balance between particle size, surface area, lipid packing geometry and internal volume available for drug entrapment (12). The lipid-to-drug ratio plays a pivotal role in determining entrapment efficiency. Higher ratios of phospholipids provide more bilayer surface and hydrophobic domains for drug incorporation, enhancing molecular interaction and drug retention (10).

FT-IR was used to prove the molecular interaction via hydrogen bonding between phospholipid and naringin to create phytosome. According to Table 3, the FT-IR spectrum of the prepared phytosome showed a number of significant wavenumber shifts particularly for hydroxyl and carbonyl groups of NG. The coprecipitated sample of PTC and NG was prepared and examined using FT-IR to confirm the molecular interactions.

According to the results, P4 was selected as the optimal formulation, combining the high encapsulation efficiency with proper physicochemical characteristics, and P4 was subsequently used as the model to study the effect of PEG derivatives.

Table 2. Particle diameter, polydispersity index (PDI), zeta potential and encapsulation efficiency (%EE) of blank phytosome, naringin phytosomes and naringin phytosomes containing PEG derivatives.

Formulation	Particle size (nm)	PDI	Zeta potential (mV)	%EE
Blank (PB)	189.80 \pm 3.59	0.35 \pm 0.02	-35.89 \pm 0.76	0.00 \pm 0.00
P1	151.87 \pm 0.25*	0.27 \pm 0.00*	-48.17 \pm 1.03*	80.56 \pm 0.58*
P2	179.23 \pm 1.82	0.29 \pm 0.02	-35.66 \pm 0.41	82.80 \pm 0.55
P3	161.87 \pm 2.68*	0.39 \pm 0.03	-29.94 \pm 0.60	85.12 \pm 0.27*
P4	170.93 \pm 1.87	0.28 \pm 0.01	-34.57 \pm 0.57	86.12 \pm 0.22*
P400	136.00 \pm 1.45*	0.28 \pm 0.01	-52.95 \pm 0.27*	96.74 \pm 0.01*
P1500	258.60 \pm 7.56*	0.65 \pm 0.11*	-55.25 \pm 0.65*	97.43 \pm 0.01*
P4000	248.17 \pm 4.65*	0.50 \pm 0.05*	-37.42 \pm 0.43	97.60 \pm 0.01*
G4414	365.23 \pm 13.14*	0.44 \pm 0.02*	-55.61 \pm 1.37*	97.05 \pm 0.00*

Significant difference compared to Blank (PB), $P < 0.05$, determined by one-way ANOVA followed by Tukey's post hoc test.

Regarding the physicochemical properties of the formulations with PEG derivatives in Table 2, P400 displayed optimal formulation characteristics, achieving minimal particle diameter of 136.00 ± 1.45 nm, low PDI 0.28 ± 0.01 , and relatively high encapsulation efficiency. The zeta potential (-52.95 ± 0.27 mV) indicated robust electrostatic stabilization. The use of PEG derivatives with lower molecular weight may optimally modulate interfacial tension while preserving colloidal stability through steric hindrance mechanism (11).

Comparative assessment of various PEG derivatives revealed significant structure-activity relationships. Notably, the addition of PEG 1500 and PEG 4000 markedly displayed the larger particle diameters with higher PDI. This phenomenon likely originates from the rigid nature and the longer chains of these two PEG derivatives, implying that they might be included into the particles. In addition, the increased viscosity and restricted molecular mobility inherent to longer PEG polymer chains may compromise nanocarrier structural integrity (15). The Gelucire® 44/14-modified formulation manifested the least favorable performance parameters. These observations are consistent with previous reports documenting that non-ionic surfactant can induce micellar coalescence and phospholipid bilayer disruption in nanostructured delivery systems (12). However, the addition of PEG derivatives

can evidently enhance encapsulation efficiency. PEGs might improve homogeneity of NG with the other ingredients to create phytosomes, leading to the high NG loading after aqueous hydration.

Table 3. FTIR peak shifts indicating phytosome formation

Component	Key Peaks (cm ⁻¹)
Phosphatidylcholine (PTC)	3369 (O-H), 1734 (C=O), 1236/1174 (P=O)
Cholesterol (CHO)	3428 (O-H), 1464 (C-H)
Naringin (NG)	3339 (O-H), 1624 (C=O), 1518 (C=C)
PTC-NG Coprecipitate	3351 (O-H, broad), 1639 (C=O, shifted)
Phytosome (with NG)	3391 (O-H), 1643 (C=O)

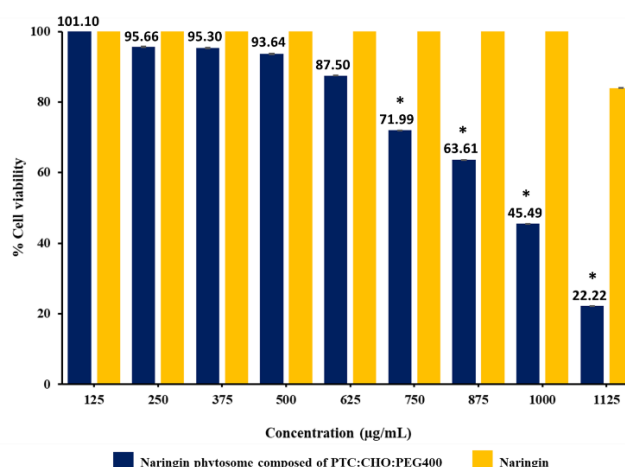


Figure 1. Cytotoxicity of naringin phytosome and unprocessed naringin on Caco-2 cells. Significantly different compared to the control (0 µg/mL) using one-way ANOVA followed by Tukey's post hoc test ($P < 0.05$).

Table 4. Physicochemical properties and encapsulation efficiency (%EE) of blank phytosome and naringin phytosomes containing PEG derivatives after storage at 4°C and 30°C for 2 months.

Formulation	At 4°C for 2 months				At 30°C for 2 months			
	Particle size (nm)	PDI	Zeta potential (mV)	%EE	Particle size (nm)	PDI	Zeta potential (mV)	%EE
P4	195.37±4.48	0.46±0.06	-45.82±1.16	75.53±0.16	309.43±70.34*	0.68±0.03*	-55.37±1.50*	75.48±0.04
P400	130.13±1.36	0.34±0.02	-41.55±0.74	68.55±0.07	160.17±3.70*	0.41±0.04*	-21.10±0.41*	61.00±0.09*
P1500	260.33±7.39	0.74±0.01	-42.52±0.12	69.24±0.02	562.43±78.52*	0.83±0.06*	-36.19±1.28*	62.34±0.03*
P4000	234.57±5.06	0.56±0.03	-46.39±2.44	69.31±0.01	1,925.67±332.88*	0.98±0.03	-48.69±1.27	61.83±0.11*
G4414	426.37±2.83	0.59±0.04	-49.35±1.31	68.24±0.05	505.43±83.67*	0.71±0.03	-56.09±2.48	62.89±0.06*

Significant difference compared to 4°C condition of the same formulation ($P < 0.05$), determined by paired t-test

The results of stability study of phytosomes are summarized in Table 4. The formulation without PEG derivatives (P4) exhibited a notable increase in particle size in both storage conditions, suggesting significant particle aggregation upon storage. Among the PEG-modified formulations, P400 demonstrated the highest stability, with only a slight increase in particle size, alongside a moderate decrease in encapsulation efficiency (%EE). This superior stability at 30°C aligns with findings that low molecular weight PEGs can enhance bilayer stability under thermal stress, whereas higher molecular weight PEGs may destabilize lipid membranes (12). During storage, visual inspection revealed slight precipitation in the formulations containing PEG 1500, PEG 4000, and Gelucire® 44/14 at 30°C, which correlated with the observed increases in particle size and PDI. In contrast, the PEG 400-based formulation remained unchanged visually. The proper hydrophilic-lipophilic balance (HLB) of PEG 400 (HLB~12) facilitates nanoparticle surface coverage, reducing interfacial tension and preventing aggregation through steric stabilization (13). Its short chain length enhances water solubility and mobility, contributing to superior colloidal stability compared to higher-MW PEGs like PEG 4000, which exhibit increased viscosity and reduced molecular flexibility (14). The decrease in encapsulation efficiency observed in all formulations suggests partial drug leakage, potentially due to phospholipid peroxidation, which has been previously reported as a mechanism for drug loss in lipid-based delivery systems (20). Since the phytosome formulation containing PEG400 can provide the most favorable characteristics, thus P400 was further selected to apply in the cytotoxicity test in human colon adenocarcinoma (Caco-2) cells. The results demonstrated a clear concentration-dependent response, with naringin phytosomes exhibiting minimal cytotoxicity at low concentrations (125–500 µg/mL), where cell viability remained above 90%. These findings align with previous reports suggesting that flavonoid compounds, including naringin, may exert cytoprotective effects or even stimulate cell proliferation at sub-therapeutic doses (15). A significant reduction in cell viability was first observed at 750 µg/mL, followed by a steep decline at higher concentrations (Figure 1). This sharp decrease suggests the onset of substantial cytotoxic effects, likely due to mitochondrial dysfunction, i.e. a mechanism previously reported for flavonoid-loaded nanoparticles

(16). The highest tested concentration (1,125 $\mu\text{g/mL}$) nearly abolished cell viability (22.22%), consistent with naringin's known ability to induce apoptosis via reactive oxygen species (ROS) mediated pathways (17). The calculated IC_{50} (948 $\mu\text{g/mL}$) corroborates existing literature on naringin's anticancer effects in colorectal cancer models, where it triggers oxidative stress, cell cycle arrest, and apoptotic cell death. Phytosomes are likely taken up by Caco-2 intestinal cells through endocytic pathways, particularly clathrin-mediated endocytosis which is a common mechanism for lipid nanoparticles (18).

Conclusion

This study successfully developed and characterized naringin-loaded phytosomes with optimized physicochemical properties for improved drug delivery. The optimization of NG:PTC ratios revealed that the molar ratio of NG:PTC at 1:4 exhibited the best balance between particle size, stability, and encapsulation efficiency. Further modification with the addition of PEG400 significantly improved colloidal stability with minimal particle size, narrow size distribution and high encapsulation efficiency. Stability studies confirmed that PEG400-modified phytosomes maintained structural integrity, while higher molecular weight PEGs and Gelucire-based formulation showed particle aggregation and reduced drug retention. These findings highlight the different actions of PEG derivatives in stabilizing phytosome. In vitro cytotoxicity assays on Caco-2 cells demonstrated a concentration-dependent effect. Naringin-loaded phytosomes showed potent cytotoxicity at higher concentrations (IC_{50} 948 $\mu\text{g/mL}$). The observed apoptosis aligns with naringin's established mechanism in colorectal cancer models.

Reference

1. Parihar, V. K., & Prabhakar, K. R. (2010). Naringin modulates oxidative stress and inflammation in 3-nitropropionic acid-induced neurodegeneration through the activation of nuclear factor-erythroid 2-related factor-2 signalling pathway. *Neuroscience*, 165(2), 654-664.
2. Li, P., & Wang, Y. (2015). Preparation and evaluation of naringin-loaded lipid-based drug delivery systems for enhancing bioavailability. *Journal of Drug Delivery Science and Technology*, 30, 432-439.
3. Semalty, A., Semalty, M., & Rawat, M. S. M. (2010). Phytosomes in herbal drug delivery. *Indian Journal of Pharmaceutical Sciences*, 72(1), 4-10.
4. Zhang, J., Tang, Q., Xu, X., & Li, N. (2013). Development and evaluation of a novel phytosome-loaded chitosan microsphere system for curcumin delivery. *International Journal of Pharmaceutics*, 448(1), 168-174.
5. Suk, J. S., Xu, Q., Kim, N., Hanes, J., & Ensign, L. M. (2016). PEGylation as a strategy for improving nanoparticle-based drug and gene delivery. *Advanced Drug Delivery Reviews*, 99, 28-51.
6. Caballero-Florán, I. H., González-González, R. B., Moreno-Luna, L. E., Morales-Luckie, R. A., & Garza-Navarro, M. A. (2023). PEGylation of PLGA nanoparticles enhances their hydrophilicity and neuronal uptake without significantly increasing particle size. *International Journal of Pharmaceutics*, 634, 122716.
7. Serajuddin, A. T. M. (2012). Solid dispersion of poorly water-soluble drugs: Early promises, subsequent problems, and recent breakthroughs. *Journal of Pharmaceutical Sciences*, 101(7), 2647-2662.
8. Yu, X., Wu, H., Zhang, L., & Fei, D. (2024). Optimization of Naringin Extraction, Synthesis of Dihydrochalcone and Its Effects on Reducing Blood Lipid Levels In Vitro. *Molecules*, 29(23), 5778.
9. Honary, S., & Zahir, F. (2013). Effect of zeta potential on the properties of nano-drug delivery systems - A review. *Tropical Journal of Pharmaceutical Research*, 12(2), 255-264.
10. Gill, B. S., & Nanda, A. (2020). Formulation and evaluation of etodolac-loaded emulsomes for enhanced anti-inflammatory and analgesic activity. *Journal of Drug Delivery Science and Technology*, 55, 101374.
11. Kulkarni, S.B., et al. (2018). PEGylation and its alternatives: A comprehensive review. *International Journal of Pharmaceutics*, 548(1), 176-189.
12. Chen, Y., et al. (2018). PEG-lipid interactions in nanocarrier systems. *Journal of Controlled Release*, 285, 230-245.
13. Zhang, Y., et al. (2021). Role of PEG chain length in nanoparticle stabilization: Interfacial tension and steric effects. *International Journal of Pharmaceutics*, 592, 120045.
14. Sharma, A., et al. (2019). Impact of PEG molecular weight on nanoparticle mobility and storage stability. *Colloids and Surfaces B: Biointerfaces*, 178, 412-420.
15. Ahmad, A., et al. (2020). Flavonoids in Cancer Therapy: Current Status and Future Perspectives. *Phytotherapy Research*, 34(5), 812-830.
16. Singh, D., et al. (2022). Flavonoid-Loaded Nanoparticles and Mitochondrial Dysfunction in Cancer Cells. *Nanomedicine*, 17(8), 1025-1040.
17. Chen, L., et al. (2021). Naringin Induces Oxidative Stress-Mediated Apoptosis in Human Colon Cancer Cells. *Journal of Agricultural and Food Chemistry*, 69(12), 3560-3570.
18. Liu, M., Svirsakis, D., Proft, T., Loh, J., Huang, Y., & Wen, J. (2024). Cellular Uptake and Transport Mechanism Investigations of PEGylated Niosomes for Improving the Oral Delivery of Thymopentin. *Pharmaceutics*, 16(3), 397.

Influence of Polymer Molecular Weight on Physical Properties and Cytotoxicity of Folic Acid Conjugated Hyaluronic Acid Nanoparticles Loading Curcumin

Nakarin Chawchaikhong¹, Natacha Busun¹, Chittima Managit¹, Sujimon Tunvichien¹, Chutima Wiranidchamong¹, Duangratana Shuwisitkul^{1,}*

¹Department of Pharmaceutical Technology, Faculty of Pharmacy, Srinakharinwirot University, Nakhonnayok, THAILAND

*Corresponding author Email: duangrats@g.swu.ac.th

Abstract. The molecular weight of hyaluronic acid polymers is one consideration to play a part in the properties of nanoparticles. Therefore, this research aimed to compare the properties of folic acid conjugated hyaluronic acid nanoparticles loading curcumin (FHAC nanoparticles) prepared by the different molecular weights of polymer. The different molecular weights of hyaluronic acid in the study were 10 kDa (small molecular weight; SHA) and 1,000 kDa (large molecular weight; LHA). The particle size, zeta potential, conjugation efficiency (CE), and cell cytotoxicity were studied. The CaCO-2 cell line was used to compare the cytotoxicity of nanoparticles prepared by LHA and SHA. FHAC nanoparticles were prepared using a chemical conjugation method. The results showed that the CE of folic acid with hyaluronic acid was higher for LHA (60% CE) than SHA polymer (35% CE). By contrast, the molecular weight of hyaluronic acid did not affect the CE of curcumin (70% CE). The particle size of FHAC nanoparticles from SHA polymer was approximately 195 nm and it increased with increasing molecular weight of hyaluronic acid (approximately 385 nm for LHA). However, the zeta potential of approximately -40 mV was similar for both FHAC nanoparticles. The cell viability of FHAC nanoparticles from LHA polymer was approximately 10% less than those from SHA polymer. In conclusion, the molecular weight of hyaluronic acid influenced particle size, conjugation efficiency, and cell cytotoxicity of FHAC. The properties of FHAC nanoparticles were partially influenced by the molecular weight of hyaluronic acid.

Keywords: Hyaluronic acid nanoparticles, Folic acid, Conjugation

INTRODUCTION

The development of drug delivery systems for cancer therapy is a technique to solve the disadvantages of traditional cancer drugs. They normally affect both cancer cells and normal cells of the body. A targeted drug delivery system can help improve therapeutic effects and reduce the side effects of traditional cancer drugs, particularly hyaluronic acid (HA) nanoparticles. HA nanoparticle delivery systems can increase the efficiency of drug release control, deliver drugs to target cells, and have more anti-cancer activities because of the targeting mechanism. The mechanism of HA nanoparticles relies on both a passive targeting mechanism from nanoparticles to tumors and an active targeting mechanism from the ability to bind to the CD44 receptor at cancer cells of hyaluronic acid [1].

Some researches are focusing on herbs used to kill cancer cells. Turmeric extract or curcumin is an active compound used to destroy cancer cells through the mechanism of increasing the destruction of cancer cells (apoptosis) and inhibiting the formation of new blood vessels of cancer cells [2]. However, curcumin has limitations in its use. It has low solubility, low permeability, and low absorption. The development of curcumin into HA nanoparticles helps increase water solubility and the ability to deliver curcumin into the body. However, it was found that the concentration of active ingredients from herbs that enter cancer cells to destroy cancer cells is still not enough to act against cancer cells.

The increase in the specificity of HA nanoparticles in delivering curcumin to destroy cancer cells by modifying HA with a ligand. Folic acid (FA) is a ligand that can bind to the folic acid receptor. This receptor is normally overexpressed on cancer cells [3]. Folic acid-conjugated hyaluronic acid nanoparticles loading curcumin (FHAC nanoparticles) increase the specificity of binding to receptors on the surface of cancer cells and increase the accumulation of curcumin in cancer cells, thus enhancing the effect of HA nanoparticles.

The molecular weight of hyaluronic acid polymers is one consideration to play a role in the properties of nanoparticles. Therefore, this research aims to compare the properties of FHAC nanoparticles prepared by the different molecular weights of polymer. The particle size, zeta potential, conjugation efficiency, and cytotoxicity of a cancer cell were studied.

MATERIALS AND METHODS

Materials

Small molecule hyaluronic acid (SHA) (MySkinRecipes, Thailand) in the molecular weight of 10 kDa and standard yaluronic acid (LHA) (MySkinRecipes, Thailand) in the molecular weight of 1,000 kDa were compared in the study. Folic acid (FA) (TOKOYO Chemical Industry Co., Ltd., Japan) and curcumin (Sigma Aldrich China Inc, China) were purchased and used as received. CaCO-2 (HTB-37) was purchased from ATCC (American Type Culture Collection), USA.

Methods

Conjugation of hyaluronic acid nanoparticles loading curcumin (FHAC nanoparticles)

FHAC nanoparticles were synthesized by conjugation. Folic acid was added to HA in the ratio of 1:100 by weight. The ratio of 1:100 by weight of HA: FA was selected caused by the preliminary study. An activated FA solution was prepared by dissolving FA in 1:1 v/v of 0.1N NaOH:DMSO (20 ml). The mixture was stirred until the clear yellow solution (solution A) was obtained. The coupling agent and catalyst, 8.2 mg of DCC and 5.0 mg of DMAP, were added to solution A. The mixture was stirred at 300 rpm overnight at the room temperature, then FA solution was obtained (solution B). Subsequently, 20 mg of HA was added to solution B and the solution was stirred for 6 h (solution C). A 6mM curcumin solution was prepared by dissolving curcumin 27.63 mg in 12.50 ml of DMSO and slowly added to the solution C. The mixture was incubated at 100 rpm and 60 °C for 6 h to create the final volume of 32.50 ml.

Measurement of particle size and zeta potential

Particle size and size distribution were determined using the Zetasizer (Malvern Panalytical Company, USA). The samples were measured using a glass cuvette quartz at a set temperature of 25°C. The test was performed on hyaluronic acid with a refractive index of 1.666, using deionized water (DI) as the solvent. The measurements were conducted using the Advance setting mode, with fluorescence interference minimized. Zeta potential was also measured using the Zetasizer with a Folded Capillary Zeta Cell at a constant temperature of 25°C, using hyaluronic acid (refractive index 1.666) and deionized water

Determination of conjugation efficiency

The conjugation efficiency of FA and curcumin were indirectly determined by the unconjugated FA and curcumin using UV-Vis spectrophotometry at 288 nm and 425 nm respectively. 5 ml of a sample in a centrifugal filter (10kDa) was centrifuged at 5000 rpm, 25°C for 5 minutes. Free FA and curcumin were collected and diluted. Drug Conjugation Efficiency (DCE) was calculated.

$$\text{Conjugation efficiency (\%)} = (\text{Ct} - \text{Cs}) / \text{Ct} \times 100$$

Ct = Total amount of active compound

Cs = Unconjugated (free) active compound

Cp = Amount of hyaluronic acid used

Cytotoxicity study

Cell viability of human colon adenocarcinoma (CaCO-2) was determined to compare cytotoxicity of FHAC nanoparticles from LHA and SHA. The cell culture media was MEM with 0.75% penicillin-streptomycin and 10% FBS. 10,000 cells of CaCO-2 were incubated at 37°C with 5% CO₂ for 24 hours before treatment. The MTS Assay Kit was used, and absorbance was read at 450 nm using a microplate reader to determine cell viability.

$$\text{Cell viability (\%)} = (\text{Absorbance of sample} / \text{Absorbance of negative control}) \times 100$$

RESULTS AND DISCUSSION

Results

FHAC nanoparticles were successfully synthesized using chemical conjugation. The particle size of less than a submicron was obtained (Table 1) after diluting the solution of FHAC nanoparticles with DI water in the dilution factor of 30X and 40X. The dilution factor less than 30X showed the higher particle size and high value of PDI indicating particle agglomeration. The dilution higher than 30X demonstrated the consistency of particle size and value of PDI. Therefore, the dilution factors of 30X and 40X have been used to compare the physical properties of FHAC nanoparticles. The particle size of FHAC nanoparticles from SHA

polymer was smaller than FHAC nanoparticles from LHA polymer. However, the zeta potentials of both FHAC nanoparticles were almost similar (Table 1).

The conjugation efficiency of folic acid with hyaluronic acid was significantly higher for LHA polymer than for SHA polymer (Table 2). By contrast, the molecular weight of hyaluronic acid did not affect the conjugation efficiency of curcumin. The conjugation efficiency was approximately 70% for both FHAC nanoparticles (Table 2).

Table 1. Comparison of particle size and zeta potential of FHAC nanoparticles from SHA and LHA polymer.

Ratio of diluted nanoparticles in DI water	SHA-FHAC Nanoparticles			LHA-FHAC Nanoparticles		
	Particle size (nm)	PDI	Zeta potential (mV)	Particle size (nm)	PDI	Zeta potential (mV)
1: 30	227.5 \pm 7.2	0.44 \pm 0.03	-41.6 \pm 7.7	430.1 \pm 139.5	0.58 \pm 0.04	-41.3 \pm 10.1
1: 40	163.6 \pm 23.7	0.41 \pm 0.06	-40.7 \pm 14.2	339.9 \pm 96.7	0.47 \pm 0.09	-34.3 \pm 5.4

Table 2. Comparison of conjugation efficiency of folic acid and curcumin with SHA and LHA polymer for FHAC nanoparticles.

Ligand/Drug	SHA-FHAC nanoparticles	LHA-FHAC nanoparticles
Folic acid	34.50 \pm 0.69*	59.32 \pm 2.79*
Curcumin	71.39 \pm 1.69	75.79 \pm 0.02

*Unpaired t-test statistical test ($p < 0.0001$) at 95% confidence level

The CaCO-2 cell line, colorectal adenocarcinoma cell line, was used to study the cytotoxicity of nanoparticles prepared from LHA and SHA polymer. The curcumin solution for the cytotoxicity was 0.008 mM. LHA and SHA solutions in concentration of 0.0003% w/v and FA solution in concentration of 0.01mM were prepared to perform the cytotoxicity test. The concentration of curcumin, FA, LHA and SHA solutions were equal to their concentration in the nanoparticles with dilution factor of 200X. FA, LHA and SHA polymers with/without folic acid conjugation were not toxic to CaCO-2 cells (Figure 1). There was the effect of curcumin, SHA nanoparticles with curcumin and LHA nanoparticles with curcumin on CaCO-2 cells. After 24 hours, the cells were killed approximately 50%. However, the conjugation of folic acid with HA nanoparticles showed the better effect on CaCO-2 cells. FHAC nanoparticles demonstrated the highest cytotoxicity among the others. The lowest cell viability was obtained from FHAC nanoparticles from LHA polymer.

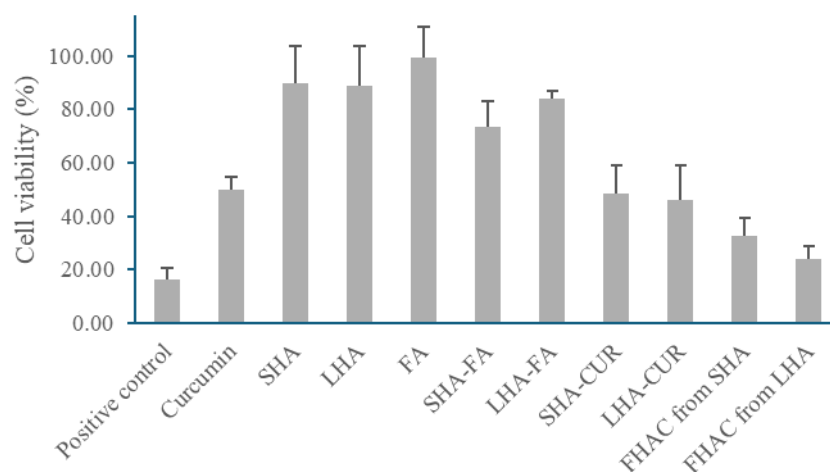


Figure 1. Comparison of cell viability (%) of CaCO-2 after incubation of the HA polymers, curcumin, SHA-FA (SHA conjugated with FA), LHA-FA (LHA conjugated with FA), SHA-Cur (SHA conjugated with curcumin), LHA-Cur (LHA conjugated with curcumin), and FHAC nanoparticles from SHA and LHA.

Discussions

FHAC nanoparticles from both LHA and SHA polymer showed similarly negative charge of zeta potential. This finding was explained by the negative charge of HA polymers [4]. The ligand, folic acid, on HA polymers also containing carboxylic acid

groups can lead to the negative charge of zeta potential (Table 1). LHA polymer could not disentangle sufficiently enough to lead to individual particles during conjugation [5], thus the larger particles form LHA polymer in comparison to SHA polymer.

The carboxylic acid group of FA could conjugate with HA polymer at the hydroxyl group [6]. LHA polymer contains more hydroxyl groups on the chains than SHA polymer. It can result in high conjugation efficiency of FA (Table 2). Curcumin was subsequently conjugated on HA polymer after FA. The saturated reactive sites of HA led to no higher conjugation efficiency of curcumin with LHA polymer in comparison to SHA polymer.

Folate receptors are usually overexpressed on cancer cells [3]. When conjugating FA on HA polymer, the nanoparticles could enter the cells through two receptors, folate receptors and CD44 receptors. The higher amount of curcumin in FHAC nanoparticles went into CaCO-2 cells. It caused more dead cells than HA nanoparticles without FA. Some studies showed that the high molecular weight of HA could inhibit cell proliferation [7]. This might lead to more cytotoxicity of LHA-FHAC nanoparticles than SHA-FHAC nanoparticles.

The study was performed using the narrow range of HA molecular weights. More HA molecular weights should be studied to demonstrate a tendency of particle size, conjugation efficiency and cytotoxicity. To explain in detail regarding cellular uptake of HA nanoparticles prepared by different molecular weights, a cellular uptake study should be performed to support receptor-mediated internalization.

CONCLUSIONS

The molecular weight of hyaluronic acid influenced the properties of FHAC nanoparticles, including particle size, conjugation efficiency, and cell cytotoxicity. The properties of FHAC nanoparticles were partially affected by the molecular weight of hyaluronic acid. More variety of HA molecular weight and cellular uptake are recommended to investigate for more assumptions on the effect of the molecular weight of hyaluronic acid on the properties of FHAC nanoparticles.

ACKNOWLEDGMENTS

This research is supported financially by the Faculty of Pharmacy, Srinakharinwirot University.

REFERENCES

1. Machado V, Morais M, Medeiros R. Hyaluronic Acid-Based Nanomaterials Applied to Cancer: Where Are We Now? *Pharmaceutics*. 2022; 14(10):2092. Available from <https://doi.org/10.3390/pharmaceutics14102092>
2. Wan Mohd Tajuddin WN, Lajis NH, Abas F, Othman I, Naidu R. Mechanistic understanding of curcumin's therapeutic effects in lung cancer. *Nutrients*. 2019;11(12):2989.
3. Boss SD, Ametamey SM. Development of folate receptor–targeted pet radiopharmaceuticals for tumor imaging-a bench-to bedside journey. *Cancers*. 2020;12(6):1508.
4. Polexe RC, Delair T. Elaboration of stable and antibody functionalized positively charged colloids by polyelectrolyte complexation between chitosan and hyaluronic acid. *Molecules* 2013; 18: 8563-8578.
5. Akentieva NP, et al. Development of chitosan-hyaluronic acid nanoparticles and study of their physico-chemical properties for targeted delivery of anticancer drugs. *IOP Conf. Ser.: Mater. Sci. Eng.* 2020;848: 012002.
6. Zhanga X, Liangb N, Gong X, Kawashimac Y, Cuid F, Suna S. Tumor-targeting micelles based on folic acid and α -tocopherol succinate conjugated hyaluronic acid for paclitaxel delivery. *Colloids Surf. B Biointerfaces* 2019; 177: 11–18.
7. Zhao N, Wang X, Qin L, Guo Z, Li D. Effect of molecular weight and concentration of hyaluronan on cell proliferation and osteogenic differentiation in vitro. *Biochem. Biophys. Res. Commun.* 2015; 465(3): 569-574.

Advances in Pharmaceutical Sciences, Analysis, and Medicinal Chemistry

Green and Rapid Stability-Indicating HPLC Method for Determination of Rosmarinic Acid in *Thunbergia Laurifolia* Leaf Extract

Sudarat Arunmongkon¹, Chaweewan Suwanvecho², Pongtip Sithisarn³,
Piyanuch Rojsanga^{2,*}

¹Center of analysis product quality (Chemical division), Faculty of Pharmacy, Mahidol University, Bangkok, THAILAND

²Department of Pharmaceutical Chemistry, Faculty of Pharmacy, Mahidol University, Bangkok, THAILAND

³Department of Pharmacognosy, Faculty of Pharmacy, Mahidol University, Bangkok, THAILAND

*Corresponding author Email: piyanuch.roj@mahidol.ac.th

Abstract. A simple and precise high-performance liquid chromatographic method (HPLC) was developed for determination of rosmarinic acid (RA) in the ethanolic extract of *Thunbergia laurifolia* leaf (ETL). Using a monolithic C-18 column with a mobile phase of 0.02% phosphoric acid and 12% methanol in acetonitrile, the rapid gradient elution achieved a retention time of 7.7 min for RA and a 14-minute analysis time. The sample preparation was simplified by direct dilution with 10% acetonitrile in water. Forced degradation studies were carried out under acidic, basic, oxidative, and photolysis conditions. The results revealed that RA was stable in acidic and oxidative conditions, but extremely labile under basic and photolytic conditions. No interference from degradation products was observed in the HPLC chromatogram at the retention times of RA, demonstrating the specificity of the method. The HPLC method exhibited linear correlations for RA in the concentration range of 2.09–104.4 µg/mL, with correlation coefficients (r)>0.99. RA recoveries ranged from 99.6–102.7%, and relative standard deviations for repeatability and intermediate precision were less than 1.8%. The RA content in ETL extracted with 55–95 % ethanol ranged from 0.24 to 7.78 mg/g of dried leaf. Interestingly, the developed method is environmentally friendly, as it minimizes solvents used, and enhance laboratory safety. The method's greenness was further confirmed by an AGREE software greenness score of 0.7 from 1. The proposed approach was shown to be a promising method for quality control of *T. laurifolia* leaf extracts

Keywords: *Thunbergia laurifolia*; Force degradation; Monolithic column; Rosmarinic acid; Green analytical chemistry

INTRODUCTION

Thunbergia laurifolia (TL), known as Rang Chuet, is a medicinal plant native to Southeast Asia. In Thailand, the herbal teas and capsules of TL leaves are listed in the National List of Essential Medicines 2023 under the category of herbal medicines for treatments of fever and aphthous ulcers [1,2]. TL leaves contain flavonoids, including apigenin and apigenin glucosides, as well as some phenolic acids, including caffeic, gallic, protocatechuic, and rosmarinic acids (RA) [3]. The TL leaf extracts have been reported to possess anti-inflammatory, antioxidant, anti-diabetic, antimicrobial, anti-depressant, and anti-dementia activities [3–9]. Furthermore, RA a major compound derived from TL leaves has been documented to have anti-inflammatory and antioxidant activities [5–9], rendering it a significant molecule for potential therapeutic applications. Its detection as a chemical marker may also help standardize TL leaf extract for uniform potency and effectiveness across different formulations. High-performance liquid chromatography (HPLC) was the primary analytical method used to quantify RA content in plant extracts [10–12], because of its benefits in terms of sensitivity, specificity, and accuracy. However, most of them require a quite long period analysis (normally more than 20 min). The implementation of high-throughput liquid chromatography technology has been suggested to mitigate these limitations, hence shortening analysis time and thereby diminishing environmental effect through reduced solvent consumption.

Moreover, drug stability assays are crucial in pharmaceutical research for reliability. A stability-indicating method (SIM) for RA in TL extract can detect and separate out degradation products, requiring forced degradation studies. This information aids in determining storage needs, formulation development, container design, and pre-formulation research, illustrating RA chemical behavior and potential breakdown mechanisms.

In this work, we described the development and validation of a rapid and stability-indicating HPLC method for the quantification of RA in the ethanolic extract of *T. laurifolia* leaf (ETL). In addition, the method was effectively employed to quantify RA in TL leaf extract that was prepared using varying concentrations of ethanol. This purposed method can be used for routine quality control analysis of ETLs to ensure their potency and stability.

MATERIALS AND METHODS

Materials

Acetonitrile and methanol (HPLC grade) were purchased from Merck (Darmstadt, Germany). Orthophosphoric acid (HPLC grade), dipotassium phosphate, hydrochloric acid, sodium hydroxide and hydrogen peroxide were obtained from Fisher Scientific (Leicestershire, UK). RA were procured from Sigma-Aldrich (Missouri, USA)

Methods

Plant extract preparation

The TL leaves were collected from Amnat Charoen province, Thailand in November 2024. The leaves were cleaned, dried in 60 °C for 8 h, powdered with an electronic mill (20 mesh sieve). The extraction was performed in a plastic vial at solid-liquid ratio 1:10 (final volume 5 mL) with 75% v/v ethanol in an ultrasonic bath (GT SONIC-D9) at 200 W, and 40 °C for 45 min. After the extraction, the samples were centrifuged at 6000 rpm for 10 min. The supernatant was collected, then 1.2 g of dipotassium phosphate (K_2HPO_4 , 98 wt%) was added. The mixture was vortexed until the salt completely dissolved. After placed at room temperature (25 °C) for 8 h, the upper phase (ETL) was transferred into a new tube and stored at -20 °C for further analysis.

The HPLC analysis and chromatographic condition

The analysis was performed using a Shimadzu *i*-Series (Model LC-2050C, Shimadzu Cooperation, Japan) equipped with a photo diode array detector. The chromatographic separation was carried out on a Chromolith Performance RP-18e column (150 × 4.6 mm, Merck, Germany) with a RP-18e guard cartridge (5 × 4.6 mm) from the same company. The column temperature was maintained at 30 °C. The flow rate was optimized to 1.5 mL/min and the sample injection volume was 10 µL. The mobile phase consisted of solvent A (0.02% phosphoric acid in water) and solvent B (12% methanol acetonitrile). Gradient elution was programmed as follows: 0–3 min, 12% B; 3–7 min, 12–45% B; 7–7.5 min, 45–55% B; 7.5–8 min, 55–85% B; 8–10 min, 85% B; 10–11 min, 85–12% B; 11–14 min, 12% B. UV absorption was monitored at 330 nm.

Force degradation

ETL was subjected to four stress testing conditions defined in the ICH guideline Q1A [13]: acid hydrolysis, alkali hydrolysis, oxidation, and photolysis. For acid hydrolysis, 100 µL of 0.2N HCl was added to 1 mL of ETL and heated at 60 °C for 1 h. For basic hydrolysis, 50 µL of 0.2 N NaOH was added to 1 mL of ETL and kept at room temperature for 30 min. For oxidative stress, 10 µL of 30% w/w H_2O_2 was added to 1 mL of ETL and incubated at 60 °C for 1 h. For photolysis, 1 mL of ETL was exposed to sunlight for 4 h. Before HPLC analysis, all stress samples were diluted with 10% acetonitrile in water to make the volume of 10 mL and filtered through a 0.45-µm PTFE syringe filter.

Method Validation

The method was validated following ICH Q2(R1) guidelines [14] for specificity, linearity, accuracy, precision, and limit of quantitation (LOQ). Specificity was assessed to ensure that there were no interferences affecting the retention times of marker. This was achieved by comparing chromatograms of forced degradation and control samples with peak purity value exceeding 0.9 and a resolution greater than 2. For linearity, calibration curves were established using six concentration levels of standard solutions covering the ranges of 2.09–104.4 µg/mL of RA. The linearity was evaluated through linear regression analysis, with correlation coefficient (*r*) more than 0.99. Accuracy was evaluated by spiking samples with 3 different concentration levels of RA (10, 20, and 40 µg/mL) and the percentage recovery was calculated from three replicates per concentration level. Precision was assessed by analyzing six samples (*n*=6) on the same day for repeatability and 12 samples (*n*=12) on different days for intermediate precision. The percentage relative standard deviation was calculated to ensure precision of the method. The LOQ was determined as the lowest concentration that yielded acceptable accuracy (%recovery) and precision (%RSD). Six samples prepared at the concentration of LOQ were determined %recovery and %RSD.

Determination of RA content in ETLs

For ETL preparation, the powder samples were extracted using varied percentages of ethanol (55%, 60%, 75%, and 95% v/v) as outlined in the section on plant extract preparation. Prior to HPLC analysis, the samples were diluted with 10% acetonitrile in water to achieve a total volume of 10 mL and subsequently filtered using a 0.45-µm PTFE syringe filter.

Method for Evaluating Greenness using AGREE software

The environmental impact and human safety of the developed HPLC method were assessed using AGREE (Analytical GREENness) software [15], a tool based on the principle of green analytical chemistry. The software evaluates various factors including solvent selection, energy consumption, reagent toxicity, and waste production to generate an overall greenness score on scale from 0 to 1 and displayed on a red-yellow-green color scale as explained in results. A green colored one represents the most environmentally friendly method. Each criterion was presented by the color in the numbered segment around the center circle. Size of each segment is corresponded to the assigned weight of that criterion.

RESULTS AND DISCUSSION

Results

For method optimization, the chromatographic condition was adjusted from Onsawang et al. [12]. The flow rate was increased to 1.5 mL/min to compensate differences between the monolithic column used in this study and the fully porous silica column. Isocratic elution using 0.02% phosphoric acid in water (A) and methanol (B) at a 40:60 ratio resulted in poor separation. Similarly, replacing methanol with 50% acetonitrile failed to improve resolution. To enhance the separation of RA, a gradient elution method, as described by Onsawang et al., was applied using acetonitrile as organic phase (B). However, resolution of RA from adjacent peaks remained unsatisfactory. To migrate these issues, 12% methanol was added to organic phase to reduce its eluting power, and the gradient was extended between 7.5 and 8.0 min. This modification improved the resolution of RA to greater than 2, with a total runtime of 14 min.

The analytical technique was validated in accordance with the ICH Q2(R1) guideline [14]. Forced degradation studies were employed to assess the specificity. Figure 1 illustrates that the percentage of remaining RA in stressed samples varied between 12% and 104% relative to the control sample. No interfering peaks were detected at the RA retention time, with peak purity index 0.9581–0.9702, therefore demonstrating the specificity of method. As shown in Table 1, RA exhibited linearity over 2.09–104.4 µg/mL, with r of 0.9999. Precision was evaluated through intra-day and inter-day variability, with all %RSD values ≤ 3 . Recovery was determined using standard addition method, the recovery of standard spiked concentration found divided by its nominal concentration were calculated and reported in Table 1. Moreover, the LOQ was 2.04 µg/mL with %RSD of 0.46 and %recovery of 99.4 (98.7–100.0%).

Table 1. Validation results of the optimized HPLC method for determination of rosmarinic acid

Validation parameter	Criteria	Result
Linearity	N/A $r \geq 0.99$	$y = 17317x - 10009$ $r = 0.9999$
Range	N/A	2.09–104.4 µg/mL
Accuracy (%recovery, n=9)	Mean recovery 90-108%	100.6 (99.6–102.7)
- 10 µg/mL (n=3)		101.6 (99.9–102.7)
- 20 µg/mL (n=3)		100.1 (99.6–100.5)
- 40 µg/mL (n=3)		100.1 (99.9–100.4)
Repeatability (%RSD, n=6)	%RSD ≤ 3	1.46, 1.74
Intermediate precision (%RSD, n=12)	%RSD ≤ 3	1.60
Limit of quantitation	N/A	2.04 µg/mL

r = correlation coefficient, RSD = relative standard deviation, N/A = not applicable

The validated method was applied to quantify RA in performed at 40 °C for 45 min. The contents of RA in extracts using ethanol concentrations of 55%, 60%, 75%, and 95% were 5.61 ± 0.25 , 7.78 ± 0.46 , 5.92 ± 0.31 , and 0.24 ± 0.02 mg/g dried leaves, respectively.

In addition to analytical performance, the environmental impact of the method was assessed using AGREE software [15] with scored 0.7 (Figure 2). The developed method is greener than Onsawang et al. with scored 0.64 [12] by improving sample throughput and minimizing of sample preparation steps.

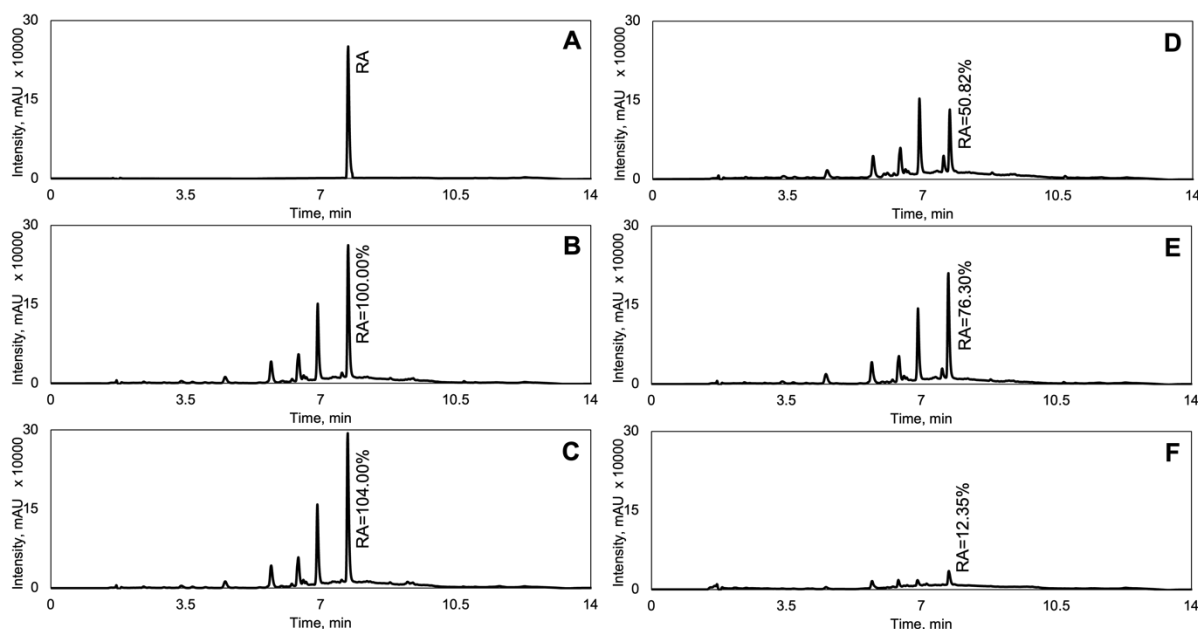


Figure 1. The chromatogram of standard solution 10 µg/mL (A) and the ethanolic extract of *T. laurifolia* leaf control (unforced) sample (B), as well as under acid hydrolysis (C), alkali hydrolysis (D), photolysis (E), and oxidation (F) detected at 330 nm, with the peak of rosmarinic acid (RA) observed at 7.7 min. Percent remaining, relatively to RA peak of the ETF control, was presented on each chromatogram.

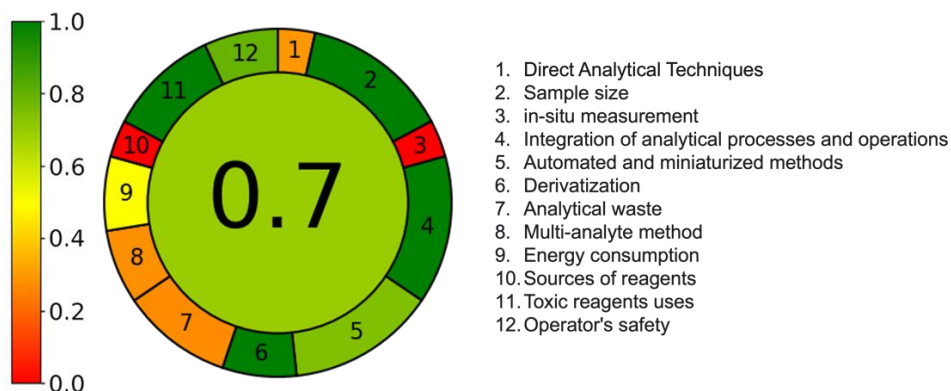


Figure 2. Greenness pictogram of the developed method. Overall greenness score and the corresponding color were presented in the center circle (1 with green color = the best overall greenness performance as displayed in the color scale with greenness score). Each performance criterion was represented by the outer element which was identified with the numbers.

Discussions

Research on RA in plant extracts has employed several approaches for quantification [10–12]. Many of these strategies need considerable time-consuming procedures. This study selected a monolithic column for its capacity to provide high-speed analysis, hence enhancing cost-efficiency in analytical procedures. The study utilized a 12% methanol in acetonitrile combination with 0.02% (v/v) phosphoric acid due to its efficacy in chromatographic separation and its ability to reduce the ionization of RA during analysis. The method's capacity to precisely estimate RA in ETL without influence from degradation products is crucial, particularly for stability studies. The method's stability-indicating properties were also assessed. The degraded sample verified that the RA remained stable in acidic condition but deteriorated in basic, oxidative, and photolytic conditions. The suggested technique was validated, and all parameters conformed to the acceptance requirements. The technique was effectively utilized to determine RA content using 55–95% v/v ethanol. Extraction with 60% ethanol yielded the maximum concentration, while extraction with 95% ethanol resulted in the lowest level. These findings imply that the amount of ethanol used affects the efficacy of RA extraction.

Additional studies could investigate the influence of different solvents on RA extraction in order to optimize the procedure for optimal yield.

Furthermore, a small sample volume and the single-step sample preparation method without derivatization have been highlighted as reasons for the AGREE software's 0.7 out of 1 greenness score. No additional solvent or hazardous reagents were used. Energy consumption was limited to HPLC operation, with no additional sample preparation equipment. The runtime was reduced to 14 min, compared to the 40-min method of Onsawang et al. [12], improving sample throughput. The only limitation was the use of acetonitrile as the mobile phase. Overall, the method is rapid, robust, and environmentally sustainable.

CONCLUSIONS

A stability-indicating HPLC method was developed and validated for the determination of RA in ETL. The method is simple, accurate, precise, and effective across a wide concentration range of RA. From a green chemistry perspective, it minimizes reagent use and energy consumption through single step sample preparation and reduced solvent volumes, offering a sustainable analytical approach.

ACKNOWLEDGMENTS

The authors would like to express their gratitude to Faculty of pharmacy, Mahidol university for providing the research facilities and technical support. Special appreciation is extended to Center of analysis product quality (chemical division) team for their encouragement and support.

REFERENCES

1. Chan EWC, Eng SY, Tan YP, et al. Phytochemistry and pharmacological properties of *Thunbergia Laurifolia*: A Review. Pharmacognosy Journal 2011;3(24):1-6.
2. Herbal Product Division (Thai Food and Drug Administration). National List of Essential Medicines 2023. Department of Medical Sciences MoPH, editor. Bangkok; 2023.
3. Nanna U, Chiruntanat N, Jaijoy, et al. Effect of *Thunbergia laurifolia* Lindl. Extract on Anti-Inflammatory, Analgesic and Antipyretic Activity. J Med Assoc Thai. 2017;100(5):98–106.
4. Posridee K, Oonsivilai A, Oonsivilai R. Acute and sub-chronic toxicity study of Rang chuet (*Thunbergia Laurifolia* Lindl.) extracts and its antioxidant activities. Toxicol Rep. 2022;9:2000–17.
5. Pattananandecha T, Apichai S, Julsrigival J, et al. Antioxidant activity and anti-photoaging effects on UVA-irradiated human fibroblasts of rosmarinic acid enriched extract prepared from *Thunbergia laurifolia* leaves. Plants. 2021;10(8):1648.
6. Aritajat S, Wutteerapol S, Saenphet K. Anti-diabetic effect of *Thunbergia laurifolia* Linn. aqueous extract. Southeast Asian J Trop Med Public Health. 2004;35.
7. Boonyarikpunchai W, Sukrong S, Towiwat P. Antinociceptive and anti-inflammatory effects of rosmarinic acid isolated from *Thunbergia laurifolia* Lindl. Pharmacol Biochem and Behav. 2014;124:67–73.
8. So-In C, Sunthamala N. Treatment efficacy of *Thunbergia laurifolia*, *Curcuma longa*, *Garcinia mangostana*, and *Andrographis paniculata* extracts in staphylococcus aureus-induced rabbit dermatitis model. Veterinary World. 2022;188–97.
9. Rojsanga P, Sithisarn P, Tanaka K, et al. *Thunbergia laurifolia* extract ameliorates cognitive and emotional deficits in olfactoryectomized mice. Pharm Biol 2015;53(8):1141-8.
10. Öztürk N, Tunçel M, Uysal UD, et al. Determination of rosmarinic acid by high-performance liquid chromatography and its application to certain *Salvia* species and rosemary, Food Anal. Methods. 2011;4:300–6.
11. Adham AN. Comparative extraction methods, phytochemical constituents, fluorescence analysis and HPLC validation of rosmarinic acid content in *Mentha piperita*, *Mentha longifolia* and *Ocimum basilicum*, J. Pharmacogn. Phytochem. 2015;3:130–9.
12. Onsawang T, Suwanvecho C, Sithisarn P, et al. Experimental design approach for the quantitative analysis of multicomponents by single marker and HPLC fingerprinting of *Thunbergia laurifolia* aqueous extract. Phytochem Anal. 2024;35(6):1472-85.
13. ICH. Q1A(R2): Stability Testing of new Drug Substances and Products step 5 [Internet], 2003 [cited 2025 Apr 4]. Available from: https://www.ema.europa.eu/en/documents/scientific-guideline/ich-q-1-r2-stability-testing-new-drug-substances-and-products-step-5_en.pdf
14. ICH guideline Q2(R1) on validation of analytical procedures [Internet], 1995 [cited 2025 Apr 4]. Available from: https://www.ema.europa.eu/en/documents/scientific-guideline/ich-guideline-q2r1-validation-analytical-procedures-text-and-methodology-step-5-first-version_en.pdf.
15. Francisco Pena-Pereira WW and Marek Tobiszewski. AGREE-Analytical GREENness Metric Approach and Software. Analytical chemistry. 2020;92:10076-82.

Determination of Anti-aging Amino Acids via High-Performance Liquid Chromatography using 2-Hydroxynaphthaldehyde as a Derivatizing Agent

Pornnapa Thanomrak¹, and Vipaporn Panapisal^{1,}*

¹Department of Pharmaceutics and Industrial Pharmacy, Faculty of Pharmaceutical Sciences, Chulalongkorn University, Bangkok, Thailand
Author Email: thanomrak2542@gmail.com

*Corresponding author Email: vipaporn.p@chula.ac.th

Abstract. Gamma-aminobutyric acid (GABA) enhances elastin fiber production, while glycine and L-proline promote collagen formation. High-performance liquid chromatography (HPLC) is widely used for amino acid analysis but requires derivatization to improve detection. This study investigates the determination of GABA, glycine, and L-proline using 2-hydroxynaphthaldehyde (HN) as a derivatizing agent. GABA and glycine were derivatized using the same agent under similar conditions, while L-proline underwent derivatization with slight variations in preparation parameters. Validation confirmed specificity, linearity, accuracy, and precision. The linear range was 6 – 100 µg/mL for GABA and glycine, and 600 – 9600 µg/mL for L-proline. The limits of detection (LOD) were 1.47, 1.72, and 132.48 µg/mL, while the limits of quantitation (LOQ) were 4.47, 5.21, and 401.47 µg/mL for GABA, glycine, and L-proline, respectively. GABA and glycine showed greater reactivity with HN and higher sensitivity than L-proline. This validated HPLC method provides a reliable approach for quantifying anti-aging amino acids.

Keywords: GABA; glycine; L-proline; 2-hydroxynaphthaldehyde

INTRODUCTION

Amino acids are vital biomolecules involved in various physiological processes and have recently gained attention for their anti-aging potential in cosmetics. γ -aminobutyric acid (GABA), a major inhibitory neurotransmitter found in plants, animals, and microbes [1, 2], enhances elastin fiber production [3], reduces MMP-1-mediated collagen degradation [4], and promotes filaggrin synthesis, a key component of the natural moisturizing factors (NMFs) [4]. Glycine and proline, key components of collagen fibers, support skin structure [5, 6] and are primarily derived from dietary sources [7]. Arginine, abundant in foods like salmon and pumpkin seeds, boosts nitric oxide production for improved dermal circulation and acts as a precursor for proline and glutamine [8, 9]. Glutamine supplement has been reported to alleviate signs of skin aging caused by oxidative stress [10], while taurine aids skin regeneration and accelerating the repair of damaged skin tissue [11].

Growing evidence suggests that combinations of amino acids can exert synergistic benefits beyond those of individual components. For example, Diaz et al. (2022) [11] reported that a combination of taurine, glycine, and arginine (AAComplex) effectively reduced skin irritation and improved skin hydration. In alignment with this trend, our research group recently developed and obtained a Thai petty patent for a synergistic amino acid blend comprising GABA, glycine, and L-proline, specifically designed to enhance anti-aging efficacy in cosmetic products. Despite the increasing use of amino acid mixtures in cosmetic formulations, there remains a limitation in validated analytical methods capable of simultaneously quantifying individual amino acids within such combinations. Amino acids can be quantified using various techniques, including gas chromatography-mass spectrometry (GC-MS) [12, 13], capillary electrophoresis-mass spectrometry [14], liquid chromatography-mass spectrometry (LC-MS) [15], and high-performance liquid chromatography (HPLC) [16, 17, 18]. Among these, HPLC is widely utilized due to its high resolution, sensitivity, and reproducibility. However, amino acids exhibit weak UV absorption and fluorescence, necessitating derivatization to enhance detection. Several derivatizing agents, such as o-phthalaldehyde (OPA) [18, 19], phenylisothiocyanate [17], 9-fluorenylmethyloxycarbonyl derivatives (FMOC) [16, 20], and 2-hydroxynaphthaldehyde (HN) [18] have been employed, each interacting differently with amino acids. HN has been reported to improve the detection of HPLC-based amino acids, particularly GABA [18, 21]. Amino acids react with HN to form Schiff base derivatives via nucleophilic attack by their amino groups. While this is effective for primary amines, its reactivity with secondary amines, such as in L-proline, is limited due to steric hindrance from the pyrrolidine ring and requires modified derivatization conditions. Previous studies have been reported the use of GABA-HN derivative for the determination of GABA content in cerebrospinal fluid, which also consisted other primary amine - containing amino acids such as glycine, tyramine, and lysine [21]. However, there is a lack of validated analytical methods for the simultaneous quantifying amino acid mixtures with diverse amine groups. As amino acid combinations are increasingly incorporated in formulations, a validated method capable of quantifying multiple amino acids in a single run is urgently needed. This research addresses this gap by developing a robust, HN-based HPLC method to analyze GABA, glycine, and L-proline simultaneously.

This study aims to develop and validate an HPLC method for the simultaneous determination of GABA, glycine, and L-proline using 2-hydroxynaphthaldehyde (HN) as a derivatizing agent. GABA and glycine were derivatized under identical protocol, while L-proline required a modified protocol. After derivatization, the amino acids were analyzed using HPLC equipped with a UV detector. GABA and glycine were detected at a wavelength of 330 nm, while L-proline was detected at 280 nm.

MATERIALS AND METHODS

Materials

γ -amino butyric acid was purchased from Shaanxi Youbio Technology Co., Ltd (China). Glycine was purchased from Kemaus (Australia). L-proline and 2-hydroxy-1-naphthaldehyde were purchased from Sigma-Aldrich (Germany). Potassium chloride, boric acid, and sodium hydroxide were purchased from Merck (Germany). Methanol was purchased from RCI Labscan Limited (Thailand). Ultrapure water obtained from Faculty of Pharmaceutical Sciences, Chulalongkorn University.

Methods

Derivatization method

Derivatization of GABA, glycine (Gly), and L-proline (Pro) with 2-hydroxynaphthaldehyde (HN) were performed based on protocol modified from Panrod et al [18]. GABA and glycine were prepared as a combined solution at a 1:1 ratio, while L-proline was prepared separately. The solution was mixed with 0.6 mL of borate buffer (pH 8) and 1 mL of 0.3 %w/v 2-hydroxynaphthaldehyde in methanol. The mixture of GABA and glycine were heated in a water bath at 80 °C for 10 minutes. While the mixture of L-proline was heated at 50 °C for 40 minutes. After that, the mixture of each amino acids cooled down at 30 °C and protected from light for 10 minutes and then adjusted to 5 mL with methanol before HPLC analysis.

HPLC method

The HPLC equipped with a UV detector was used for analysis. Separation was performed on ACE Excel 5 C18-AR (4.6 mm \times 250 mm) at 25 °C. The mobile phase consists of methanol and water (62:38, v/v). The mobile phase was filtered through 0.45 μ m membrane filters and vacuum degassed before use. The injection volume was 5 μ L and isocratically eluted at a flow rate of 0.95 mL/min. The UV detector was set at 330 nm for GABA-HN and Gly-HN derivatives and 280 nm for Pro-HN derivatives. Each sample was analyzed in triplicated.

Validation method of HPLC

The validation method was conducted in accordance with the ICH guideline Q2(1). Specificity was assessed by comparing the HPLC chromatograms of each amino acid derivatized with HN and a blank derivatized with HN. GABA and glycine solutions at concentration of 6, 10, 20, 60, and 100 μ g/mL were analyzed, while L-proline solutions at concentration of 600, 1200, 2400, 4800, and 9600 μ g/mL were analyzed. A calibration curve was plotted between the peak area and concentrations. Each concentration was analyzed in triplicated. The linearity was determined based on the coefficient of determination ($r^2 \geq 0.999$). The accuracy was performed at three different concentrations covering the range and the percentage of recovery should range from 85-115%. The intra-day precision was performed by analyzing three concentrations within the same day and three consecutive days for the inter-day precision. The percentage of coefficient of variation (% CV) should be less than 2%. The limit of detection (LOD) and the limit of quantitation (LOQ) were analyzed by determination of the signal-to-noise (S/N) ratio, with a S/N ratio of 3:1 or 2:1 for LOD and 10:1 for LOQ.

RESULTS AND DISCUSSION

Results

The regression analysis is shown in **Table 1**. The linearity was plotted between peak area vs concentrations. GABA-HN and Gly-HN derivatives were plotted at concentration ranging from 6 to 100 μ g/mL. The linear equations were $y = 15058x + 15223$ and $y = 16213x - 19830$ for GABA-HN and Gly-HN derivatives, respectively. The results showed the coefficient of determination (r^2) of 0.9998 for both GABA-HN and Gly-HN derivatives. Pro-HN derivative was plotted at concentrations ranging from 600-9600 μ g/mL and the linear equation was $y = 41.012x + 6727$, with a coefficient of determination (r^2) of 0.9991. The limit of detection (LOD) was 1.47, 1.72, and 132.48 μ g/mL for GABA-HN, Gly-HN, and Pro-HN derivatives, respectively. The limit of quantitation (LOQ) was 4.47, 5.21, and 401.47 for GABA-HN, Gly-HN, and Pro-HN derivatives, respectively.

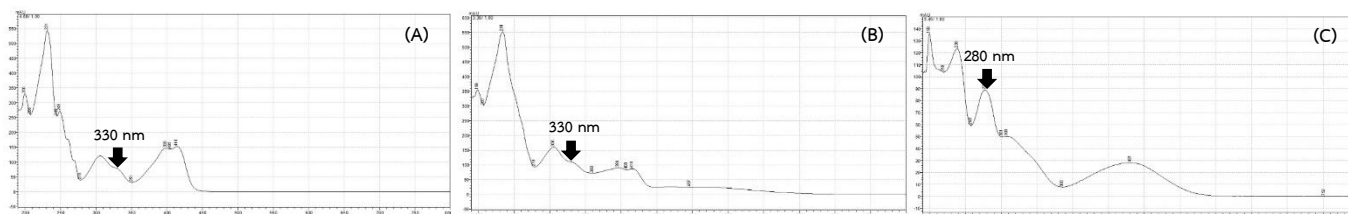
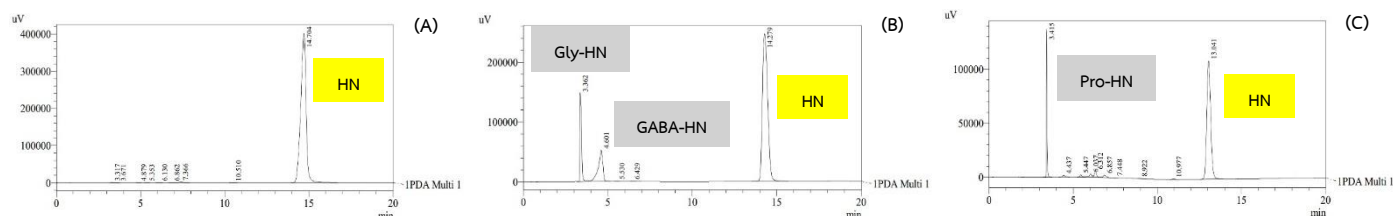
Table 1. Regression analysis of the linearity data of GABA-HN, Gly-HN, and Pro-HN derivatives

Parameters	GABA-HN derivative	Gly-HN derivative	Pro-HN derivative
Concentration range ($\mu\text{g/mL}$)	6-100	6-100	600-9600
Slope	15058	16213	41.012
Intercept	15222.68	-19830.2	6727.028
Coefficient of determination (r^2)	0.9998	0.9998	0.9991
LOD ($\mu\text{g/mL}$)	1.47	1.72	132.48
LOQ ($\mu\text{g/mL}$)	4.47	5.21	401.47

Table 2. Intra-day and Inter-day precision and accuracy of GABA-HN, Gly-HN, and Pro-HN derivatives

Parameters	GABA-HN derivative	Gly-HN derivative	Pro-HN derivative
Precision (Coefficient of variation, %)			
Intra-day	1.08-1.40	0.99-1.81	0.90-1.45
Inter-day	0.97-1.56	1.25-1.96	0.72-1.79
Accuracy, (Recovery, %)	101.68-105.98	100.24-110.41	93.54-104.22

The specificity of all amino acid derivatives was assessed by comparing the chromatograms of each amino acid derivatized with HN and a blank derivatized with HN to ensure no interference from the other compounds in the solution. These results are shown in **Figure 1** and **Figure 2**. The amino acid derivatized with HN were completely separate from HN. The peak purity index was 1.000000, 0.999808, and 0.999398 for GABA-HN, Gly-HN, and Pro-HN derivative, respectively. GABA-HN and Gly-HN derivatives were analyzed at 330 nm, with retention times of 4.60 and 3.36 minutes, respectively. Pro-HN derivative was analyzed at 280 nm, with a retention time of 3.41 minutes. The accuracy and precision were performed at concentrations of 10, 20, and 60 $\mu\text{g/mL}$ for GABA-HN and Gly-HN derivatives. While Pro-HN derivative was performed at concentrations of 2400, 4800, and 9600 $\mu\text{g/mL}$. The results of Intra-day and Inter-day precision and accuracy are shown in **Table 2**. GABA-HN and Gly-HN derivatives showed the percentage of recovery in the range of 101.68-105.98 and 100.24-110.41, respectively. Pro-HN derivative showed the percentage of recovery of 93.54-104.22. For intra-day precision, GABA-HN and Gly-HN derivatives showed the coefficient of variation (% CV) in the range of 1.08-1.40% and 0.99-1.81%, respectively, while Pro-HN derivative showed % CV in the range of 0.90-1.45%. For inter-day precision, GABA-HN and Gly-HN derivatives showed % CV in the range of 0.97-1.56% and 1.25-1.96%, respectively, while Pro-HN derivative showed % CV in the range of 0.72-1.79%. These results demonstrate that the methods are accurate and precise for analyzing GABA, glycine, and L-proline content.

**Figure 1.** Spectrum chromatograms demonstrated the detection wavelength selection of each amino acid derivatized with 2-hydroxynaphthaldehyde (HN): (A) GABA-HN derivative, (B) Gly-HN derivative, and (C) Pro-HN derivative**Figure 2.** HPLC Chromatograms demonstrated the specificity of amino acids derivatized with 2-hydroxynaphthaldehyde (HN): (A) Blank-HN derivative, (B) GABA-HN and Gly-HN derivatives, and (C) Pro-HN derivative

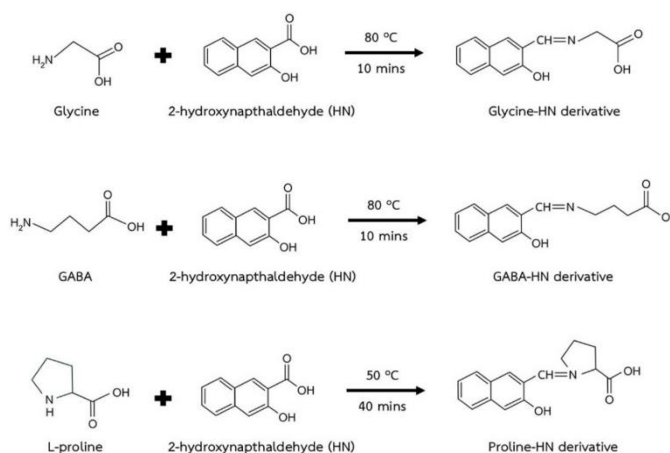


Figure 3. Scheme of the reaction between amino acids with 2-hydroxynaphthaldehyde (HN)

Discussions

The amino acids consist of an amino group (-NH_2), a carbonyl group (-COOH), a hydrogen atom and an R group (side chain). They are both anionic and cationic molecules in their structure, a state referred to as “zwitterion” or “dipolar ions”. Glycine is the smallest amino acid. γ -aminobutyric acid (GABA) contains a primary amino group on the gamma (γ) carbon. Pyrrolidine-2-carboxylic acid (L-proline) has a secondary amino group, that is part of the pyrrolidone ring. Borax buffer at pH 8 was considered the optimal condition for the reaction of amino acids with HN [22]. Amino acids exist in a nucleophilic form in borate buffer at pH 8, allowing them to react with an aldehyde to form a Schiff base. The primary or secondary amine group of amino acids acts as a nucleophile, attacking the aldehyde group (-CHO) of 2-hydroxynaphthaldehyde. This reaction forms a Schiff base (imine or -C=N-) through condensation [23, 24]. The reactions of amino acids with HN are presented in **Figure 3**. GABA and glycine are primary amines, while L-proline is a secondary amine, which may make imine formation slower and less efficient than primary amines due to steric hindrance and lower nucleophilicity, resulting in lower reactivity. As a result, Pro-HN derivative showed lower signal intensities in HPLC and required higher concentrations of L-proline, along with a specific derivatization method, to be effectively detected.

Additionally, the resulting Schiff base may undergo keto-enamine tautomerism, which can affect the UV absorbance [25]. This explains why derivatized L-proline has different detection properties than glycine and GABA. Panrod et al (2017) [18] suggested that GABA-HN derivative remain stable for 240 minutes after derivatization. While glycine has a similar chemical structure to GABA, its derivative may also be stable under the same conditions. On the other hand, Pro-HN derivative has a limited stability period after derivatization. However, all amino acid derivatives should be detected immediately after derivatization to ensure accuracy and precision.

CONCLUSIONS

GABA, glycine, and L-proline derivatized with HN can be used to determine the content of GABA, glycine, and L-proline. After validation following ICH guidelines, these methods demonstrate notable specificity, sensitivity, accuracy, and precision. The LOD and LOQ results showed that GABA and glycine exhibited greater reactivity with HN and higher sensitivity than L-proline. This is due to L-proline being a secondary amine, which requires a modified, specific derivatization method for analysis. These validated HPLC methods provide an approach for the quantification of anti-aging amino acid combinations, such as GABA, glycine, and L-proline, in cosmetic formulations. Additionally, this method is suitable for analysis of raw materials, finished products, or potentially biological fluids where amino acid-based actives are incorporated.

ACKNOWLEDGMENTS

The author would like to thank the Research Instrument Center of the Faculty of Pharmaceutical Sciences, Chulalongkorn University for providing research facilities, and the Master of Science program in Cosmetic Science, Faculty of Pharmaceutical Sciences, Chulalongkorn University for funding and supporting.

REFERENCES

1. Rashmi D, Zanan R, John S, et al. Chapter 13 - γ -aminobutyric acid (GABA): biosynthesis, role, commercial production, and applications. In: Atta ur R, editor. *Studies in Natural Products Chemistry*. 57: Elsevier; 2018. p. 413-52.
2. Dhakal R, Bajpai VK, Baek KH. Production of gaba (γ - Aminobutyric acid) by microorganisms: a review. *Brazilian Journal of Microbiology*. 2012;43(4):1230-41.
3. Uehara E, Hokazono H, Hida M, et al. GABA promotes elastin synthesis and elastin fiber formation in normal human dermal fibroblasts (HDFs). *Bioscience, Biotechnology, and Biochemistry*. 2017;81(6):1198-205.
4. Zhao H, Park B, Kim MJ, et al. The effect of γ -aminobutyric acid intake on UVB- induced skin damage in hairless mice. *Biomolecules & Therapeutics (Seoul)*. 2023;31(6):640-7.5.
5. Sá OMdS, Lopes NNF, Alves MTS, et al. Effects of glycine on collagen, PDGF, and EGF expression in model of oral mucositis. *Nutrients*. 2018;10(10):1485.
6. Aydin H, Tatar C, Savas OA, et al. The effects of local and systemic administration of proline on wound healing in rats. *Journal of Investigation Surgery*. 2019;32(6):523-9.7.
7. Górska-Warsewicz H, Laskowski W, Kulykovets O, et al. Food products as sources of protein and amino acids-the case of poland. *Nutrients*. 2018;10(12)8.
8. Bojarska J. Amino acids and short peptides as anti-aging “Superfood”. *International Journal of Nutrition Sciences*. 2020;5(1):1039.
9. Gad MZ. Anti-aging effects of l-arginine. *Journal of Advanced Research*. 2010;1(3):169-77.
10. Zhou J, Chen H, Du J, et al. Glutamine availability regulates the development of aging mediated by mTOR signaling and autophagy. *Frontiers in Pharmacology*. 2022;13:924081.
11. Diaz I, Namkoong J, Wu JQ, et al. Amino acid complex (AAComplex) benefits in cosmetic products: In vitro and in vivo clinical studies. *Journal of Cosmetic Dermatology*. 2022;21(7):3046-52.12.
12. E. Otter D. Standardised methods for amino acid analysis of food. *British Journal of Nutrition*. 2012;108(S2):S230-S7.
13. Simek P, Hušek P, Zahradníčková H. Heptafluorobutyl chloroformate-based sample preparation protocol for chiral and nonchiral amino acid analysis by gas chromatography. *Methods in Molecular Biology*. 2012;828:137-52.14.
14. Shanmuganathan M, Britz-McKibbin P. New advances in amino acid profiling in biological samples by capillary electrophoresis-mass spectrometry. *Methods in Molecular Biology*. 2019;2030:327-50.
15. Thiele B, Hupert M, Santiago-Schübel B, et al. Direct analysis of underivatized amino acids in plant extracts by LC-MS/MS (improved method). *Methods in Molecular Biology*. 2019;2030:403-14.
16. Jámboř A, Molnár-Perl I. Amino acid analysis by high-performance liquid chromatography after derivatization with 9-fluorenylmethyloxycarbonyl chloride: Literature overview and further study. *Journal of Chromatography A*. 2009;1216(15):3064-77.
17. Heinrikson RL, Meredith SC. Amino acid analysis by reverse-phase high-performance liquid chromatography: Precolumn derivatization with phenylisothiocyanate. *Analytical Biochemistry*. 1984;136(1):65-74.
18. Panrod K, Tansirikongkol A, Panapisal V. Comparison of validated high-performance liquid chromatography methods using two derivatizing agents for gamma-aminobutyric acid quantification. *Thai Journal of Pharmaceutical Sciences*. 2017;40(4):203-8.
19. Fleury MO, Ashley DV. High-performance liquid chromatographic analysis of amino acids in physiological fluids: On-line precolumn derivatization with o-phthalaldehyde. *Analytical Biochemistry*. 1983;133(2):330-5.
20. Bank RA, Jansen EJ, Beekman B, et al. Amino acid analysis by reverse-phase high-performance liquid chromatography: improved derivatization and detection conditions with 9-fluorenylmethyl chloroformate. *Analytical Biochemistry*. 1996;240(2):167-76.
21. Khuhawar MY, Rajper AD. Liquid chromatographic determination of γ -aminobutyric acid in cerebrospinal fluid using 2-hydroxynaphthaldehyde as derivatizing reagent. *Journal of Chromatography B*. 2003;788(2):413-8.
22. Rajper A, Arain G, Rind F, et al. Spectrophotometric and liquid chromatographic determination of dopamine from pharmaceutical preparations using 2-hydroxynaphthaldehyde as derivatizing reagent. *Asian Journal of Chemistry*. 2007;19:4817-24.
23. Rao PV, Rao CP, Wegelius EK, et al. 2-hydroxy-1-naphthaldehyde-derived Schiff bases: synthesis, characterization, and structure. *Journal of Chemical Crystallography*. 2003;33(2):139-47.
24. Neelofar, Ali N, Khan AA, et al. Synthesis of Schiff bases derived from 2-hydroxy-1- naphth- aldehyde and their tin(II) complexes for antimicrobial and antioxidant activities. *Bulletin of The Chemical Society of Ethiopia*. 2018;31:445-56.
25. Asiri AM, Badahdah KO. Synthesis of some new anils: part 1. Reaction of 2-hydroxy-benzaldehyde and 2-hydroxynaphthaldehyde with 2-aminopyridine and 2-aminopyrazine. *Molecules*. 2007;12(8):1796-804.

Anti-Inflammatory and Antioxidant Activities of Commercial Saffron Tea products

Lawan Siangjong¹, Kawisara Chongtangsatkul¹, Onkamon Kantauris¹, Avalin Prabsutha¹ and Auayporn Apirakaramwong^{1,*}

¹Faculty of Pharmacy, Silpakorn University, 6 Ratchamankana Road., Phra Pathom Chedi, Mueang, Nakhon Pathom 73000, THAILAND

*Corresponding author Email: apirakaramwong@su.ac.th

Abstract. Nowadays, saffron (*Crocus sativus* L.) products are growingly popular among health-aware consumers, with appealing claims of anti-inflammatory, antioxidant, and anticancer properties. However, due to the deficit of regulations affirming their therapeutic efficacy and safety, these products remain widely accessible, especially in the online market. The present study aimed to preliminarily identify saffron samples following ISO 3632-2:2010 standard and assess their *in vitro* biological activities including anti-inflammatory, antioxidant and cytotoxic activities. Three commercial saffron tea samples were purchased from online marketplaces and cultivation site. They were extracted with hot and cold-water before being tested for biological activities. All three samples were confirmed as genuine saffron but exhibited variations in quality. Both hot and cold-water extracts demonstrated anti-inflammatory activities using protein denaturation method, with hot-water extracts showing greater potency. This suggest a superior benefit of thermally prepared saffron tea. The MTT cytotoxicity assay on HepG2 cell cultures revealed that all samples showed a significant cell growth inhibition compared to the control ($p < 0.05$), but this effect was not concentration-dependent. The DPPH antioxidant assay indicated that all samples exhibited antioxidant activity, with variations in potency depending on concentration and sample differences. Nevertheless, the quality of saffron tea products varies among manufacturers, depending on the cultivation source and other factors. Therefore, the regulation for quality control of these products should be established to ensure the reliability and consumer safety.

Keywords: Saffron (*Crocus sativus* L.); Anti-inflammation; Antioxidation; Cytotoxicity

INTRODUCTION

The use of saffron, like other herbal products, has become increasingly widespread among health-aware consumers. It is believed that natural products have a high safety profile compared to chemically synthesized drugs. Furthermore, herbal products marketed as food supplements are not subject to strict regulations regarding their effectiveness in treating or preventing diseases, making them easily accessible. Saffron is derived from the stigmas of the flower *Crocus sativus*, in which each flower yields only three stigmas. It is widely used in cooking, medicine, and cosmetics with its characteristics of deep red color, distinct aroma and earthy taste. Moreover, saffron cultivation is limited to specific regions, such as Iran, Italy, and Spain. The quality of saffron is classified based on the quality of the stigmas, which affects the levels of bioactive compounds [1]. These compounds contribute to saffron therapeutic effects, including blood sugar-lowering, anti-inflammatory, antioxidant, and anticancer properties [2,3]. Due to its high value and market demand, saffron is often adulterated with other substances to reduce production costs. In the saffron raw material trade, the ISO (IEC) 3632(2)-2010 standard is widely recognized as the benchmark for evaluating the quality, purity, and authenticity of saffron [4].

This study aims to evaluate the anti-inflammatory, antioxidant, and cytotoxic effects of commercial saffron tea products available on the market. The results will help determine the reliability of online saffron products and raise consumer awareness of saffron safety and quality.

MATERIALS AND METHODS

Materials

Saffron tea products were purchased from online marketplaces and a cultivation site. HepG2 cells were obtained from American Type Culture Collection, ATCC (Manassas, VA). Dulbecco's Modified Eagle Medium (DMEM), fetal bovine serum (FBS), trypsin-EDTA, penicillin weer streptomycin were obtained from Gibco BRL (Rockville, MD, USA). MTT (3-(4,5-Dimethylthiazol-2-yl)-2,5-Diphenyltetrazolium Bromide), bovine serum albumin (BSA) and 2,2-diphenyl-1-picrylhydrazyl (DPPH) were purchased from Sigma-Aldrich (USA). All other chemicals were purchased from standard sources.

Methods

Sample preparation

Three saffron tea products used in biological tests and UV-Visible spectrophotometry were prepared according to ISO(IEC)3632(2)-2010 standard. Five mg of each saffron tea product was extracted in water at the temperature of 70 °C (hot water) or 22°C (cold water) for 15 min.

Physiochemical tests

1. Identification procedures were conducted in accordance with ISO 3632-2:2010 and ISO 3632-1:2011 standards.
 - a. *Microscopic examination*: Saffron tea products were depigmented using methanol and examined under a light microscope. Morphological features were compared with reference descriptions to confirm authenticity.
 - b. *Sulfuric acid and nitric acid test*: Concentrated sulfuric acid or nitric acid was directly applied to saffron samples. The development of a purple-blue color with sulfuric acid and a light blue with nitric acid was indicative of genuine saffron.
 - c. *UV-Visible spectrophotometry*: Saffron samples were extracted in hot or cold water and analyzed using UV-Visible spectrophotometry. Absorbance was measured at wavelengths of 254, 330, and 440 nm, corresponding to the characteristic peaks of saffron constituents.
2. Adulteration detection tests
 - a. *Floatation test*: Saffron stigmas were placed in water to assess buoyancy. Authentic stigmas remained afloat, whereas adulterants typically sank.
 - b. *Color test*: Samples were immersed in water, and the rate and pattern of color release were monitored. Genuine saffron releases color slowly and uniformly, while adulterated samples exhibit rapid or uneven color diffusion.
 - c. *Whatman paper test*: Samples were gently rubbed onto pre-moistened Whatman filter paper to observe staining. Authentic saffron produces a light yellow stain without spreading, whereas artificial colorants often produce intense or diffuse stains.

Protein denaturation assay

Bovine serum albumin (BSA) was prepared at 1% w/v in PBS (pH 6.4). Saffron extracts were diluted in distilled water to yield four to five different concentrations. Diclofenac (1,000 µg/mL) and BSA alone served as positive and negative controls, respectively. For each test, 480 µL of extract was mixed with 1% w/v BSA and 960 µL PBS, then incubated under controlled condition. Absorbance was measured at 660 nm using a spectrophotometer. All experiments were performed in triplicate. The percentage inhibition of protein denaturation was calculated as follows:

$$\% \text{Inhibition} = \left(\frac{A_c - A_s}{A_c} \right) \times 100$$

where A_c is the absorbance of the control, and A_s is the absorbance of the sample.

DPPH Radical Scavenging Assay

A 0.004% DPPH solution was prepared by diluting a 0.5% stock solution with methanol. A 1.002 mg/mL vitamin C standard was diluted to at least five concentrations for a standard curve. Each 20 µL standard was mixed with 3 mL DPPH, incubated in the dark for 30 min, and measured at 517 nm. Saffron tea extract was prepared at 200-1000 µg/mL. A 0.2 mL aliquot of each was mixed with 2.8 mL DPPH under the same conditions. The assay was performed in triplicate, with a DPPH-methanol as the control. Antioxidant capacity (mg vitamin C equivalent/g dry sample) was determined from the standard curve. Percentage inhibition was calculated as follows:

$$\% \text{Inhibition} = \left(\frac{A_c - A_s}{A_c} \right) \times 100$$

where A_c is the absorbance of the control, and A_s is the absorbance of the sample.

Cytotoxicity Assay (MTT Assay)

HepG2 liver cancer cells were culture in DMEM supplemented with 10% PBS, 100 U/mL penicillin, and 100 µg/mL streptomycin at 37°C with 5% CO₂. For the MTT assay, HepG2 cells (1×10⁴ cells/well) were seeded in 96-well plates and incubated overnight. Cells were then treated with 100 µL of saffron extracts at 15.625, 31.25, 62.5, 125, and 250 µg/mL for 24 h. Afterward, 10 µL of MTT solution was added and incubated for 2 hours. Formazan crystals formed by mitochondrial enzymes in viable cells were then dissolved in DMSO, and the absorbance was measured at 570 nm. Cell viability (%) was calculated compared to control. All experiments were performed in triplicate.

Data Analysis

Data were reported as mean ± standard deviation (SD). Statistical significance was analyzed using two-way ANOVA, with a significance level set at $p < 0.05$. If significant differences were observed, post-hoc analysis was conducted using Tukey's Honestly Significant Difference (TukeyHSD) test.

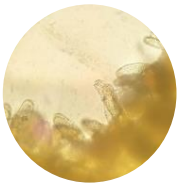

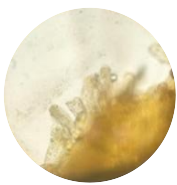
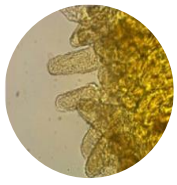
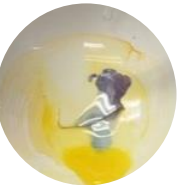



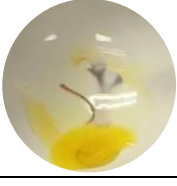


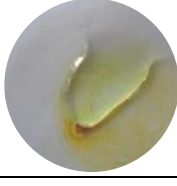



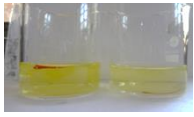








RESULTS AND DISCUSSION

Results

To assess the authenticity of saffron in three samples, several physiochemical tests were conducted. Microscopic examination under a light microscope revealed the presence of stigmas with finger-shaped papillae in all samples (Table 1), consistent with the morphological characteristics reported by Girme et al [5]. In sulfuric acid test, the major constituents of saffron reacted with sulfuric acid, producing an immediate blue coloration in all three samples. Similarly, the nitric acid test resulted in a light blue color across all samples, indicating their genuineness [6]. UV-Vis spectrophotometry analysis further confirmed saffron authenticity, displaying characteristic absorbance peaks at 243, 330 and 440 nm corresponding to picrocrocin, safranal and crocin, respectively (Figure 1).

To evaluate potential adulteration, flotation, color diffusion and Whatman paper tests were performed. When saffron strands were placed in water, Sample 2 and 3 remained floating, whereas Sample 1 partially sank. Additionally, Sample 1 exhibited rapid color diffusion, releasing a yellow-orange hue into the water, suggesting the presence of artificial coloring agents. Similarly, when rubbed on Whatman paper, Sample 1 left a more intense yellow stain compared to the other samples. These findings strongly indicate the presence of food coloring in Sample 1, suggesting possible adulteration.

Table 1. Physiochemical tests of three samples of saffron tea products compared with findings from reference studies.

Method		Sample 1	Sample 2	Sample 3	Reference study	
IDENTIFICATION TESTS	Microscopic examination					Girme A, et.al. 2022 [5]
	Sulfuric test					Shukla SK, et.al. 2015 [6]
	Nitric acid test					Shukla SK, et.al. 2015 [6]
ADULTERATION TESTS	Flotation test					Shukla SK, et.al. 2015 [6]
	Color test					Shukla SK, et.al. 2015 [6]
	Whatman paper test					Shukla SK, et.al. 2015 [6]

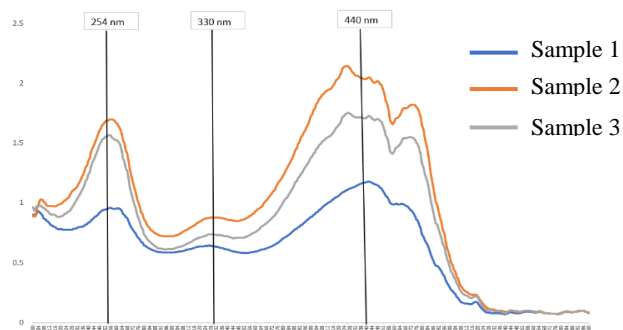


Figure 1. UV-Vis spectra of three saffron tea products showing characteristic absorbance peaks at 243, 330 and 440 nm.

Antioxidant activity of saffron tea products

The DPPH radical scavenging activity assay revealed that saffron tea products in Samples 1 and 2, at a concentration of 0.80 mg/mL, exhibited antioxidant activities of 12.10 ± 9.51 and 11.15 ± 5.50 , respectively. These values were comparable to the antioxidant activity of the standard ascorbic acid at its lowest concentration (0.10 mg/mL), which showed a scavenging activity of 11.33 ± 0.03 . In contrast, Sample 3, even at its highest concentration (1 mg/mL), did not exhibit antioxidant activity comparable to that of ascorbic acid. Furthermore, a statistically significant difference ($p < 0.001$) was observed between Samples 1 and 2 compared to Sample 3 across all tested concentrations, indicating differences in product quality.

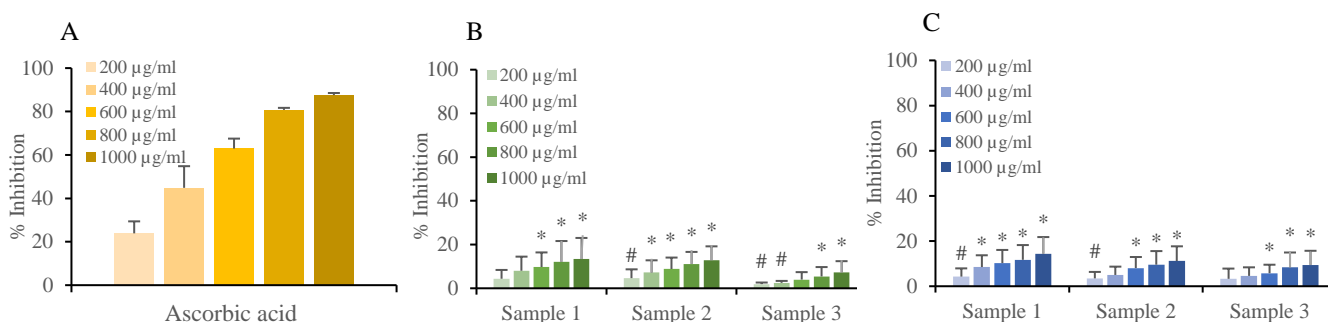


Figure 2. Antioxidant activity of saffron tea extract in hot water (B) or cold water (C) as compared to standard ascorbic acid (A) using DPPH assay. (*; $p \leq 0.05$ compared to the negative control, #; $p \leq 0.05$ compared to the 1,000 µg/mL concentration).

Anti-inflammatory activity of saffron tea products

The anti-inflammatory activity of saffron tea products was evaluated using the protein denaturation assay with BSA serving as the protein source. Among the hot-water extracts, only Sample 2 demonstrated statistically significant anti-inflammatory activity at all tested concentrations when compared to the control group (Figure 3). Notably, the percent inhibition at the concentration of 600, 800 and 1,000 µg/mL was similar to that of diclofenac (1,000 µg/mL), the positive control (data not shown). In contrast, Sample 1 and 3 exhibited significantly lower activity than diclofenac at all tested concentrations.

For the cold-water extracts, Sample 2 demonstrated significant anti-inflammatory effects, but with a lesser extent than its hot-water counterpart. At the concentration of 1,000 µg/mL, both Samples 1 and 2 demonstrated inhibitory activity similar to diclofenac. Meanwhile, Sample 3 exhibited anti-inflammatory effects only within the concentration range of 400 -1,000 µg/mL, but not at lower concentration, when compared to the control.

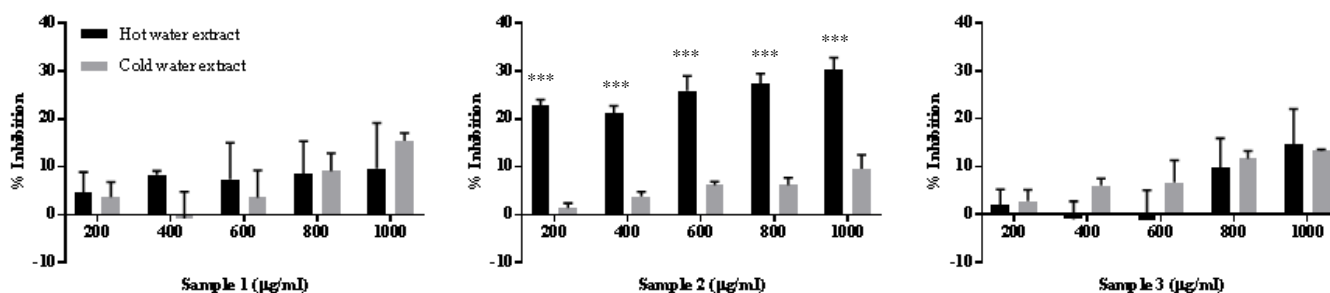


Figure 3. Effect of saffron water extract on BSA denaturation assay. (***) $p \leq 0.001$ compared to the negative control).

Cytotoxic activity of saffron water extract on HepG2 cells

Using MTT assay, the toxicity of saffron extract was evaluated in cultured HepG2 cells. The percentage of cell viability, compared to the vehicle control, indicated that all three samples exhibited cytotoxic effects against liver cancer cells. However, the observed cytotoxicity was not concentration-dependent.

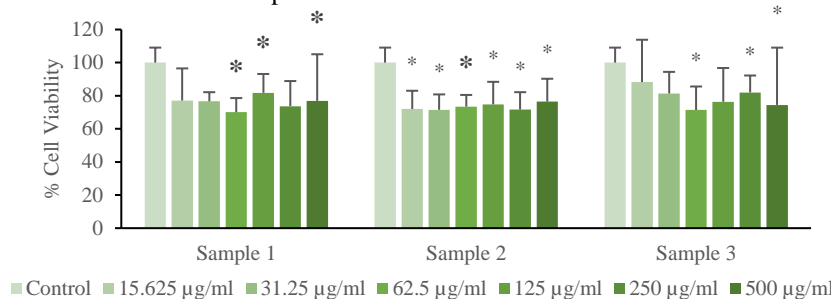


Figure 4. Effect of three saffron tea extracts on HepG2 cell viability after 24 h treatment as compared to control. $n = 3$ (*, $p < 0.001$)

Discussions

This study confirms that all tested saffron tea products from various marketplaces contained authentic saffron. However, differences in quality were observed, with some products potentially containing added coloring agents. Given the widely claimed pharmacological properties of saffron, we evaluate its key biological activities. The anti-inflammatory activity was assessed using the protein denaturation assay with BSA as the protein source. The results indicated that Samples 2 exhibited the highest anti-inflammatory activity, particularly in the hot-water extract. At higher concentrations, its activity was comparable to diclofenac, a commonly used non-steroidal anti-inflammatory drug (NSAID). In contrast, cold water extracts of Sample 2 showed lower anti-inflammatory effects than the hot-water extract and diclofenac. The other samples were less effective, especially in cold-water extracts. These findings support the traditional consumption of saffron as hot tea, which may enhance its effectiveness. Additionally, all three saffron tea samples demonstrated antioxidant activity in the DPPH assay, regardless of extraction temperature. Furthermore, the study suggests that saffron tea may have potential anticancer effects against hepatic cancer cells. However, the effective concentrations tested were far exceeded those typically consumed in tea form.

CONCLUSIONS

In summary, these findings highlight the potential anti-inflammatory, antioxidant, and anticancer properties of saffron tea, while also emphasizing the influence of extraction temperature on its bioactivity. Being a high-value herb with several claimed pharmacological activities, saffron is often adulterated which may compromise its therapeutic potential. Therefore, consumers should be careful when selecting the source of saffron to ensure authenticity and effectiveness.

ACKNOWLEDGMENTS

The authors would like to express their sincere gratitude to the Faculty of Pharmacy, Silpakorn University, for providing financial support and research facilities that made this study possible.

REFERENCES

- Bergomi A, Comite V, Santagostini L, Guglielmi V, Fermo P. Determination of Saffron Quality through a Multi-Analytical Approach. *Foods*. 2022; 11(20):3227. <https://doi.org/10.3390/foods11203227>.
- Alyoussef A. Investigation of the ability of crocin to treat skin cancer chemically induced in mice via the inhibition of the wnt/ β -catenin and fibrotic pathway. *Cureus* 15(5): e38596. DOI:10.7759/cureus.38596.
- Tajaddini A, Roshanravan N, Mobasseri M, Haleem Al-qaim Z, Hadi A, Aeinehchi A, et al. The effect of saffron (*Crocus sativus* L.) on glycemia, lipid profile, and antioxidant status in patients with type-2 diabetes mellitus: A randomized placebo-controlled trial. *Phytother Res*. 2023;37:388–98. DOI: 10.1002/ptr.7600.
- International Organization for Standardization. ISO3632-2:2010._ Spices-Saffron (*Crocus sativus* L.)-Part 2: Test method_. Geneva:ISO;2010.
- Girme A, Mirgal A, Darji B, Gafner S, Hingorani L. Adulteration of saffron and saffron extracts. *Botanical Adulterants Prevention Bulletin*. Austin, TX: ABC-AHP-NCNPR Botanical Adulterants Prevention Program; 2022.
- Shukla SK, Lqbal M. Forensic analysis of the saffron: Rapid authenticity testing. *Int J Res Appl Sci Eng Technol*. 2015;3(4):228-30.

Development of a Microcontroller-Driven Automated Titration System for the Quantitative Assay of Sodium Bicarbonate Tablets

Warakorn Chawalikit¹, Pattamawan Srirach¹, Sattayawatee Sripilai¹, and Saowapak Vchirawongkwin^{1,*}

¹Department of Pharmaceutical Chemistry, College of Pharmacy, Rangsit University, Pathumthani 12000, Thailand

*Corresponding author Email: saowapak.k@rsu.ac.th

Abstract. Titration is a widely used and methodologically simple technique in pharmaceutical analysis; however, manual titration can present limitations in precision, reproducibility, and reagent efficiency when performed in high-throughput or routine settings. This study addressed these challenges by developing a microcontroller-driven instruction set for an automated titration system. The system quantified sodium bicarbonate content in tablet formulations using acid-base reactions in aqueous solutions. It constructed accurate pH versus titrant volume curves from titration data and precisely determined the equivalence point using first and second derivative spline fit techniques. Device calibration was conducted in two phases. The peristaltic pump was calibrated by delivering titrant at a constant voltage (3.76 V) over three trials, achieving 100% flow accuracy with 0% RSD. The glass electrode was calibrated using standard buffer solutions (pH 4.01, 7.00, and 9.21), showing a strong linear voltage-to-pH correlation ($R^2 = 0.9999$) and minimal variation (%RSD < 0.15%). The system's performance was verified by analyzing sodium bicarbonate tablets, achieving 97.3% of the labeled claim with a %RSD of 0.28%. No significant difference was found between results obtained using the proposed method and the official USP method, confirming its equivalency. The average analysis time per sample was approximately 5–6 minutes. The automated titration system reduces human error in endpoint determination, enhancing system reliability and decreasing titration time, thereby improving operational efficiency. Incorporating spline fit data processing further enhances the precision of equivalence point identification, making this system superior to conventional methods.

Keywords: Microcontroller; Automatic titration; Pharmaceutical analysis; Equivalence point; Spline fit

INTRODUCTION

Technological advancements have significantly transformed scientific practices, improving analytical efficiency, accuracy, and reproducibility. Titration remains a fundamental method for quantifying analytes in pharmaceutical and chemical laboratories. Traditionally, titration involves the stepwise addition of a titrant to an analyte solution until the equivalence point is reached, typically detected by a visual indicator. However, manual titration has limitations, including subjective endpoint determination, time-consuming procedures, and substantial chemical waste, particularly with colored or opaque samples [1].

Recent innovations have addressed these challenges using automation with affordable microcontroller platforms like Arduino and Raspberry Pi. These open-source systems provide flexible, low-cost solutions for laboratory automation [2,3]. Examples include web-enabled titration systems that allow remote control and real-time monitoring [1], Bluetooth-enabled autotitrators with voice feedback for inclusive education [4], and syringe-pump-based systems costing a fraction of commercial autotitrators [5]. Galvanostat systems with photometric endpoint detection have also demonstrated excellent reproducibility in various titrations [6]. These advances align with Industry 4.0 demands for technological literacy, critical thinking, and innovation in Science, Technology, Engineering, and Mathematics (STEM) education [7].

Compared to commercial autotitrators costing USD 5,000–15,000 [8,9], the developed system was built for under USD 250 using open-source components. It offers comparable precision, customizable settings, and ease of programming [4,5], making it ideal for teaching, research, and low-resource pharmaceutical labs [6].

This study developed a microcontroller-based automated titration system for quantifying sodium bicarbonate tablets. Integrating a peristaltic pump, pH electrode, and custom instruction set with spline fit analysis ensures accurate, real-time data acquisition. Its open-source, modular design offers a cost-effective alternative to commercial autotitrators and is adaptable to other titration applications.

MATERIALS AND METHODS

Materials

The study employed laboratory-grade analytical equipment and high-purity chemical reagents appropriate for pharmaceutical analysis. The primary analytical instrumentation involved an automated titration system driven by a microcontroller (TitraLab Board) connected to a peristaltic pump (DP-DIY, INTLLAB, USA) and a glass electrode for potentiometric measurements.

Chemical reagents consisted of analytical reagent-grade sulfuric acid (98%, QR&C, New Zealand), sodium carbonate (99.5%, KEMAUS, Australia), pharmaceutical-grade sodium bicarbonate tablets (local manufacturer in Thailand), and indicators such as methyl red (Merck, Germany) and methyl orange (Riedel-de Haën, Germany). Buffer solutions for electrode calibration (pH 4.01, 7.00, and 9.21) were sourced from Mettler Toledo, USA.

Methods

Automated Titration System and Calibration Procedures

The automated titration system was developed using Arduino IDE software version 2.2.1, featuring a Thin Film Transistor (TFT) display, a potentiometer for flow control, push buttons, and an SD card for data logging. The peristaltic pump was calibrated by timing the 10 mL sulfuric acid delivery at various speeds, ensuring precise flow. The glass electrode was calibrated using standard buffers (pH 4.01, 7.00, 9.21), and linear regression confirmed electrode accuracy. These procedures followed best practices for automated titration system validation [4], ensuring precise potentiometric measurements throughout pharmaceutical analyses. Systematic evaluations at various pump speeds were performed by measuring the volume and time of sulfuric acid delivery to determine the optimal titrant flow rate, ensuring consistent and reproducible analytical results [5].

Standardization and Quantitative Analysis of Pharmaceutical Samples [10, 11]

The titration system was first standardized by titrating 0.2 g of sodium carbonate dissolved in 50 mL purified water with sulfuric acid, using methyl red as an indicator and recording pH data to determine the equivalence point with the automated titration system precisely; this was repeated three times for consistency. Twenty sodium bicarbonate tablets were weighed for sample analysis to determine the average tablet mass (352 mg/tablet). The tablets were powdered, and 300 mg portions were dissolved in 50 mL of water, yielding a final 6 mg/mL concentration of sodium bicarbonate. Each sample was titrated under the same conditions, and endpoints were determined using visual and potentiometric methods to validate system accuracy and repeatability.

Method Validation Procedures [12]

The automated titration system was validated following ICH Q2(R2) guidelines and USP, incorporating current best practices [10,11]. Validation covered key parameters: linearity, accuracy, precision, specificity, and robustness. Linearity was assessed across 100–350 mg sodium carbonate, with regression analysis showing $R^2 \geq 0.995$. Accuracy was evaluated by spiking blank solutions with known amounts of sodium carbonate at 40%, 100%, and 140% of the nominal 250 mg level (i.e., 100 mg, 250 mg, and 350 mg). Each spiked sample was dissolved in 50 mL of water and titrated using the same method, with recoveries between 98% and 102%, ensuring freedom from systematic error. Precision was determined by analyzing three replicates of sodium bicarbonate tablets per day across three consecutive days. Each sample contained 300 mg of the active ingredient in a 50 mL solution. Intra-day and inter-day %RSD values were all $\leq 2\%$. Specificity was confirmed by comparing titration profiles of pure standards and pharmaceutical samples, showing no interference from excipients or indicators [13]. Robustness was demonstrated by varying flow rate, calibration intervals, and temperature, with minimal effect ($<2\%$ deviation) on results consistent with established protocols [4].

RESULTS AND DISCUSSION

Optimization and Calibration of the Automated Titration System

The optimization process included determining the ideal titrant flow rate and calibrating the peristaltic pump and glass electrode to ensure reliable and precise measurements. The optimal titrant flow rate was assessed at three voltage settings: 3.76 V, 4.71 V, and 8.47 V. At 3.76 V, the system achieved a stable flow rate of 0.10 mL/sec, compared to 0.14 mL/sec and 0.24 mL/sec at higher voltages. This setting was optimal for further experiments due to its precision and suitability for accurate pH measurement near the equivalence point.

Peristaltic pump calibration at 3.76 V across three trials demonstrated outstanding performance, achieving 100% accuracy with a %RSD of 0%, confirming the pump's reliability and consistency. Glass electrode calibration was performed using standard buffer solutions (pH 4.01, 7.00, and 9.21), yielding measured accuracies of 99.75%, 100.00%, and 99.89%, respectively, with minimal %RSD values (0.14%, 0.14%, 0.06%). The electrode showed a strong linear relationship between voltage and pH ($R^2 = 0.9999$), confirming its high precision. Proper electrode maintenance, continuous solution stirring, and selective averaging of stable potential readings were essential to reduce variability, consistent with best practices [4, 1].

Figure 1A shows the microcontroller with related devices, illustrating the system's compact integration of hardware components and highlighting the practical design that supports accurate and efficient titration performance. The optimized flow rate and precise calibration ensured that the automated titration system met pharmaceutical standards, demonstrating excellent potential for routine pharmaceutical and analytical applications.

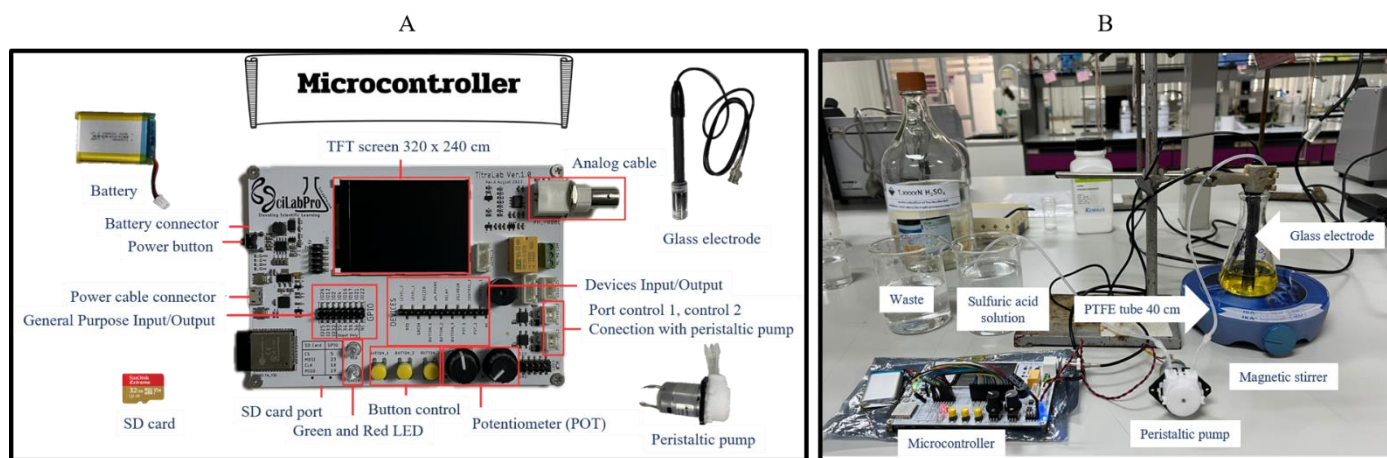


Figure 1. Microcontroller with related devices (A) and setup of the automated titration system (B).

Standardization and Quantitative Analysis of Pharmaceutical Samples

The sulfuric acid (H_2SO_4) titrant was first standardized using primary standard sodium carbonate (Na_2CO_3 , 99.5% purity). Three replicates yielded normality values of 1.1565 N, 1.1755 N, and 1.1791 N, with an average normality of 1.1704 ± 0.0121 N and a relative standard deviation (%RSD) of 1.04%, well within the pharmaceutically acceptable limit ($\leq 2\%$). This standardization ensured the accuracy and reproducibility of analytical results and confirmed the system's robust precision, aligning with ICH Q2(R2) guidelines and USP.

Following titrant validation, the quantitative analysis of sodium bicarbonate tablets was performed using the automated titration system and standardized sulfuric acid solution. As shown in Figure 1B, the titration system consists of a microcontroller connected to a peristaltic pump that delivers the titrant through a 40 cm polytetrafluoroethylene (PTFE) tube. The titrant is dispensed into an Erlenmeyer flask positioned on a magnetic stirrer, and pH is continuously monitored using a glass electrode. The waste solution is directed into a separate container. This configuration enables real-time pH tracking and precise, automated titration suitable for pharmaceutical assays. Three replicates yielded assay values of 99.7%, 102.9%, and 102.2% of the labeled amount, with an average content of 101.6% and %RSD of 1.68%, falling within the USP acceptance range of 95.0–105.0%. It is noted that, unlike the USP manual method, this automated procedure did not include a boiling step to expel dissolved CO_2 gas before titration. However, this omission did not negatively impact result accuracy. The system uses real-time potentiometric monitoring with continuous stirring, allowing stabilization of the pH signal before equivalence point detection. The titration curve showed no evidence of delayed endpoints or plateauing, and the results were statistically comparable to those obtained via the USP procedure. Therefore, the absence of the boiling step under the controlled automated conditions did not compromise the reliability of the assay. Further, the system operates semi-closed, reducing CO_2 loss variability during titration. While the system showed high reliability, minor delays in titrant delivery, inherent to microcontroller-based control, occasionally caused minor deviations in titrant volume. Although these had minimal impact, they could introduce cumulative errors in extended analyses. Future improvements to pump activation timing are recommended to enhance precision, consistent with current literature [14, 15].

Method Validation

The microcontroller-based automated titration system was validated according to ICH Q2(R2) guidelines and USP. Validation parameters included specificity, linearity, precision, accuracy, robustness, and sensitivity, confirming the method's reliability for pharmaceutical analysis.

Specificity was demonstrated by comparing titration curves obtained from sodium carbonate standards and sodium bicarbonate tablet formulations. In the standard solution (Figure 2A), the equivalence point was identified at 4.08 mL; in the tablet solution (Figure 2B), it appeared at 3.50 mL. Both endpoints were determined using second derivative spline fit analysis. The absence of additional peaks or distortions in the curves indicated that excipients in the tablet formulation or indicators did not interfere with endpoint detection. The results confirmed that the system selectively responds to the active analyte, supporting its specificity.

Linearity was assessed using sodium carbonate standards across the concentration range of 100 to 350 mg (equivalent to 40–140% of nominal concentration). Calibration curves were constructed by plotting analyte concentration (x) against the volume of titrant at the equivalence point (y). These results demonstrate a strong linear relationship between analyte concentration and titration response, well above the acceptance threshold of $R^2 \geq 0.995$.

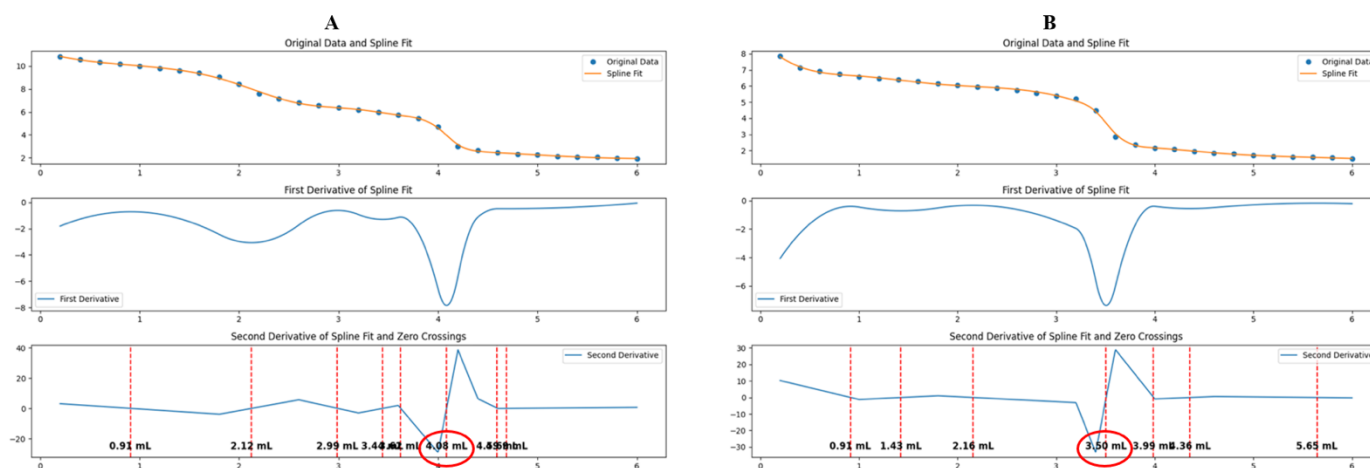


Figure 2. Titration curves processed with spline fitting and derivative analysis: (A) Standardization of sulfuric acid with sodium carbonate; (B) Quantitative analysis of sodium bicarbonate tablets.

Precision was assessed through intra-day and inter-day testing across three days, using daily triplicate titrations of sodium bicarbonate tablets. All results met the pharmacopeial acceptance criterion of $\%RSD \leq 2\%$, confirming the method's precision under routine laboratory conditions.

Measured accuracy by spiking sodium carbonate at 40%, 100%, and 140% levels. All recovery values were within the USP-accepted range of 98–102%, indicating high analytical accuracy and freedom from systematic error.

Robustness was evaluated by varying the titrant flow rate ($\pm 10\%$), calibration intervals (daily vs. every 3 days), and temperature (20–30°C). Deviations in measured results remained under 2%, confirming the method's reliability under typical laboratory fluctuations.

Sensitivity was evaluated based on the response's standard deviation and the calibration curve's slope. Using the regression approach, the limit of detection (LOD) was calculated to be 3.45 mg/mL, and the limit of quantification (LOQ) was 10.44 mg/mL. These values demonstrate that the system can confidently detect and quantify low concentrations of analytes.

Table 2. Summary of validation results

Parameter	Test Condition/Details	Results
Linearity	Sodium carbonate 100-350 mg (40-140% Range)	$y = 0.016x + 0.0017$; $R^2 = 0.9985$ $y = 0.016x - 0.0345$; $R^2 = 0.9991$ $y = 0.016x + 0.0126$; $R^2 = 0.9983$
Precision (Repeatability & Intermediate)	Day 1-3, 3 times titration (Sodium bicarbonate tablets)	Day 1: 101.58% LA; $\%RSD = 1.68$ Day 2: 100.28% LA; $\%RSD = 1.49$ Day 3: 101.60% LA; $\%RSD = 1.69$ Inter-day: 101.15% LA; $\%RSD = 1.55$
Accuracy	Spiked levels 40%, Spiked levels 100%, Spiked levels 140%	Recovery = 99.55%; $\%RSD = 0.76$ Recovery = 100.54%; $\%RSD = 0.78$ Recovery = 99.05%; $\%RSD = 1.07$
Robustness	Flow rate $\pm 10\%$, Calibration every 3 days, Temperature 20-30°C	Deviation = 1.4% Deviation = 1.2% Deviation <1.2%
Sensitivity	Calculated via regression analysis	LOD = 3.45 mg/mL; LOQ = 10.44 mg/mL

CONCLUSIONS

This research successfully developed and validated a microcontroller-based automated titration system tailored for pharmaceutical analysis. The system demonstrated excellent analytical performance, with strong linearity ($R^2 \geq 0.998$), high precision (intra- and inter-day $\%RSD \leq 1.69\%$), and accuracy (recoveries within 98–102%) across a broad concentration range. Robustness testing confirmed stable performance under varied laboratory conditions, and sensitivity assessments established low limits of detection and quantification (LOD: 3.45 mg/mL; LOQ: 10.44 mg/mL), supporting its suitability for trace-level analysis.

By integrating a microcontroller-driven instruction set, peristaltic pump, and potentiometric pH sensor, combined with spline fit and derivative analysis, the system achieved precise automated endpoint detection, reduced human error, and improved reproducibility compared to manual titration. Compared to commercial autotitrators, which typically cost USD 5,000–15,000, the developed system's total component cost was under USD 250, representing a cost reduction of over 95%. It offers a cost-effective, customizable, and reliable alternative to commercial autotitrators, making it highly applicable for pharmaceutical quality control, research, and educational use.

However, some limitations were identified. Minor delays in titrant delivery inherent to the microcontroller control system occasionally caused minor deviations in titrant volume, which could affect accuracy in extended or highly sensitive assays. Additionally, the current system was tested mainly for acid-base titrations, and its performance with more complex reactions or multi-component systems remains to be evaluated. Future development should focus on improving pump response time, enhancing real-time control algorithms, expanding application to various titration types, and integrating data transfer interfaces for laboratory information management systems (LIMS). Addressing these aspects will further strengthen the system's capabilities and broaden its use in pharmaceutical and chemical laboratories.

ACKNOWLEDGMENTS

The authors gratefully acknowledge the Department of Pharmaceutical Chemistry, College of Pharmacy and Research Institute, Rangsit University, for their generous financial support. We would like to thank Assoc.Prof.Dr.Viwat Vchirawongkwin for his valuable assistance with ESP32 microcontroller and TitraLab board.

REFERENCES

1. Famularo N, Kholod Y, Kosenkov D. Integrating chemistry laboratory instrumentation into the industrial internet: Building, programming, and experimenting with an automatic titrator. *J Chem Educ.* 2016;93(1):175-81.
2. Fitzpatrick DE, O'Brien M, Ley SV. A tutored discourse on microcontrollers, single board computers and their applications to monitor and control chemical reactions. *React Chem Eng.* 2020;5(2):201-20.
3. Fisher D, Fletcher R, Anapalli S. Python software integrates with microcontrollers and electronic hardware to ease development for open-source research and scientific applications. *Adv Internet Things.* 2021;11(1):42-58.
4. Soong R, Agmata K, Doyle T, Jenne A, Adamo A, Simpson AJ. Rethinking a timeless titration experimental setup through automation and open-source robotic technology: Making titration accessible for students of all abilities. *J Chem Educ.* 2019;96(7):1497-501.
5. Del Castillo-Santaella T, Maldonado-Valderrama J, Fernandez-Rodriguez MA. Autotitrator based on an Arduino open source pump. *HardwareX.* 2023;15:e00464. Available from: <https://doi.org/10.1016/j.hwx.2023.e00464>
6. González-Arjona D, Roldán González E, López-Pérez G, Domínguez Pérez MM, Calero-Castillo M. Coulometer from a digitally controlled galvanostat with photometric endpoint detection. *Sensors.* 2022;22(19):7541.
7. Suyanta. The role of chemistry and its learning to improve 21st century skills in revolutionary industry 4.0 era. *Atl High Chem Pharm Sci.* 2019;1:214-20.
8. Mettler-Toledo International Inc. Excellence Titrator T7 [Internet]. Columbus (OH): Mettler Toledo; 2023 [cited 2025 May 16]. Available from: <https://www.mt.com>
9. Metrohm AG. TitrIC Vario Compact Titrator [Internet]. Herisau: Metrohm; 2023 [cited 2025 May 16]. Available from: <https://www.metrohm.com>
10. United States Pharmacopeia. Monograph: Sodium Carbonate [Internet]. USP 46–NF 41. Rockville, MD: United States Pharmacopeial Convention; 2023 [cited 2024 Sep 29]. Available from: https://doi.usp.org/USPNF/USPNF_M76010_03_01.html
11. United States Pharmacopeia. Monograph: Sodium Bicarbonate Tablets [Internet]. USP 46–NF 41. Rockville, MD: United States Pharmacopeial Convention; 2023 [cited 2024 Sep 29]. Available from: https://doi.usp.org/USPNF/USPNF_M75900_01_01.html
12. European Medicines Agency. ICH guideline Q2(R2): Validation of analytical procedures [Internet]. Amsterdam: EMA; 2022 [cited 2024 Sep 29]. Available from: https://www.ema.europa.eu/en/documents/scientific-guideline/ich-guideline-q2r2-validation-analytical-procedures-step-2b_en.pdf
13. Marques MRC, Pappa H, Chang M, Spafford L, Klein M, Meier L. Recommendations for titration methods validation [Internet]. Rockville, MD: United States Pharmacopeia and Metrohm; 2021 [cited 2024 Sep 29]. Available from: https://www.usp.org/sites/default/files/usp/document/resources/titration_met_val_feb_10_2021.pdf
14. McIntyre MP, van Schoor G, Uren KR, Klopppers CP. Modelling the pulsatile flow rate and pressure response of a roller-type peristaltic pump. *Sens Actuators A Phys.* 2021;325:112708.
15. Pratami LWD, Ariswati HG, Titisari D. Effect of temperature on pH meter based on Arduino Uno with internal calibration. *J Electron Electromed Med Inform.* 2020;2(1):23-7.

Screening of Colorimetric Reagents for Rapid Detection of Bisacodyl on Paper-Based Device

Kunnaphat Kumborn¹, Junjira Saebui¹, Nawaporn Pathom-eam¹, Kanawan Pochanakom¹, Jankana Burana-osot¹, Somlak Kongmuang¹, Panadda Phattanawasin^{1,*}

¹Department of Industrial Pharmacy, Faculty of Pharmacy, Silpakorn University, Nakhon Pathom, THAILAND, 73000

*Corresponding author Email: Phattanawasin_p@silpakorn.edu

Abstract. The increasing use of dietary supplements for weight control has raised concerns about their intentional adulteration with pharmaceutical compounds, such as bisacodyl, which may pose health risks to consumers. Existing analytical methods for bisacodyl detection, including chromatographic and immunoassay-based techniques, are highly sensitive but require specialized equipment and expertise, limiting their suitability for rapid or on-site screening. Given the lack of simple and low-cost colorimetric methods for bisacodyl detection, this study aimed to investigate the use of colorimetric reagents for its rapid detection on a paper-based platform. Six reagents were screened for their reactivity toward bisacodyl. Among these, Dragendorff's reagent selectively interacted with the pyridine group in bisacodyl, producing a visually detectable response, especially when the bisacodyl solution was prepared in 0.01 N hydrochloric acid. Additionally, acid- and base-catalyzed hydrolysis of bisacodyl enhanced color development with Folin-Ciocalteu reagent and Fast Blue B, which reacted with the phenolic groups in bis-(p-hydroxyphenyl)-pyridyl-2-methane (BHPM), a hydrolysis product of bisacodyl. This is the first study to demonstrate a reagent-based colorimetric screening method for bisacodyl on a paper platform. These preliminary findings highlight the potential of colorimetric reagents for further developing a simple, rapid, and cost-effective paper-based method for bisacodyl detection.

Keywords: Bisacodyl; Colorimetric detection; Paper-based device

INTRODUCTION

Obesity and overweight have become major public health concerns due to their association with various chronic diseases. Consequently, the use of dietary supplements for weight control has gained popularity among the general public. Despite regulatory controls to ensure the quality and safety of these supplements, the issue of illegal adulteration with pharmacologically active substances persists. The Department of Medical Sciences in Thailand has reported numerous cases of drug adulteration in slimming products, including sibutramine, fluoxetine, and commonly available drugs such as orlistat and bisacodyl (1). Although bisacodyl, a diphenolic stimulant laxative, is generally safe at recommended doses, excessive or prolonged use, especially when consumers are unaware of its adulteration in dietary supplements, may increase the risk of drug dependence and gastrointestinal issues (2).

Current analytical methods for detecting bisacodyl adulteration, such as ion exchange chromatography (3) and liquid chromatography-mass spectrometry (4), are highly precise, sensitive, and specific. However, these methods are expensive, time-consuming, and require sophisticated laboratory setups and expertise, making them impractical for routine or on-site testing. Paper-based analytical devices (PADs) offer an attractive alternative due to their simplicity, portability, and cost-effectiveness. A recent report described a paper-based immunosensor for detecting stimulant laxatives in slimming products (5), demonstrating rapid and sensitive on-site testing without requiring specialized equipment. However, the preparation of antigen-antibody pairs for immunochromatographic assays can be challenging, as producing high-quality, specific antibodies requires expertise, time, and resources.

Colorimetry based on a chemical reaction is one of the most commonly used detection methods in PADs (6). Specific reagents that react with target analytes to produce a visible color change on a paper-based platform have been reported for the rapid detection of adulterants such as dexamethasone, allopurinol, and sibutramine in herbal medicines and slimming products (7-9). Given the lack of simple and low-cost colorimetric methods for bisacodyl detection, this study focused on screening various colorimetric reagents for rapidly detecting bisacodyl on a paper-based platform. The color change on the paper device was observed, captured with a scanner, and analyzed using image analysis software, providing preliminary insights into colorimetric reagents for visualizing bisacodyl on paper.

MATERIALS AND METHODS

Materials

All chemicals used were of analytical grade. Bisacodyl and Fast Blue B were obtained from Sigma-Aldrich (St Louis, MO, USA). Bismuth nitrate, potassium iodide, nitric acid, ferric chloride (FeCl₃), 2 N Folin-Ciocalteu reagent, sodium carbonate, sodium

*Corresponding author: phattanawasin_@silpakorn.edu
Presenting author: phattanawasin_@silpakorn.edu

hydroxide (NaOH), hydrochloric acid (HCl), and ethanol were obtained from Merck (Darmstadt, Germany). 0.01, 1 and 6 M HCl, 1 and 6 M NaOH, and 20% sodium carbonate were prepared in distilled water. Whatman No. 1 filter paper was purchased from GH Healthcare (Buckinghamshire, United Kingdom).

Methods

Preparation of colorimetric reagents

Dragendorff's reagent was prepared accordingly. A solution of 7.2 g of potassium iodide in 50 mL of distilled water was mixed with a solution of 8 g of bismuth nitrate in 20 mL of nitric acid, then adjusted to 100 mL with distilled water. 0.5% and 1% Fast Blue B solution and 2% and 5% FeCl_3 solution were made in distilled water. 2N Folin-Ciocalteu reagent was directly used from Merck.

Preparation of bisacodyl and hydrolyzed bisacodyl solutions

Bisacodyl solutions (1 mg/mL) were prepared in 0.01 N HCl and ethanol. Acid hydrolysis of bisacodyl (A) was carried out by preparing bisacodyl solutions (1 mg/mL) in 1 M HCl, left for 24 hours at room temperature, and then neutralizing with 1 M NaOH (10). Basic hydrolysis (B) was performed by adding 20 μL of 6 M NaOH to 2 mL of the 1 mg/mL bisacodyl solution (11). The solutions were heated at 70°C for 30 minutes, then cooled and neutralized with 6 M HCl. The resulting acid and basic-hydrolyzed bisacodyl solutions were used for subsequent analysis.

Paper fabrication and screening of colorimetric reagents for bisacodyl detection

The paper-based device was fabricated using Whatman No. 1 filter paper, which was cut into a specified design comprising a rectangular area (5x24 mm) and six circular test zones (7x7 mm), connected by small channels (1.5 x 12 mm by width and 1.5 x 21 mm by length) as shown in Figure 1. The cutting was done using a laser cutter. The rectangular area of the patterned paper was affixed to a transparent, hydrophobic plastic sheet with adhesive tape. Each circular zone was designated for the application of colorimetric reagents, followed by the test solutions (sample or blank solvent). For color comparison, the three circular zones on the left were used for testing blanks, while the three zones on the right were designated for the sample solution.

A schematic of the procedure for the screening of colorimetric reagents for rapid detection of bisacodyl on the paper-based device is shown in Fig. 1. The screening was performed using various colorimetric reagents including Dragendorff's, 2% and 5% FeCl_3 , 0.5%, and 1% Fast Blue B, as well as 2 N Folin-Ciocalteu. For Fast Blue B and Folin-Ciocalteu, 20% sodium carbonate was added after the test solutions before observation. The resulting color was observed within 5 minutes and captured by a flatbed scanner with 300 dpi resolution using a color photo mode in a joint photographic experts group (JPEG) format. The color intensity of each zone was measured using an open-source image processing program, ImageJ 1.54h software (National Institutes of Health, USA). The relative percentage change between I_{BIS} and I , where I_{BIS} and I are the intensity with and without bisacodyl, respectively, was calculated ($\text{rel. } \Delta I\% = (I_{\text{BIS}} - I/I) \times 100$) from three replicates.

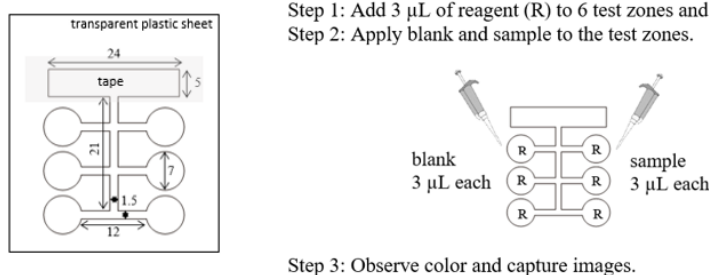


Figure 1. The design of the paper-based device and the procedure for colorimetric reagent screening.

RESULTS AND DISCUSSION

In this work, six colorimetric reagents were screened for bisacodyl detection. The reagents were chosen based on their reactivity towards two functional groups: pyridine in bisacodyl and phenol in its hydrolyzed product, BHPM (Fig. 2). To detect the nitrogen-containing pyridine group in bisacodyl, Dragendorff's reagent was used. For the phenolic group in BHPM, 2% and 5% FeCl_3 , 0.5% and 1% Fast Blue B, and 2N Folin-Ciocalteu were screened.

Whatman No. 1 filter paper, the most widely used paper type in colorimetric PADs, was chosen in this study due to its affordability, small pore size, and moderate retention and flow rate, which facilitate uniform reagent distribution and enhanced

detection performance (12). The paper design (Fig. 1) allowed for a side-by-side visual comparison of color development between the blank and sample test zones.

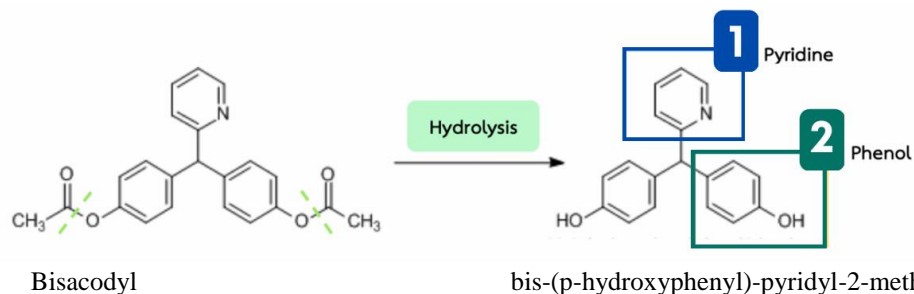


Figure 2. The structure of bisacodyl and its hydrolyzed product.

Figure 3 shows the color responses in the blank and sample zones with various colorimetric reagents. An orange stain appeared in the sample zones when Dragendorff's reagent was applied (Fig. 3aII). Dragendorff's reagent is known to form colored complexes with nitrogen-containing compounds through ion-pair formation between protonated nitrogen atoms and the tetraiodobismuthate anion in the reagent (9). In the case of bisacodyl, the pyridyl nitrogen may become protonated under acidic conditions, facilitating ion-pair formation with the tetraiodobismuthate anion, leading to the observed orange coloration. The solvent used for sample preparation significantly influenced the intensity and clarity of the color formation. Bisacodyl prepared in 0.01 N HCl produced a more intense orange stain compared to bisacodyl prepared in ethanol, as shown in Fig. 3a. This difference could be attributed to the acidic environment promoting protonation of the nitrogen and enhancing its reactivity with Dragendorff's reagent. Additionally, the staining intensity may have been influenced by the diffusion behavior of the solvents on the paper (13). The acidic aqueous solution likely diffused more slowly, allowing bisacodyl to remain concentrated in a smaller area, which enhanced its interaction with Dragendorff's reagent, resulting in a more distinct orange stain.

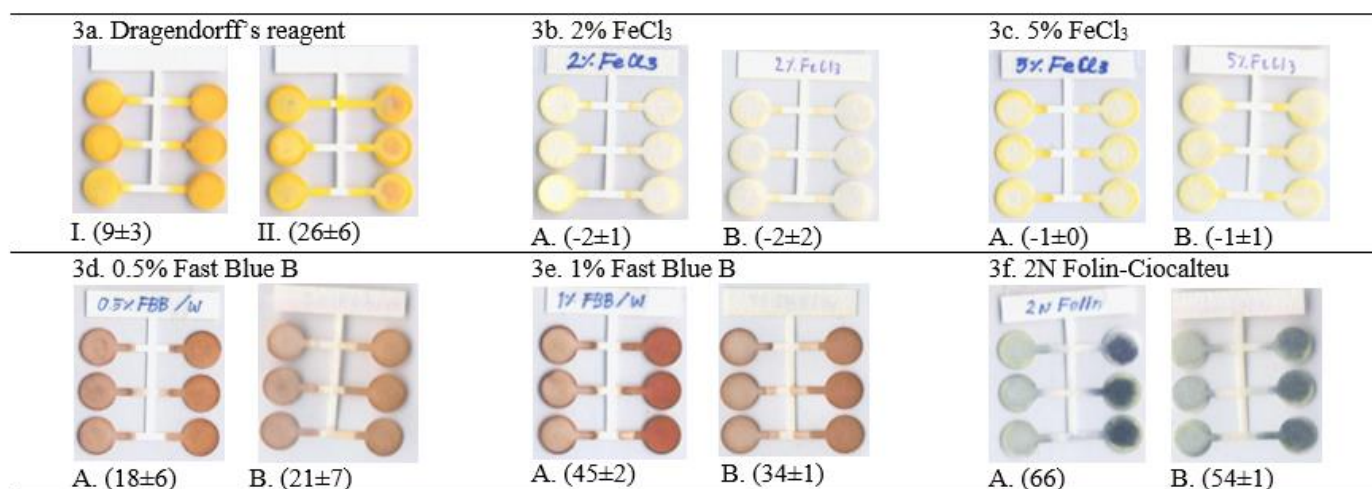


Figure 3. Color responses in the blank and sample zones with various colorimetric reagents. I and II: Bisacodyl in ethanol and 0.01 N HCl, respectively. A and B: Acid- and basic-hydrolyzed samples, respectively. The relative percentage change (rel. $\Delta I\%$) in color intensity is indicated in parentheses.

Bisacodyl itself does not contain a phenol group. However, upon the acid and basic hydrolysis, bisacodyl is converted into BHMP, which contains phenolic groups capable of reacting with specific reagents to produce a color change. The screening results showed that 0.5% and 1% Fast Blue B and 2 N Folin-Ciocalteu reagents produced a dark red color (Fig. 3d and 3e) and an intense blue color (Fig. 3f), respectively. The color intensity increased with the concentration of Fast Blue B. To enhance color development, 20% sodium carbonate was introduced to maintain an alkaline environment. The reaction with Fast Blue B involved an azo coupling of phenolic groups in BHMP with the diazonium salt in Fast Blue B, which, at basic pH, resulted in the formation of red-colored azo complexes (14). The alkaline medium enhanced the nucleophilicity of the hydroxyl groups, facilitating the reaction.

Similarly, the formation of a blue-colored complex with the Folin-Ciocalteu reagent is based on the redox reaction between the phenolic groups and phosphomolybdate/ phosphotungstate complexes under basic pH. The basic medium likely increases the abundance of phenols in their phenolate form, facilitating the redox reaction and the formation of a blue-colored complex (14, 15). In contrast, no detectable color change was observed with 2% and 5% FeCl₃. Although BHPM contains phenolic groups, the lack of color formation may be due to its inability to form suitable complexes with FeCl₃. Steric hindrance or electronic effects could prevent its effective complexation with FeCl₃, resulting in the absence of color formation.

CONCLUSIONS

Various colorimetric reagents, including Dragendorff's reagent, ferric chloride, Folin-Ciocalteu reagent, and Fast Blue B, were screened for the rapid detection of bisacodyl on a paper-based platform. Among these, Dragendorff's reagent, Fast Blue B, and Folin-Ciocalteu reagent exhibited distinct color changes due to their reactivity with pyridine and phenolic groups, respectively. In contrast, ferric chloride did not result in a detectable color change, likely due to unsuitable reaction conditions or limited reactivity under the tested conditions. These preliminary findings support the study objective of screening colorimetric reagents for rapid bisacodyl detection on a paper-based platform and demonstrate their potential for further development into a simple, low-cost, and portable detection method. However, further study is needed to validate the specificity, sensitivity, and interference potential of these colorimetric reagents on a paper-based platform for bisacodyl detection in dietary supplements, ensuring its reliability for real-world applications.

ACKNOWLEDGMENTS

The authors are very grateful to the Faculty of Pharmacy, Silpakorn University for financial assistance and for providing facilities to support the senior project of academic year 2024.

REFERENCES

1. Ueasirikornkun P, Ninwichian P, Sukpol J. Situation of adulteration of weight loss substance in dietary supplements sold in stores and online. *J Health Sci Thai*. 2023;32(4):587–595.
2. Noergaard M, Traerup AJ, Jimenez-Solem E, Bring CM. Long term treatment with stimulant laxatives – clinical evidence for effectiveness and safety? *Scand J Gastroenterol*. 2019;54:27–34.
3. Dal Molin TR, da Silveira GD, Leal GC, Müller LS, Muratt DT, de Carvalho LM, Viana C. A new approach to ion exchange chromatography with conductivity detection for adulterants investigation in dietary supplements. *Biomed Chromatogr*. 2019;33(11):e4669.
4. Kim HJ, Lee JH, Park HJ, Cho SH, Cho S, Kim WS. Monitoring of 29 weight loss compounds in foods and dietary supplements by LC-MS/MS. *Food Addit Contam Part A Chem Anal Control Expo Risk Assess*. 2014;31(5):777–783.
5. Chen S, Guan T, Qian Z, Quan Q, Wang J, Li X, Wu S, Yan Y, Yao X, Zhang S, Lei H. A sensitive and quantitative immunochromatographic assay for simultaneous detection of three stimulant laxatives in slimming food. *Food Chem*. 2023;398:133861.
6. Pradela-Filho LA, Veloso WB, Arantes IVS, Gongoni JLM, de Farias DM, Araujo DAG, Paixão TRLC. Paper-based analytical devices for point-of-need applications. *Microchim Acta*. 2023;190:179.
7. Kuswandi B, Kartika AS, Kristiningrum N, Pratoko DK, Sary IP. Simple and rapid dipstick test for detection of dexamethasone adulteration in traditional herbal medicines. *Pharm Sci Asia*. 2021;48(2):115-121.
8. Pratiwi R, Septyani R, Febriany R, Saputri F, Nuwarda R. Design and optimization of colorimetric paper-based analytical device for rapid detection of allopurinol in Herbal Medicine. *Int J Anal Chem*. 2019;19:1–7.
9. Karamahito P, Sitanurak J, Nacapricha D, Wilairat P, Chaisiwamongkhon K, Phonchai A. Paper device for distance-based visual quantification of sibutramine adulteration in slimming products. *Microchem Journal*. 2021;162:105784.
10. Metwally FH, Abdelkawy M, Naguib IA. Development and validation of three stability-indicating methods for determination of bisacodyl in pure form and pharmaceutical preparations. *J AOAC Int*. 2007;90(1):113-127.
11. de Wolff FA, de Haas EJM, Verweij M. A screening method for establishing laxative abuse. *Clin Chem*. 1981;27(6):914–917.
12. Evans E, Gabriel EFM, Coltro WKT, Garcia CD. Rational selection of substrates to improve color intensity and uniformity on microfluidic paper-based analytical devices. *Analyst*. 2014;139(9):2127–2213.
13. Kumar S, Bhushan P, Bhattacharya S. Fluid transport mechanisms in paper-based microfluidic devices. 2019. 10.1007/978-981-15-0489-1_2.

14. Zugazua-Ganado M, Bordagaray A, Ezenarro J, Garcia-Arrona R, Ostra M, Vidal M. Adaptation of the Folin-Ciocalteu and Fast Blue BB spectrophotometric methods to digital image analysis for the determination of total phenolic content: Reduction of reaction time, interferences and sample analysis. *LWT*. 2024;193:115756.
15. Rizvi NB, Fatima A, Busquets R, Khan MR, Ashraf S, Khan MS, Fatih O. Effect of the media in the folin-ciocalteu assay for the analysis of the total phenolic content of olive products. *Food Anal Methods*. 2023;16:1-8.

Study on Biological Activities of Medium-Ripe and Ripe *Pouteria campechiana* Fruit Extracts for Use as Cosmetic Raw Materials

Parichatr Maneetong¹, Mathukorn Sainakham¹, Pimpak Phumat¹, and Kanokwan Kiattisin^{1,*}

¹Department of Pharmaceutical Sciences, Faculty of Pharmacy, Chiang Mai University, Chiang Mai, Thailand, 50200

*Corresponding author Email: kanokwan.k@cmu.ac.th

Abstract. *Pouteria campechiana* is a tropical fruit rich in bioactive compounds and essential nutrients. This study investigated and compared the phytochemical compositions and biological activities of ethanolic extracts from different parts of *P. campechiana* fruit including the peel, pulp, and seed collected from medium-ripe and ripe fruits. The phytochemical profiles were assessed by measuring the total phenolic content and total flavonoid content. Antioxidant, anti-tyrosinase, and anti-aging activities of each extract were evaluated using standard *in vitro* assays. The results showed that the medium-ripe seed extract exhibited the strongest free radical scavenging activity in the DPPH assay, with an IC₅₀ value of 0.04 ± 0.00 mg/mL. The FRAP assay also confirmed its superior antioxidant capacity, yielding a value of 114.86 ± 1.44 mg FeSO₄/g extract. Furthermore, this extract demonstrated the most potent anti-tyrosinase activity. In anti-aging assays, the medium-ripe seed extract showed the highest collagenase and elastase inhibitory activities, with percentage inhibitions of $61.92 \pm 12.46\%$ and $49.62 \pm 13.24\%$, respectively. These bioactivities are consistent with its elevated total phenolic and total flavonoid contents. Interestingly, the ripe seed extract showed the highest antioxidant activity in the β -carotene bleaching assay, with a percentage inhibition of $84.56 \pm 11.25\%$, and exhibited the most potent hyaluronidase inhibitory activity at $21.61 \pm 0.79\%$. These findings suggest that extracts from *P. campechiana*, particularly those from medium-ripe and ripe seeds, are rich in phytochemicals and exhibit promising biological activities. Therefore, they hold potential for further development as natural active ingredients in cosmetic formulations.

Keywords: *Pouteria campechiana*; fruit extracts; cosmetic raw materials; anti-oxidant; anti-aging

INTRODUCTION

Pouteria campechiana, commonly known as canistel or eggfruit, is a tropical plant cultivated in several countries, including Thailand. The fruit can be consumed fresh or incorporated into a variety of foods and beverages. However, peel and seeds are typically discarded as waste. This plant is recognized as a valuable source of bioactive compounds and has been traditionally used for medicinal purposes [1]. Phytochemical investigations have identified several polyphenolic compounds in *P. campechiana*, including dihydromyricetin, (+)-catechin-3-O-gallate, (+)-gallocatechin, (+)-catechin, (–)-epicatechin, gallic acid, and myricitrin [2,3]. Previous studies have demonstrated that the fruit pulp is rich in minerals, carotenoids, polyphenols, flavonoids, carbohydrates, amino acids, and vitamins B and C, all of which contribute to its notable antioxidant properties. Additionally, various parts of the plant such as bark, unripe fruit, seeds, and leaves have been utilized in traditional medicine for a range of therapeutic purposes [3,4]. While *P. campechiana* has been extensively studied in the context of food science for its nutritional and antioxidant benefits, its potential cosmetic applications, particularly in terms of anti-aging and anti-tyrosinase activities, remain underexplored. Therefore, this study aims to evaluate the cosmetic potential of residual fruit parts, including the peel and seeds, in comparison to the pulp. Samples from medium-ripe and ripe stages were analyzed for their phytochemical content and cosmetic properties, including antioxidant, anti-aging, and anti-tyrosinase activities, to assess their suitability as natural active ingredients in cosmetic formulations. The use of fruit peels and seeds not only contributes to waste reduction but also provides a sustainable source of functional ingredients. The findings from this study are expected to support the incorporation of *P. campechiana* extracts into cosmetic and cosmeceutical products for skincare applications.

MATERIALS AND METHODS

Materials

1,1-Diphenyl-2-Picrylhydrazyl (DPPH) was purchased from Fluka (Buchs, Switzerland). Aluminium chloride, calcium chloride, L-dopa, and sodium chloride were purchased from Loba Chemie (Mumbai, India). Tris-HCl were purchased by RCI Labscan (Bangkok, Thailand). Ascorbic acid, L-tyrosine, gallic acid, collagenase, elastase, N-[3-(2-Furyl) acryloyl]-Leu-Gly-Pro-Ala (FALGPA), N-succinyl-Ala-Ala-Ala-p-nitroanilide (AAPVN), epigallocatechin gallate (EGCG), linoleic acid, and tricine were purchased from Sigma-Aldrich (St. Louis, MO, USA). Ethanol and dimethyl sulfoxide (DMSO) were purchased from Union Science (Chiang Mai, Thailand). Folin-Ciocalteu reagent was purchased from Merck (Darmstadt, Germany).

P. campechiana fruits were collected in November 2023 from local agricultural sources in Chai Prakan District, Chiang Mai, Thailand. The ripe and medium-ripe *P. campechiana* fruits were peeled and dried in a hot air oven at 50 °C for three days. Then, the peel, pulp, and seed were separated and coarsely ground.

Methods

Preparation of P. campechiana extracts

Peel, pulp, and seed of *P. campechiana* were ground into a coarse powder and extracted using a Soxhlet apparatus with 95% v/v ethanol [5]. The solvent was removed using a rotary evaporator (Buchi, R-300, Switzerland). The extracts were stored in a well-closed container protected from light at 4 °C. The yield of the extract was calculated.

Determination of total phenolic content (TPC)

The total phenolic content (TPC) of the extracts was determined using the Folin–Ciocalteu assay [5]. Each extract was prepared by dissolving it in ethanol to a concentration of 1 mg/mL. The sample solution was mixed with Folin–Ciocalteu reagent followed by sodium carbonate. The mixture was allowed to stand at room temperature for 30 minutes. Absorbance was then measured at 765 nm using a UV–visible spectrophotometer (Shimadzu UV-2600i, Japan). The results were expressed as milligrams of gallic acid equivalents (GAE) per gram of extract (mg GAE/g extract).

Determination of total flavonoid content (TFC)

The total flavonoid content (TFC) of the extracts was determined using the aluminum chloride colorimetric assay [5]. Each extract was prepared by dissolving it in ethanol to a concentration of 1 mg/mL. The extract solution was mixed with sodium nitrite and deionized water, and the mixture was incubated for 5 minutes. Subsequently, aluminum chloride and sodium hydroxide were added. The absorbance was measured at 510 nm using a UV–visible spectrophotometer. The results were expressed as milligrams of quercetin equivalent (QE) per gram of extract (mg QE/g extract).

Determination of antioxidant activity

DPPH radical scavenging assay

The extract solutions were prepared in ethanol. Each concentration, along with the standard, was mixed with a DPPH solution and incubated in the dark at room temperature for 30 minutes. After incubation, the absorbance was measured at 520 nm using a microplate reader (BMG SPECTROstar Nano, Germany) [6]. Trolox was used as the positive control. The antioxidant activity was expressed as the half-maximal inhibitory concentration (IC₅₀).

Ferric reducing antioxidant power (FRAP) assay

The extract solution was prepared by dissolving each sample in ethanol at a concentration of 1 mg/mL. The FRAP reagent was mixed with the extract and incubated at room temperature for 5 minutes. Absorbance was then measured at 593 nm using a microplate reader [6]. Trolox was used as the positive control. The antioxidant activity was expressed as FRAP value, reported in milligrams of FeSO₄ equivalent per gram of extract (mg FeSO₄/g extract).

β-carotene bleaching assay

The β-carotene bleaching assay was conducted following the method described by Barros et al. [7]. β-carotene was dissolved in chloroform, followed by the addition of linoleic acid and Tween 80. After the chloroform was evaporated, distilled water was added to form a stable emulsion. The emulsion was mixed with each extract (1 mg/mL). Absorbance was measured at 490 nm using a microplate reader in kinetic mode. Trolox was used as a positive control. The antioxidant activity was expressed as the percentage of inhibition of β-carotene oxidation.

Determination of anti-tyrosinase activity

The anti-tyrosinase activity was evaluated using L-tyrosine and L-DOPA as substrates [8]. The sample was dissolved in 20% v/v Tween 20 at a concentration of 1 mg/mL. The sample was mixed with phosphate-buffered saline (PBS, pH 6.5) and mushroom tyrosinase enzyme solution (50 units/mL). After incubation at room temperature for 10 minutes, the substrate was added, and the mixture was further incubated for 20 minutes. Absorbance was measured at 765 nm using a microplate reader. Kojic acid was used as a positive control. The anti-tyrosinase activity was expressed as the percentage inhibition of tyrosinase activity.

Determination of anti-aging activity

Anti-collagenase assay

Collagenase inhibitory activity was measured using the procedure described by Preedalikit et al. [8]. The collagenase enzyme was prepared in 50 mM tricine buffer (pH 7.5) containing 400 mM sodium chloride and 10 mM calcium chloride. The sample was dissolved in 20% v/v DMSO at a concentration of 1 mg/mL. Each extract was mixed with the collagenase enzyme solution and incubated at room temperature for 15 minutes. The reaction was initiated by the addition of the substrate (FALGPA). Absorbance was measured at 340 nm in kinetic mode.

using a microplate reader. Epigallocatechin gallate (EGCG) served as the positive control. The collagenase inhibitory activity was expressed as the percentage inhibition of enzyme activity.

Anti-elastase assay

Elastase inhibitory activity was evaluated using a method based on Preedalikit et al. [8]. The sample was dissolved in 20% v/v DMSO at a concentration of 1 mg/mL. Elastase, prepared in 100 mM Tris-HCl buffer (pH 8.0), was pre-incubated with each extract for 20 minutes at room temperature. The reaction was then initiated by adding 4.4 mM AAPVN in the same buffer. Absorbance was measured at 410 nm in kinetic mode using a microplate reader. Ascorbic acid was used as a positive control. The elastase inhibitory activity was expressed as the percentage inhibition of enzyme activity.

Anti-hyaluronidase assay

Hyaluronidase inhibitory activity was determined using a modified turbidimetric method [8]. The sample was dissolved in 20% v/v DMSO at a concentration of 25 µg/mL. The hyaluronidase enzyme was initially pre-incubated with each extract for 10 minutes at 37 ± 5 °C. Subsequently, hyaluronic acid in buffer solution was added, and the mixture was incubated for 45 minutes at 37 ± 5 °C. Acetic acid containing bovine serum albumin was then added to precipitate the undigested hyaluronic acid. After 10-minute incubation, the turbidity of the mixture was measured at 600 nm using a microplate reader. Tannic acid was used as a positive control. The hyaluronidase inhibitory activity was expressed as the percentage inhibition of enzyme activity.

Statistical analysis

All experiments were conducted in triplicate, and the results are presented as mean \pm standard deviation (SD). Statistical analysis was performed using one-way analysis of variance (ANOVA), followed by Tukey's Honestly Significant Difference (HSD) post hoc test to determine significant differences among groups. A p-value of less than 0.05 ($p < 0.05$) was considered statistically significant. All data analyses were performed using SPSS software (version 17).

RESULTS AND DISCUSSION

1. Plant extraction

The extraction yields for each part are presented in Table 1. The medium-ripe pulp extract (PuM) yielded the highest percentage at 55.90%, followed by the ripe peel extract (PeR), ripe seed extract (SeR), medium-ripe peel extract (PeM), ripe pulp extract (PuR), and medium-ripe seed extract (SeM), respectively. These results indicate notable variations in chemical composition across different parts and ripening stages of the fruit, which may influence extraction efficiency [9]. As these extracts are derived from natural sources, they may be sensitive to environmental conditions. Therefore, all samples were stored at 4 °C prior to analysis to preserve their stability.

Table 1. Percentage yields of each *P. campechiana* extract

Sample	PeM	PuM	SeM	PeR	PuR	SeR
Yield (%)	10.15	55.9	7.27	37.89	8.29	12.16

2. Total phenolic content and total flavonoid content of *P. campechiana* extracts

The total phenolic and flavonoid contents of each extract are presented in Figure 1. The SeM exhibited the highest levels of both total phenolics and flavonoids among all samples ($p < 0.05$). Similarly, the ripe seed extract SeR demonstrated higher phenolic and flavonoid contents than the peel and pulp extracts at both ripening stages. These findings confirm that phytochemical content varies significantly among different fruit parts and ripeness levels. This trend is consistent with previous reports indicating that seeds often accumulate high concentrations of bioactive secondary metabolites such as β -carotene, lutein, and quercetin [10]. The analysis of *P. campechiana* seed extracts revealed a strong correlation between specific phytochemical constituents and significant biological activity. In particular, the seeds were rich in flavonoids, including myricitrin, quercetin, and kaempferol. These results highlight that the phytochemical profile of the seeds directly influences their biological effects.

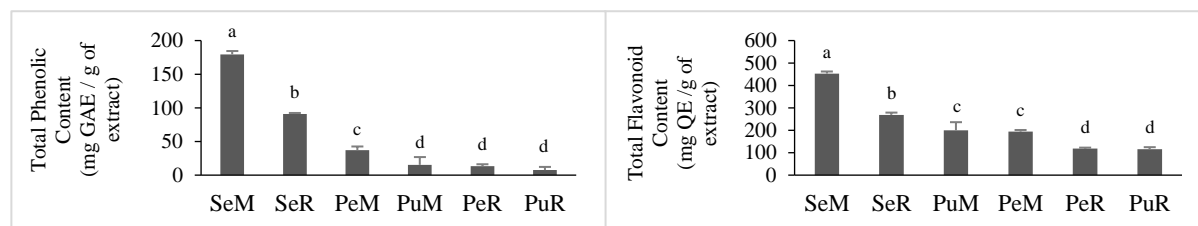


Figure 1. Total phenolic content and total flavonoid content of *P. campechiana* extracts. Different superscript letters (a-d) indicate significant differences by one-way ANOVA with multiple comparisons test using Tukey ($p < 0.05$).

3. Antioxidant activity of *P. campechiana* extracts

The antioxidant activity of *P. campechiana* extracts was evaluated using DPPH, FRAP, and β -carotene bleaching assays. Antioxidants mitigate oxidative stress by scavenging free radicals, interrupting chain reactions, chelating metal ions, and inhibiting lipid peroxidation [7,9]. The results are summarized in Table 2. The SeM exhibited the lowest IC₅₀ value in the DPPH assay (0.04 ± 0.00 mg/mL), although the difference was not statistically significant when compared with the PeM, SeR, and Trolox. Notably, the SeM also showed the highest antioxidant capacity in the FRAP assay, with a value of 114.86 ± 1.44 mg FeSO₄/g extract ($p < 0.05$), indicating strong electron-donating ability. In the β -carotene bleaching assay, the SeR, SeM, and PeM effectively inhibited lipid peroxidation, displaying antioxidant activities comparable to Trolox. These findings are closely associated with the high total phenolic content of the extracts, reinforcing their potential for protecting the skin from oxidative damage. Among the phenolic constituents, gallic acid identified in *P. campechiana* is known to contribute significantly to antioxidant mechanisms. It can donate hydrogen atoms or electrons from its hydroxyl groups to neutralize reactive oxygen species. It can chelate transition metal ions (e.g., Fe²⁺, Cu²⁺), preventing them from catalyzing free radical formation. In addition, it can intercept lipid peroxyl radicals (LOO[•]), thereby reducing oxidative chain propagation [3].

Table 2. Antioxidant activities of *P. campechiana* extracts using DPPH assay, FRAP assay, and β -carotene bleaching assay

Sample	DPPH assay IC ₅₀ (mg/mL)	FRAP assay FRAP value (mg FeSO ₄ /g of extract)	β -carotene bleaching assay Inhibition (%)
Trolox	0.01 ± 0.00^a	134.35 ± 1.18^a	88.71 ± 7.48^a
SeR	0.14 ± 0.01^a	22.32 ± 0.50^c	84.56 ± 11.25^{ab}
SeM	0.04 ± 0.00^a	114.86 ± 1.44^b	83.82 ± 5.79^{ab}
PuM	0.72 ± 0.02^b	15.48 ± 0.40^d	82.35 ± 1.80^b
PeM	0.14 ± 0.00^a	20.59 ± 2.88^c	81.11 ± 3.14^{ab}
PuR	3.26 ± 0.06^d	6.54 ± 0.40^e	79.41 ± 1.04^{bc}
PeR	2.25 ± 0.27^c	5.25 ± 0.39^e	69.85 ± 1.04^c

Different superscript letters (a-e) indicate significant differences in each assay by one-way ANOVA with multiple comparisons test using Tukey ($p < 0.05$)

4. Anti-tyrosinase activity of *P. campechiana* extracts

Tyrosinase is a key enzyme involved in melanin synthesis within melanocytes and plays a central role in skin pigmentation [8]. Therefore, inhibiting tyrosinase activity is a widely targeted approach in skin-brightening and anti-hyperpigmentation treatments. The anti-tyrosinase activity of *P. campechiana* extracts is presented in Figure 2. Among all samples, the SeM exhibited the highest tyrosinase inhibitory activity, closely followed by the SeR. This activity is strongly correlated with the high total phenolic and flavonoid contents observed in SeM. Phenolic and flavonoid compounds can suppress tyrosinase activity by binding directly to its active site (competitive inhibition) or by chelating copper ions essential for its catalytic function. Additionally, some compounds exert non-competitive inhibition by interacting with allosteric sites, inducing conformational changes that reduce enzyme activity. Gallic acid, one of the major phenolics identified in *P. campechiana*, acts primarily as a competitive inhibitor of tyrosinase. Quercetin, another key flavonoid, exhibits either competitive or mixed-type inhibition [8].

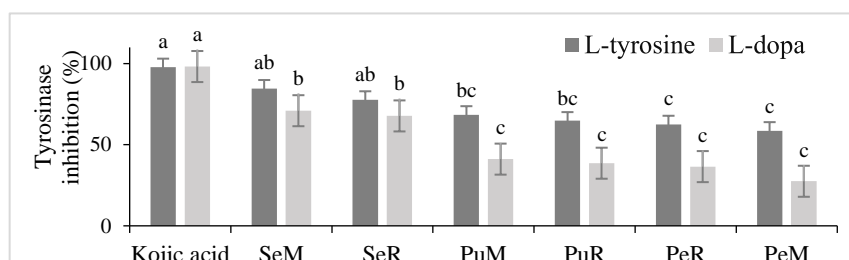


Figure 2. Tyrosinase inhibitory activity of *P. campechiana* extracts. Different superscript letters (a-c) indicate significant differences by one-way ANOVA with multiple comparisons test using Tukey ($p < 0.05$).

5. Anti-aging activity of *P. campechiana* extracts

Collagenase, elastase, and hyaluronidase are key enzymes involved in the degradation of collagen, elastin, and hyaluronic acid, respectively, which are structural components essential for maintaining skin firmness and elasticity. Their activity accelerates the skin aging process, contributing to wrinkle formation and loss of skin resilience [8]. Therefore, inhibiting these enzymes is a promising strategy for anti-aging skincare. The anti-aging activities of *P. campechiana* extracts against collagenase, elastase, and hyaluronidase are summarized in Table 3. The SeM exhibited

the highest collagenase (61.92%) and elastase (49.62%) inhibitory activities; however, these differences were not statistically significant compared to the other extracts. The SeR showed the strongest hyaluronidase inhibitory activity (21.61%), although it was also not significantly different from other tested extracts and the positive control. The notable anti-aging effects of the seed extracts may be attributed to their high content of phenolic compounds and triterpenoids, which are known to inhibit skin-degrading enzymes. Gallic acid typically acts via non-competitive inhibition. It chelates metal ions such as Zn^{2+} and alters the enzyme's conformation, thereby reducing its activity. Quercetin inhibits these enzymes primarily through competitive or mixed-type mechanisms by binding to their active sites, forming hydrogen bonds, and engaging in hydrophobic interactions. Additionally, it can chelate essential metal ions required for enzymatic activity [1]. Additionally, flavonoids present in the extracts have been reported to suppress hyaluronidase activity, thereby helping to preserve skin hydration and elasticity.

Table 3. Anti-aging activities by anti-collagenase assay, anti-elastase assay and anti-hyaluronidase assay of *P. campechiana* extracts

Sample	Collagenase inhibition (%)	Elastase inhibition (%)	Hyaluronidase inhibition (%)
Ascorbic acid	ND	79.13±7.02 ^a	ND
EGCG	68.20±5.67 ^a	ND	ND
Tannic acid	ND	ND	29.78±16.58 ^a
SeM	61.92±12.46 ^a	49.62±13.24 ^b	19.78±0.76 ^a
SeR	58.74±3.86 ^a	35.92±0.86 ^b	21.61±0.79 ^a
PeM	53.25±7.32 ^a	39.27±13.20 ^b	14.41±0.15 ^a
PuM	51.83±8.74 ^a	34.25±16.96 ^b	17.31±0.66 ^a
PuR	45.33±2.64 ^a	48.71±13.24 ^b	17.31±1.33 ^a
PeR	45.12±0.81 ^a	29.76±9.64 ^b	15.91±1.35 ^a

ND means not determined. Superscript letters (a-b) indicate significant difference ($p < 0.05$) in each assay evaluated by one-way ANOVA with multiple comparisons test using Tukey

CONCLUSIONS

The seed extract of *P. campechiana* from medium-ripe fruits exhibited the highest levels of phenolic and flavonoid contents, along with potent antioxidant activity. Its strong inhibitory effects on tyrosinase and matrix-degrading enzymes highlight its potential for application in skin-whitening and anti-aging products. This extract shows promise as a novel natural active ingredient for cosmetic formulations. However, future studies should focus on the identification and quantification of chemical markers to determine the specific bioactive compounds responsible for the observed biological activities. This will enhance the understanding of the extract's mechanism of action and support standardization for cosmetic applications. In addition, cytotoxicity evaluation is essential to ensure its safety. A comprehensive stability study is recommended in future research to determine optimal storage conditions for maintaining extract integrity.

ACKNOWLEDGMENTS

The authors thankfully acknowledge the Master of Science Program in Cosmetic Science, Faculty of Pharmacy at Chiang Mai University, Chiang Mai, Thailand for providing us with the funding and necessary resources.

REFERENCES

- [1] Do TVT, Suhartini W, Phan CU, et al. Nutritional value, phytochemistry, health benefits, and potential food applications of *Pouteria campechiana* (Kunth) Baehni: A comprehensive review. *J Funct Foods*. 2023;103:105481.
- [2] Manthra V, Ireen C, Thilagameena S, et al. Free radical scavenging potential and antihemolytic activity of methanolic extract of *Pouteria campechiana* (Kunth) Baehni. and *Tricosanthus tricuspidata* Linn. *Biocatal Agric Biotechnol*. 2019;18:101031.
- [3] Elsayed AM, El-Tanbouly ND, Moustafa SF, et al. Chemical composition and biological activities of *Pouteria campechiana* (Kunth) Baehni. *J Med Plants Res*. 2016;10(16):209-215.
- [4] Sethuraman G, Nizar M, Syaheerah T, et al. Nutritional composition of canistel (*Pouteria Campechiana* (Kunth) Baehni). *Int J Food Sci Nutr*. 2020;5(6):53-57.
- [5] Poomanee W, Chaiyana W, Intasai N, et al. Biological activities and characterization of the pod extracts from sompoi (*Acacia concinna* linn) grown in northern Thailand. *Int J Pharm Sci*. 2015;7:237-241.
- [6] Theansungnoen T, Nitthikan N, Wilai M, et al. Phytochemical analysis and antioxidant, antimicrobial, and antiaging activities of ethanolic seed extracts of four *Mucuna* species. *Cosmetics*. 2022;9:14.
- [7] Barros L, Baptista P, Ferreira ICFR. Effect of *Lactarius Piperatus* fruiting body maturity stage on antioxidant activity measured by several biochemical assays. *Food Chem Toxicol*. 2007;45:1731-1737.
- [8] Preedalikit W, Chittasupho C, Leelapornpisid P, et al. Comparison of Biological Activities and Protective effects on PAH-induced oxidative damage of different coffee cherry pulp extracts. *Foods*. 2023; 12:4292.
- [9] Koca I, Ustun S, Tekguler B. Physical and chemical changes during ripening of blackberry fruits. *Scientia Agricola*. 2008;65(1):87-90.
- [10] Balasundram N, Sundram K, Samman S. Phenolic compounds in plants and agri-industrial by-products: Antioxidant activity, occurrence, and potential uses. *Food Chem*. 2006;99: 191-203.

Patient-Centric Approaches in Biopharmaceutics, Pharmacology, and Toxicology

The Functional Analysis of *UGT1A1**80 and *93 Polymorphisms on Deferasirox Metabolism and Transcriptional Regulation

*Siriporn Yukuntorn*¹, *Kittika Yampayon*¹, *Watchara Sakares*¹, *Krittin Pitinanon*¹, *Polsak Teerawonganan*², *Sumate Kunsan-ngiem*², *Pithi Chanvorachote*^{1,3}, *Jittima Piriapongsa*⁴, *Alisa Tubsuwan*⁵, *Varalee Yodsurang*^{1,6,*}

¹Department of Pharmacology and Physiology, Faculty of Pharmaceutical Sciences, Chulalongkorn University, Thailand

²Bioanalysis Section, Bioequivalence and Clinical Research Division, Research Development and Innovation Department, The Government Pharmaceutical Organization, Thailand

³Cell-Based Drug and Health Product Development Research Unit, Faculty of Pharmaceutical Sciences, Chulalongkorn University, Thailand

⁴National Biobank of Thailand, National Center for Genetic Engineering and Biotechnology, National Science and Technology Development Agency, Thailand

⁵Institute of Molecular Biosciences, Mahidol University, Thailand

⁶Preclinical Toxicity and Efficacy Assessment of Medicines and Chemicals, Chulalongkorn University, Thailand

*Corresponding author Email: varalee.y@pharm.chula.ac.th

Abstract. Deferasirox (DFX), an approved medicine indicated for chronic iron overload, is primarily metabolized through UDP Glucuronosyltransferase Family 1 Member A1 (UGT1A1). *UGT1A1**80 (rs887829) and *93 (rs10929302), SNPs in the promotor region, have been associated with plasma levels of drugs reported in clinical studies. However, their impact on DFX metabolism remains uncharacterized. This study investigated the function of these two SNPs on DFX metabolism using *in vivo* and transcriptional regulation using cell-based assays. Thalassemia patients with chronic iron overload receiving DFX at Siriraj Hospital were screened and genotyped for SNPs. The linkage disequilibrium (LD) between these SNPs was examined and demonstrated the strong LD of *UGT1A1**80 and *93. Patients were categorized based on *UGT1A1* diplotypes and measured for trough concentration (C_{trough}) of DFX and its primary glucuronide metabolite (M3) using LC-MS/MS. The M3/DFX C_{trough} ratio was analyzed and compared across diplotypes to infer DFX metabolism. Variations in M3/DFX C_{trough} ratios across diplotypes suggest SNP-dependent alterations in DFX metabolism. For the *in vitro* analysis, CRISPR-Cas9/12-mediated disruption was performed to interrupt the SNP positions in HepG2 cells. We did not detect alteration in *UGT1A1* mRNA level between SNP-disrupted and wild-type cells using mixed cell populations, suggesting further elucidation using stable single cells. In conclusion, our study showed *UGT1A1**80 and *93 corresponding to DFX metabolism *in vivo*; although, a larger sample size and the *in vitro* analysis should be further investigated. These findings suggest the potential clinical relevance of *UGT1A1* polymorphisms in optimizing DFX treatment.

Keywords: Deferasirox (DFX); *UGT1A1**80; *UGT1A1**93; trough concentration (C_{trough}); deferasirox acyl-β-D-glucuronide (M3).

INTRODUCTION

Deferasirox (DFX), used to treat chronic iron overload, exhibits variable therapeutic responses. DFX is metabolized by UDP-glucuronosyltransferase 1A1 (*UGT1A1*) into deferasirox acyl-β-D-glucuronide (M3) and is excreted via bile and urine ^[1]. Promoter SNPs, *UGT1A1**80 (rs887829) ^[2,3] and *93 (rs10929302) ^[3,4], have been correlated with variabilities in the plasma concentrations of several drugs, but their impact on DFX metabolism remains unclear. This study analyzed the impact of *UGT1A1**80 and *93 on DFX metabolism through *in vivo* analysis using 46 thalassemia patients and investigated transcriptional regulation via *in vitro* analysis involving CRISPR/Cas9/12-mediated SNP disruption in HepG2 cells.

MATERIALS AND METHODS

Materials

This study used hepatocellular carcinoma HepG2 cell lines (ATCC, USA), Dulbecco's modified Eagle medium (DMEM) (Gibco Life Technologies; USA), Penicillin-Streptomycin (Cytiva, USA), Fetal Bovine Serum (FBS) (Sigma-Aldrich, USA). Plasmids and reagents used in this study included PX458 plasmid (Addgene, USA), oligonucleotides (Macrogen, Korea), the Polyethylenimine "Max" (PEI MAX) transfection reagent (Polysciences, USA), Opti-MEM[®] (Invitrogen Life Technologies, USA), Phusion high-fidelity DNA polymerase (NEB, USA), QIAamp[®] DNA Investigator (Qiagen, USA), TRIzol (Invitrogen, USA),

iScript™ Reverse Transcription Supermix (Bio-Rad, US), iTaq Universal SYBR Green Supermix (Bio-Rad, US) and T4 DNA ligase (NEB, USA).

Methods

Patient: inclusion and exclusion criteria

This study included 46 beta-thalassemia patients with transfusional iron overload who received DFX treatment for a minimum of six months. Patients were excluded if they were taking medications known to interact with DFX, i.e., strong inducers of UGT isoenzymes (e.g., rifampicin, barbiturates, carbamazepine, phenytoin, efavirenz, nevirapine, ritonavir, and rifabutin) or bile acid sequestrants (e.g., cholestyramine, colestevlam, colestipol). Additionally, individuals with hepatic or renal dysfunction were not included in the study.

Blood sample collection

For the analysis of deferasirox trough concentration (C_{trough}) and its metabolite, deferasirox acyl-β-D-glucuronide (M3), blood samples were collected from participants at steady-state prior to the administration of their next DFX dose. The collected blood samples were immediately centrifuged, and the resulting plasma was stored at -80°C until analyzed using LC-MS/MS.

LC-MS/MS Assay for DFX and M3

The LC-MS/MS method was developed and validated to quantify plasma concentrations of DFX C_{trough} and its metabolite M3. The study used the Nexera™ UPLC system (Shimadzu Corporation, Kyoto, Japan) coupled with a TSQ Quantum Ultra mass spectrometer (Thermo Fisher Scientific, USA). Data acquisition and processing were performed using Xcalibur™ 4.0.27.42 and LCquan™ 3.0.26.0 software (Thermo Fisher Scientific, USA). Validation followed FDA and EMA bioanalytical guidelines, assessing linearity, recovery, detection/quantification limits, matrix effects, precision, accuracy, selectivity, stability, and reproducibility. Additionally, the M3/DFX C_{trough} ratio was analyzed across *UGT1A1* diplotypes to evaluate DFX metabolism.

Cell culture

HepG2 cells were cultured in DMEM supplemented with 10% FBS, along with 1% penicillin and streptomycin. The cell lines were maintained at 37°C with a humidified atmosphere containing 95% air and 5% CO₂. The cell lines were maintained below 80% confluency and passaged as needed.

Plasmid construction

PX458 plasmid containing a green fluorescent protein gene (GFP) was used for expression of the gRNA and SpCas9 protein. Complementary oligonucleotides (Table 1) encoding the gRNAs targeting *UGT1A1**80 and *93 promoter region sequence were annealed and ligated into PX458 using T4 ligase enzyme. The gRNA sequences in constructed plasmids were confirmed by the Sanger sequencing (U2Bio, Thailand).

Table 1. Oligonucleotides encoding gRNAs targeting *UGT1A1**80 and *93

Oligo name	Sequences
*80-Cas9-gRNA1-Fw	CACCAAAGCCTTCTGTTAATTTC
*80-Cas9-gRNA1-Rw	AAACGAAATTAAACAGAAGGCTTT
*80-Cas9-gRNA2-Fw	CACCAAAGCCTTCTGTTAATTTT
*80-Cas9-gRNA2-Rw	AAACAAAATTAAACAGAAGGCTTT
*93-Cas9-gRNA2-Fw	CACCGAGGAGGAATGAGCTTGGAC
*93-Cas9-gRNA2-Rw	AAACGTCCAAGCTCATTCTCCTC

Transfections

HepG2 cells were seeded into 24-well flat-bottom cell culture plate at 1.3×10^5 cells/well. Transfections were carried out 18–24 hours post-seeding with 1 µg of the expression PX458 plasmid containing gRNA for *UGT1A1**80 and *UGT1A1**93 and SpCas9 protein per transfection (per well, in a 24-well plate). Polyethylenimine “Max” (PEI MAX) was used as the transfection reagent at 2 µg per transfection.

Cell sorting by flow cytometry

Regarding the vector PX458 encoding GFP, the transfected HepG2 cells were harvested and sorted for selection of GFP-positive cells by fluorescence-activated cell sorting (FACS) using a BD FACSMelody™ (Beckton Dickinson, USA). The mixed populations of cell clones of GFP-expressing cells were selected and cultured.

Targeted amplicon sequencing

The gDNA was extracted from the disrupted cells and measured for its concentration by NanoDrop 2000 spectrophotometer (Thermo Fisher Scientific, USA). The PCR was performed to amplify the genomic regions of *UGT1A1**80 and *UGT1A1**93 using Phusion™ High-Fidelity DNA Polymerase. PCR products were purified using GenepHlow™ Gel/PCR Kits according to the manufacturer's protocol and sequenced using next-generation sequencing (NGS) using Fast NGS sequencing (U2Bio, Thailand).

RNA extraction, cDNA synthesis, and Reverse Transcription Quantitative PCR (RT-qPCR)

The mixed populations of disrupted cells were harvested, and extracted for RNA using TRIzol according to the manufacturer's protocol. The total RNA amount was quantified using Nanodrop. The 1 µg of RNA was reverse transcribed using iScript™ Reverse Transcription Supermix, diluted in nuclease-free water (1:10), and stored at -20°C. For the qPCR, reaction mixtures (10 µl) contained 5 µl of iTaq SYBR supermix buffer, 0.5 mM of the respective forward and reverse primers, and 4 µl of the thawed cDNA. Beta-actin was used as an endogenous control. Primer sequences for *UGT1A1* are CCTTGCCTCAGAATTCCTTC as forward and ATTGATCCCAAAGAGAAAACCAC as reverse primers for qPCR.

Statistical analysis

All measurement data presented were expressed as mean ± standard deviation (SD). The Kruskal–Wallis test was used and the statistical significance was defined as $P < 0.05$.

RESULTS AND DISCUSSION

The linkage disequilibrium (LD) between SNPs

We analyzed the linkage disequilibrium (LD) of *UGT1A1**80, *93, and the previously reported known functional promotor SNPs, including *60 (rs4124874) and *28 (rs3064744). LD analysis of *UGT1A1* promotor SNPs in a Thai thalassemia cohort revealed strong co-inheritance ($r^2 \approx 1$) among *UGT1A1**80, *93, and *28, forming a tightly linked haplotype. In contrast, *UGT1A1**60 showed weak LD ($r^2 < 0.5$) with this haplotype, segregating independently (Table 3). These findings suggest *UGT1A1**80/*93/*28 function as a coordinated regulatory unit, while *UGT1A1**60 contributes to metabolic variability through distinct mechanisms.

	<i>UGT1A1</i> *60	<i>UGT1A1</i> *93	<i>UGT1A1</i> *80	<i>UGT1A1</i> *28
<i>UGT1A1</i> *60	N/A	0.38	0.43	0.43
<i>UGT1A1</i> *93		N/A	0.89	0.89
<i>UGT1A1</i> *80			N/A	1.00
<i>UGT1A1</i> *28				N/A

Table 2. Pairwise linkage disequilibrium (r^2 values) among *UGT1A1* variants (*UGT1A1**60, *93, *80, and *28). N/A; Not Applicable.

Classification of patients based on *UGT1A1* diplotypes

Patients were stratified into six diplotype groups based on *UGT1A1* variants, including haplotype-tagged SNPs (*80, *93, *28; LD $r^2 \approx 1$) and the functionally validated *60 polymorphism.

Diplotype pattern	<i>UGT1A1</i> *60 (T>G)	<i>UGT1A1</i> *93 (G>A)	<i>UGT1A1</i> *80 (C>T)	<i>UGT1A1</i> *28 (6TA>7TA)
1	T/T	G/G	C/C	6TA/6TA
2	T/G	G/G	C/C	6TA/6TA
3	T/G	G/A	C/T	6TA/7TA
4	G/G	G/A	C/T	6TA/7TA
5	G/G	G/G	C/C	6TA/6TA
6	G/G	A/A	T/T	7TA/7TA

Table 3. Diplotype Patterns of *UGT1A1* Variants

Noted: (Reference allele > Alternative allele). Dark blue indicates homozygous variant genotypes, moderate blue represents heterozygous genotypes, and pale blue denotes homozygous wild-type genotypes.

Variations in the DFX metabolism across *UGT1A1* diplotypes

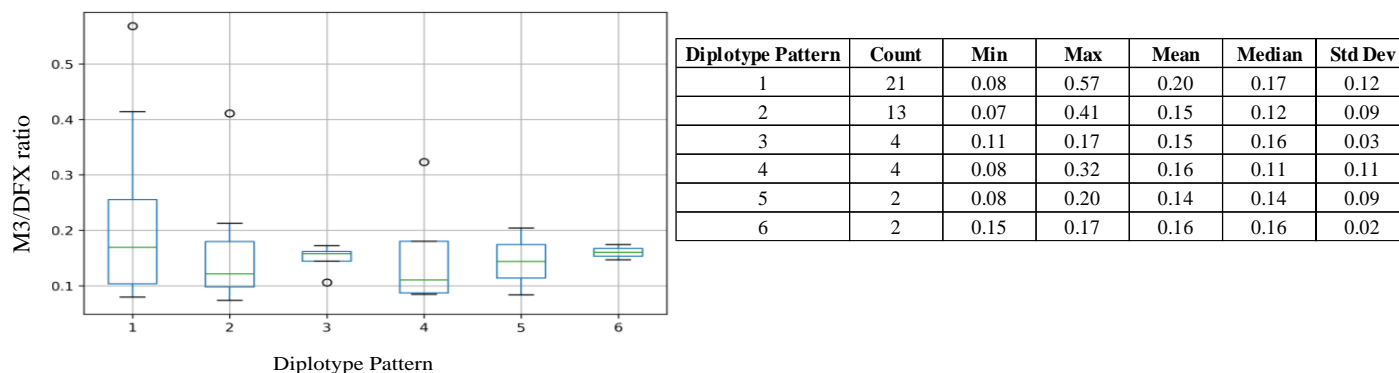


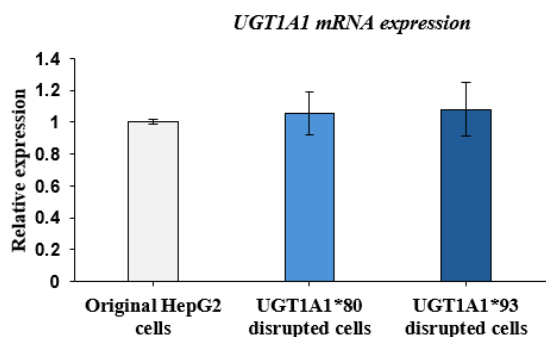
Figure 1. Boxplot analysis of the M3/DFX C trough ratio across diplotype patterns.

A comparison between diplotype patterns 1 vs 2, as well as patterns 3 vs 4, revealed that patients carrying the *UGT1A1**60 variant allele G (T/G and G/G) exhibited a decreasing trend in the M3/DFX ratio compared to homozygous wild-type carriers (T/T). The median M3/DFX ratios for T/G and G/G carriers ranged from 0.11–0.12, whereas T/T carriers showed higher median values of 0.16–0.17. These findings suggest that the *UGT1A1**60 variant is associated with reduced *UGT1A1* metabolic function as well as DFX metabolism. The observed influence of the *UGT1A1**60 variant is consistent with previous studies [3], [5]. However, two patients with pattern 5, having homozygous *UGT1A1**60 variant (G/G), did not show a decreasing trend of M3/DFX ratios compared to those with the heterozygous (T/G) and homozygous wild-type in patterns 1 and 2, respectively. This discrepancy may be attributed to the influence of additional SNPs within the *UGT1A1* or other genes involved with DFX metabolism. For example, the multidrug resistance-associated protein 2 (*MRP2*) gene, having a well-known role in the excretion of DFX and M3 [1], was not considered in this analysis.

Analysis of diplotype patterns 2 vs 3, and 5 vs 6 revealed that patients carrying heterozygous genotypes of *UGT1A1**93 (G/A), *80 (C/T), and *28 (6TA/7TA) exhibited a trend toward higher M3/DFX ratios compared to those with the homozygous wild-type genotypes *UGT1A1**93(G/G), *80(C/C), and *28(6TA/6TA). , as well as the *UGT1A1**93(A/A), *80(T/T), and *28(7TA/7TA) homozygous variants also exhibited a trend toward higher M3/DFX ratios compared to those with the homozygous wild-type genotypes of *UGT1A1**93(G/G), *80(C/C), and *28(6TA/6TA). These results suggest that the combination of *UGT1A1**93, *80, and *28 variants may contribute to increased *UGT1A1* metabolic activity as well as DFX metabolism. Conversely, comparing diplotype patterns 5 vs 4 demonstrated the decreasing trend of the median ratios in heterozygous genotypes of *93, *80, and *28 compared to those with the homozygous wild-type, with consistency to previous studies [2], [3], [4], [6], [7]. This discrepancy may be attributed to the influence of additional SNPs within the *UGT1A1* or other genes. In addition, the number of patients included in this analysis remains limited, particularly some diplotype patterns, therefore, further *in vivo* studies, with larger sample sizes are warranted to obtain more definitive results.

Transcriptional regulation of *UGT1A1**80 and *93

Figure 2. *UGT1A1* mRNA expression levels in the mixed populations of cells disrupted at *UGT1A1**80 and *93.



For the *in vitro* analysis, CRISPR-Cas9 was successfully introduced into HepG2 cells to disrupt promoter regions containing the *UGT1A1**80 and *93 variants, as confirmed by GFP fluorescence in mixed-cell populations. These promoter regions may contain transcription factor (TF) binding sites, and SNP-induced disruptions could alter *UGT1A1* transcription. However, no significant changes in *UGT1A1* mRNA levels were detected between edited and wild-type cells (Figure 2). This may be due to the

mosaic nature of CRISPR editing, where edited and unedited cells coexist, and bulk RNA analysis masks transcriptional changes occurring in subpopulations. The resulting dilution effect emphasizes the importance of using single-cell clones, particularly homozygous knockouts, to isolate and evaluate SNP-specific regulatory effects more precisely [8]. In addition, *UGT1A1**80 and *93 may affect post-transcriptional regulation, such as mRNA stability, rather than transcription, suggesting further studies under stimulated conditions and protein-level analyses.

Several additional factors could explain the lack of observed mRNA changes. Post-transcriptional effects, such as altered mRNA stability, cryptic splicing, or internal ribosome entry sites (IRES)-generated translation [9], could allow protein synthesis without affecting transcript levels. Moreover, protein expression may also differ due to changes in turnover or post-translational modification. These possibilities underscore the need for complementary approaches, including Western blotting to assess protein levels, ChIP assays to confirm disrupted TF binding, and stimulated cell models to uncover SNP effects. Editing efficiency may also be limited by flanking sequence constraints [9] or chromatin accessibility, such as DNA methylation or repressive histone marks, potentially impairing Cas9 access [10]. Single-cell sequencing and further analyses could clarify cellular heterogeneity and compensatory responses.

CONCLUSIONS

This study suggested the function of promoter polymorphisms, *UGT1A1**80 and *93, linked to the well-known *28, on DFX metabolism *in vivo*, with the trend of variations in M3/DFX Ctrough ratios across diplotypes. While CRISPR-Cas9 disruption of these SNPs in HepG2 cells did not alter *UGT1A1* mRNA levels in mixed populations, further investigations using stable single-cell clones are needed to clarify their transcriptional regulatory roles. These findings highlight the clinical relevance of *UGT1A1* polymorphisms in optimizing DFX treatment for thalassemia patients.

ACKNOWLEDGMENTS

This work (Grant No. RGNS 65-021) was supported by Office of the Permanent Secretary, Ministry of Higher Education, Science, Research and Innovation (OPS MHESI), Thailand Science Research and Innovation (TSRI) and Chulalongkorn University. We thank the Government Pharmaceutical Organization (GPO) for providing the M3/DFX Ctrough level measurement using LC/MS/MS. The Bioimaging Center of the University of Konstanz is acknowledged for providing confocal microscopy instrumentation and support.

REFERENCES

1. Waldmeier F, Bruin GJ, Glaenzel U, et al. Pharmacokinetics, metabolism, and disposition of deferasirox in beta-thalassemic patients with transfusion-dependent iron overload who are at pharmacokinetic steady state. *Drug Metab Dispos.* 2010;38(5):808-16.
2. Cusato J, Allegra S, Massano D, et al. Influence of single-nucleotide polymorphisms on deferasirox C trough levels and effectiveness. *Pharmacogenomics J.* 2015;15(3):263-71.
3. Bhatt DK, Mehrotra A, Gaedigk A, et al. Age- and Genotype-Dependent Variability in the Protein Abundance and Activity of Six Major Uridine Diphosphate-Glucuronosyltransferases in Human Liver. *Clin Pharmacol Ther.* 2019;105(1):131-41.
4. Li M, Seiser EL, Baldwin RM, et al. ABC transporter polymorphisms are associated with irinotecan pharmacokinetics and neutropenia. *Pharmacogenomics J.* 2018;18(1):35-42.
5. Wang H, Bian T, Jin T, et al. Association analysis of UGT1A genotype and haplotype with SN-38 glucuronidation in human livers. *Pharmacogenomics.* 2014;15(6):785-98.
6. Iyer L, Das S, Janisch L, et al. UGT1A1*28 polymorphism as a determinant of irinotecan disposition and toxicity. *Pharmacogenomics J.* 2002;2(1):43-7.
7. Mattioli F, Puntoni M, Marini V, et al. Determination of deferasirox plasma concentrations: do gender, physical and genetic differences affect chelation efficacy? *Eur J Haematol.* 2015;94(4):310-7.
8. Joberty G, Fálth-Savitski M, Paulmann M, et al. A Tandem Guide RNA-Based Strategy for Efficient CRISPR Gene Editing of Cell Populations with Low Heterogeneity of Edited Alleles. *Crispr j.* 2020;3(2):123-34.
9. Tuladhar R, Yeu Y, Tyler Piazza J, et al. CRISPR-Cas9-based mutagenesis frequently provokes on-target mRNA misregulation. *Nat Commun.* 2019;10(1):4056.
10. Han Y, Slivano OJ, Christie CK, et al. CRISPR-Cas9 genome editing of a single regulatory element nearly abolishes target gene expression in mice--brief report. *Arterioscler Thromb Vasc Biol.* 2015;35(2):312-5.

Analysis of the Effects of Transforming Growth Factor- β , a Main Component of Platelet-Rich Plasma, on Pain-Related Diseases Using Network Pharmacology

Krittamate Chatdamrongsakool¹, Hasriadi Hasriadi^{2,4}, Rataya Luechapudiporn^{2,3}, and Pasarapa Towiwat^{2,4,}*

¹ Inter-Department of Pharmacology, Graduate School, Chulalongkorn University, 10330, Bangkok, THAILAND

² Department of Pharmacology and Physiology, Faculty of Pharmaceutical Sciences, Chulalongkorn University, 10330, Bangkok, THAILAND

³ Center of Excellence in Natural Products for Ageing and Chronic Diseases, Faculty of Pharmaceutical Sciences, Chulalongkorn University, 10330, Bangkok, THAILAND

⁴ Animal Models of Chronic Inflammation-associated Diseases for Drug Discovery Research Unit, Faculty of Pharmaceutical Sciences, Chulalongkorn University, 10330, Bangkok, THAILAND

*Corresponding author Email: pasarapa.c@chula.ac.th

Abstract. Platelet-rich plasma (PRP) is an autologous blood-derived bioproduct used for pain management due to its high content of growth factors. However, the underlying mechanisms of those growth factors in pain-related diseases remain unclear. In this study, network pharmacology was employed to evaluate the role of transforming growth factor- β (TGF- β), a major growth factor presents in PRP, in pain-related conditions, including neuropathic pain, osteoarthritis, and rheumatoid arthritis. Target genes of TGF- β and disease-associated genes were identified and analyzed. A protein-protein interaction (PPI) network was constructed using the STRING database, and the top 10 genes were identified, revealing a strong association between TGF- β and disease-associated genes, as indicated by high interaction scores in the PPI network. Furthermore, Gene Ontology (GO) and Kyoto Encyclopedia of Genes and Genomes (KEGG) pathway enrichment analyses were performed to determine the biological activities and pathways involved. The results demonstrate that TGF- β in PRP regulates biological pathways related to pain perception and immune response. This study provides valuable insights into the role of TGF- β , a key component of PRP, in pain-related conditions.

Keywords: Platelet-rich plasma; Neuropathic pain; Osteoarthritis; Rheumatoid arthritis; Network pharmacology

INTRODUCTION

Pain is an unpleasant sensation associated with numerous conditions such as tissue damage, infections, cancer, and inflammatory conditions. Pain is also linked with multiple chronic diseases, such as osteoarthritis (OA), diabetic neuropathy, fibromyalgia, and rheumatoid arthritis (RA) (1). The symptoms of pain observed in these diseases are clinically characterized by allodynia, hyperalgesia, and emotional strain (2). Although non-steroidal anti-inflammatory drugs (NSAIDs), cyclooxygenase-2 (COX-2) inhibitors, gabapentinoids, opioids, tricyclic antidepressants (TCAs), serotonin-norepinephrine reuptake inhibitors (SNRIs), local anesthetics, and intra-articular corticosteroids are commonly used to manage neuropathic pain (NP) and chronic inflammatory pain, modest efficacy and unwanted side effects remain a concern (3-5). Therefore, finding alternatives will be beneficial to overcome current conditions, and novel analgesic agents need to be discovered and developed.

Platelet-rich plasma (PRP) is a bioproduct prepared by centrifuging peripheral blood to concentrate platelets (6, 7). PRP has been investigated for its potential benefits in alleviating pain and inflammation in various conditions, including rotator cuff tendinopathy (8, 9), carpal tunnel syndrome (CTS) (10, 11), adhesive capsulitis (12), osteoarthritis (13-16), diabetic neuropathic pain (17), and spinal cord injury (SCI) (18, 19). The beneficial effects of PRP are attributed to its abundance of growth factors found in PRP (20). As such, the high concentration of TGF- β in PRP likely makes it the most influential growth factor, contributing to the therapeutic efficacy of PRP. As shown in the previous study, TGF- β showed a significant correlation with pain score reduction in osteoarthritis patients following PRP injection (21). Although clinically studied, the underlying mechanisms of TGF- β in pain-related conditions remain unclear. In this study, network pharmacology was employed to elucidate the potential targets and pathways involved in TGF- β -mediated pain relief.

MATERIALS AND METHODS

Methods

Identification of TGF- β -target genes and target genes associated with pain-related diseases.

In the present study, the main growth factor present in PRP (22), TGF- β , was used. The structure of TGF- β was obtained from the PUBCHEM database. Subsequently, the SMILES representation of TGF- β was entered into the databases of Swiss Target Prediction (<https://www.swisstargetprediction.ch/>), the Similarity Ensemble Approach (SEA Search Server) (<http://sea.bkslab.org/>), and Super-PRED (<https://prediction.charite.de/>) to identify target genes of TGF- β . All identified target

genes were combined, and duplicate genes were removed. Target genes associated with neuropathic pain, osteoarthritis, and rheumatoid arthritis were acquired from several databases, including OMIM (<https://www.omim.org/>) and GeneCards (<http://www.genecards.org/>). All identified target genes were combined, and duplicate genes were removed.

Construction of protein-protein interaction (PPI) network and Enrichment analyses

The intersection genes between neuropathic pain-associated genes, osteoarthritis-associated genes, rheumatoid arthritis-associated genes, and growth factor-affected genes were determined using the online Venn diagram tool (23). Furthermore, the overlapping genes were analyzed using the STRING databases and visualized with Cytoscape 3.10.1. In addition, the top 10 genes were analyzed and determined using the cytoHubba plugin v.0.1 within Cytoscape.

Enrichment analyses, including Gene Ontology (GO) and Kyoto Encyclopedia of Gene and Genomes (KEGG), were performed using the online tool for bioinformatic data analysis (<http://www.bioinformatics.com.cn/>). The enrichment analyses provide information regarding biological processes, cellular components, molecular functions, and involved pathways.

RESULTS AND DISCUSSION

Network of protein-protein interaction and the top 10 influenced genes

In the present study, the underlying mechanism of TGF- β in pain-related diseases was investigated using network pharmacology. As shown in **Figure 1A**, the total number of target genes for TGF- β was 268. Furthermore, the target genes associated with diseases include 2,262 neuropathic pain-associated genes, 5,459 osteoarthritis-associated genes, and 6,566 rheumatoid arthritis-associated genes. The intersection of TGF- β target genes and disease-associated genes was identified. As shown in the Venn diagram, the intersection of target genes between TGF- β and neuropathic pain, osteoarthritis, and rheumatoid arthritis was 122, 136, and 160, respectively. Furthermore, as illustrated in the network of TGF- β and disease-associated genes, there are strong interactions with the target genes (**Figure 1B**).

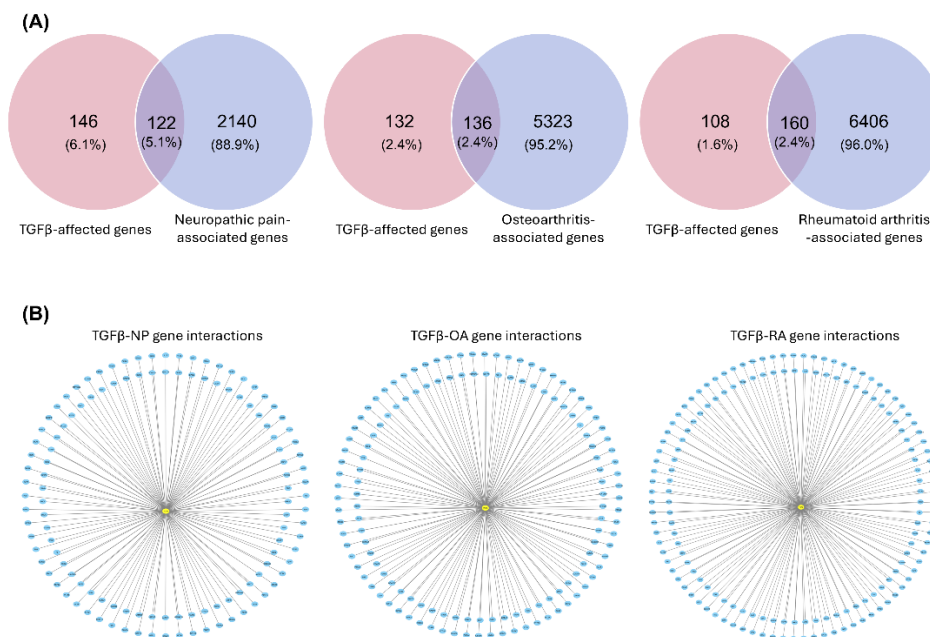


Figure 1. The intersection of genes between TGF- β -affected genes and neuropathic pain, osteoarthritis, and rheumatoid arthritis-associated genes, and TGF- β interactions with neuropathic pain-, osteoarthritis-, and rheumatoid arthritis-associated genes.

Intersection targets between TGF- β and neuropathic pain-, osteoarthritis-, and rheumatoid arthritis-associated genes were used to construct protein-protein interactions. In the network of TGF- β and neuropathic pain, there were 121 nodes and 1041 edges constructed, with 17.2 average node degrees and 0.503 average clustering coefficients (**Figure 2A**). In the network of TGF- β and

osteoarthritis, there were 135 nodes and 1046 edges constructed, with 15.5 average node degrees and 0.535 average clustering coefficients. In the network of TGF- β and rheumatoid arthritis, there were 158 nodes and 1343 edges constructed, with 17 average node degrees and 0.471 average clustering coefficients.

Furthermore, the top 10 gene interactions were determined using CytoHubba's maximal clique centrality (MCC) analysis. As shown in **Figure 2B**, the top 10 genes involved in TGF- β and neuropathic pain were NFKB1, HSP90AA1, STAT3, IKBKB, PTGS2, BCL2L1, SIRT1, IL1B, PARP1, and CASP8. The top 10 genes associated with TGF- β and osteoarthritis were NFKB1, CASP8, HSP90AA1, STAT3, SIRT1, IL1B, PARP1, PTGS2, BCL2L1, and IKBKB. Additionally, the top 10 genes related to TGF- β and rheumatoid arthritis were NFKB1, IL1B, HSP90AA1, PARP1, STAT3, CASP9, BCL2L1, CASP8, PTGS2, and MCL1. These genes represent the most influential genes in each disease, indicating their potential roles in the mechanisms of TGF- β targeting neuropathic pain, osteoarthritis, and rheumatoid arthritis

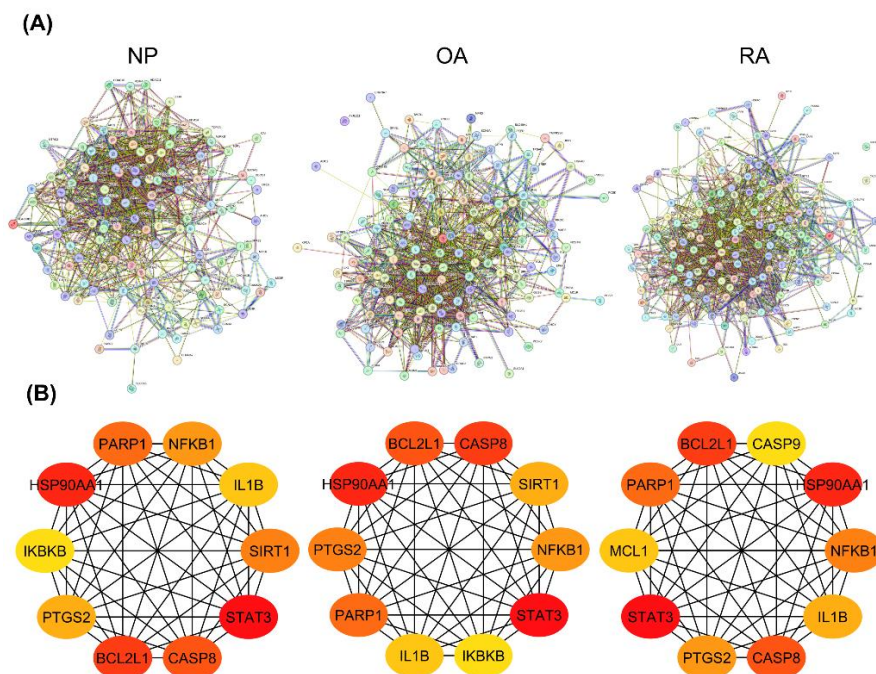


Figure 2. Protein-protein interaction networks of TGF- β in neuropathic pain, osteoarthritis, and rheumatoid arthritis (A). The top 10 most influential genes in TGF- β -related interactions for neuropathic pain, osteoarthritis, and rheumatoid arthritis (B). NP: neuropathic pain; OA: osteoarthritis; RA: rheumatoid arthritis.

GO and KEGG pathway enrichment of PRP on neuropathic pain, osteoarthritis, and rheumatoid arthritis

To determine the mechanistic and organizational role of TGF- β in PRP, enrichment analyses related to neuropathic pain, osteoarthritis, and rheumatoid arthritis were performed. In Figure 3A, the top 10 biological processes, molecular functions, and cellular components are shown. Among the top 10 biological processes, 'sensory perception of pain' was identified, indicating that PRP may play a role in alleviating neuropathic pain. Furthermore, in the biological process associated with TGF- β in osteoarthritis (Figure 3B), the results indicated that TGF- β plays a role in sensory perception of pain and regulation of cytokine production. In the biological process related to TGF- β in rheumatoid arthritis, the results showed that TGF- β is involved in cytokine production and the regulation of the inflammatory response.

Pathway enrichment analyses were performed using KEGG, as shown in Figure 3. The analyses demonstrated that TGF- β in PRP modulates pathways associated with pain. The role of TGF- β in modulating pain pathways is through regulating apoptosis and neuroactive-ligand receptor interactions. The role of TGF- β on apoptosis was observed in simulation studies in neuropathic pain and OA, whereas its role in neuroactive-ligand receptor interactions was observed in OA and RA. These findings are consistent with previous studies showing that TGF- β protects against neuronal cell death and downregulates microglial activation (24). Furthermore, TGF- β has been shown to increase the Bcl-2/Bax ratio, thereby protecting chondrocytes from apoptosis (25). These

results are also consistent with previous studies, which demonstrated the ability of TGF- β to maintain regulatory T cells, suppress inflammation, and regulate apoptosis (26-28). Altogether, the enrichment results suggest that TGF- β in PRP regulates biological processes and pathways associated with pain-related diseases, including neuronal protection and apoptosis regulation.

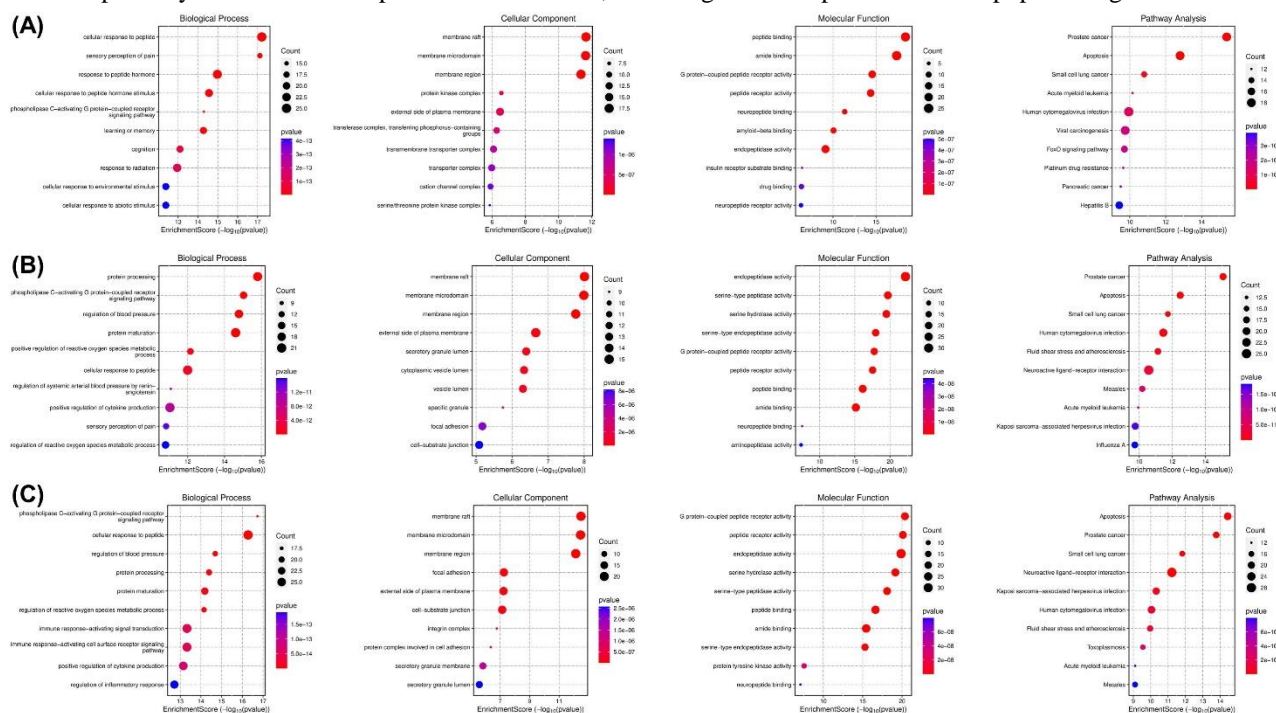


Figure 3. Enrichment analyses including Gene Ontology (biological processes, cellular components, and molecular functions) and KEGG pathways, highlighting the role of TGF- β . The enrichment analyses for GO and KEGG are demonstrated for each disease, including neuropathic pain (A), osteoarthritis (B), and rheumatoid arthritis (C).

CONCLUSIONS

In conclusion, network pharmacology demonstrated that TGF- β , a key growth factor in PRP, targets multiple genes involved in pain-related diseases, including neuropathic pain, osteoarthritis, and rheumatoid arthritis. TGF- β regulates biological processes and pathways associated with pain and apoptosis in pain-related diseases. This study supported the application of PRP in the management of pain. Further studies are required to validate these network pharmacology-based results through wet lab experiments.

ACKNOWLEDGMENTS

The authors gratefully acknowledge Chulalongkorn University for their support and the grants provided

FUNDING

This study was supported by the 90th Anniversary of Chulalongkorn University Scholarship, Chulalongkorn University, Thailand (GCUGR1125671134M), the Ratchadaphiseksomphot Endowment Fund for the Center of Excellence in Natural Products for Ageing and Chronic Diseases, Chulalongkorn University (GCE 3330170003), and the Animal Models of Chronic Inflammation-associated Diseases for Drug Discovery Research Unit, Chulalongkorn University (RU66_014_3300_00).

REFERENCES

1. Baral P, Udit S, Chiu IM. Pain and immunity: implications for host defence. *Nature Reviews Immunology*. 2019;19(7):433-47.
2. Hasriadi, Dasuni Wasana PW, Vajragupta O, Rojsitthisak P, Towiwat P. Mechanistic Insight into the Effects of Curcumin on Neuroinflammation-Driven Chronic Pain. *Pharmaceuticals* [Internet]. 2021; 14(8).
3. Melnikova I. Pain market. *Nature Reviews Drug Discovery*. 2010;9(8):589-90.

4. Martel-Pelletier J, Barr AJ, Cicuttini FM, Conaghan PG, Cooper C, Goldring MB, et al. Osteoarthritis. *Nature Reviews Disease Primers*. 2016;2(1):16072.
5. Jones IA, Togashi R, Wilson ML, Heckmann N, Vangsness CT. Intra-articular treatment options for knee osteoarthritis. *Nature Reviews Rheumatology*. 2019;15(2):77-90.
6. Everts P, Onishi K, Jayaram P, Lana JF, Mautner K. Platelet-Rich Plasma: New Performance Understandings and Therapeutic Considerations in 2020. *Int J Mol Sci*. 2020;21(20).
7. Locatelli L, Colciago A, Castiglioni S, Maier JA. Platelets in Wound Healing: What Happens in Space? *Frontiers in Bioengineering and Biotechnology*. 2021;9.
8. Thepsoparn M, Thanphraisan P, Tanpowpong T, Itthipanichpong T. Comparison of a Platelet-Rich Plasma Injection and a Conventional Steroid Injection for Pain Relief and Functional Improvement of Partial Supraspinatus Tears. *Orthop J Sports Med*. 2021;9(9):23259671211024937.
9. Tanpowpong T, Thepsoparn M, Numkarunarunrote N, Itthipanichpong T, Limskul D, Thanphraisan P. Effects of Platelet-Rich Plasma in Tear Size Reduction in Partial-Thickness Tear of the Supraspinatus Tendon Compared to Corticosteroids Injection. *Sports Med Open*. 2023;9(1):11.
10. Wu YT, Ho TY, Chou YC, Ke MJ, Li TY, Huang GS, et al. Six-month efficacy of platelet-rich plasma for carpal tunnel syndrome: A prospective randomized, single-blind controlled trial. *Sci Rep*. 2017;7(1):94.
11. Senna MK, Shaat RM, Ali AAA. Platelet-rich plasma in treatment of patients with idiopathic carpal tunnel syndrome. *Clin Rheumatol*. 2019;38(12):3643-54.
12. Lee MJ, Yoon KS, Oh S, Shin S, Jo CH. Allogenic Pure Platelet-Rich Plasma Therapy for Adhesive Capsulitis: A Bed-to-Bench Study With Propensity Score Matching Using a Corticosteroid Control Group. *Am J Sports Med*. 2021;49(9):2309-20.
13. Bansal H, Leon J, Pont JL, Wilson DA, Bansal A, Agarwal D, et al. Platelet-rich plasma (PRP) in osteoarthritis (OA) knee: Correct dose critical for long term clinical efficacy. *Scientific Reports*. 2021;11(1):3971.
14. Khatib S, van Buul GM, Kops N, Bastiaansen-Jenniskens YM, Bos PK, Verhaar JA, et al. Intra-articular Injections of Platelet-Rich Plasma Releasate Reduce Pain and Synovial Inflammation in a Mouse Model of Osteoarthritis. *The American Journal of Sports Medicine*. 2018;46(4):977-86.
15. Zhao H, Zhu W, Mao W, Shen C. Platelet-rich plasma inhibits Adriamycin-induced inflammation via blocking the NF- κ B pathway in articular chondrocytes. *Molecular Medicine*. 2021;27(1):66.
16. van Buul GM, Koevoet WL, Kops N, Bos PK, Verhaar JA, Weinans H, et al. Platelet-rich plasma releasate inhibits inflammatory processes in osteoarthritic chondrocytes. *Am J Sports Med*. 2011;39(11):2362-70.
17. Hassanien M, Elawamy A, Kamel EZ, Khalifa WA, Abolfadl GM, Roushdy ASI, et al. Perineural Platelet-Rich Plasma for Diabetic Neuropathic Pain, Could It Make a Difference? *Pain Med*. 2020;21(4):757-65.
18. Salarinia R, Hosseini M, Mohamadi Y, Ghorbani A, Alamdari DH, Mafinezhad A, et al. Combined use of platelet-rich plasma and adipose tissue-derived mesenchymal stem cells shows a synergistic effect in experimental spinal cord injury. *J Chem Neuroanat*. 2020;110:101870.
19. Behroozi Z, Ramezani F, Nasirinezhad F. Human umbilical cord blood-derived platelet -rich plasma: a new window for motor function recovery and axonal regeneration after spinal cord injury. *Physiol Behav*. 2022;252:113840.
20. Andia I, Maffulli N. Platelet-rich plasma for managing pain and inflammation in osteoarthritis. *Nat Rev Rheumatol*. 2013;9(12):721-30.
21. Louis ML, Magalon J, Jouve E, Bornet CE, Mattei JC, Chagnaud C, et al. Growth Factors Levels Determine Efficacy of Platelets Rich Plasma Injection in Knee Osteoarthritis: A Randomized Double Blind Noninferiority Trial Compared With Viscosupplementation. *Arthroscopy*. 2018;34(5):1530-40.e2.
22. Wasai S, Sato M, Maehara M, Toyoda E, Uchiyama R, Takahashi T, et al. Characteristics of autologous protein solution and leucocyte-poor platelet-rich plasma for the treatment of osteoarthritis of the knee. *Scientific Reports*. 2020;10(1):10572.
23. Oliveros J C. Venny. An interactive tool for comparing lists with Venn diagrams. <https://bioinfogp.cnb.csic.es/tools/venny/>. 2007.
24. Brionne TC, Tesseur I, Masliah E, Wyss-Coray T. Loss of TGF-beta 1 leads to increased neuronal cell death and microgliosis in mouse brain. *Neuron*. 2003;40(6):1133-45.
25. Lires-Deán M, Caramés B, Cillero-Pastor B, Galdo F, López-Armada MJ, Blanco FJ. Anti-apoptotic effect of transforming growth factor- β 1 on human articular chondrocytes: role of protein phosphatase 2A. *Osteoarthritis and Cartilage*. 2008;16(11):1370-8.
26. Chen W, Frank ME, Jin W, Wahl SM. TGF-beta released by apoptotic T cells contributes to an immunosuppressive milieu. *Immunity*. 2001;14(6):715-25.
27. Nadkarni S, Mauri C, Ehrenstein MR. Anti-TNF-alpha therapy induces a distinct regulatory T cell population in patients with rheumatoid arthritis via TGF-beta. *J Exp Med*. 2007;204(1):33-9.
28. Rubtsov YP, Rudensky AY. TGF β signalling in control of T-cell-mediated self-reactivity. *Nature Reviews Immunology*. 2007;7(6):443-53.

**Cutting-Edge Technologies in Drug discovery,
Natural Products, Cosmetics, and Nutraceuticals**

Isolation and Characterization of Chemical Constituents from *Pinalia densa* and Evaluation of Their Cytotoxic Activity Against Human Prostate Cancer Cell Lines

Suthathip Ploithoom^{1,2}, *Narumol Bhummaphan*³, *Boonchoo Sritularak*^{2,4,*}

¹Pharmaceutical Sciences and Technology Program, Faculty of Pharmaceutical Sciences, Chulalongkorn University, Bangkok 10330, Thailand

²Department of Pharmacognosy and Pharmaceutical Botany, Faculty of Pharmaceutical Sciences, Chulalongkorn University, Bangkok 10330, Thailand

³College of Public Health Sciences, Chulalongkorn University, Bangkok 10330, Thailand

⁴Center of Excellence in Natural Products for Ageing and Chronic Diseases, Faculty of Pharmaceutical Sciences, Chulalongkorn University, Bangkok 10330, Thailand

*Corresponding author Email: boonchoo.sr@chula.ac.th

Abstract. Phytochemical investigation of the whole plant of *Pinalia densa* resulted in the isolation of five compounds identified as 2,7-dihydroxy-3,4,6-trimethoxy-9,10-dihydrophenanthrene (**1**), 2,7-dihydroxy-3,4,6-trimethoxyphenanthrene (**2**), nudol (**3**), liparisphenanthrene B (**4**) and 9,9'-*O*-di-(*E*)-feruloyl-(*-*)-secoisolariciresinol (**5**). All compounds were evaluated for the cytotoxic activity against human prostate cancer cell lines (PC-3 and DU145) together with the human normal keratinocyte HaCaT cell line by using MTT assay. 9,9'-*O*-di-(*E*)-feruloyl-(*-*)-secoisolariciresinol (**5**) showed cytotoxic activity against human prostate cancer cell lines (PC-3 and DU145) as well as HaCaT cell line in a concentration-dependent manner, while liparisphenanthrene B (**4**) exhibited a significant cytotoxic effect on PC-3 cell line with an IC₅₀ value of 30.97 ± 9.0 µM with less cytotoxic effect on HaCaT cell line.

Keywords: *Pinalia densa*; Orchidaceae; cytotoxicity; PC-3; DU145

INTRODUCTION

Cancer is one of the serious diseases characterized by uncontrolled cell growth and spread to other parts of the body.^[1] Prostate cancer is the second most diagnosed cancer and the fifth most prevalent cause of cancer-related deaths in males worldwide. Around 1.4 million new cases were reported in 2022, and more than 396,000 people died as a result.^[2, 3] Some of example current treatments for prostate cancer are chemotherapy, radiation and surgery. However, most of them either have side effects or are ineffective. Natural products are particularly essential against cancer.^[4, 5] There have been reports of several orchid species having the ability to treat various types of cancer.^[6] Orchids have been used in traditional medicine in various cultures including traditional Chinese, Ayurvedic, and Native American medicine for centuries as they possess a significant number of health benefits. It is well known that orchids are widely used to treat serious ailments, for example cough, asthma, digestive issues, stomachache, fever, headache and high blood pressure.^[7, 8] *Pinalia densa* is an orchid species that belongs to the family Orchidaceae, native to Southeast Asia, including Malaysia, Indonesia, and Thailand. Numerous orchids play a major role in traditional medical systems due to their high content of alkaloids, flavonoids, glycosides, carbohydrates, and other chemical components.^[9] However, no research has been conducted on the chemical constituents of *Pinalia densa*. The objectives of this study are to isolate and identify the constituents of *Pinalia densa* extract as well as evaluate cytotoxic activity against prostate cancer.

MATERIALS AND METHODS

Materials

The Bruker MicroTOF mass spectrometer (ESI-MS) (Billerica, MA, USA) was used to measure the mass spectra. 1D and 2D NMR spectra were recorded on Bruker Avance Neo 400 MHz NMR spectrometer (Billerica, MA, USA). Column chromatography (CC) was carried out on silica gel 60 size 0.063-0.200 mm (No. 1.07734.2500) and size 0.040-0.063 mm (No. 1.09385.2500) (Merck, NJ, USA). Sephadex LH-20 (Merck, NJ, USA) was also utilized for isolation. Thin-layer chromatography (TLC) was performed on silica gel 60 F₂₅₄ (Merck, NJ, USA). Solvents including methanol, acetone, ethyl acetate, dichloromethane and hexane used in this study were of commercial grade and redistilled before use.

Extraction and isolation

The dried whole plant of *Pinalia densa* (2.2 kg) was macerated with methanol (MeOH) (3 x 10 L) at room temperature for 3-5 days to yield a methanolic extract (112.5 g). Then the methanolic extract was separated by vacuum liquid chromatography (silica gel, gradient dichloromethane-ethyl acetate, 99:1 to 0:100) to give 7 fractions (A-G). Fraction C (7.6 g) was subjected to CC (silica gel, gradient hexane-acetone, 9:1 to 0:10) to produce fractions C1-C11. Fraction C7 (110 mg) was subjected to CC (dichloromethane-hexane, 1:9), and 2,7-dihydroxy-3,4,6-trimethoxy-9,10-dihydrophenanthrene (**1**) (20.1

mg) was obtained. Fraction C9 (360 mg) was further purified by CC (silica gel, dichloromethane) to yield 2,7-dihydroxy-3,4,6-trimethoxyphenanthrene (**2**) (6.0mg) and other 5 fractions (C9A to C9E). Fraction C9B (134 mg) was then separated on silica gel (hexane-dichloromethane, 1:1), and then by preparative thin-layer chromatography (hexane-dichloromethane, 3:7) to furnish nudol (**3**) (15.3 mg). Fraction E (5.98 g) was separated again with a silica gel column (gradient ethyl acetate-dichloromethane, 9:1 to 0:10) to yield 8 fractions (E1-E8). Liparisphenanthrene B (**4**) (5.0 mg) was purified from fraction E4 (1.0 g) by Sephadex LH-20 (MeOH) and CC (silica gel, hexane-ethyl acetate, 6:4). Fraction E6 (1.0 g) was separated on Sephadex LH-20 (acetone; MeOH, respectively) to give 9,9'-*O*-di-(*E*)-feruloyl-(-)-secoisolariciresinol (**5**) (3.9 mg).

Cell culture

The human prostate cancer cell lines PC-3 and DU145 as well as the human normal keratinocyte HaCaT cell line were used in this study. PC-3 cells were cultured in Ham's F-12 medium, DU145 cells in Eagle's Minimum Essential Medium (EMEM), and HaCaT cells in Dulbecco's Modified Eagle Medium (DMEM). All media were supplemented with 10% fetal bovine serum (Merck, DA, Germany), 100 units/mL of penicillin/streptomycin (Gibco, Grand Island, NY, USA) and 2 mM L-glutamine (Gibco, Grand Island, NY, USA). Cells were maintained at 37°C in a humidified atmosphere with 5% CO₂.

Methods

Cell viability assay

Cell viability was evaluated by using the MTT assay. PC-3, DU145 and HaCaT cells (5x10³ cells) were seeded into each well of a 96-well plate, and cell attachment was facilitated by an overnight incubation. After that, the cells were treated with varying concentrations of the methanol extract of *Pinalia densa* (0-125 µg/mL) and isolated compounds (0-200 µM). The cell viability assay was performed after 48 hours. After treatment, the cells were exposed to 100 µL of the MTT solution for 4 hours at 37 °C. Next, dimethyl sulfoxide (DMSO) (100 µL) was added to each well to dissolve the formazan crystals. The absorbance of the resulting MTT product was assessed at 570 nm using a microplate reader. The percentage of viable cells were determined to be relative to the control cells. Additionally, the half-maximal inhibitory concentration (IC₅₀) values for cytotoxicity against prostate cancer cells of the active compounds were evaluated.

Statistical analysis

All data were analyzed using Graph Pad Prism, and the results will be displayed as the mean ± standard deviation (SD). One-way ANOVA and Tukey's post hoc test will be used for statistical analysis with $p < 0.05$ as the significant level.

RESULTS AND DISCUSSION

Results

Isolation of the methanolic extract of *Pinalia densa* yielded five known compounds that were characterized by NMR and HR-ESI-MS. They were identified as 2,7-dihydroxy-3,4,6-trimethoxy-9,10-dihydrophenanthrene (**1**)^[10], 2,7-dihydroxy-3,4,6-trimethoxyphenanthrene (**2**)^[11], nudol (**3**)^[12], liparisphenanthrene B (**4**)^[13] and 9,9'-*O*-di-(*E*)-feruloyl-(-)-secoisolariciresinol (**5**)^[14]. The structures of isolated compounds are shown in **Figure 1**.

2,7-dihydroxy-3,4,6-trimethoxy-9,10-dihydrophenanthrene (**1**); Brown amorphous powder. HR-ESI-MS m/z 303.1239 [M+H]⁺ (calcd 303.1154 for C₁₇H₁₉O₅). ¹H NMR (acetone-*d*₆, 400 MHz): 6.59 (1H, s, H-1), 7.94 (1H, s, H-5), 6.72 (1H, s, H-8), 2.62 (4H, s, H-9, H-10), 3.77 (3H, s, 4-OMe), 3.87 (6H, s, 3-OMe, 6-OMe); ¹³C NMR (acetone-*d*₆, 100 MHz): 111.1 (C-1), 148.9 (C-2), 139.9 (C-3), 151.1 (C-4), 119.7 (C-4a), 124.2 (C-4b), 111.1 (C-5), 145.7 (C-6), 144.9 (C-7), 114.4 (C-8), 130.9 (C-8a), 28.9 (C-9), 30.1 (C-10), 134.4 (C-10a), 60.2 (3-OMe), 59.5 (4-OMe), 55.6 (6-OMe).

2,7-dihydroxy-3,4,6-trimethoxyphenanthrene (**2**); Brown amorphous powder. HR-ESI-MS m/z 301.1081 [M+H]⁺ (calcd 301.0998 for C₁₇H₁₇O₅). ¹H NMR (acetone-*d*₆, 400 MHz): 7.15 (1H, s, H-1), 9.05 (1H, s, H-5), 7.27 (1H, s, H-8), 7.51 (1H, d, $J = 8.8$, H-9), 7.45 (1H, d, $J = 8.8$, H-10), 8.31 (1H, s, 2-OH), 7.95 (1H, s, 7-OH), 4.02 (3H, s, 3-OMe), 4.04 (3H, s, 4-OMe), 4.06 (3H, s, 6-OMe); ¹³C NMR (acetone-*d*₆, 100 MHz): 108.7 (C-1), 149.0 (C-2), 141.6 (C-3), 151.1 (C-4), 117.7 (C-4a), 123.8 (C-4b), 107.3 (C-5), 147.8 (C-6), 145.6 (C-7), 111.7 (C-8), 127.5 (C-8a), 125.8 (C-9), 124.4 (C-10), 129.7 (C-10a), 60.4 (3-OMe), 59.5 (4-OMe), 55.2 (6-OMe).

Nudol (**3**); Brown yellow crystal. HR-ESI-MS m/z 271.0969 [M+H]⁺ (calcd 271.0892 for C₁₆H₁₅O₄). ¹H NMR (acetone-*d*₆, 400 MHz): 7.16 (1H, s, H-1), 9.34 (1H, d, $J = 9.2$, H-5), 7.20 (1H, dd, $J = 9.2, 2.8$, H-6), 7.25 (1H, d, $J = 2.8$, H-8), 7.51 (1H, d, $J = 8.8$, H-9), 7.54 (1H, d, $J = 8.8$, H-10), 3.98 (3H, s, 3-OMe), 4.01 (3H, s, 4-OMe); ¹³C NMR (acetone-*d*₆, 100 MHz): 108.9 (C-1), 149.0 (C-2), 141.9 (C-3), 151.3 (C-4), 118.3 (C-4a), 123.4 (C-4b), 128.0 (C-5), 116.7 (C-6), 154.9 (C-7), 111.6 (C-8), 133.7 (C-8a), 126.2 (C-9), 126.8 (C-10), 129.4 (C-10a), 60.4 (3-OMe), 59.2 (4-OMe).

Liparisphenanthrene B (**4**); Brown amorphous powder. HR-ESI-MS m/z 539.1752 [M+H]⁺ (calcd for 539.1628 C₃₂H₂₇O₈). ¹H NMR (acetone-*d*₆, 400 MHz): 7.40 (1H, d, $J = 9.2$, H-3'), 9.56 (1H, d, $J = 9.2$, H-4'), 9.49 (1H, d,

$J = 9.2$, H-5), 7.25 (1H, dd, $J = 9.2$, 2.8, H-6), 7.21 (1H, d, $J = 2.8$, H-8), 7.11 (1H, s, H-8'), 7.34 (1H, d, $J = 9.6$, H-9), 7.36 (1H, d, $J = 9.2$, H-9'), 7.03 (1H, d, $J = 6.4$, H-10), 7.00 (1H, d, $J = 6.4$, H-10'), 4.12 (3H, s, 3-OMe), 4.11 (3H, s, 4-OMe), 4.08 (3H, s, 5'-OMe), 4.05 (3H, s, 6'-OMe); ^{13}C NMR (acetone- d_6 , 100 MHz): 114.2 (C-1), 117.4 (C-1'), 148.0 (C-2), 153.1 (C-2'), 141.9 (C-3), 116.8 (C-3'), 151.0 (C-4), 127.8 (C-4'), 118.8 (C-4a), 124.0 (C-4a'), 123.8 (C-4b), 118.5 (C-4b'), 128.3 (C-5), 151.5 (C-5'), 116.9 (C-6), 142.1 (C-6'), 155.0 (C-7), 149.1 (C-7'), 111.3 (C-8), 108.6 (C-8'), 133.6 (C-8a), 129.2 (C-8a'), 126.1 (C-9), 126.7 (C-9'), 124.6 (C-10), 124.1 (C-10'), 129.1 (C-10a), 132.9 (C-10a'), 60.5 (3-OMe), 59.3 (4-OMe), 59.3 (5'-OMe), 60.4 (6'-OMe).

9,9'-*O*-di-(*E*)-feruloyl(-)-secoisolariciresinol (**5**); Yellow amorphous powder. HR-ESI-MS m/z 715.2793 $[\text{M}+\text{H}]^+$ (calcd 715.2833 for $\text{C}_{40}\text{H}_{43}\text{O}_{12}$). ^1H NMR (acetone- d_6 , 400 MHz): 6.78 (2H, d, $J = 2.0$, H-2, H-2'), 7.34 (2H, d, $J = 1.6$, H-2'', H-2'''), 6.75 (2H, d, $J = 8.0$, H-5, H-5'), 6.87 (2H, d, $J = 8.0$, H-5'', H-5'''), 6.66 (2H, dd, $J = 8.0$, 2.0, H-6, H-6'), 7.16 (2H, dd, $J = 8.0$, 1.6, H-6'', H-6'''), 2.71, 2.83 (each 2H, dd, $J = 14.0$, 8.0, H-7, H-7'), 7.63 (2H, d, $J = 16.0$, H-7'', H-7'''), 2.32 (2H, m, H-8, H-8'), 6.46 (2H, d, $J = 16.0$, H-8'', H-8'''), 4.19, 4.41 (each 2H, dd, $J = 11.6$, 6.4, H-9, H-9'), 7.35 (2H, s, 4-OH, 4'-OH), 8.17 (2H, s, 4''-OH, 4'''-OH), 3.77 (6H, s, 3-OMe, 3'-OMe), 3.92 (6H, s, 3''-OMe, 3'''-OMe); ^{13}C NMR (acetone- d_6 , 100 MHz): 131.6 (C-1, C-1'), 126.5 (C-1'', C-1'''), 112.3 (C-2, C-2'), 110.5 (C-2'', C-2'''), 147.4 (C-3, C-3'), 149.2 (C-3'', C-3'''), 144.9 (C-4, C-4'), 147.9 (C-4'', C-4'''), 114.7 (C-5, C-5'), 115.2 (C-5'', C-5'''), 121.5 (C-6, C-6'), 123.1 (C-6'', C-6'''), 34.5 (C-7, C-7'), 144.9 (C-7'', C-7'''), 40.4 (C-8, C-8'), 115.0 (C-8'', C-8'''), 63.9 (C-9, C-9'), 166.7 (C-9'', C-9'''), 55.5 (3-OMe, 3'-OMe), 55.2 (3''-OMe, 3'''-OMe).

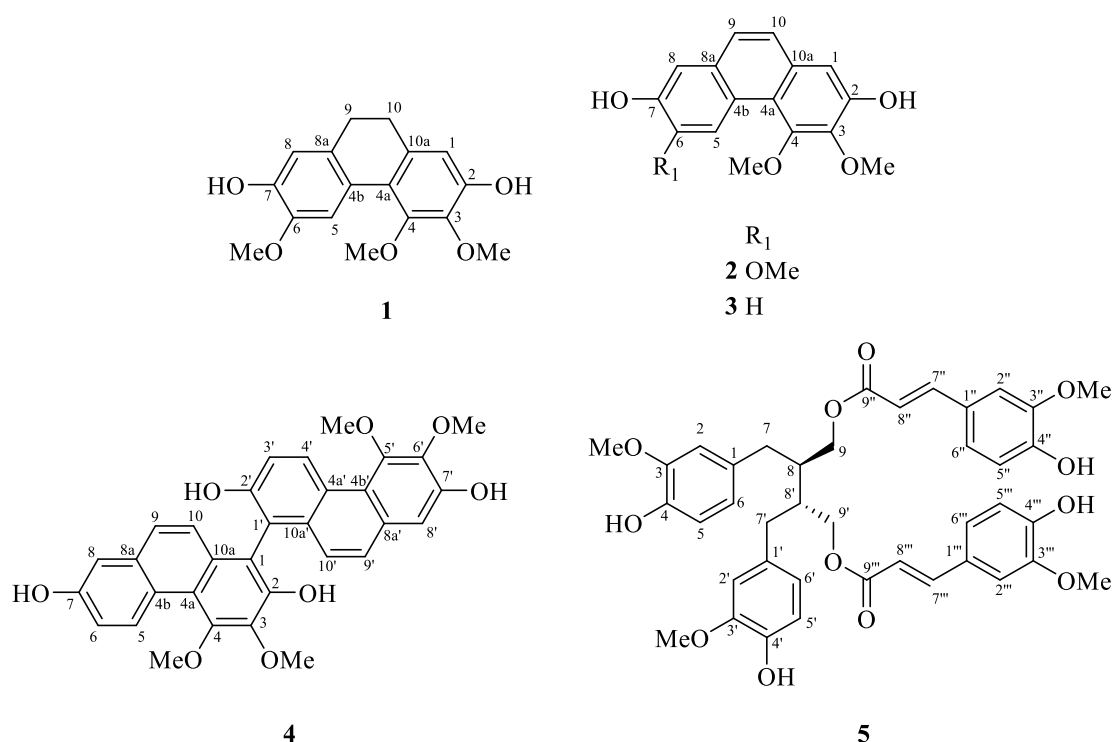


Figure 1. Chemical structures of compounds 1–5 isolated from *Pinalia densa*

The methanolic extract of *Pinalia densa* was screened for cytotoxic activity against melanoma cell (A375), colorectal adenocarcinoma cell (HCT 116), gastric carcinoma cell (NCI-N87), prostate cancer cell (PC-3), breast cancer cell (MDA-MB-468), ovarian cancer cell (SK-OV-3), and human normal keratinocyte (HaCaT). At a concentration of 15.62 $\mu\text{g/mL}$, it exhibited significant cytotoxic effects on prostate cancer cell (PC-3). Therefore, two prostate cancer cell lines (PC-3 and DU145) were used to further assess the cytotoxic effects of the isolated compounds from *Pinalia densa*. According to **Table 1**, liparisphenanthrene B (**4**) exhibited a significant cytotoxic effect on PC-3 cell ($\text{IC}_{50} = 30.97 \pm 9.0 \mu\text{M}$) and less cytotoxic effect on human normal keratinocyte HaCaT cell ($\text{IC}_{50} = 88.56 \pm 3.0 \mu\text{M}$). Additionally, liparisphenanthrene B (**4**) has been reported to have a cytotoxic profile on human stomach (HGC-27) and colon (HT-29) cancer cell lines ($\text{IC}_{50} = 15.23 \pm 0.035 \mu\text{M}$ and $27.44 \pm 0.029 \mu\text{M}$).^[13] Furthermore, 9,9'-*O*-di-(*E*)-feruloyl(-)-secoisolariciresinol (**5**) shown cytotoxic activity against PC-3 and DU145 prostate cancer cell lines which was dependent on concentration. According to a prior study, 9,9'-*O*-di-(*E*)-feruloyl(-)-secoisolariciresinol (**5**) exhibited significant cytotoxic effects on human cancer cell lines including human leukemia (HL-60), liver (SMMC-7721), lung (A-549), breast (MCF-7), and colon (SW-480) cancer cell lines ($\text{IC}_{50} = 3.58$, 4.55, 6.39, 5.09, and 4.80 μM , respectively).^[15] However, 9,9'-*O*-di-(*E*)-feruloyl(-) secoisolariciresinol (**5**)

showed cytotoxic effects on normal keratinocyte HaCaT cell in our study at concentrations comparable to those effective on prostate cancer cells. Therefore, liparisphenanthrene B (**4**) could be a candidate therapeutic agent against prostate cancer.

Table 1. Cytotoxic activity of isolated compounds on PC-3, DU145 and HaCaT cell lines.

Compounds	Cytotoxicity IC ₅₀ ± SD (μM)		
	PC-3	DU145	HaCaT
1	>100	>100	>100
2	>100	>100	>100
3	>100	>100	>100
4	30.97 ± 9.0	>100	88.56 ± 3.0
5	62.35 ± 4.0	123.1 ± 4.0	49.13 ± 3.0

CONCLUSION

Five known compounds, 2,7-dihydroxy-3,4,6-trimethoxy-9,10-dihydrophenanthrene (**1**), 2,7-dihydroxy-3,4,6-trimethoxyphenanthrene (**2**), nudol (**3**), liparisphenanthrene B (**4**) and 9,9'-*O*-di-(*E*)-feruloyl(-)-secoisolariciresinol (**5**), were obtained from *Pinalia densa* in this research. Their structures were determined after a thorough spectroscopic evaluation. Liparisphenanthrene B (**4**) demonstrated a notable cytotoxic effect against PC-3 cell with an IC₅₀ value of 30.97 ± 9.0 μM, but less cytotoxic effect on human normal HaCaT cells. Moreover, 9,9'-*O*-di-(*E*)-feruloyl(-)-secoisolariciresinol (**5**) had a concentration-dependent cytotoxic effect against PC-3, DU145, and HaCaT cells.

ACKNOWLEDGEMENTS

S.P. thanks to the Pharmaceutical Sciences and Technology Program, Faculty of Pharmaceutical Sciences, Chulalongkorn University, and the Development and Promotion of Science and Technology Talents (DPST) for a master's degree scholarship. This research is funded by Thailand Science Research and Innovation Fund Chulalongkorn University (HEA_FF_68_006_3300_002). We are grateful to the Pharmaceutical Science Research Instrument Center (Faculty of Pharmaceutical Sciences, Chulalongkorn University) for providing us with research facilities.

REFERENCES

1. Dash SL, Mohapatra R, Mishra SK. Anticancer activity study of some selected Indian medicinal plants used traditionally. *Journal of Pharmaceutical Negative Results*. 2023;1123-32.
2. Schafer EJ, Laversanne M, Sung H, Soerjomataram I, Briganti A, Dahut W, et al. Recent Patterns and Trends in Global Prostate Cancer Incidence and Mortality: An Update. *European Urology*. 2025;87(3):302-13.
3. Bray F, Laversanne M, Sung H, Ferlay J, Siegel RL, Soerjomataram I, et al. Global cancer statistics 2022: GLOBOCAN estimates of incidence and mortality worldwide for 36 cancers in 185 countries. *CA: A Cancer Journal for Clinicians*. 2024;74(3):229-63.
4. Bonam SR, Wu YS, Tunki L, Chellian R, Halmuthur MSK, Muller S, et al. What has come out from phytomedicines and herbal edibles for the treatment of cancer. *ChemMedChem*. 2018;13(18):1854-72.
5. Mishra SK, Dash SL, Mohapatra R. *In vitro* anticancer activity of various plant extracts. *International Journal of Pharmaceutical Quality Assurance*. 2023;14(01):61-5.
6. Shukla MK, Monika, Thakur A, Verma R, Lahlhenmawia H, Bhattacharyya S, et al. Unravelling the therapeutic potential of orchid plant against cancer. *South African Journal of Botany*. 2022;150:69-79.
7. Gantait S, Das A, Mitra M, Chen J-T. Secondary metabolites in orchids: biosynthesis, medicinal uses, and biotechnology. *South African Journal of Botany*. 2021;139:338-51.
8. Li K, Wu F, Chen M, Xiao Z, Xu Y, Xu M, et al. Identification, biological function profiling and biosynthesis of secondary metabolites in medicinal orchids. *Metabolites*. 2023;13(7):829.
9. Teoh ES. *Pinalia* Lindl. In: Teoh ES, editor. *Orchid Species from Himalaya and Southeast Asia Vol 2 (G - P)*. Cham: Springer International Publishing; 2021. p. 311-21.
10. Lu D, Liu J, Li P. Dihydrophenanthrenes from the stems and leaves of *Dioscorea nipponica* Makino. *Natural Product Research*. 2010;24(13):1253-7.
11. Majumder PL, Pal S. Rotundatin, a new 9,10-dihydrophenanthrene derivative from *Dendrobium rotundatum*. *Phytochemistry*. 1992;31(9):3225-8.
12. Bhandari SR, Kapadi AH, Majumder PL, Joardar M, Shoolery JN. Nudol, a phenanthrene of the orchids *Eulophia nuda*, *Eria carinata* and *Eria stricta*. *Phytochemistry*. 1985;24(4):801-4.
13. Liu L, Yin Q-M, Zhang X-W, Wang W, Dong X-Y, Yan X, et al. Bioactivity-guided isolation of biphenanthrenes from *Liparis nervosa*. *Fitoterapia*. 2016;115:15-8.
14. Fuchino H, Satoh T, Tanaka N. Chemical Evaluation of *Betula* Species in Japan. I. Constituents of *Betula ermanii*. *Chemical and Pharmaceutical Bulletin*. 1995;43(11):1937-42.
15. Xiong R, Jiang J, Chen Y. Cytotoxic lignans from *Cryptocarya impressinervia*. *Nat Prod Res*. 2021;35(6):1019-23.

Green Extraction of Bioactives from Thai Traditional Plant *Clinacanthus nutans* (Burm.f.) Lindau

Penuel Panuel¹, Surat Punyahathaikul², Kunjimas Ketsuwan², Jukrapun Komaikul², Promsin Masrinoul², Tharita Kitisripanya^{1,*}

¹Department of Pharmacognosy, Faculty of Pharmacy, Mahidol University, Bangkok, Thailand

²Center for Vaccine Development, Institute of Molecular Biosciences, Mahidol University, Nakhon Pathom, Thailand

*Corresponding author Email: tharita.kit@mahidol.edu

Abstract. *Clinacanthus nutans* (CN) is an endemic Acanthaceae species in Thailand with significant ethnopharmacological relevance, traditionally used as an anti-inflammatory and antiviral agent for conditions like herpes simplex. Current extraction methods often rely on organic solvents, presenting sustainability and safety challenges, including flammability and energy-intensive removal steps. This research compared a green extraction approach using a natural deep eutectic solvent (NADES) composed of proline and glycerol with conventional 95% ethanol extraction via ultrasonic-assisted extraction. We then determined the total phenolics, total flavonoids, and total chlorophyll contents for quality control and comparison of the green extract. CN-NADES extract had TPC (13.00 ± 0.21 mg/g GAE) and TFC (6.81 ± 0.22 mg/g QAE), which were significantly higher than those of CN-ethanol extract (3.17 ± 0.48 mg/g GAE, 5.01 ± 0.71 mg/g QAE) (p -value < 0.05). Both extracts inhibited HSV-1 plaque formation dose-dependently at non-cytotoxic concentrations. The CN-ethanol extract exhibited higher specific potency ($IC_{50} = 7.98 \pm 0.83$ μ g/mL, equivalent to 0.1 mg CN powder/mL) compared to the CN-NADES extract ($IC_{50} = 1.66 \pm 0.20$ % (v/v), equivalent to 1.7 mg CN powder/mL). This study highlights a critical compromise, while CN-ethanol extract yields higher specific anti-HSV-1 potency, potentially linked to chlorophyll derivatives, the CN-NADES extract offers a greener alternative, yielding phenolic/flavonoid-rich extracts with lower chlorophyll content, suggesting advantages in safety, stability, and formulation suitability. The choice of extraction method should therefore be guided by the intended application, balancing the need for maximal specific potency with the principles of green chemistry and consideration of practical usability.

Keywords: *Clinacanthus nutans*; deep eutectic solvent; antiviral; traditional medicine; green extraction

INTRODUCTION

Clinacanthus nutans (Burm.f.) Lindau, commonly known as 'Phaya Yo', is a medicinal plant widely used in Southeast Asia for various ailments, including skin rashes, insect bites, and viral infections [1, 2]. Notably, it holds a place in traditional medicine specifically for treating Herpes Simplex Virus (HSV) infections [3, 4]. The Thai Herbal Pharmacopoeia typically recommends extraction using 95% ethanol to obtain the bioactive constituents responsible for this anti-herpes activity [5]. While effective, conventional organic solvents like ethanol pose environmental and safety concerns due to their volatility, flammability, and potential toxicity [6].

The search for greener, safer, and more sustainable extraction methods has led to growing interest in Natural Deep Eutectic Solvents (NADES) [7]. NADES are mixtures of natural compounds (like amino acids, sugars, organic acids) that form a eutectic liquid with unique solvent properties, often exhibiting low volatility, non-flammability, biodegradability, and high solubilizing power for various plant metabolites [8, 9]. Proline and glycerol are natural, readily available, and generally recognized as safe (GRAS) compounds that can form effective NADES systems [10]. Previous studies have indicated the potential of NADES for extracting phenolic and flavonoid compounds, which are often implicated in the antiviral activity of medicinal plants [11]. Gallic acid, a simple phenolic acid, has itself been reported to inhibit HSV-1 entry [12].

Despite the traditional use and established pharmacopoeial standard of *C. nutans*, limited research has been conducted to compare eco-friendly NADES extraction with the conventional ethanol method for this plant, particularly in relation to its anti-HSV-1 potential. This study aims to address this knowledge gap by preparing and comparing a proline-glycerol-based NADES extract of *C. nutans* (CN-NADES extract) with the standard 95% ethanol extract of *C. nutans* (CN-ethanol extract). Here, we quantified and compared the extraction efficiency in terms of total phenolic content (TPC), total flavonoid content (TFC), and total chlorophyll content (TC), evaluated and compared the *in vitro* anti-HSV-1 activity of both extracts using a plaque reduction assay on Vero cells and finally assessed the potential of proline-glycerol-based NADES as a viable green alternative to ethanol for obtaining anti-HSV-1 active extracts from *C. nutans*. This research will contribute to the development of alcohol-free, ready-to-use extracts that are non-toxic, biodegradable, green, and a sustainable source of cost-effective antiviral agents.

MATERIALS AND METHODS

Materials

L-Proline ($\geq 99\%$), and glycerol ($\geq 99.5\%$) were purchased from TCI AMERICA (Portland, OR, USA). Ethanol (absolute, analytical grade) was obtained from RCI Labscan (Bangkok, Thailand). Ultra-pure water was obtained using a Milli-Q water purification system (Millipore, Bedford, MA, USA). Gallic acid, quercetin standard ($\geq 98\%$ purity), and dimethyl sulfoxide (DMSO) were purchased from Sigma-Aldrich (St. Louis, MO, USA). Minimum Essential Medium (MEM), fetal bovine serum (FBS), penicillin-streptomycin, Carboxymethyl cellulose (CMC), and trypsin-EDTA were purchased from Gibco (Thermo Fisher Scientific, Waltham, MA, USA). The Human herpesvirus 1 strain KOS (HSV-1, ATCC, VR1493) and Vero cells (African green monkey kidney epithelial cells, ATCC CCL-81) were obtained from the Center for Vaccine Development, Mahidol University. All other chemicals were standard analytical reagent-grade commercial products.

Methods

Plant Material

Clinacanthus nutans leaves were collected in Phu Khiao District, Chaiyaphum Province, Thailand. The material was identified, and a voucher specimen (PMB-006443) was deposited at Sireeruckhachati Nature Learning Park, Mahidol University. Leaves were washed, oven-dried (50°C , 2 days), ground into a fine powder (electric grinder HC-2500Y), and sieved (18-mesh) for uniformity. The powder was stored in ziplock bags at 4°C , protected from light, until use.

Preparation of Solvents

The proline-glycerol-based NADES was prepared by mixing L-proline and glycerol at a molar ratio of 1:2.5. Deionized water was added to achieve a final water content of 30% (v/v). The mixture was heated at 50°C with constant stirring until a clear, homogeneous liquid was formed [13]. The 95% ethanol solution was prepared by diluting the absolute ethanol with deionized water.

Extraction Procedure

One gram (1.0 g) of dried *C. nutans* powder was accurately weighed and added to 10 mL of either 95% ethanol or NADES solvent in a 15 mL centrifuge tube. Extraction was performed using ultrasonication for 60 min, heating at $50\text{--}60^{\circ}\text{C}$. After extraction, the mixtures were filtered through cotton. The entire CN-ethanol extract was evaporated to dryness using a hot air oven at 40°C . The CN-NADES extract was stored at 4°C until use.

Phytochemical Content Determination

Total phenolic content (TPC) was determined using a modified Folin-Ciocalteu method [14], with quantification based on a gallic acid calibration curve ($0\text{--}250\text{ }\mu\text{g/mL}$), and results expressed as mg GAE/g DW. Total flavonoid content (TFC) was determined via a modified aluminum chloride colorimetric method [15], with quantification based on a quercetin calibration curve ($0\text{--}250\text{ }\mu\text{g/mL}$), and expressed as mg QAE/g DW. Chlorophyll content was measured spectrophotometrically (absorbance at 664 and 648 nm) following a modified procedure [16]. All analyses were performed in triplicate.

Cell Culture and Virus Propagation

Vero cells (ATCC, CCL-81) were maintained in minimal essential medium (MEM) supplemented with 10% fetal bovine serum (FBS) and 1% penicillin-streptomycin at 37°C in a humidified atmosphere with 5% CO_2 . Human herpesvirus 1 strain KOS (HSV-1, ATCC, VR1493) stock titer was determined by standard plaque assay, expressed as Plaque Forming Units per mL (PFU/mL).

Plaque Reduction Inactivation Assay

Preliminary cytotoxicity of the extracts and gallic acid at the highest concentrations used in the antiviral assay was assessed on uninfected Vero cells using the Presto blue assay. The anti-HSV-1 activity was evaluated using a plaque reduction assay based on direct virus inactivation, following the protocol outlined by [17] with slight modification. Briefly, various serial dilutions of the CN-NADES extract (10%, 5%, 2.5%, 1.25%, and 0.625% v/v), CN-ethanol extract (100, 50, 25, 12.5, 6.25, and 3.125 $\mu\text{g/mL}$) and gallic acid (100, 50, 25, 12.5, 6.25, and 3.125 μM) were prepared in serum free MEM. Blank NADES solvent and vehicle controls (MEM with 0.5% DMSO) were included. Subsequently, equal volumes (300 μL) of the appropriately diluted virus stock (30-40 PFU/100 μL inoculum) and the test substance dilutions (or controls) were mixed and kept for 30 minutes at room temperature. Confluent monolayers of Vero cells in 24-well plates were washed, and then 100 μL of the virus-substance mixture was inoculated per well in triplicate. After 1 hour of adsorption at 37°C with gentle rocking, the inoculum was removed. Cells were overlaid with 1 mL of MEM containing 1.5% CMC and 2% FBS. Plates were incubated at 37°C with 5% CO_2 for 48 hours. Cells were then fixed with 4% paraformaldehyde for 1 hour. The overlay was removed, and monolayers were stained with 0.5% crystal violet solution for 15 minutes. Plates were rinsed with water and air-dried. Plaques were counted, and percentage inhibition was calculated relative to the virus control wells.

Statistical analyses

Data are presented as mean \pm standard deviation (SD) from three independent experiments (n=3). Statistical comparisons between the two extraction methods (TPC, TFC, TC) were made using an independent samples t-test. IC_{50} values were calculated using non-linear regression. Statistical significance was set at $p < 0.05$. Analyses were performed using GraphPad Prism Version 10.4.2.

RESULTS AND DISCUSSION

Results

Table 1. Phytochemical contents in *Clinacanthus nutans* extracts (mean \pm SD, n=3).

Sample	TPC (mg GAE/g DW)	TFC (mg QAE/g DW)	Total Chlorophyll (mg/g DW)
CN-NADES extract	13.00 \pm 0.21***	6.81 \pm 0.22*	0.1424 \pm 0.0016
CN-Ethanol extract	3.17 \pm 0.48	5.01 \pm 0.71	0.7868 \pm 0.0960***

*** $p < 0.001$, * $p < 0.05$ (Independent samples t-test). DW = Dry Weight.

Table 2. Anti-HSV-1 activity (IC_{50}) of *Clinacanthus nutans* extracts and gallic acid (mean \pm SD, n=3).

Sample	IC_{50} (Primary Units)	Equivalent CN powder (μ g/mL)
CN-NADES extract	1.66 \pm 0.20 % (v/v)	1660 \pm 200
CN-Ethanol extract	7.98 \pm 0.83 μ g/mL	106.4 \pm 11.1
Gallic acid	21.92 \pm 4.78 μ M	-

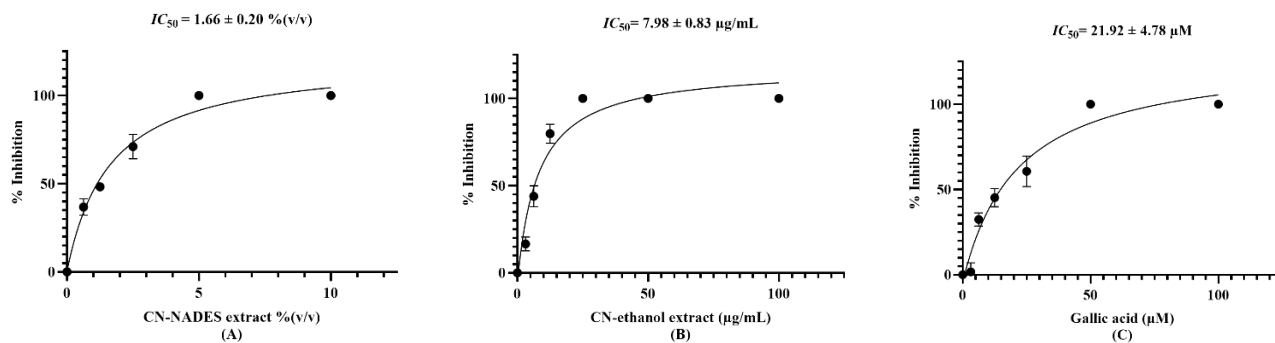


Figure 1. Dose-response curves showing inhibition of HSV-1 plaque formation by (A) CN-NADES extract, (B) CN-ethanol extract, and (C) gallic acid. Data points represent mean \pm SD (n=3).

Discussions

The positive control, gallic acid, exhibited an IC_{50} of 21.92 \pm 4.78 μ M (equivalent to 3.73 \pm 0.81 μ g/mL), confirming the validity of the assay and consistent with literature reports of its anti-HSV-1 activity [12]. When comparing the extracts, the CN-ethanol extract (IC_{50} = 7.98 \pm 0.83 μ g/mL) was approximately 2-fold less potent than pure gallic acid on a weight basis, which is expected for a complex crude extract. Studies have identified gallic acid as one of the major phenolic compounds present in *C. nutans* extracts [18]. Therefore, gallic acid likely contributes intrinsically to both the measured TPC value and the observed anti-HSV-1 activity of the extracts, particularly the CN-NADES extract, which showed significantly higher TPC (Table 1). However, the available phytochemical analyses of *C. nutans* indicate a diverse range of phenolic and flavonoid compounds [19]. Without specific quantification of individual phenolics in the current extracts, it cannot be concluded that gallic acid is the predominant phenolic compound. The markedly higher TPC value obtained with NADES (13.00 mg GAE/g DW) compared to ethanol (3.17 mg GAE/g DW) strongly suggests that the proline-glycerol NADES system is more efficient at extracting a broader spectrum or higher quantity of various phenolic compounds from *C. nutans*, beyond just gallic acid.

To assess the potency of the two extraction methods relative to the starting material, IC_{50} values were expressed as equivalent original CN powder weight per mL of assay medium. This comparison revealed a substantial difference where the CN-ethanol extract (IC_{50} = 0.1 mg CN powder/mL) was about 17 times more potent than the CN-NADES extract (IC_{50} = 1.7 mg CN powder/mL). This indicates that while NADES is superior for bulk extraction of total phenolics and flavonoids, the conventional

ethanol method is significantly more efficient at isolating the specific compounds from *C. nutans* that possess the highest intrinsic anti-HSV-1 activity. Previous research identified three chlorophyll derivatives (phaeophytins), isolated from a chloroform extract of *C. nutans*, that exhibited anti-HSV-1F activity at subtoxic concentrations by interfering with viral adsorption or penetration prior to host cell entry [17]. In this study, the CN-ethanol extract contained significantly higher total chlorophyll (0.7868 ± 0.0960 mg/g DW) than the CN-NADES extract (0.1424 ± 0.0016 mg/g DW) (Table 1). Given the structural similarity between these phaeophytins and chlorophyll, it is plausible that these or related chlorophyll derivatives are enriched in the CN-ethanol extract, contributing to its superior specific potency against HSV-1. However, the high TPC in the CN-NADES extract, measured in gallic acid equivalents, combined with the known activity of gallic acid itself, suggests phenolic acids likely contribute to the CN-NADES extract's activity, but they clearly do not solely account for the large difference in specific potency compared to the CN-ethanol extract.

This study highlights a critical trade-off in phytopharmaceutical development between extraction efficiency for broad phytochemical classes and the specific biological potency of the resulting extract. The proline-glycerol-based NADES efficiently extracts phenolics and flavonoids while minimizing chlorophyll co-extraction. Such extracts could be advantageous for applications where antioxidant or anti-inflammatory activities associated with phenolics are primary targets, or where the presence of chlorophyll is undesirable. However, the significantly higher chlorophyll content in the ethanol extract, while linked to its greater specific anti-HSV-1 potency, introduces potential drawbacks for practical application, particularly in topical formulations commonly used for HSV lesions. Natural chlorophylls are known to be unstable and susceptible to degradation by factors such as light, heat, oxygen, and acidic pH, leading to pheophytinization and loss of the characteristic green color to olive-brown hues [20]. This instability can impact product shelf-life, visual appeal, and potentially efficacy. Furthermore, chlorophyll and its derivatives can act as photosensitizers, increasing the skin's sensitivity to sunlight and potentially leading to phototoxic reactions like exaggerated sunburn, rashes, or even blistering upon exposure [21]. Topical application has also been associated with skin irritation, itching, or burning in some individuals [22]. These factors and challenges related to intense and unstable color represent significant hurdles for developing safe and effective topical products based on chlorophyll-rich extracts like the CN-ethanol extract.

Despite the lower specific anti-HSV-1 potency per milligram of starting material, the CN-NADES extract presents compelling practical advantages stemming from its composition and the nature of the NADES system. Composed of proline, glycerol, and water, components generally recognized as safe and biodegradable, the NADES itself is non-volatile and non-flammable [23]. This allows the resulting extract potentially to be incorporated directly into topical formulations like creams or lotions without requiring energy-intensive and time-consuming solvent evaporation steps [24]. This simplification of the manufacturing process can reduce production costs and environmental impact, aligning with green chemistry principles. Furthermore, the NADES components themselves (proline, glycerol) are often used in cosmetic and pharmaceutical formulations and may even contribute beneficial properties like moisturization or enhanced skin penetration [25]. Therefore, while the CN-ethanol extract might be preferred for applications demanding the highest possible specific potency (e.g., for isolating lead compounds), the NADES system offers a distinct set of advantages regarding ease of use, environmental sustainability, formulation simplicity, and potentially an improved safety profile due to the significantly lower chlorophyll content. These characteristics make the NADES approach an attractive alternative, particularly in contexts where direct incorporation into final products is desired and adherence to green chemistry principles is a priority. The choice between ethanol and NADES extraction should thus be carefully considered based on the specific requirements and priorities of the intended application, balancing *in vitro* potency against practical formulation and safety considerations. Nevertheless, the potential of NADES system to support sustainable product development positions it as a forward-looking and promising alternative that merits further investigation and optimization.

CONCLUSIONS

This study compared proline-glycerol NADES and 95% ethanol for extracting phytochemicals and anti-HSV-1 compounds from *Clinacanthus nutans*. NADES yielded higher total phenolic (TPC) and flavonoid (TFC) content, consistent with its properties. Conversely, ethanol extracted significantly more total chlorophyll (TC). Both extracts showed dose-dependent *in vitro* anti-HSV-1 activity. However, ethanol extract exhibited about 17-fold higher specific potency ($IC_{50} = 0.1$ mg CN powder/mL) compared to the CN-NADES extract ($IC_{50} = 1.7$ mg CN powder/mL). These findings highlight a significant trade-off. While NADES offers a greener, safer method yielding high phenolics/flavonoids with minimal chlorophyll, potentially advantageous for formulation. Ethanol maximizes specific anti-HSV-1 potency, likely via chlorophyll derivatives. Optimal method selection depends on prioritizing specific antiviral potency (ethanol) versus green chemistry, broad phytochemical yield, and formulation ease (NADES). Further research should identify the specific anti-HSV-1 compounds and characterize the NADES extract's phenolics.

ACKNOWLEDGMENTS

This research was supported by the “2023 Mahidol Postgraduate” scholarship from the Faculty of Graduate Studies at Mahidol University. The authors would like to thank the Project of Institute Establishment for Sireeruckhachati Nature Learning Park, Mahidol University, for their support in preparing the plant voucher specimens.

REFERENCES

1. Bongcheewin B, Darbyshire I, Satitpatipan V, Kongsawadworakul P. Taxonomic revision of *Clinacanthus* (Acanthaceae) in Thailand. 2019.
2. Chelyn JL, Omar MH, Mohd Yousof NSA, Ranggasamy R, Wasiman MI, Ismail Z. Analysis of flavone C-glycosides in the leaves of *Clinacanthus nutans* (Burm. f.) Lindau by HPTLC and HPLC-UV/DAD. *The Scientific World Journal*. 2014;2014(1):724267.
3. Chotchoungchatchai S, Saralamp P, Jenjittikul T, Pornsiripongse S, Prathanuraturug S. Medicinal plants used with Thai Traditional Medicine in modern healthcare services: A case study in Kabchoeng Hospital, Surin Province, Thailand. *Journal of ethnopharmacology*. 2012;141(1):193-205.
4. Patrick V, Noweg T, Nelson J. Utilization of Traditional Medicinal Plants by Bidayuh Communities in Sarawak, Malaysia. *Journal of Herbs, Spices & Medicinal Plants*. 2023;29(3):250-61.
5. Thailand. National List of Essential Medicines for Herbs: Food and Drug Administration; 2023 [Available from: <https://herbal.fda.moph.go.th/media.php?id=565337537405657088&name=2023-11-15%20ebook%20D3.pdf>].
6. Virmani T, Chhabra V, Kumar G, Sharma A, Pathak K. Impact of nonconventional solvents on environment. *Organic Synthesis, Natural Products Isolation, Drug Design, Industry and the Environment*. 2023;2:265-84.
7. Chemat F, Abert-Vian M, Fabiano-Tixier AS, Strube J, Uhlenbrock L, Gunjevic V, et al. Green extraction of natural products. Origins, current status, and future challenges. *TrAC Trends in Analytical Chemistry*. 2019;118:248-63.
8. Dai Y, Witkamp G-J, Verpoorte R, Choi YH. Tailoring properties of natural deep eutectic solvents with water to facilitate their applications. *Food chemistry*. 2015;187:14-9.
9. Pradeepkumar P, Subbiah A, Rajan M. Synthesis of bio-degradable poly (2-hydroxyethyl methacrylate) using natural deep eutectic solvents for sustainable cancer drug delivery. *SN Applied Sciences*. 2019;1:1-13.
10. Socas-Rodríguez B, Torres-Cornejo MV, Álvarez-Rivera G, Mendiola JA. Deep eutectic solvents for the extraction of bioactive compounds from natural sources and agricultural by-products. *Applied Sciences*. 2021;11(11):4897.
11. Duan L, Dou L-L, Guo L, Li P, Liu E-H. Comprehensive evaluation of deep eutectic solvents in extraction of bioactive natural products. *ACS Sustainable Chemistry & Engineering*. 2016;4(4):2405-11.
12. Kratz JM, Andrighetti-Fröhner CR, Kolling DJ, Leal PC, Cirne-Santos CC, Yunes RA, et al. Anti-HSV-1 and anti-HIV-1 activity of gallic acid and pentyl gallate. *Memórias do Instituto Oswaldo Cruz*. 2008;103:437-42.
13. Palmelund H, Andersson MP, Asgreen CJ, Boyd BJ, Rantanen J, Löbmann K. Tailor-made solvents for pharmaceutical use? Experimental and computational approach for determining solubility in deep eutectic solvents (DES). *International Journal of Pharmaceutics*. 2019;1:100034.
14. Traiyasuk W, Komaikul J, Anantachoke N, Kitisripanya T. Establishment of *Afgekia mahidolae* BL Burtt & Chermis in vitro culture and effect of elicitation on its bioactive compounds. *Natural Product Research*. 2023;37(11):1829-37.
15. Sithisarn P, Carlsen CU, Andersen ML, Gritsanapan W, Skibsted LH. Antioxidative effects of leaves from *Azadirachta* species of different provenience. *Food chemistry*. 2007;104(4):1539-49.
16. Raya KB, Ahmad SH, Farhana SF, Mohammad M, Tajidin NE, Parvez A. Changes in phytochemical contents in different parts of *Clinacanthus nutans* (Burm. f.) lindau due to storage duration. *Bragantia*. 2015;74(4):445-52.
17. Sakdarat S, Shuyprom A, Pientong C, Ekalaksananan T, Thongchai S. Bioactive constituents from the leaves of *Clinacanthus nutans* Lindau. *Bioorganic & medicinal chemistry*. 2009;17(5):1857-60.
18. Jantakee K, Panwong S, Sattayawat P, Sumankan R, Saengmuang S, Choowongkamon K, et al. *Clinacanthus nutans* (Burm. f.) Lindau Extract Inhibits Dengue Virus Infection and Inflammation in the Huh7 Hepatoma Cell Line. *Antibiotics*. 2024;13(8):705.
19. Al-Shami AMA, Khalid KA, Hadi H. Pharmacological effects of *Clinacanthus nutans* Lindau and its potential cosmeceutical values: A comprehensive review. *Journal of Pharmaceutical Sciences and Research*. 2020;12(1):10-9.
20. Yang Z, Li F, Shen S, Wang X, Nihmot Ibrahim A, Zheng H, et al. Natural chlorophyll: a review of analysis methods, health benefits, and stabilization strategies. *Critical Reviews in Food Science and Nutrition*. 2024:1-15.
21. Gonçalves M. Phototoxic and photoallergic contact reactions. *Contact Dermatitis*: Springer; 2020. p. 365-89.
22. Al-Tameemi K, Nassour R, Hamad A. The medical importance of chlorophylls and their derivatives. *SEA Journal of Islamic Finance*. 2022;8:4-8.
23. Dai Y, Van Spronsen J, Witkamp G-J, Verpoorte R, Choi YH. Natural deep eutectic solvents as new potential media for green technology. *Analytica chimica acta*. 2013;766:61-8.
24. Bragagnolo FS, Strieder MM, Pizani RS, de Souza Mesquita LM, González-Miquel M, Rostagno MA. Revisiting natural deep eutectic solvents (NADES) as extraction media and ready-to-use purposes. *TrAC Trends in Analytical Chemistry*. 2024:117726.
25. Villa C, Caviglia D, Robustelli della Cuna FS, Zuccari G, Russo E. NaDES application in cosmetic and pharmaceutical fields: an overview. *Gels*. 2024;10(2):107.

The Role of Topical Nicotinamide Adenine Dinucleotide (NAD⁺) in Alleviating Short-Term Skin Damage Following UVB Exposure in Mice

Napat Hunsajarupan¹, Adiluck Pisutpunya¹, and Pawit Phadungsaksawasdi^{1,}*

¹ Department of Dermatology, Chulabhorn International College of Medicine, Thammasat University Rangsit Campus, Pathumthani, THAILAND

*Corresponding author Email: pawit.p@tu.ac.th

Abstract. Ultraviolet (UV) radiation is a major environmental factor that induces inflammation and skin damage. Post-UV exposure skin care is essential for alleviating these effects but is often overlooked. Nicotinamide adenine dinucleotide (NAD⁺) has demonstrated promising anti-inflammation and cellular repair effects in vitro. However, strategies to enhance cellular repair following UVB-induced skin damage remain unclear. This study aimed to investigate the efficacy of 5% topical NAD⁺ in alleviating short-term skin damage after UV exposure in C57BL/6NJcL mice. Mice were exposed to broadband UVB radiation at a minimum erythema dose (MED) every other day for seven days, mimicking short-term sun exposure, similar to a summer vacation in humans. Topical NAD⁺ was applied daily for seven days. Skin damage was assessed using double skin fold thickness and erythema severity scores (0-3). Skin biopsies were collected from three different groups (n=3 per group) for histological analysis. Results showed that the NAD⁺-treated group exhibited significant reduction in both double skin fold thickness and erythema severity scores. Double skin fold thickness increased 41.9% in the UVB-exposed group, while the NAD⁺-treated group showed a significantly smaller increase of 9.3% ($p < 0.001$). Mean erythema score in UVB-exposed was 2.67, whereas NAD⁺-treated group exhibited a significantly lower score of 1.33 ($p < 0.001$). Histological analysis further demonstrated reduction in epidermal thickness with the mean epidermal thickness in the NAD⁺-treated group measured at 10.93 μm , compared to 33.9 μm in the UVB-exposed ($p < 0.05$). These preliminary results suggest that topical NAD⁺ effectively alleviates short-term UVB-induced skin damage at both macroscopic and microscopic levels.

Keywords: Nicotinamide Adenine Dinucleotide, ultraviolet B, aftersun, photodamage, cellular repair

INTRODUCTION

Aging is an inevitable and dynamic biological process. Skin aging is one of the most noticeable features of the aging process. Human skin aging is divided into two distinct mechanisms: intrinsic and extrinsic. While intrinsic or chronological aging involves multiple physiological changes that are deemed to be unavoidable as these changes are controlled by genetic and hormonal factors, extrinsic skin aging or photoaging is influenced by environmental factors. Ultraviolet radiation (UVR) is considered the most significant factor that leads to photoaging of the skin.(1)

Acute and chronic exposure to UVR can induce serious damage to the skin including erythema (sunburn), skin dryness, hyperpigmentation, deep wrinkles, telangiectasia and even skin cancers. These changes are due to the production of reactive oxygen species (ROS), increase in inflammation cytokines, degradation of collagen fibers and DNA damage induced by photoproducts. Therefore, searching for ways to prevent or reduce UVR damage on the skin is one of the main focuses in the modern world.

At the moment, most of the photoprotection methods are mainly focusing on the pre-exposure to sunlight, such as the use of sunscreens, oral photoprotections or even the application of topical botanical agent extracts. However, there is limited knowledge or research on interventions and DNA repair following sun exposure. Most of the after-sun products in the market are mainly focusing on the soothing, hydrating and moisturizing effects. Hence it would be ideal if an after-sun protective method, which is able to enhance DNA repairing ability of the cells, is being made available.

NAD⁺ is an essential pyridine nucleotide that mediates the production of energy and fuels enzymes with crucial cellular functions like DNA repair. NAD⁺ exists in all cells of the human body, and its normal level is vital for maintaining the functions of mitochondria, homeostasis of organisms, normal activities of tissues and organs, and delaying aging. Recent studies have shown that NAD⁺ plays role in ROS reduction in the skin cells, leading to the alleviation of oxidative stress and damage DNA. Application of NAD⁺ also made it instantly available for being used by the cells for DNA repair without having to go through multiple synthesis processes from its precursors.(2)

Nevertheless, there are only a few reports on the effect of topical NAD⁺ on UVB-induced skin damage. The purpose of this study is to assess the efficacy of NAD⁺ applied topically for the alleviation of short-term skin damage induced by UVB exposure in mouse skin. In this experiment, a situation similar to a short summer vacation in humans will be simulated. Artificial UVB lamp will be used every other day for 4 times within 7 days to induce skin damage on the dorsal skin of the experimental mice. 5%

Topical NAD⁺ will then be applied every day for 7 days. We will then measure the double skin fold thickness, evaluate the skin damage, the epidermis thickness and the number of apoptotic keratinocytes.

The present study may provide theoretical knowledge of the prevention or treatment of skin damage induced by UVB radiation with topical NAD⁺. It may also provide foundational insights into novel approaches for managing photoaging and UV-induced skin injury, potentially guiding the formulation of next-generation after-sun treatments with active DNA repair properties.

MATERIALS AND METHODS

Materials

1. Animal
 - a. C57BL/6NJcL female mice, 6 weeks old (Purchased from Nomura Siam International)
2. Experimental Substances
 - a. Nicotinamide Adenine Dinucleotide (Cayman chemical; CAS 53-84-9) was purchased from S.M. Chemical supplies Co., Ltd.
 - b. Vehicle (standard cream base)

Methods

Animal Experiment

All animal care was performed in accordance with the Ethical Principles and Guidelines for the Use of Animals for Scientific Purposes, and was approved by Thammasat University's Ethical committee. A total of twelve 6-week-old C57BL/6NJcL female mice were used in this experiment. The animals were housed under conventional room temperature ($22 \pm 2^\circ\text{C}$), relative humidity (30-70%) with 12 hours light/dark cycle conditions. Free access to food and water were also provided. All experiments were performed to minimize the number of animals used and their suffering due to the procedure used in the present experiment.

Experiment Design and Groups

For the UVB protection experiment, the mice were divided into four groups (n=3 per group). The experimental groups were as follows: (A) control mice, (B) UVB-exposed mice, (C) UVB-exposed and vehicle-treated mice, and (D) UVB-exposed and 5% topical NAD⁺-treated mice.

BB-UVB radiation exposure was given for 3 mins and 30 seconds (Minimal erythema dose = 150 mJ/cm^2) for 4 times at day 1, 3, 5, 7 using the BB-UVB lamps (Two Phillips UVB TL 40W/12RS, 280-320nm with peak emission at 311nm). Our two BB-UVB lamps put a combined output of around 0.7 mW/cm^2 . This was measured using a digital UV energy monitor. The measurement was done inside the UVB box with two UVB lamps installed at the top, 30 cm away from the bottom of the box.(3) In order to determine the duration for UVB exposure, we divided the MED (150 mJ/cm^2) by the total energy output of the lamps (0.7 mW/cm^2) and this gave us 214 seconds. Therefore, we decided to use the duration of 3 minutes and 30 seconds for this experiment ($\text{mW/cm}^2 \times \text{second} = \text{mJ/cm}^2$).

At the start of the experiment, the dorsal hairs of the mice were shaved 3 days prior to UVB exposure. Mice in group B, C, and D were then exposed to BB-UVB for 3 minutes and 30 seconds. Two mice were placed in the UVB box at a time under anesthesia to prevent them from moving around and to ensure that each of them received similar amount of UVR.

The vehicle and 5% NAD⁺ were applied on the dorsal skin of the mice every day for 7 days. For vehicle-treated group (C), vehicle was applied on the dorsal skin of the mice at 20 minutes after exposure to UVB. For NAD⁺-treated group (D), 5% topical NAD⁺ was applied on the dorsal skin of the mice at 20 minutes after exposure to UVB.

NAD⁺ (CAS number: 53-84-9) was purchased from S.M. Chemical supplies Co., Ltd. (Bangkok, Thailand). NAD⁺'s purity was measured by high-performance liquid chromatography (by Sigma-Aldrich) and was shown to be $\geq 95\%$.

Result Assessment

Skin damage was assessed using double skin fold thickness and erythema severity scores. Double skin fold thickness was measured five times at day 1, 3, 5, 7, 8 before UVB exposure using engineer's micrometer.(4) The erythema severity score was also evaluated four times (day 1, 3, 5, 7) by three independent individuals. The erythema severity score was scored as 0 (none), 1 (mild), 2 (moderate), 3 (severe).(5)

For histological analysis, skin samples from the dorsal back of mice were collected by punch biopsy technique (using 6 mm punch biopsy equipment), then they were stained with H&E staining and evaluate under a microscope for epidermal thickness and the number of apoptotic keratinocytes (sun-burn cells) presented in the epidermis. The epidermal thickness was calculated by performing measurement at 10 randomly selected sites from each section and the mean value of the epidermal thickness from each group was calculated for comparison.(6)

Statistical analyses

All of the values are presented as mean \pm standard deviation. A multiple sample comparison was applied to test the differences between groups. Stata statistical software was used to determine the statistical significance. Values of $p < 0.05$ were considered statistically significant. The comparison between two groups was performed by T-test.

RESULTS AND DISCUSSION

Results

The effect of topical NAD⁺ on the UVB-exposed dorsal skin was assessed by measuring double skin fold thickness and analyzing erythema severity scores. The percentage change in double skin fold thickness at day 3, 5, 7, and 8 were significantly higher in UVB-exposed and vehicle-treated groups compared to the NAD⁺-treated group. Double skin fold thickness at day 8 increased by 41.9% in the UVB-exposed group, while the NAD⁺-treated group showed a significantly lower increase of 6.0% ($p < 0.05$). The NAD⁺-treated group also showed similar level of percentage change in double skin fold thickness compared to the control group (Figure 1). Control group showed a change in the double skin fold thickness by 4.9%, which is not significantly different from NAD⁺-treated group. Meanwhile, double skin fold thickness did not differ between the vehicle-treated and UVB-only groups, suggesting that the effect is not due to moisturization.

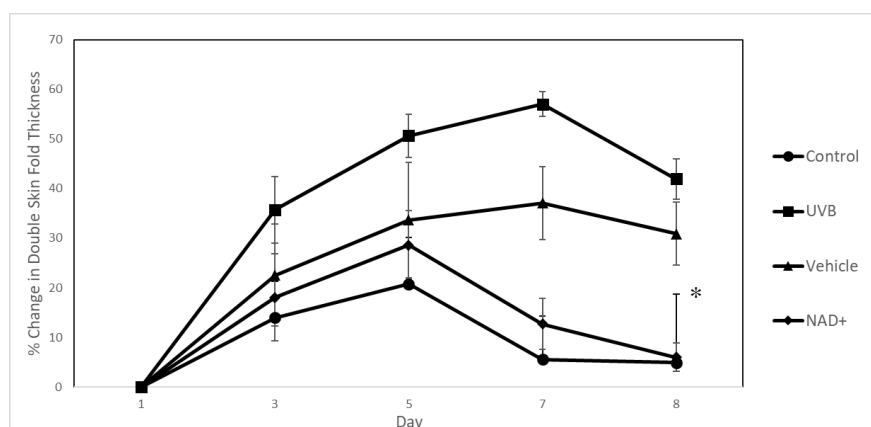


Figure 1. The percentage change in double skin fold thickness in the control, UVB, Vehicle and NAD⁺ group at day 1,3,5,7 and 8. Bars indicate the standard deviation. * indicates a significant different from the UVB and vehicle group ($p < 0.05$).

The erythema severity score was significantly higher in the UVB-exposed and vehicle-treated group at day 7 of the experiment compared to the NAD⁺-treated group. Mean erythema severity score in UVB-exposed group at day 7 was 2.67, whereas NAD⁺-treated group exhibited a significantly lower score of 1.33 ($p < 0.001$). The mean erythema severity score of vehicle group was 2.44, which was also significantly higher than that of the NAD⁺-treated group ($p < 0.05$) (Figure 2).

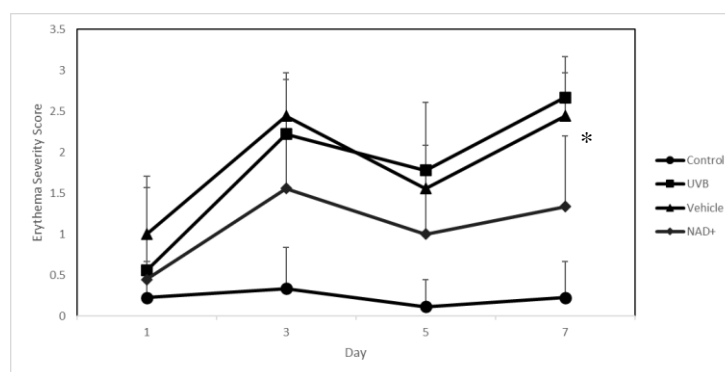


Figure 2. The erythema severity score in control, UVB, vehicle and NAD⁺ group at day 1, 3, 5, and 7. Bars indicate the standard deviation; * indicates a significant different from the UVB group ($p < 0.001$).

The histological analysis of the dorsal skin was performed on day 8 using H&E staining. Epidermal thickness was measured at 10 randomly selected sites per specimen, and the mean value was calculated for each group. The UVB-exposed and vehicle-treated groups showed a significant increase in epidermal thickness, indicative of both epidermal hyperplasia and hypertrophy. The mean epidermal thicknesses were 33.97 μm and 32.62 μm , respectively. In contrast, the NAD⁺-treated group exhibited a markedly lower epidermal thickness, with a mean value of 10.93 μm , representing a 3.11-fold reduction compared to the UVB-exposed group (Figure 3A).

The mean number of apoptotic keratinocytes in the epidermis was counted and expressed as the number of cells per mm². The UVB-exposed group exhibited a significantly higher number of apoptotic keratinocytes (14.8 cells/mm²) compared to the NAD⁺-treated group (7.6 cells/mm², $p < 0.05$). Similarly, the vehicle-treated group also showed a significantly greater number of apoptotic cells (13.3 cells/mm²) than the NAD⁺-treated group ($p < 0.05$) (Figure 3B).

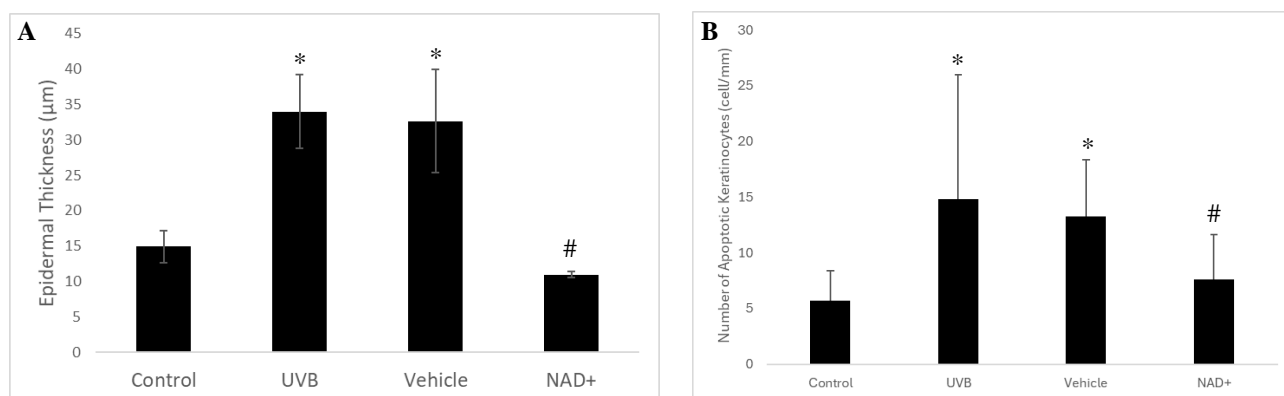


Figure 3. (A) The mean value of epidermal thickness in control, UVB, vehicle and NAD⁺ group at day 8. * indicates a significant different from the control group ($p < 0.05$); # indicates a significant difference from UVB and vehicle group ($p < 0.05$). (B) The mean number of apoptotic keratinocytes in control, UVB, vehicle and NAD⁺ group. * indicates a significant different from the control group ($p < 0.05$); # indicates a significant difference from UVB and vehicle group ($p < 0.05$).

Discussions

This study demonstrates the photoprotective effect of topical NAD⁺ in alleviating short term UVB-induced skin damage in mice. UVB radiation is one of the primary extrinsic factors contributing to photoaging and epidermal damage, primarily by generating reactive oxygen species (ROS), triggering pro-inflammatory cytokine release, and inducing DNA photolesions such as cyclobutane pyrimidine dimers (CPDs) and 6-4 photoproducts.(7)

Our findings revealed that NAD⁺ treatment significantly reduced percentage change in double skin fold thickness and erythema severity score compared to both UVB-exposed and vehicle-treated groups. Histological analysis confirmed that mice in the NAD⁺ group exhibited a markedly thinner epidermis, suggesting that NAD⁺ effectively inhibited keratinocyte hyperproliferation and UVB-induced hyperplasia and hypertrophy, which are the common side effects observed after UVB-exposure. These results are consistent with previous studies showing that oxidative stress-induced epidermal thickening can be alleviated through anti-oxidative and anti-inflammatory interventions.(8)

NAD⁺ is a vital coenzyme involved in mitochondrial function, and cellular energy metabolism. It is also a substrate for key DNA repair enzymes such as poly(ADP-ribose) polymerases (PARPs) and sirtuins, which maintain genomic stability, cellular repair and DNA repair.(9) Topical application of NAD⁺ may allow direct uptake by skin cells, bypassing the need for intracellular synthesis from precursors such as nicotinamide riboside and nicotinamide mononucleotide. This immediate bioavailability could enhance cellular repair activity in UVB-damaged cells, explaining the significant reduction in skin erythema severity scores observed in our study.

Moreover, the lower erythema severity scores suggest an anti-inflammatory effect of NAD⁺. Prior reports have shown that NAD⁺ and its associated enzymes can help regulate the inflammatory responses by inhibiting NF- κ B activation and downregulating cytokines such as TNF- α and IL-6.(10) These effects contribute to the overall reduction of UVB-induced skin inflammation and support the role of NAD⁺ in alleviating short-term UVB-induced skin damage.

While most current photoprotection strategies focuses on prevention (e.g., sunscreen, antioxidants), post-exposure interventions are often limited to hydration and soothing agents. There are very few options for active cellular repair. Our findings

indicate that NAD⁺ could fill the gap as a promising after-sun product, providing both anti-inflammatory and cellular repair-enhancing properties.

CONCLUSIONS

In summary, this study provides preliminary evidence supporting the potential of topical NAD⁺ as an effective agent for alleviating short term UVB-induced skin damage at both macroscopic and microscopic levels. Topical NAD⁺ may serve as a promising post-exposure care for photodamaged skin. Future research should further explore its molecular mechanisms and potential applications in clinical dermatology and human skin treatment.

ACKNOWLEDGMENTS

We would like to sincerely thank the Laboratory Animal Center, Thammasat University, for their kind support and collaboration throughout this research. We are especially grateful to Dr. Werayut Yingmema, DVM, Deputy Director of the center, for his guidance, and to Ms. Sukanya Maison, Animal Husbandry Technical Officer, for her excellent care of the animals and technical assistance during the experiment.

REFERENCES

1. Christensen L, Suggs A, Baron E. Ultraviolet Photobiology in Dermatology. In: Ahmad SI, editor. Ultraviolet Light in Human Health, Diseases and Environment. Cham: Springer International Publishing; 2017. p. 89-104.
2. Katayoshi T, Nakajo T, Tsuji-Naito K. Restoring NAD(+) by NAMPT is essential for the SIRT1/p53-mediated survival of UVA- and UVB-irradiated epidermal keratinocytes. *J Photochem Photobiol B*. 2021;221:112238.
3. Choi J, Bordeaux ZA, Braun G, Davis C, Parthasarathy V, Deng J, et al. Construction of a Secondary Enclosure for UVB Irradiation of Mice. *JID Innovations*. 2023;3(1).
4. Horváth S, Kemeny A, Pintér E, Gyulai R. A Localized Aldara (5% Imiquimod)–Induced Psoriasiform Dermatitis Model in Mice Using Finn Chambers. *Current Protocols in Pharmacology*. 2020;90.
5. Yamamoto M, Haruna T, Yasui K, Takahashi H, Iduhara M, Takaki S, et al. A Novel Atopic Dermatitis Model Induced by Topical Application with Dermatophagoides Farinae Extract in NC/Nga Mice. *Allergology International*. 2007;56(2):139-48.
6. Her Y, Shin BN, Lee YL, Park JH, Kim DW, Kim KS, et al. Oenanthe Javanica Extract Protects Mouse Skin from UVB Radiation via Attenuating Collagen Disruption and Inflammation. *Int J Mol Sci*. 2019;20(6).
7. Yaar M, Gilchrist BA. Photoageing: mechanism, prevention and therapy. *Br J Dermatol*. 2007;157(5):874-87.
8. D'Orazio J, Jarrett S, Amaro-Ortiz A, Scott T. UV radiation and the skin. *Int J Mol Sci*. 2013;14(6):12222-48.
9. Imai S, Guarente L. NAD⁺ and sirtuins in aging and disease. *Trends Cell Biol*. 2014;24(8):464-71.
10. Yoshino J, Baur JA, Imai SI. NAD(+) Intermediates: The Biology and Therapeutic Potential of NMN and NR. *Cell Metab*. 2018;27(3):513-28.

The Role of Topical Nicotinamide Adenine Dinucleotide (NAD⁺) in Alleviation of UVB-induced Acute Sun damage in Mice

Kodchakorn Chukanchitipat¹, Adiluck Pisutpunya², and Pawit Phadungsaksawasdi^{1,}*

¹Department of Dermatology, Chulabhorn International College of Medicine, Thammasat University Rangsit campus, Pathumthani Thailand

²Department of Pathology, Faculty of Medicine, Thammasat University, Rangsit campus, Pathumthani Thailand

*Corresponding author, E-mail: pawit.p@tu.ac.th

Abstract. Exposure to high doses of ultraviolet B (UVB) radiation induces acute sun damage and immediate severe cellular injury. Current treatments primarily offer symptomatic relief, lacking direct interventions for cellular repair. Nicotinamide Adenine Dinucleotide (NAD⁺) is a key coenzyme in oxidative stress reduction and DNA damage repair. However, its potential in alleviating UVB-induced acute sun damage remains unclear. This study assessed the effectiveness of a 1% topical NAD⁺ treatment in reducing sun damage induced by a high dose of UVB radiation (at least twice the minimal erythema dose, MED) in C57BL/6NJcL mice. Skin damage was assessed using an erythema severity score (0-3) and objective histological analysis of dorsal skin biopsies from three groups (n=3/group). Results demonstrated that 1% topical NAD⁺, significantly reduced erythema severity. The cumulative erythema score in UVB-exposed mice was 19, while NAD⁺-treated mice showed a significant lower score of 8 ($p<0.05$). Histological analysis revealed improved control of epidermal edema and a significant reduction in sunburn cells counts. Mean epidermal edema was significantly lower in NAD⁺-treated mice (10.9 μ m) compared to UVB-exposed mice (35.5 μ m) ($p<0.001$). The UVB-exposed group displayed 53.4 sunburn cells/mm, while the NAD⁺-treated group exhibited a significantly lower count of 16.3 cells/mm ($p<0.001$). These preliminary findings strongly suggest that immediate topical NAD⁺ application alleviates UVB-induced acute sun damage at both macroscopic and microscopic levels, highlighting its potential protective role in acute sun damage. Further investigation is needed to explore underlying mechanisms in sun damage prevention.

Keywords: Acute sun damage; Nicotinamide Adenine Dinucleotide; Skin erythema; Ultraviolet B (UVB)

INTRODUCTION

Sunburn, primarily affects Fitzpatrick skin type I-III, is an acute inflammatory response to intense UVB (280-320 nm) overexposure, characterized by erythema, a burning sensation with pain, swelling, and, in severe cases, blistering and skin peeling. UVB exposure leads to significant cellular injury, triggering the release of inflammatory cytokines (IL-1b, IL-6 and TNF- α), oxidative stress, DNA damage, and apoptotic keratinocytes(1). In response to UVB-induced skin damage, the skin activates several repair mechanisms, including inflammatory responses, oxidative stress pathways, and DNA repair processes. One of the essential molecules involved in the repair activities is NAD⁺. NAD⁺ is essential for oxidative stress regulation and acts as substrate for DNA repair enzymes through poly(ADP)polymerases (PARPs) and sirtuins (2). Precursors of NAD⁺, such as nicotinamide and nicotinamide mononucleotide (NMN), have shown promise in mitigating UVR-induced skin damage in preclinical studies. Nicotinamide inhibits inflammatory mediators (IL-6 and TNF- α) and promotes DNA repair(3), while intraperitoneal NMN, enhances antioxidant enzyme activity and reduces anti-inflammatory cytokines in UVB-exposed mice(4), supporting the potential of NAD⁺ in alleviating UVB-induced skin damage. Despite the evidence, limited research exists on the direct topical application of NAD⁺ to alleviate sunburn symptoms such as erythema, edema, and sunburn cell formation. This research aim to evaluate the efficacy of topical NAD⁺ in acute sun damage condition. This may provide a potential approach to post-sunburn care.

MATERIALS AND METHODS

Materials

Experimental substance – Nicotinamide adenine dinucleotide (Cayman chemical; CAS 53-84-9), Cream base - an oil-in-water emulsion containing key components such as glyceryl stearate, PEG-100 stearate, caprylic/capric triglyceride, dimethicone, and cetearyl alcohol, designed to enhance skin absorption and maintain formulation stability.

Animals and Housing The study protocol number 022/2022 was approved and conducted under the Animals Ethics Committee of Thammasat university, Thailand and the animal care were in accordance to the ethical guidelines. In this study, female C57BL/6NJcL mice, aged at 6 weeks, were purchased from Nomura Siam International. They were housed under Laboratory Animal Center, Thammasat university, and experiments were performed under institutional animal care and use committee (IACUC) guidelines.

Methods

Experimental design and Groups

Mice were randomly arranged in three experimental groups (n = 3/group), including:

- A Control: Mice not exposed to UVB radiation and not treated with topical NAD⁺.
- B UVB: Mice exposed to UVB radiation without treatment.
- C 1% NAD⁺ (20 minutes post-UVB exposure): Mice exposed to UVB radiation and treated with 1% topical NAD⁺ 20 minutes post exposure. This 20-minute delay was chosen to simulate a more realistic scenario of post-sun exposure intervention, as individuals typically do not apply treatments immediately upon UV exposure.

Experiment protocol: Two groups of mice; UVB and UVB+1%NAD⁺ were irradiated in UV box, receiving 360 mJ/cm² for 8 minutes 30 seconds. The broadband UVB lamps of two Phillips UVB TL 40W/12RS, 280-320 nm with peak emission at 311 nm were constructed in a UV box and set 30 cm distant from the mice area(5). Irradiated mice were put under inhaled isoflurane during radiation. Group C (Treated group) received 0.5 g, 1% topical NAD⁺ applied 20 minutes post-UVB radiation at dorsal of mice. The 1% concentration was chosen based on previous research by Wozniacka et al. (2006), which demonstrated the efficacy of 1% topical NAD⁺ in improving erythematous plaques in psoriatic patients(6).

Skin erythema evaluation: Erythema, a marker of sunburn, was assessed 24 hours post-UVB exposure using a scale of 0 to 3: 0 = No erythema, 1 = Mild redness, 2 = Moderate redness, 3 = Severe redness with swelling. Three independents evaluators, blinded to the treatment groups, scored erythema on the dorsal skin of mice (9 images) based on reference photographs. A cumulative erythema score was calculated from the individual evaluations.

Histological Analysis: Dorsal skin with 6 mm biopsies were collected at 24 hours post-exposure. Samples were fixed in 10% formalin, embedded in paraffin, and sectioned at 5 µm thickness. Hematoxylin and eosin (H&E) staining was performed to assess epidermal edema and apoptotic keratinocytes formation. Epidermal edema was vertically measured by determining the thickness of the epidermis in micrometers (µm), five randomly positioned were measured in one tissue then the average was calculated. Apoptotic keratinocytes were counted by an observer blinded to the treatment groups per square millimeter (cells/mm) in a standardized region of the epidermis at five randomized positions in one tissue, the average then was calculated.

Statistical analyses: All data are analyzed using mean ± standard error of the mean (SEM). Statistical significance between groups was determined using Kruskal-Wallis test for multiple comparisons. A p-value of less than 0.05 was considered statistically significant. Data were conducted using GraphPad Prism ver10.3.

RESULTS AND DISCUSSION

Results (Skin erythema severity): There was a significant reduction in the mean cumulative erythema score in the 1% NAD⁺ treatment group compared to the UVB-only group. The mean cumulative erythema score from three individuals for the UVB-only group was 19, whereas the 1% topical NAD⁺ group exhibited a significantly lower erythema score of 8 ($p < 0.05$), as shown in Figure 1. This preliminary data illustrates that the topical NAD⁺ treatment effectively alleviates erythema and skin damage from UVB over exposure. These findings are consistent with prior research showing that NAD⁺ precursor, nicotinamide mononucleotide (NMN) plays a protective role in cellular damage, ROS(2, 4).

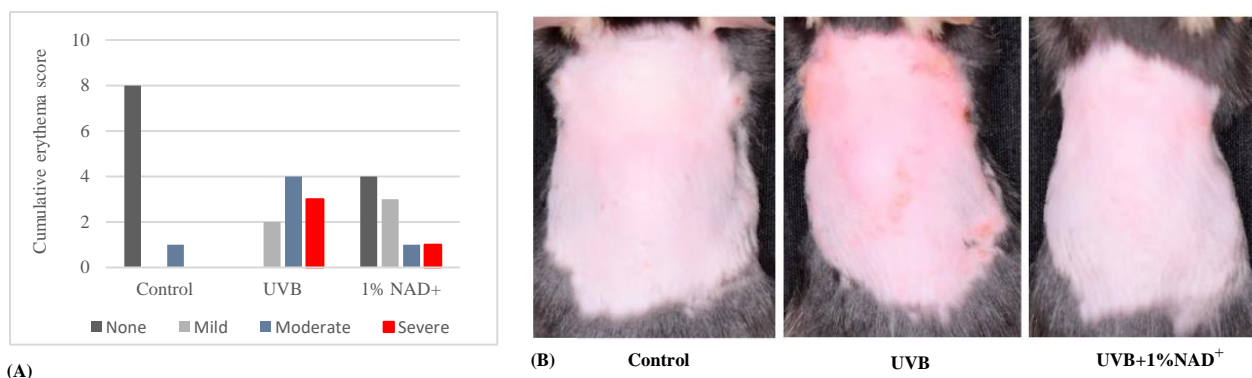


Figure 1. The effect of 1% topical NAD⁺ on UVB-skin exposure. (A) The frequency distribution of erythema severity 24 hours post-UVB exposure in the UVB-only and UVB+1%NAD⁺ groups, as evaluated by three different evaluators. (B) Representative dorsal skin images 24 hours after exposure to UVB radiation. (A) Control, (B) UVB-exposed group, and (C) UVB + 1% NAD⁺ (20 minutes post-exposure) treated group.

Epidermal edema: Histological assessments, epidermal changes such as dyskeratotic and vacuolated keratinocyte edema with spongiosis were shown in acute sun damage condition, which peak at 24 hours post-irradiation(7). Hematoxylin and eosin (H&E) staining revealed that the NAD⁺-treated groups presented significantly reduced epidermal edema and lower number of apoptotic keratinocytes compared to the UVB-exposed group. The mean epidermal edema in the UVB-only group was 35.5 μm , while the 1% NAD⁺ treated group showed a significant reduction to 10.9 μm ($p < 0.001$) (Figure 2D). A research by Perluigi, et al. (2010) demonstrated that UVB exposure produces ROS, leading to the damage of proteins, DNA, RNA, and cellular inflammation(8). NAD⁺'s properties show crucial roles in protecting against these processes, acting as both enzymes and substrates for antioxidant defense, anti-inflammation activity and DNA repair(2, 3, 9). Our preliminary results align with these findings, suggesting that topical NAD⁺ may alleviate UV-induced skin damage by reducing oxidative stress and inflammation.

Therefore, epidermal edema was significantly less in NAD⁺-treated compared to UVB groups.

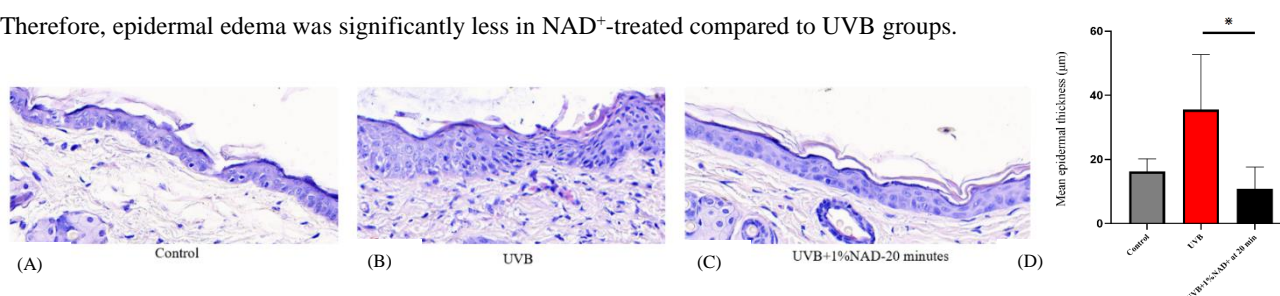


Figure 2 illustrates (A-C) H&E stained of mice dorsal skin in three groups: Control (A), UVB (B) and (C) UVB+1%NAD⁺ at 24 hours post-irradiation. 40x magnification. The mean comparison of epidermal thickness in the control, UVB, and UVB+NAD⁺ are shown in (D). The data represents mean \pm standard deviation of epidermal thickness(μm). * indicates significant different $p < 0.05$.

Apoptotic keratinocytes: The main characteristics of acute sun damage include the presence of apoptotic keratinocytes. They determine a direct result of DNA damage and are crucial determinant of the damage severity, inflammatory response, and the extent of cellular injury(7, 10). In our study, the mean number of apoptotic keratinocytes per millimeter were counted in all groups. The UVB-exposed group had a significant higher count of 53.4 cells/mm, whereas the 1% NAD⁺-treated group showed a significantly lower count of 16.3 cells/mm ($p < 0.001$), indicating that 1% topical NAD⁺ can mitigate the product of acute sun damage (Figure 3). The preliminary data suggests that NAD⁺ may also help reducing the inflammatory and apoptotic processes induced by UVB-exposed.

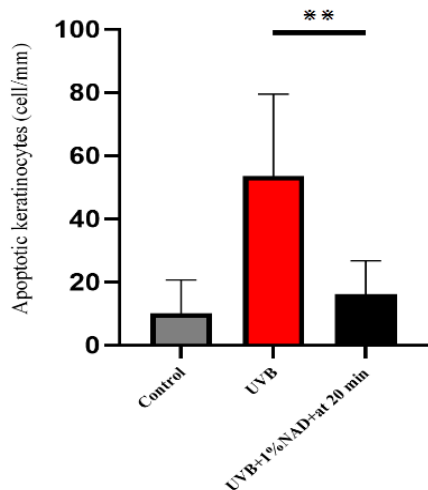


Figure 3. Average of apoptotic keratinocytes counts per millimeter in control, UVB, and UVB+1%NAD⁺. The data represents mean \pm standard deviation. ** Indicates significant different $p < 0.001$.

Previous studies support topical NAD⁺ against skin damage and inflammation. Notably, 1% and 0.3% topical NAD⁺ improved chronic psoriatic plaques over 4 weeks(6), and topical NADH, in Vaseline ointment (applied twice daily) showed a potential treatment for contact dermatitis and rosacea (11), suggesting potential for post - inflammatory conditions. Our findings also raise important questions about the concentration and application timing of NAD⁺. The significant reduction in erythema and epidermal edema observed 24 hours post-UVB exposure suggests that NAD⁺ may be most effective when applied immediately after UVB exposure. However, it is crucial to acknowledge that the small sample size ($n=3$ per group) in this pilot study limits the statistical power and generalizability of

these observations. Future studies with larger cohorts are needed to confirm these trends. Furthermore, the absence of a vehicle control group makes it difficult to definitively attribute the observed effects solely to NAD⁺, as the vehicle itself might have influenced the results. Only single concentration and application time were tested, future research should explore the optimal concentration and the best application timing of NAD⁺ and whether it can prevent long-term effects of UVB damage, such as photoaging or skin cancer.

CONCLUSION

In summary, our preliminary data suggests that 1% topical NAD⁺ has the potential as a therapeutic agent for mitigating acute UVB-induced skin damage, by reducing erythema, epidermal edema, and apoptotic keratinocytes, suggesting a role in modulating inflammation and cellular repair. However, further research should broaden the assessment beyond clinical and histological evaluations to include molecular mechanisms and investigate its capacity to prevent long-term UVB skin damage.

ACKNOWLEDGMENTS

We thank the laboratory Animal Center, Thammasat university, and for invaluable and especially Dr. Werayut Yingmema, DVM, and Miss Sukanya Maison, Animal Husbandry Technical Officer.

REFERENCES

1. Kang S, Amagai M, Bruckner AL, Enk AH, Margolis DJ, McMichael AJ, Orringer JS. Cutaneous Photobiology. In: Runger TM, editor. Fitzpatrick's Dermatology, 9e. 1. New York, NY: McGraw-Hill Education; 2019. p. 265-88.
2. Belenky P, Bogan KL, Brenner C. NAD⁺ metabolism in health and disease. Trends Biochem Sci. 2007;32(1):12-9.
3. Oblong JE. The evolving role of the NAD⁺/nicotinamide metabolome in skin homeostasis, cellular bioenergetics, and aging. DNA Repair (Amst). 2014;23:59-63.

4. Zhou X, Du H-H, Long X, Pan Y, Hu J, Yu J, Zhao X. β -Nicotinamide mononucleotide (NMN) administrated by intraperitoneal injection mediates protection against UVB-induced skin damage in mice. *Journal of Inflammation Research*. 2021;5165-82.
5. Choi J, Bordeaux ZA, Braun G, Davis C, Parthasarathy V, Deng J, et al. Construction of a Secondary Enclosure for UVB Irradiation of Mice. *JID Innov*. 2023;3(1):100107.
6. Wozniacka A, Szajerski P, Adamus J, Gebicki J, Sysa-Jedrzejowska A. In search for new antipsoriatic agents: NAD⁺ topical composition. *Skin Pharmacology and Physiology*. 2006;20(1):37-42.
7. Gilchrest BA, Soter NA, Stoff JS, Mihm MC. The human sunburn reaction: Histologic and biochemical studies. *Journal of the American Academy of Dermatology*. 1981;5(4):411-22.
8. Perluigi M, Di Domenico F, Blarzino C, Foppoli C, Cini C, Giorgi A, et al. Effects of UVB-induced oxidative stress on protein expression and specific protein oxidation in normal human epithelial keratinocytes: a proteomic approach. *Proteome Science*. 2010;8(1):13.
9. Nishida T, Naguro I, Ichijo H. NAMPT-dependent NAD⁺ salvage is crucial for the decision between apoptotic and necrotic cell death under oxidative stress. *Cell Death Discovery*. 2022;8(1):195.
10. Laethem AV, Claerhout S, Garmyn M, Agostinis P. The sunburn cell: Regulation of death and survival of the keratinocyte. *The International Journal of Biochemistry & Cell Biology*. 2005;37(8):1547-53.
11. Woźniacka A, Sysa-Jędrzejowska A, Adamus J, Gębicki J. Topical application of NADH for the treatment of rosacea and contact dermatitis. *Clinical and Experimental Dermatology*. 2003;28(1):61-3.

The Efficacy of Nicotinamide Adenine Dinucleotide (NAD⁺) in Mitigating Long-term Skin Side Effects from UVB Radiation in Mice

Kanyawan Harnsiriwattana^{1,}, Adiluck Pisutpunya^{1,2} and Pawit Phadungsaksawasdi^{1,*}*

¹Department of Dermatology, Chulabhorn International College of Medicine, Thammasat University, Rangsit campus, Pathumthani, Thailand

²Department of Pathology, Faculty of Medicine, Thammasat University, Rangsit campus, Pathumthani, Thailand

*Corresponding author E-mail: pawit.p@tu.ac.th

Abstract. Long-term exposure to ultraviolet B (UVB) radiation is known to cause lasting damage to skin, including DNA damage, premature aging, and an increased risk of skin cancer. The buildup of DNA damage can lead to the transformation of normal skin cells into abnormal ones, contributing to cancer development. While Nicotinamide Adenine Dinucleotide (NAD⁺) plays a crucial role in cellular energy metabolism and DNA repair, its potential protective effects against repeated UVB-induced skin damage remain largely unexplored. This study investigates the effectiveness of topical NAD⁺ in repairing skin damage caused by prolonged UVB exposure in C57BL/6NJcL mice. The mice were subjected to sub-minimal erythema dose (sub-MED) UVB radiation three times per week for 12 weeks. Immediately following each UVB exposure, the treatment group received a topical NAD⁺ cream, while the vehicle group and other controls served as comparisons. Skin biopsies were collected and analyzed at the end of the study to assess histological changes. The NAD⁺-treated mice exhibited thinner epidermal layers and less epidermal dysplasia than those in the vehicle control group. Interestingly, while the vehicle-treated group, which provided a moisturizing effect, showed some reduction in skin thickness, it did not significantly decrease epidermal dysplasia compared to the UVB-only group. This suggests that NAD⁺ aids in epidermal repair beyond just moisturization. These initial results indicate that NAD⁺ may play a role in repairing long-term UVB-induced skin damage at the molecular level. However, further research is necessary to determine its potential in preventing skin cancer.

Keywords: Nicotinamide Adenine Dinucleotide; UVB Radiation; chronic skin side effects; photocarcinogenesis; DNA damage

INTRODUCTION

In recent times, the increasing intensity of ultraviolet radiation (UVR) has become a major concern, largely due to the continued depletion of the ozone layer. With UVR stronger than ever, it poses a serious health risk to humans. Acting as both a direct mutagen and an indirect tumor promoter, UVR is classified as a human carcinogen and is a main contributor to skin damage, particularly from UVB exposure (1).

Persistent exposure to UV radiation leads to more serious consequences. Photoaging, characterized by solar elastosis, accelerates skin aging, resulting in wrinkles and reduced elasticity which mostly caused by inflammation and generation of reactive oxygen species (ROS). Photocarcinogenesis is the process by which UV radiation causes DNA damage especially from photoproduct called cyclobutane pyrimidine dimers (CPDs), heightening the risk of skin cancer as a long-term effect (9).

Among the many preventive methods, sunscreen remains one of the most widely recognized and effective solutions. Extensive research has been conducted over the years to enhance its quality and effectiveness. However, despite awareness of its importance, several factors cause people to forget to apply sunscreen before sun exposure. Additionally, potential side effects like skin irritation or allergic reactions can discourage consistent use (2).

Nicotinamide adenine dinucleotide (NAD⁺) is a vital coenzyme involved in redox reactions essential for adenosine triphosphate (ATP) production, various metabolic processes such as glycolysis, fatty acid oxidation, and the citric acid cycle, DNA repair and immune function. Maintaining adequate NAD⁺ level is crucial for genomic stability and cellular energy. Thus, NAD⁺ could be thought to aid in chemoprophylaxis by facilitating DNA damage response and reducing UV-induced immunosuppression. Considering this, the 2020 recommendations from the Journal of the American Academy of Dermatology support the use of oral nicotinamide (precursor of NAD⁺) at a dosage of 500 mg twice daily for 12 months in individuals with a cutaneous skin cancer. The incidence of new Nonmelanoma skin cancer (NMSC) and Actinic Keratosis (AK) were notably lower in the group receiving nicotinamide compared to the placebo group with further reductions when continue follow up (3).

However, we would like to study Nicotinamide in a topical formulation. Topical administration of NAD⁺ may be more effective than oral dosing in skin conditions because of localized delivery and quicker absorption into the skin without unwanted side effects such as nausea, vomiting or diarrhea from oral medication (6). Therefore, our research aims to examine NAD⁺ as a topical medication ingredient by studying their cellular mechanisms and potential to help the skin recover after sun exposure, as well as their ability to prevent epidermal transformation into dysplasia lesions.

MATERIALS AND METHODS

Materials

1. Animals
 - Female C57BL/6NJcL mice aged 6 weeks were purchased from Nomura Siam International.
2. Experimental substance
 - NAD⁺ were purchased via Cayman chemical; CAS 53-84-9 with 5% concentration.
 - Vehicle cream - standard cream base
3. Other equipment
 - UV exposure chamber made of black polyvinyl chloride boards with size 60*20*20 inches
 - Two broadband UVB lamps 120cm of Philips F40T12/12RS TL40W/12RS
 - UVAB light meter of Tenmars TM-223
 - Digital camera Nikon D5500, compact DSLR
 - Puluz studio box 25*25cm
 - Codos CP-5200 pet hair trimmer
 - Veet hair removal cream aloe vera & vitamin E sensitive skin

Methods

Animal experiment

The study protocol received approval from Thammasat University's Ethical Committee and was carried out in accordance with the Ethical Principles and Guidelines for the Use of Animals for Scientific Purposes. Female C57BL/6NJcL mice aged 6 weeks were housed at Laboratory Animal Center, Thammasat University, and the experiment was performed under institutional animal care and use committee (IACUC) guidelines.

The mice were assigned to four groups, with each group consisting of three mice: Group A served as the normal control; Group B was exposed to UVB without any topical treatment; Group C received a vehicle application 20 minutes after UVB exposure; and Group D was treated with 5% NAD⁺ 20 minutes after UVB exposure. Prior to the experiment, all mice were anesthetized using an inhaled isoflurane mask, and the hair on their dorsal side was removed using a pet trimmer and hair removal cream every two weeks. At the beginning of each procedure, anesthesia was administered in a chamber then, biweekly photographs of each mouse were taken using a compact DSLR camera before radiation exposure.

Groups B through D were exposed to UVB radiation for 4 minutes every other day, three times per week for a total of 12 weeks, using a dose of 120 mJ/cm² (representing the sub-minimal erythema dose for this mouse strain to induce precancerous lesions). Two broadband UVB lamps were used, positioned 30 cm above the floor within a UV exposure chamber. To ensure uniform UV energy distribution, the position of each group within the chamber was rotated during each exposure session. After each UVB irradiation, a 20-minute interval was observed before applying 200 μ l of either the vehicle cream or 5% NAD⁺ cream to the dorsal skin of the mice, according to the group-specific protocol.

Histological assessment

At week 12 of the experiment, tissue samples were obtained from the dorsal skin of all mice using a 4-mm punch biopsy. The collected skin specimens were fixed in 10% neutral-buffered formalin, embedded in paraffin, sectioned, and mounted onto serial slides. Hematoxylin and eosin (H&E) staining was performed for histological evaluation. Epidermal thickness was measured using the scale bar tool provided by the Motic Digital Slide Assistant software, which is designed for analyzing microscope slide images. Epidermal thickness was assessed by taking measurements at 10 different locations on each skin sample. The average epidermal thickness for each group was then calculated and compared across control and treatment groups. A pathologist evaluated the histological slides for abnormal epidermal cell features in each group. Additionally, the average percentage of lesion area in each biopsy was determined by dividing the length of the lesion by the total length of the skin biopsy.

Statistical analyses

Statistical analyses were performed using GraphPad Prism 10.0 software. The sample size (n) was 12. All group comparisons were conducted with Kruskal-Wallis test, and comparisons between two groups were used Mann-Whitney test. A difference with a p-value of < 0.05 was considered statistically significant.

RESULTS AND DISCUSSION

Results and Discussions

Epidermal thickness

To assess the efficacy of topical NAD⁺ in preventing long-term skin damage, epidermal thickness was measured in skin biopsies from each mouse in all groups at week 12 of the experiment. Group B (UVB without topical treatment) exhibited the greatest epidermal thickness, followed by Group C (vehicle), Group D (5% NAD⁺), and Group A (no UVB exposure), respectively. These results were consistent with the minimum and maximum values recorded for each group, see Table 1.

Group	Mean (μm) \pm SD	Min	Max	[95% Conf. Interval]
A	13.23 \pm 2.81	8.4	17.2	[12.18, 14.28]
B	41.71 \pm 7.40	28.5	57.6	[38.94, 44.46]
C	28.82 \pm 6.50	17.6	45	[26.39, 31.25]
D	16.25 \pm 4.40	10.6	26.9	[14.50, 17.79]

Table 1. Epidermal thickness results of each group

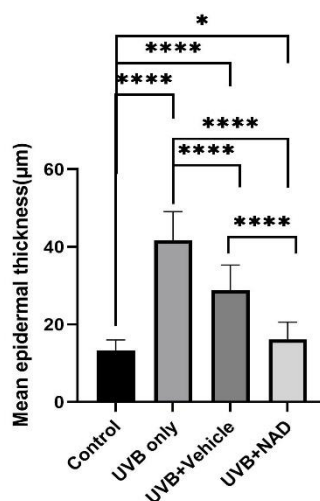


Figure 1. Bar chart of average epidermal thickness of each group

Figure 1 illustrated the average epidermal thickness across the control, UVB-irradiated, vehicle-treated, and NAD⁺-treated groups. The UVB-unexposed control group showed a statistically significant difference in epidermal thickness compared to all UVB-exposed groups, although the difference was minimal when compared to the NAD⁺-treated group. In contrast, both the UVB-only and vehicle-treated groups exhibited significantly greater epidermal thickness compared to the NAD⁺ group. Bars indicate the mean, and error bars represent the SD. Mann-Whitney test was used for analysis. *, $p < 0.05$. ****, $p < 0.0001$. SD, standard deviation.

Prolonged UVB exposure is known to trigger hyperproliferative responses in the epidermis, leading to acanthosis and abnormal keratinocyte differentiation. Previous studies investigated the effects of chronic low-dose UV irradiation in mice, revealing that it induced photoaging, characterized by wrinkle formation that persisted even after exposure ended. UV irradiation also caused epidermal thickening (hyperkeratosis), a protective adaptation to further damage (7). Moreover, other research demonstrated that continuous application of topical agents with anti-inflammatory and antitumor properties can reduce keratinocyte proliferation in mice (4).

NAD⁺ plays a role in cellular repair, stress response, and inflammation regulation by activating sirtuins (SIRT), which are NAD⁺-dependent deacetylase enzymes. SIRT contribute to various skin-related processes, including reducing skin inflammation, protecting against UV damage, and aiding wound healing (10). Thus, our study suggested that NAD⁺ can mitigate epidermal damage, as evidenced by reduced epidermal thickness compared to both the non-treated and vehicle-treated groups. Although the NAD⁺ group differed from the UVB-unexposed group, the difference was minimal, and its raw data was most similar to that of the control group, suggesting it was the most effective treatment among the others.

Histopathology of dysplastic cells

Lesions exhibiting features of epidermal dysplasia were assessed using digital microscopy at 40x magnification (Figure 2). No dysplastic lesions were observed in Group A (non-exposed control). Group C (vehicle-treated) showed the highest average percentage of dysplasia, followed by Group B (UVB-only) and Group D (NAD⁺-treated), see Table 2. The non-irradiated control group differed significantly from all UVB-exposed groups. Statistically, there was no significant difference between the UVB-only and vehicle-treated groups. However, both of these groups showed a significant increase in dysplastic lesion percentage compared to the NAD⁺-treated group, see Figure 3. Bars indicate the mean, and error bars represent the SD. Mann-Whitney test was used for analysis. *, $P < 0.05$. **, $P < 0.002$. ns, not statistic significant. SD, standard deviation.

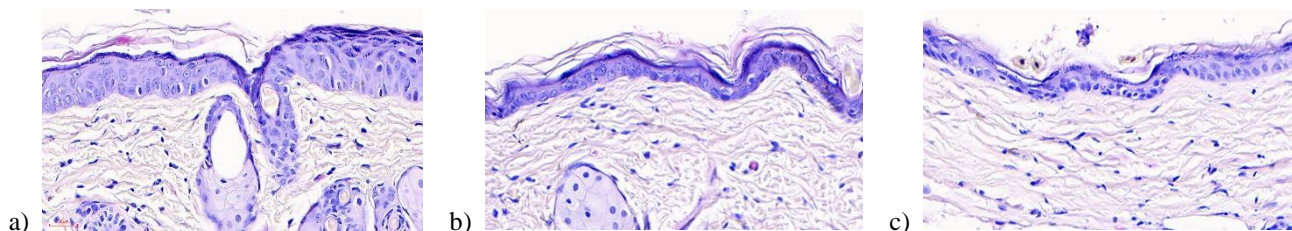


Figure 2. Representative H&E staining of UVB only (a) vehicle (b) and NAD group (c). Red bars represent 30 μ m.

Group	Mean (%) \pm SD	Min	Max	[95% Conf. Interval]
A	0	0	0	[0, 0]
B	70.62 \pm 2.81	48.4	95.7	[51.07, 90.16]
C	76.57 \pm 8.08	64.6	89	[68.08, 85.05]
D	15.03 \pm 7.91	5.2	24.5	[6.73, 23.3]

Table 2. Epidermal dysplasia results of each group

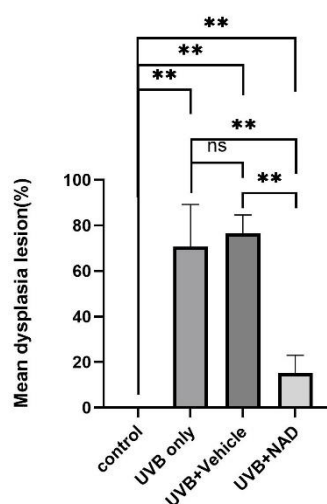


Figure 3. Bar chart of average percentage of dysplastic lesion of each group

The DNA repair system comprises several mechanisms, including base excision repair (BER), nucleotide excision repair (NER), and double-strand break repair (DSBR), all of which involve complex pathways and numerous proteins. A key enzyme in this system is Poly(ADP-ribose) polymerase (PARP), which acts as a DNA damage sensor and plays a vital role in DNA repair and replication. PARP uses NAD⁺ as a substrate to synthesize poly(ADP-ribose) (PAR) chains and transfers them to target proteins via ADP-ribosylation. In addition, several DNA repair proteins—such as DNA ligases I and III—require ATP for their activity. Therefore, enhancing ATP production in UV-irradiated cells may improve DNA repair efficiency and reduce the risk of mutation formation (8).

In this study, dysplastic cells were identified as indicators of long-term UVB-induced damage that may represent an early sign of photocarcinogenesis. The NAD⁺ treated group exhibited a significantly lower percentage of abnormal lesions compared to the UVB-only group and vehicle group. Interestingly, while the vehicle group provided a moisturizing effect that reduced epidermal thickening, it did not influence the reduction of skin mutations. This suggests that topical NAD⁺ effectively reduces skin side effects from repeated UVB exposure beyond surface-level hydration and involve molecular mechanisms such as DNA repair enhancement.

Limitations of this study include a small sample size (n=12). The variation in hair cycle among the mice may have affected the skin area exposed to UV. Future studies should explore the enduring effects of NAD⁺ treatment, including its effect on tumor development over extended periods and in models that simulate the full UV spectrum.

CONCLUSIONS

In conclusion, this research investigated the potential of topical NAD⁺ cream to prevent skin damage from long-term UVB exposure using a murine model. The results indicated that topical NAD⁺ had beneficial effects in reducing epidermal thickness and epidermal dysplasia which were the key markers of photodamage. However, further studies are needed to assess the cream's effectiveness in larger sample sizes and different models. Ultimately, this research provides a basis for continued exploration and progress in chemoprevention.

ACKNOWLEDGMENTS

The authors would like to express their gratitude to Department of Dermatology, Chulabhorn International College of Medicine for providing the facilities and resources necessary for this research, and also the staff from the department for their invaluable assistant throughout this research. Appreciation is also extended to the laboratory staff, Dr. Werayut Yingmema, DVM., Deputy Director of the Laboratory Animal Center, Thammasat University and Miss Sukanya Maison, Animal Husbandry Technical Officer, Professional level whose contributions are essential to the successful completion of this experiment.

REFERENCES

1. Watson M, Holman DM, Maguire-Eisen M. Ultraviolet radiation exposure and its impact on skin cancer risk. *Semin Oncol Nurs.* 2017; 32(3):241-54.
2. Rai R, Srinivas C. Photoprotection. *Indian J Dermatol Venereol Leprol.* 2007;73:73-9.
3. Chen AC, Martin AJ, Choy B, et al. A phase 3 randomized trial of nicotinamide for skin cancer chemoprevention. *N Engl J Med.* 2015 Oct 22;373(17):1618-26.
4. Bordeaux ZA, Choi J, Braun G, et al. Topical GZ21T Inhibits the Growth of Actinic Keratoses in a UVB Induced Model of Skin Carcinogenesis. *JID innovations.* 2023;3(4).
5. Gyöngyösi N, Lőrincz K, Keszeg A, et al. Photosensitivity of murine skin greatly depends on the genetic background: clinically relevant dose as a new measure to replace minimal erythema dose in mouse studies. *Exp Dermatol.* 2016 Jul; 25(7):519-25.
6. Kang S, Park J, Cheng Z, et al. Novel Approach to Skin Anti-Aging: Boosting Pharmacological Effects of Exogenous Nicotinamide Adenine Dinucleotide (NAD⁺) by Synergistic Inhibition of CD38 Expression. *Cells.* 2024 Oct 30;13(21):1799.
7. Kambayashi H, Yamashita M, Odake Y, et al. Epidermal changes caused by chronic low-dose UV irradiation induce wrinkle formation in hairless mouse. *J Dermatol Sci.* 2001 Aug;27 Suppl 1:S19-25.
8. Fania L, Mazzanti C, Campione E, et al. Role of Nicotinamide in Genomic Stability and Skin Cancer Chemoprevention. *Int J Mol Sci.* 2019 Nov 26;20(23):5946.
9. Kang S. *Fitzpatrick's Dermatology.* 9th ed. The United States: McGraw-Hill Education; 2019.
10. Su S, Ndiaye M, Singh CK, Ahmad N. Mitochondrial Sirtuins in Skin and Skin Cancers. *Photochem Photobiol.* 2020 Sep;96(5):973-980.

Investigation of Trikatu Remedy: Potential Anti-Amyloid Beta and Antioxidant Effects in a *Caenorhabditis elegans* Alzheimer's Model

Harunchai Paecharoenchai¹, Worapan Sitthithaworn², and Roongpetch Keowkase^{1,*}

¹Department of Biopharmacy, Faculty of Pharmacy, Srinakharinwirot University, Nakhon Nayok, THAILAND

²Department of Pharmacognosy, Faculty of Pharmacy, Srinakharinwirot University, Nakhon Nayok, THAILAND

*Corresponding author Email: roongpet@g.swu.ac.th

Abstract. Alzheimer's disease (AD) is a leading cause of dementia, marked by pathological protein aggregation, including amyloid-beta (A β) plaques and neurofibrillary tangles. Current treatments offer only symptomatic relief, emphasizing the need for alternative approaches targeting disease mechanisms. Trikatu remedy, containing ginger, black pepper, and Java long pepper, has previously demonstrated antioxidant, anti-inflammatory, and neuroprotective properties. However, its effects on A β toxicity and oxidative stress remain unexplored. This study investigated the pharmacological effects of the Trikatu remedy on anti-A β toxicity and antioxidant activity in *Caenorhabditis elegans* (*C. elegans*), a widely used model organism in Alzheimer's disease research. The transgenic *C. elegans* CL4176 strain expressing human A β in body wall muscle was used to assess paralysis, while oxidative stress resistance assay was conducted in wild-type *C. elegans*. Trikatu extract was prepared using equal amounts of each herb (1:1:1) through water extraction and spray drying. It was tested at varying concentrations (10, 100, and 1,000 μ g/mL) along with its primary active components, including piperine and 6-shogaol. Kaplan-Meier survival analysis was used to determine therapeutic potential. We found that Trikatu 10 μ g/mL significantly delayed A β -induced paralysis with median paralysis time (PT_{Mdn}) 28 hours compared with a control group (PT_{Mdn} = 26 hours, $p < 0.0001$). Oxidative resistance also found in 10 μ g/mL of Trikatu by median survival time (ST_{Mdn}) at 3 hours compared with the control (ST_{Mdn} = 2 hours, $p = 0.0005$). These findings suggest potential activity on anti-A β toxicity and antioxidant effect of Trikatu, which require further investigation into its molecular mechanisms of action.

Keywords: Trikatu remedy; Alzheimer's disease; *Caenorhabditis elegans*; Amyloid beta; Antioxidant

INTRODUCTION

Aging is a risk factor for various diseases, including cognitive impairment, which can lead to dementia. Alzheimer's disease is the most common cause of dementia, caused by an accumulation of proteins called amyloid beta (A β) and neurofibrillary tangles (NFTs) or hyperphosphorylated tau protein. These toxic proteins could lead to cell dysfunction and death.^[1] Current treatment offered only symptomatic relievers of the disease by compensation of imbalanced neurotransmitters.^[2] Therefore, preventive treatment of Alzheimer's disease remains challenging. The transgenic *Caenorhabditis elegans* (*C. elegans*) model for Alzheimer's disease was the most common model of study with several advantages including short life cycle, ease of observation, numerous orthologues in humans, and low maintenance cost. This model provides the amyloid cascade hypothesis, which was expressed by progressive paralysis. A β aggregation can induce oxidative stress and inflammation. It also involves with the insulin/insulin-like growth factor-1 signaling (IIS) pathway, which is the established pathway that associates with aging and proteotoxicity.^[3] Both processes are the target for disease-modifying interventions.

Trikatu is a traditional Ayurvedic polyherbal remedy composed of three potent spices: ginger (*Zingiber officinale* Roscoe), black pepper (*Piper nigrum* L.), and long pepper (*Piper retrofractum* Vahl) in equal proportions.^[4] It is widely used to alleviate gastrointestinal disorders, and also known for its anti-inflammatory, antiallergic, antioxidant, and anthelmintic properties.^[5] The primary bioactive components are gingerol and shogaol. Studies have demonstrated the antioxidant properties of 6-gingerol and 6-shogaol, contributing to neuroprotection and cholinesterase inhibition.^[6] Moreover, gingerol and 6-shogaol from ginger inhibit A β peptide aggregation and enhance neuroprotection in Alzheimer's models^[7], while piperine from black pepper modulates amyloidogenic pathways.^[8] Although various studies have explored the pharmacological benefits of Trikatu and its active compounds, the mechanisms underlying its effects on neurodegenerative disease, particularly with A β toxicity hypothesis in Alzheimer's disease remain unclear. This study aims to investigate the pharmacological effects of Trikatu remedy on anti-amyloid beta toxicity and antioxidant activity in *Caenorhabditis elegans* Alzheimer's model.

MATERIALS AND METHODS

Materials

Trikatu remedy was prepared by boiling equal amounts of dried long pepper, black pepper, and ginger. The mixture of herbal powder 300 mg was boiled in 2,000 mL deionized water for 5 minutes. Then, vacuum filtration was used to separate the supernatant

*Corresponding author: roongpet@g.swu.ac.th

Presenting author: harunchai@g.swu.ac.th

from the sediment. The supernatant was spray dried with a Buchi mini spray dryer B-290 (Buchi labortechnik AG, Flawil, Switzerland). The yield of brownish extracted powder was 49 mg/g after water removal and contained piperine at 2.7 µg/mg of powder. Standard piperine (CAS RN 94-62-2) and 6-shogaol (CAS RN 555-66-88) were purchased from Tokyo Chemical Industry (TCI), Japan. Paraquat (CAS RN 75365-73-0) was purchased from Sigma-Aldrich. The transgenic *C. elegans* strains CL4176, CL802, and wild-type N2 were obtained from the Caenorhabditis Genetic Center (CGC, University of Minnesota). They were incubated at 20 °C for N2 and 16 °C for transgenic strains.

Methods

C. elegans model strains and maintenance

The transgenic *C. elegans* CL4176 strain was used for paralysis assay, CL802 strain was used as a control strain for CL4176, and wild-type (N2) strain was used for oxidative stress resistance assay. They were maintained on a petri dish filled with nematode growth media (NGM) and seeded with *Escherichia coli* (*E. coli*) strain OP50 as a food source. Worms were prepared for each experiment by transferring adult worms onto fresh NGM plates and allowing them to lay eggs for 4-6 hours to ensure age-synchronization.

Trikatu stock solutions and standard extracts preparation

Stock solutions of Trikatu were prepared using distilled water and OP50 as solvents. They were diluted to the desired test concentrations of 10, 100, and 1,000 µg/mL. Standard extracts were prepared using DMSO and OP50 as solvents and diluted to 100 µg/mL with a final DMSO content of 1% to prevent toxicity. Each extract was seeded and left overnight at room temperature before worm transfer.

Oxidative stress resistance assay

Age-synchronized wild-type *C. elegans* eggs were treated with various concentrations of Trikatu, or with the standard compounds, until they reached the L4 stage at approximately 56 hours. They were then collected and transferred into 96-wells plate containing 40 µL of M9 buffer (3 g KH₂PO₄, 6 g Na₂HPO₄, 5 g NaCl, and 0.25 g MgSO₄ · 7H₂O) with 100 mM paraquat, with 6 worms per well. Worms were monitored at 1-hour intervals until the last worm died.

Paralysis assay

After egg synchronization of the transgenic *C. elegans* CL4176 strain, eggs were maintained at 16 °C for 36 hours until they reached the L3 stage. The temperature was then upshifted to 25 °C to induce Aβ-producing gene expression. Scoring began 24 hours after the temperature upshifting at 2-hour intervals. Worm that was immobilized or exhibited only head movement when touched with a platinum loop was scored as paralyzed.

Statistical analyses

Data were reported as mean ± SD from at least 3 independent experiments. Each experiment included a minimum of 100 worms per group. Median paralysis time (PT_{Mdn}) and survival time (ST_{Mdn}) were calculated from the median value of each survival curve. Survival and paralysis curves were generated using GraphPad Prism 10 software. Kaplan-Meier survival analysis and log-rank (Mantel-Cox) tests were used to determine the significant difference between treated and control groups. A *p*-value < 0.05 was considered statistically significant.

RESULTS AND DISCUSSION

Results

Paralysis assay was conducted to determine the potential effects of the extracts on Aβ-toxicity alleviation using CL4176 strain. Trikatu extract at 10 µg/mL significantly delayed paralysis to 28 hours (*p*<0.0001). Other concentrations did not show the benefit on paralysis delay (26 hours by 100 and 1,000 µg/mL of Trikatu, *p*=0.2019 and *p*=0.1121, respectively). Moreover, piperine and 6-shogaol also showed a significant delay in paralysis to 28 hours (*p*<0.0001). The *C. elegans* CL802 strain was used as a control for CL4176. Paralysis was not observed in this strain following the temperature upshift (Figure 1, Table 1).

For paraquat-induced oxidative stress experiments in wild-type *C. elegans*, we found that Trikatu extract at 10 µg/mL significantly extended survival to 3 hours, compared with 2 hours in non-treated group (*p*=0.005). In contrast, higher concentrations of Trikatu extract did not show the benefit of oxidative resistance. Trikatu 100 µg/mL was not different from the control group (*p*=0.2489), and 1,000 µg/mL of the extract worsened the resistance effect (*p*=0.0432). Epigallocatechin Gallate (EGCG), a polyphenolic compound from green tea was used as a positive control. It was found that EGCG 100 µg/mL increased survival to 4 hours (*p*<0.0001). We found that 1% DMSO used as solvent significantly extended survival from 2 to 3 hours compared with OP50

($p < 0.0001$). However, piperine 100 $\mu\text{g/mL}$ and 6-shogaol 100 $\mu\text{g/mL}$ failed to protect against oxidative stress induced by paraquat (Figure 2, Table 2).

Table 1. Paralysis assay on *C. elegans* CL4176 strain treated with Trikatu at 10, 100, and 1,000 $\mu\text{g/mL}$ and standard compounds

Experiment	Treatment	Median paralysis time (PT _{Mdn} , hours)	Significant
1	OP50	26	
	Trikatu 10 $\mu\text{g/mL}$	28	$p < 0.0001^*$
	Trikatu 100 $\mu\text{g/mL}$	26	$p = 0.2019$
	Trikatu 1,000 $\mu\text{g/mL}$	26	$p = 0.1121$
2	DMSO 1% v/v	26	
	Piperine 100 $\mu\text{g/mL}$	28	$p < 0.0001^{\#}$
	6-shogaol 100 $\mu\text{g/mL}$	28	$p < 0.0001^{\#}$
3	OP50	26	
	DMSO 1% v/v	26	$p = 0.2575$
4	CL4176	26	
	CL802	-	$p < 0.0001^*$

Table 2. Oxidative stress resistance assay on wild-type *C. elegans* treated with Trikatu at 10, 100, and 1,000 $\mu\text{g/mL}$ and standard compounds

Experiment	Treatment	Median survival time (ST _{Mdn} , hours)	Significant
1	Control (OP50)	2	
	Trikatu 10 $\mu\text{g/mL}$	3	$p = 0.0005^*$
	Trikatu 100 $\mu\text{g/mL}$	3	$p = 0.2489$
	Trikatu 1,000 $\mu\text{g/mL}$	2	$p = 0.0432^*$
2	DMSO 1% v/v	3	
	Piperine 100 $\mu\text{g/mL}$	4	$p = 0.8240$
	6-shogaol 100 $\mu\text{g/mL}$	3	$p = 0.0216^{\#}$
3	Control (OP50)	2	
	EGCG 100 $\mu\text{g/mL}$	4	$p < 0.0001^*$
4	Control (OP50)	2	
	DMSO 1% v/v	3	$p < 0.0001^*$

*Significantly different from OP50 control at a p -value < 0.05 .

$^{\#}$ Significantly different from DMSO 1% v/v control at a p -value < 0.05 .

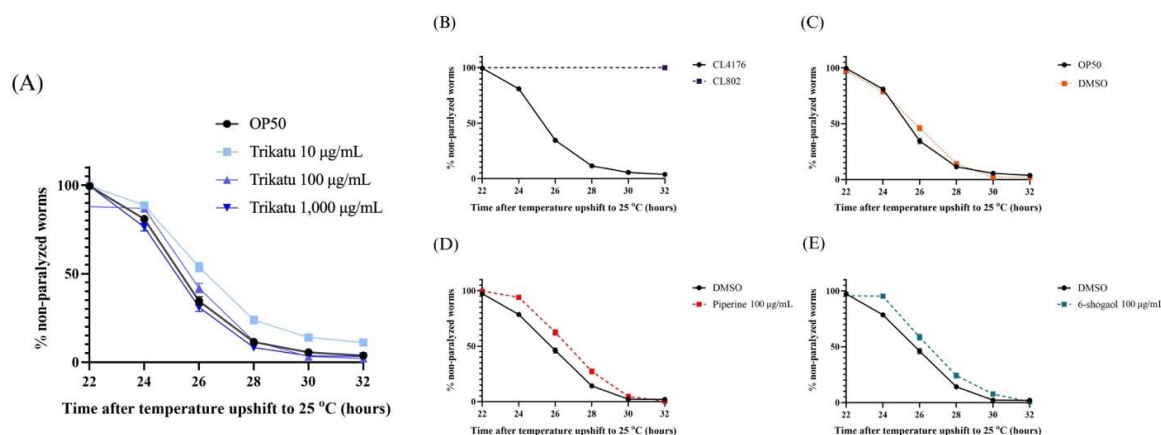


Figure 1. Effect of Trikatu, EGCG, DMSO, piperine and 6-shogaol on paralysis assay using *C. elegans* CL4176 strain. Worms were treated with OP50 containing vehicle (control) or Trikatu (10, 100, and 1,000 $\mu\text{g/mL}$) (A), compared with CL802 strain (B), DMSO 1% v/v vehicle (C). Piperine 100 $\mu\text{g/mL}$ (D) and 6-shogaol 100 $\mu\text{g/mL}$ (E) were compared with DMSO 1% v/v as a solvent. Worms were maintained at 16 °C until they reached L3 stage and then upshifted to 25 °C to induce A β -producing gene expression. The paralysis was scored at 2-hour intervals. Data were shown as percentage of worms not paralyzed.

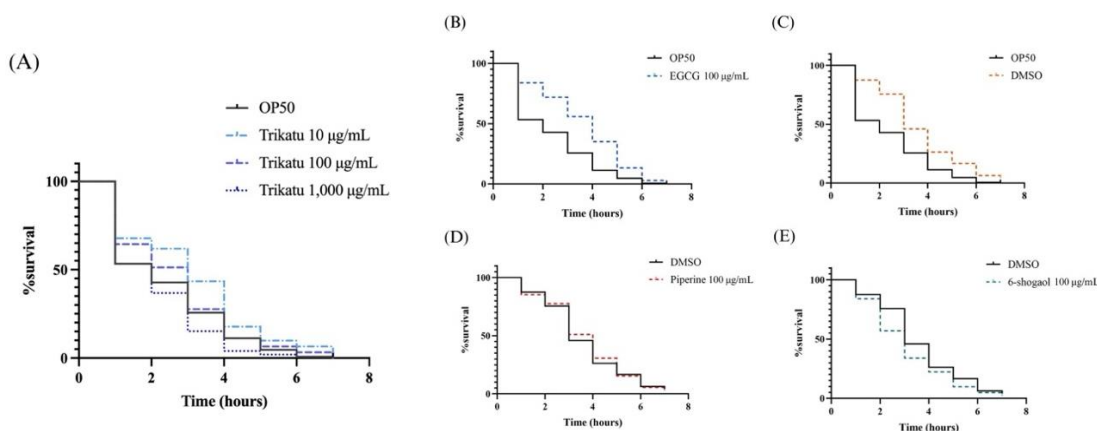


Figure 2. Effect of Trikatu, EGCG, DMSO, piperine and 6-shogaol on oxidative resistance induced by paraquat at 100 mM using wild-type *C. elegans*. Worms were treated with OP50 containing vehicle (control) or Trikatu (10, 100, and 1,000 µg/mL) (A), EGCG 100 µg/mL (B), DMSO 1% v/v vehicle (C). Piperine 100 µg/mL (D) and 6-shogaol 100 µg/mL (E) were compared with DMSO 1% v/v as a solvent. Worms were transferred to 96-well plate containing 40 µL of M9 buffer with 100 mM paraquat and then monitored at 1-hour intervals until the last worm died. Data were shown as percentage of survival.

Discussions

This study was a pilot study of using Trikatu remedy, extracted with distilled water to mimic traditional use, in a 1:1:1 ratio of each herb in a *C. elegans* animal model. The protective effect of Trikatu against A β and oxidative stress resistance were observed at a concentration of 10 µg/mL, which may represent an optimal concentration for further investigation. Paralysis assays with piperine and 6-shogaol also demonstrated protective effects, consistent with existing evidence of gingerol and 6-shogaol in inhibiting A β aggregation in mice model^[7], as well as piperine's role in modulating the amyloidogenic pathway.^[8]

For oxidative resistance, paraquat was used to generate the oxidative stress by inducing mitochondrial dysfunction and increasing reactive oxygen species (ROS) production. This herbicide exposure can lead to gene expression and lifespan change.^[9] Although our study showed no difference between piperine and 6-shogaol and DMSO 1% v/v as a vehicle control in oxidative resistance, previous reports have indicated that gingerol and 6-shogaol exert marked positive effects on lifespan and stress resistance. 6-shogaol also reported with the capacity of stress resistance by increasing superoxide dismutase (SOD) and heat-shock protein (HSP) expression in a *C. elegans* model. This discrepancy may result from methodological differences, such as the use of thermal, osmotic, and oxidative stress model using 1 mM of juglone.^[10-12] Juglone and paraquat are both commonly used for stress induction, but differ in concentrations, exposure rate, and ROS-generating mechanisms may produce a different outcome.^[13] Moreover, differences in worm developmental stage, variation in an amount of food source, and the interaction between *E. coli* and the tested compound could also affect the survival outcomes.^[14] In addition, antioxidant capacity of previous findings in ginger may result from other components, such as gingerols.^[11] Thus far, antioxidant effect of piperine and 6-shogaol may still be unclear based on our findings.

The antioxidant activity of Trikatu may in part contribute to the extended paralysis time. Studies on ginger components have demonstrated increased activity of superoxide dismutase (SOD) and catalase enzyme, along with upregulated expression of SOD-3 and heat shock protein HSP-16.2.^[10, 11] These effects may contribute to reduced A β toxicity and are also associated with anti-aging mechanisms.^[15] Gene regulation effects have also been observed with ginger extract, which promotes the translocation of DAF-16 and SKN-1 within the IIS pathway.^[16] This pathway involves with aging and proteotoxicity, particularly through its role in modulating A β peptides, which may represent a mechanism underlying the delay in paralysis observed in the *C. elegans* model.

Both experiments revealed that higher dose of Trikatu worsened worm paralysis and declined survival rates. Trikatu toxicity has been assessed only in murine model, where it was reported to be well tolerated both in acute toxicity at a dose of 2,000 mg/kg body weight and in long term administration at doses up to 300 mg/kg body weight for 28 days.^[17] In contrast, high doses of piperine have been reported as toxic when given intravenously to adult mice, with a lethal dose (LD₅₀) of 15.1 mg/kg body weight.^[18] Additionally, Trikatu exhibited anthelmintic effects by inducing paralysis in adult earthworms at a concentration of 4 mg/mL.^[19] In our experiments, Trikatu at concentrations above 10 µg/mL led to the formation of a small, thick, round film on the OP50 lawn, which appeared to slow worm movement. Therefore, higher doses may exert direct toxic effects or contribute to the behavioral changes observed in our study. Our study suggested that Trikatu at 10 µg/mL is an appropriate dose for further investigation and lower concentration should be evaluated to better determine the effect of the remedy.

Our findings support the anti-A β toxicity and oxidative resistance effects of Trikatu at 10 µg/mL. However, other possible mechanisms may also contribute to A β toxicity resistance. The toxicity profile of Trikatu in *C. elegans* remains unclear and requires

further studies to confirm an appropriate neuroprotective dose without adverse effects. Additionally, the potential synergistic effects of the components in Trikatu have not yet been studied and should be investigated by comparing its effects with those of individual constituents such as piperine and 6-shogaol.

CONCLUSIONS

This study shows that Trikatu extract at a concentration of 10 µg/mL reduces amyloid beta toxicity and enhances resistance to oxidative stress. The anti-Aβ toxicity property is likely attributed to its main components, piperine and 6-shogaol. Future study will investigate the relationship between delayed paralysis and oxidative stress, elucidate the underlying molecular mechanisms, assess effects on longevity, and explore the potential synergistic actions of piperine and 6-shogaol to validate the pharmacological efficacy of this remedy.

ACKNOWLEDGMENTS

The authors acknowledge the Research Unit for Drug Discovery and Development, Faculty of Pharmacy, Srinakharinwirot University, for providing research facilities. This research project was supported by the Fundamental Fund from the National Science Research and Innovation Fund (Grant No. 032/2567), and by The Graduate School of Srinakharinwirot University.

REFERENCES

1. Yarns BC, Holiday KA, Carlson DM, Cosgrove CK, Melrose RJ. Pathophysiology of Alzheimer's Disease. *Psychiatr Clin North Am.* 2022;45(4):663-76.
2. Neurological Institute of Thailand. Clinical practice guideline for Dementia. Bangkok: Tanapress; 2020. 326 p.
3. Sano T, Ochiai T, Nagayama T, Nakamura A, Kubota N, Kadowaki T, et al. Genetic Reduction of Insulin Signaling Mitigates Amyloid-β Deposition by Promoting Expression of Extracellular Matrix Proteins in the Brain. *J Neurosci.* 2023;43(43):7226-41.
4. Pichansoonthon C, Jirawongse V. Traditional Thai Pharmacy Manual: Herbal Formulas. Vol. 5. 3 ed. Bangkok: Amarin Printing and Publishing; 2013. 352 p.
5. Kaushik R, Jain J, Khan AD, Rai P. Trikatu - A combination of three bioavailability enhancers. *Int J Green Pharm.* 2018;12(3):S437-41.
6. Tappayuthpijarn P, Sattaponpan C, Sakpakdeecharoen I, Ittharat A. Cholinesterase Inhibitory and Antioxidant Activities of Thai Traditional Remedies Potentially Used for Alzheimer's Disease. *TJEAS.* 2012;17(1):18-25.
7. Fajrin FA, Permatasari D, Asdar D, Dewi IP. Neuroprotective Activity of Ethanolic Extract of Red Ginger Containing 6-Shogaol on Scopolamine-Induced Memory Impairment in Alzheimer's Mice. *Biomed Pharmacol J.* 2023;16(1):145-56.
8. Manap ASA, Madhavan P, Vijayabalan S, Chia A, Fukui K. Explicating anti-amyloidogenic role of curcumin and piperine via amyloid beta (Aβ) explicit pathway: recovery and reversal paradigm effects. *PeerJ.* 2020;8:e10003.
9. Hernández-Cruz EY, Eugenio-Pérez D, Ramírez-Magaña KJ, Pedraza-Chaverri J. Effects of Vegetal Extracts and Metabolites against Oxidative Stress and Associated Diseases: Studies in *Caenorhabditis elegans*. *ACS Omega.* 2023;8(10):8936-59.
10. Lee EB, Kim JH, Kim YJ, Noh YJ, Kim SJ, Hwang IH, et al. Lifespan-extending property of 6-shogaol from *Zingiber officinale* Roscoe in *Caenorhabditis elegans*. *Arch Pharm Res.* 2018;41(7):743-52.
11. Lee EB, Kim JH, An CW, Kim YJ, Noh YJ, Kim SJ, et al. Longevity and Stress Resistant Property of 6-Gingerol from *Zingiber officinale* Roscoe in *Caenorhabditis elegans*. *Biomol Ther (Seoul).* 2018;26(6):568-75.
12. Lee EB, Kim JH, An CW, Kim YJ, Noh YJ, Kim SJ, et al. Longevity and Stress Resistant Property of 6-Gingerol from *Zingiber officinale* Roscoe in *Caenorhabditis elegans*. *Biomol Ther (Seoul).* 2018;26(6):568-75.
13. Senchuk MM, Dues DJ, Van Raamsdonk JM. Measuring Oxidative Stress in *Caenorhabditis elegans*: Paraquat and Juglone Sensitivity Assays. *Bio Protoc.* 2017;7(1).
14. Xiong LG, Chen YJ, Tong JW, Gong YS, Huang JA, Liu ZH. Epigallocatechin-3-gallate promotes healthy lifespan through mitohormesis during early-to-mid adulthood in *Caenorhabditis elegans*. *Redox Biol.* 2018;14:305-15.
15. Cohen E, Dillin A. The insulin paradox: aging, proteotoxicity and neurodegeneration. *Nat Rev Neurosci.* 2008;9(10):759-67.
16. Xu T, Tao M, Li R, Xu X, Pan S, Wu T. Longevity-promoting properties of ginger extract in *Caenorhabditis elegans* via the insulin/IGF-1 signaling pathway. *Food Funct.* 2022;13(19):9893-903.
17. Chanda D, Shanker K, Pal A, Luqman S, Bawankule DU, Mani D, et al. Safety evaluation of Trikatu, a generic Ayurvedic medicine in Charles Foster rats. *J Toxicol Sci.* 2009;34(1):99-108.
18. Piyachaturawat P, Glinesukon T, Toskulkao C. Acute and subacute toxicity of piperine in mice, rats and hamsters. *Toxicol Lett.* 1983;16(3-4):351-9.
19. Reddy NLN, Yamini K, Gopal V. Anthelmintic activity of aqueous and ethanolic extract of Trikatu Churna. *J Appl Pharm Sci.* 2011;1(3):140-2.

A Comparative Study of Total Flavonoid Content, Total Phenolic Content, and Antioxidant Potentials of *Aegle marmelos* (L.) Corrêa Extracts from Thailand's Floristic Regions Using Optimized Ultrasonic-Assisted and Heat Reflux Extraction Methods

Pandita Chitphet¹, Darawan Pinthong², Supachoke Mangmool³, Tharita Kitisripanya¹, and Duangjai Tungmunthum^{1,}*

¹Faculty of Pharmacy, Mahidol University, Bangkok, THAILAND

²Faculty of Science, Mahidol University, Bangkok, THAILAND

³Faculty of Pharmacy, Chiang Mai University, Chiang Mai, THAILAND

*Corresponding author Email: duangjai.tun@mahidol.ac.th

Abstract. *Aegle marmelos* (L.) Corrêa or the so-called bael, is a medicinal plant with natural sources of flavonoid and phenolic content, contributing to its antioxidant properties. This study examines Total Flavonoid Content (TFC), Total Phenolic Content (TPC), and Antioxidant Activities i.e. 2,2'-azino-bis(3-ethylbenzothiazoline-6-sulphonic acid) (ABTS) and 1,1-diphenyl-2-picrylhydrazyl (DPPH) assays using Ultrasonic-Assisted Extraction (UAE) and Heat Reflux Extraction (HRE) to investigate their effects. Bael fruit samples from seven provinces across Thailand's floristic regions were analyzed. UAE with ethanol yielded the highest TPC in Chanthaburi (1171.84 ± 0.00 mg% garlic acid equivalent (mg% GAE)), showing a correlation with DPPH activity ($p < 0.05$). In contrast, HRE with water was more effective for phenolic extraction, and Nakhon Ratchasima sample contained the highest TFC (0.11 ± 0.00 µg% quercetin equivalents (µg% QE)) with a statistical difference ($p < 0.05$). For antioxidant potential, Kanchanaburi sample extracted by UAE with ethanol exhibited the highest ABTS activity (1674.64 ± 0.10 mg Trolox equivalent/mL), while Nong Bua Lam Phu sample using HRE with water showed the highest DPPH activity (1392.87 ± 0.00 mg TE/mL). In conclusion, HRE-ethanol more efficiently enhances phenolic and antioxidant yields, while UAE-ethanol is more suitable for flavonoid extract recovery. Regional diversity significantly affected bioactive content, showing the need for tailored extraction to optimize bael's medicinal potential. Bael's strong antioxidant activity suggests its potential to alleviate oxidative stress and inflammation by inhibiting pro-inflammatory pathways leading to cardiovascular, immune and endocrine disorders, arthritis, and neurodegenerative diseases. These findings support bael's use in functional foods and anti-inflammatory treatment.

Keywords: Bael (*Aegle marmelos* (L.) Corrêa); TFC; TPC; Antioxidant; UAE

INTRODUCTION

Aegle marmelos (L.) Corrêa, commonly known as bael, is a medicinal plant belonging to the Rutaceae family and is highly valued for its diverse pharmacological properties, primarily attributed to its rich content of flavonoids and phenolic compounds. The extensive use of bael in traditional medicine for treating ailments associated with oxidative stress, inflammation, metabolic disorders, arthritis, and neurodegenerative diseases has stimulated considerable research interest in exploring its bioactive components and therapeutic potentials (Sharma et al., 2018; Singh & Agrawal, 2020).

The antioxidant activity of bael extracts is primarily linked to the presence of flavonoids and phenolic compounds, which act as potent scavengers of free radicals, thereby mitigating oxidative stress and preventing cellular damage. Moreover, these bioactive compounds have been reported to exhibit anti-inflammatory, anti-carcinogenic, and neuroprotective properties, which contribute to their potential applications in managing chronic health conditions such as cardiovascular diseases, arthritis, and neurodegenerative disorders like Alzheimer's and Parkinson's diseases (Chandrasekaran & Mathuram, 2020; Zhang et al., 2021). Notably, the antioxidant mechanisms of bael are associated with its ability to inhibit pro-inflammatory pathways, enhance cellular antioxidant defenses, and modulate neuronal signaling pathways, suggesting its promising role in preventing or ameliorating oxidative stress-related diseases (Hano & Tungmunthum, 2021; Tungmunthum et al., 2022).

Given the increasing demand for natural antioxidants and their therapeutic benefits, optimizing extraction techniques to enhance the recovery of phenolic and flavonoid compounds from bael fruit has become a critical focus of research. Various extraction methodologies, including Ultrasonic-Assisted Extraction (UAE) and Heat Reflux Extraction (HRE), have been employed to improve the yield and antioxidant activity of bael extracts (Patel & Goyal, 2017; Wang et al., 2022). The studies conducted by Tungmunthum et al. have provided valuable insights into the optimization of extraction methods for improving the recovery of bioactive compounds and enhancing antioxidant efficacy (Tungmunthum et al., 2018; Tungmunthum & Hano, 2020). Furthermore, the work of Hano and colleagues has demonstrated the importance of optimizing extraction parameters to maximize phenolic yield and antioxidant activity (Hano & Tungmunthum, 2021; Hano et al., 2022).

This study aims to comparatively evaluate the efficiency of UAE and HRE methods in maximizing Total Flavonoid Content (TFC), Total Phenolic Content (TPC), and antioxidant activities of *Aegle marmelos* (L.) Corrêa extracts. To achieve this, bael fruit samples were collected from seven provinces representing Thailand's diverse floristic regions, allowing for the investigation of

regional variations in bioactive content. Antioxidant activities were assessed using two widely recognized assays: 2,2'-azino-bis(3-ethylbenzothiazoline-6-sulphonic acid) (ABTS) and 1,1-diphenyl-2-picrylhydrazyl (DPPH).

The findings of this study are expected to establish correlations between extraction methodologies, geographical origins, and antioxidant properties of bael extracts, thereby providing valuable insights into their therapeutic potential. Moreover, this research seeks to contribute to the development of optimized extraction protocols that enhance the utilization of *Aegle marmelos* (L.) Corrêa in functional foods and anti-inflammatory treatments.

MATERIALS AND METHODS

Materials

The plant material utilized in this study was bael fruit (*Aegle marmelos* (L.) Corrêa), collected in April 2022 from seven provinces representing all floristic regions of Thailand, namely the Northern, Northeastern, Central, Eastern, Western, Southern, and Peninsular regions. This simultaneous collection ensured consistency in fruit maturity and minimized the impact of seasonal variation on phytochemical content. The samples were harvested during their mature fruiting stage to ensure optimal levels of phenolic and flavonoid content. Plant authentication was conducted through morphological comparison with herbarium specimens preserved at the Bangkok Forest Herbarium (BKF), Thailand, following the standard protocols outlined by Tungmunnithum et al. (2020).

The collected bael fruit samples were subjected to air drying using the sun drying method described by Sarker et al. (2006), and hot air oven drying at 30°C for 60 min until a constant weight was achieved. The dried samples were then coarsely ground using a porcelain pestle and mortar to obtain particles close to fine powder. The processed samples were stored in tightly-sealed, opaque containers at room temperature to prevent photodegradation and maintain sample integrity.

The chemicals and reagents used in this study included Folin-Ciocalteu reagent (Merck, Germany), quercetin standard (Sigma-Aldrich, USA), gallic acid (Sigma-Aldrich, USA), DPPH (1,1-diphenyl-2-picrylhydrazyl) (Sigma-Aldrich, USA), ABTS (2,2'-azino-bis(3-ethylbenzothiazoline-6-sulphonic acid)) (Sigma-Aldrich, USA), ethanol (Merck, Germany), and potassium persulfate (Merck, Germany). All chemicals were of analytical grade and used without further purification.

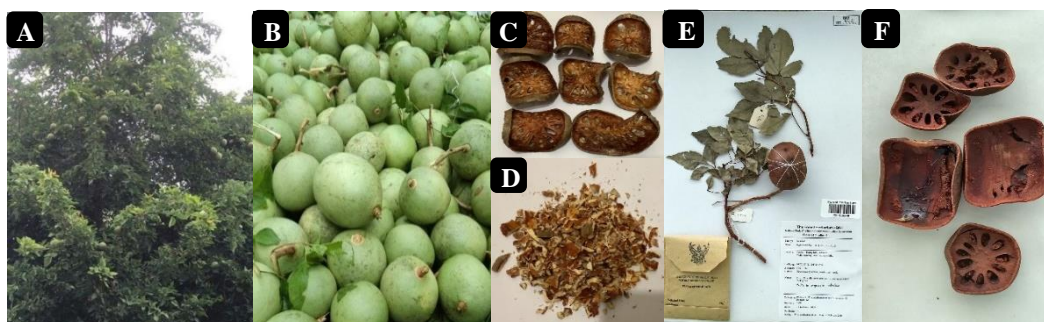


Figure 1. The bael (*Aegle marmelos* (L.) Corrêa) (A) plant in natural habitat, (B) fruits, (C) samples before drying and (D) dry specimens after coarsely ground, (E-F) herbarium specimen from BKF in part of (E) Overall and (F) Fruits.

Table 1. The collected 10 populations of the bael (*Aegle marmelos* (L.) Corrêa).

Population Number	Floristic Region in Thailand	Number on Floristic Regions Map	Population Name
1	Central (C)	52	Nonthaburi
2	Northeastern (NE)	18	Nong Bua Lam Phu
3	Eastern (E)	29	Nakhon Ratchasima
4	Northern (N)	14	Phichit
5	Central (C)	42	Chainat
6	Southeastern (SE)	62	Chanthaburi
7	Southwestern (SW)	38	Kanchanaburi
8	Northern (N)	5	Nan
9	Northeastern (NE)	27	Khonkaen
10	Peninsula (PEN)	71	Phatthalung

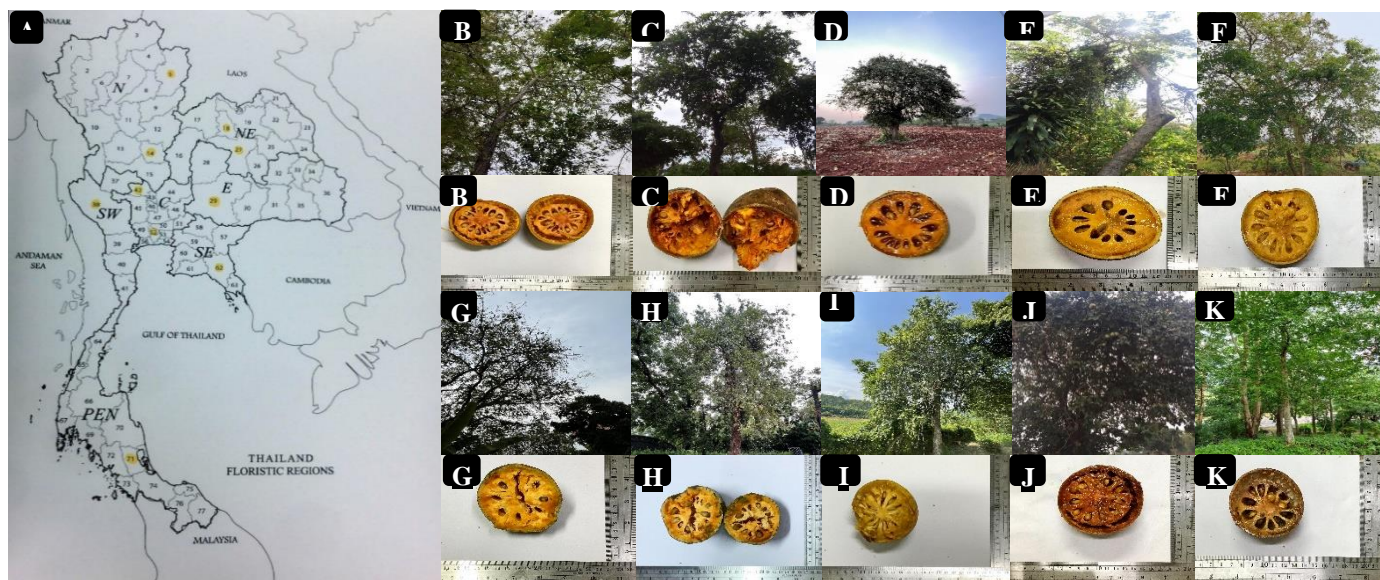


Figure 2. The bael (*Aegle marmelos* (L.) Corrêa) fruits and trees from (A) all 7 Floristic Regions in Thailand Map, included (B-K) 10 populations, were collected from bael plant in (B) Nonthaburi, (C) Nong Bua Lam Phu, (D) Nakhon Ratchasima, (E) Pichit, (F) Chainat, (G) Chanthaburi, (H) Kanchanaburi, (I) Nan, (J) Khonkaen and (K) Phatthalung.

Methods

1. Extraction Methods

1.1. Ultrasonic-Assisted Extraction (UAE)

The UAE method was performed following the optimized protocol established by Tungmunthum et al. (2020). The coarsely ground bael fruit samples (500 mg) were extracted using an ultrasonic bath (Hielscher Ultrasonics GmbH, Germany) operating at a frequency of 45 kHz and a power of 200 W. Extraction was conducted using 10 mL of 75% ethanol as the solvent. The extraction process was carried out for 60 min at a controlled temperature of 45°C. The resulting extracts were filtered through a 0.45 µm of nylon syringe membranes (Whatman, USA) and stored at 4–8°C until further analysis.

1.2. Heat Reflux Extraction (HRE)

The HRE method was employed as a conventional extraction technique for comparison, following the procedure described by Hano et al. (2021). Coarsely ground bael fruit samples (500 mg) were extracted with 10 mL of 75% ethanol under reflux conditions at 45°C for 2 hours. After extraction, the filtrates were collected by filtration through a 0.45 µm of nylon syringe membranes (Whatman, USA) and stored at 4–8°C until further analysis.

2. Phytochemical Characterization and Antioxidant Activity Assays

2.1. Total Phenolic Content (TPC) Determination

TPC was assessed using the Folin-Ciocalteu method adapted from Tungmunthum et al. (2020). Bael extract (500 mg) was dissolved in 10 mL of 75% ethanol (50 mg/mL), and gallic acid standards (5–100 µg/mL) were prepared. A 96-well microplate was loaded with 20 µL of extract or standard, followed by 100 µL of Folin-Ciocalteu reagent (1:9 dilution) and 100 µL of distilled water. After 6 min of incubation, 80 µL of 7% sodium carbonate and 80 µL of distilled water were added, mixed, and incubated for 30 min in the dark. Absorbance was measured at 760 nm, and TPC was expressed as gallic acid equivalents (GAE) per gram of extract (g GAE/g extract) and will be calculated into mg% GAE.

2.2. Total Flavonoid Content (TFC) Determination

TFC was quantified using the aluminum chloride colorimetric assay (Tungmunthum et al., 2020). Extract solutions (50 mg/mL) and quercetin standards (3.125–100 µg/mL) were prepared. In a 96-well microplate, 100 µL of extract or standard was mixed with 100 µL of 2% aluminum chloride, incubated at room temperature for 15 min, and measured at 415 nm. TFC was calculated using a quercetin calibration curve and expressed as quercetin equivalents (QE) per gram of extract (g QE/g extract) and will be calculated into µg% QE.

2.3. ABTS Radical Scavenging Activity Assay

ABTS radical scavenging activity was determined following Tungmunthum et al. (2020). ABTS reagent was prepared by mixing 7 mM ABTS with 2.45 mM potassium persulfate (1:1 ratio) and incubating for 12–16 hours in the dark before dilution to an absorbance of 0.7 ± 0.02 at 734 nm. A 96-well microplate was loaded with 20 µL of extract or standard (Trolox, 2.5–30 µg/mL) and 180 µL of ABTS reagent, incubated for 15 min, and measured at 734 nm. Antioxidant activity was calculated using a Trolox calibration curve and expressed as TEAC (mg TE/mL).

2.4. DPPH Radical Scavenging Activity Assay

The antioxidant capacity of bael extracts was evaluated using the DPPH radical scavenging assay (Tungmunthum et al., 2020). Extract solutions (50 mg/mL) and Trolox standards (2–20 µg/mL) were prepared. A 96-well microplate was loaded with 75 µL of extract or standard and 75 µL of freshly prepared DPPH solution. After 30 min of incubation in the dark, absorbance was recorded at 517 nm. The results were expressed as Trolox equivalent antioxidant capacity (TEAC, mg TE/mL).

RESULTS AND DISCUSSION

Results

1. Phytochemical Characterization correlation with Antioxidant Activity

Table 2. Phytochemical Characterization (TPC and TFC), and Antioxidant Activities (ABTS and DPPH) of 10 populations of bael (*Aegle marmelos* (L.) Corrêa) extracts from various optimized extraction conditions.

Sample	Optimized Extraction Method	TPC (mg% GAE)	TFC (µg% QE)	ABTS (mg TE/mL)	DPPH (mg TE/mL)
52	HE	180.29 ± 0.00	0.01 ± 0.00	581.36 ± 2.27	1223.88 ± 0.40
52	HW	498.06 ± 0.00	0.01 ± 0.00	1220.87 ± 1.88	1380.12 ± 0.19
52	UE	35.74 ± 0.00	0.01 ± 0.00	169.65 ± 5.06	1217.45 ± 1.55
52	UW	70.15 ± 0.00	0.01 ± 0.00	1052.14 ± 1.74	1214.13 ± 0.32
18	HE	17.40 ± 0.00	0.06 ± 0.00	722.25 ± 1.30	1221.64 ± 0.92
18	HW	374.76 ± 0.00	0.06 ± 0.00	1187.83 ± 3.86	1392.87 ± 0.00
18	UE	13.33 ± 0.00	0.05 ± 0.00	1119.88 ± 3.14	1221.38 ± 0.00
18	UW	379.52 ± 0.00	0.07 ± 0.00	1185.17 ± 0.05	1347.99 ± 0.77
29	HE	14.29 ± 0.00	0.05 ± 0.00	702.96 ± 0.39	1236.22 ± 0.52
29	HW	298.39 ± 0.00	0.11 ± 0.00	1077.30 ± 0.92	1217.25 ± 1.29
29	UE	23.56 ± 0.00	0.01 ± 0.00	510.04 ± 1.25	1234.84 ± 2.17
29	UW	73.64 ± 0.00	0.01 ± 0.00	1223.22 ± 1.01	1092.05 ± 3.14
14	HE	1.46 ± 0.00	0.01 ± 0.00	196.94 ± 0.53	1202.41 ± 7.17
14	HW	98.22 ± 0.00	0.01 ± 0.00	1173.50 ± 1.89	1181.42 ± 8.92
14	UE	135.10 ± 0.00	0.05 ± 0.00	68.69 ± 0.53	1232.65 ± 1.56
14	UW	29.49 ± 0.00	0.02 ± 0.00	1209.98 ± 0.82	1299.22 ± 4.16
42	HE	14.03 ± 0.00	0.05 ± 0.00	990.64 ± 1.50	1200.00 ± 0.00
42	HW	678.61 ± 0.00	0.06 ± 0.00	1205.49 ± 1.01	1218.19 ± 0.23
42	UE	0.79 ± 0.00	0.01 ± 0.00	1132.65 ± 2.36	1234.94 ± 2.66
42	UW	35.62 ± 0.00	0.01 ± 0.00	1101.83 ± 1.01	1203.02 ± 4.54
62	HE	382.77 ± 0.00	0.01 ± 0.00	945.25 ± 0.14	1225.20 ± 9.52
62	HW	156.67 ± 0.00	0.06 ± 0.00	910.73 ± 1.30	1216.97 ± 0.58
62	UE	1171.84 ± 0.00	0.01 ± 0.00	99.39 ± 2.41	1225.71 ± 3.67
62	UW	514.20 ± 0.00	0.01 ± 0.00	1416.31 ± 0.10	1236.50 ± 4.27
38	HE	488.43 ± 0.00	0.01 ± 0.00	1085.96 ± 0.58	1207.00 ± 5.84
38	HW	211.92 ± 0.00	0.01 ± 0.00	1171.33 ± 1.35	1218.47 ± 0.16
38	UE	20.76 ± 0.00	0.06 ± 0.00	1674.64 ± 0.10	1231.58 ± 1.51
38	UW	191.78 ± 0.00	0.05 ± 0.00	755.90 ± 0.24	1217.67 ± 0.23
5	HE	18.04 ± 0.00	0.05 ± 0.00	1074.73 ± 2.94	1212.66 ± 5.15
5	HW	350.75 ± 0.00	0.01 ± 0.00	1213.48 ± 1.21	1209.34 ± 8.33
5	UE	106.10 ± 0.00	0.01 ± 0.00	946.52 ± 0.77	1212.56 ± 10.99
5	UW	119.14 ± 0.00	0.01 ± 0.00	1192.46 ± 0.53	1200.00 ± 0.00
27	HE	247.66 ± 0.00	0.05 ± 0.00	494.91 ± 1.30	1234.69 ± 2.06
27	HW	399.73 ± 0.00	0.01 ± 0.00	1179.56 ± 0.77	1231.14 ± 1.35
27	UE	2.05 ± 0.00	0.05 ± 0.00	968.66 ± 1.88	1216.18 ± 8.48
27	UW	186.22 ± 0.00	0.01 ± 0.00	1222.27 ± 0.48	951.56 ± 7.79
71	HE	29.81 ± 0.00	0.05 ± 0.00	225.03 ± 1.11	1172.65 ± 9.68
71	HW	170.71 ± 0.00	0.01 ± 0.00	1192.88 ± 2.46	1215.84 ± 7.30
71	UE	56.14 ± 0.00	0.01 ± 0.00	1205.40 ± 0.87	1215.34 ± 4.92
71	UW	6.35 ± 0.00	0.01 ± 0.00	1203.33 ± 0.05	1199.43 ± 3.45

The total flavonoid content (TFC) and total phenolic content (TPC) showed significant correlations with antioxidant activities, supporting their role in free radical scavenging. Using the aluminum chloride and Folin-Ciocalteu methods, the highest TFC was observed in HRE-water extracts from Nakhon Ratchasima (0.11 ± 0.00 µg% QE) while the highest TPC was found in UAE-ethanol extracts from Nan (106.10 ± 0.00 mg% GAE), correlating with strong DPPH activity ($p < 0.05$), while Chanthaburi's UAE-ethanol

extract yielded the highest TPC (1171.84 ± 0.00 mg% GAE), with Kanchanaburi's UAE-ethanol extract showing the strongest ABTS activity (1674.64 ± 0.10 mg TE/mL). Pearson correlation analysis confirmed strong associations between TPC and both ABTS and DPPH, as well as between TFC and antioxidant assays ($p < 0.01$), highlighting the contribution of phenolics and flavonoids to antioxidant potential, in agreement with previous phytopharmaceutical research.

Discussions

These findings indicate that morphological traits, particularly fruit coloration, significantly influence the bioactive compound content in bael (*Aegle marmelos* (L.) Corrêa) fruit, aligning with previous studies that suggest pigmentation can serve as an indicator of phenolic and antioxidant levels (Kumar & Yadav, 2023; Soni & Kumar, 2018). While current research focuses on the fruit, other plant parts such as leaves and bark also hold notable phytochemical potential (Sharma & Kumar, 2017). Future studies could explore these variations across different plant parts, supporting natural product development and herbal medicine applications (Raut & Sushil, 2020).

CONCLUSIONS

HRE-ethanol enhances phenolic and antioxidant yields, while UAE-ethanol favors flavonoid extraction. Regional differences significantly impact bioactive content, highlighting the need for tailored extraction. Bael's strong antioxidant activity supports its potential in reducing oxidative stress and inflammation, suggesting applications in functional foods and anti-inflammatory treatments. The strong correlation between phenolic/flavonoid content and antioxidant activity points to their pharmaceutical and nutraceutical potential. Further studies should isolate and characterize key active compounds.

ACKNOWLEDGMENTS

This study acknowledges financial support from the Franco-Thai Cooperation Programme (PHC SIAM) and Faculty of Pharmacy, Mahidol University, as well as the valuable contributions of all advisors, lab facilities, and technical staffs.

REFERENCES

- Sharma R, Singh R, Bhardwaj R. *Aegle marmelos* (L.) Corrêa: A sacred medicinal plant with multifarious therapeutic potentials. *J Ethnopharmacol*. 2018;213:1–15. doi:10.1016/j.jep.2017.11.010.
- Singh D, Agrawal SS. Phytochemical and pharmacological potential of *Aegle marmelos*: A review. *J Pharmacogn Phytochem*. 2020;9(5):2297–2303.
- Chandrasekaran CV, Mathuram LN. Scientific basis for the therapeutic use of *Aegle marmelos*: Current status and future prospects. *Indian J Tradit Knowl*. 2020;19(1):23–31.
- Zhang Y, Liu T, Zhang L, Xu Y. Flavonoids and phenolic acids as antioxidants and anti-inflammatory agents: Implications in neurodegenerative disorders. *Oxid Med Cell Longev*. 2021;2021:5548791. doi:10.1155/2021/5548791.
- Hano C, Tungmunthum D. Plant polyphenols, sustainable sources, and extraction optimization targeting antioxidant properties: A review. *Ind Crops Prod*. 2021;172:113990. doi:10.1016/j.indcrop.2021.113990.
- Tungmunthum D, Drouet S, Lorenzo JM, Hano C. Ultrasound-assisted extraction of bioactive flavonoids and phenolics from plants: Green and sustainable approaches for antioxidant recovery. *Molecules*. 2022;27(3):723. doi:10.3390/molecules27030723.
- Patel S, Goyal A. The current trends and future perspectives of extraction technologies for bioactive compounds: A review. *Crit Rev Food Sci Nutr*. 2017;57(7):1417–1431. doi:10.1080/10408398.2014.953493.
- Wang L, Wang Y, Zhang X, Deng Y. Optimization of ultrasonic-assisted extraction of phenolic compounds from plant materials: A review. *Ultrason Sonochem*. 2022;82:105876. doi:10.1016/j.ultsonch.2022.105876.
- Kumar, A., & Yadav, A. (2023). Diversity in morpho-pomological and biochemical traits of bael genotypes in North-Western India. *Indian Journal of Horticulture*, 80(1), 43-50. <https://pubmed.ncbi.nlm.nih.gov/38404771/>
- Soni, A., & Kumar, P. (2018). Phytochemical study of *Aegle marmelos*: Chromatographic elucidation of polyphenolics and assessment of antioxidant and cytotoxic potential. *Journal of Environmental Science and Technology*, 12(2), 98-104. <https://pmc.ncbi.nlm.nih.gov/articles/PMC5822502/>
- Soni, A., & Kumar, P. (2018). Phytochemical study of *Aegle marmelos*: Chromatographic elucidation of polyphenolics and assessment of antioxidant and cytotoxic potential. *Journal of Environmental Science and Technology*, 12(2), 98-104. <https://pmc.ncbi.nlm.nih.gov/articles/PMC5822502/>
- Sharma, S., & Kumar, M. (2017). Antioxidant potential and phenolic contents of leaf, bark, and fruit of *Aegle marmelos*. *Journal of Tropical Forest Science*, 29(1), 56-65. <https://jtfs.frim.gov.my/jtfs/article/view/866>

Isolation and Identification of Phenolic Compounds from *Cylindrolobus mucronatus* and Their Cytotoxic Activity Against Glioblastoma Cells

Shune Lae Yee Soe^{1,2}, *Khent Primo Alcantara*³, *Virunh Kongkatitham*², *Pornchai Rojsitthisak*^{3,4}, *Boonchoo Sritularak*^{2,4,*}

¹ Pharmaceutical Sciences and Technology Program, Faculty of Pharmaceutical Sciences, Chulalongkorn University, Bangkok 10330, Thailand

² Department of Pharmacognosy and Pharmaceutical Botany, Faculty of Pharmaceutical Sciences, Chulalongkorn University, Bangkok 10330, Thailand

³ Department of Food and Pharmaceutical Chemistry, Faculty of Pharmaceutical Sciences, Chulalongkorn University, Bangkok 10330, Thailand

⁴ Center of Excellence in Natural Products for Ageing and Chronic Diseases, Faculty of Pharmaceutical Sciences, Chulalongkorn University, Bangkok, Thailand

* Corresponding author: Boonchoo.sr@chula.ac.th

Abstract. Natural products derived from plants are an essential source of bioactive compounds with diverse pharmacological activities. This study investigates the phytochemical constituents of *Cylindrolobus mucronatus* orchid for the first time. The cytotoxic screening revealed that the ethyl acetate extract exhibited significant activity against U87 glioblastoma cells, reducing cell viability to 16.3 ± 1.1 % at 50 $\mu\text{g/mL}$. Three phenolic compounds were isolated from the ethyl acetate fraction. Structural determination through nuclear magnetic resonance spectroscopy (NMR) and mass spectrometry confirmed their structures as confusarin (**1**), nudol (**2**), and bleformin I (**3**). The results showed that bleformin I exhibited significant cytotoxic activity, with an IC_{50} value of 17.08 ± 3.7 μM . This research is the first report on these compounds in *Cylindrolobus mucronatus*, providing new insights into phytochemistry and its potential cytotoxic activity.

Keywords: Orchid, Phenolic compounds, Cytotoxic activity, Glioblastoma cells

INTRODUCTION

Cancer is a complex disease characterized by uncontrolled cell growth, affecting various organs and requiring diverse treatment approaches [1]. Among them, gliomas are aggressive brain tumors, with glioblastoma (GBM) being the most prevalent and lethal disease, classified as grade IV astrocytoma by the World Health Organization (WHO) due to its rapid invasion and resistance to conventional therapies [2,3]. Despite the standard treatment of surgical resection followed by temozolomide chemotherapy and radiotherapy, GBM has a poor prognosis, with a five-year survival rate of only 4.7% and a median survival of approximately 15 months [2,4]. Given its intrinsic chemoresistance and limited treatment options, there is an urgent need for alternative therapeutic strategies [5]. Natural products have been a crucial source of anticancer agents, with approximately 60% of anticancer drugs derived from plants and other natural sources [6-8]. Orchids, belonging to the Orchidaceae family, have gained attention for their diverse bioactive compounds, including alkaloids, flavonoids, phenanthrenes, and terpenoids, which exhibit potential anticancer properties against various cancer types [9]. Several genera, such as *Dendrobium*, *Habenaria*, and *Coelogyne*, have been traditionally used in herbal medicine for various ailments, including cancer treatment [10]. *Cylindrolobus mucronatus* is an epiphytic orchid belonging to the Orchidaceae family. This genus comprises approximately 39 species, with a geographical distribution in southwest China and Southeast Asia [11]. However, research on the orchid species *Cylindrolobus mucronatus* remains unexplored. This study represents the first investigation into its chemical constituents and cytotoxic activity against glioblastoma U87 cells, addressing a significant gap in understanding its potential as an anticancer agent.

MATERIALS AND METHODS

Experimental

The whole plant material of *Cylindrolobus mucronatus* was purchased from Chatuchak Market. Mass spectra were obtained using a Bruker microTOF mass spectrometer equipped with an electrospray ionization (ESI) source (Bruker Daltonics, Billerica, MA, USA). Nuclear magnetic resonance (NMR) spectra were recorded on Bruker Avance Neo 400 MHz spectrometers (Bruker BioSpin, Billerica, MA, USA). Cytotoxicity assays were performed using a CLARIOstar microplate reader (CLARIOstar, BMG Labtech, Ortenberg, Germany). The U87-MG human glioblastoma cell line (ATCC® HTB-14) was obtained from the American Type Culture Collection (ATCC, Manassas, VA, USA). Cell viability was evaluated using the Cell Counting Kit-8 (CKK-8; ab228554, Abcam, Cambridge, UK). Data analysis was conducted using GraphPad Prism® software version 9.5.1 (GraphPad Software, San Diego, CA, USA). All chemicals and solvents used in this study were of analytical grade.

Extraction and Isolation

Air-dried, powdered whole plant material of *Cylindrolobus mucronatus* (2 kg) was macerated in 10 L of methanol for 3 days at room temperature. This extraction process was repeated 3 times, resulting in the extraction of 169.36 g of methanol extract after removing the solvent. This extract was then separated into ethyl acetate (62.41 g) and aqueous (30.25 g) fractions by partition method using each 1 L of solvents. Preliminary tests indicated that the ethyl acetate fraction exhibited notable cytotoxic effects against U87 glioblastoma cells, while the aqueous fraction demonstrated no such activity. Consequently, further phytochemical analysis was conducted on the ethyl acetate fraction. The ethyl acetate extract was fractionated using vacuum liquid chromatography on silica gel with a dichloromethane-ethyl acetate gradient, yielding five fractions A - E. Confusarin (**1**) was isolated from fraction B using a hexane-ethyl acetate gradient via silica gel column chromatography. Additionally, nudol (**2**) was extracted from fraction

B through repeated silica gel column chromatography and purified using Sephadex LH-20 column chromatography with methanol as the solvent. Lastly, bleformin I (**3**) was isolated from fraction C through preparative thin-layer chromatography utilizing a dichloromethane-methanol solvent system.

Cell Culture

Glioblastoma U87-MG cells (ATCC® HTB-14) were cultured in Dulbecco's Modified Eagle Medium (DMEM) supplemented with 10% fetal bovine serum (FBS) and 1% penicillin-streptomycin and maintained at 37°C in a humidified atmosphere containing 5% CO₂.^[12]

Cytotoxicity Assay

The cytotoxic effects were determined using the Cell Counting Kit-8 (CCK-8) assay. Cells were cultured in a 96-well plate at a density of 1×10^4 cells per well and left to incubate overnight. The methanolic, ethyl acetate, and aqueous extracts were dissolved in 0.5% DMSO and tested at a concentration of 50 µg/mL. Bleformin I was also dissolved in 0.5% DMSO and prepared at 10, 20, 40, 60, 80, and 100 µM concentrations. A 100 µL volume of each treatment was introduced into the wells, followed by a 24-hour incubation period. Subsequently, 10 µL of CCK-8 solution (ab228554, Abcam, Cambridge, UK) was added to each well, and the plates were incubated in the dark at 37°C for 1 hour. Finally, the absorbance was recorded at 450 nm using a microplate reader (CLARIOstar, BMG Labtech, Ortenberg, Germany)^[13]. The IC₅₀ value was determined using non-linear regression analysis with the log(inhibitor) vs. response-variable slope (four-parameter) model in GraphPad Prism® 9.5.1 (San Diego, CA, USA). The data were analyzed by variance (ANOVA) followed by post-hoc test and expressed as the mean ± SD.

RESULTS AND DISCUSSION

Three phenolic compounds were isolated from the ethyl acetate extract of *Cylindrolobus mucronatus* and identified as confusarin (**1**), nudol (**2**), and bleformin I (**3**). The spectral data are consistent with previously published data^[14,15,16]. The structures of isolated compounds are shown in Figure 1.

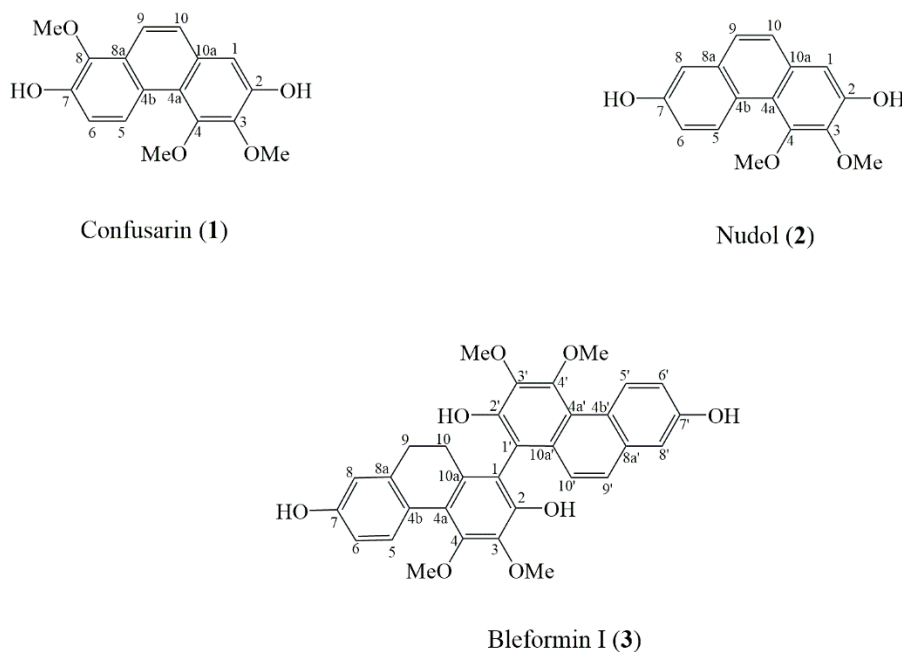


Figure 1. Structures of confusarin, nudol and bleformin I

Confusarin (**1**); White crystal. HR-ESI-MS m/z : $[M+H]^+$ Calcd. for C₁₇H₁₇O₅, 301.1076, found: m/z 301.1070. ¹H NMR (acetone-*d*₆, 400 MHz) : 7.19 (1H, s, H-1), 9.15 (1H, d, J = 9.6, H-5), 7.27 (1H, d, J = 9.6, H-6), 7.91 (1H, d, J = 9.2, H-9), 7.61 (1H, d, J = 9.2, H-10), 4.02 (3H, s, 3-OCH₃), 3.98 (3H, s, 4-OMe), 3.94 (3H, s, 8-OMe); ¹³C NMR (acetone-*d*₆, 100 MHz) : 108.9 (C-1), 149.3 (C-2), 142.0 (C-3), 151.5 (C-4), 117.3 (C-4a), 124.2 (C-4b), 127.1 (C-5), 118.3 (C-6), 146.4 (C-7), 141.5 (C-8), 124.2 (C-8a), 119.4 (C-9), 129.3 (C-10), 126.8 (C-10a), 60.5 (3-OMe), 59.2 (4-OMe), 60.4 (8-OMe).

Nudol (**2**); Brown yellow crystal. HR-ESI-MS m/z : $[M+H]^+$ Calcd. for C₁₆H₁₅O₄, 271.0970, found: m/z 271.0967. ¹H NMR (acetone-*d*₆, 400 MHz) : 7.16 (1H, s, H-1), 9.34 (1H, d, J = 9.2, H-5), 7.20 (1H, dd, J = 9.2, 2.8, H-6), 7.26 (1H, d, J = 2.8, H-8), 7.51 (1H, d, J = 8.8, H-9), 7.55 (1H, d, J = 8.8, H-10), 4.02 (3H, s, 3-OMe), 3.99 (3H, s, 4-OMe); ¹³C NMR (acetone-*d*₆, 100 MHz) : 108.9 (C-1), 149.0 (C-2), 141.9 (C-3), 151.3 (C-4), 133.7 (C-4a), 118.3 (C-4b), 128.0 (C-5), 116.7 (C-6), 154.9 (C-7), 111.5 (C-8), 129.4 (C-8a), 126.2 (C-9), 126.8 (C-10), 123.4 (C-10a), 60.4 (3-OMe), 59.18 (4-OMe).

Bleformin I (**3**); Brown solid. HR-ESI-MS m/z : $[M+H]^+$ Calcd. for C₃₂H₂₉O₈, 541.1862, found: m/z 541.1883. ¹H NMR (acetone-*d*₆, 400 MHz) 8.19 (1H, d, J = 8.4, H-5), 6.78 (1H, dd, J = 8.4, 2.8, H-6), 6.68 (1H, d, J = 2.8, H-8), 2.51 (2H, m, H-9), 2.32 (1H, m, H-10), 2.22 (1H, m, H-10), 9.45 (1H, d, J = 10.0, H-5'), 7.23 (1H, dd, J = 10.0, 2.8, H-6'), 7.22 (1H, d, J = 2.8, H-8'), 7.43 (1H, d, J = 9.2, H-9'), 7.24 (1H, d, J = 9.2, H-10'), 3.95 (3H, s, 3-OMe), 3.83 (3H, s, 4-OMe), 4.06 (3H, s, 3'-OMe), 4.04 (3H, s, 4'-OMe).

OMe); ^{13}C NMR (acetone- d_6 , 100 MHz) : 117.6 (C-1), 147.0 (C-2), 139.8 (C-3), 150.6 (C-4), 119.9 (C-4a), 124.8 (C-4b), 128.5 (C-5), 113.1 (C-6), 155.7 (C-7), 144.1 (C-8), 139.6 (C-8a), 29.7 (C-9), 26.6 (C-10), 134.3 (C-10a), 115.5 (C-1'), 147.6 (C-2'), 141.6 (C-3'), 150.5 (C-4'), 118.5 (C-4a'), 123.7 (C-4b'), 128.3 (C-5'), 116.7 (C-6'), 154.9 (C-7'), 111.3 (C-8'), 133.6 (C-8a'), 126.0 (C-9'), 124.5 (C-10'), 128.4 (C-10a'), 60.5 (3-OMe), 59.5 (4-OMe), 60.3 (3'-OMe), 59.2 (4'-OMe).

The cytotoxic activity of crude extracts and isolated compounds was assessed against U87 glioblastoma cells using the CCK-8 assay. The results, including cell viability percentages and IC_{50} values, are shown in **Table 1**. Among the crude extracts evaluated at 50 $\mu\text{g/mL}$, the ethyl acetate (EtOAc) extract exhibited the highest cytotoxicity. Notably, bleformin I (**3**) displayed the most potent cytotoxic effect at 100 μM . The IC_{50} value for bleformin I (**3**) was determined, while doxorubicin exhibited a significantly lower IC_{50} value as the positive control.

Table 1. Cytotoxic activity of crude extracts and isolated compounds against U87 glioblastoma cells

Crude Extract	Cell viability % at 50 $\mu\text{g/mL}$ (Mean \pm SD)	Compound	Cell viability % at 100 μM (Mean \pm SD)	Compound	IC_{50} (Mean \pm SD)(μM)
MeOH Extract	36.4 \pm 3.9	Confusarin (1)	62.5 \pm 4.3	Bleformin I (3)	17.08 \pm 3.7
EtOAc Extract	16.3 \pm 1.1	Nudol (2)	53.6 \pm 6.6	Doxorubicin	0.3 \pm 1.9
Aqueous Extract	69.4 \pm 6.9	Bleformin I (3)	11.9 \pm 0.6		

The cytotoxic activities of methanolic, ethyl acetate, and aqueous extracts were evaluated using the CCK-8 assay against U87 cells to identify the most active crude extract. Among the three extracts tested at 50 $\mu\text{g/mL}$, the ethyl acetate extract exhibited the highest cytotoxicity, with a cell viability of 16.3 \pm 1.1 %, indicating its potential as the most active fraction. In contrast, the methanol (MeOH) and aqueous extracts showed higher cell viability of 36.4 \pm 3.9 % and 69.4 \pm 6.9 %, respectively, suggesting lower cytotoxic effects. At 100 μM , bleformin I (**3**) exhibited the strongest cytotoxicity, reducing cell viability to 11.9 \pm 0.6 %, while confusarin and nudol showed moderate activity with viabilities of 62.5 \pm 4.3% and 53.6 \pm 6.6%, respectively. Confusarin and nudol are monophenanthrene and both exhibited only moderate cytotoxic activity. In contrast, bleformin I, a biphenanthrene, showed potent cytotoxic activity. The stronger activity of bleformin I may be attributed to the presence of two phenanthrene units, which could result in a synergistic effect and enhance its biological activity. The dimeric structure might allow bleformin I to interact more effectively with cellular targets compared to monophenanthrenes, leading to improved cytotoxic potency. These observations suggest that the structural complexity of biphenanthrenes like bleformin I may play an important role in their anticancer potential. Due to its potent cytotoxic effect (cell viability < 50%), bleformin I (**3**) was selected for IC_{50} determination using the CCK-8 assay, with doxorubicin (0.3 \pm 1.9 μM) as the standard drug. Although bleformin I (**3**) had a higher IC_{50} (17.08 \pm 3.7 μM) than doxorubicin, it demonstrated significant cytotoxicity against U87 glioblastoma cells, highlighting its potential for further investigation across various cancer cell types.

CONCLUSIONS

In summary, the isolation of bioactive compounds from the ethyl acetate extract led to the identification of three phenolic compounds: confusarin (**1**), nudol (**2**), and bleformin I (**3**). Among these, bleformin I (**3**) demonstrated the strongest cytotoxic effect. Although its IC_{50} value is higher than that of the standard drug doxorubicin, it still holds potential for further development as an anticancer agent. To gain deeper insights into its therapeutic potential, future studies will focus on investigating its detailed mechanism of action, including its role in apoptosis induction, cell cycle regulation, and interactions with key molecular targets involved in cancer progression.

ACKNOWLEDGEMENTS

S.L.Y.S. thanks to the Pharmaceutical Sciences and Technology Program, Faculty of Pharmaceutical Sciences, Chulalongkorn University, and the Graduate School Chulalongkorn University, for the CU-ASEAN Scholarship. This research is funded by the Thailand Science Research and Innovation Fund Chulalongkorn University (HEA-FF-68-006-3300-002).

REFERENCES

- Huang B, Zhang Y. Teaching an old dog new tricks: Drug discovery by repositioning natural products and their derivatives. *Drug Discov Today*. 2022;27(7):1936-44.
- Omuro A, DeAngelis LM. Glioblastoma and other malignant gliomas: a clinical review. *JAMA*. 2013;310(17):1842-50.
- Weller M, Wick W, Aldape K, et al. Glioma. *Nat Rev Dis Primers*. 2015;1(1):1-18.
- Tan AC, Ashley DM, López GY, et al. Management of glioblastoma: State of the art and future directions. *CA Cancer J Clin*. 2020;70(4):299-312.
- Li H-Y, Feng Y-H, Lin C-L, et al. Mitochondrial mechanisms in Temozolomide resistance: unraveling the complex interplay and therapeutic strategies in glioblastoma. *Mitochondrion*. 2024;75:101836.
- Newman DJ. Natural products as source of new drugs over the period 1981-2002. *J Nat Prod*. 2003;66(7):1022-37.
- Ho JW, Leung Y, Chan C. Herbal medicine in the treatment of cancer. *Curr Med Chem Anticancer Agents*. 2002;2(2):209-14.

8. Yin S-Y, Wei W-C, Jian F-Y, et al. Therapeutic applications of herbal medicines for cancer patients. *Evid Based Complement Alternat Med.* 2013;2013(1):302426.
9. Singh A, Duggal S. Medicinal orchids-an overview. *Ethnobot Leaflet.* 2009;13:399-412.
10. Teoh ES. Medicinal orchids of Asia. Switzerland: Springer; 2016.
11. Teoh ES. Orchid species from Himalaya and Southeast Asia. Vol. 1, (A-E). Switzerland: Springer; 2021. p.263-4.
12. Jimoh TO, Costa BC, Chansrinoyom C, et al. Three new dihydrophenanthrene derivatives from *Cymbidium ensifolium* and their cytotoxicity against cancer cells. *Molecules.* 2022;27(7):2222.
13. Praseatsook K, Vachiraarunwong A, Taya S, et al. Anticancer and antioxidant effects of bioactive peptides from black soldier fly larvae (*Hermetia illucens*). *Nutrients.* 2025;17(4):645.
14. Wu Y-P, Liu W-J, Zhong W-J, et al. Phenolic compounds from the stems of *Flickingeria fimbriata*. *Nat Prod Res.* 2017;31(13):1518-22.
15. Aminah NS, Hidayah R, Tanjung M. Confusarin and nudol, two phenanthrene group compounds, from *Dioscorea esculenta* L. and their antioxidant activities. *J Chem Technol Metall.* 2017;52(6):1135-9.
16. Lin C-W, Hwang T-L, Chen F-A, et al. Chemical constituents of the rhizomes of *Bletilla formosana* and their potential anti-inflammatory activity. *J Nat Prod.* 2016;79(8):1911-21.

Development of Pyrrolidinyl Diaminopyrimidine Oxide Microemulsion System for Enhancing Solubility in Hair Care Applications

Sorrakan Sutunno¹, Pornpen Werawatganone^{1,}, and Walaisiri Muangsiri^{1,*}*

¹Faculty of Pharmaceutical Science, Chulalongkorn University, Bangkok, THAILAND

*Corresponding author Email: pornpen.w@chula.ac.th; walaisiri.m@chula.ac.th

Abstract. Hair loss remains a widespread concern, driving continuous research into novel treatment approaches. Pyrrolidinyl Diaminopyrimidine Oxide (PDPO), commonly known as Kopyrrol, is a promising hair growth active ingredient that enhances follicular proliferation and scalp microcirculation. However, its poor water solubility, limited to 2% w/w in 70:30 ethanol-water, restricts its bioavailability and therapeutic potential. This study aims to develop a 1% w/w Kopyrrol-loaded microemulsion system to enhance solubility since 70:30 ethanol-water is not proper vehicle for cosmetic preparations. Kopyrrol solubility was evaluated in various solvents, including Cetiol AB, Tween®20, Labrasol® ALF, and propylene glycol. A ternary phase diagram was constructed using an oil phase (Cetiol AB), a surfactant mixture (Tween®20, Labrasol®ALF, and propylene glycol), and water. The optimized formulation was determined at an oil: surfactant: water (O:S:W) ratio of 12.9:71.3:15.8, corresponding to an oil-to-surfactant phase ratio of 1.5:8.5. This system significantly enhanced Kopyrrol solubility to 17.50 ± 1.49 mg/mL, allowing the incorporation of 1% w/w Kopyrrol. The optimized microemulsion exhibited a pH of approximately 5, a viscosity of 126.3 mPa.s at 25 °C under a shear stress of 3.173 Pa, and a particle size of 1190 nm. The translucent solution appeared as a pale yellowish tint, indicating uniform dispersion of Kopyrrol within the system. These findings demonstrated the potential of using a microemulsion system to overcome Kopyrrol's solubility challenges, paving the way for more effective hair care formulations.

Keywords: Kopyrrol, microemulsion, solubility, enhancement, hair care

INTRODUCTION

Hair loss remains a widespread concern, driving continuous research into novel treatment approaches. Hair loss is a common condition that significantly affects self-confidence and quality of life. It is estimated that more than 70% of men experience hair loss at some point in their lives (1-4). One promising active ingredient used in hair care formulations is Pyrrolidinyl Diaminopyrimidine Oxide (PDPO) or Kopyrrol (KP). Recent studies suggest that Kopyrrol could accelerate hair regrowth by promoting the proliferation of human dermal papilla cells (HDPCs) and optimizing the hair growth cycle (5, 6). Despite its potential benefits, one of the main challenges of using Kopyrrol is its limited permeability due to its water-soluble nature. Kopyrrol is classified as a water insoluble compound (<0.1 mg/mL). It has been reported to have a solubility profile of 70% w/w in ethanol-water mixtures, which may hinder its effectiveness in topical applications (7). This study aims to enhance the solubility of Kopyrrol using a microemulsion system for hair care applications.

MATERIALS AND METHODS

Materials

Pyrrolidinyl Diaminopyrimidine Oxide (PDPO) or Kopyrrol was purchased from Kuma Organic (India). C12-15 Alkyl Benzoate (CETIOL®AB) was purchased from BASF (Ludwigshafen, Germany). Bergamot oil was purchased from Thai - China Flavours and Fragrances Industry Co., Ltd. (Nonthaburi, Thailand). Caprylocaproyl polyoxyl-8 glycerides (Labrasol®ALF) was provided by Gattefossé SAS (Saint-Priest Cedex, France). Polyoxyethylene (20) sorbitan monolaurate (Tween®20) was provided by Croda. Absolute Ethanol was purchased from Merck. Ethanol 95% (L PURE 95) was purchased from Liquor Distillery Organization (Chachoengsao, Thailand). Propylene glycol was purchased from S. Tong Chemicals Co., Ltd. (Nonthaburi, Thailand), Batch No. C81506JR41. Ultrapure water was provided by the Pharmaceutical Research Instrument Center, Faculty of Pharmaceutical Sciences, Chulalongkorn University.

Methods

Kopyrrol Calibration Curve

A concentration calibration curve was established for Kopyrrol in the concentration range of 1.6 - 16 µg/mL. Initially, 20 mg of Kopyrrol was accurately weighed using a balance (XS105, Mettler Toledo, USA) and dissolved in 95% w/w ethanol in a 50 mL volumetric flask. Standard solutions of Kopyrrol at concentrations of 1.6, 3.2, 4.8, 6.4, 8.0, 12.8, and 16.0 µg/mL were prepared.

The absorbance of Kopyrrol was measured at 260 nm by using a UV-Vis Spectrophotometer (Agilent Cary 60, Agilent Technologies, USA) (5).

Solubility Study of Kopyrrol

An excess amount of Kopyrrol was added to various solvents. The mixture was placed in light protected amber vials. The vials were sealed with rubber stoppers and aluminum caps and then shaken using a shaker (Glas-Col, Rugged Rotator 099A RD5512, USA) for 72 hours at ambient temperature (app. 25 ± 5 °C). After equilibration, the undissolved Kopyrrol was filtered out using a 0.45 μ m Nylon syringe filter (PRECLEAN SCEQ-CF2101, ANPEL Laboratory Technology, China). A 1 mL aliquot of the clear filtrate was diluted in 95% w/w ethanol. The absorbance of Kopyrrol was measured at 260 nm using a UV-Vis Spectrophotometer. The concentration was calculated based on the calibration curve.

Preparation of Kopyrrol Microemulsion

Microemulsion systems were prepared using the surfactant/co-surfactant (Smix), which consisted of Tween®20:Labrasol® ALF:Propylene glycol with corresponding compositions of 22.5:7.5:10 and 20:10:10 where Tween®20:Labrasol® ALF ratios were 3:1 and 2:1, respectively. Ternary phase diagrams were constructed using Cetiol® AB as oil phase. The water phase was gradually titrated into the mixture of oil and surfactant mixture. Then the mixtures were visually checked for homogeneous and heterogeneous mixtures. Microemulsions were defied for the clear and homogeneous systems. Excess amount of Kopyrrol was added to the selected microemulsions and the solubility of Kopyrrol was determined in the same manner as mentioned previously.

Physical properties characterization of kopyrrol microemulsion.

The physical properties of kopyrrol microemulsion was monitored at 25 °C including color, transparency, pH, viscosity and particle size were evaluated by using the digital pH meter with pH Sensor LE 438 (Mettler Toledo, Switzerland), HAAKE™ MARST™ Rheometer (Thermo Scientific, Germany) and Zetasizer Nano-ZS, Malvern Panalytical, UK).

Statistical analyses

The solubility of Kopyrrol was calculated and reported as mg/mL \pm standard deviation (SD) based on triplicate samples in each experiment.

RESULTS AND DISCUSSION

Results and Discussion

Kopyrrol Calibration Curve

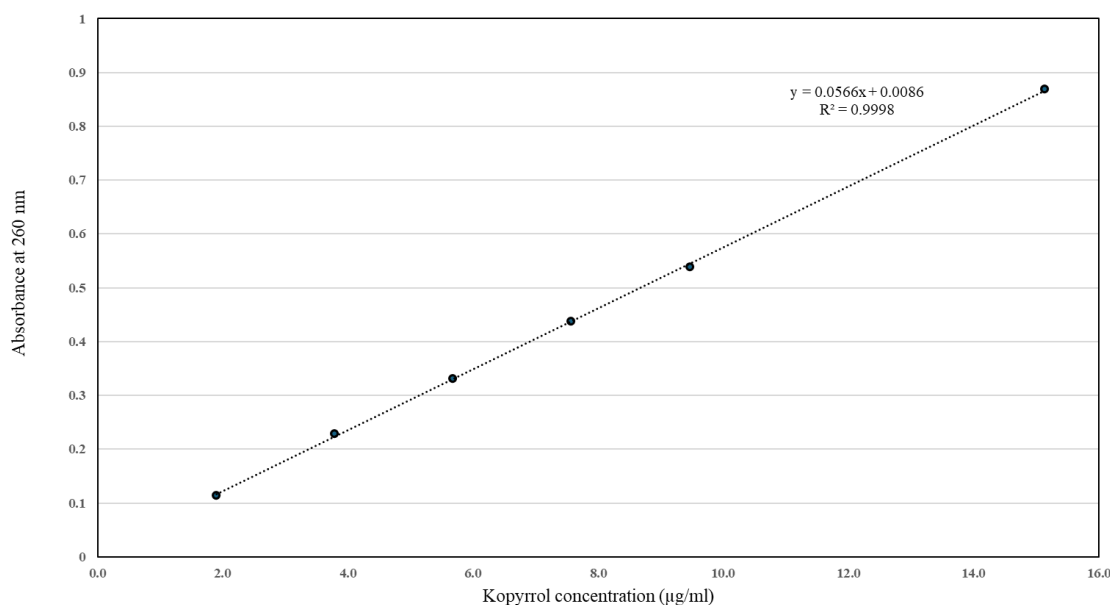


Figure 1. Kopyrrol Calibration standard curve.

The calibration is shown in Figure 1 at absorption wavelength of 260 nm. The curve present a good correlation absorbance vs concentration at r square of 0.9998.

Table 1. Solubility of Kopyrrol in various surfactants and solvents at $25 \pm 5^\circ\text{C}$ (mean \pm SD, n=3)

Chemical Name	Solubility (mg/mL)
Bergamot oil	13.4 ± 2.03
Cetiol AB	31.0 ± 1.44
Propylene glycol	31.5 ± 3.62
Tween® 20 (20% w/w)	5.3 ± 0.57
Labrasol® ALF (20% w/w)	6.6 ± 0.24
Ethanol 70% (w/w)	20.5 ± 1.96

Solubility study of Kopyrrol

The solubility of kopyrrol in various solvents is presented in Table 1. Cetiol AB and propylene glycol show higher ability to dissolve kopyrrol than 70% w/w ethanol. Micellar systems partially increase solubility of Kopyrrol in water which is <0.1 mg/mL.

Preparation of Kopyrrol microemulsion

Microemulsion is another approach that applies to the micellar solubilization technique. This method consists of a combination of oil, surfactant, and water, with the addition of a co-surfactant to enhance system stability and solubilization efficiency (8, 9). Propylene glycol (PG) was investigated ability to enhance the solubility of Kopyrrol, with the expectation as co-surfactant in the preparation of a microemulsion system. The diagrams shown in the figure 2 present the appropriate concentration ranges for the microemulsion components. This was achieved using the water titration method while varying the oil/surfactant/cosurfactant ratios. The optimal microemulsion formulation was determined to consist of an oil-to-surfactant-to-water (O:S:W) ratio of 12.9:71.3:15.8, corresponding to an oil-to-surfactant phase ratio of 1.5:8.5. The surfactant/cosurfactant mixture (Tween®20 and Labrasol®ALF : PG) was optimized at a 3:1 ratio. When evaluating the solubility of Kopyrrol in this optimized microemulsion system, it was found to be 17.5 ± 1.49 mg/mL, which was significantly higher than in the system where the surfactant/cosurfactant ratio (Smix) was set at 2:1. In the latter case, the solubility of Kopyrrol was measured at 12.3 ± 0.39 mg/mL. Additionally, the O:S:W ratio for the system with Smix at 2:1 was determined to be 12.1:67.6:20.4. Both formulations resulted in a translucent microemulsion, indicating successful formation of a stable system regardless of the Smix ratio. However, the 3:1 Smix ratio provided better Kopyrrol solubility. Furthermore, based on the Kopyrrol solubility data, the optimal formulation whereas 3:1 Smix ratio can successfully load 1% Kopyrrol.

Physical properties characterization of Kopyrrol microemulsion

The microemulsion appearance (color and translucency) from visual observation had appeared as a pale yellowish tint, and microscopically using a polarized light microscope (Olympus SC180, Model BX53F2, Japan), no birefringence was observed. This confirmed the formation of a microemulsion and the absence of a liquid crystal structure (8-10). The pH of the microemulsion incorporating Kopyrrol was determined to be 5.5, indicating its suitability and safety for use in hair care products (5, 6, 11-13).

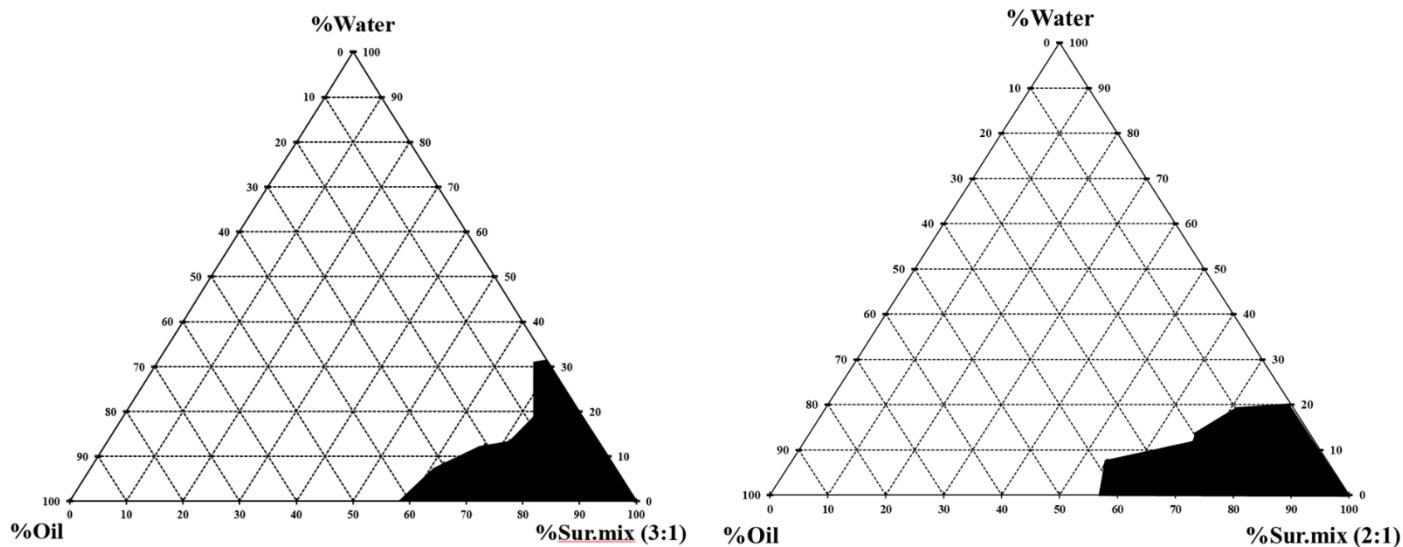


Figure 2. Ternary phase diagram of the oil (Cetiol AB), surfactant/co-surfactant (Smix), which consisted of Tween®20: Labrasol® ALF: Propylene glycol with corresponding compositions of 22.5:7.5:10 and 20:10:10 where Tween®20:Labrasol® ALF ratios were 3:1 and 2:1, respectively **Note:** Shaded area shows microemulsion zone.

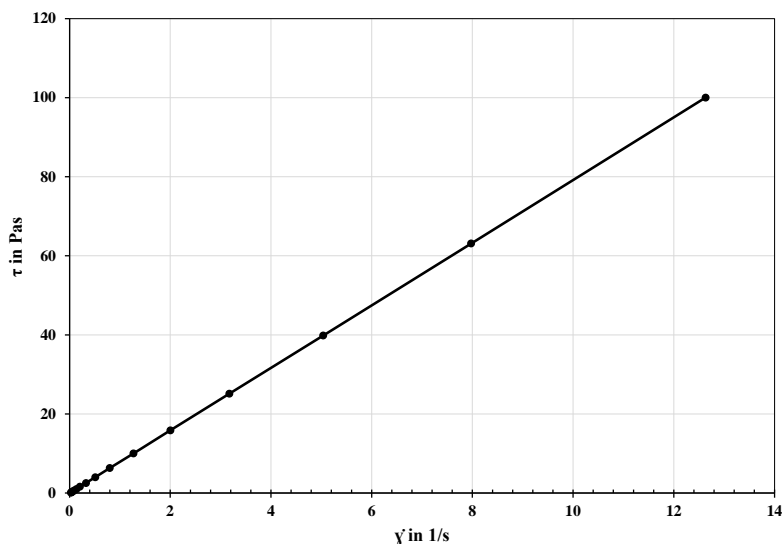


Figure 3. The rheological profile of the microemulsion, consisting of an oil:surfactant:water (O:S:W) ratio of 12.9:71.3:15.8, with Smix at a 3:1 ratio.

The viscosity of the microemulsion was measured at 126.3 mPa·s (or 0.1263 Pa·s) at 25°C under a shear stress of 3.173 Pa. This value aligns with typical viscosities observed in microemulsions, suggesting figure 3., showed a stable and consistent flow behavior. This indicated Newtonian fluid behavior.(9, 10). The particle size measurement result was shown in Figure4., indicated that the majority of the particles had a size of 1190±2.496 nm.

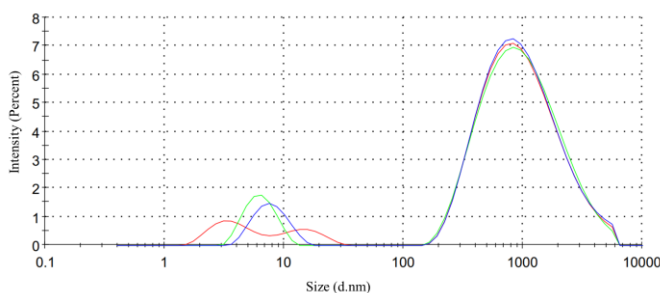


Figure 4. Particle size data of the optimum microemulsion formulation.

CONCLUSIONS

This study has successfully investigated and enhanced the solubility of Kopyrrol through microemulsions. The microemulsion system achieved a remarkable solubility enhancement, reaching 17.5 ± 1.49 mg/mL, thereby confirming its capability to effectively encapsulate Kopyrrol under the specified conditions. This significant improvement not only underscores the feasibility of 1% Kopyrrol loading but also highlights its substantial potential for high-performance hair care applications.

ACKNOWLEDGMENTS

The authors sincerely appreciate the Pharmaceutical Research Instrument Center, Faculty of Pharmaceutical Sciences, Chulalongkorn University, for providing access to analytical instruments essential for this study. Lastly, heartfelt thanks are extended to the authors' parents for their unwavering encouragement, as well as to the faculty and staff of the Cosmetic Science Program for their generous technical support throughout the research process.

REFERENCES

1. Sadgrove N, Batra S, Barreto D, Rapaport J. An Updated Etiology of Hair Loss and the New Cosmeceutical Paradigm in Therapy: Clearing 'the Big Eight Strikes'. *Cosmetics*. 2023;10(4):106.
2. Natarelli N, Gahoonia N, Sivamani RK. Integrative and Mechanistic Approach to the Hair Growth Cycle and Hair Loss. *J Clin Med*. 2023;12(3).
3. Gupta AK, Talukder M, Venkataraman M, Bamimore MA. Minoxidil: a comprehensive review. *J Dermatolog Treat*. 2022;33(4):1896-906.
4. Suchonwanit P, Thammarucha S, Leerunyakul K. Minoxidil and its use in hair disorders: a review. *Drug Des Devel Ther*. 2019;13:2777-86.
5. Zhang S, Zhou H, Chen X, Zhu S, Chen D, Luo D, et al. Microneedle Delivery Platform Integrated with Codelivery Nanoliposomes for Effective and Safe Androgenetic Alopecia Treatment. *ACS Applied Materials & Interfaces*. 2024;16(13):15701-17.
6. Cao J, Wu B, Yuan P, Liu Y, Hu C. Advances in Research of Hydrogel Microneedle-Based Delivery Systems for Disease Treatment. *Pharmaceutics*. 2024;16(12).
7. Purna.C.Ray, Mittapelli V, Chauhan Y, Tyagi O. Tungstate-Catalyzed Oxidation of Triptans with Hydrogen Peroxide: A Novel Method for the Synthesis of N,N-dimethyltryptamine N-oxides. *Indian Journal of Chemistry Section B*. 2009;48B:134-6.
8. Zhao J, Jiang K, Chen Y, Chen J, Zheng Y, Yu H, Zhu J. Preparation and Characterization of Microemulsions Based on Antarctic Krill Oil. *Marine Drugs* [Internet]. 2020; 18(10).
9. Musakhanian J, Osborne DW. Understanding Microemulsions and Nanoemulsions in (Trans)Dermal Delivery. *AAPS PharmSciTech*. 2025;26(1):31.
10. Prapaporn Boonme VBJ. Characterization and Stability of Vitamin A Palmitate Microemulsions Composed of Isopropyl Palmitate, Water and Polyoxyethylene-10-Oleyl Ether. *Journal of Pharmaceutical Science*. 2010;37:21-8.
11. Špaglová M, Čuchorová M, Čierna M, Poniš S, Bauerová K. Microemulsions as Solubilizers and Penetration Enhancers for Minoxidil Release from Gels. *Gels*. 2021;7(1).
12. Maitra M, Goyal AK, Rath G. A novel approach for follicular delivery of minoxidil for treatment of alopecia. *Journal of Drug Delivery Science and Technology*. 2017;41:113-23.
13. Lukić M, Pantelić I, Savić SD. Towards Optimal pH of the Skin and Topical Formulations: From the Current State of the Art to Tailored Products. *Cosmetics* [Internet]. 2021; 8(3).

Enhancing α -Gel Stability: The Role of Surfactant Ratios, Heating, and Stirring Conditions

Viriyanka Magha¹ and Vipaporn Panapisal^{1,}*

¹Department of Pharmaceutics and Industrial Pharmacy, Faculty of Pharmaceutical Sciences,
Chulalongkorn University, Bangkok 10330, THAILAND

*Corresponding author Email: Vipaporn.P@chula.ac.th

Abstract. α -Gels, known for their lamellar liquid crystal structure, offer high water retention, controlled rheology, and stability, making them valuable for skincare formulations. However, the stability and physical properties of α -Gels are highly sensitive to formulation parameters, and the optimal conditions for consistent and stable gel formation remain insufficiently explored. This study addresses this research gap by investigating the impact of formulation parameters, specifically the ratio of potassium cetyl phosphate (KCP) to L-arginine, heating time, and temperature, affect the physical properties and stability of α -Gel. α -Gel formulations were prepared using KCP to L-arginine ratios of 1:1, 2:1, and 3:1; heating durations of 1, 2, 3, and 4 hours; and temperatures of 75°C, 80°C, and 85°C at constant stirring speed of 100 rpm. Physical properties, including color, pH, viscosity, and microscopic structure, were evaluated. Preliminary stability results indicated that the optimal formulation (2:1 KCP to L-arginine ratio and 2-hour heating at 80°C) showed consistent viscosity with minimal fluctuations: 9,517 \pm 9.16 cP (Day 7), 9,685 \pm 2.00 cP (Day 14), 9,979 \pm 22.00 cP (Day 21), and 10,415 \pm 33.00 cP (Day 28), indicating strong structural integrity and resistance to phase separation. This formulation also exhibited a smooth, homogenous appearance, skin-compatible pH of 7, and a well-defined lamellar organization under polarized optical microscopy. These results highlight the significance of formulation parameters in achieving stable α -Gel systems, supporting their use in advanced skincare products.

Keywords: α -Gel; Lamellar Liquid Crystal; Film-forming Polymers; Water Resistance

INTRODUCTION

α -Gel, or α -form hydrated gel, is a lamellar liquid crystalline phase, which is a specially structured form obtained as a result of the self-assembly of surfactants and fatty alcohols in the aqueous systems. Its characteristic structure consists of hexagonally packed hydrophobic chains and hydrated hydrophilic layers, enabling it to trap large amounts of water and provide high viscosity and elasticity. These physical properties make α -Gel an ideal candidate for pharmaceutical and cosmetic formulations, including topical emulsions and creams, where it enhances product moisturizing, stability, and spreadability [1].

A key factor in α -Gel formulation is the potassium cetyl phosphate-to-L-arginine ratio, which impacts the packing structure of the gel and its stability. The focus of this study is the relationship between potassium cetyl phosphate (KCP), which is an anionic surfactant, and L-arginine. This ratio significantly impacts hydrogen bonding and electrostatic interactions that affect the gel's structural integrity. Notably, an imbalance in the KCP-to-L-arginine ratio can lead to undesirable shifts in pH and viscosity, potentially destabilizing the α -Gel system [2]. At lower KCP concentrations, limited amounts of anionic surfactants result in reduced micellization and weaker electrostatic forces, leading to minimal viscosity enhancement and a more neutral or slightly alkaline pH that may be attributed to the greater prevalence of basicity of L-arginine. In contrast, at higher KCP concentrations, excessively high anionic concentrations lead to denser lamellar packing, which promotes further viscosity increase via H-bonding interactions and an even greater drop in pH caused by acidic characteristics of excess KCP. Therefore, the ratio of KCP to L-arginine plays a vital role in defining the structural and physicochemical properties of α -Gel; critically, viscosity and pH profiles [1,2].

Heating is a critical factor in α -Gel formation, as the transition to the α -phase requires sufficient energy input through an endothermic process. Heating disrupts existing molecular assemblies, allowing new lamellar bilayers to form. Both temperature and duration must be carefully controlled, insufficient heating results in incomplete α -phase formation, while excessive heat or prolonged exposure can degrade sensitive components or disrupt lamellar alignment [3,4]. Typically, the system should be heated above the melting points of both the surfactant and fatty alcohol, followed by controlled cooling to promote the formation of ordered lamellar structures.

Accordingly, achieving a stable α -Gel with the desired physicochemical properties requires optimizing both the KCP-to-L-arginine ratio and the heating conditions. This study focuses on adjusting formulation parameters and evaluating their impact on physical appearance, pH, and viscosity, aiming to establish a reproducible procedure for α -Gel preparation to support future research in pharmaceutical and cosmetic applications.

MATERIALS AND METHODS

Materials

Potassium cetyl phosphate (KCP) (MySkinRecipes, Thailand), L-arginine (MySkinRecipes, Thailand), and deionized water.

Methods

Initial Screening of Critical Variables Affecting α -Gel Formation

Given the complex and sensitive nature of α -Gel self-assembly, where small formulation or processing changes can greatly impact lamellar structure and stability, a systematic screening was essential to define reliable conditions for future optimization. This preliminary study aimed to identify suitable parameters for producing physically homogeneous α -Gels with desirable physicochemical properties.

A full-factorial experimental design was used to test 36 unique conditions by varying two formulation factors, the KCP to L-arginine ratio (1:1, 2:1, 3:1 at a total concentration of 3% w/w), and three processing parameters: heating duration (1–4 hours), temperature (75°C, 80°C, 85°C), and a fixed stirring speed (100 rpm). Each condition was tested in a single-beaker batch, reflecting practical constraints during early exploration. Though each test was performed once, careful control and standardization of procedures ensured consistent and comparable results. This screening confirmed that α -Gel formation is feasible under specific conditions and provided a foundational reference for identifying key formulation and processing parameters for future refinement.

Preparation of α -Gel

A measured amount of KCP was melted at 200 °C on a hotplate stirrer. Separately, L-arginine was dissolved in water, stirred until homogeneous, and its pH was checked using pH paper. Using a 100 mL beaker with a magnetic stirrer (2/3 the base width), the α -Gel was prepared. A water bath was heated on a hotplate, with the temperature continuously monitored. The beaker was covered with a watch glass to minimize evaporation. Once KCP was fully melted, it was placed in the water bath and stirred at 100 rpm. The L-arginine solution was added slowly into the melted KCP. After mixing, the temperature was checked and maintained as needed. Finally, the mixture was cooled to room temperature while stirring gently at 60 rpm, allowing the α -Gel structure to form.

Physical Appearance Evaluation of α -Gel

The α -Gel formulations were observed visually by characterizing its color, separation phase, and consistency [5,6].

pH Measurement of α -Gel

The pH of α -Gel formulations will be measured using a digital pH meter (Mettler Toledo, Germany). An approximately 30 mL amount of α -Gel will be placed into a 50 mL glass beaker, then stir gently to homogenize the sample. Next, the pH electrode will be immersed directly into the α -Gel sample, and afterwards, wait for the reading to stabilize, typically around 30–60 seconds.

Viscosity Measurement of α -Gel

The viscosity of α -Gel formulations was measured using Viscometer (Brookfield DV-II+ Viscometer, US). An approximately 40 mL amount of α -Gel was poured into viscometer tube, then its viscosity was measured using suitable spindle and rpm speed. The reading of α -Gel's viscosity measurement results should be done within 30 until 60 seconds after the spindle start spinning.

Characterization of α -Gel: POM

Polarized optical microscopy (POM) (Olympus, Japan) was used to examine the micromorphology of the samples. Lamellar structures, such as α -Gels, typically exhibit a characteristic Maltese cross under polarized light. A small amount of sample was placed on a slide, covered with a cover glass, and gently pressed to ensure uniformity. Observations were first made under regular light, followed by polarized light. Representative images were captured at 10× magnification [2,5].

Stability Evaluation of selected α -Gel Formulations

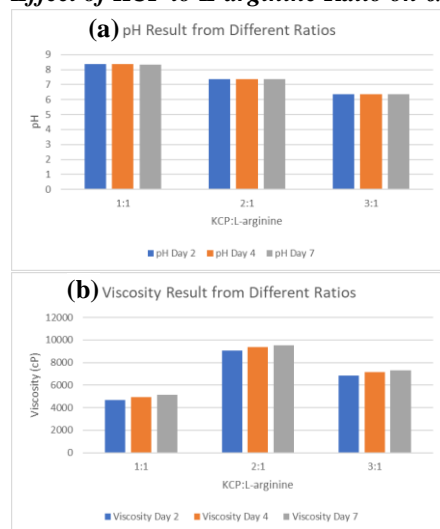
Based on preliminary screening results, formulation candidates with suitable viscosity (8,000–12,000 cP), pH (7.0–8.0), distinct Maltese cross patterns under polarized optical microscopy (POM), and no visible phase separation after one week were selected for further stability evaluation. These selected formulations represent optimal combinations of KCP-to-L-arginine ratios and heating conditions capable of consistently forming α -Gel. To assess their physical stability, the selected formulations were prepared in triplicate and stored in sealed glass containers under two conditions: ambient temperature and accelerated conditions (40 ± 2°C). Physical stability was monitored over a 28-day period, with evaluations conducted on days 7, 14, 21, and 28. The assessments included visual inspection, pH measurement, viscosity analysis, and microstructural examination via POM to confirm the integrity and robustness of the α -Gel structure over time.

Statistical Analyses

All experiments were conducted in triplicate (n = 3), and data are expressed as mean ± standard deviation (SD). One-way ANOVA was used to analyze differences among groups. For stability data collected over multiple time points, repeated measures ANOVA was applied. A p-value of < 0.05 was considered statistically significant.

RESULTS AND DISCUSSION

Effect of KCP to L-arginine Ratio on α -Gel Properties



The KCP:L-arginine ratio significantly influenced the physicochemical characteristics of the α -Gel. Among the tested ratios (1:1, 2:1, and 3:1), the 2:1 ratio consistently yielded the most favorable results. This formulation maintained a stable pH around 7.35–7.36 over days 2, 4, and 7 (Figure 1a), aligning well with the skin's natural pH range (4.5–6.5), thereby minimizing potential irritation. In comparison, the 1:1 ratio exhibited alkaline pH values (>8.3), which may disrupt the skin barrier, while the 3:1 ratio resulted in a slightly acidic pH (~6.35–6.37) [7]. Viscosity measurements further supported the superiority of the 2:1 ratio, showing values between 9064 and 9527 cP (Figure 1b), which fall within the optimal range for topical gels balancing spreadability and adhesion. The 1:1 ratio yielded significantly lower viscosities (4654–5117 cP), producing a less cohesive gel, whereas the 3:1 ratio showed moderately high viscosity (6855–7322 cP) but remained below the desirable threshold [8]. The enhanced performance of the 2:1 ratio may be attributed to a more balanced amphiphilic interaction between KCP and L-arginine, promoting the efficient formation of lamellar phases and contributing to a more stable α -Gel structure.

Figure 1. (a) pH and (b) viscosity from different ratios of KCP to L-arginine in 7 days.

Effect of Heating Time on α -Gel Structure and Stability

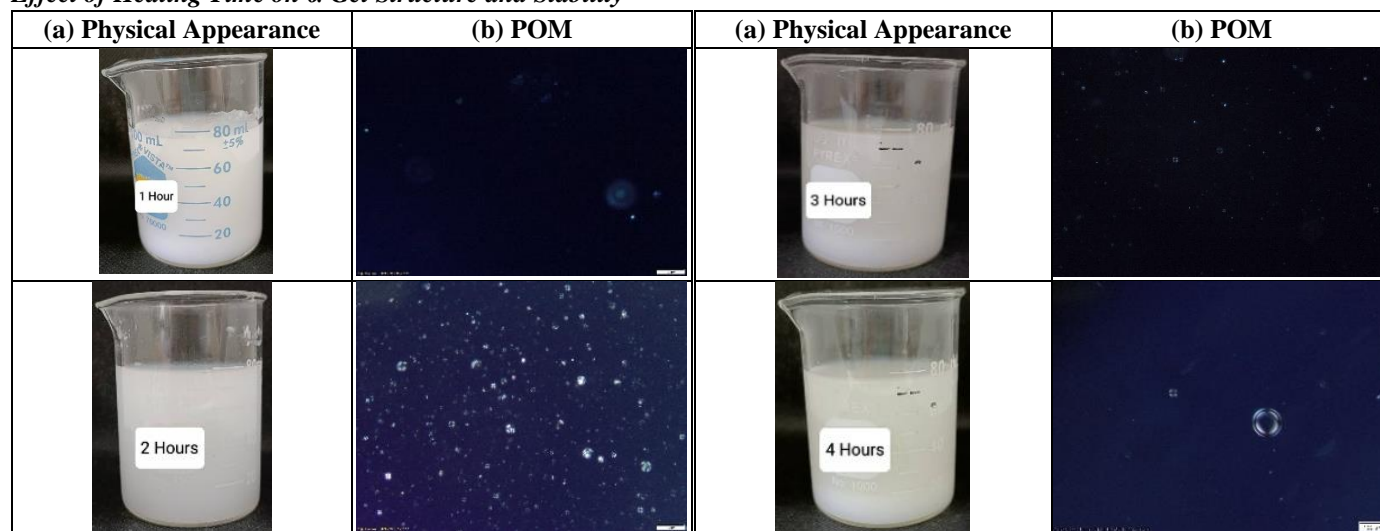


Figure 2. Result of (a) physical appearance and (b) POM at day 7 from different heating time.

Heating duration played a critical role in determining the internal structure and physical stability of α -Gels. Among the tested conditions (1, 2, 3, and 4 hours), the 2-hour heating period yielded the most favorable outcomes. By day 7, α -Gels heated for 2 hours maintained a homogeneous appearance with no visible phase separation (Figure 2a), whereas other durations exhibited signs of sedimentation. Polarized optical microscopy (POM) further supported these findings. The 2-hour formulation displayed prominent Maltese cross patterns (Figure 2b), indicative of a well-formed lamellar liquid crystalline phase. In contrast, gels heated for 1 hour or 4 hours showed weak or absent birefringence, suggesting either incomplete assembly or thermal disruption of the lamellar structure.

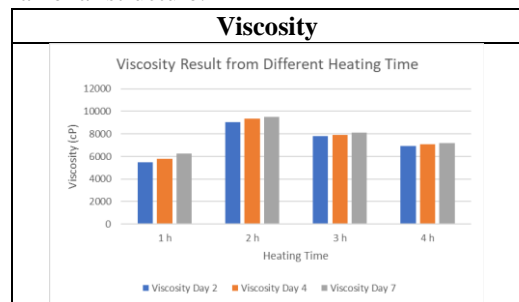


Figure 3. Result of viscosity within 7 days from different heating time.

Viscosity measurements (Figure 3) showed that the 2-hour samples consistently retained values within the desired topical gel range of 8000–12000 cP (9064–9527 cP), indicating both adequate spreadability and skin adhesion. Insufficient heating (1 hour) may not provide enough energy to drive proper molecular assembly, while excessive heating (3–4 hours) likely disrupts the lamellar network through thermal degradation, as previously observed in thermosensitive gel systems [1,9]. Thus, a 2-hour heating period offers an optimal balance, supplying sufficient thermal energy to promote self-assembly while preserving the gel's structural integrity.

Result Effect of Heating Temperature on α -Gel Microstructure and Rheology

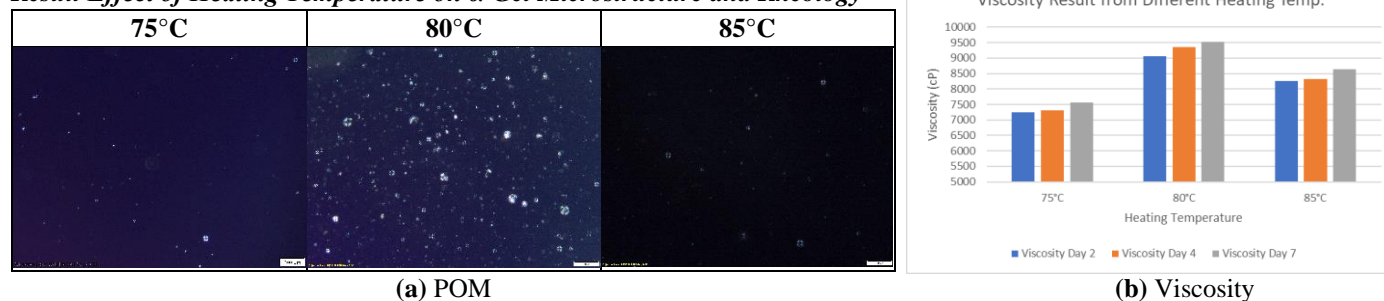
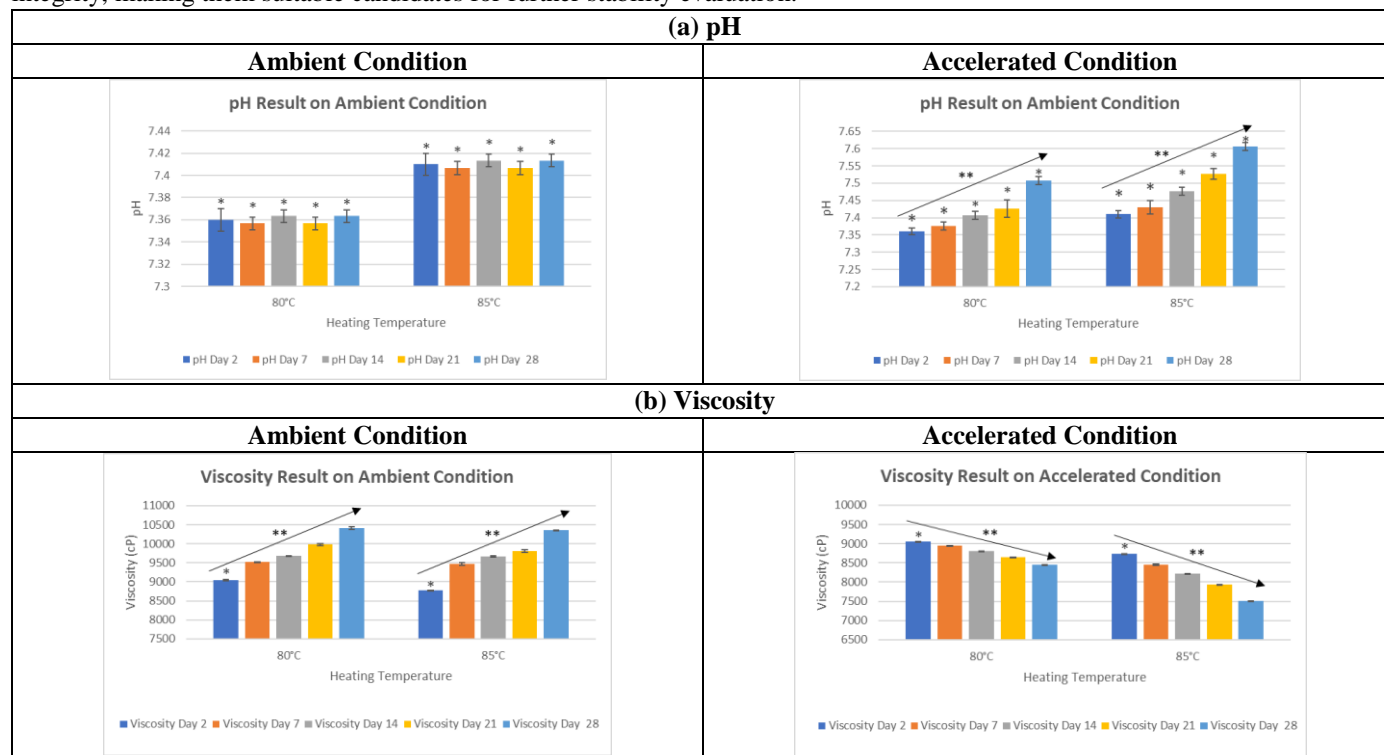


Figure 4. Result of (a) POM at day 7 and (b) viscosity within 7 days from different heating temperature.

Heating temperature plays a critical role in determining the microstructure and rheological behavior of α -Gels (Figure 4). Among the temperatures tested (75 °C, 80 °C, and 85 °C), heating at 80 °C yielded the most favorable results. At this temperature, the α -Gel exhibited high viscosities ranging from 9064 to 9527 cP, along with distinct Maltese cross patterns under polarized optical microscopy (POM), indicating the formation of a well-organized lamellar liquid crystalline phase. The superior structural properties observed at 80 °C can be attributed to sufficient thermal energy promoting the alignment and packing of surfactant molecules and fatty alcohols, enhancing hydrophobic interactions and hydrogen bonding [1]. In contrast, heating at 75 °C resulted in lower viscosities (7248–7561 cP) and poorly defined lamellar structures, likely due to inadequate thermal input for complete self-assembly. At 85 °C, viscosity decreased slightly (8249–8633 cP), and fewer birefringent domains were observed, possibly due to thermal degradation or disruption of previously formed structures. These findings are consistent with earlier reports indicating that overheating may shrink the gel network and reduce viscoelasticity, ultimately compromising the physical integrity of the α -Gel system [10].

Result of Stability Study



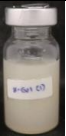



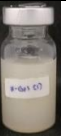




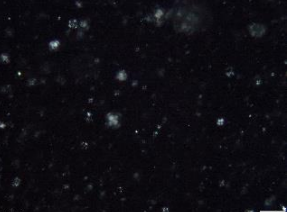

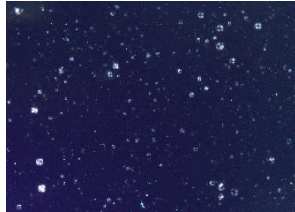


α -Gel formulations prepared with a 2:1 KCP-to-L-arginine ratio and heated for 2 hours at either 80°C or 85°C were selected based on their optimal physical characteristics, including a smooth appearance, well-defined lamellar structures (Maltese cross patterns), and ideal viscosities within the 8000–12000 cP range. These properties indicate robust gel strength and structural integrity, making them suitable candidates for further stability evaluation.



* 80°C and 85°C are statistically different ($p < 0.05$); ** statistically different within times

Figure 5. Stability result of (a) pH and (b) viscosity from 80°C and 85°C heating temperature within 28 days.

Figure 6. Stability result of (a) physical appearance and (b) POM from 80°C and 85°C heating temperature at day 7 and day 28.

Properties	Ambient Condition				Accelerated Condition			
	Day 7		Day 28		Day 7		Day 28	
(a) Physical Appearance	80°C 	85°C 	80°C 	85°C 	80°C 	85°C 	80°C 	85°C 
(b) POM								
								

The selected α -Gel formulations (2:1 KCP-to-L-arginine ratio, heated for 2 hours at 80°C and 85°C) exhibited good stability over 28 days under both ambient and accelerated conditions. Physically, both remained stable with no phase separation, discoloration, or consistency loss (Figure 6a) [5]. Under ambient conditions, pH remained stable: 80°C averaged 7.36 ± 0.01 , while 85°C was 7.41 ± 0.01 . Under accelerated conditions, both increased significantly ($p < 0.05$), with 80°C rising to 7.50 ± 0.01 and 85°C to 7.61 ± 0.01 , indicating higher pH drift at elevated temperature (Figure 5a) [3]. Viscosity under ambient conditions increased: 80°C from $9,042 \pm 25.66$ to $10,415 \pm 33$ cP, and 85°C from $8,768 \pm 8.54$ to $10,365 \pm 2.00$ cP. Under accelerated conditions, viscosity declined: 80°C from $9,051 \pm 3.00$ to $8,444 \pm 1.53$ cP, and 85°C from $8,731 \pm 9.50$ to $7,513 \pm 5.67$ cP, with greater loss at 85°C (Figure 5b) [1]. POM analysis confirmed structural stability: both gels showed clear Maltese crosses under ambient conditions. Under accelerated conditions, crosses remained visible but became smaller and more diffuse—yet still indicative of lamellar structures (Figure 6b) [2]. Overall, the 80°C formulation maintained better pH, viscosity, and microstructural stability, making it more suitable for long-term topical use.

CONCLUSIONS

This study concluded that the optimal parameters for preparing stable α -Gel are a KCP:L-arginine ratio of 2:1, heating temperature of 80 °C, and heating duration of 2 hours. These conditions produced α -Gels with desirable pH (around 7), viscosity (8000–12000 cP), uniform physical appearance, and abundant Maltese cross patterns under POM. The selected formulation also demonstrated good physical appearance and structural stability under both ambient and accelerated storage conditions.

ACKNOWLEDGMENTS

The author gratefully acknowledges the financial support provided by Chulalongkorn University's Graduate Scholarship Program for ASEAN or Non-ASEAN Countries, which made this study possible.

REFERENCES

1. Ichihara K, Sugahara T, Akamatsu M, Sakai K, Sakai H. Rheology of α -Gel Formed by Amino Acid-Based Surfactant with Long-Chain Alcohol: Effects of Inorganic Salt Concentration. *Langmuir*. 2021 Jun 15;37(23):7032–8.
2. Ren H, Tang X, Chen M. Preparation and Characterization of Alpha Gel Formed by Fatty Alcohol and Amino Acid Surfactants. *J Surfactants Deterg*. 2021 Sep 1;24(5):865–70.
3. Suzuki T. Liquid Crystal and α -gel-Based Emulsion and Soft Gel formulations. Vol. 2, Acc. Mater. Surf. Res. 2017.
4. Iwata T. Stabilization of Emulsion by α -Gel [Internet]. 2017. Available from: <https://www.researchgate.net/publication/312471830>
5. NIKKO CHEMICALS. α -gel forming agent that gives a new feel to products NIKKOL PUREPHOS® α . 2023.
6. Aramaki K, Matsuura Y, Kawahara K, Matsutomo D, Konno Y. Effect of Adding Lecithin and Nonionic Surfactant on α -Gels Based on a Cationic Surfactant-Fatty Alcohol Mixture. *J Oleo Sci [Internet]*. 2021 [cited 2025 Apr 10];70(1):67–76. Available from: <https://www.ncbi.nlm.nih.gov/pubmed/33431774>
7. Kuo SH, Shen CJ, Shen CF, Cheng CM. Role of pH Value in Clinically Relevant Diagnosis. *Diagnostics [Internet]*. 2020 [cited 2025 May 6];10(2):107. Available from: <https://pmc.ncbi.nlm.nih.gov/articles/PMC7167948/>
8. Krisanti EA, Kirana DP, Mulia K. Nanoemulsions containing *Garcinia mangostana* L. pericarp extract for topical applications: Development, characterization, and in vitro percutaneous penetration assay. *PLoS One [Internet]*. 2021 Dec 1 [cited 2025 May 6];16(12):e0261792. Available from: <https://journals.plos.org/plosone/article?id=10.1371/journal.pone.0261792>
9. Mao B, Bentaleb A, Louerat F, Divoux T, Snabre P. Overcooked agar solutions: impact on the structural and mechanical properties of agar gels. 2016 Mar 2 [cited 2025 May 6]; Available from: <https://arxiv.org/pdf/1603.00778>
10. Sugahara T, Akamatsu M, Iwase H, Takamatsu Y, Sakai K, Sakai H. Structural Change of an α -Gel (α -Form Hydrated Crystal) Induced by Temperature and Shear Flow in an Oleic Acid Based Gemini Surfactant System. *Langmuir [Internet]*. 2020 May 5 [cited 2025 May 7];36(17):4695–701. Available from: [doi/pdf/10.1021/acs.langmuir.0c00507](https://doi.org/10.1021/acs.langmuir.0c00507)

Nanofibril Cellulose from Pineapple Core: A Sustainable Solution for Antimicrobial Air Filtration

*Chayaphat Phechkrajang*¹, *Saranyapong Boonprasit*¹, *Nannaphat Nantawisit*¹, *Waraphon Sinsiri*¹,
*Jiraphong Suksiriworapong*², *Nanthawan Jinakul*³, *Nantana Nuchtavorn*^{4,*}

¹ Benchamaracharungsarit School, 222 Chumpol Rd., Na Mueang, Mueang, Chachoengsao, 24000, THAILAND

² Department of Pharmacy, Faculty of Pharmacy, Mahidol University, 447 Sri-Ayudhaya Rd., Rajathevee, Bangkok, 10400, THAILAND

³ Department of Microbiology, Faculty of Pharmacy, Mahidol University, 447 Sri-Ayudhaya Rd., Rajathevee, Bangkok, 10400, THAILAND

⁴ Department of Pharmaceutical Chemistry, Faculty of Pharmacy, Mahidol University, 447 Sri-Ayudhaya Rd., Rajathevee, Bangkok, 10400, THAILAND

*Corresponding author Email: nantana.nuc@mahidol.ac.th

Abstract. Pineapple (*Ananas comosus* Linn.) is widely cultivated in Thailand, with the Batavia variety (Smooth Cayenne), also known as Sriracha pineapple, being particularly popular in the eastern region. The pineapple core, often discarded as waste at both household and industrial levels, is a valuable source of cellulose. This study aims to extract nanofibril cellulose (NFC) from pineapple cores to develop an air filter capable of removing fine dust particles while exhibiting antibacterial properties. Batavia pineapple cores were processed into NFC using a ball mill, followed by chemical treatments (acid hydrolysis, alkaline hydrolysis, or enzymatic hydrolysis with cellulase), and subsequently high-pressure homogenization. The particle size and functional groups of the samples were analyzed using a Zetasizer (Nano series) and Fourier Transform Infrared Spectroscopy (FT-IR). The NFC was then fabricated into filter sheets using a grille method, dried, and evaluated for particulate filtration efficiency and antibacterial activity. Zinc oxide (ZnO) powder was used to simulate dust particles. The concentration of ZnO in deionized water, before and after filtration through the membrane, was determined by complexometric titration to evaluate the membrane's filtration efficiency. Antibacterial activity against *S. epidermidis* was assessed using gentamicin as a positive control. The results showed that the proposed method yielded nanofibril cellulose with an average particle size of approximately 400 nm. Membrane filters were successfully produced by drying the NFC slurry at 60°C in a hot air oven. The filters achieved a ZnO filtration efficiency of 51.7% and demonstrated 44.4% antibacterial activity compared to the control against *S. epidermidis*.

Keywords: Nanofibril cellulose, Smooth Cayenne, Antibacterial membrane

INTRODUCTION

The applications of nanofibril cellulose materials have increased over the past decade due to their desirable properties, including high strength and stiffness, low weight, and high surface area, which enable strong interactions with surrounding species. Novel nanofibril cellulose derived from plant sources has gained interest due to its potential as a sustainable material, high natural abundance, and biodegradability [1–3]. This study aimed to isolate and extract nanofibril cellulose from the core of pineapple (*Ananas comosus* Linn.). The extracted nanofibril cellulose was further processed to form a filtration membrane. The filtration efficiency and antibacterial properties of the resulting membrane were evaluated. *Ananas comosus* Linn., a pineapple variety, is abundantly found in eastern Thailand. Its core is usually not consumed and is often discarded as waste. This study adds value to pineapple core waste by converting it into a functional material.

MATERIALS AND METHODS

Materials

Zinc oxide was purchased from Honeywell (NC, USA). Hydrochloric acid was purchased from ACI Labscan (Thailand). Silver nitrate and sodium hydroxide were obtained from Carlo Erba (Cornaredo, Italy). Ethylenediaminetetraacetate sodium and enzyme cellulase, 4.8 units/mg, were from Sigma-Aldrich (MO, USA). Sodium borohydride was purchased from TCI (Tokyo, Japan). Polyvinylpyrrolidone was from O-BASF (Ludwigshafen, Germany).

Methods

Production of nanofibril cellulose (NFC)

The core of the pineapple was washed and dried for 30 minutes before being cut into small pieces and finely ground using a food blender. The resulting fine material was washed several times with deionized water until the rinse water was clear. The material was then dried at 60 °C in a hot air oven for 3 hours. The dried material was ground using a ball mill (QM-3SP2, Nanjing T-Bota Sciotech Instruments & Equipment Co., Ltd, China), and both the milling speed and grinding time were evaluated. The particle sizes were measured using a Mastersizer 3000 (Malvern Instruments, UK). The smallest particle size fraction was further subjected to hydrolysis using acid (5 g of dried material in 50 mL of 2.5 M HCl), base (5 g in 50 mL of 2.5 M NaOH), and enzymatic treatment (5 g in 50 mL of 10 mg/mL cellulase). The hydrolysis conditions were 105 °C for 30 minutes for acid and base, and 50 °C for 30 minutes for enzymatic hydrolysis. After 30 minutes, the hydrolyzed materials were washed with deionized water until the pH of the rinse water was neutral. Fourier-transform infrared spectroscopy (Nicolet iS5, Thermo Fisher Scientific, USA) was used to analyze the functional groups of the cellulose material. To further reduce the particle size, a cellulose suspension in reverse osmosis water (5 g in 400 mL) was processed using a high-pressure homogenizer (APV 2000, UK), and the particle size was monitored with a Zetasizer (Malvern Instruments, UK). Finally, the resulting suspension was lyophilized using a freeze dryer (Christ Alpha 1–4 LD plus, Osterode am Harz, Germany) to remove the water.

Membrane filter formation

The nanofibril cellulose (NFC) slurry was prepared by dispersing 0.4 g of dried nanocellulose fibrils in deionized water. A nanofibril cellulose membrane filter was formed using one sheet of stainless-steel wire mesh and two sheets of gauze as support layers. Two types of membranes, with surface densities of 1 mg/cm² and 2 mg/cm², were prepared. The membranes were dried at 60 °C for 1 hour and 2 hours for the 1 mg/cm² and 2 mg/cm² membranes, respectively. A schematic diagram of the nanofibril cellulose membrane filter formation is shown in Figure 1.

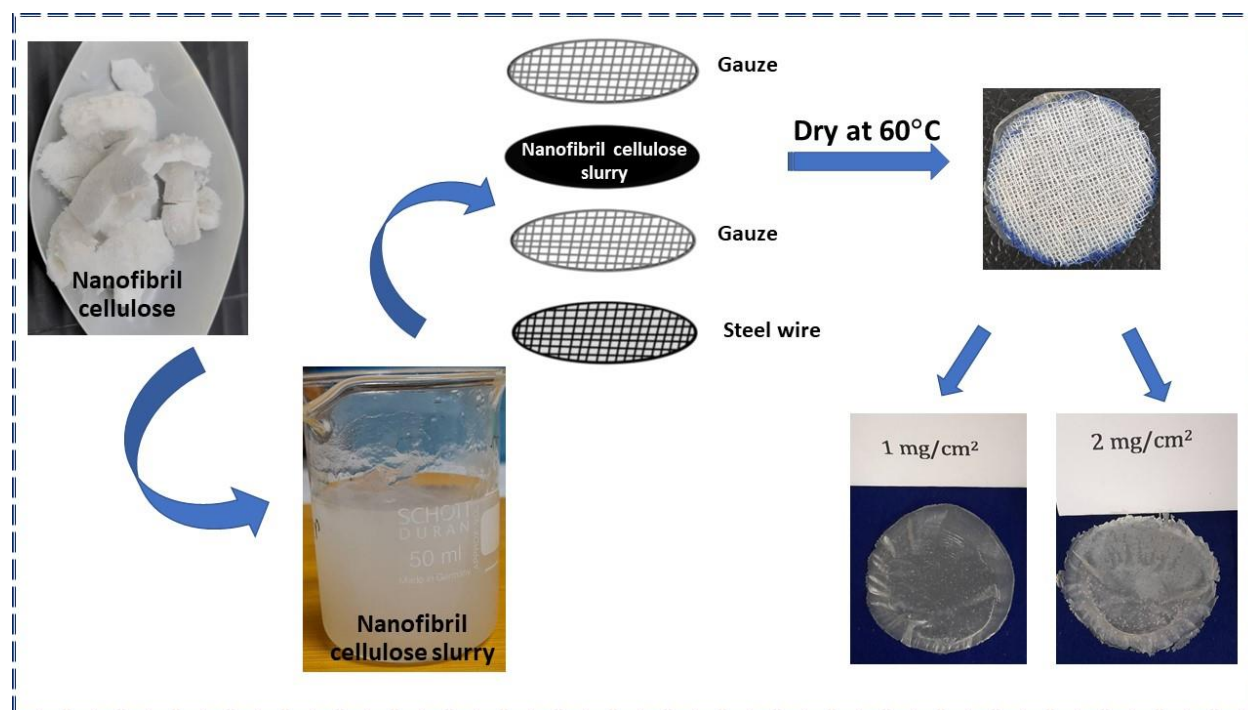


Figure 1. The schematic diagram of nanofibril cellulose membrane filter formation.

Evaluation of filtration properties

The filtration efficiency of the nanocellulose fibril membrane was evaluated using zinc oxide (ZnO) particles with a size range of 3–4 μm . Approximately 50 mg of ZnO, accurately weighed, was dispersed in 50 mL of deionized water and filtered through the membrane using a water jet pump (Sigma Aldrich, MO, USA). Amount of ZnO in the filtrate was quantitatively determined by complexometric titration with 0.05 M ethylenediaminetetraacetic acid disodium salt [4]. The remaining ZnO on the membrane was calculated by subtracting amount of ZnO in the filtrate from the total weight of ZnO taken, this was amount filtered ZnO by the membrane. Then, the filtration efficiency of the membrane was calculated using the following equation:

$$\text{Filtration efficiency of the membrane (\%)} = \frac{\text{Amount filtered ZnO (mg) by the membrane}}{\text{Weight of ZnO taken (mg)}} \times 100$$

Evaluation of antibacterial properties

The antibacterial properties of nanofibril cellulose membranes, both with and without silver nanoparticles, were evaluated against *S. epidermidis*, using gentamicin as a positive control. The silver nanoparticle solution was prepared by reacting silver nitrate with sodium borohydride [5]. Specifically, 0.255 g of silver nitrate was dissolved in 15 mL of deionized water and slowly added dropwise to a solution containing 0.575 g of sodium borohydride in 15 mL of 1 M NaOH under continuous stirring. Finally, 20 mL of 10% polyvinylpyrrolidone was added and mixed thoroughly to stabilize the silver nanoparticle solution. Varying volumes (10–30 μL) of the silver nanoparticle solution were added to the nanofibril cellulose membranes for antibacterial testing.

RESULTS AND DISCUSSION

Production of nanofibril cellulose (NFC)

The dried pineapple core obtained from the first step was ground using a ball mill machine. The milling speed (ranging from 1200 to 1500 rpm) and grinding time (ranging from 10 to 30 minutes) were varied. The results showed that the smallest particle size was achieved at a speed of 1500 rpm for 30 minutes. The sample obtained under this condition was then hydrolyzed using acid, base, and the enzyme cellulase according to the procedure described in the Experimental section. After hydrolysis, the sample was analyzed using infrared spectroscopy. As shown in Figure 2, the IR spectrum of the sample exhibited characteristic absorption bands corresponding to functional groups present in the cellulose structure: O–H stretching at 3200–3400 cm^{-1} , C–H stretching (aliphatic) at 2800–2900 cm^{-1} , C–O stretching at 1000–1280 cm^{-1} , and C–C stretching at 1000 cm^{-1} .

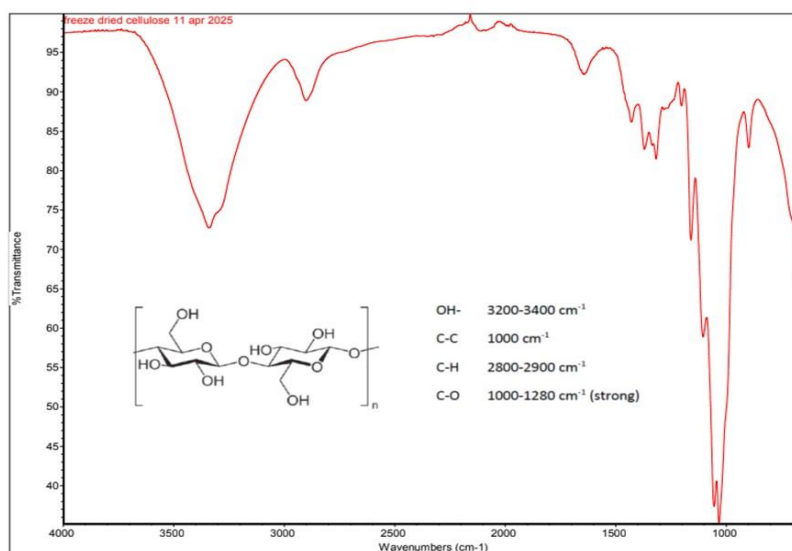


Figure 2. The representative IR spectrum of cellulose material after hydrolysis condition exhibits the absorption bands correspond to the functional groups in cellulose structure i.e., O–H stretching at 3200–3400 cm^{-1} , C–H stretching (aliphatic) at 2800–2900 cm^{-1} , C–O stretching at 1000–1280 cm^{-1} , and C–C stretching at 1000 cm^{-1} .

After size reduction using a high-pressure homogenizer at 1000 bar for 10 cycles, the base-hydrolyzed sample exhibited the smallest particle size, approximately 270 nm. Therefore, the sample obtained under the base hydrolysis condition was selected for further experiments. The output from the high-pressure homogenizer was subsequently dried using a freeze-dryer to obtain the final nanofibril cellulose product. From 5 g of starting material, 1.76 g of product was recovered after freeze-drying, corresponding to a yield of 35.2%.

Membrane filter formation

Membrane filters were prepared both with and without support sheets. As shown in Figure 1, the membrane filter without support sheets appeared clear and transparent. However, the resulting membrane lacked elasticity and could not be used in filtration equipment. To improve mechanical strength, three layers of support sheets were incorporated. The membranes with support sheets were used for filtration property evaluation and antibacterial property evaluation experiments.

Evaluation of filtration properties

In this study, three water insoluble compounds which were available in our laboratory, $\text{Al}(\text{OH})_3$, ZnO , CaCO_3 , were measured the particles size. Eventually, zinc oxide (ZnO) was selected as a representative small airborne particle due to its average particle size of approximately 3-4 μm . Filtration performance was tested for: (1) support sheets without membrane, (2) membranes containing 1 mg/cm^2 of nanofibril cellulose, and (3) membranes containing 2 mg/cm^2 of nanofibril cellulose. As shown in Figure 3, the membranes with nanofibril cellulose demonstrated significantly improved filtration efficiency compared to the support sheets alone. The average filtration efficiencies for the 1 mg/cm^2 and 2 mg/cm^2 membranes were 41.4% and 51.7%, respectively.

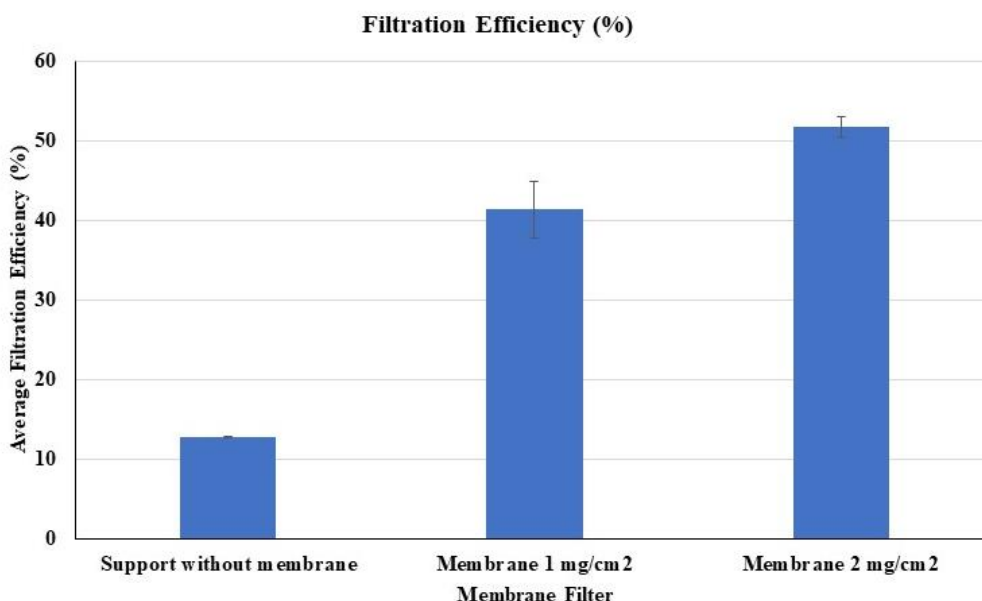


Figure 3. Filtration properties of the formation nanofibril cellulose membrane. The filtration efficiency (average % \pm SD ($n = 3$)) of the support without membrane, the membrane containing cellulose 1 mg/cm^2 and the membrane containing cellulose 1 mg/cm^2 were 12.8 % \pm 0.1, 41.4 % \pm 3.5 and 51.7 % \pm 1.3, respectively.

Evaluation of antibacterial properties

Airborne particles may contain microorganisms; therefore, the antibacterial properties of the candidate filter membranes were further evaluated. Both the synthetic membrane and the membrane incorporating silver nanoparticles were tested for their ability to inhibit *S. epidermidis*, using gentamicin as a positive control. The results indicated that the synthetic membrane alone did not exhibit antibacterial activity (Figure 4). However, the membranes doped with silver nanoparticles demonstrated antibacterial effects, with the activity increasing in accordance with the concentration of silver nanoparticles.

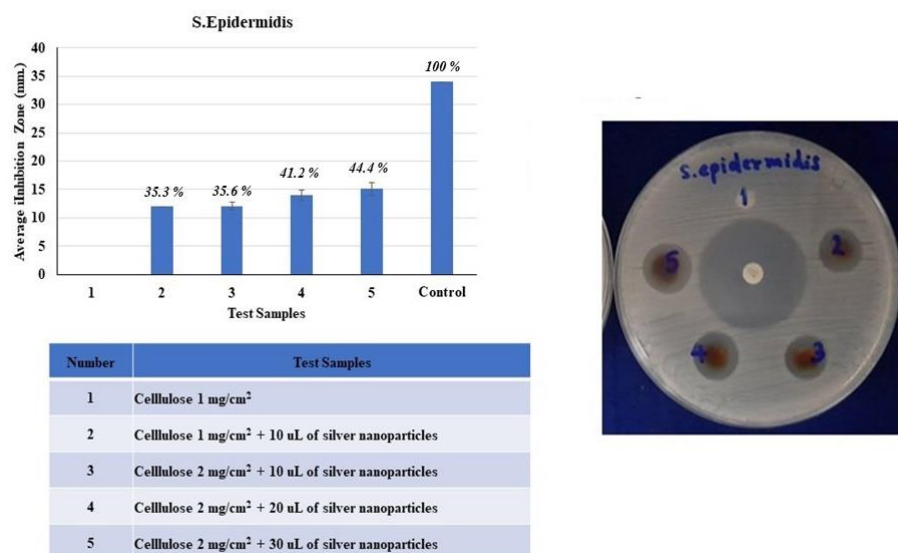


Figure 4. Antibacterial properties of the formation nanofibril cellulose membrane. The membrane containing cellulose material 2 mg/cm² with 30 μ L of silver nanoparticles exhibited the maximum antibacterial activity of 44.4% compared with the control, gentamicin.

CONCLUSIONS

This study successfully developed a nanofibril cellulose filter membrane derived from pineapple core, an abundant, sustainable, and biodegradable agricultural waste material. The process yielded approximately 35% nanofibril cellulose from the dried pineapple core. The resulting membrane effectively filtered zinc oxide particles with an average size of 3-4 μ m, achieving average filtration efficiencies of 41.4% for the 1 mg/cm² membrane and 51.7% for the 2 mg/cm² membrane. Furthermore, the incorporation of silver nanoparticles endowed the membrane with antibacterial activity against *S. epidermidis*, with the degree of inhibition increasing alongside the concentration of silver nanoparticles. The results of this study successfully demonstrate a valuable approach for converting agricultural waste into functional and environmentally friendly filtration materials. In addition, to validate these findings, future studies should focus on enhancing the mechanical strength and flexibility of the membrane to expand its practical applications. More precise PM2.5 filtration experiments and particle size measurements using scanning electron microscopy should also be conducted.

ACKNOWLEDGMENTS

The authors would like to thank Department of Pharmacy, Department of Pharmaceutical Chemistry, Central Research Laboratory Unit, Faculty of Pharmacy, Mahidol University for research facilities.

REFERENCES

1. Yi T, Zhao H, Mo Q, Pan D, Liu Y, Huang L, Xu H, Hu B, Song H. From Cellulose to Cellulose Nanofibrils—A Comprehensive Review of the Preparation and Modification of Cellulose Nanofibrils. *Materials*. 2020;13:5062.
2. Jose SA, Cowan N, Davidson M, Godina G, Smith I, Xin J, Menezes PL. A Comprehensive Review on Cellulose Nanofibers, Nanomaterials, and Composites: Manufacturing, Properties, and Applications. *Nanomaterials* 2025;15:356.
3. Islam MT, Alam MM, di Torino P, Patrucco A, Montarsolo A, Zoccola M. Preparation of Nanocellulose: A Review. *AATCC J. Res.* 2014;1(5):17-23.
4. Zinc oxide compounded paste monograph. In: United States Pharmacopeia [Online]. Rockville, MD: USP Convention; 2025 [cited 2025 Mar 24]. Available from: <https://www.uspnf.com>
5. Raheem SA, Alfatlawi AH. Surface-water purification using cellulose paper impregnated with silver nanoparticles. *Drink. Water Eng. Sci.* 2021;14:95–102.

Exploring the Combined Pharmacological Potential of *Mimosa pudica* L. and *Centella asiatica* in Hyperglycemic Wound Healing: A Hyperglycemic Planarian Regeneration Model Approach

Thanyathorn Lohabunditwong^{1,}*

¹The Newton Sixth Form, Bangkok, Thailand

*Corresponding author Email: aunging.loha@gmail.com

Abstract. Hyperglycemic wounds are characterized by delayed healing due to high glucose levels, impairing cell migration, vascular function, immune response, and collagen synthesis. Chronic inflammation and oxidative stress further hinder tissue regeneration and increase infection risk. Plant-derived compounds such as flavonoids and triterpenoids are emerging as potential alternatives for hyperglycemic wound management. This study aimed to evaluate the wound-healing potential of *Mimosa pudica* L. and *Centella asiatica*, individually and in combination, using a hyperglycemic planarian regeneration model. Planarians were rendered hyperglycemic by exposure to 50 mM D-glucose before being assigned to four groups: A (0.2 µg/mL *M. pudica* + 1 mg/mL *C. asiatica*), B (0.2 µg/mL *Mimosa pudica* L.), C (1 mg/mL *Centella asiatica*), and D (negative control). Regeneration was assessed by photoreceptor recovery over time, serving as a proxy for tissue regeneration. A exhibited the most significant regenerative response, with complete photoreceptor restoration observed within the shortest period. B and C showed slower regeneration and mild signs of toxicity. D displayed the poorest recovery, confirming the baseline impairment of the hyperglycemic model. These results, based on preliminary observation, suggest that the combination of *M. pudica* and *C. asiatica* demonstrates a synergistic effect on tissue regeneration, likely due to the complementary action of flavonoids and triterpenoids on fibroblast-like blastema cells. These findings support the potential application of combined phytotherapeutics in hyperglycemic wound care. Future studies should involve larger sample sizes and usage of mammalian models and molecular analyses to confirm efficacy and elucidate underlying mechanisms.

Keywords: Hyperglycemic wound healing; Phytotherapy; Planarian regeneration; *Mimosa pudica* L.; *Centella asiatica*

INTRODUCTION

Hyperglycemic conditions impair numerous bodily processes, including cellular proliferation, angiogenesis, and immune responses—particularly those involving neutrophils, a type of leukocyte.[1][2][3] This impairment is primarily due to glucose toxicity, which, if prolonged, is indicative of diabetes.[2] As a result, diabetic wounds exhibit a significantly slower regeneration rate compared to those in non-diabetic individuals. These wounds are also more susceptible to infection, which can escalate into severe complications, often leading to amputation.[4]

According to the latest data from *The Lancet*, approximately 828 million adults aged 18 and older are living with diabetes.[5] The condition is strongly associated with aging, and with the global elderly population projected to increase from 1.1 billion in 2023 to 1.4 billion by 2030, diabetes is set to become one of the most critical health concerns of the future.[6][7]

With the rising diabetic population, the demand for wound care solutions in hyperglycemic conditions is undeniably increasing. Treatment options span from basic wound dressings to advanced therapies such as skin grafts.[8] Among these, herbal extracts have emerged as popular and promising alternatives. For example, *Centella asiatica*, widely used in Thailand, contains triterpenes—such as asiatic acid (AA), asiaticoside (AS), madecassoside (MS or brahminoside), and madecassic acid (MA or brahmie acid)—which are known for their anti-inflammatory, antiviral, antimicrobial, and immunomodulatory properties.[9][10] In addition, *Centella asiatica* also contains alkaloids, tannins, flavonoids, terpenoids, and reducing sugars.[11] Flavonoids, in particular, are known for their strong antioxidative and anti-inflammatory effects, further contributing to the wound healing process.[11][12]

However, many other medicinal plants with wound-healing potential remain underutilized. One such example is *Mimosa pudica* Linn, commonly known as the shameplant. Often dismissed as a weed and appreciated solely for its unique sensitivity, this plant actually contains valuable active compounds—including alkaloids, the non-

protein amino acid mimosine, flavonoids, C-glycosides, sterols, terpenoids, tannins, and fatty acids—that suggest its potential to accelerate tissue regeneration.[13]

To confirm its efficiency both individually and in combination on this specific type of wound, the extracts were tested on hyperglycemic planarians regeneration model as they one of the common in vivo model for studying tissue regeneration.[14] Moreover, the results were assess based on photoreceptors regeneration since the eyes are visible under a light microscope and discrete.[15]

MATERIALS AND METHODS

Materials

D-glucose (analytical grade) [LOBA CHEMIE PVT.LTD., India], 70% Ethanol (EtOH), 95% Ethanol (EtOH), Dimethyl sulfoxide (DMSO), dried *Mimosa pudica* L. (Thailand) plant, *Centella asiatica* extract [GREENTECH, France], Sodium acetate [SIGMA CHEMICAL, USA], Aluminium chloride [Riedel, Germany], Planarians, Reversed osmosis (RO) water, Deionised (DI) water, Shrimp pellet food, Rotary evaporator, Micro Pipette, Light microscope, Spectrophotometer

Methods

Animal

Ethical approval was not required for this study, as it only involved planarians, an invertebrate species not subject to Ethical Principles and Guidelines for the Use of Animals, National Research Council of Thailand.

Mimosa pudica L. extraction

Dried *Mimosa p.* plants were soaked in 70% Ethanol (EtOH) for 48 hours prior and the mixture of extract and EtOH were separated by rotary evaporation under 150 rpm, 60°C, and 100 mbar. The extract was then dissolved in 20 ml of DMSO and diluted to the wanted concentration.

Total Flavonoid Content Analysis (Aluminium Chloride Colorimetric Method)

For total flavonoid content determination of the sample, Quercetin was used to create a standard calibration curve. The standard solutions of Quercetin were prepared by serial dilutions using DMSO (5-50 µg/mL). The sample solution was diluted by 100 fold using DMSO. The standard or sample solution (800 µL) was mixed with 2.4 mL of 95% Ethanol, 160 µL of 10% AlCl₃ and 1M Sodium acetate. After mixing, the solution incubated for 10 min at room temperature. The absorbance of the reaction mixtures was measured against blank at 440 nm wavelength with a Thermo Fisher UV-Vis Spectrophotometer (GENESYS 150 Spectrophotometer, Thermo Fisher). The estimated concentration of total flavonoid content in the test samples was calculated from the calibration plot and expressed as µg Quercetin equivalent (µg QE)/mL of extract. However, the extract was diluted by 100 fold so the actual estimated total flavonoid content is about 1.91±0.12 mg QE/mL. All the determinations were carried out in triplicate. [16][17][18]

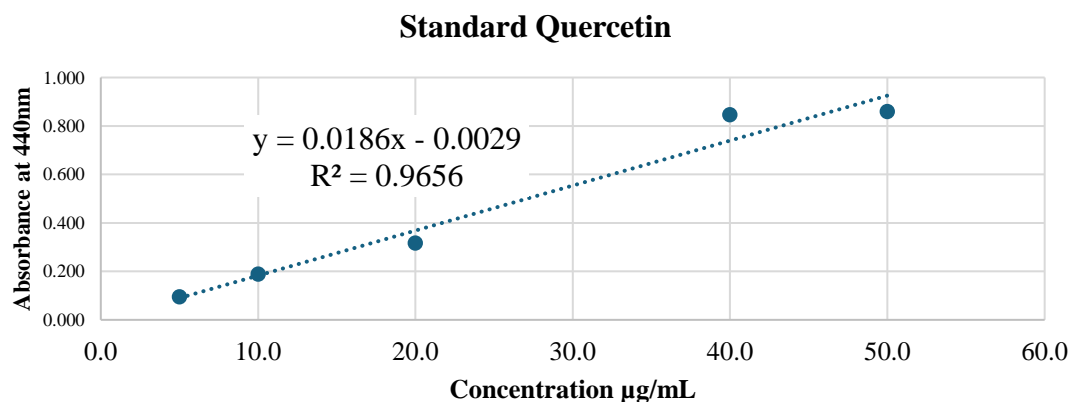


Figure 1. Total flavonoid content for standard Quercetin

Hyperglycemic planarian induction

Planarians were immersed in 50 mM of D-glucose 48 hours. As an observation, the planarians curled in a c-shape and have less movement activity.

Planarian's photoreceptor regeneration assessment

Hyperglycemic planarians were decapitated and divided into 4 groups to test 4 different conditions including group A (0.2 µg/mL *M. pudica* + 1 mg/mL *C. asiatica*), group B (0.2 µg/mL *Mimosa pudica* L.), group C (1 mg/mL *Centella asiatica*), and group D (negative control). The planarians were observed under a light microscope for eye spots every day and were feed with pellet food every 3 days.

Statistical analyses

Statistical analysis was conducted using the independent two-sample t-test in Microsoft Excel to compare the effects of different treatments on planarian regeneration under hyperglycemic conditions. Each group consisted of five planarians (n = 5). Among the comparisons, Group A (0.2 µg/mL *M. pudica* + 1 mg/mL *C. asiatica*) and Group D (negative control) showed a significant difference ($p < 0.05$), indicating a potential synergistic and regenerative-promoting effect of the combined treatment under hyperglycemic stress.

RESULTS AND DISCUSSION

Results

Group A significantly improves photoreceptor regeneration and behavioral recovery in hyperglycemic planarians indicating a synergistic effect between extracts while group B and C shows slower regeneration rate when compare to group A. However, group B and C still effectively healed the wound while group D regeneration rate is almost 0 making it insignificant. The results in Table 1. shows the observative results of all group of planarians tested with different conditions (A - 0.2 µg/mL *M. pudica* + 1 mg/mL *C. asiatica*, B - 0.2 µg/mL *Mimosa pudica* L., C - 1 mg/mL *Centella asiatica*, and D - negative control). Moreover, groups treated with extracts both individually and combination shows faster regeneration rate than the negative control group.

Table 1. Observative results of photoreceptor regeneration from Day 3 to Day 5

Day	Group A	Group B	Group C	Group D (Control)
D3	+/-	-	-	-
D4	+	+/-	+/-	-
D5	++	+	+/-	-
D6	++++	++	+	-
D7	++++	++	++	-

Day 1 and Day 2 are not presented on the table as there is no significant change during the time.

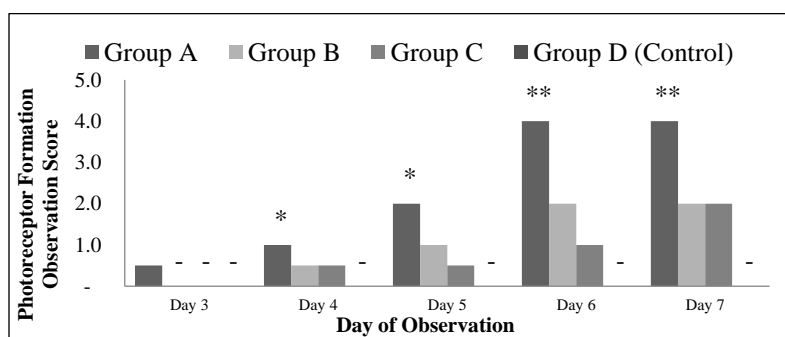


Figure 2. Photoreceptor Formation Observation Score changed during D3 to D7

t-test score * $P < 0.05$ in D4, D5 *Mimosa pudica* L. and *Centella asiatica* compare with control group (negative)

Discussions

The findings of this study demonstrate that both *Mimosa pudica* L. and *Centella asiatica* extracts can effectively promote regeneration in hyperglycemic planarians. This suggests that these natural extracts retain regenerative potential even in a glucose-rich environment, which typically impairs tissue recovery. Their effectiveness when used individually points to each plant's independent bioactive properties, while the enhanced effect observed when combined suggests a synergistic interaction that may amplify regenerative outcomes.

The results are consistent with existing literature that highlights the wound-healing, anti-inflammatory, and antioxidant properties of both plants.[11][12][13] Compounds in *Mimosa pudica* L. and *Centella asiatica* like mimosine and flavanoids could be the main active compound for this outcome indicating the necessity in tissue repairment, although the exact molecular interactions remain unclear.

Despite these promising outcomes, several limitations should be noted. The planarian model, while useful for observing regenerative trends, does not replicate the complexity of mammalian wound healing. Additionally, this study did not explore molecular mechanisms, optimal dosages, or long-term outcomes of treatment, which are necessary for translating the findings into clinical applications.

Future research should aim to investigate in more advanced models, such as mammalian cells assay and diabetic rodent wound models to help validate the therapeutic potential of these extracts in human-related contexts.

CONCLUSIONS

By using a simple model organism like hyperglycemic planarian regeneration model, this experiment explored the regenerative potential of *Mimosa pudica* L. and *Centella asiatica* in a hyperglycemic environment. The encouraging results support the idea of using natural plant extracts in wound care, particularly for diabetic patients. However, studies involving mammalian systems and molecular analysis will be crucial for deeper understanding and application.

ACKNOWLEDGEMENTS

I would like to express my sincere appreciation to Dr. Watcharee Amornwatcharapong, Project Supervisor, for their guidance and insightful feedback throughout the course of this experiment. Their support greatly contributed to the development and completion of this project.

I would also like to thank The Newton Sixth Form and Faculty of Dentistry, Chulalongkorn University for providing the necessary resources and environment to carry out this research. Lastly, I am grateful to my family for their continuous encouragement and support.

REFERENCES

1. Dasari N, Jiang A, Skochdopole A, Chung J, Reece EM, Vorstenbosch J, et al. Updates in diabetic wound healing, inflammation, and scarring. *Semin Plast Surg* [Internet]. 2021 [cited 2025 Apr 9];35(3):153–158. Available from: <https://www.ncbi.nlm.nih.gov/pmc/articles/PMC8432997/>
2. Kawahito S, Kitahata H, Oshita S. Problems associated with glucose toxicity: Role of hyperglycemia-induced oxidative stress. *World J Gastroenterol* [Internet]. 2009 [cited 2025 Apr 9];15(33):4137–4142. Available from: <https://www.ncbi.nlm.nih.gov/pmc/articles/PMC2738809/>
3. Tahergorabi Z, Khazaei M. Imbalance of angiogenesis in diabetic complications: the mechanisms. *Int J Prev Med* [Internet]. 2012 Dec [cited 2025 Apr 9];3(12):827–838. Available from: <https://www.ncbi.nlm.nih.gov/pmc/articles/PMC3530300/>
4. Primadhi RA, Seprina R, Hapsari P, Kusumawati M. Amputation in diabetic foot ulcer: A treatment dilemma. *World J Orthop* [Internet]. 2023 May 18 [cited 2025 Apr 9];14(5):312–318. Available from: <https://pmc.ncbi.nlm.nih.gov/articles/PMC10251268/>
5. Zhou B, Carrillo-Larco RM, Popkin BM, et al. Worldwide trends in diabetes prevalence and treatment from 1990 to 2022: a pooled analysis of 1108 population-representative studies with 141 million participants. *Lancet* [Internet]. 2024 Nov 13 [cited 2025 Apr 9];404(10467):e1–e12. Available from : <https://www.thelancet.com/journals/lancet/article/PIIS0140-6736%2824%2902317-1/fulltext>

6. World Health Organization. Population ageing [Internet]. Geneva: World Health Organization; 2024 [cited 2025 Apr 9].
Available from: <https://www.who.int/news-room/questions-and-answers/item/population-ageing>
7. Yan Z, Cai M, Han X, Chen Q, Lu H. The interaction between age and risk factors for diabetes and prediabetes: a community-based cross-sectional study. *Diabetes Metab Syndr Obes* [Internet]. 2023 Jan 11 [cited 2025 Apr 9];16:85–93.
Available from: <https://www.ncbi.nlm.nih.gov/pmc/articles/PMC9843502/>
8. InformedHealth.org. Chronic wounds: Learn More – What are the treatment options for chronic wounds? In: InformedHealth.org [Internet]. Cologne, Germany: Institute for Quality and Efficiency in Health Care (IQWiG); 2006-. [cited 2025 Apr 9].
Available from: <https://www.ncbi.nlm.nih.gov/books/NBK326436/>
9. Arribas-López E, Zand N, Ojo O, Snowden MJ, Kochhar T. A Systematic Review of the Effect of *Centella asiatica* on Wound Healing. *Int J Environ Res Public Health* [Internet]. 2022 Mar 10 [cited 2025 Apr 9];19(6):3266.
Available from: <https://pmc.ncbi.nlm.nih.gov/articles/PMC8956065/>
10. Ríos JL. Effects of triterpenes on the immune system. *J Ethnopharmacol* [Internet]. 2010 Mar 2 [cited 2025 Apr 9];128(1):1–14.
Available from: <https://pubmed.ncbi.nlm.nih.gov/20079412/>
11. Quyen NTC, Quyen NTN, Quy NN, Quan PM. Evaluation of total polyphenol content, total flavonoid content, and antioxidant activity of *Centella asiatica*. *IOP Conf Ser Mater Sci Eng* [Internet]. 2020 [cited 2025 Apr 9];991(1):012020.
Available from: <https://doi.org/10.1088/1757-899X/991/1/012020>
12. Panche AN, Diwan AD, Chandra SR. Flavonoids: an overview. *J Nutr Sci* [Internet]. 2016 Dec 29 [cited 2025 Apr 9];5:e47.
Available from: <https://pmc.ncbi.nlm.nih.gov/articles/PMC5465813/>
13. Santos JG, Silva TM, Lima TC, et al. Structural characterization of a novel derivative of myricetin from *Mimosa pudica* with anticancer activity. *Bioorg Med Chem Lett* [Internet]. 2016 Oct 15 [cited 2025 Apr 9];26(20):4979–4982.
Available from: <https://www.sciencedirect.com/science/article/pii/S0753332216308800>
14. Karami A, Tebyanian H, Goodarzi V, Shiri S. Planarians: an in vivo model for regenerative medicine. *Int J Stem Cells*. 2015 Nov;8(2):128–133.
Available from: <https://www.ncbi.nlm.nih.gov/pmc/articles/PMC4651277/>
15. Reddien PW. Principles of regeneration revealed by the planarian eye. *Curr Opin Cell Biol*. 2021 Dec;73:19–25.
Available from: <https://www.ncbi.nlm.nih.gov/pmc/articles/PMC11064094/>
16. Chandra S, Khan S, Avula B, Lata H, Yang MH, ElSohly MA, Khan IA. Assessment of total phenolic and flavonoid content, antioxidant properties, and yield of aeroponically and conventionally grown leafy vegetables and fruit crops: A comparative study. *Evid Based Complement Alternat Med* [Internet]. 2014 [cited 2025 May 7];2014:253875. Available from: <https://onlinelibrary.wiley.com/doi/10.1155/2014/253875>
17. Suphiratwanich P, Lomarat P, Julsrigival J. Assessment of total phenolic and flavonoid contents, antioxidant activity, and anti-acetylcholinesterase activity from *Codiaeum variegatum* (L.) Blume leaves found in Thailand. *Khon Kaen Agric J* [Internet]. 2021 Apr 5 [cited 2025 May 7];49(2):517–523.
Available from: https://ag2.kku.ac.th/kaj/PDF.cfm?filename=022-107_63_Revised%202_final3.pdf&id=4515&keeptrack=12
18. Sulaiman M. Antioxidant activity and nitric oxide inhibition of *Kaempferia parviflora* (black ginger) extract in ATDC-5 cells [thesis]. Pathum Thani: Rangsit University; 2020. Available from: <https://rsuir-library.rsu.ac.th/bitstream/123456789/578/1/Sulaiman%20Mano.pdf>

Innovative Extraction of Phenolic Compounds from Longan Seeds Using Ultrasonic-Assisted Extraction and Response Surface Methodology

Sompong Paruchanon¹, Arthitaya Kawee-ai¹, Supakiat Supasin² and Surapol Natakankitkul^{1,}*

¹Division of Cannabis and Medicinal Plants for Local Development, Graduate School, Payap University, Chiang Mai 50000, Thailand ² Faculty of Engineering, Rajamangala University of Technology Lanna, Chiang Mai, Thailand, 50300

*Corresponding author Email: surapolhsri@gmail.com

Abstract. Longan (*Dimocarpus longan* Lour.) seeds contain high levels of phenolic compounds with significant antioxidant properties. This study aimed to optimize the extraction of phenolics from longan seeds using ultrasonic-assisted extraction (UAE). A Box-Behnken experimental design was employed to evaluate the effects of temperature (A: 40–60°C), time (B: 5–20 min), and solid-to-liquid ratio (C: 1:10–1:30) on the extraction process. The optimal conditions were identified as a temperature of 50°C, an extraction time of 14 min, and a solid-to-liquid ratio of 1:20. Under these conditions, the total phenolic content (TPC) reached 4.36 ± 0.10 mg GAE/g, representing a threefold increase compared to the conventional maceration method (1.44 ± 0.05 mg GAE/g). Scanning electron microscope (SEM) imaging revealed that UAE created a more porous and disrupted seed structure, which facilitated enhanced bioactive compound extraction. These findings provide critical insights into the development of efficient protocols for recovering phenolic compounds from longan seeds, reduced processing time, and minimized solvent usage. Moreover, it aligns with the principles of the circular economy by transforming underutilized agricultural by-products into valuable natural antioxidant sources and offers significant potential for industrial applications in sectors such as food, pharmaceuticals, and cosmetics.

Keywords: Longan Seeds; Phenolic Compounds; Ultrasonic-Assisted Extraction

INTRODUCTION

According to the Department of Agricultural Extension, fresh longan production in 2022 reached approximately 1,032,326.7 tons, with Chiang Mai and Lamphun being the largest in-season longan-producing regions in northern Thailand (1). Notably, the pericarp and seeds, which make up about 20% of the fruit's total weight, are often discarded as waste (2). Phenolic compounds are a diverse group of secondary metabolites essential for plant physiology and human health. Longan (*Dimocarpus longan*) seeds, typically considered agricultural by-products, have been identified as a rich source of these bioactive compounds (3). This presents an opportunity to add value to agricultural waste while promoting a sustainable source of beneficial compounds. Utilizing longan seeds aligns with the principles of a circular economy and waste valorization, highlighting the need for efficient extraction methods to maximize their bioactive potential (4).

Traditional phenolic extraction techniques, such as maceration and Soxhlet extraction, are time-consuming, solvent-intensive, and often degrade sensitive bioactive compounds due to prolonged heat exposure (5). Ultrasonic-assisted extraction (UAE) has emerged as an advanced alternative that overcomes these limitations. UAE employs ultrasonic waves to break cell walls, improving mass transfer and enhancing phenolic compound extraction (6). This method significantly reduces extraction time and solvent use while preserving bioactive compound integrity, making it a more sustainable and efficient approach (5, 6).

However, despite UAE's advantages and the potential of longan seeds as a phenolic source, limited research has systematically optimized extraction parameters for this material. Most studies have focused on traditional methods or have not fully explored multiple interacting factors, highlighting a research gap. This study aims to optimize the UAE of phenolic compounds from longan seeds using Box-Behnken Design (BBD). The phenolic compounds extracted under optimized UAE conditions were compared with those obtained through maceration, and surface changes were analyzed using scanning electron microscopy (SEM). Furthermore, this study underscores the importance of utilizing agricultural by-products as sustainable bioactive compound sources, supporting global efforts in waste reduction and resource efficiency.

MATERIALS AND METHODS

Materials

The study used Edor variety longan seeds harvested in-season from Makuea Chae Subdistrict, Lamphun Province. The seeds were washed, dried at 70°C for three days (7), ground, and stored in zip-lock bags within a desiccator to prevent moisture for further use.

The experiment utilized a prototype ultrasonic system integrated with a pulsed electric field (PEF) system. The portable machine operated via a touchscreen interface, where parameters were set before inserting the 0.8 L chamber into the PEF or ultrasound hub. The process was controlled using "start" and "stop" commands in Swift. The ultrasonic power of this device was fixed at 40 MHz.



Figure 1. A portable prototype integrating a pulsed electric field (PEF) and ultrasonic system.

Methods

The experimental conditions for UAE were optimized using the BBD, a response surface methodology that assesses variable interactions while minimizing experimental runs. The study examined temperature (40, 50, 60 °C), extraction time (5, 12.5, 20 min), and solid-to-liquid ratio (1:10, 1:20, 1:30) across 14 experimental runs. Longan seed powder (1 g) was mixed with 50% ethanol (3) and extracted using a 40 kHz ultrasonic system under the specified conditions. The extract was then filtered, and the supernatant was analyzed for TPC.

Table 1. Total phenolic compounds extracted from longan seeds using UAE factors.

Run no.	Factors ^a			TPC (mg GAE/g)
	A	B	C	
1	40	5	1:20	2.93±0.12
2	60	5	1:20	2.56±0.05
3	40	20	1:20	3.28±0.02
4	60	20	1:20	3.08±0.11
5	40	12.5	1:10	2.56±0.17
6	60	12.5	1:10	2.67±0.06
7	40	12.5	1:30	2.93±0.06
8	60	12.5	1:30	2.33±0.13
9	50	5	1:10	2.33±0.05
10	50	20	1:10	2.86±0.05
11	50	5	1:30	2.68±0.03
12	50	20	1:30	3.01±0.13
13	50	12.5	1:20	3.98±0.05
14	50	12.5	1:20	4.24±0.06

^a A is temperature (°C), B is extraction time (min), and C is solid-to-liquid ratio.

Conventional Extraction

Maceration was used as the conventional extraction method, adapted from Keawsa-ard et al. (7). One gram of longan seed powder was immersed in a 50% ethanol solution at a 1:20 ratio for 6 h at 50°C. The extract was then filtered, and the liquid was analyzed for TPC.

Determination of Total Phenolic Content

The TPC of longan seed extracts was determined using the Folin–Ciocalteu colorimetric method (8). The extract was mixed with diluted Folin–Ciocalteu reagent in a 96-well plate, incubated, then combined with sodium carbonate and left at 24 ± 2 °C for 2 h. Absorbance was measured at 760 nm using a microplate reader, and TPC was quantified using a gallic acid standard curve, expressed as micrograms of gallic acid equivalent (GAE) per gram of extract.

Data and Statistical analyses

All experiments were performed in triplicate, with results presented as the mean \pm standard deviation. The experimental data were evaluated using a second-order polynomial model (Equation 1) to estimate the regression coefficients (b) through Design-Expert software version 13 (Stat-Ease Inc., Minneapolis, MN, USA).

$$Y = \beta_0 + \beta_1 X_1 + \beta_2 X_2 + \beta_3 X_3 + \beta_{12} X_1 X_2 + \beta_{13} X_1 X_3 + \beta_{23} X_2 X_3 + \beta_{11} X_1^2 + \beta_{22} X_2^2 + \beta_{33} X_3^2 \quad (1)$$

In this model, Y represents the response variable, X₁, X₂, and X₃ are the independent variables or studied factors, β_0 is the constant term, β_1 , β_2 , and β_3 are the linear coefficients, β_{12} , β_{13} , and β_{23} are the interaction coefficients, and β_{11} , β_{22} , and β_{33} are the quadratic coefficients. Group differences were assessed using an independent t-test at $p < 0.05$ with the PSPP program (GNU, Boston, MA, USA).

RESULTS AND DISCUSSION

Effect of UAE factors on TPC of longan seeds

The experimental results demonstrated that the TPC values ranged from 2.33 ± 0.13 mg GAE/g to 4.24 ± 0.06 mg GAE/g, depending on the extraction conditions. The highest TPC (4.24 ± 0.06 mg GAE/g) was achieved at 40°C with a 12.5-min extraction time and a 1:20 solid-to-liquid ratio (Experiment 14). In contrast, the lowest TPC (2.33 ± 0.13 mg GAE/g) was obtained at 60°C with the same extraction time but a 1:30 solid-to-liquid ratio (Experiment 9). The findings suggest that moderate temperatures (40–50°C), intermediate extraction times (12.5–20 min), and a 1:20 solid-to-liquid ratio are optimal for higher phenolic yields.

Temperature significantly impacts phenolic extraction by affecting both solubility and the degradation of phenolic compounds. The highest TPC was achieved at 40°C, indicating that lower temperatures may help preserve phenolic stability while still facilitating their release from plant materials (5). Higher temperatures, such as 60°C, did not improve TPC yield and could lead to the degradation of phenolic compounds, as seen in Experiment 9. These results align with previous studies indicating that temperatures above 65°C can degrade phenolic compounds (9).

Extraction time also influenced TPC, with shorter times (e.g., 5 min) yielding lower amounts. Longer extraction times (12.5–20 min) generally led to higher TPC due to improved cell wall breakdown and enhanced phenolic release (10). However, excessively long extraction times could cause oxidation or degradation of phenolic compounds. The solid-to-liquid ratio was another key factor, with a 1:20 ratio providing the highest TPC yields. Increasing the ratio to 1:30 generally resulted in lower yields, possibly due to dilution effects that reduced extraction efficiency (10).

The data were analyzed using a second-order polynomial equation, and the significance of the model coefficients was evaluated using ANOVA (Table 2).

Table 2. Regression coefficients of the predicted models for TPC extracted from longan seeds using UAE.

Source	Sum of Squares	df	Mean Square	F-value	p-value	
Model	4.02	9	0.4471	28.74	0.0028	significant
A-Temperature	0.1405	1	0.1405	9.03	0.0398	
B-Time	0.3741	1	0.3741	24.05	0.0080	
C-Ratio	0.0351	1	0.0351	2.26	0.2074	
AB	0.0072	1	0.0072	0.4644	0.5330	
AC	0.1260	1	0.1260	8.10	0.0466	
BC	0.0100	1	0.0100	0.6428	0.4676	
Residual	0.0622	4	0.0156			
Lack of Fit	0.0284	3	0.0095	0.2803	0.8447	not significant
Pure Error	0.0338	1	0.0338			
Cor Total	4.09	13				

$R^2 = 0.9848$; Adjusted $R^2 = 0.9505$; C.V. % = 4.21; Adeq Precision = 16.4237

Table 4 presents the regression coefficients and corresponding p-values, emphasizing the statistical significance of the relationship between each term and the response. The model's F-value of 28.74 and a p-value less than 0.05 indicate that the model terms are significant. Significant factors influencing the TPC yield ($p < 0.05$) included one interaction coefficient (AC), and two main effects (A and B). The high R^2 value of 0.9848 and Adjusted R^2 of 0.9505, along with a coefficient of variation (CV) of 4.21 and a non-significant lack of fit ($p > 0.05$), confirmed that the mathematical model accurately predicts TPC based on various combinations of the variables. The "Adeq Precision" value, which measures the signal-to-noise ratio, was 15.8461, well above the desirable threshold of 4, indicating a strong and reliable model. This suggests that the model is effective for navigating the design space. The final equation derived from the multiple regression analysis is provided in Equation 2.

$$\text{TPC} = -17.79 + 0.64 \text{ Temperature} + 0.23 \text{ Time} + 0.45 \text{ Ratio} + 0.0006 \text{ Temperature} \times \text{Time} - 0.0018 \text{ Temperature} \times \text{Ratio} - 0.0007 \text{ Time} \times \text{Ratio} - 0.0062 \text{ Temperature}^2 - 0.0093 \text{ Time}^2 - 0.0086 \text{ Ratio}^2 \quad (2)$$

In the polynomial equation, a negative sign signifies an antagonistic relationship between the response and the factor, while a positive sign indicates a synergistic relationship (11). From the equation, it was found that temperature, extraction time, and the solid-to-liquid ratio had a positive effect on the TPC concentration in longan seed extracts under UAE conditions.

Combined effect of factors on TPC of longan seeds

Figure 2 illustrates 3D response surface plots for the TPC of longan seed extracts, highlighting the effects of temperature, extraction time, and solid-to-liquid ratio. The color gradient represents predicted TPC values, with blue (lowest) at 2.33 mg GAE/g and red (highest) at 4.24 mg GAE/g.

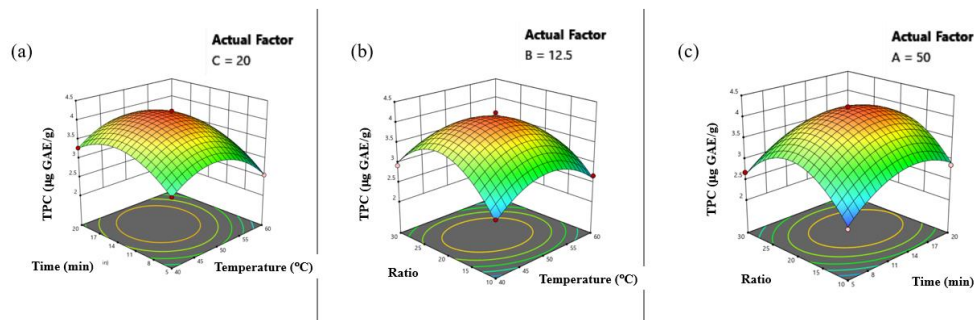


Figure 2. The 3D plots display the predicted TPC of longan seed extracts by UAE parameters. Figure 2a shows temperature vs. time, Figure 2b depicts temperature vs. solid-to-liquid ratio, and Figure 2c illustrates time vs. solid-to-liquid ratio.

TPC follows a parabolic trend, peaking at moderate temperatures (40–50°C) and intermediate times (12.5–20 min) (Figure 2A). Beyond this, degradation occurs due to excessive heat or prolonged extraction (Figure 2a). The highest TPC is observed at ~40°C and a 1:20 ratio. Higher ratios (>1:30) reduce TPC due to dilution and lower diffusion efficiency (Figure 2b). Optimal TPC is achieved at 12.5–20 min with a 1:20 ratio. Longer times or higher solvent volumes do not improve extraction and may cause degradation or dilution (Figure 2c).

Verification of the model

The optimal extraction conditions were determined by maximizing desirability. The initial optimal parameters were 48.94°C, 13.99 min, and a 1:20.43 solid-to-liquid ratio, with a predicted TPC yield of 4.14 mg GAE/g. To enhance practical applicability, the conditions were adjusted to 50°C, 14 min, and a 1:20 ratio. Under these modified conditions, the experimental yield was 4.36 ± 0.10 mg GAE/g, closely matching the predicted value with an error of +5.31%, thereby confirming the accuracy and reliability of the RSM model.

Comparison between maceration and optimal UAE conditions

The comparison was conducted using UAE at 50°C for 14 min with a 1:20 ratio, and conventional maceration at 50°C for 6 h with the same ratio. The results indicate a significant difference ($p < 0.05$) in TPC yield between UAE and maceration. UAE yielded a higher TPC (4.36 ± 0.10 mg GAE/g) compared to maceration (1.44 ± 0.05 mg GAE/g), demonstrating its superior efficiency. This increased extraction efficiency is attributed to the cavitation effect, which enhances cell wall disruption and facilitates bioactive compound release, whereas maceration relies solely on passive diffusion, leading to lower yields (5, 12).

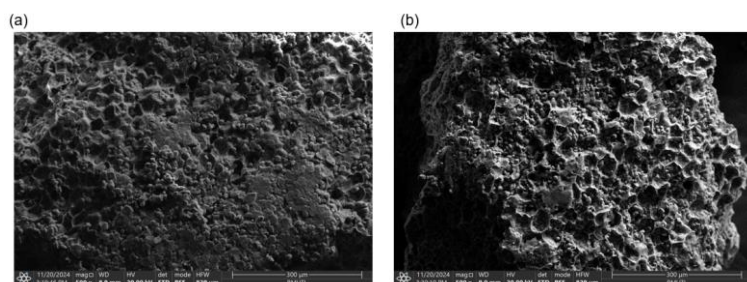


Figure 3. The surface of longan seed powder subjected to ultrasonic treatment (a) is examined using SEM at $\times 500$ magnification and compared to the conventional maceration method (b).

UAE-treated samples exhibited extensive cavitation, deep cavities, and a well-defined porous network, indicating enhanced cellular disruption (Figure 3a). These structural modifications, caused by acoustic cavitation, improve mass transfer and extraction efficiency, reinforcing UAE as a promising technique for bioactive compound extraction in food and pharmaceutical applications (5, 10). SEM analysis of conventionally macerated samples (Figure 3B) revealed modest structural modifications, with smaller, more superficial pores and a largely intact surface, indicating minimal cellular disruption. This contrasts with the extensive cavitation and porous networks observed in ultrasonically treated samples (Figure 3A).

CONCLUSIONS

The study successfully optimized ultrasound-assisted extraction for phenolic compounds from longan seeds using the Box-Behnken design. The optimal condition was achieved at 50°C, 14 min, and a 1:20 solid-to-liquid ratio, nearly doubling the yield compared to conventional maceration. SEM analysis showed that ultrasonic treatment created a more porous seed surface, enhancing extraction efficiency. These findings highlight the potential of longan seeds as a sustainable source of natural antioxidants and contribute to developing efficient extraction protocols for applications in the food, pharmaceutical, and cosmetic industries. Scaling up UAE for industrial applications is feasible with optimized parameters, enhanced energy efficiency, and integration with conventional extraction methods. Challenges include equipment cost, process control, and material variability. However, advancements in reactor design and automation improve scalability, making UAE a promising technology for large-scale extraction industries.

ACKNOWLEDGMENTS

The authors would like to thank the Innovation Center, Payap University, Chiang Mai, Thailand for equipment supporting

REFERENCES

1. Tansuchat R, Pankasemsuk T, Panmanee C, Rattanasamakarn T, Palason K. Analyzing Food Loss in the Fresh Longan Supply Chain: Evidence from Field Survey Measurements. *Agriculture*. 2023;13(10):1951.
2. Tang Y-Y, He X-M, Sun J, Li C-B, Li L, Sheng J-F, et al. Polyphenols and alkaloids in byproducts of longan fruits (*Dimocarpus Longan* Lour.) and their bioactivities. *Molecules*. 2019;24(6):1186.
3. Keawsa-ard S, Dadookain A, Yawootti A, Wimonthanasi P. Appropriate extraction methods and conditions of antioxidant compounds in longan. *Thai Science and Technology Journal*. 2020;28(11):2052-63.
4. Wang M, Chen T, Wang Q, Shi Y. Antioxidant, bacteriostatic and preservative effects of extractable condensed tannins isolated from longan pericarps and seeds. *Plants*. 2023;12(3):512.
5. Osorio-Tobón JF. Recent advances and comparisons of conventional and alternative extraction techniques of phenolic compounds. *Food Sci Technol*. 2020;57(12):4299-315.
6. Fikry M, Jafari S, Shiekh KA, Kijpatanasilp I, Khongtongsang S, Khojah E, et al. Ultrasound-assisted extraction of bioactive compounds from longan seeds powder: Kinetic modelling and process optimization. *Ultrasonics Sonochemistry*. 2024;108:106949.
7. Narkprasom K, Tanongkankit Y, Saenscharoenrat P, Narkprasom N. Optimization of total phenolic from *Euphoria longana* Lam. seed by microwave assisted extraction. *Burapha Sci J*. 2018;24(1):48-63.
8. Salee N, Chaiyana W, Yawootti A, Naruenartwongsakul S, Klangpetch W, Walter P, et al. Optimization of the pulse electric field assisted extraction of black rice grain for antioxidant and sirtuin1 enzyme stimulation activities. *Scientific Reports*. 2022;12(1):6459.
9. Sai-Ut S, Kingwascharapong P, Mazumder MAR, Rawdkuen S. Optimization of Ethanolic Extraction of Phenolic Antioxidants from Lychee and Longan Seeds Using Response Surface Methodology. *Foods*. 2023;12(15):2827.
10. Du B, Jeepipalli SP, Xu B. Critical review on alterations in physiochemical properties and molecular structure of natural polysaccharides upon ultrasonication. *Ultrasonics Sonochemistry*. 2022;90:106170.
11. Porwal O. Box-Behnken Design-based formulation optimization and characterization of spray dried rutin loaded nanosuspension: State of the art. *South African Journal of Botany*. 2022;149:807-15.
12. Jha AK, Sit N. Extraction of bioactive compounds from plant materials using combination of various novel methods: A review. *Trends Food Sci Technol* 2022;119:579-91.

Development of Film-Forming Spray Containing Herbal Mixture for Hair Coloring

Kodpaka Lueadnakrob¹, Suvimol Somwongin¹, Watchara Kanjanakawinkul², Kittisak Jantanasakulwong³, Wantida Chaiyana^{1,4,}*

¹Department of Pharmaceutical Sciences, Faculty of Pharmacy, Chiang Mai University, Chiang Mai, THAILAND

²Chulabhorn Royal Pharmaceutical Manufacturing Facilities by Chulabhorn Royal Academy, Chon Buri, THAILAND

³Faculty of Agro-Industry, Chiang Mai University, Chiang Mai, THAILAND

⁴Multidisciplinary and Interdisciplinary School, Chiang Mai University, Chiang Mai, THAILAND

*Corresponding author Email: wantida.chaiyana@cmu.ac.th

Abstract. A film-forming spray is designed to create a thin protective layer on surfaces, including hair, offering benefits such as enhanced color retention, improved protection, and superior moisture preservation. This study aimed to develop a film-forming spray specifically for hair color applications using herbal mixtures. Various factors affecting the film-forming formulation were evaluated, including the type and concentration of polymers. The formulations were then characterized for their external appearance, viscosity, pH, drying time, and washing performance. The hair sprayed with the film-forming formulation was further characterized for its morphology using scanning electron microscopy (SEM). The findings indicated that the combination of polyvinyl alcohol (PVA) and chitosan at a ratio of 24:1, along with glycerin as a plasticizer, was the most suitable formulation. This formulation was transparent, with a pH of 5.50 ± 0.04 . The formulation was a transparent liquid with Newtonian flow, exhibiting a viscosity of 4.90 ± 0.10 mPas, which allowed it to be sprayed effectively from the nozzle. The drying time was quick, taking only 2 minutes, making it suitable for practical applications. The herbal mixture, with a ratio of 2:2:1 from *Lawsonia inermis* leaves, *Clitoria ternatea* flowers, and *Indigofera tinctoria* leaves, was successfully incorporated into the formulation. The hair treated with the formulation showed no noticeable differences compared to untreated hair, indicating that the formulation did not affect the natural appearance or properties of the hair. Therefore, the film-forming spray containing herbal mixtures proved to be a promising option for hair coloring.

Keywords: Film-forming spray; Polyvinyl alcohol; *Lawsonia inermis*; *Clitoria ternatea*; *Indigofera tinctoria*

INTRODUCTION

Film-forming sprays represent a promising alternative to conventional topical and transdermal dosage forms. These innovative formulations are capable of forming a thin uniform film on the skin or hair surface following application (1). Of particular interest is their potential to improve dye durability and ease of use. Typically, film-forming sprays are composed of an active compound and a film-forming polymer dissolved in a suitable solvent. When applied, the solvent rapidly evaporates, leaving behind a polymeric film that adheres to the target surface, such as the hair shaft (2). This film not only enhances adhesion but also contributes significantly to the longevity and stability of hair color. The spray format offers several advantages, including convenient application and improved user compliance, which are critical factors for achieving consistent and long-lasting coloring results. Moreover, the ability of the film to remain on the outer surface of hair minimizes direct contact with the scalp and skin, potentially reducing the risk of allergic reactions and irritations commonly associated with traditional hair dye formulations. Therefore, the present study aimed to develop and evaluate a film-forming spray formulation containing herbal mixture for hair coloring. Additionally, their hair dyeing efficacy and effects on the hair cuticles were evaluated.

MATERIALS AND METHODS

Materials

Lawsonia inermis leaves were generously provided by the Chulabhorn Royal Pharmaceutical Manufacturing Facilities, Chulabhorn Royal Academy, Chon Buri, Thailand. Dried powders of *Clitoria ternatea* flowers and *Indigofera tinctoria* leaves were purchased from a local market in Chiang Mai, Thailand. Polyvinyl alcohol (PVA 205), a partially hydrolyzed, medium-viscosity grade, was purchased from Chanjao Longevity Co., Ltd. (Bangkok, Thailand). Chitosan and citric acid were purchased from Sigma-Aldrich (St. Louis, MO, USA). Glycerin and Spectrastat BHL were purchased from Namsiang Co., Ltd. (Bangkok, Thailand).

Methods

Development of blank film-forming formulations

The film-forming formulations were developed using varying concentrations of 100 g/L PVA, with a fixed concentration of 0.5% w/w of 5 g/L of chitosan in 50 g/L of citric acid aqueous solution. Additionally, 3% w/w Spectrastat BHL and 1% w/w

*Corresponding author: wantida.chaiyana@cmu.ac.th
Presenting author: kodpaka_luead@cmu.ac.th

glycerin were incorporated as a preservative and plasticizer, respectively. The resulting formulations were characterized based on their external appearance through organoleptic assessments, viscosity through a rheometer, and pH through a pH meter. The sample sizes used for the determination of viscosity and pH were 4 mL and 20 mL, respectively. Drying time was evaluated by spraying the 5 g of each formulation onto hair tresses and recording the time required for the weight to stabilize. A washing test was also conducted. Briefly, the initial weight of the hair tresses (W0) was recorded before applying 5 g of the formulation. After spraying and allowing the tresses to dry at room temperature, the weight was recorded as W1. Following washing, the tresses were dried again, and the final weight was recorded as W2. Washing performance was calculated as the percentage of weight loss after washing using the formula: Washing performance = $(W1-W2)/(W1-W0) \times 100$. The experiments were carried out in triplicate.

Development of film-forming formulations containing natural dyes

Lawsonia inermis leaves, *Clitoria ternatea* flowers, and *Indigofera tinctoria* leaves in a ratio of 2:2:1, which was suggested from our previous study (3), was used as a natural dye in the development of film-forming formulations for hair coloring. The most suitable blank film-forming formulation was selected based on their characteristic, including suitable viscosity, pH, drying time, and washing performance. The resulting formulations were characterized based on their external appearance, viscosity, and pH as described above. Additionally, the color of the formulations, in term of lightness (L^*), was evaluated using a colorimeter. The experiments were carried out in triplicate.

Performance test of film-forming formulations containing natural dyes

The performance of the film-forming formulation was evaluated on human bleached hair tresses obtained from a salon in Chiang Mai, Thailand. The film-forming formulations containing natural dyes was sprayed on the hair tresses and left dry at the room temperature. The drying time and washing performance were evaluated as described above. The color of hair tresses after the application of the formulation were evaluated in term of lightness (L^*) using a colorimeter. Additionally, the hair shafts were investigated under the scanning electron microscope (SEM). The experiments were carried out in triplicate.

Statistical analyses

The results were reported as mean and standard deviation (SD). Differences between groups were analyzed using ANOVA followed by Tukey's HSD test for post-hoc comparisons (* $p < 0.05$).

RESULTS AND DISCUSSION

Blank film-forming formulations

The film-forming formulations, as shown in **Figure 1**, were transparent liquids with viscosities ranging from 2.10 ± 0.01 to 6.36 ± 0.05 mPas (**Table 1**). The higher concentrations of PVA in the formulation resulted in significantly higher viscosity, longer drying time, and less washing performance. However, no significant effect on the pH was detected. The washing performance decreased with increasing PVA concentration, plateauing after 60% w/w of PVA, representing the amount remaining on the hair. Higher concentrations of PVA did not offer any advantages in durability after washing, so the formulation with 60% w/w PVA was selected for further incorporation of the natural dye extract.

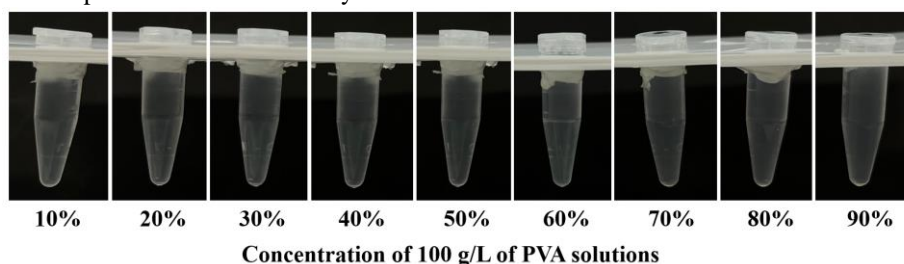


Figure 1. External appearance of blank film-forming formulations containing different concentration of 100 g/L of PVA solutions.

Table 1. Viscosity, pH, drying time, and washing performance of blank film-forming formulations.

PVA solution (% w/w)	Viscosity (mPas)	pH	Drying time (s)	Washing performance (%)
10	2.10 ± 0.10^a	5.40 ± 0.01	66.67 ± 2.08^a	91.33 ± 4.90^a
20	2.43 ± 0.10^b	5.43 ± 0.03	69.33 ± 4.04^a	83.62 ± 5.21^a
30	3.06 ± 0.03^c	5.48 ± 0.01	90.33 ± 1.52^b	$81.59 \pm 3.76^{a,b}$
40	3.90 ± 0.17^d	5.49 ± 0.01	96.67 ± 2.08^b	$85.79 \pm 6.43^{a,b}$
50	4.16 ± 0.11^e	5.49 ± 0.05	108.67 ± 1.52^c	$76.61 \pm 8.31^{a,b}$

60	4.90 ± 0.10^f	5.50 ± 0.04	121.00 ± 1.73^e	67.71 ± 2.55^e
70	5.53 ± 0.05^g	5.50 ± 0.02	124.00 ± 3.51^e	68.25 ± 3.68^e
80	5.93 ± 0.05^h	5.53 ± 0.03	139.00 ± 1.73^d	67.91 ± 5.71^e
90	6.36 ± 0.10^i	5.54 ± 0.05	149.33 ± 7.50^f	67.77 ± 2.77^e

NOTE: The concentration of PVA solutions was 100 g/L. The sample sizes used for the determination of viscosity, pH, drying time, and washing performance were 4 mL, 20 mL, 5 g, and 5 g, respectively. Different letters, a, b, c, d, e, f, g, h, and i, represent significant differences among the formulations, as determined by one-way ANOVA followed by Tukey's test ($p < 0.05$).

Film-forming formulations containing natural dyes

The film-forming formulations containing various concentrations of natural dyes are shown in **Figure 2**. The color of the solutions became progressively darker with increasing dye concentration. The formulation without the natural dyes appeared transparent with no color. At 1% concentration, a light brown coloration was observed, which deepened to a darker brown at 2%. Further increases in concentration resulted in even more pronounced darkening, with the 3%, 4%, and 5% samples appearing nearly black, suggesting a saturation point was approached. These results demonstrated a clear correlation between dye concentration and color intensity, supporting the effectiveness of natural dyes in modulating solution appearance. The visual appearance was in good accordance with the lightness (L^*) of the formulation measured by a colorimeter, as shown in **Table 2**, exhibiting lower L^* values with increasing natural dye concentrations, which plateaued at 3%. In contrast, the increasing natural dyes concentrations had no significant effect on the viscosity and pH of the formulations.

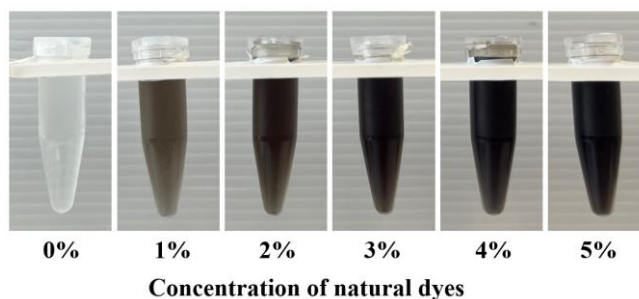


Figure 2. External appearance of film-forming formulations containing different concentrations of natural dyes.

Table 2. Viscosity, pH, drying time, and washing performance of film-forming formulations containing different concentrations of natural dyes.

Natural dyes concentration (% w/w)	Viscosity (mPas)	pH	Lightness (L^*) of formulation
0	4.83 ± 0.28	5.50 ± 0.01	95.18 ± 0.82^a
1	5.16 ± 0.28	5.53 ± 0.01	37.02 ± 1.19^b
2	5.33 ± 0.28	5.54 ± 0.01	26.17 ± 1.19^c
3	5.33 ± 0.76	5.52 ± 0.01	24.97 ± 1.67^d
4	5.33 ± 0.76	5.50 ± 0.01	22.35 ± 1.32^d
5	5.33 ± 0.57	5.50 ± 0.01	22.04 ± 0.56^d

NOTE: The film-forming formulations composing of 60% w/w of 100 g/L, 0.5% w/w of 5 g/L of chitosan in 50 g/L of citric acid aqueous solution, 3% w/w of Spectrastat BHL, 1% w/w of glycerin, and 35.5% w/w of DI water. Different letters, a, b, c, and d, represent significant differences among the formulations, as determined by one-way ANOVA followed by Tukey's test ($p < 0.05$).

The visual appearance of hair samples treated with the film-forming spray containing the increasing concentrations of natural dyes revealed a clear trend in color intensification as shown in **Figure 3**. The hair treated with the blank formulation (0% natural dyes) retained its original light blonde tone. At 1% and 2% dye concentrations, the hair adopted progressively deeper shades of brown. A noticeable darkening occurred at 3%, with the color transitioning to a medium to dark brown. Further increases to 4% and 5% resulted in even deeper brown hues, with only minimal changes between these concentrations, suggesting a saturation point had been reached. This visual progression aligns with the corresponding solution appearances and supports the effectiveness of natural dyes in hair coloring applications.

The influence of natural dye concentration on hair tress characteristics was quantitatively assessed and is summarized in **Table 3**. The drying time increased significantly with higher dye concentrations, starting from 117.33 ± 2.52 s for the blank formulation and reaching 135.33 ± 3.21 s at the concentration of 5% w/w natural dyes. Notably, significant differences in drying time were

observed between 0% and all dyed formulations, with values plateauing from 2% onwards. The washing performance, expressed as color retention percentage after washing, showed no significant among the blank formulation and those containing various concentration of the natural dyes. Regarding lightness (L^*), a clear decrease was observed with increasing dye concentrations. A significant drop in L^* was observed up to 3%, after which the values plateaued, suggesting saturation of color deposition. This finding aligns with the visual observations in **Figures 3**.



Figure 3. External appearance of hair tress sprayed with film-forming spray containing different concentration of herbal mixture.

Table 3. Viscosity, pH, drying time, and washing performance of film-forming formulations containing different concentrations of natural dyes.

Natural dyes concentration (% w/w)	Drying time (s)	Washing performance (%)	Lightness (L^*) of hair tress
0	117.33 ± 2.52^a	65.63 ± 15.53	50.14 ± 2.12^a
1	124.33 ± 4.73^b	65.32 ± 18.91	24.65 ± 1.78^b
2	$132.00 \pm 3.46^{b,c}$	60.98 ± 17.77	20.53 ± 0.71^c
3	132.67 ± 1.15^c	60.49 ± 14.92	16.21 ± 0.61^d
4	134.00 ± 1.00^c	60.44 ± 11.26	16.45 ± 1.07^d
5	135.33 ± 3.21^c	58.92 ± 20.50	15.61 ± 1.12^d

NOTE: The film-forming formulations composing of 60% w/w of 100 g/L, 0.5% w/w of 5 g/L of chitosan in 50 g/L of citric acid aqueous solution, 3% w/w of Spectrastat BHL, 1% w/w of glycerin, and 35.5% w/w of DI water. Different letters, a, b, c, and d, represent significant differences among the formulations, as determined by one-way ANOVA followed by Tukey's test ($p < 0.05$).

The SEM micrographs of a hair sprayed with film-forming spray containing different concentration of herbal mixture as shown in **Figure 4** noted that all formulation had no damage effects on the hair.

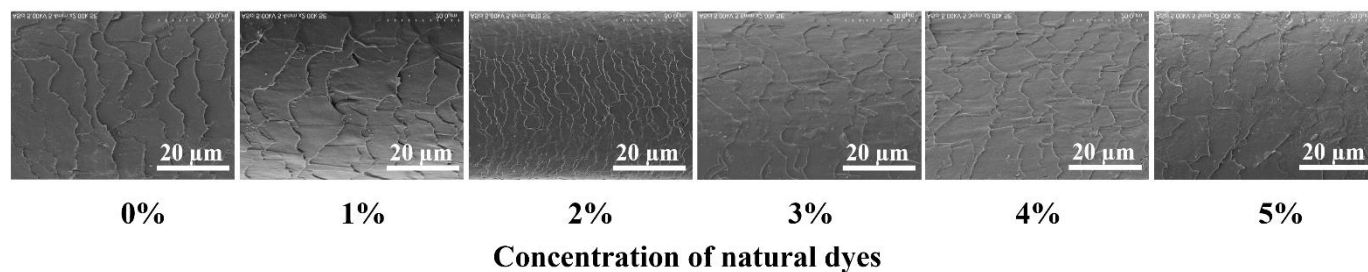


Figure 4. SEM micrographs showing the surface morphology of a hair sprayed with film-forming spray containing different concentrations of herbal mixture. Each image represents the surface topography and microstructural features of overlapping hair cuticles. Treated hair samples show a smoother and more uniform surface compared to the untreated control, with no visible signs of cuticle damage. All images were captured at a magnification of $2,000\times$ with a scale bar of $20\ \mu\text{m}$ for reference.

Discussions

The present study introduces a novel hair dye formulation utilizing plant-derived natural colorants, addressing the growing demand for safer, eco-conscious alternatives to synthetic hair dyes. The formulation successfully delivered progressive and uniform

coloration across various concentrations, with optimal performance observed at 3% w/w dye loading. This research not only validates the effectiveness of natural dyes in hair coloring but also provides a comprehensive analysis of their physicochemical behavior, including drying time, washing durability, and lightness (L^*) measurements. The novelty of the formulation lies in its ability to achieve saturated and stable color deposition on hair fibers using a minimal concentration (3%) of natural dyes, reducing the need for excess pigment and improving formulation efficiency. Moreover, the study demonstrated that the visual outcomes are in strong agreement with instrumental color measurements, establishing a reliable basis for visual quality control in natural dye applications. Compared to conventional synthetic dyes, which often contain harmful chemicals like ammonia, para-phenylenediamine, and resorcinol, the natural dye formulation offers several distinct advantages, including biocompatibility, reduced allergenicity, and environmental sustainability (4,5). As natural dyes are biodegradable and derived from renewable resources it could minimize the ecological impact (6,7). However, to ensure long-term stability, further research should focus on incorporating natural stabilizers or preservatives to enhance color retention and protect the formulation from environmental degradation. In addition, scaling-up process would be necessary for further commercialization.

CONCLUSIONS

This study highlighted the development of a novel natural hair dye formulation capable of producing rich, uniform coloration with minimal dye concentration. The results emphasize that a 3% w/w concentration of the natural dyes delivered the most effective balance between visual aesthetics, physicochemical performance, and formulation efficiency. Compared to synthetic dyes, natural dyes offer significant advantages including improved safety, biodegradability, and eco-friendliness, making them a highly promising alternative for the future of sustainable cosmetics. These findings contributed valuable insights into the formulation science of natural hair dyes and open opportunities for further innovation in plant-based beauty products. Future studies should explore long-term color stability, incorporation of multifunctional botanicals, and consumer acceptance to facilitate broader market adoption.

ACKNOWLEDGMENTS

The authors sincerely appreciate the financial support from the Research and Researchers for Industries (RRi), grant number N23G670016, with partial support from SkinPro Laboratory Co., Ltd. We also express our gratitude to the Chulabhorn Royal Pharmaceutical Manufacturing Facility for the valuable contribution in providing the raw plant materials for this study.

REFERENCES

1. Chamsai B, Soodvilai S, Opanasopit P, Samprasit W. Topical film-forming chlorhexidine gluconate sprays for antiseptic application. *Pharmaceutics*. 2022;14(6):1124.
2. Kathe K, Kashmira H, Harsha K. Film forming systems for topical and transdermal drug delivery. *Asian journal of pharmaceutical sciences*. 2017;12(6):487-497.
3. Lueadnakrob K, Juntrapirom S, Rongthong T, Kanjanakawinkul W, Chaiyana W. Functional performance and safety evaluation of optimized plant-based dye mixtures for intense hair coloration. *Cosmetics*. 2025;12(2):78.
4. Pranta D, Rahaman T. Extraction of eco-friendly natural dyes and biomordants for textile coloration: A critical review. *Nano-Struct. Nano-Objects*. 2024;39:101243.
5. Meyer A, Fischer K. Oxidative transformation processes and products of para-phenylenediamine (PPD) and para-toluenediamine (PTD) a review. *Environmental Sciences Europe*. 2015; 27:1-16.
6. Renita A, Gajaria K, Sathish S, Kumar A, Lakshmi S, Kujawa J, Kujawski W. Progress and prospective of the industrial development and applications of ECO-friendly colorants: an insight into environmental impact and Sustainability issues. *Foods*. 2023;12(7): 1521.
7. Dey P, Dey P, Hoque B, Baria B, Rahman M, Shovon S, Das D. Sustainable and eco-friendly natural dyes: a holistic review on sources, extraction, and application prospects. *Textile Research Journal*. 00405175251321139.

Antioxidant and Anti-tyrosinase Activities of *Morus nigra* L. Fruit Extract and Mixed Extract for Use as Cosmetic Raw Materials

*Chadamon Mookaew*¹, *Kanokwan Kiattisin*^{1,*}

¹Department of Pharmaceutical Sciences, Faculty of Pharmacy, Chiang Mai University, Chiang Mai, Thailand, 50200

* Corresponding author: kanokwan.k@cmu.ac.th

Abstract. *Morus nigra* L. (black mulberry) is a fruit rich in polyphenols, anthocyanins, and flavonoids, offering notable health benefits. This study investigated and compared the antioxidant and anti-tyrosinase activities of black mulberry extract, Indian gooseberry extract, goji berry extract, and mixed extract at various ratios. Antioxidant capacity, assessed using DPPH and FRAP assays, revealed that Indian gooseberry extract exhibited the strongest activity, followed by black mulberry and goji berry extracts. In contrast, black mulberry extract indicated the highest anti-tyrosinase activity, followed by Indian gooseberry extract and goji berry extract. Based on these findings, combinations of black mulberry and Indian gooseberry extracts were prepared at different ratios to assess potential synergistic effects. The mixed extract at a ratio of 1:7 showed the highest DPPH radical scavenging activity with an IC_{50} of 0.24 ± 0.00 mg/mL and demonstrated a synergistic effect with a combination index (CI) of 0.82 ± 0.06 . Interestingly, the mixed extract at a ratio of 8:1 indicated the highest anti-tyrosinase activity with an IC_{50} of 0.84 ± 0.02 mg/mL and exhibited a synergistic effect with a CI of 0.58 ± 0.14 . These results suggest that specific combinations of black mulberry and Indian gooseberry extracts enhance biological activity beyond their individual effects. In conclusion, the mixed extract exhibited synergistic antioxidant and anti-tyrosinase activities, supporting its potential as a multifunctional active ingredient in cosmetic formulations.

Keywords: *Morus nigra* L.; Black mulberry fruit; Antioxidant; Anti-tyrosinase; Synergistic effect

INTRODUCTION

The cosmetics industry plays an increasingly significant role in daily life, appealing to individuals of all genders. Among Thai women, skin darkening is a prevalent concern, influenced by intrinsic factors such as genetics and ethnicity, as well as extrinsic factors including sun exposure and lifestyle. Another major challenge to skin health is oxidative stress caused by free radicals encountered in everyday life, such as pollutants, dust, smoke, and ultraviolet radiation. These factors contribute to premature skin aging, cellular damage, inflammation, wrinkles, and dullness. To combat these effects, there is rising interest in incorporating natural extracts derived from plants and fruits into cosmetic formulations to enhance their efficacy. One of the interesting natural ingredients is *Morus nigra* L., commonly known as black mulberry, which is widely used in cosmetic products. Previous research has demonstrated that mulberry root extract possessed antioxidant, anti-tyrosinase, anti-inflammatory, and antifungal activities [1]. However, limited research has explored the potential of black mulberry fruit extract, particularly in combination with other bioactive ingredients such as goji berry (*Lycium barbarum* L.) and Indian gooseberry (*Phyllanthus emblica* L.) extracts. Given the remarkable bioactive properties of black mulberry fruit extract, its combination with other cosmetic ingredients is particularly significant, as it may enhance the bioactivity of individual components, leading to improved antioxidant efficacy and tyrosinase inhibition. This synergistic approach could lead to the development of more effective formulations for addressing oxidative stress and hyperpigmentation—two major concerns in skincare [2]. Therefore, the objective of this study is to identify the optimal combination of extracts with the strongest antioxidant and tyrosinase inhibitory activities, providing valuable insights into their potential applications as cosmetic ingredients. Importantly, there is currently a lack of research on the effects of mixed extract in promoting skin health, highlighting the need for this study to advance the field of cosmetic science.

MATERIALS AND METHODS

Materials

Mushroom tyrosinase, 2,2-diphenyl-1-picrylhydrazyl radical (DPPH), gallic acid, quercetin, kojic acid, and Trolox were purchased from Sigma-Aldrich, USA. Ethanol, and sodium hydroxide were purchased from RCI Labscan, Ireland. L-dopa, Folin Ciocalteu reagent, sodium carbonate (Na_2CO_3), ferrous sulfate ($FeSO_4$), sodium acetate, aluminum chloride ($AlCl_3$), and sodium nitrite ($NaNO_2$) were purchased from Loba Chemie, India. Potassium chloride (KCl) was purchased from EMSURE, Germany. Cyanidin-3-O-glucoside was purchased from ChemFaces, China.

Plant material

Black mulberry fruit was bought from the Chiang Mai Sericulture Research Center, Chiang Mai, Thailand. It was dried at 55 °C for 60 hours in a hot air oven and ground into powder for extraction. Goji berry fruit extract was prepared by Cosmetic

*Corresponding author: email address of corresponding author
Presenting author: email address of presenting author

laboratory, Chiang Mai University, Chiang Mai, Thailand. Indian gooseberry extract was purchased from Namsiang, Bangkok, Thailand.

Methods

Extraction

Black mulberry fruit was extracted using 95% (v/v) ethanol by maceration and stirred using a magnetic stirrer at 105 rpm for 24 hours per cycle, repeated for three cycles. The solution was filtered through Whatman No.1 filler paper, and then the solvent was removed using a rotary evaporator to obtain black mulberry fruit ethanol extract (EM). Black mulberry fruit was separately extracted using water by maceration with the same previous condition. The solution was condensed using a freeze dryer to obtain black mulberry fruit water extract (WM).

Chemical composition determination

Determination of total phenolic content

The total phenolic content of extracts was determined using the Folin–Ciocalteu assay [3]. The Folin–Ciocalteu reagent and 7.5% (w/v) sodium carbonate were mixed with each extract. After incubation for 30 minutes in the dark, absorbance was measured at 765 nm using a microplate reader. The experiment was performed in triplicate. The results were expressed as milligrams of gallic acid equivalent (GAE) per gram of extract.

Determination of total flavonoid content

The total flavonoid content of extracts was determined using the aluminum chloride colorimetric assay [4]. The extract solution was mixed with 5% (w/v) sodium nitrite and deionized water, followed by a 5 minutes incubation period. Then, 10% (w/v) aluminum chloride and 4% (w/v) sodium hydroxide were added to the mixed extract. The absorbance was measured at 510 nm using a microplate reader. The experiment was performed in triplicate. The total flavonoid content was expressed as milligrams of quercetin equivalent (QE) per gram of extract.

Determination of total anthocyanin content

The total anthocyanin content of extracts was determined using the pH differential method [5]. Each extract was diluted using various pH buffer solutions. The first test tube contained potassium chloride buffer (pH 1.0), while the second test tube contained sodium acetate buffer (pH 4.5). Each extract solution was mixed with each buffer in a ratio of 1:4. After 15 minutes in the dark, the absorbance was measured at 520 and 700 nm using a UV-visible spectrophotometer. The experiment was performed in triplicate. The results were presented as milligrams of cyaniding-3-O glucoside chloride equivalent (CGE) per gram of extract.

Determination of in vitro antioxidant activity

DPPH radical scavenging assay

Various concentrations of selected black mulberry fruit extract, goji berry extract, and Indian gooseberry extract were mixed with freshly prepared DPPH• solution. The mixed extract was incubated at room temperature for 30 minutes in the dark. The absorbance was measured using a microplate reader at 520 nm [3]. Trolox was used as a positive control. The percentage of inhibition was calculated using the following equation:

$$\text{Inhibition (\%)} = [(A_{\text{control}} - A_{\text{sample}}) / A_{\text{control}}] \times 100$$

Where A_{control} and A_{sample} represent the absorbance of the control and the sample, respectively. Based on the relationship between the extract concentration and the percentage of inhibition, the half-maximal inhibitory concentration (IC_{50}) was calculated.

Ferric reducing antioxidant power (FRAP) assay

Selected black mulberry fruit extract, goji berry extract, and Indian gooseberry extract were evaluated ferric reducing antioxidant power using FRAP assay [6]. Each sample was mixed with FRAP reagent. The sample was incubated at room temperature for 5 minutes. The absorbance was measured at 595 nm using a microplate reader. Trolox was used as a positive control. Ferrous sulfate was employed as a standard. Ferric reducing antioxidant power results were presented as the effective concentration 1 (EC1).

Determination of anti-tyrosinase activity

The modified dopachrome method was used to measure anti-tyrosinase activity of selected black mulberry fruit extract, goji berry extract, and Indian gooseberry extract using L-dopa as substrate [6]. Each extract was mixed with phosphate buffer solution and tyrosinase enzyme (50 units/mL). The sample was incubated for 10 minutes at 25 °C before adding 2.5 mM L-dopa. The absorbance was measured using a microplate reader at 450 nm. Kojic acid was used as a positive control. Anti-tyrosinase activity of each sample was expressed as a percentage of tyrosinase inhibition and the IC_{50} was calculated.

Determination of synergistic effect of mixed extract

Preparation of black mulberry fruit extract combined with Indian gooseberry extract

The selected black mulberry fruit extract with the highest levels of chemical compositions, antioxidant activity, and anti-tyrosinase activity was selected to combine with Indian gooseberry extract in various ratios (1:1 to 1:9 for antioxidant activity test and 1:1 to 9:1 for anti-tyrosinase activity test).

Determination of antioxidant and anti-tyrosinase activities of mixed extract

Each ratio was evaluated antioxidant activity using DPPH and FRAP assays. Moreover, anti-tyrosinase activity of each ratio was evaluated using the same method as mentioned above. The IC₅₀ results from each assay were then used to calculate the Combination Index (CI) value, which indicates the nature of the interaction between the ingredients. A CI value less than 1 (CI < 1) indicates a synergistic effect, a CI value equal to 1 (CI = 1) indicates an additive effect, and a CI value greater than 1 (CI > 1) indicates an antagonistic effect.

Statistical analysis

The data were presented as the mean \pm standard deviation (SD) and analyzed using analysis of variance (ANOVA) at the 95% confidence level ($p < 0.05$). Variance analysis was performed using SPSS statistical software (Version 19.0, IBM). Additionally, statistical significance was determined using an unpaired t-test for comparisons between the data of two groups.

RESULTS AND DISCUSSION

Yields of black mulberry fruit extracts

The black mulberry fruit water extract (WM) yielded 67.55%, which was higher than that of the ethanol extract (EM), which yielded 52.55%. Both extracts were obtained as semi-solid substances with a characteristic purple color and distinct odor.

Total phenolic content of black mulberry fruit extracts

The total phenolic content of WM (30.28 mg GAE/ g extract) was significantly higher than the EM (21.75 mg GAE/ g extract) ($p < 0.05$). Previous research indicated that mulberry contains hydroxycinnamic acids such as chlorogenic acid, caffeic acid, and gallic acid [7].

Total flavonoid content of black mulberry fruit extracts

The EM (83.47 mg QE/ g extract) indicated total flavonoid content significantly higher than the WM (44.86 mg QE/ g extract) ($p < 0.05$). According to previous research, black mulberry fruit extracted with a non-polar solvent exhibited a higher flavonoid content compared to extraction with polar solvents [8]. Mulberry contains flavonoids such as rutin, quercetin, and resveratrol [7].

Total anthocyanin content of black mulberry fruit extracts

The WM exhibited higher total anthocyanin content with 169.28 ± 0.20 mg CGE/g extract than the EM (0.00 ± 0.10 mg CGE/g extract). In black mulberry, anthocyanins such as cyanidin 3-glucoside (C3G) are pigments found in flowers and fruits that impart red, blue, or purple colors [2]. These compounds are water-soluble and exhibit high antioxidant activity. Therefore, anthocyanins were detected in the WM and were present at higher levels compared to the EM.

In vitro antioxidant activity of black mulberry extract, Indian gooseberry extract, goji berry extract, and mixed extract

Based on the results of yield and phytochemical contents, the WM was selected to evaluate antioxidant and anti-tyrosinase activities, as well as to assess the efficacy of the mixed extract. Antioxidant activities, as determined by DPPH and FRAP assays, are presented in Table 1. The Indian gooseberry extract exhibited the highest DPPH radical scavenging activity, followed by the WM and goji berry extracts, respectively. Interestingly, the ferric reducing antioxidant power showed the same trend as the DPPH assay. The results indicated that the Indian gooseberry extract had the highest ferric reducing capacity, followed by the WM. Therefore, Indian gooseberry extract was chosen to be mixed with the WM. The mixed extract at various ratios were tested for antioxidant activity and determined the synergistic effect. The antioxidant activity results of mixed extract are shown in Table 2. A synergistic effect between the WM extract and Indian gooseberry extract was found at ratios ranging from 1:5 to 1:9 when evaluated by DPPH assay. On the other hand, the mixed extract did not show the synergistic effect in the FRAP method.

Indian gooseberry contains several components that contribute to its strong antioxidant activity, including Vitamin C, phenolic compounds (gallic acid and ellagic acid), flavonoids (quercetin and kaempferol), and tannins (emblicanin A and B). Based on the above findings, it can be concluded that the active compounds present in Indian gooseberry extract contribute to the enhanced bioactivity observed when its proportion is increased in the mixed extract, particularly compounds in the tannin group. Tannins can bind to various organic molecules, including free radicals. Through this binding, they help stabilize these molecules and enhance antioxidant activity [9].

Table 1. Antioxidant activities of black mulberry fruit water extract (WM), Indian gooseberry extract, goji berry extract, and trolox when evaluated using DPPH and FRAP assays

Samples	DPPH assay	FRAP assay
	IC ₅₀ (mg/mL)	EC ₁ (mg/mL)
Trolox	0.05 ± 0.00 ^a (ug/mL)	0.02 ± 0.060 ^a
WM	1.55 ± 0.09 ^c	0.32 ± 0.007 ^c
Indian gooseberry extract	0.26 ± 0.03 ^b	0.04 ± 0.002 ^b
Goji berry extract	8.31 ± 0.35 ^d	ND

Different alphabets (a, b, c, and d) indicate significant differences among samples in each experiment based on one-way ANOVA ($p < 0.05$). ND means “not detected”.

Table 2. Antioxidant activities and CI value of mixed extract evaluated using DPPH and FRAP assays

Ratios of black mulberry water extract : Indian gooseberry extract	DPPH assay	CI value	FRAP assay	CI value
	IC ₅₀ (mg/mL)		EC ₁ (mg/mL)	
1:1	0.58 ± 0.01	1.30 ± 0.03	0.09 ± 0.003	1.26 ± 0.04
1:2	0.40 ± 0.01	1.11 ± 0.10	0.07 ± 0.002	1.24 ± 0.04
1:3	0.37 ± 0.01	1.14 ± 0.03	0.07 ± 0.004	1.35 ± 0.46
1:4	0.35 ± 0.02	1.12 ± 0.09	0.07 ± 0.004	1.44 ± 0.06
1:5	0.28 ± 0.00	0.92 ± 0.01	0.07 ± 0.002	1.48 ± 0.08
1:6	0.25 ± 0.01	0.83 ± 0.03	0.07 ± 0.005	1.53 ± 0.03
1:7	0.24 ± 0.00	0.82 ± 0.06	0.06 ± 0.001	1.55 ± 0.10
1:8	0.27 ± 0.01	0.94 ± 0.14	0.06 ± 0.004	1.59 ± 0.04
1:9	0.27 ± 0.01	0.94 ± 0.02	0.06 ± 0.010	1.61 ± 0.22

Anti-tyrosinase activity of black mulberry extract, Indian gooseberry extract, goji berry extract, and mixed extract

Anti-tyrosinase activity of black mulberry water extract, Indian gooseberry extract, and goji berry extract is shown in Table 3. The MW indicated the highest tyrosinase inhibitory activity, followed by Indian gooseberry extract and goji berry extract, respectively. Therefore, the MW and Indian gooseberry extract were selected to mixed and evaluate the synergistic effect of anti-tyrosinase activity. The results are shown in Table 4. A synergistic effect between the WM extract and Indian gooseberry extract was found at ratios ranging from 2:1 to 9:1. It can be observed that increasing the proportion of mulberry enhances the efficacy, primarily due to anthocyanidins, flavonoids found in black mulberry, which inhibit tyrosinase activity by chelating Cu²⁺ ions and acting as competitive inhibitors. Additionally, mulberroside F (also known as moracin M-6), another compound found in mulberry, has been shown to suppress melanin production in melanocytes [10]. Gallic acid, a major component of Indian gooseberry, also exhibits tyrosinase inhibitory activity [11]. In accordance with a previous study, the combination of mulberry and Korean ginseng extracts exhibited greater anti-tyrosinase activity than the individual extracts, which was attributed to the synergistic interaction of their respective phytochemical constituents [12].

Table 3. Anti-tyrosinase activity of black mulberry fruit water extract (WM), Indian gooseberry extract, goji berry extract, and kojic acid

Samples	IC ₅₀ (mg/ml)
Kojic acid	0.02 ± 0.00 ^a
WM	1.31 ± 0.05 ^b
Indian gooseberry extract	16.56 ± 0.60 ^c
Goji berry extract	19.74 ± 0.72 ^d

Different alphabets (a, b, c, and d) indicate significant differences among samples based on one-way ANOVA ($p < 0.05$).

Table 4. Anti-tyrosinase activity and CI value of mixed extract

Ratio of black mulberry water extract : Indian gooseberry extract	IC ₅₀ (mg/mL)	CI Value
1:1	3.67 ± 0.06	1.51 ± 0.03
2:1	1.33 ± 0.04	0.71 ± 0.10
3:1	1.18 ± 0.34	0.69 ± 0.03
4:1	1.09 ± 0.13	0.67 ± 0.09
5:1	1.08 ± 0.10	0.69 ± 0.01
6:1	1.05 ± 0.03	0.69 ± 0.02
7:1	0.92 ± 0.08	0.62 ± 0.13
8:1	0.84 ± 0.02	0.58 ± 0.14
9:1	0.84 ± 0.04	0.58 ± 0.02

CONCLUSIONS

This study revealed that the water extract of black mulberry fruit contains active compounds belonging to the phenolic, flavonoid, and anthocyanin groups, which exhibit strong antioxidant properties and tyrosinase inhibitory activity. Moreover, the combination of black mulberry water extract with Indian gooseberry extract demonstrated a synergistic effect in enhancing both free radical scavenging and tyrosinase inhibition activities. Specifically, a synergistic effect was observed at a 1:7 ratio (mulberry:Indian gooseberry) for antioxidant activity and at an 8:1 ratio for tyrosinase inhibition. These findings suggest that the mixed extract at the identified optimal ratios holds potential for use as an active ingredient in anti-aging and skin-brightening skincare products. This study offers a novel contribution by combining black mulberry with a potent antioxidant source such as Indian gooseberry and by identifying the most effective extract ratios for cosmetic application. However, future studies should focus on evaluating the safety of these mixed extract and developing suitable formulations for clinical trials in human volunteers.

ACKNOWLEDGMENTS

The authors thankfully acknowledge the Master of Science Program in Cosmetic Science, Faculty of Pharmacy at Chiang Mai University, Chiang Mai, Thailand for providing us with the funding and necessary resources.

REFERENCES

- [1] Suriyaprom, S., Kaewkod, T., Promputtha, I., et al. Evaluation of antioxidant and antibacterial activities of white mulberry (*Morus alba* L.) fruit extracts. *Plants*. 2021;10(12):2736.
- [2] Ercisli, S., & Orhan, E. Chemical composition of white (*Morus alba*), red (*Morus rubra*) and black (*Morus nigra*) mulberry fruits. *Food chemistry*. 2007;103(4):1380-1384.
- [3] Kiattisin, K., Nantararat, T., & Leelapornpisid, P. Evaluation of antioxidant and anti-tyrosinase activities as well as stability of green and roasted coffee bean extracts from *Coffea arabica* and *Coffea canephora* grown in Thailand. *Journal of Pharmacognosy and Phytotherapy*. 2016;8(10):182-192.
- [4] Theansungnoen, T., Nitthikan, N., Wilai, M., et al. Phytochemical analysis and antioxidant, antimicrobial, and antiaging activities of ethanolic seed extracts of four *Mucuna* species. *Cosmetics*. 2022;9(1):14.
- [5] Poomanee, W., Wattananapakasem, I., Panjan, W., et al. Optimizing anthocyanins extraction and the effect of cold plasma treatment on the anti-aging potential of purple glutinous rice (*Oryza sativa* L.) extract. *Cereal Chemistry*. 2021;98(3):571-582.
- [6] Kiattisin, K., Intasai, N., Nitthikan, N., et al. Antioxidant, anti-tyrosinase, anti-aging potentials and safety of arabica coffee cherry extract. *Chiang Mai Journal of Science*. 2019;46(5):930-945.
- [7] Jan B., Parveen R., Zahiruddin S., et al. Nutritional constituents of mulberry and their potential applications in food and pharmaceuticals: A review. *Saudi Journal of Biological Sciences*. 2021;28:3909–3921.
- [8] Extraction of active compound from herb: Solvent Extraction. [Internet]. [2024 Oct 23]. Available from: https://www3.rdi.ku.ac.th/cl/knowledge/2564/solvent_extraction.pdf
- [9] Niwaspragrit, C., Munyanont, M., Jaisin, Y., et al. Study on physical properties, hydrolyzable tannin contents and free radical scavenging activities of *Phyllanthus emblica* Linn. from Kanchanaburi province. *Thai Journal of Pharmaceutical Sciences*. 2013;35(1):3-13.
- [10] Literature Review. [Internet]. [2025 Jan 1]. Available from: https://archive.lib.cmu.ac.th/full/T/2557/phars50857try_ch2.pdf
- [11] Peng, Z., Li, Y., Tan, L., et al. Anti-tyrosinase, antioxidant and antibacterial activities of gallic acid-benzylidenehydrazine hybrids and their application in preservation of fresh-cut apples and shrimps. *Food chemistry*. 2022;378:132127.
- [12] Kim, J. H., Kim, T. I., et al. Synergistic effects of novel herbal decoctions from *Panax ginseng* and *Morus alba* on tyrosinase activity and melanogenesis in vitro. *Heliyon*. 2022;8(2).

Potential of *Peristrophe bivalvis* (L.) Leaf Extracts for Cosmeceutical Applications: Biological Activity and Safety Profile

Pawaranch Wachirasawetkul¹, Suvimol Somwongin¹, Narin Taokaenchan², Watchara Kanjanakawinkul³,
Wantida Chaiyana^{1,4,*}

¹Department of Pharmaceutical Sciences, Faculty of Pharmacy, Chiang Mai University, Chiang Mai, Thailand

²Department of Medicinal Plant Science, Faculty of Agricultural Production, Maejo University, Chiang Mai, Thailand

³Chulabhorn Royal Pharmaceutical Manufacturing Facilities by Chulabhorn Royal Academy, Chon Buri, Thailand

⁴Multidisciplinary and Interdisciplinary School, Chiang Mai University, Chiang Mai, Thailand

*Corresponding author Email: wantida.chaiyana@cmu.ac.th

Abstract. This study aimed to examine the biological activity and safety profile of *Peristrophe bivalvis* (L.) leaf extracts. Extraction methods including infusion with water for 15 min and maceration with 95% ethanol or ethyl acetate (3 × 24 h). The biological activities evaluated were anti-aging and whitening effects. Anti-aging activity was determined by assessing collagenase and hyaluronidase inhibition, while whitening potential was evaluated through tyrosinase inhibition. Furthermore, the safety profile of the extracts was evaluated using the hen's egg test–chorioallantoic membrane to assess the potential for irritation. The ethanolic extract exhibited the highest enzyme inhibition at 1.0 mg/mL, with 137.0 ± 4.2% collagenase (suggesting both a protective effect and strong enzymatic inhibition) and 80.0 ± 2.1% hyaluronidase inhibition ($p < 0.05$). In contrast, the infusion extract showed lower inhibition of 99.0 ± 8.6% and 68.0 ± 4.0%, respectively. Notably, both extracts exhibited greater collagenase inhibition than epigallocatechin gallate (EGCG) at the same concentration, with EGCG showing 92.5 ± 3.9% inhibition. However, tyrosinase inhibition was relatively low in all extracts (inhibition below 25%). Regarding safety, the infusion extract caused no irritation, whereas ethyl acetate and ethanol extracts induced visible irritation. In conclusion, the infusion extract of *P. bivalvis* demonstrated significant anti-aging activity through the inhibition of key enzymes involved in skin aging, with no signs of irritation, highlighting its potential as a safe and effective ingredient for anti-aging formulations in cosmetic uses.

Keywords: *Peristrophe bivalvis*; magenta plant; cosmeceutical; anti-skin wrinkles; collagenase inhibitor

INTRODUCTION

Cosmetics are now an essential part of daily life, prompting greater attention to their ingredient sources and safety profiles (1). Plant-derived ingredients are widely considered safer and milder, making them particularly suitable for sensitive skin types (1,2). As awareness of the potential health risks associated with synthetic chemicals increases, there has been a growing shift towards the use of natural ingredients in cosmetics and personal care products. Consumers are increasingly seeking alternatives made from herbal extracts, which are perceived to be safer and more environmentally friendly (2). Consequently, there has been a significant increase in research focused on developing innovative formulations using herbal and natural products (3,4). Phytochemicals derived from plants have shown to possess biological activities comparable to or even more potent than their synthetic counterparts, with the added benefit of being less irritating and better suited for topical applications (2,3).

Peristrophe bivalvis (L.), a member of the Acanthaceae family, is widely distributed across Southern Asia and Africa (5). Traditionally, the leaves of *P. bivalvis* have been used as a natural dye, exhibiting a range of colors from purple and magenta to red and yellow (6,7). Beyond its use as a dye, *P. bivalvis* has a long history of medicinal applications, including the treatment of blood disorders, hypertension, and hyperlipidemia (6,8). Notably, the leaves are rich in bioactive compounds, particularly anthocyanins, which have been shown to possess antioxidant properties and may contribute to anti-aging effects (9-11). Despite these findings, the potential of *P. bivalvis* for anti-aging and skin-whitening applications, particularly through its ability to inhibit tyrosinase activity, a key enzyme in skin aging and pigmentation, remains underexplored. Comparing different extraction solvents is essential to identify the most efficient and effective method for isolating bioactive compounds. Solvents can significantly influence the yield and bioactivity of the extracted substances, and selecting the optimal solvent ensures the best possible outcome for specific applications, such as in cosmetics or pharmaceuticals.

Therefore, this study aimed to investigate the biological activities of *P. bivalvis* leaf extracts, focusing on their potential anti-aging and skin-whitening effects. The inhibitory effects of these extracts on key skin-aging enzymes, including collagenase and hyaluronidase, as well as on tyrosinase involved in skin whitening, were assessed. Additionally, the safety profile of the extracts was evaluated to determine their suitability for cosmetic and therapeutic applications.

MATERIALS AND METHODS

Materials

The leaves of *P. bivalvis* were purchased from a local market in Thailand. The plant materials were washed with water and then dried in a tray dryer (Mallory Quality Product, Bangkok, Thailand) at 60 °C for 24 h until dryness. Subsequently, dried *P. bivalvis* leaves were then ground into a fine powder using a blender.

Methods

Extraction of P. bivalvis leaves

Maceration

The dried *P. bivalvis* leaf powder (250 g) was macerated in 95% v/v ethanol or ethyl acetate with constant stirring using a magnetic stirrer set at 100 rpm for three cycles of 24-h (12). The macerate was then filtered through Whatman No. 1 filter paper and the solvent was subsequently removed using a rotary evaporator (Eyela, Tokyo, Japan).

Infusion

The dried *P. bivalvis* leaf powder (250 g) was infused in boiling water with constant stirring for 15 min (12). The infusion was then filtered through Whatman No. 1 filter paper and the solvent was removed using a freeze dryer (Christ, Osterode am Harz, Germany).

Determination of biological activities of P. bivalvis leaf extracts

Collagenase inhibition

The collagenase inhibitory activity of *P. bivalvis* leaf extracts was determined as described by Chaiyana et al. (13), with some modifications. In brief, 20 µL of a 1 mg/mL sample solution was mixed with 20 µL of collagenase solution and incubated for 15 min. Then, 80 µL of 50 mM Tricine buffer pH 7.5 and 40 µL of 2 mM FALGPA were added to the mixture. The absorbance was then immediately measured continuously at 345 nm using a multimode microplate reader (BMG LABTECH, Ortenberg, Germany). The collagenase inhibitory activity was calculated using the following equation (Eq. 1).

$$\text{Collagenase inhibition (\%)} = [(A-B)/A] \times 100 \quad (1)$$

where A is the reaction rate of the system in the presence of the sample and B is the reaction rate of the system without the sample. Epigallocatechin gallate (EGCG) at the same concentration to the extract (1 mg/mL) was used as a positive control. The experiment was performed in triplicate.

Hyaluronidase inhibition

The hyaluronidase inhibitory activity of *P. bivalvis* leaf extracts was determined as described by Chaiyana et al. (13), with some modifications. In brief, 120 µL of a 1 mg/mL sample solution was mixed with 100 µL of a 30-unit hyaluronidase solution and incubated at 37°C for 10 min. Then, 100 µL of 0.03% w/v hyaluronic acid in 300 mM sodium phosphate pH 5.35 was added, and the mixture was incubated at 37°C for 45 min. Subsequently, 880 µL of 0.1% w/v bovine serum albumin solution was added, and the resulting mixture was incubated at room temperature for 10 min. The absorbance was measured at 600 nm using a multimode microplate reader (BMG LABTECH, Ortenberg, Germany). The hyaluronidase inhibitory activity was calculated using the following equation (Eq. 2).

$$\text{Hyaluronidase inhibition (\%)} = [(A-B)/A] \times 100 \quad (2)$$

where A is the absorbance of the system in the presence of the sample and B is the absorbance of the system without the sample. Oleanolic acid at the same concentration to the extract (1 mg/mL) was used as a positive control. The experiment was performed in triplicate.

Tyrosinase inhibition

The tyrosinase inhibitory activity of *P. bivalvis* leaf extracts was determined as described by Chaiyana et al. (13), with some modifications. In brief, 120 µL of a 1 mg/mL sample solution was mixed with tyrosinase solution in 50 mM PBS pH 6.5 and incubated for 5 min at room temperature. Subsequently, 2.5 mM of L-Dopa or L-Tyrosine was added, and the mixture was incubated for 30 min. The absorbance was measured at 492 nm using a multimode microplate reader (BMG LABTECH, Ortenberg, Germany). The tyrosinase inhibitory activity was calculated using the following equation (Eq. 3).

$$\text{Tyrosinase inhibition (\%)} = (A - B)/A \times 100 \quad (3)$$

where A is the absorbance of the system in the presence of the sample and B is the absorbance of the system without the sample. Kojic acid at the same concentration to the extract (1 mg/mL) was used as a positive control. The experiment was performed in triplicate.

Irritation test

The irritation potential of *P. bivalvis* leaf extracts were investigated using the hen's egg-chorioallantoic membrane (HET-CAM) test (14). Fertilized hen's eggs, aged between 7 and 9 days, were obtained from the Faculty of Agriculture, Chiang Mai University. Ethical approval was not required as the embryo was less than half the incubation period (21 days). The shell was carefully opened, and the inner membrane in contact with the CAM was moistened with a normal saline solution (NSS). The membrane was then gently removed using forceps. The method was validated using sodium lauryl sulfate (SLS) and NSS as positive and negative controls, respectively. After the sample solution was applied to the CAM, the irritation signs, including hemorrhage, vascular lysis, and coagulation, were observed under a stereomicroscope at 5 and 60 min. The time of the first observation of each irritation sign was recorded in seconds, and the irritation score (IS) was calculated using the following equation (Eq. 4).

$$IS = [(301-H) \times 5]/300 + [(301-L) \times 7]/300 + [(301-C) \times 9]/300 \quad (4)$$

where H is the time point of the first observation of hemorrhage, L is the time point of the first observation of vascular lysis, and C is the time point of the first observation of coagulation. The IS was classified as no irritation (IS = 0.0 - 0.9), mild irritation (IS = 1.0 - 4.9), moderate irritation (IS = 5.0 - 8.9), and severe irritation (IS = 9.0 - 21.0). The experiment was performed in triplicate.

Statistical analyses

All experiments were performed in triplicate. The data were expressed as the mean \pm standard deviation (SD) and statistically analyzed using SPSS Statistics version 17.0 for Windows. The data were compared using one-way ANOVA followed by Tukey's multiple comparison test, with a *p*-value of < 0.05 considered statistically significant.

RESULTS AND DISCUSSION

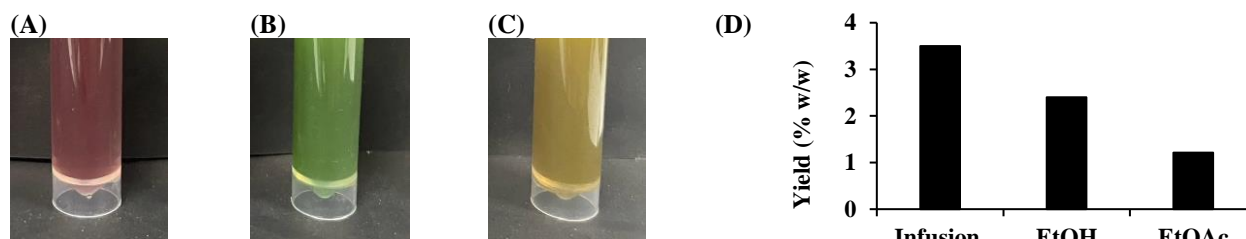
Results

Yield of *P. bivalvis* extracts

The visual appearance of *P. bivalvis* leaf extracts prepared by different extraction methods is shown in **Figure 1**. The infusion extract exhibited a reddish-brown hue, while the ethanol maceration extract appeared deep green in color. In contrast, the ethyl acetate extract presented a yellowish-brown coloration. These differences in color reflect variations in the types and concentrations of phytochemicals extracted by each solvent. The corresponding extraction yields were also different, with the infusion method providing the highest yield (3.5% w/w), followed by ethanol (2.4% w/w) and ethyl acetate (1.21% w/w) extraction methods.

Biological activities of *P. bivalvis* leaf extracts

The anti-skin aging and anti-tyrosinase activities of *P. bivalvis* leaf extracts are shown in **Figure 1**. The ethanol extract exhibited the highest collagenase inhibition ($137 \pm 2.1\%$), followed by the infusion ($99 \pm 1.8\%$) and EtOAc extracts ($77 \pm 3.4\%$), while EGCG showed $75 \pm 4.6\%$ inhibition. For hyaluronidase inhibition, the EtOH extract displayed the strongest activity ($80 \pm 1.6\%$), greater than oleanolic acid ($60 \pm 1.2\%$), infusion ($36 \pm 1.4\%$), and EtOAc ($20 \pm 2.1\%$), respectively. Regarding tyrosinase inhibition using L-tyrosine as a substrate, kojic acid showed the highest activity ($53.54 \pm 6.3\%$), while the infusion and EtOAc extracts exhibited moderate inhibition ($20.20 \pm 2.0\%$ and $24.42 \pm 1.5\%$, respectively), and the EtOH extract showed negligible activity. Similarly, for tyrosinase inhibition with L-DOPA, kojic acid demonstrated strong inhibition ($61.89 \pm 4.9\%$), whereas the EtOH, infusion, and EtOAc extracts showed low to minimal activities at $13.03 \pm 1.2\%$, $2.35 \pm 0.9\%$, and nearly 0%, respectively. These results indicate that extraction methods markedly affect the enzyme inhibitory properties of *P. bivalvis* leaf extracts.



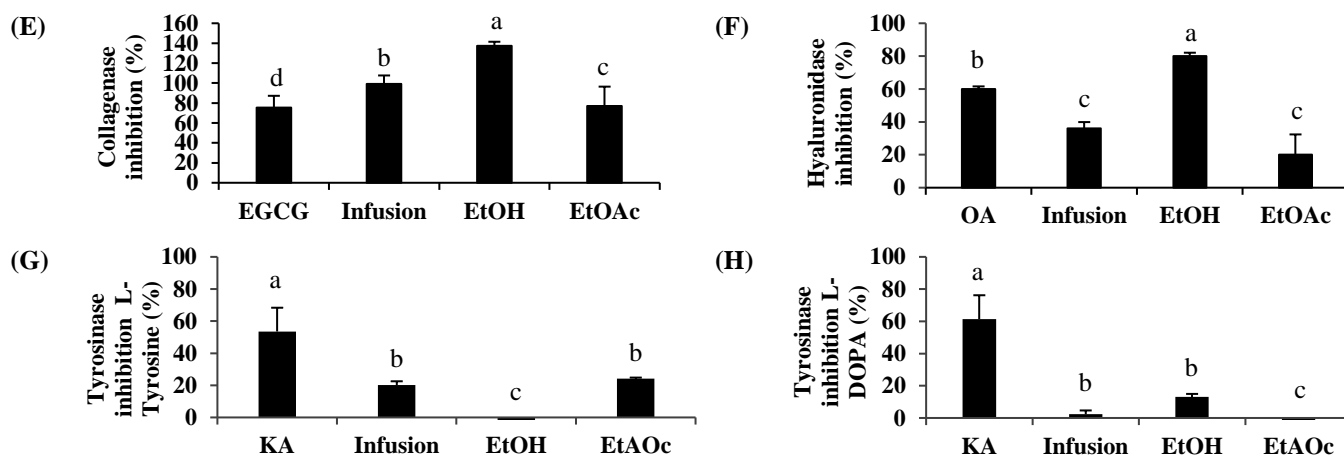


Figure 1. The aqueous solutions of *P. bivalvis* leaf extracts obtained by infusion (Infusion; A) and maceration with ethanol (EtOH; B) and ethyl acetate (EtOAc; C), along with their corresponding extraction yields (D). The inhibitory activities of epigallocatechin gallate (EGCG), oleanolic acid (OA), kojic acid (KA), Infusion, EtOH, and EtOAc were evaluated against collagenase (E), hyaluronidase (F), tyrosinase using L-tyrosine (G), and tyrosinase using L-DOPA (H).

Irritation properties of *P. bivalvis* leaf extracts

The irritation potential of *P. bivalvis* leaf extracts are shown in **Table 1**. The positive control exhibited a significantly high irritation score (16.54 ± 1.34), corresponding to severe irritation. In contrast, the negative control and the infusion extract showed no observable irritation, with irritation scores of 0.00 ± 0.00 . Ethanol and ethyl acetate extracts demonstrated mild irritation, with scores of 1.03 ± 0.29 and 1.14 ± 0.32 , respectively. These findings suggest that the infusion extract is the safest among the tested samples for topical application, while the mild irritation observed in the ethanol and ethyl acetate extracts may be attributed to solvent residues or specific semi-polar constituents.

Table 1. Irritation score (IS) of *P. bivalvis* leaf extracts

Sample	IS	Classification
Positive control	16.54 ± 1.34^a	Severe irritation
Negative control	0.00 ± 0.00^c	No irritation
Infusion	0.00 ± 0.00^c	No irritation
EtOH	1.03 ± 0.29^b	Mild irritation
EtOAc	1.14 ± 0.32^b	Mild irritation

NOTE: Positive control = 1% w/v SLS solution, Negative control = NSS, *P. bivalvis* leaf extracts obtained by infusion (Infusion) and maceration with ethanol (EtOH) and ethyl acetate (EtOAc). Different letters *a and b) denote significant differences among the irritation score of each extract ($p < 0.05$).

Discussions

The findings from this study highlight the influence of extraction method on the physicochemical properties and biological activities of *P. bivalvis* leaf extracts. The aqueous extract obtained by infusion yielded the highest extraction percentage (3.5% w/w) and presented a reddish-brown color, indicating a rich presence of hydrophilic phytochemicals such as anthocyanin (15). Ethanol and ethyl acetate extractions yielded lower amounts (2.4% and 1.21% w/w, respectively), but their distinct green and yellowish-brown colors suggest the presence of chlorophylls and mid-polar compounds such as flavonoids (5). Among the biological activities tested, the ethanol extract demonstrated the strongest inhibitory effect against collagenase ($137 \pm 2.1\%$) and hyaluronidase ($80 \pm 1.6\%$), suggesting its potential in anti-aging applications. The collagenase inhibition exceeding 100% likely results from the extract not only inhibiting enzyme activity but also further retarding the reaction rate compared to the untreated control, potentially through enzyme destabilization, substrate interaction, or antioxidant-mediated protection. The infusion also exhibited notable collagenase inhibition ($99 \pm 1.8\%$), though its hyaluronidase inhibition was significantly lower ($36 \pm 1.4\%$). Interestingly, despite its lower yield and weaker performance in collagenase and hyaluronidase assays, the ethyl acetate extract maintained mild activity across all tested enzymes, reflecting its content of selective lipophilic constituents. In the tyrosinase inhibition assays, both L-DOPA and L-tyrosine were used in the tyrosinase assay to evaluate the enzyme activity at different stages of melanogenesis. L-tyrosine serves as a substrate in the initial monophenolase phase (hydroxylation to L-DOPA), while L-DOPA

is used in the subsequent diphenolase phase (oxidation to dopaquinone). Using both substrates allowed for a comprehensive assessment of tyrosinase inhibition across its catalytic cycle. Both infusion and ethyl acetate extracts showed moderate inhibition on L-tyrosine, while only weak activity was observed on L-DOPA, indicating a limited effect on the later stage of melanogenesis. Low inhibition at the diphenolase phase implies that the extracts are unlikely to completely suppress melanin formation, which may limit their use as standalone skin-lightening agents. Importantly, the irritation assessment revealed that the infusion extract, similar to the negative control, caused no irritation, while the ethanol and ethyl acetate extracts induced only mild irritation. Residual solvents from ethanol and ethyl acetate extractions may contribute to the observed irritation, highlighting the need for careful solvent removal and formulation to ensure skin safety.

CONCLUSIONS

The biological activities and safety profile of *P. bivalvis* leaf extracts are strongly influenced by the extraction solvents. The infusion with DI water showed the highest extraction yield, notable collagenase inhibition, and complete absence of irritation, highlighting its potential as a safe and effective ingredient for anti-aging skincare formulations. Although ethanol and ethyl acetate extracts exhibited stronger enzyme inhibition in certain assays, their mild irritation potential suggested the need for cautious formulation. Overall, the *P. bivalvis* infusion extract represents a promising natural source for the development of multifunctional cosmeceutical products targeting skin aging and pigmentation. This study was the first to evaluate the anti-aging and safety properties of *P. bivalvis* leaf extracts using different extraction solvents. The identification of the aqueous infusion as a non-irritating, bioactive extract with high collagenase inhibition highlights its novel potential as a multifunctional ingredient for cosmeceutical applications.

ACKNOWLEDGMENTS

The authors would like to express our sincere gratitude to the Department of Pharmaceutical Science, Faculty of Pharmacy, Chiang Mai University for the financial support and the facilities used in the present study.

REFERENCES

1. Selvakumar PM. Application of plant-based molecules and materials in cosmetics. *Cosmetics*. 2024;11(6):211.
2. Liu W, Li Y, Luo Y, et al. Natural products in cosmetics. *Nat Prod Bioprospect*. 2022;12:1–10.
3. Ekor M, Martins E. The growing use of herbal medicines: issues relating to adverse reactions and challenges in monitoring safety. *Front Pharmacol*. 2014;4:177.
4. Saeed N, Khan MR, Shabbir M. Antioxidant activity, total phenolic and total flavonoid contents of whole plant extracts *Torilis leptophylla* L. *BMC Complement Altern Med*. 2012;12:221.
5. Minh TN, Nobukazu N, Xuan TD. The potential use of a food-dyeing plant *Peristrophe bivalvis* (L.) Merr. in Northern Vietnam. *Int J Pharmacol Phytochem Ethnomed*. 2016;4:14–16.
6. Thuy NM, Han DHN, Minh VQ, et al. Effect of extraction methods and temperature preservation on total anthocyanins compounds of *Peristrophe bivalvis* L. Merr. leaf. *J Appl Biol*. 2022;10(2):146–53.
7. Thuy NM, Tien VQ, Van Tai N, et al. Effect of foaming conditions on foam properties and drying behavior of powder from magenta (*Peristrophe roxburghiana*) leaves extracts. *Horticulturae*. 2022;8:546.
8. Tanaka Y, Ke NV. *Edible wild plants of Vietnam: the bountiful garden*. Bangkok: Orchid Press; 2007.
9. Adrianta KA, Santosa KA, Saputra H, et al. The antioxidant capacity of *Peristrophe bivalvis* (L.) Merr. as natural-based nephroprotection. *Tradit Med J*. 2021;26(1):35–41.
10. Adrianta KA, Santosa KA, Suparta IW, et al. Phytochemical identification of magenta leaf extract (*Peristrophe bivalvis* (L.) Merr.) and acute toxicity test on male white mice with LD50 determination. *J Ilmiah Medicamento*. 2021;7(2):136–41.
11. Khoo HE, Azlan A, Tang ST, et al. Anthocyanidins and anthocyanins: colored pigments as food, pharmaceutical ingredients, and the potential health benefits. *Food Nutr Res*. 2017;61:1–20.
12. Chaiyana W, Inthorn J, Somwongin S, et al. The fatty acid compositions, irritation properties, and potential applications of *Teleogryllus mitratus* oil in nanoemulsion development. *Nanomaterials*. 2024;14(2):184.
13. Somwongin S, Sirilun S, Chantawannakul P, et al. Ultrasound-assisted green extraction methods: an approach for cosmeceutical compounds isolation from *Macadamia integrifolia* pericarp. *Ultrason Sonochem*. 2023;92:106266.
14. Chaiyana W, Punyoyai C, Somwongin S, et al. Inhibition of 5 α -reductase, IL-6 secretion, and oxidation process of *Equisetum debile* Roxb. ex Vaucher extract as functional food and nutraceuticals ingredients. *Nutrients*. 2017;9(10):1105.
15. Le PH, Dao DN, Huynh TQ, et al. Extraction and purification of anthocyanins from *Peristrophe bivalvis* (L.) Merr. leaf (Acanthaceae) using aqueous two-phase systems. *Nat Prod Res*. 2023;37(1):154–8.

Antioxidant and Anti-inflammatory Effects of *Ipomoea pes-caprae* (L.) R.Br. Extracts from Eco-Friendly Extraction

*Suttida Changprasoe*¹, *Suvimol Somwongin*¹, *Watchara Kanjanakawinkul*²,
*Songyot Anuchapreeda*³, *Singkome Tima*³, *Wantida Chaiyana*^{1,4,*}

¹ Department of Pharmaceutical Sciences, Faculty of Pharmacy, Chiang Mai University

² Chulabhorn Royal Pharmaceutical Manufacturing Facilities by Chulabhorn Royal Academy

³ Department of Medical Technology, Faculty of Associated Medical Science, Chiang Mai University

⁴ Multidisciplinary and Interdisciplinary School, Chiang Mai University

*Corresponding author Email: wantida.chaiyana@cmu.ac.th

Abstract. *Ipomoea pes-caprae* (L.) R. Br is a medicinal herb known for treating skin conditions. Green extraction typically refers to environmentally friendly methods recently used for extracting bioactive compounds from medicinal plants for sustainable purposes. Therefore, this study aimed to enhance the extraction efficacy of bioactive compounds from *I. pes-caprae* using green extraction methods, with a focus on antioxidant and anti-inflammatory effects. The dried powder of *I. pes-caprae* was extracted using 95% w/v ethanol through a conventional maceration method for 24 h over 3 cycles (CON), maceration for 30 min at room temperature (MC) or at 50 °C (HT), and ultrasonication for 30 min (UL). The extracts were evaluated for the antioxidant activities through 2,2-diphenyl-1-picrylhydrazyl (DPPH) and ferric-reducing antioxidant power (FRAP) assay. The anti-inflammatory effects were evaluated through the inhibition of interleukin-6 (IL-6) and tumor necrosis factor-alpha (TNF- α) using enzyme linked immunosorbent assay. The findings showed that CON exhibited the most potent antioxidant activity, with DPPH inhibition of $31.3 \pm 0.9\%$ and a reducing power of 257.6 ± 35.6 mM FeSO₄ per g of extract. It also demonstrated the strongest anti-inflammatory effects, inhibiting IL-6 by $42.4 \pm 2.0\%$ and TNF- α by $16.4 \pm 0.9\%$. Interestingly, HT exhibited a comparable reducing power, achieved with the assistance of heat. On the other hand, UL exhibited a comparable TNF- α inhibition, achieved with the assistance of ultrasonication. In conclusions, green extraction methods improved time efficiency compared to the conventional extraction method, while maintaining comparable antioxidant and anti-inflammatory activities of the extracts.

Keywords: *I. pes-caprae*; environmentally friendly extraction; green extraction; sustainability; ultrasonication

INTRODUCTION

In recent years, there has been a notable shift within the cosmetics industry toward the use of natural, plant-based ingredients, largely driven by consumer preferences for products that are safe, sustainable, and environmentally responsible (1). This growing demand has, in turn, encouraged the adoption of green extraction technologies, which are innovative methods developed to reduce the environmental impact of extracting bioactive compounds from natural sources (1). These approaches are grounded in key sustainability principles, such as the use of renewable plant materials, non-toxic and biodegradable solvents, energy-efficient processing, and waste minimization through solvent recovery and by-product utilization (1-3).

Ipomoea pes-caprae (Linn.) R. Br., commonly known as beach morning glory, bay hops, or railroad vine, is a halophytic species in the Convolvulaceae family, predominantly native to coastal regions and widely distributed along tropical and subtropical shorelines (4). Despite its abundance and traditional medicinal uses, including its astringent, laxative, and diuretic properties (5), *I. pes-caprae* has received limited attention in the context of modern therapeutic and cosmetic applications. Traditionally, the plant has been applied topically to treat skin conditions such as itching, inflammation, and irritation caused by jellyfish stings and burns (5,6), indicating the presence of bioactive compounds with dermatological relevance.

Antioxidant and anti-inflammatory properties are highly valued in natural cosmetic ingredients because of their ability to address oxidative stress and inflammation, the two major factors contributing to skin aging, irritation, and skin damage (7). Therefore, this study aimed to investigate the antioxidant and anti-inflammatory effects of *I. pes-caprae* extracts obtained through eco-friendly extraction methods.

MATERIALS AND METHODS

Materials

The whole plant of *I. pes-caprae*, including leaves and stems, which had been naturally grown along the beach of the Sattahip Sea, was collected. The plant materials were washed with water, cut into small pieces, and dried in a hot air oven set at 50 °C. The dried *I. pes-caprae* was then ground into a fine powder by a grinder.

Methods

Extraction of *I. pes-caprae*

The dried powder of *I. pes-caprae* (80 g) was extracted using 95% w/v ethanol with a plant-to-solvent ratio of 1:10 through a conventional maceration method for 24 h over 3 cycles (CON), maceration for 30 min at room temperature (MC) or at 50 °C (HT), and ultrasonication at 40 kHz frequency and 240 W power for 30 min (UL). The extraction solvent was then removed by rotary evaporation.

2,2-Diphenyl-1-picrylhydrazyl (DPPH) assay

The DPPH[•] radical scavenging ability of *I. pes-caprae* extracts at the final concentration of 100 µg/mL was determined using the DPPH assay following the method of Chaiyana et al. (2017) (8). The DPPH[•] radical scavenging ability was evaluated by measuring the decrease in the deep violet color of the DPPH solution to pale yellow using a multimode reader at 520 nm after 30 min of reaction. The results were expressed as the percentage of DPPH[•] inhibition. L-ascorbic acid was used as a positive control. The experiments were done in triplicate using a single extract preparation.

Ferric reducing antioxidant power (FRAP) assay

The ferric reducing ability of *I. pes-caprae* extracts at the final concentration of 100 µg/mL was determined using the FRAP assay following the method of Saeio et al. (2011) (9). The reducing ability was evaluated by measuring the formation of a blue-colored Fe²⁺-TPTZ complex using a multimode reader at 595 nm after 5 min of reaction. The results were expressed as EC₁, which was millimoles of Fe²⁺ equivalents per gram of extract. L-ascorbic acid was used as a positive control. All experiments were performed in triplicate using a single extract preparation.

Anti-inflammatory activities determination

The anti-inflammatory activity of *I. pes-caprae* extracts at the final concentration of 10 µg/mL was evaluated based on interleukin 6 (IL-6) and tumor necrosis factor alpha (TNF-α) inhibition using the enzyme-linked immunosorbent assay (ELISA), following the method of Chaiyana et al. (2019) (10). RAW 264.7 cells (1 × 10⁵ cells/well) were seeded in a 24-well plate and incubated for 24 h. The extracts (1 µL) or vehicle were added and incubated for 2 h, followed by the addition of 200 µL of lipopolysaccharide (LPS), and further incubated for 24 h. Supernatant (500 µL) was collected for the 3-(4,5-dimethylthiazol-2-yl)-2,5-diphenyltetrazolium bromide (MTT) assay, while 100 µL was used for ELISA. A 96-well plate was coated with the capture antibody overnight at 4 °C, followed by sequential incubations with assay diluent, sample, detection antibody, avidin-horseradish peroxidase, and 3,3',5,5'-tetramethylbenzidine (TMB) substrate. The reaction was stopped with 2 N H₂SO₄, and the absorbance was measured at 450 nm. Dexamethasone was used as a positive control. The results were expressed as the percentage of IL-6 or TNF-α inhibition. All experiments were performed in triplicate using a single extract preparation.

Statistical analyses

The results were reported as the mean and standard deviation. One-way ANOVA followed by Tukey's test was used to identify the statistical differences (p < 0.05).

RESULTS AND DISCUSSION

Results

I. pes-caprae extracts

The whole plant of *I. pes-caprae* was successfully extracted using ethanol through eco-friendly extraction methods and their extraction yields are shown in **Figure 1**. CON yield the highest extract of 17.45% w/w, followed by HT (10.45% w/w), MC (7.45% w/w), and UL (6.58% w/w).

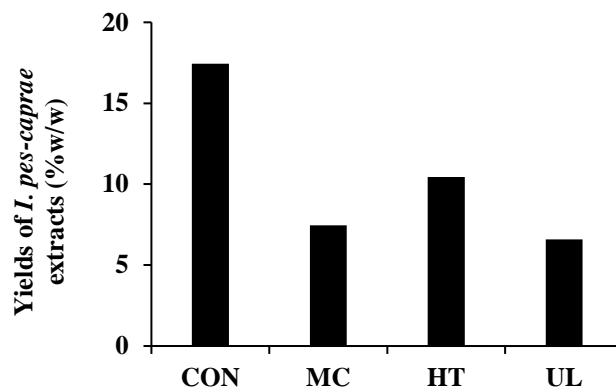


Figure 1. Yields *I. pes-caprae* extracts obtained through various eco-friendly extraction methods, including conventional maceration for 24 h over 3 cycles (CON), maceration for 30 min at room temperature (MC), and maceration for 30 min at 50 °C (HT), and ultrasonication for 30 min (UL).

Antioxidant activities of *I. pes-caprae* extracts

The antioxidant activities of *I. pes-caprae* extracts are presented in **Figure 2**. Ascorbic acid, used as a positive control, demonstrated superior DPPH• radical scavenging capacity with an inhibition of $92.8 \pm 0.6\%$, which was significantly higher than all the *I. pes-caprae* extracts ($p < 0.05$). Among the various *I. pes-caprae* extracts, CON exhibited the most pronounced DPPH• radical scavenging activity ($31.3 \pm 0.9\%$), which was significantly higher than the other extraction methods. MC displayed moderate inhibitory potential ($23.3 \pm 0.6\%$), while HT and UL extracts showed comparable but significantly lower activities ($18.9 \pm 1.7\%$ and $18.7 \pm 0.7\%$, respectively).

Similarly, the reducing power of the extracts, which was quantified as FeSO₄ equivalents per gram of extract, corroborated the trends observed in the DPPH assay. Ascorbic acid demonstrated a significantly higher reducing capacity of 2236.8 ± 37.9 mM FeSO₄/g extract ($p < 0.05$). Among the various *I. pes-caprae* extracts, CON, MC, and HT exhibited comparable reducing powers, with values of 257.6 ± 35.6 , 202.7 ± 0.4 , and 232.2 ± 0.9 mM FeSO₄/g extract, respectively. In contrast, UL showed a lower ferric reducing potential, with a value of 182.7 ± 6.8 mM FeSO₄/g extract.

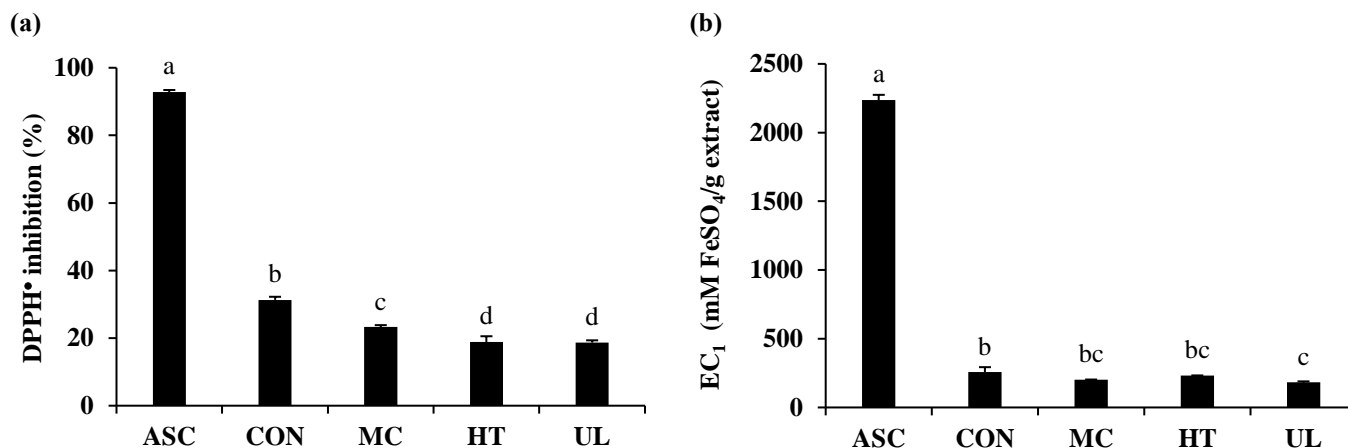


Figure 2. DPPH• inhibition (a) and EC₁ (c) of ascorbic acid (ASC) and *I. pes-caprae* extracts obtained through various eco-friendly extraction methods, including conventional maceration for 24 h over 3 cycles (CON), maceration for 30 min at room temperature (MC), and maceration for 30 min at 50 °C (HT), and ultrasonication for 30 min (UL). The letters a, b, c, and d represent significant differences in antioxidant activities among the extracts, as determined by one-way ANOVA followed by Tukey's test ($p < 0.05$). Extracts labeled with different letters are considered significantly different from each other.

Anti-inflammatory activities of *I. pes-caprae* extracts

The anti-inflammatory activities of *I. pes-caprae* extracts in terms of inhibitory activities against IL-6 and TNF- α are shown in **Figure 3**. Dexamethasone, the positive control, exhibited the most potent inhibitory effect on IL-6 production with an inhibition

rate of $67.6 \pm 1.6\%$, which was significantly higher than all tested extracts ($p < 0.05$). Among the *I. pes-caprae* extracts, CON demonstrated superior inhibitory activity ($42.4 \pm 2.0\%$), significantly more effective than the other extraction methods. MC showed moderate inhibition ($24.4 \pm 2.4\%$), while UL and HT exhibited the least inhibitory effects ($16.6 \pm 10.3\%$ and $12.6 \pm 6.9\%$, respectively).

Similarly, the pattern of TNF- α inhibition revealed that dexamethasone significantly outperformed all plant extracts, with an inhibition of $49.6 \pm 6.7\%$ ($p < 0.05$). However, all *I. pes-caprae* extracts exhibited no significant differences in TNF- α inhibition, with inhibition of $16.4 \pm 0.9\%$ for CON, $11.7 \pm 2.5\%$ for UL, $7.3 \pm 1.1\%$ for MC, and $4.1 \pm 5.8\%$ for HT, respectively.

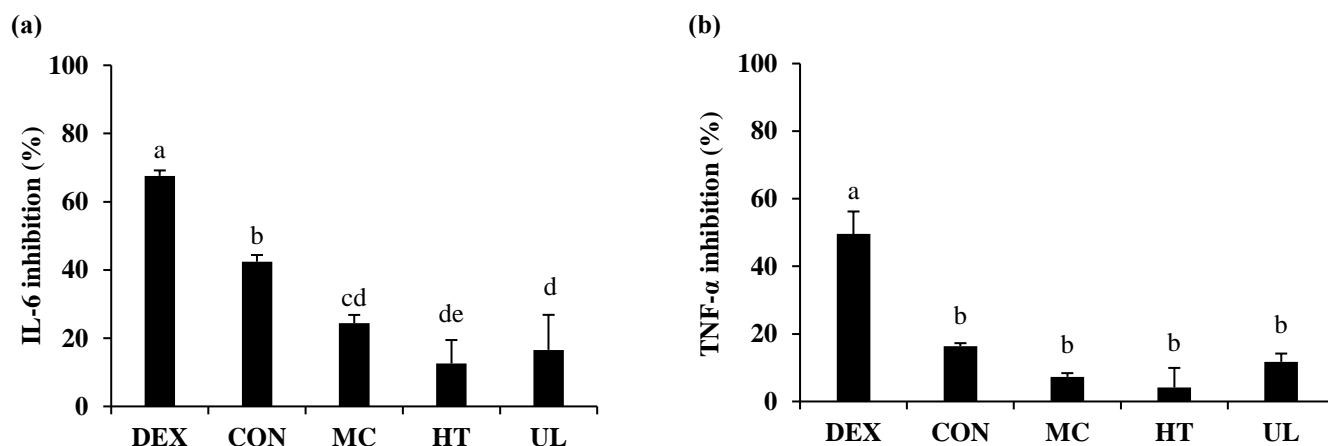


Figure 3. IL-6 inhibition (a) and TNF- α inhibition (b) of dexamethasone (DEX) and *I. pes-caprae* extracts obtained through various eco-friendly extraction methods, including conventional maceration for 24 h over 3 cycles (CON), maceration for 30 min at room temperature (MC), and maceration for 30 min at 50 °C (HT), and ultrasonication for 30 min (UL). The letters a, b, c, and d represent significant differences in antioxidant activities among the extracts, as determined by one-way ANOVA followed by Tukey's test ($p < 0.05$). Extracts labeled with different letters are considered significantly different from each other.

Discussions

I. pes-caprae was successfully extracted using eco-friendly methods, including HT, MC, and UL, which offer rapid processing and reduced solvent and energy consumption. In this study, eco-friendly extraction refers not only to the use of ethanol as a green solvent but also to the application of techniques that reduce energy consumption and extraction time. Ethanol was chosen as a green solvent in the current study based on previous reports suggesting that ethanol is effective for extracting compounds with antioxidant and anti-inflammatory activities (11). Although CON also used ethanol, its prolonged duration and higher energy demand make it less sustainable, thus serving as a comparative benchmark rather than an eco-friendly method. Although HT, MC, and UL yielded less extract than CON, they offer significant advantages in terms of time efficiency, requiring only 30 min compared to the prolonged duration of CON (3×24 h). Additionally, these methods are more energy-efficient and considered green extraction. The dried plant powder in this study was not sieved and its particle size was not controlled; however, the use of a consistent batch across all extractions ensured method consistency. Nonetheless, future studies should standardize particle size to enhance the reproducibility. The findings on the antioxidant and anti-inflammatory activities of *I. pes-caprae* extracts suggested that this plant possessed notable bioactive potential, with the efficacy of these activities influenced by the extraction method employed. The significant differences in antioxidant capacity among the various extracts remarked the critical role of extraction. The superior DPPH \cdot radical scavenging activity, ferric reducing power, and IL-6 inhibition observed in the CON could be attributed to its extended extraction duration of totaling 72 h (three cycles of 24 h), which likely facilitated greater extraction efficiency. Despite these significant differences, the slightly lower bioactivities found in the green extraction methods (MC, UL, and HT) remain within a promising range. Notably, these methods require only 30 min of extraction time, offering substantial advantages in terms of energy efficiency, time savings, and environmental sustainability. Although all the green extraction methods show promising results, further optimization is recommended to enhance yields, increase bioactive compounds, and improve biological activity. This could involve adjusting parameters such as temperature, ultrasonication frequency, and extraction time. Therefore, while conventional extraction may yield marginally higher activity, green extraction techniques present a more sustainable and practical approach for developing bioactive plant-based products. The demonstrated antioxidant and anti-inflammatory activities of *I. pes-caprae* remarked its potential as a multifunctional agent in skin care applications. Its antioxidant capacity contributes to the neutralization of oxidative stressors, thereby protecting the skin from premature aging and environmental damage (12). Concurrently, its ability to modulate pro-inflammatory cytokines such as IL-6 and TNF- α supports the reduction of inflammation,

promoting skin barrier integrity and resilience (13). These bioactivities position *I. pes-caprae* as a promising candidate for the development of advanced dermatological and cosmeceutical formulations.

CONCLUSIONS

I. pes-caprae exhibited significant antioxidant and anti-inflammatory activities, with its bioefficacy notably influenced by the extraction method. While CON yielded the highest activity, likely due to prolonged extraction time, green methods such as short-term maceration, ultrasound-assisted, and heat-assisted extraction demonstrated comparable bioactivities within a much shorter timeframe. These environmentally friendly techniques offer clear advantages in terms of sustainability, energy efficiency, and practicality for large-scale applications. Importantly, the bioactive properties of *I. pes-caprae*, including its ability to combat oxidative stress and modulate inflammatory responses, highlighted its strong potential as a multifunctional ingredient in skincare and cosmeceutical products. Further investigations on phytochemical profiling to pinpoint the active constituents responsible for the bioactivities would be suggested to identify the bioactive compounds responsible for its biological activities.

ACKNOWLEDGMENTS

The authors are grateful for the funding support from the Research and Researchers for Industries (RRI) program, grant number N23G670013 and partial funding from Skin Pro Laboratory Co., Ltd. We also express our gratitude to the Chulabhorn Royal Pharmaceutical Manufacturing Facility for the valuable contribution in providing the raw plant materials for this study.

REFERENCES

1. Chemat F, Abert-Vian M, Fabiano-Tixier AS, Strube J, Uhlenbrock L, Gunjevic V, et al. Green extraction of natural products. Origins, current status, and future challenges. *Trends Analyt Chem.* 2019 Sep; 118:248–63.
2. Gonzalez-Díaz A, García-Núñez JA. Hydrophilic deep eutectic solvents: A new generation of green and safe extraction systems for bioactive compounds obtaining from natural oil & fats – A review. *Sustain Chem Pharm.* 2023 Dec; 36:101278.
3. Marchev AS, Yordanova ZP, Georgiev MI. Green (Cell) factories for advanced production of plant secondary metabolites. *Crit Rev Biotechnol.* 2020 May 18;40(4):443–58.
4. Akinniyi G, Lee J, Kim H, Lee JG, Yang I. A medicinal halophyte *Ipomoea pes-caprae* (Linn.) r. Br.: a review of its botany, traditional uses, phytochemistry, and bioactivity. *Mar Drugs.* 2022 May 17;20(5):329.
5. Khan SA, Salem Al Faraji SR, Hamed Almukhaini MS, Mohd A, Jamal F, Premkumar SSD, et al. *In vitro* establishment, hydroponic, salt tolerance, antifungal and phytochemical investigations in important sand binder medicinal plant *Ipomoea pes-caprae*. *Traditional Medicine.* 2023;4(1).
6. Xavier-Santos JB, Passos JGR, Gomes JAS, Cruz JVC, Alves JSF, Garcia VB, et al. Topical gel containing phenolic-rich extract from *Ipomoea pes-caprae* leaf (Convolvulaceae) has anti-inflammatory, wound healing, and antiophidic properties. *Biomed Pharmacother.* 2022 May; 149:112921.
7. Li X, Li C, Zhang W, Wang Y, Qian P, Huang H. Inflammation and aging: signaling pathways and intervention therapies. *Signal Transduct Target Ther.* 2023 Jun 8;8(1):239.
8. Chaiyana W, Punyoyai C, Somwongin S, Leelapornpisid P, Ingkaninan K, Waranuch N, et al. Inhibition of 5 α -reductase, IL-6 secretion, and oxidation process of *Equisetum debile* roxb. Ex vaucher extract as functional food and nutraceuticals ingredients. *Nutrients.* 2017 Oct 10;9(10):1105.
9. Saeio K, Chaiyana W, Okonogi S. Antityrosinase and antioxidant activities of essential oils of edible Thai plants. *Drug Discov Ther.* 2011;5(3):144–9.
10. Chaiyana W, Anuchapreeda S, Punyoyai C, Neimkhum W, Lee KH, Lin WC, et al. *Ocimum sanctum* Linn. as a natural source of skin anti-ageing compounds. *Ind Crops Prod.* 2019 Jan; 127:217–24.
11. Saengkhae C, Uawongyart N, Osiri S, Srisook K, Tangwattanachuleeporn M. Antioxidant and anti-inflammatory activities of different solvent extracts from *Ipomoea pes-caprae* (L.) R. Br. in lipopolysaccharide stimulated RAW 264.7 macrophages. *Trends Sci.* 2021;18(24):1404-1404.
12. Rona C, Vailati F, Berardesca E. The cosmetic treatment of wrinkles. *J of Cosmetic Dermatology.* 2004 Jan;3(1):26–34.
13. Proksch E, Brandner JM, Jensen J. The skin: an indispensable barrier. *Exp Dermatol.* 2008 Dec;17(12):1063–72.

Characterization of Cannabis Flower Wax for Cosmetic Production

Chanakarn Amphansri¹, Nuttapol Boonrueang¹, Darunee Hongwiset¹, Kanokwan Kiattisin¹, and Chadarat Ampasavate^{1,}*

¹Department of Pharmaceutical Sciences, Faculty of Pharmacy, Chiang Mai University, Chiang Mai 50200, Thailand

*Corresponding author Email: chadarat.a@cmu.ac.th

Abstract. Cannabis wax is a by-product of the cannabis extraction, primarily obtained during the winterization process. This study investigates the physicochemical properties of cannabis wax samples to assess their suitability for cosmetic and pharmaceutical formulations. The batch-to-batch chemical composition of cannabis wax varies depending on the cannabis strain, extraction method, and purification techniques. The HPLC analysis showed cannabidiol (CBD) content of 5.66–13.28 %w/w and tetrahydrocannabinol (THC) at 0.42 ± 0.09 %w/w, which requires legal considerations. The wax exhibited slight solubility in non-polar solvents and a relatively low melting point (62.40–64.60 °C), indicating compatibility with a wide range of solid and liquid lipids used in pharmaceutical and cosmetic formulations. By applying the USP <401> analyses indicated high acid values (2.79–5.57 mg KOH/g wax), low iodine values (2.28–10.74 g Iodine/100 g wax), and low peroxide values (0.97–1.95 mEq oxygen/kg), reflecting a composition rich in long-chain fatty acids with a low degree of unsaturation. These properties contribute to its stability and resistance to oxidation and rancidity. The wax was incorporated into a lipstick prototype to explore its formulation potential, demonstrating its feasibility as a sustainable alternative to petroleum-based wax. The findings highlight the potential of cannabis wax as a value-added ingredient in cosmetic and pharmaceutical applications, promoting its use in eco-friendly formulations.

Keywords: Cannabis wax; By-product; Physicochemical properties; Sustainable formulation; Cosmetic application

INTRODUCTION

Cannabis is a genus in the Cannabaceae family, which includes three subspecies ^[1]: hemp, marijuana, and ruderalis. Hemp (*Cannabis sativa* subsp. *sativa*) and marijuana (*Cannabis sativa* subsp. *indica*) are commonly used in pharmaceutical and cosmetic applications.^[2] Cannabinoid extraction from cannabis flower buds yields crude oil containing key bioactive compounds such as CBD and THC. The winterization process is then applied to remove impurities, including plant waxes, enhancing extract purity.^[3]

Cannabis wax, generated as a by-product of cannabinoid extraction, offers a sustainable means to valorize biomass while reducing waste and methane emissions, thereby supporting the carbon-neutrality goal.^[4] Converting this material into high-value cosmetics would not only lower the environmental burden but also create additional revenue streams for growers. Rich in long-chain hydrocarbons, residual cannabinoids (CBD, THC) and aromatic terpenes with a relaxing scent, cannabis wax and terpenes are well-suited to lipid-based formulations. These attributes justify its investigation as a primary raw material for cosmetic applications.^[5]

This study aimed to investigate the physicochemical properties of cannabis wax, including peroxide value, acid value, saponification value, ester value, iodine value, and solubility. Comprehensive characterization of these parameters is essential for ensuring the consistency and quality of cannabis wax, particularly to minimize batch-to-batch variation in pharmaceutical and cosmetic applications. To explore its practical use, cannabis wax was incorporated into a lipstick formulation, and the optimal ratio of lipid components was systematically evaluated.

MATERIALS AND METHODS

Materials

Cannabis waxes and CBD distillate from the cannabinoid extraction process were gifted from Atlanta Co. Ltd. (Chiang Mai, Thailand). Three wax samples (H02, H03, H04) obtained via the ethanol extraction method were dried at 50 °C under vacuum to remove residual solvents. Natural beeswax (MySkinRecipes, Bangkok, Thailand) was used as a control and for analytical validation.

Methods

Source of samples

Three cannabis waxes differed by subspecies and harvest time; H02 and H03 were from *C. sativa* subsp. *indica* (harvested 8 November 2023 and 25 March 2024, respectively), while H04 was from *C. sativa* subsp. *sativa* (harvested in 2023, unknown exact date). The CBD distillate was derived from the cannabinoid extraction process of H02 on 10 June 2024.

Physical properties determination

Melting point

Melting points were determined using a melting point apparatus (Stuart, United Kingdom). Each wax sample was placed in a glass capillary tube, and the melting point was recorded from the onset of melting until the sample was completely liquefied.

*Corresponding author: chadarat.a@cmu.ac.th
Presenting author: chanakarn_am@cmu.ac.th

Solubility property

The solubility of each wax (10 mg) was determined following the criteria outlined in USP47-NF42.^[6] Solvents tested at $25 \pm 2^\circ\text{C}$ included mineral oil, chloroform, acetone, DMSO, PEG, methanol, ethanol, ethoxydiglycol, dimethyl isosorbide, olive, sesame, avocado, and jojoba oils. Solvent (10 μL) was added gradually with mixing until complete dissolution or up to 1 mL total. The volume of solvent required was recorded, and solubility was classified according to USP47-NF42 criteria.^[6]

Chemical properties determination

Analytical methods for chemical parameters were developed using certified natural beeswax as the control. The USP47-NF42 <401> fats and fixed oil monographs, including saponification, acid, ester, iodine, and peroxide values, were applied to determine the corresponding values in cannabis wax.^[7]

Determination of saponification value

The sample (1.5 g) was mixed with 25 mL of 0.5 M alcoholic potassium hydroxide and heated. The solution was kept at the boiling stage for 60 minutes for complete saponification. After adding 1 mL phenolphthalein, excess potassium hydroxide was titrated with 0.5 M hydrochloric acid solution. The saponification value was calculated using Eq. 1:

$$\text{Saponification value} = [M_r \times (V_B - V_S) \times N] / W \quad (1)$$

where M_r is the molecular weight of potassium hydroxide, V_B is the volume of hydrochloric acid solution required by the blank (mL), V_S is the volume of hydrochloric acid solution required for the sample (mL), N is the exact concentration of hydrochloric acid (M), W is the mass of the sample (g)

Determination of acid value

The sample (3 g) was accurately weighed into an Erlenmeyer flask. Then, neutralized dehydrated alcohol (25 mL) was added and heated until completely melted. Next, phenolphthalein TS (1 mL) was added, and titrated with 0.5 M alcoholic potassium hydroxide VS. The acid value was calculated by using the following equation (Eq. 2):

$$\text{Acid value} = (M_r \times V) \times (N/W) \quad (2)$$

where M_r is the molecular weight of potassium hydroxide, V is the volume of potassium hydroxide solution required (mL), N is the exact concentration of potassium hydroxide (M), and W is the mass of the sample (g)

Determination of ester value

A 0.5 M alcoholic potassium hydroxide VS solution (25 mL) was pipetted into the titrated solution from the acid value analysis. The aldehyde-free alcohol (50 mL) was added and boiled for 4 hours. The excess base was titrated with 0.5 M hydrochloric acid VS. The Ester value was calculated by using the following equation (Eq. 1).

Determination of iodine value

The sample (3 g) was dissolved in dichloromethane (10 mL) and iodobromide TS (25 mL), then kept in the dark for 30 minutes. Potassium iodide TS (30 mL) and water (100 mL) were added before titration with 0.1 M sodium thiosulfate until pale yellow. After adding 3 mL starch TS, the titration continued until the blue color disappeared. The iodine value was calculated using Eq. 3:

$$\text{Iodine value} = [A_r \times (V_B - V_S) \times N] / (10 \times W) \quad (3)$$

where A_r is the molecular weight of iodine, V_B is the volume of 0.1 M sodium thiosulfate solution required by the blank (mL), V_S is the volume of 0.1 M sodium thiosulfate solution required for the sample (mL), N is the concentration of sodium thiosulfate (M), and W is the mass of the sample (g)

Determination of peroxide value

The sample (1 g) was dissolved in chloroform, then mixed with 2 M hydrochloric acid solution and saturated potassium iodide. After incubation in the dark for 5 minutes at room temperature, the mixture was titrated with 0.01 M sodium thiosulfate using starch as an indicator. The peroxide value was calculated according to Eq. 4:

$$\text{Peroxide value} = 1000 \times [(V_S - V_B) \times M] / W \quad (4)$$

where V_B is the volume of 0.01 M sodium thiosulfate solution required by the blank (mL), V_S is the volume of 0.01 M sodium thiosulfate solution required for the sample (mL), N is the concentration of sodium thiosulfate (M), and W is the mass of sample (g)

Spectroscopic characterization

The spectroscopic characterization provided insights for standardizing raw material quality of cannabis wax across production lots in the industrial sector. The methods include UV-Vis spectroscopy and IR spectroscopy.

UV-Vis spectroscopy

Cannabis wax samples were dissolved in chloroform (1 mg/mL), and absorption spectra were recorded in the 200–400 nm range at room temperature using an Agilent Cary 60 UV–Vis spectrophotometer.

IR spectroscopy

FT-IR spectra were obtained using the ATR mode of the FT-IR spectrometer (Bruker, Germany) in the 400–4000 cm^{-1} range. Cannabis waxes were finely ground and mixed with potassium bromide to ensure homogeneity prior to analysis.

Determination of active content using High-Performance Liquid Chromatography (HPLC)

Cannabinoid content in cannabis waxes was analyzed using HPLC-UV. Identification and quantification were performed by comparison with reference standards (CBD, CBD-A, THC, THC-A). The analysis employed a Shimadzu HPLC system with UV detection at 228 nm, using a C18 column (Symmetry®, 5 μm , 250 \times 4.6 mm; Waters, Ireland). The isocratic mobile phase consisted of acetonitrile and 0.1% trifluoroacetic acid in DI water (69:3), with a flow rate of 1.0 mL/min and an injection volume of 20 μL .

Application

Lipsticks were prepared using a general method by melting white beeswax, cannabis wax, lanolin, cocoa butter, and CBD distillate in order of decreasing melting point. The coloring agent (iron oxides) was dispersed in castor oil and heated before combining the lipid phase at the same temperature. The mixture was poured into molds, cooled, trimmed, and flamed. Final products were then evaluated for their characteristics.^[8]

Statistical analysis

The experimental results were presented as the mean \pm standard error and analyzed for differences using SPSS statistic software version 17.0 for application, using a One-way ANOVA with Turkey's multiple comparison tests. The p-value < 0.05 level was considered statistically significant.

RESULTS AND DISCUSSION

Results and Discussion

Physical properties

Wax by-products and CBD distillate

The cannabis waxes (H02, H03) were sticky yellow semi-solids, while H04 was a sticky brown semi-solid. All samples exhibited a distinct cannabis terpene scent and darkened upon drying. The CBD distillate was observed as a viscous yellow oil.

Melting point of waxes

The melting point of cannabis wax ranged from 62.30 ± 0.20 °C to 64.60 ± 0.20 °C, suitable for cosmetic use as it melts at low temperatures, reducing the risk of ingredient degradation during production.

Solubility property

According to USP47-NF42^[6], cannabis wax is sparingly soluble in oils but slightly soluble in organic solvents such as acetone, chloroform, DMSO, PEG, methanol, ethanol, ethoxydiglycol, and dimethyl isosorbide. This reflects the solubility principle: 'like dissolves like,' wherein compounds tend to dissolve in solvents with similar polarity characteristics.

Values of cannabis wax and CBD distillate

Natural beeswax was used as a reference for the analytical method development, whose results were consistent with the Certificate of Analysis (CoA). As shown in Figure 1A–1C, beeswax had the highest acid, ester, and saponification values, indicating a high fatty acid content. In contrast, cannabis waxes exhibited lower values across all three parameters, suggesting a lower fatty acid and ester content. Specifically, acid values are 4.64 ± 0.01 KOH/g for H02, 2.79 ± 0.00 KOH/g for H03 and 5.57 ± 0.01 KOH/g for H04. The ester values are 24.64 ± 0.03 KOH/g for H02, 26.18 ± 0.03 KOH/g for H03, and 34.65 ± 0.04 KOH/g for H04, and saponification values are 51.83 ± 0.93 KOH/g for H02, 46.10 ± 0.24 KOH/g for H03 and 22.60 ± 0.91 KOH/g for H04. As shown in Figure 1D, cannabis waxes showed higher iodine values 12.65 ± 0.01 g I₂/100 g for H02, 10.74 ± 0.01 g I₂/100 g for H03, and 12.28 ± 0.00 g I₂/100 g for H04 than natural beeswax, all samples also exhibited low peroxide values (0.97 mEq O₂/kg), indicating good oxidative stability. As shown in Figure 1A–1C, the CBD distillate exhibited higher acid values (10.21 ± 0.01 mg KOH/g) and lower ester (5.39 ± 0.00 mg KOH/g sample) and saponification values (5.64 ± 0.89 mg KOH/g) compared to the wax samples, suggesting a greater content of free fatty acids and a lower ester content or the presence of longer-chain fatty acids in the oil. Figures 1C and 1D show the higher iodine (15.50 ± 0.01 g I₂/100 g) and peroxide values (1.95 ± 0.00 mEq oxygen/kg sample) of the CBD distillate than the wax samples, indicating greater susceptibility to oxidation.

Based on the results, the three cannabis waxes and the CBD distillate may be suitable for use in cosmetic products requiring long shelf lives, as they can help reduce the risk of product instability and maintain product quality.

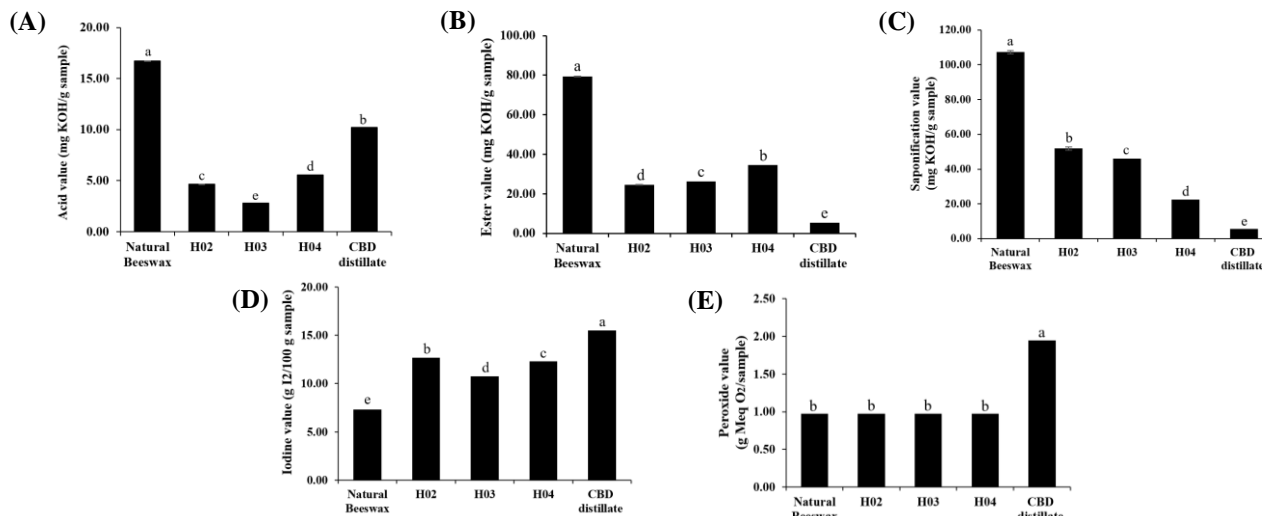


Figure 1. Acid values (A), Ester values (B), Saponification values (C), Iodine values (D), and Peroxide values (E) of the natural beeswax, various cannabis waxes, and CBD distillate

Spectroscopic characteristics of wax samples

UV-Vis Absorption Spectra

The cannabis wax samples were diluted in chloroform and scanned for absorption bands in the UV range of 200 to 400 nm. The absorption bands of all three samples are similar, showing the maxima at 243 and 273 nm, respectively (**Figure 2A**). These maximums are likely related to unsaturated fatty acids and the cannabinoid structure of CBD or THC.^[9]

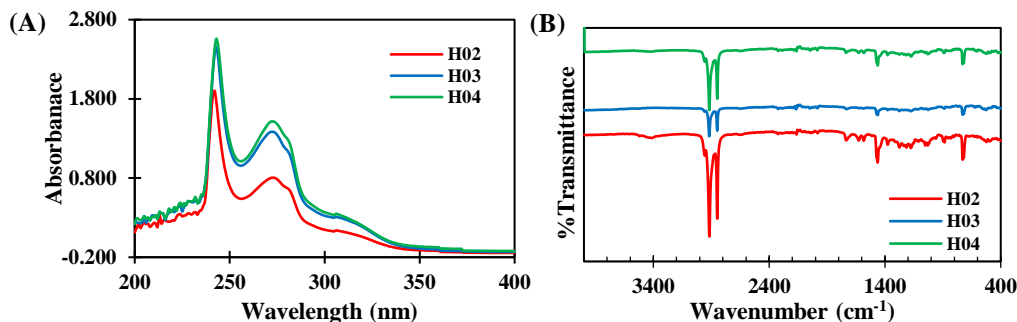


Figure 2. UV-vis spectra (A) and IR spectra (B) of cannabis wax

IR Spectra

The FT-IR spectra of cannabis wax exhibit the presence of prominent peaks at 2957 cm⁻¹ and 2848 cm⁻¹ (-CH), 1463 cm⁻¹ (-CH₂), 1376 cm⁻¹ (-CH₃), 3413 cm⁻¹ (-OH), and 1735 cm⁻¹ (C=O), indicating the presence of alkanes, alcohols, and carboxylic groups of carboxylic acids and esters, respectively. The signal at 1626 cm⁻¹ corresponds to unsaturated C=C bonds; the signals at 1052-1215 cm⁻¹ indicate the presence of terpenoids and the peak at 729 cm⁻¹ indicates the existence of long-chain alkanes. All three waxes exhibited similar FT-IR spectra but with different peak intensities as shown in **Figure 2B**. Additionally, the waxes are similar to the standard on another paper when compared to another finding.^[10]

Active compounds in cannabis waxes

Analysis of residual cannabinoids in wax samples revealed CBD contents of 5.70 ± 1.50% for H02, 13.66 ± 1.87% for H03, and 10.24 ± 0.35% for H04, with an average THC content of 0.42 ± 0.09% (n = 3). All samples showed significantly higher CBD than THC levels (24.31 ± 3.88%). As a non-psychoactive compound with legal accessibility and beneficial properties, including anti-inflammatory, moisturizing, and skin-balancing effects. CBD-containing wax is more suitable than high-THC wax for cosmetic applications. However, due to THC levels exceeding 0.2% w/w^[11], direct use of cannabis wax remains restricted. Incorporating wax at concentrations not exceeding 10% allows CBD to act as the primary active ingredient while maintaining THC levels within legal limits. Due to limited sample size, further studies are required to confirm differences between hemp and marijuana-derived waxes.

Cannabis lipstick formulation

Conventional lipstick formulation was developed using plant-based waxes, cannabis wax and CBD distillate as alternatives to petroleum-derived ingredients. As shown in **Figure 3**, among the six formulations, formulation 5 demonstrated the most desirable characteristics, including a texture and application quality comparable to commercial products. The presence of CBD wax contributed to a smooth, soft touch and excellent spreadability. Evaluation results, summarized in **Table 1**, indicate that this formulation resembles standard parameters and is comparable to marketed lipsticks.

Table 1. Evaluation of cannabis lipstick formulation 5

No.	Parameter	Results
1	Color	Red
2	Texture	Soft
3	pH	5.0
4	Ease of application	Good
5	Melting point (°C)	59-62
6	Surface anomalies	No defect
7	Solubility test	Chloroform soluble
8	Aging stability	Smooth



Figure 3. Lipstick formulation-5

CONCLUSIONS

In this work, the cannabis wax samples derived from two subspecies were evaluated. Among all three wax samples, the acid, ester, saponification and iodine values exhibited significant differences, whereas the peroxide values were comparable. Notably, their chemical profiles differed markedly from those of the CBD distillate and conventional beeswax, suggesting that cannabis-derived wax possesses a relatively stable composition. Additionally, low melting points and good solubility in oils mean that the studied CBD distillate can also be used together. The similarity of the spectroscopic UV and FT-IR spectra indicated the identity, consistency and quality of raw material for application in pharmaceuticals and cosmetics. Therefore, cannabis wax demonstrates suitability as a natural alternative to petroleum-based fats in the formulation developed in this study. In addition, the presence of CBD offers added functional benefits such as anti-inflammatory and moisturizing properties. Overall, cannabis wax shows promise as a natural alternative to petroleum-based fats in eco-friendly cosmetic and pharmaceutical applications.

ACKNOWLEDGMENTS

The authors would like to express our sincere gratitude to the Multidisciplinary Research Institute, Chiang Mai University, and Atlanta Co., Ltd., Chiang Mai, Thailand, for the financial support and provision of materials used in this study. The authors also extend their appreciation to the Cosmeceutical Science Program, Department of Pharmaceutical Sciences, Faculty of Pharmacy, Chiang Mai University, for partial financial support and access to research facilities essential to the completion of this work.

REFERENCES

1. Rehman, M., Fahad, S., Du, G., et al. (2021). Evaluation of hemp (*Cannabis sativa* L.) as an industrial crop: A review. *Environmental Science and Pollution Research*, 28(38), 52832–52843. <https://doi.org/10.1007/s11356-021-14933-3>
2. Happyana, N., Agnolet, S., Muntendam, R., Van Dam, A., Schneider, B., & Kayser, O. (2013). Analysis of cannabinoids in laser-microdissected trichomes of medicinal *Cannabis sativa* using LCMS and cryogenic NMR. *Phytochemistry*, 87, 51–59.
3. Keller, N. M. (2013). The legalization of industrial hemp and what it could mean for Indiana's biofuel industry. *Indiana International & Comparative Law Review*, 23, 555.
4. Valizadehderakhshan, M., Shahbazi, A., Kazem-Rostami, M., Todd, M. S., Bhowmik, A., & Wang, L. (2021). Extraction of cannabinoids from *Cannabis sativa* L. (Hemp). *Agriculture*, 11(5), 384. <https://doi.org/10.3390/agriculture11050384>
5. Tutek, K., & Masek, A. (2022). Hemp and its derivatives as a universal industrial raw material (with particular emphasis on the polymer industry): A review. *Materials*, 15(7), 2565. <https://doi.org/10.3390/ma15072565>
6. The United States Pharmacopeial Convention. (2024). Description and relative solubility of reagents. In *United States Pharmacopeia and National Formulary (USP 47–NF 42)*. Rockville, MD: The United States Pharmacopeial Convention.
7. The United States Pharmacopeial Convention. (2024). <401> Fats and fixed oils. In *United States Pharmacopeia and National Formulary (USP 47–NF 42)*. Rockville, MD: The United States Pharmacopeial Convention.
8. Sunil, R., Shekhar, T. C., & Ashutosh, B. (2013). Formulation and evaluation of a herbal lipstick: A new approach. *International Journal of Pharmaceutical Erudition*, 3(1), 26–30.
9. Ryu, B. R., Islam, M. J., Azad, M. O. K., Go, E.-J., Rahman, H. M., Rana, M. S., et al. (2021). Conversion characteristics of some major cannabinoids from hemp (*Cannabis sativa* L.) raw materials by new rapid simultaneous analysis method. *Molecules*, 26(14), 4113.
10. Lian, S., Gao, X., Song, C., Li, H., Chen, A., & Lin, J. (2021). The characteristics of Raman spectroscopy of isomer CBD- and THC-Au nanoparticles using the density functional theory. *Spectrochimica Acta Part A: Molecular and Biomolecular Spectroscopy*, 268, 120682.
11. กระทรวงสาธารณสุข. (2564). เรื่อง การใช้ส่วนของกัญชงในเครื่องสำอาง พ.ศ. ๒๕๖๔. Retrieved from <https://www.thansettakij.com/content/480391>

Cosmetic Applications of Silk Cocoon Extracts: Enzyme-Assisted Extraction and Development of Nanostructured Lipid Carriers

Sarocho Chareegun¹, Suvimol Somwongin¹, Jirasit Inthorn¹, Anurak Bunrod², Saranya Juntrapirom², Watchara Kanjanakawinkul², Wantida Chaiyana^{1,3,}*

¹ Department of Pharmaceutical Sciences, Faculty of Pharmacy, Chiang Mai University, Chiang Mai, 50200 Thailand

² Chulabhorn Royal Pharmaceutical Manufacturing Facilities by Chulabhorn Royal Academy, Chon Buri 20180, Thailand

³ Multidisciplinary and Interdisciplinary School, Chiang Mai University, Chiang Mai, 50200 Thailand

*Corresponding author email: wantida.chaiyana@cmu.ac.th

Abstract. Enzymatic extraction is a sustainable and eco-friendly method. This study aimed to extract silk cocoons using Alcalase® and evaluate their cosmeceutical potential and irritation potency. Nanostructured lipid carriers (NLCs) were developed as a promising approach for effective cosmetic formulations. Silk cocoons were extracted with 0.5% v/v Alcalase® at pH 8.0 and 50 °C for 2 h. The extracts were assessed for antioxidant and anti-wrinkle properties, along with irritation potential using the hen's egg test on the chorioallantoic membrane. For NLC development, glyceryl monostearate and rice bran oil were used, and the hydrophilic-lipophilic balance (HLB) was optimized using a mixture of Tween® 80 and Span® 80 (Smix). The NLCs were developed using a probe sonicator set at 80 W for 5 min and characterized for physical appearance, particle size, polydispersity index (PDI), and zeta potential. The results showed that the silk cocoon extract demonstrated a potent collagenase inhibition of $69.05 \pm 2.0\%$, comparable to the positive control. The optimal silk cocoon extract loaded NLCs, composed of 3.5% glyceryl monostearate, 1.5% rice bran oil, 1.5% Smix, and 0.1% silk cocoon extract, had the smallest particle size (485 ± 2.35 nm), the narrowest PDI (0.69 ± 0.01), and a pronounced zeta potential (-40.6 ± 1.90 mV). Both the silk cocoon extract and its NLC formulation induced no irritation. In conclusion, this study highlighted the potential of silk cocoon extract incorporated into NLCs for effective and safe cosmetic applications.

Keywords: Silk cocoon; Nanostructured lipid carriers; Cosmeceutical; Nano delivery system; Enzyme-assisted extraction

INTRODUCTION

Silk cocoons, produced by the silkworm *Bombyx mori*, are natural protein fibers primarily composed of two key proteins, including fibroin and sericin. While fibroin forms the structural core of the silk fiber, sericin acts as a gummy coating that binds the fibers together [1]. In the silk industry, sericin is commonly removed during the degumming process and often discarded as waste material. However, growing scientific interest has revealed that sericin is far from a useless byproduct. Numerous studies have demonstrated its beneficial physicochemical and biological properties, including antioxidant, anti-inflammatory, anti-aging, antibacterial, and moisturizing activities [2,3]. These multifunctional bioactivities make sericin a promising candidate for application in cosmeceuticals and dermatological formulations.

Despite its potential, effective delivery of sericin to the skin remains a challenge due to its hydrophilic nature and relatively large molecular size, which can limit skin penetration. In recent years, nanocarrier systems have emerged as innovative strategies to overcome such limitations and improve the bioavailability of active compounds. Among these, nanostructured lipid carriers (NLCs) have gained significant attention in topical delivery systems [4]. NLCs are an advanced generation of lipid-based nanoparticles designed to enhance drug loading capacity, stability, and skin permeability, which are developed as an improvement over solid lipid nanoparticles (SLNs) by incorporating a blend of solid and liquid lipids [5]. This unique composition reduces the crystallinity of the lipid matrix, allowing for better entrapment of both hydrophilic and lipophilic compounds and promoting controlled release properties [4,5].

Therefore, the aim of this study was to develop and characterize NLC formulations incorporating silk cocoon extracts and to evaluate their irritation potential. The findings from this research may contribute to the advancement of sustainable, effective, and skin-friendly cosmeceutical products derived from natural sources.

MATERIALS AND METHODS

Materials

Silk Cocoons Materials

Yellow silk cocoons (Lueang Saraburi variety) were kindly provided by the Queen Sirikit Sericulture Center, Chiang Mai, Thailand. Prior to extraction, the cocoons were cut into smaller pieces to facilitate further processing.

Chemical Materials

Alcalase[®] proteolytic enzyme from *Bacillus licheniformis* was purchased from Merk KGaA (Darmstadt, Germany). Collagenase enzyme from *Clostridium histolyticum*, sericin from *Bombyx mori*, ascorbic acid, epigallocatechin gallate (EGCG), 2,2-Diphenyl-1-picrylhydrazyl (DPPH), and N-[3-(2-furyl)acryloyl]-Leu-Gly-Pro-Ala (FALGPA) were from Sigma-Aldrich (St. Louis, MO, USA). Sodium chloride (NaCl), calcium chloride (CaCl₂), and sodium lauryl sulfate (SLS) were from Thermo Fisher Scientific (Waltham, MA, USA). Glyceryl monostearate (GMS), rice bran oil, polysorbate 80 (Tween[®] 80), and sorbitan monooleate (Span[®] 80) were purchased from Namsiang (Bangkok, Thailand). Methanol was analytical-grade and purchased from RCI Labscan Co., Ltd. (Bangkok, Thailand).

Methods

Enzyme-Assisted Extraction of Silk Cocoons

Silk cocoons were extracted using an enzyme-assisted extraction method adapted from Vaithanomsat and Punyasawon (2008) [6]. In brief, small pieces of silk cocoon were immersed in DI water and subjected to microwave treatment (UltimateTaste300, Electrolux Co., Ltd., Guangdong, China) at 1000 W for 2 min. After removing the water, the pre-treated cocoons were extracted using a 1:25 (w/v) ratio of 0.5% v/v Alcalase[®] enzyme solution (pH 8.0) at 50 °C for 2 h. The extract was then cooled to room temperature and filtered through cheesecloth. The resulting liquid fraction was subsequently freeze-dried using a LyoQuest Arctic freeze dryer (Telstar, Barcelona, Spain).

Antioxidant Activities Determination

The antioxidant activity of the silk cocoon extract was evaluated using the 2,2-diphenyl-1-picrylhydrazyl (DPPH) assay, following the method described by Chaiyana et al. (2017) [7]. Briefly, 20 µL of a 1 mg/mL sample solution in DI water was mixed with 180 µL of 167 µM DPPH solution in methanol. The mixture was incubated at room temperature in the dark for 30 min. The absorbance was then measured at 520 nm using a microplate reader (SPECTROstar Nano, BMG Labtech, Ortenberg, Germany). The DPPH[•] radical scavenging activity was calculated using the following equation:

$$\text{DPPH inhibition (\%)} = [(A - B)/A] \times 100 \quad (1)$$

where A and B represent the absorbance of the systems without and with the sample solution, respectively. The antioxidant activity of the silk cocoon extract was compared with ascorbic acid, used as a positive control, and sericin, the major bioactive component of the silk cocoon extract. The experiment was performed in three independent replications.

Anti-Skin Ageing Activities Determination

The collagenase inhibitory activity of sericin and silk extracts was investigated using a modified substrate enzyme according to the method of Thring et al. (2009) [8]. Briefly, 10 µL of the sample solution was mixed with 20 µL of 5 units/mL collagenase in 50 mM tricine buffer (pH 7.5), containing 400 mM NaCl and 10 mM CaCl₂, and incubated for 15 min. Subsequently, 120 µL of 0.67 mM FALGPA in tricine buffer was added and the absorbance was measured at 340 nm in kinetic mode for 20 min using a microplate reader (SPECTROstar Nano, BMG Labtech, Ortenberg, Germany). Collagenase inhibitory activity was calculated using the following equation:

$$\text{Collagenase inhibition (\%)} = [(A - B)/A] \times 100 \quad (2)$$

where A and B represent the reaction rate of the systems without and with the sample solution, respectively. The anti-collagenase activity of the silk cocoon extract was compared with EGCG, used as a positive control, and sericin, the major bioactive component of the silk cocoon extract. The experiment was performed in three independent replications.

Development of Silk Cocoon Extract-Loaded NLCs

Silk cocoon extract-loaded NLCs were prepared using a melt-emulsion process, following a previously described procedure of Yeerong et al. (2025) with some modifications [9]. Briefly, an aqueous phase containing 0.5% w/w Tween[®] 80 was prepared and heated to 85 °C. To this heated aqueous phase, 0.1% w/w silk cocoon extract was added. The resulting water phase was then mixed with the melted lipid phase, which consisted of 3.5% w/w GMS, 1.5% w/w rice bran oil, and 1% w/w Span[®] 80, while maintaining a temperature of 80 °C. The mixture was immediately sonicated using a probe sonicator (Vibra Cell VCX 600, Sonic & Materials, Newton, CT, USA) at 80 W for 5 min, with a 9.9 s pulse-on mode and a 2 s pulse-off mode.

Characterization of Silk Cocoon Extract-Loaded NLCs

Silk cocoon extract-loaded NLCs were characterized in terms of particle size, polydispersity index (PDI), and zeta potential using a Malvern ZS Nano ZetaSizer (Malvern Instruments Ltd., Malvern, UK). The samples were diluted with DI water at a ratio of 1:1000 prior to characterization to ensure a uniform dispersion of individual particles in the measurement medium. DI water was

chosen as the dilution medium to prevent any potential interference from ions on the zeta potential measurements. All experiments were performed in triplicate.

Irritation Test by Hen's Egg Chorioallantoic Membrane (HET-CAM) Test

Silk cocoon extracts and silk cocoon extract-loaded NLCs were evaluated for their irritation potential using the HET-CAM test [10]. Briefly, an eggshell was opened and 0.9% w/v NaCl solution was dropped onto its tissue. The outer membrane was then carefully removed using forceps, avoiding contact with the blood vessels. Following this, 30 μ L of the tested solution was applied onto the CAM. The irritation response was observed immediately for 5 min under a stereomicroscope (NS80, Ningbo Yongxin Optics, Ningbo, China) to assess early signs of irritation, including hemorrhage, vascular lysis, and coagulation. The onset time for each irritation signal was recorded in seconds and used to calculate the irritation score (IS) using the following equation:

$$IS = [(301 - t(h))/300 \times 5] + [(301 - t(l))/300 \times 7] + [(301 - t(c))/300 \times 9] \quad (3)$$

where $t(h)$ represents the time in seconds at which hemorrhage was first detected, $t(l)$ represents the time at which vascular lysis was first observed, and $t(c)$ represents the time at which coagulation of blood vessels was first detected. IS was classified as follows: 0.0–0.9 as mild irritation, 1.0–4.9 as moderate irritation, 5.0–8.9, and 9.0–21.0 as severe irritation. Additionally, 1% w/v SLS and 0.9% w/v NaCl solution were used as the positive and negative controls, respectively. The experiment was performed in duplicates.

Statistical analyses

Data are presented as mean \pm standard deviation (S.D.) and sample differences were analyzed using a t-test and one-way ANOVA followed by Tukey's post hoc test. Statistical analysis was performed using IBM SPSS Statistics version 23.0 (SPSS Inc., Chicago, IL, USA), with statistical significance set at $p < 0.05$.

RESULTS AND DISCUSSION

Results

Silk Cocoon Extract and Its Biological Activities

The physical appearance of yellow silk cocoons (Lueang Saraburi variety) and its enzyme-assisted extract are shown in **Figure 1**. The extract had a golden-brown, amber-like coloration and a distinctly crystalline texture. It appeared as a loose aggregation of irregular powder with hygroscopic properties. The extraction yielded $22.8 \pm 1.6\%$ w/w, which corresponded to 22.8 g of extract obtained from every 100 g of silk cocoon, demonstrating the efficiency of the enzyme-assisted method.

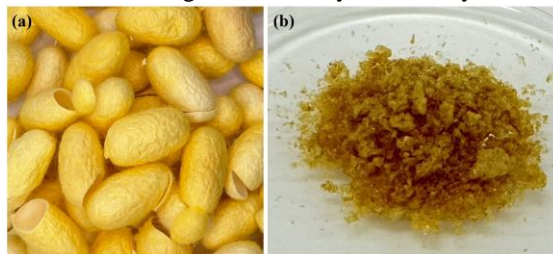


Figure 1. Physical appearance of yellow silk cocoons (Lueang Saraburi variety) (a) and its enzyme-assisted extract (b).

The antioxidant activity and collagenase inhibitory effects of ascorbic acid, EGCG, sericin, and silk cocoon extract are presented in **Figure 2**. Ascorbic acid exhibited the highest DPPH radical scavenging activity ($p < 0.05$), with an inhibition of $95.07 \pm 0.34\%$. The silk cocoon extract showed moderate activity ($78.82 \pm 0.55\%$), significantly higher than that of sericin ($17.93 \pm 1.27\%$) ($p < 0.05$). On the other hand, EGCG showed the strongest inhibitory effect of $96.67 \pm 0.67\%$ ($p < 0.05$), followed by the silk cocoon extract ($69.05 \pm 0.02\%$) and sericin ($47.38 \pm 2.36\%$), respectively.

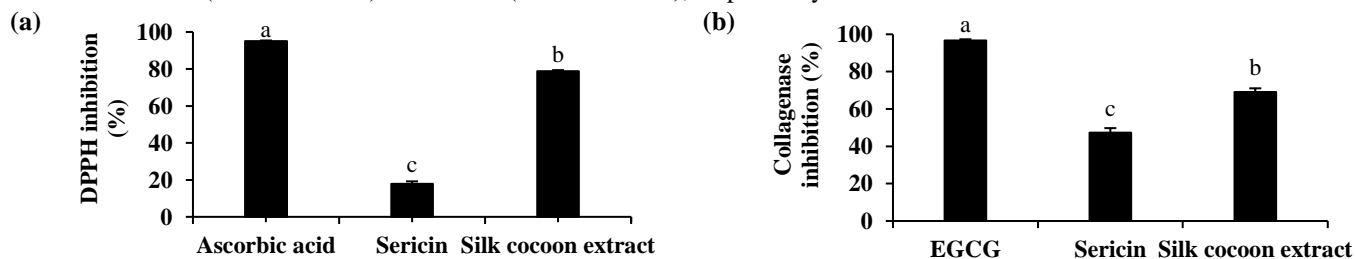


Figure 2. DPPH inhibition (a) and collagenase inhibition (b) of ascorbic acid, EGCG, sericin, and silk cocoon extract. The letters a, b, and c denote significant differences in the biological activities among the samples ($p < 0.05$).

Silk Cocoon Extract-Loaded NLCs

The physical characteristics of the silk cocoon extract-loaded NLC are shown in **Figure 3**. The visual appearance of the formulations as presented in **Figure 3a**, shows a milky white dispersion. As shown in **Figure 3b**, the particle size of SC-NLC was significantly larger than that of NLC ($p < 0.05$), with average sizes of 485.0 ± 2.35 nm and 456.0 ± 2.75 nm, respectively. The PDI values of both formulations, presented in **Figure 3c**, were in a comparable range, with no statistically significant difference observed. Both NLC and silk cocoon extract-loaded NLC exhibited PDI values indicative of moderate size distribution of 0.606 ± 0.067 and 0.694 ± 0.006 , respectively. **Figure 3d** shows the zeta potential values of the formulations, which were approximately -36.8 ± 1.9 and -40.6 ± 1.9 mV, respectively.

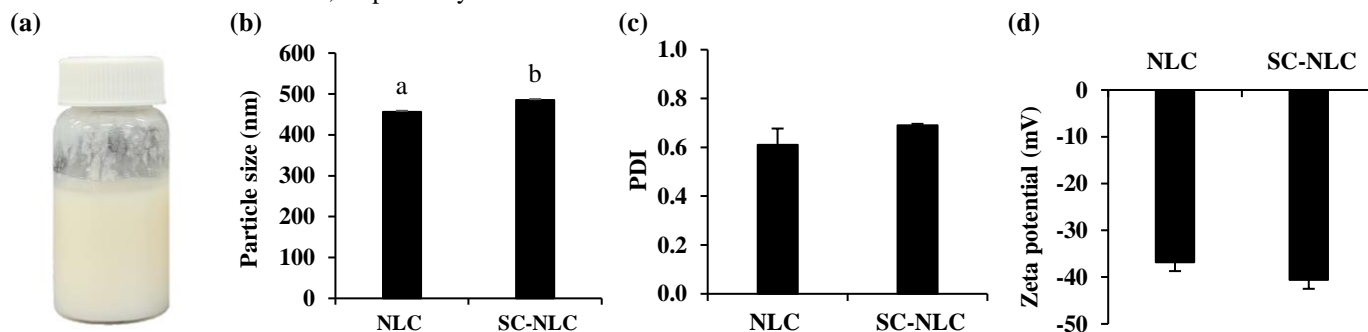


Figure 3. Physical appearance of silk cocoon extract loaded NLCs (SC-NLC) (a) and its particle size (b), polydispersity index (PDI) (c), and zeta potential (d) in a comparison with blank NLCs (NLC). The letter a and b denote significant differences among the particle size of NLCs ($p < 0.05$).

Irritation Properties of Silk Cocoon Extract-Loaded NLCs

The irritation potential of silk cocoon extract, NLC blank, and silk cocoon extract-loaded NLC on the CAM are shown in **Figure 4**. The positive control (1% w/v SLS solution) induced pronounced irritation effects, including hemorrhage, vascular lysis, and coagulation, which were evident as early as 5 min post-application with the irritation score of 14.4 ± 0.5 . In contrast, the negative control (0.9% w/v NaCl solution) caused no observable damage to the CAM throughout the exposure period. In addition, the silk cocoon extract, NLC blank, and silk cocoon extract-loaded NLC did not irritate with the irritation score of 0.0 ± 0.0 .

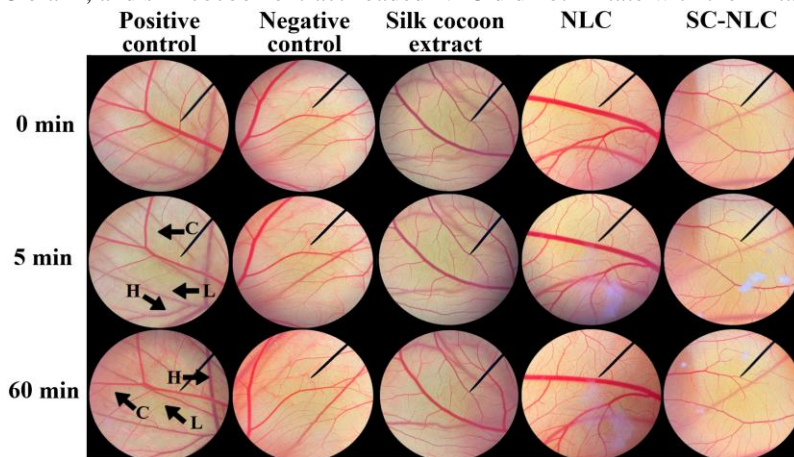


Figure 4. Effects of the positive control (1% w/v SLS solution), negative control (0.9% w/v NaCl solution), silk cocoon extract, NLC blank (NLC), and silk cocoon extract-loaded NLCs (SC-NLC) on the chorioallantoic membrane (CAM) at contact times of 0, 5, and 60 min. Following application, visible damage to the CAM is indicated by black arrows. Hemorrhage (H), vascular lysis (L), and coagulation (C) represent specific irritation responses observed.

Discussions

The current study highlighted the promising biological activities of silk cocoon extract, particularly for cosmetic and dermatological applications. The extract showed moderate antioxidant activity with DPPH[•] inhibition of $78.82 \pm 0.55\%$ and significant collagenase inhibition of $69.05 \pm 2.02\%$. The extract is suggested for anti-aging due to its antioxidant activity, which helps protect the skin from oxidative damage, a key factor in aging. Additionally, its significant collagenase inhibition can help preserve collagen integrity, reducing wrinkles and promoting skin elasticity, both of which are crucial for anti-aging benefits.

Although sericin is a major component of silk, it is not responsible for the antioxidant and collagenase inhibitory activities observed in the extract. These effects are likely due to other bioactive compounds, such as amino acids, peptides, or polyphenols, present in the silk cocoon [11]. When the silk cocoon extract was incorporated into NLCs, the particle sizes slightly enlarged, indicating that it was encapsulated inside the particles. However, the silk cocoon extract had no effect on the PDI and zeta potential. Its moderate PDI and pronounced negative zeta potential (less than -40) signified its stability due to the uniform particle size distribution and strong electrostatic repulsion between the particles, preventing aggregation and ensuring consistent dispersion over time. Additionally, both the silk cocoon extract and its NLC formulations induced no irritation signs in the HET-CAM test, suggesting their safety for sensitive skin applications. Although the NLC preparation involved heating to 85°C, previous studies suggested that sericin remained stable up to 200 °C [12,13], indicating that the process likely preserved the bioactivity. However, as various bioactive components other than sericin could be included, further evaluation of the biological activities of the NLC was suggested.

CONCLUSIONS

The silk cocoon extract demonstrated promising biological activities, including antioxidant and collagenase inhibitory effects, making it a potential candidate for anti-aging and skincare applications. Encapsulation into NLCs was successful without affecting its PDI or zeta potential. The extract and its NLC formulations showed no irritation in the HET-CAM test, confirming their safety for sensitive skin. These findings suggest that silk cocoon extract-loaded NLCs could be a valuable ingredient in cosmetic formulations, with further research needed to explore their clinical potential.

ACKNOWLEDGMENTS

Sarocho Chareegun expresses sincere gratitude for the Teaching Assistant and Research Assistant (TA/RA) scholarship provided by Chiang Mai University. The authors wish to acknowledge the Queen Sirikit Sericulture Center (Chiang Mai) for their generous support in providing the silk cocoon material.

REFERENCES

1. Chuang CC, Prasannan A, Hong PD, Chiang MY. Silk-sericin degummed wastewater solution-derived and nitrogen enriched porous carbon nanosheets for robust biological imaging of stem cells. *Int. J. Biol. Macromol.* 2018;107:2122–2130.
2. Sangwong G, Sumida M, Sutthikhum V. Antioxidant activity of chemically and enzymatically modified sericin extracted from cocoons of *Bombyx mori*. *Biocatal. Agric. Biotechnol.* 2016;5:155–161.
3. Saha J, Mondal MIH, Sheikh MRK, Habib MA. Extraction, structural and functional properties of silk sericin biopolymer from *Bombyx mori* silk cocoon waste. *J. Textile. Sci. Eng.* 2019;9(1):390.
4. Viegas C, Patricio AB, Prata JM, Nadhman A, Chintamaneni PK, Fonte P. Solid lipid nanoparticles vs. nanostructured lipid carriers: A comparative review. *Pharmaceutics* 2023;15(6):1593.
5. Chauhan I, Yasir M, Verma M, Singh AP. Nanostructured lipid carriers: a groundbreaking approach for transdermal drug delivery. *Adv. Pharm. Bull.* 2020;10:150-165.
6. Vaithanomsat P, Punyasawon C. Process optimization for the production of Philosamiricini (Eri Silk) pupae hydrolysate. *Kasetsart J. (Nat. Sci.)* 2008;42:341–352.
7. Chaiyana W, Punyoyai C, Somwongin S, Leelapornpisid P, Ingkaninan K, Waranuch N, Srivilai J, Thitipramote N, Wisuitiprot W, Schuster R, et al. Inhibition of 5α-reductase, IL-6 secretion, and oxidation process of *Equisetum debile* Roxb. ex vaucher extract as functional food and nutraceuticals ingredients. *Nutrients* 2017;9(10):1105.
8. Thring TS, Hili P, Naughton DP. Anti-collagenase, anti-elastase and anti-oxidant activities of extracts from 21 plants. *BMC Complement. Altern. Med.* 2009;9(1):27.
9. Yeerong K, Czyrski GS, Heinz A, Müllertz A, Rades T, Chaiyana W. Transdermal delivery of *Acheta domesticus* protein hydrolysate using nanostructured lipid carriers and Derma Stamp – Does the combination of lipid-based formulation and a physical technique add value for permeation and retention? *Journal of Drug Delivery Science and Technology* 2025;104:106470.
10. Somwongin S, Chantawannakul P, Chaiyana W. Antioxidant activity and irritation property of venoms from *Apis* species. *Toxicon* 2018;145:32–39.
11. Bungthong C, Wrigley C, Sontee T, Sirimornpun S. Amino acid profile and biological properties of silk cocoon as affected by water and enzyme extraction. *Molecules* 2021;26:3455.
12. Lee HG, Jang MJ, Park BD, Um IC. Structural characteristics and properties of redissolved silk sericin. *Polymers* 2023;15:3405.
13. Saha J, Mondal MIH, Ahmed F, Rahman M. Extraction, characterization and functionality assessment of aloe vera, chitosan and silk sericin. *Arab. J. Chem.* 2023;16:105087.

Emerging Trends in Biotechnology and AI

Evaluation of Picosecond Nd:YAG Laser Parameters on Laser-Induced Optical Breakdown (LIOB) Formation and Tissue Response

Jitaraphol Potiwihok¹, Sasin Charoensuksira¹ and Pawit Phadungsaksawasdi^{1,*}

¹Department of Dermatology, Chulabhorn International College of Medicine, Thammasat University
Rangsit campus, Pathumthani, Thailand

*Corresponding author, E-mail: pawit.p@tu.ac.th

Abstract. Picosecond Nd:YAG lasers are increasingly used in dermatology, often combined with cosmeceuticals to enhance therapeutic efficacy. When paired with a microlens array (MLA) handpiece, these ultrashort-pulse lasers induce laser-induced optical breakdown (LIOB), leading to intradermal vacuolization. The effects of fluence, spot size, pulse duration, and focal depth on LIOB formation remain under investigation. This study evaluates the influence of these parameters on LIOB and the resulting tissue response *in vitro*. Experiments were conducted using acrylic blocks and tissue-mimicking phantoms (porcine gelatin with artificial pigmentation). Fluence, spot size, focal depth, and pulse duration were systematically varied. Beam profiles of a fractional MLA-assisted picosecond laser were analyzed using ImageJ software. Results showed that increasing spot size from 4 mm to 8 mm, while keeping fluence constant, increased penetration depth by 42%, with minimal changes in microbubble intensity. Conversely, increasing fluence with a fixed spot size led to only an 11.42% penetration depth increase but significantly enhanced microbubble intensity up to 43%, particularly in superficial layers. Findings from tissue-mimicking phantoms correlated with acrylic block results, reinforcing observed trends. These results suggest that larger spot sizes enhance laser penetration, while higher fluence increases LIOB intensity, particularly at superficial depths. This study provides valuable insights into optimizing picosecond Nd:YAG laser parameters, which may improve therapeutic efficacy and safety in fractional laser treatments.

Keywords: picosecond laser, Nd:YAG Laser, Laser-Induced Optical Breakdown (LIOB), laser-tissue interaction

INTRODUCTION

Laser technology has significantly advanced dermatologic treatments through selective, minimally invasive approaches. The development began with the ruby laser in 1960, evolving with powerful continuous-wave lasers (e.g., CO₂, argon, Nd:YAG) and was markedly improved by the introduction of selective photothermolysis in 1983. Currently, lasers address various skin conditions such as vascular and pigmented lesions, tattoos, unwanted hair, and scars due to their ability to selectively target specific skin components with minimal collateral damage. Picosecond lasers, delivering pulses in trillionths of a second (300–900 ps), differ fundamentally from traditional nanosecond lasers by generating a predominantly photomechanical rather than thermal effect. This results in precise fragmentation of pigments with minimal surrounding tissue damage. LIOB represents a new therapeutic method by creating micro-injuries with ultra-short pulses that form plasma and microscopic bubbles without significant thermal damage. Despite their potential, key gaps exist regarding the influence of adjustable laser settings (fluence, spot size, focal depth, pulse width) on LIOB characteristics and outcomes. Research indicates that fluence, optics, and skin type critically affect LIOB, yet comprehensive studies systematically evaluating all parameters remain scarce. Addressing this gap, this research proposes investigating LIOB by systematically varying these laser parameters across progressively complex models from acrylic and gelatin phantoms. Results will enhance understanding of parameter-outcome relationships, optimizing safe, effective clinical application of picosecond lasers.

MATERIALS AND METHODS

Materials

Two commercial picosecond Nd:YAG lasers with different pulse widths (250 ps and 450 ps) and a wavelength of 1064 nm were used in this study. Two types of materials were tested: transparent acrylic blocks and gelatin skin phantoms with artificial ink. A standard mirrorless camera was used, and a controlled photographic environment was set up.

*Corresponding author: pawit.p@tu.ac.th

Presenting author: potiwihok@gmail.com

Methods

This study employed two commercial picosecond Nd:YAG lasers with different pulse widths (250 ps and 450 ps) operating at 1064 nm, with adjustable handpieces for spot size, focal depth, and fractional optics. All laser shots were delivered in single-pulse mode at 1 Hz, and the systems were calibrated to ensure accuracy. Two types of materials were used: acrylic blocks (to visualize depth and beam intensity), and gelatin skin-phantoms with artificial pigment. The gelatin was molded and cooled at 4°C for at least 12 hours before laser exposure. Four experimental conditions were designed to assess LIOB outcomes: (1) fixed fluence with varying spot sizes (4, 6, 8 mm), (2) fixed spot size (6 mm) with varying fluence (0.6, 1.2, 1.6 J/cm²), (3) fixed fluence and spot size with varying focal depths (-1, 0, +1 positions corresponding to 13, 16, and 19 mm), and (4) fixed all parameters with varying pulse widths (250 vs. 450 ps). Each condition was tested in acrylic in triplicate, with randomized trials to reduce bias. LIOB penetration depth was measured using longitudinal images analyzed in ImageJ, averaging three measurements per site and calculating standard deviation. Beam intensity was quantified from 16-bit grayscale images, with intensity measured across the full beam.

Statistical analyses

All statistical analyses were conducted using Stata software (version 17). One-way ANOVA tests were used to assess the effects of independent variables (spot size, fluence, focal depth, and pulse width) on penetration depth and optical beam intensity. Each condition was measured in triplicate (n=3). Comparisons were made across varying spot sizes, fluence levels, focal depths, and pulse widths. Statistical significance was set at $\alpha = 0.05$, with exact P-values reported. Independent t-tests were also used to compare pulse widths (250 ps vs. 450 ps) under identical conditions, providing robust evidence of observed differences.

RESULTS AND DISCUSSION

Results

1. The Spot Size Factor

Spot size has a statistically significant effect on penetration depth in acrylic at a fluence of 0.95 J/cm² ($p < 0.01$). Specifically, increasing the spot size from 4 mm to 8 mm led to a substantial increase in depth up to 42.1%. However, the same analysis showed no significant effect of spot size on laser intensity ($p = 0.36$), indicating that, under these experimental conditions, spot size influences penetration depth but does not significantly affect the overall intensity of the laser beam.

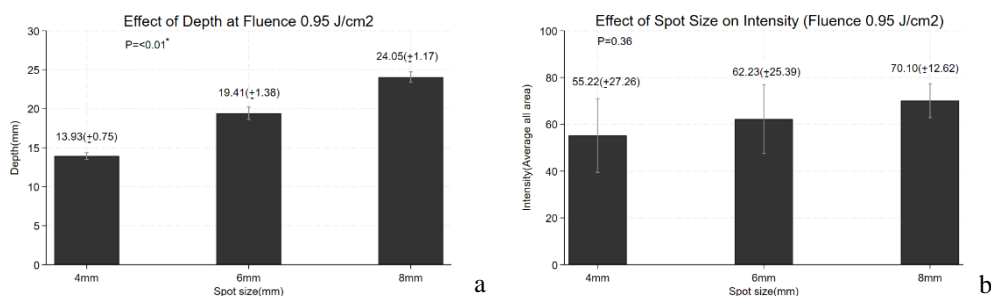


Figure 1. The bar chart illustrates the influence of spot sizes factor (4 mm, 6 mm, and 8 mm): (a) to depth of microbubble formation and (b) intensity of microbubble in acrylic model.

2. The Fluence Factor

When fluence levels (0.6, 1.2, and 1.6 J/cm²) were tested in acrylic using a fixed 6 mm spot size, the penetration depth did not show any significant difference ($p = 0.85$), indicating that fluence had no clear effect on laser depth. Increasing the fluence from 0.6 to 1.6 J/cm² resulted in only an 11.42% increase in penetration depth. However, fluence had a strong effect on laser intensity in acrylic; higher fluence levels led to significantly greater intensity ($p < 0.01$), with up to a 42.44% increase observed. In the gelatin skin-phantom, penetration depth showed a rising trend with increasing fluence. For laser intensity in gelatin, a slight upward trend was also observed at higher fluence levels.

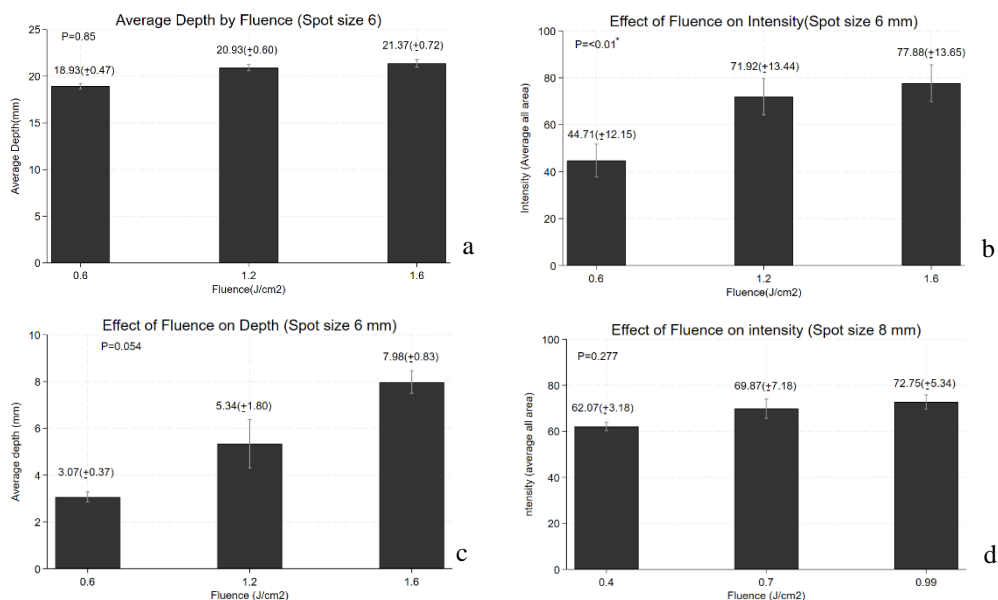


Figure 2. (a) Average penetration depth in acrylic at fluence levels of 0.6, 1.2, and 1.6 J/cm² using a 6 mm spot size. Depth differences are minor and not statistically significant ($p = 0.8466$). (b) Laser intensity in acrylic increases significantly with higher fluence, confirming enhanced energy delivery in LIOB treatments. (c) In gelatin, penetration depth shows a rising trend with fluence (0.6 to 1.6 J/cm²). Though not significant at the 95% level ($p = 0.054$), it suggests potential significance at 90%. (d) Laser intensity in gelatin across 0.4, 0.7, and 0.99 J/cm² shows a slight increase, but ANOVA indicates no significant difference.

3. The Focus Point of the Laser

When the fluence and spot size were kept constant, changing the focal depth in acrylic had a significant effect on penetration depth ($p < 0.01$). The shallowest focal point (FD -1 or 13 mm) resulted in the deepest penetration, while the deepest focal point (FD +1 or 19 mm) produced the shallowest depth. Changing the focal depth from +1 (19 mm) to -1 (13 mm) increased the penetration depth by up to 31.45%. Additionally, both of these values differed from the middle focal depth (FD 0 or 16 mm) by 18.23% and 16.17%, respectively. For laser intensity, there was a slight trend of increasing intensity with deeper focal depth, but the differences were not statistically significant ($p = 0.074$). This suggests that while focal depth clearly affects how deep the laser penetrates, its effect on intensity is less certain.

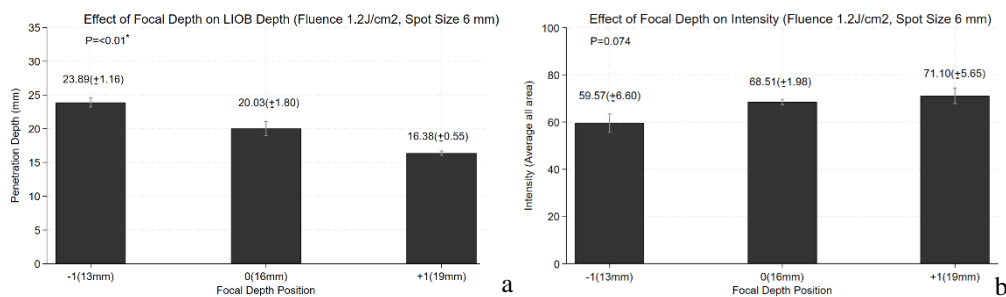


Figure 3. (a) The bar graph shows how focal depth affects penetration in acrylic. The shallowest focus (FD -1, 13 mm) produced the deepest penetration, while the deepest focus (FD +1, 19 mm) had the shallowest depth. This clearly shows that a shorter focal depth leads to greater laser penetration. (b) The second graph displays average laser intensity at each focal depth. Intensity increased as the focal depth became deeper, with FD +1 showing the highest intensity and FD -1 the lowest. However, the differences were not statistically significant, meaning the changes might be due to normal variation rather than a real effect.

4. The Pulse Widths Factor

When all laser settings were kept the same (spot size 6 mm, fluence 1.2 J/cm²), changing the pulse width had a significant effect on both penetration depth and intensity. The shorter pulse width (250 ps) resulted in a much deeper penetration (about 2.08 mm) than the longer pulse width (450 ps, about 1.48 mm), which is 28.90% deeper penetration, with strong statistical significance ($p = 0.0006$). Similarly, the intensity was also significantly higher with the 250 ps pulse (mean = 63.51) compared to 450 ps (mean = 48.61) which is 14.9% higher intensity, indicating that shorter pulse durations deliver more energy and create stronger LIOB effects.

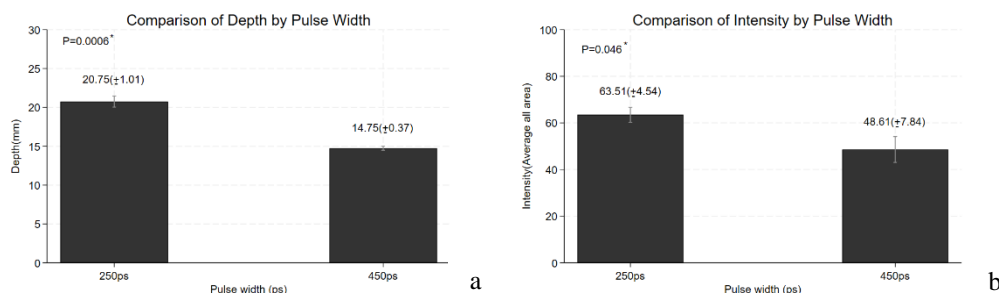


Figure 4. (a) The bar chart shows that the 250 ps pulse width creates deeper penetration in acrylic than the 450 ps pulse width. The difference is statistically significant, meaning the shorter pulse allows the laser to reach deeper under the same conditions. (b) The second graph shows that laser intensity is also higher with the 250 ps pulse compared to the 450 ps pulse. This difference is statistically significant, suggesting that shorter pulse durations produce stronger laser effects, even when other settings like spot size and fluence are the same.

Discussion

This study provides insights into optimizing the parameters of picosecond Nd:YAG lasers, particularly when used in conjunction with MLA optics to achieve LIOB. The findings enhance understanding of how fluence, spot size, focal depth, and pulse duration influence both penetration depth and intensity, which are critical aspects in dermatological laser applications. The study demonstrated that increasing the laser spot size significantly enhances penetration depth without substantially altering the intensity of LIOB. Specifically, spot sizes ranging from 4 mm to 8 mm at constant fluence (0.95 J/cm²) showed a clear correlation with increased penetration depth, corroborating previous findings in laser-tissue interaction studies. This observation aligns with the theoretical premise that larger spot sizes reduce scattering and enhance deeper penetration into tissues. However, the laser intensity remained relatively unchanged across these spot sizes, suggesting spot size alone does not significantly affect the intensity of microbubble formation under consistent fluence. Conversely, varying fluence levels at a constant spot size (6 mm) revealed a different dynamic. Higher fluence levels significantly increased laser intensity, particularly evident in acrylic blocks, though this did not translate into statistically significant differences in penetration depth. These findings suggest that higher fluence primarily contributes to more intense superficial LIOB formation, rather than deeper penetration. In gelatin tissue-mimicking phantoms, a trend toward increased depth with higher fluence was observed, although this was not statistically significant. The near-significance of this result indicates potential practical importance warranting further investigation, possibly involving larger sample sizes or repeated measures to confirm the subtle impact of fluence on penetration depth. Focal depth adjustments showed notable effects on the laser-induced penetration depth, with deeper penetration achieved at shorter focal distances (-1 position, 13 mm). This finding highlights the importance of focal precision when using fractional laser devices clinically, emphasizing that optimal therapeutic results may rely heavily on accurate depth targeting. Though there was an observable trend indicating increasing intensity with increasing focal depth, the lack of statistical significance suggests other contributing variables could be at play, warranting further exploration. Pulse width comparison between 250 ps and 450 ps provided substantial evidence supporting the importance of pulse duration in controlling both depth and intensity. The shorter pulse width (250 ps) consistently yielded greater depth and significantly higher LIOB intensity, underscoring the photomechanical advantage of shorter pulse durations, resulting in more effective pigment fragmentation and microbubble generation. These results are consistent with earlier studies indicating that shorter pulse durations are more efficient in generating photomechanical effects, essential in clinical applications targeting dermal pigment or structural modification. Collectively, these findings reinforce the complexity of optimizing picosecond laser parameters. Effective clinical use of picosecond lasers in dermatology should consider balancing increased penetration depth with intensity of

tissue damage. Future research is needed to explore the different laser wavelengths and biological responses to these parameters *in vivo*.

CONCLUSIONS

This study evaluated how key laser parameters—fluence, spot size, focal depth, and pulse width—affect LIOB outcomes, specifically penetration depth and beam intensity, using acrylic and gelatin phantoms. Larger spot sizes significantly increased penetration depth without notably affecting intensity, emphasizing the role of optical focus. Higher fluence enhanced beam intensity, especially in superficial layers, but had limited impact on depth. Shallower focal depths produced deeper effects, and shorter pulses (250 ps) led to greater depth and intensity, highlighting the efficiency of ultra-short pulses. These findings illustrate the interplay of laser settings and their clinical relevance in optimizing picosecond Nd:YAG treatments. Further *in vivo* studies are needed to confirm these implications for dermatologic practice.

ACKNOWLEDGMENTS

The authors would like to acknowledge the Department of Dermatology, Chulabhorn International College of Medicine, Thammasat University, for providing laboratory facilities and technical support throughout the study. We are also grateful for the valuable advice and academic input from our research colleagues. Special thanks go to the medical technologists and research assistants for their help in sample preparation, laser calibration, and image analysis.

LIMITATION OF STUDY

Acrylic and gelatin phantoms, while not fully representative of living tissue, enabled controlled assessment of laser effects and serve as a basis for future *in vivo* studies.

REFERENCES

1. Wu DC, Goldman MP, Wat H, Chan HH. A systematic review of picosecond laser in dermatology: Evidence and recommendations. *Lasers Surg Med.* 2021;53(1):9–49.
2. Zhou Y, Hamblin MR, Wen X. An update on fractional picosecond laser treatment: Histology and clinical applications. *Lasers Med Sci.* 2023;38(1):45.
3. Ahn KJ, Zheng Z, Kwon TR, Kim BJ, Lee HS, Cho SB. Pattern analysis of laser-tattoo interactions for picosecond- and nanosecond-domain 1064-nm Nd:YAG lasers in tissue-mimicking phantom. *Sci Rep.* 2017;7:12556.
4. Balu M, Lentsch G, Korta DZ, König K, Kelly KM, Tromberg BJ, et al. *In vivo* multiphoton microscopy of picosecond-laser-induced optical breakdown in human skin. *Lasers Surg Med.* 2017;49(8):757–65.
5. Kim H, Hwang JK, Jung M, Hwang W, Kang HW. Laser-induced optical breakdown effects of micro-lens arrays and diffractive optical elements on ex vivo porcine skin after 1064 nm picosecond laser irradiation. *Biomed Opt Express.* 2020;11(12):7286–300.
6. Liao YH, Lu PH, Chou HY, Tsai MR, Chiu CW, Yu JS, et al. Characterization of picosecond laser-induced optical breakdown using harmonic generation microscopy. *Lasers Surg Med.* 2023;55(6):561–7.
7. Rhee YH, Park BC, Jung JY, Yoo SH, Mo JH, Chung PS. Effect of fractional picosecond laser therapy using a diffractive optical lens on histological tissue reaction. *J Cosmet Laser Ther.* 2024;26(1-4):54–60.
8. Yeh YT, Peng JH, Peng P. Histology of ex vivo skin after treatment with fractionated picosecond Nd:YAG laser in high and low-energy settings. *J Cosmet Laser Ther.* 2020;22(7):324–30.
9. Tanghetti EA, Jennings J. A comparative study with a 755 nm picosecond Alexandrite laser with a diffractive lens array and a 532 nm/1064 nm Nd:YAG with a holographic optic. *Lasers Surg Med.* 2018;50(1):37–44.
10. Brauer JA, Kazlouskaya V, Alabdulrazzaq H, Bae YS, Bernstein LJ, Anolik R, et al. Use of a picosecond pulse duration laser with specialized optic for treatment of facial acne scarring. *JAMA Dermatol.* 2015;151(3):278–84.
11. Kim H, Hwang JK, Choi J, Kang HW. Dependence of laser-induced optical breakdown on skin type during 1064 nm picosecond laser treatment. *J Biophotonics.* 2021;14(9):e202100129.
12. Lee HC, Childs J, Chung HJ, Park J, Hong J, Cho SB. Pattern analysis of 532- and 1064-nm picosecond-domain laser-induced immediate tissue reactions in ex vivo pigmented micropig skin. *Sci Rep.* 2019;9(1):4186.

